

3D PRINTED HYDROGEL MICRO-ENVIRONMENTS AND BIOREACTOR  
CONDITIONING TO DEVELOP NATIVE HETEROGENEITY IN TISSUE ENGINEERED  
HEART VALVES

A Dissertation

Presented to the Faculty of the Graduate School  
of Cornell University

In Partial Fulfillment of the Requirements for the Degree of  
Doctor of Philosophy

by

Laura Ann Hockaday

August 2014



# 3D PRINTED HYDROGEL MICRO-ENVIRONMENTS AND BIOREACTOR CONDITIONING TO DEVELOP NATIVE HETEROGENEITY IN TISSUE ENGINEERED HEART VALVES

Laura Ann Hockaday, Ph. D.

Cornell University 2014

Heart valve disease is a tremendous national and global burden. Prosthetic replacement is essentially the only treatment for a critically damaged or malformed valve, and current aortic valve replacement options for pediatric patients are grimly inadequate. Tissue engineering has the potential to generate living heart valve replacements capable of growth and integration needed to treat children with valve disease. Over the last 15 years, researchers have developed and implemented novel synthetic polymers as scaffolds for engineered heart valves. Although much progress has been made, a persistent problem is the difficulty incorporating native-like heterogeneity and controlled remodeling into TEHV.

The work presented here demonstrates a 3D bioprinting approach that generates complex 3D geometry tissue constructs using extrudable materials and encapsulated cells based on native aortic valve tissue heterogeneity. As a fabrication strategy 3D printing overcomes the limitations associated with classical heart valve tissue engineering assembly of scaffolds. To enable direct cell-hydrogel printing and thereby maximize geometric control within valve constructs, viability experiments were used to establish photoencapsulation fabrication parameters tolerated by cells. Photocrosslinking experiments demonstrate that contrary to numerous 2D cytotoxicity studies, in a 3D hydrogel culture environment and fabrication setting, Irgacure 2959 photoinitiator can produce more viable encapsulated cells than VA086 photoinitiator in a

higher stiffness hydrogel. A dynamic conditioning system designed specifically for the culture of 3D bioprinted valves was 1<sup>st</sup> validated using porcine aortic heart valves. Photoencapsulation viability experiments and bioreactor validation studies presented in this work provide a range of fabrication and conditioning parameters, that were utilized for the fabrication and dynamic culture of 3D bioprinted hydrogel heart valves. Our studies indicate that the bioprinted valves can be produced with high viability encapsulated mesenchymal stem cells for the purposes of a TEHV or with primary aortic valve cells for the purpose of *in vitro* testing and mechanistic study.

## BIOGRAPHICAL SKETCH

Laura Ann Hockaday was born in Los Alamos, New Mexico in 1986 to Mary and Robert Hockaday. She grew up with her younger sister Katie and her younger brother Robert in a white house with blue trim. She graduated from Los Alamos High school in 2004, and then left New Mexico to attend college at University of California Riverside. She worked in her father's company, Energy Related Devices Inc. during high school and in college. She graduated from UCR in 2008 with the first undergraduate class of bioengineers. She then attended graduate school at Cornell University in the Biomedical Engineering Department in Ithaca, New York. During that time she was awarded a GAANN fellowship, a Morgan fellowship, and graduate research NSF fellowship. She became a research assistant in Jonathan Butcher's Cardiovascular Developmental Bioengineering Laboratory in 2008, and joined the heart valve bioprinting project. She has two cats and one monstrously large goldfish. She finds that sugar free pudding mixed with strawberries tastes suspiciously like chewing gum and that kimchi jiggaie is the most wonderful food on the planet.

DEDICATION

To My Family

## ACKNOWLEDGEMENTS

I have been incredibly blessed with my family, my friends, and my colleagues. I would like to thank all these people who have been blessings in my life and during the 6 years at Cornell. You have helped me in a myriad of ways both large and small. I could not have done it without you.

I would especially like to thank my family. Their love, support, and laughter are my power supply and driver. Mom, Dad, Katie, Bobby – nobody laughs like they do. I am not convinced you can describe people like mechanics mixture theory, that all their wonderful qualities explain the whole. By whatever mechanism by which they've become who they are with the countless wonderful qualities that define them, I would like to thank my family for just being themselves.

My parents and grandparents told me great stories as a kid and as an adult. They told me stories about hard decisions, honesty, believing in yourself, and perseverance. (They also told me stories about gophers, superfood, and magical rhinoceroses). I love their stories. As anyone in lab who has worked with me knows, I tend to learn and synthesize information in terms of stories and then I want to share those stories. "I have a story about that....." is probably heard so often that it induces a bit of eye rolling. I did not survive graduate work alone, and many a shared experience between a friend or a family member and often times a story helped me succeed in my work and research.

I would like to thank my brother Bobby for keeping me grounded. That might sound funny, but whenever I come home infused with a serious dose of 'I'm so cosmopolitan-Cornellian - science-arrogance-whatever' Bobby humbles and amazes me. He and my sister are the bravest people I know. When I get to be with my family I realize that not

only can brilliance take different forms and paths, but that just being smart isn't what matters the most. Caring about people and problem solving - that's what matters. Also, Bobby gives really good hugs, and he always has a hug for me.

I would like to thank my sister Katie. Katie listens. When I'm scared or sad or happy or boring, I can tell her anything. Katie through her interest in health and nutrition helped me identify the cause of my migraines and devise a preventative lifestyle. This has serious ramifications for my work. Although I've gotten migraines since I was six, when the pressure started to build in my graduate work approximately 3 years ago, the frequency that I was getting migraines with neurological symptoms increased to one every 12 days. Controlling my blood sugar prevents the migraines. Katie's outlook on health has influenced own perception of the medical field and clinical strategies. I believe this concept of viewing illness as a spectrum of disease, and not merely viewing illness as binary (sick or not sick, diabetic/not diabetic) will influence me throughout my career.

I want to thank my mother and father who have taught me by their example and through their story telling about hard work, integrity, warmth, loving, and having a sense of fun. I want to thank my dad for teaching me about bottle rockets, snorkeling, superfood, kite flying, and persistence. I would like to thank my dad for being willing to enthusiastically talk gadgets and willing to talk work when I was troubleshooting and stuck. I want to thank my mom for being fierce in her love, in defense of her family, and being a fighter against daunting odds. My mom is a mountain mover - if Katie, Bobby, Dad, or I are in trouble she will move mountains to protect and keep us safe and well. Dad has taught me about working with mechanical systems and generating ideas. Mom has taught me about interacting with the rest of the world. I want to thank my mom for her invaluable

help editing this thesis, and for helping me in the many moments in my life where I didn't know what to do to move beyond blind panic and pursue a directed course of action.

I would like to thank Heeyong Kang. Heeyong has been a joy to work with and to be with in real life. His determination and optimism are incredible. Without his dedication and determination the 3D printing project would never have gotten past the "imagine this 3D printed frosting pyramid as a heart valve" stage. In real life he taught my cat to walk on a leash. I want to thank Heeyong for his support, his humor, and for just being wonderful.

I would like to thank my grandparents, Larma and Francis Pottenger and Martha and Bob Hockaday for their love and support, and ultimately for their value of family and education. I would like to thank Grandpa and Grandma Pottenger for listening to me and talking to me as though my ideas have value and my work has merit. They are a sterling example of team work and the will to triumph over adversity. I want to thank my Grandma Pottenger for always having snacks, stories, and post-it notes. I want to thank my Grandpa Pottenger for always making time to paint with the grandkids. I would like to thank Grandpa and Grandma Hockaday for being adventurous and telling me stories about their respective chemistry experiences so that I would buckle down and pass chemistry (setting off explosions during a lecture by Linus Pauling at Cal Tech and wanting to discover the 93<sup>rd</sup> element).

I want to thank my aunts, uncles, and cousins for their love and support. I want to thank Uncle Marcus, Auntie Gail, Uncle Tyler, Auntie Faith, Uncle Jeff, Auntie Lois, Uncle Paul, Auntie Lisa, Auntie Louise, Uncle Bill, Auntie Lynn, Uncle Scott, Auntie Peggy, and my cousins Yvonne, Sean, Alex, Stephanie, Maribeth, Jordan, Michelle, Ryan,

Sara, Everett, Garrett, Gavin, Leila Ann, Bryanna, Noelle, Graham, Cameron, Brittany, Lizzy, Hudson, Aliyah, Sachi, and Ravi.

As requested by the members from my office I have included a cheat sheet family tree for the Hockadays, the Pottengers, and the Takahashis (Appendix D, page 427). I have told so many stories about my family in lab that people lose track.

I want to thank Patrick Turner. He always had great life lessons and stories to share. Many a manatee in Florida was saved by his problem solving. I wish everyone could meet someone like Patrick. He made a big difference in my life.

I want to thank my grad school family for their support and friendship; Erica Pratt, Jen Richards, Carissa Ball, Nathan Ball, Brooke Mason, Blake Mason, Casey Kraning-Rush, Jason Kraning-Rush, Fai Jeerapond Leelawattanachai, BoRi Seo, Obafemi Otelaja, and Jacqueline Shen, without whom being so far away from home would have been unbearable.

I would like to thank everyone from the Butcher lab. I would especially like to thank Russ Gould, Phil Buskhol, Gretchen Mahler, Emily Farrar, Chelsea Gregg, Stephanie Lindsay, Leah Pagnozzi, and Andrew Recknagel.

I want to thank Jonathan Butcher for his faith, patience, and invaluable mentorship. Dr. Butcher's positive attitude and energy has inspired me and has created a community within the lab that is positive, energetic, and allows for open discussion of ideas. Dr. Butcher has helped me improve my ability to communicate ideas, structure and plan experiments, work with collaborators, and effectively communicate with and lead a

team. I want to express my deep gratitude for his support, understanding, and availability to help during personal and family crises during the last six years.

I want to thank everyone currently and formerly on the bioprinter team, all of whom made the bioprinter project awesome. I would like to thank Nick Colangelo, Phil Cheung, Dave Filipiak, Edward Yip, Chris Caiola, Jagan Padmanabhan, Kevin Yeh, Kevin Lamott, Scott Newman, Mohammed Cherkaoui, Patrick Armstrong, Harshal Sawant, Lauren Lee, Jhalak Agarwal, Shoshana Das, Kang Li, Alain Kaldany, Daniel Cheung, Anya Laibangyang, Edi Kaptanovich, and Charlie Yunfan Xu.

I want to thank Bin Duan and Angela Zhou for their friendship and support. Duan has been a critical resource both for his knowledge and experience but also for his willingness to discuss ideas, brainstorm, and debate different experimental directions. Angela and Duan opened their home and generously provided me with shelter during the last stormy phase of earning my degree for which I will always be grateful.

For their input, technical assistance, and sharing of equipment and space I want to thank Jen Richards, Shivaun Archer, Claudia Fischbach, Jenny Puetzer, Jeff Ballyns, Cindy Reinhart-King, Paula Miller, Michael Shuler, Sydney Moise, Bruce Kornreich, Flavia Giacomazzil, Jeffrey Lipton, Warren Zipfel, Rebecca Williams, Sam Portnoff and his company Widetronix Inc., Xiaofan Luan, Bruce Land, and Ralph Personius. I want to thank Luke and Naomi Shirk for their generosity in providing porcine and ovine tissue for this research, and Jonathan Chen and the Weill Cornell Medical Center for providing the human tissue. I want to thank Belinda Floyd, Peter Doerschuk, Jinhee Roper, Vincent Rodgers, Dimitrios Morikis, and Victor Vullev for their support and help. I would also like to thank the building staff who make Weill Hall such a lovely, safe place to work, especially Lou from the 3<sup>rd</sup> floor, and Pam who runs the freezer program.

I want to thank my funding sources. My research was supported by the Morgan Family Foundation, The Hartwell Foundation, the National Science Foundation (CBET-0955172), NSF Graduate Research Fellowship, and the American Heart Association (AH0830384N).

## TABLE OF CONTENTS

BIOGRAPHICAL SKETCH.....	i
DEDICATION.....	ii
ACKNOWLEDGEMENTS.....	iii
TABLE OF CONTENTS.....	ix
LIST OF FIGURES.....	xix
LIST OF TABLES.....	xxvi
LIST OF ABBREVIATIONS.....	xxvii
CHAPTER 1	
PEDIATRIC VALVE DISEASE AND THE NEED FOR TISSUE ENGINEERED HEART VALVES.....	2
1.1 Summary.....	2
1.2 Pediatric Valve Disease.....	3
1.2.1 Congenital Heart Defects - Most Common and Lethal Birth Defects.....	3
1.2.2 Valve Disease in the Developing World Predominantly Impacts Children.....	4
1.3 Treatment of Valve Disease.....	5
1.3.1 Valve Replacement.....	5
1.3.2. Grim Inadequacy of Valve Replacement for Pediatric Valve Disease.....	7
1.4 Aortic and Pulmonary Valve Tissue Engineering.....	8
1.4.1 Design Criteria of a Tissue Engineered Heart Valve (TEHV).....	9
1.4.2 Design Path for Tissue Engineered Heart Valves.....	10

1.4.3 Tissue Engineered Heart Valve Approaches.....	11
1.4.4 Decellularized Valves .....	15
1.4.5 Biodegradable Synthetic Polymer TEHV .....	17
1.4.6 Biological Protein Based TEHV .....	18
1.4.7 <i>In-vivo-engineered</i> TEHV .....	19
1.4.8 Hybrid TEHV Manufacturing Strategies.....	21
1.4.9 Cell Sources for TEHV .....	24
1.5 Need for Improved Remodeling and Heterogeneity in TEHV .....	25
1.6 Organization of the Dissertation .....	28
CHAPTER 2	
APPLICATIONS OF 3D PRINTING TO ENGINEERING SOFT AND HETEROGENEOUS TISSUES .....	41
2.1 3D Printing Fabrication Systems .....	41
2.1.1 3D printing to create living tissue - encapsulation and direct cell printing vs post fabrication cell seeding of scaffolds.....	42
2.1.2 3D Printing devices to grow engineered tissue: 3D printing in molds and support structures/devices for culture and mechanical loading .....	44
2.2 Recent progress in TE for soft tissue .....	44
2.2.1 Skin tissue engineering: Advances in multi-level structure, in-situ printing into contoured wounds, <i>in vivo</i> animal model.....	45
2.2.2 Cartilage tissue engineering – advances in ear, intervertebral disc, and meniscus TE and hybrid technologies for engineering cartilage .....	48
2.2.3 Cardiovascular tissue engineering .....	52

2.2.4 3D printing for Higher Order Complex Tissue .....	56
---	----

## CHAPTER 3

RAPID 3D PRINTING OF ANATOMICALLY ACCURATE AND MECHANICALLY HETEROGENEOUS AORTIC VALVE HYDROGEL SCAFFOLDS.....	68
--	----

3.1 Abstract.....	68
-------------------	----

3.1 Introduction .....	69
------------------------	----

3.2 Materials and Methods .....	72
---------------------------------	----

3.2.1 Base hydrogel formulation.....	72
--------------------------------------	----

3.2.2 Mechanical testing of base hydrogel blends.....	73
---	----

3.2.3 3D printing system and hydrogel modification .....	73
--	----

3.2.4 Measuring crosslinking time of hydrogels.....	74
---	----

3.2.5. Valve geometry design.....	76
-----------------------------------	----

3.2.6. Heterogeneous valve printing.....	77
--	----

3.2.7 Shape fidelity evaluation of aortic valve scaffolds .....	79
---	----

3.2.8 Cell viability and spreading.....	79
---	----

3.2.9 Statistical analysis .....	81
----------------------------------	----

3.3. Results .....	81
--------------------	----

3.3.1 Mechanical properties of hydrogels.....	81
---	----

3.3.2 Effect of photoinitiator concentration on hydrogel crosslinking time .....	82
--	----

3.3.3 Rapid printing of heterogeneous and scaled valve scaffolds.....	82
---	----

3.3.4 Shape fidelity.....	84
---------------------------	----

3.3.5 Alginate removal and cell cytocompatibility of hydrogel scaffolds .....	87
---	----

## CHAPTER 4

PHOTO-ENCAPSULATION AND VIABILITY OPTIMIZATION OF VALVE CELLS AND MESENCHYMAL STEM CELL FOR DIRECT 3D PRINTING .....	101
4.1 Summary.....	101
4.2 Introduction .....	101
4.3 Materials and Methods .....	105
4.3.1 Synthesis of Polymer Precursors .....	105
4.3.2 Preparation of Sterile Polymer Precursor Solution .....	106
4.3.3 Light Meter Measurements and Light Sources for Photo-crosslinking.....	107
4.3.4 Mechanical Testing of Hydrogel Disks .....	108
4.3.5 Heart Valve and Mesenchymal Cell Culture .....	109
4.3.6 Encapsulation and Handling for Disk Experiments and <i>In vitro</i> Culture.....	112
4.3.7 LIVE/DEAD Staining.....	113
4.3.8 Metabolic Activity Assessment .....	114
4.3.9 Doubling Time Assay .....	115
4.3.10 General Oxidative Stress .....	115
4.3.11 Catalase Treatment of Cells.....	117
4.3.12 Statistics.....	118
4.4 Results .....	119
4.4.1 Range of Light Intensities for Photo-crosslinking During Printing.....	119
4.4.2 Mechanical Testing Photo-crosslinked Hydrogel Disks .....	123

4.4.3 Encapsulated Valve and Mesenchymal Cell Viability .....	129
4.4.4 Encapsulated Valve and Mesenchymal Cell Morphology .....	132
4.4.5 Cell Viability at Day 1, 3, 4, and 7 Culture .....	145
4.4.6 Metabolic Activity of Encapsulated Cells in 3D Culture .....	147
4.4.7 Doubling Time Compared to 3D Survival .....	149
4.4.8 Percentage of Encapsulated Cells Experiencing General Oxidative Stress (DCF) with and without Catalase Treatment .....	152
4.4.10 Cell Suspension Relative DCF Fluorescence After Bench Top Incubation .....	172
4.4.11 Effect of Catalase Treatment on Cell Viability and Morphology .....	172
4.4.12 Light Source Intensity Comparisons .....	178
4.4.13 Effect of Handling Buffer and Incubation on Encapsulated Cell Viability .....	179
4.5 Discussion .....	193
4.6 Conclusion .....	206
4.7 Future Directions .....	207
CHAPTER 5	
ARBITRARY AND ANATOMICALLY BASED CONTROL OF INTERNAL HETEROGENEITY OF 3D PRINTED TISSUES .....	217
5.1 Summary .....	217
5.2 Introduction .....	217
5.3 Materials and Methods .....	219
5.3.1 Fab@Home™ 3D Printing Platform and Vector File Format .....	219
5.3.2 Materials for Printing .....	220

5.3.3 Precursor Solution Preparation for Printing without Cells.....	221
5.3.4 Polymer Synthesis and Solution Preparation for Cell Encapsulation.....	221
5.3.5 Light Sources for Photo-crosslinking Printed Hydrogel Solutions.....	223
5.3.6 Adipose Derived Mesenchymal Cell Culture .....	223
5.3.7 Cell Encapsulation and Handling for 3D Printing.....	224
5.3.8 First Algorithm: Conversion of Images to Printable Vectors .....	225
5.3.9 Second Algorithm: Application of Gradients within Shapes and Generation of Printable Vectors.....	227
5.3.10 Region Dither Vector (RDV) Algorithm: Converting Tissue Heterogeneity into Vectors.....	227
5.3.11 MicroCT and MRI Scanning of Aortic Valve Tissue.....	234
5.3.12 Vector Printing MEGEL/PEG-DA Hydrogels .....	237
5.3.13 Quantifying Cell Distribution within Crosslinked Heterogeneous Hydrogel Constructs .....	240
5.4 Results .....	242
5.4.1 Layer Fidelity of Prescribed Component Heterogeneity .....	242
5.4.1 RDV Algorithm: Converting Tissue Heterogeneity into Vectors.....	244
5.4.2 Printing of Heterogeneous Anatomical Geometry .....	244
5.4.3 Cell Distribution within Crosslinked Heterogeneous Hydrogel Constructs.....	245
5.5 Discussion.....	246
5.6 Conclusion .....	251
CHAPTER 6	
HEART VALVE BIOREACTORS FOR DYNAMIC CONDITIONING .....	256

6.2 Heart valve tissue bioreactors .....	256
6.2.1 Component bioreactors .....	257
6.2.2 Whole valve scale bioreactors.....	264
6.3 Conclusions.....	274
CHAPTER 7	
BIOREACTOR FOR PARALLEL DYNAMIC CONDITIONING OF ADULT AND PEDIATRIC SIZED 3D PRINTED HYDROGEL HEART VALVES .....	279
7.1 Summary.....	279
7.2 Introduction .....	280
7.3 Materials and Methods .....	283
7.3.1 Heart Valve Bioreactor Design Overview .....	283
7.3.2 Heart valve conditioning chamber and holder for 3D printed hydrogel or ex vivo heart valves.....	285
7.3.4 Two Control Strategies for Pulsatile Conditioning: Timer Relay and Pressure Relief .....	288
7.3.5 Micro-controller for Regulation of Ventricular and Aortic Pressure .....	292
7.3.6 Characterizing Water Pump Flow Loop System to Drive Diaphragm in Media Loop .....	294
7.3.7 Measurement of Ventricular Stroke Volume for Different Size Conditioning Chambers.....	295
7.3.8 Systolic Flow Rate in Heart Valve Bioreactor Calculated from Stroke Volume and Cycle Time .....	295

7.3.9 Testing the Holder and Ultrasound Port and Characterizing Bioreactor System Pressure with Heart Valves .....	296
7.3.10 Bioreactor System Pressure Characterization.....	297
7.3.11 Optical Imaging of Heart Valves in Bioreactor Chamber .....	298
7.3.12 Ultrasound Imaging of Heart Valves in Bioreactor Chamber .....	298
7.3.13 Heart Valve and Mesenchymal Cell Culture.....	298
7.3.14 Biocompatibility Testing of Media Flow Loop and Conditioning Chamber Parts	300
7.3.17 Encapsulation and 3D Bioprinting of HADMSC into Hydrogel Valves .....	305
7.3.18 3D Printed Hydrogel Valve Attachment into Bioreactor Holder Assembly .....	306
7.3.19 Cell viability, collagen, and glycosaminoglycan (GAG) secretion .....	306
7.3.20 Statistics.....	307
7.4 Results .....	307
7.4.1 Characterization of Water Pump Flow Loop System to Drive Diaphragm Deflection in Media Loop.....	307
7.4.2 Ventricular Stroke Volume for Different Size Conditioning Chambers.....	311
7.4.3 Systolic Flow Rate in Heart Valve Bioreactor .....	311
7.4.4 Porcine Valve Sutured into Holder Assembly .....	314
7.4.5 Optical and Ultrasound Imaging of Heart Valve in Hard -walled Bioreactor Chamber. ....	316
7.4.7 Biocompatibility Testing of Media Flow Loop and Conditioning Chamber Parts.	325
7.4.8 3D Printed Hydrogel Valve Attachment into Biocompatible Bioreactor Holder ..	331
7.4.9 Dynamic Conditioning of 3D Bioprinting Hydrogel Valves with Encapsulated of HADMSC.....	335

7.5 Discussion .....	335
7.6 Conclusion .....	340
 CHAPTER 8	
CONCLUSIONS AND FUTURE DIRECTIONS .....	364
8.1 One Step Closer to a Viable TEHV .....	364
8.2 Need for Predictive Swelling, Growth, and Remodeling Models to Guide 3D Printing of Complex Geometries.....	365
8.3 Additional Studies to Identify Mechanism of Cell Type Specific Response to Photoencapsulation and Characterizing Material Sinking of Initiator Radicals .....	367
8.4 Evaluating the Biological Consequences of Complex Heterogeneity in a Hemodynamic Environment .....	369
8.5 Proposed MRI Study to Evaluate Engineered Valve Heterogeneity Compared to Native .....	370
8.6 Conclusion .....	370
 APPENDIX A	
BIOPRINTER TEAM .....	395
 APPENDIX B	
BIOREACTOR PARTS AND ASSEMBLY .....	399
B.1 Summary .....	399
B.2 Assembly of Bioreactor Pump Driven Water Flow Loop .....	399
B.2.1 Step 1 Drill and tap Nalgene tank walls and caps for adapters, and tap outlets for the capacitance membrane base. ....	407

B.2.2 Step 2 Seal adapters with silicone sealant to tanks, pressure transducers, and capacitance membrane chamber. ....	407
B.2.3 Step 3 Assemble capacitance membrane chamber. ....	409
B.2.4 Step 4: Assemble the water flow loop. ....	409
B.2.5 Build electronics control setup. ....	410
B.3 Partial assembly of bioreactor conditioning chamber and holder assembly and sterilization of media flow loop parts. ....	415
B.3.1 Step 1 Drill and tap the cast conditioning chamber base part outlets, aortic part outlet, body part outlets, and media reservoir. ....	415
B.3.2 Step 2 Seal adapters into ports of bioreactor chamber and reservoir parts. ....	418
B.3.3 Step 3 Assemble conditioning chamber base. ....	420
B.3.4 Step 4 - Sterilization of bioreactor conditioning chamber, reservoir, and tubing. ....	421
B.4 Installment of a valve into the holder mesh and media flow loop and chamber assembly. ....	422
B.5 Transfer the conditioning chamber setup to the large incubator and connect to electronics and applied aortic pressure line. ....	422
APPENDIX C	
HIGH POWER LED ARRAY AND HEAT SINK ASSEMBLY .....	424

## LIST OF FIGURES

Figure 1.1 Aortic valve complex structure and function. ....	27
Figure 1.2 Recent hybrid TEHV strategies to achieve improved anatomical and microstructural heterogeneity. ....	29
Figure 3.1 3D Printer setup and valve geometry modeling. ....	75
Figure 3.2 Uniaxial tensile testing and crosslinking time testing of PEG-DA hydrogels. ....	78
Figure 3.3 Printing heterogeneous valve and scaled valve constructs. ....	83
Figure 3.4 Fidelity analysis of fully hydrated printed valve scaffold geometry compared to model geometry using $\mu$ CT-derived STL files. ....	85
Figure 3.5 Slice-by-slice analysis comparing $\mu$ CT image slices of printed porcine valve scaffolds to model layers and assess internal geometric fidelity. ....	86
Figure 3.6 Representative SEM imaging of hydrogels. ....	88
Figure 3.7 Live/Dead imaging of PAVIC cultured on 12 mm ID printed valve constructs. ....	89
Figure 3.8 Morphology of PAVIC cultured on PEG-DA and collagen hydrogels. ....	90
Figure 4.1 UV light intensity vs distance for different sources used for crosslinking printed hydrogels. ....	120
Figure 4.2 Concentration and intensity study of mechanical properties of crosslinked hydrogels. ....	124
Figure 4.3 Time study of mechanical properties of crosslinked hydrogels. ....	125
Figure 4.4 Swelling properties of crosslinked hydrogels. ....	128
Figure 4.5 (A) Viability of encapsulated HADMSC, HAVIC, HASSMC stained at day 3 of culture. ....	130
Figure 4.5 (B) Circularity of viable encapsulated HADMSC, HAVIC, HASSMC stained at day 3 of culture. ....	131
Figure 4.6 Viability in HAVIC/Irgacure hydrogels. ....	133

Figure 4.7 (A) Viability in HAVIC/VA086 hydrogels. ....	134
Figure 4.7 (B) and (C) Viability in HAVIC/VA086 hydrogels. ....	135
Figure 4.8 (A) Viability in HASSMC/Irgacure hydrogels. ....	136
Figure 4.8 (B) and (C) .....	137
Figure 4.9 (A) Viability in HASSMC/VA086 hydrogels.....	138
Figure 4.9 (B) and (C) Viability in HASSMC/VA086 hydrogels.....	139
Figure 4.10 (A) Viability in HADMSC/Irgacure hydrogel.....	140
Figure 4.10 (B) and (C) Viability in HADMSC/Irgacure hydrogel.....	141
Figure 4.11 (A) Viability in HADMSC/VA086 hydrogel. ....	142
Figure 4.11 (B) and (C) Viability in HADMSC/VA086 hydrogel. ....	143
Figure 4.12 Cell type 2D doubling time and 3D hydrogel viability. ....	151
Figure 4.13 Representative images of encapsulated DCF/CTR labeled HBSS and catalase treated cells taken directly after crosslinking of hydrogel. ....	153
Figure 4.14 Representative images of HBSS and catalase treated cells labeled with DCF/DTR suspended in HBSS and benchtop incubated during encapsulation handling. ....	154
Figure 4.15 Split channels of representative images of encapsulated DCF/DTR labeled HAVIC taken directly after crosslinking of hydrogel.....	155
Figure 4.16 Split channels of representative images of encapsulated DCF/DTR labeled HASSMC cells taken directly after crosslinking of hydrogel. ....	156
Figure 4.17 Split channels of representative images of encapsulated DCF/DTR labeled HADMSC cells taken directly after crosslinking of hydrogel. ....	157
Figure 4.18 Oxidative stress differences between cell type: HAVIC, HASSMC, and HADMSC treated with catalase or HBSS (control) before encapsulation and light exposure. ....	158
Figure 4.19 Oxidative stress and effect of catalase loading for HADMSC as a function of light source intensity.....	160

Figure 4.20 (A) Viability and circularity of HBSS treated control cells verses encapsulating hydrogel modulus.....	161
Figure 4.20 (B) Viability and circularity of HBSS treated control cells verses encapsulating hydrogel modulus.....	162
Figure 4.21 (A) Viability and morphology verses percentage of cells experiencing oxidative stress for catalase treated and HBSS controls cells in Irgacure and VA086 encapsulation conditions.....	163
Figure 4.21 (B) Viability and morphology verses percentage of cells experiencing oxidative stress for catalase treated and HBSS controls cells in Irgacure and VA086 encapsulation conditions.....	164
Figure 4.22 Oxidative stress and effect of catalase loading for HASSMC as a function of light source intensity.....	168
Figure 4.23 Oxidative stress and effect of catalase loading for HAVIC as a function of light source intensity.....	169
Figure 4.24 Linear fit of percent of encapsulated cells experiencing general oxidative stress verses relative fluorescence of general oxidative stress indicator in encapsulated cell-hydrogels.....	170
Figure 4.25 General oxidative stress cell suspension controls for HAVIC, HASSMC, HADMSC.....	173
Figure 4.26 Representative images of Day 3 encapsulated, HBSS and catalase treated cells stained with Live/Dead.....	175
Figure 4.27 Effect of catalase loading on cell viability and circularity.....	176
Figure 4.28 Handling buffer and extended incubation effect on 3 day viability.....	180
Figure 4.29 Percentage of cells stained positive for oxidative stress verses modulus for HBSS control cells in Irgacure and VA086 encapsulation conditions.....	183
Figure 4.30 (A) Viability verses relative fluorescence excluding VA086/HLED condition.....	185

Figure 4.30 (B) Viability verses relative fluorescence excluding VA086/HLED condition. .....	186
Figure 4.31 (A) Oxidative stress ratio for HBSS treated cells.....	188
Figure 4.31 (B) Viability verses oxidative stress ratio for HBSS treated cells.....	189
Figure 4.31 (B) Viability verses oxidative stress ratio for HBSS treated cells.....	189
Figure 4.32 (A) Relative fluorescence intensity of oxidative stress verses modulus for HBSS control cells in encapsulation conditions, excluding HLED VA086 condition. ...	191
Figure 4.32 (B) Relative fluorescence intensity of oxidative stress verses modulus for HBSS control cells in encapsulation conditions, excluding HLED VA086 condition. ...	192
Figure 4.33 Schematic of precursor and crosslinked hydrogel environment. ....	200
Figure 5.1 Image defined heterogeneity - image based vector printing patterns in multiple materials. ....	226
Figure 5.2 Prescribed component heterogeneity - function generated geometries in Matlab and Excel.....	228
Figure 5.3 Prescribed component heterogeneity - function generated geometries converted to vectors and fabricated in hydrogels. ....	229
Figure 5.4 Brief algorithm function schematic. The RDV algorithm combines two strategies for generating printable vector files.....	230
Figure 5.5 RDV Algorithm. flowchart for fabricating geometries exhibiting anisotropic heterogeneity based on prescribed images.....	231
Figure 5.6 Flowchart summary and diagram for converting dithered paths into vectors paths. ....	233
Figure 5.7 User interface of RDV algorithm software written in Matlab. ....	235
Figure 5.8 Interpretation of $\mu$ CT and MRI intensity values for heterogeneous vector generation. ....	236
Figure 5.9 Image defined material heterogeneity in printed hydrogel valve constructs. .....	238

Figure 5.10 Setup for printing line pattern heterogeneous hydrogel constructs .....	239
Figure 5.11 Cell distribution within crosslinked heterogeneous hydrogel constructs...	241
Figure 5.12 Assessment of fabrication accuracy changes depending on path mixing during printing and the post-fabrication material properties of the hydrogel. ....	243
Figure 5.13 Diagram of heterogeneous material printing scaffold shape fidelity and feedback.....	249
Figure 6.1 Native valve loading and flow conditions change during cardiac cycle and as the valve develops.....	258
Figure 6.2 Four main bioreactor types.....	265
Figure 7.1 Over view of the heart valve bioreactor conditioning system which uses a pump driven water flow loop to circulate media in a sterile media loop. ....	284
Figure 7.2 Component diagram of Heart valve conditioning chamber and holder for 3D printed hydrogel or ex-vivo heart valves.....	286
Figure 7.3 Media flow loop and aortic pressurization diagram. ....	289
Figure 7.4 -74 Two strategies for bioreactor system control: pressure independent control of diastolic loading or pressure feedback control of diastolic loading. ....	290
Figure 7.5 Electronics diagram for single conditioning chamber. ....	293
Figure 7.6 Characterizing water pump flow loop system to drive diaphragm in media loop. ....	308
Figure 7.7 Schematic representation of diaphragm state .....	310
Figure 7.8 Heart valve bioreactor base and chamber design progression and stroke volume.....	312
Figure 7.9 Testing the holder setup with a porcine heart valve and system pressure characterization.....	315
Figure 7.10 Microscope and ultrasound imaging of valve in bioreactor.....	317
Figure 7.11 Microscope and ultrasound images of systole and diastole .....	318

Figure 7.12 Representative pressure traces of high tank, low tank, aortic, and ventricular chambers in an alternating solenoid control setup.....	320
Figure 7.13 Representative pressure traces of aortic and ventricular chambers in an alternating solenoid control setup with applied aortic pressure. ....	322
Figure 7.14 Representative pressure traces of aortic and ventricular chambers in an aortic pressure feedback control setup.....	324
Figure 7.15 Representative images of biocompatibility well experiments. ....	327
Figure 7.16 MTT assay biocompatibility screening of bioreactor materials. ....	328
Figure 7.17 Bioreactor chamber fabrication and material selection progression. ....	329
Figure 7.18 High power LED printing of hydrogel valves for conditioning. ....	332
Figure 7.19 3D printed hydrogel valve sealing into bioreactor holder assembly.....	333
Figure 7.20 Dynamic culture of 3D bioprinted heterogeneous hydrogel valves printed with encapsulated HADMSC. ....	334
Figure 7.21 Heart valve bioreactor conditioning system with a built in flow throttle in the pump driven water flow loop.....	339
Figure 7.22 Electronics diagram for parallel conditioning chambers. ....	341
Figure A.1. Bioprinter team 2008-2014. ....	397
Figure B.1 Bioreactor electronics setup for pressure feedback control of diastolic loading.....	416
Figure B.2 Electronics setup for bioreactor system control: pressure independent control of diastolic loading.....	417
Figure B.3 Fittings were clamped for additional mechanical hold in addition to PDMS sealing of luer fittings.....	419
Figure C.1 First version of high powered LED array was built with small heat sinks and rapidly overheated.....	425
Figure C.2 High powered LED schematic. ....	426
Figure C.3 Water cooling loop and copper heat sink.....	427

Figure C.4 High powered LED array intensity calculation estimates for different resistances..... 428

## LIST OF TABLES

Table 1.1 Comparison of TEHV Approaches .....	12
Table 4.1 Extrapolation of light source measurements and intensity at printing and crosslinking surface.....	122
Table 4.2 Damage to mechanics ratio.....	202
Table 6.1 Native valve loading and flow conditions change as the valve develops .....	259
Table 6.2 Miniaturized/partial tissue bioreactors .....	260
Table 6.3 Whole valve bioreactors .....	266
Table 7.1 Media loop: Parts in Contact with Cell Culture Media/Bioreactor Interior ....	326
Table B.1 Parts in Bioreactor .....	400
Table B.2 Tubing Cheat Sheet for Water Flow Loop .....	411
Table B.3 Bioreactor Electronics and Signal Processing Parts Not in Contact with Media or Water.....	412

## LIST OF ABBREVIATIONS

ABS	Acrylonitrile butadiene styrene
ADMSC	Adipose derived mesenchymal stem cells
ANCOVA	Analysis of covariance
ANOVA	Analysis of variance
AVD	Aortic valve disease
BMMSC	Bone marrow mesenchymal stem cells
CHD	Congenital Heart Defect
CT	Computed tomography
CTR	CellTracker Red CMTPX
DCF	5-(and-6)-chloromethyl-2',7'- dichlorodihydrofluorescein diacetate, acetyl ester CM-H2DCFDA
DEAD	Ethidium homodimer-1
DMEM	Dulbecco's modified Eagle's Medium
DMSO	Dimethyl sulfoxide
ECM	Extracellular matrix
FBS	Fetal bovine serum
HADMSC	Human adipose derived mesenchymal stem cells
HASSMC	Human aortic sinus smooth muscle cells
HAVIC	Human aortic valve interstitial cells
HBSS	Hank's balanced salt solution
HV	Heart valve
ID	Inner diameter
LED	Light emitting diode

LIVE	Calcein-AM
MA	Methacrylic anhydride
MEGEL	Methacrylated gelatin
MRI	Magnetic resonance imaging
MTT	3-[4,5-dimethylthiazol-2-yl]-2,5-diphenyltetrazolium bromide; thiazolyl blue
PAVIC	Porcine aortic valve interstitial cells
PBS	Phosphate buffered saline
PEG	Polyethylene-glycol
PEG-DA	Polyethylene-glycol diacrylate
PS	Penicillin/streptomycin
rhFGF	Recombinant human fibroblast growth factor basic
SEM	Scanning electron microscope
SFF	Solid freeform fabrication
SLA	Stereolithography
SSMS	Sinus smooth muscle cells
STL	Standard tessellated language
TE	Tissue engineering/ Tissue engineered
TEHV	Tissue engineered heart valve
UV	Ultra-violet
VEGF	Vascular endothelial growth factor
VIC	Valve interstitial cells

# CHAPTER 1

## PEDIATRIC VALVE DISEASE AND THE NEED FOR TISSUE ENGINEERED HEART VALVES

Portions of this chapter were previously published in *Advanced Drug Delivery Reviews* (Butcher, Mahler et al. 2011) and in the book chapter entitled “Aortic Heart Valve Tissue Regeneration” (Duan, Hockaday et al. 2014) in *Tissue and Organ Regeneration: Advances in Micro and Nanotechnology*.

### **1.1 Summary**

Valve related congenital heart defects are a serious clinical burden affecting 1/100 live births. Aortic valve replacement options for pediatric patients are grimly inadequate. Bio-prosthetic fixed tissue valve prosthetics degrade in less than a few years in young, active patients. Mechanical valve prosthetics, on the other hand, require lifelong anticoagulation therapy. Neither of these options have any potential for growth with the child. Nearly 20% of children with prosthetic valves die within 10 years of aortic valve replacement and an additional 40% require repeat surgical operations. Tissue engineering has the potential to generate a living *de novo* valve replacement capable of growth and integration. Over the last 15 years, researchers have developed and implemented novel synthetic polymers as scaffolds for engineered heart valves. Though much progress has been made, a persistent problem is the difficulty in fabricating a complex-shaped valve with a relatively rigid root and compliant leaflets with a single material formulation. The natural 3D anatomical geometry, non-uniform mechanical properties, and heterogeneous cellular composition of the aortic valve are important factors for its efficient function. Recent advances in photo-polymerizable hydrogel technology enable the combination of tunable scaffold mechanical properties and cell-

mediated degradation. In addition, solid freeform fabrication (3D printing) technology has the capacity to generate complex 3D geometries with extrudable materials.

## ***1.2 Pediatric Valve Disease***

### **1.2.1 Congenital Heart Defects - Most Common and Lethal Birth Defects**

While the majority of patients with aortic valve disease in the United States are over the age of 65, approximately 1% of all live births in the U.S. suffer from congenital heart valve defects. Congenital heart defects are the most common and lethal types of birth defects, causing 10–30% of preterm fetal demise in the US (Hoffman 1995; Hoffman and Kaplan 2002; Tanner, Sabine et al. 2005). The most common defects are malformations of the cardiac valves (Glen, Burns et al. 2004; McBride, Marengo et al. 2005; Konstantinov, Karamlou et al. 2006; Owens, Gomez-Fifer et al. 2006; Ilbawi, Spicer et al. 2007). While often requiring heroic surgical intervention at birth, valve related congenital heart defects lead to pathological remodeling over time and premature valve failure. The underlying causes and malformative mechanisms for many human congenital disease conditions are not understood (Butcher, Mahler et al. 2011). Many studies have identified families for which a valve related congenital heart valve disease is heritable, while broader screens have suggested that only a small fraction of congenital heart defects can be explained by a specific genetic disorder. The least explored causes for congenital valve malformation are micro-environmental mechanical forces. Aortic valves develop and function under constantly changing mechanical loading conditions (Aikawa, Whittaker et al. 2006), which suggests that altered mechanical signaling could be an alternative causal mechanism for congenital valve malformations (Colvee and Hurler 1983; Clark 1996; Kosaki, Mendoza et al. 1996).

### **1.2.2 Valve Disease in the Developing World Predominantly Impacts Children**

The vast majority of aortic valve disease patients in the developing world are children and young adults (Cohen, Malone et al. 2006; Zilla, Brink et al. 2008). This age group is critically important to sustaining economic development in a country. The global burden of heart valve disease is severely underappreciated. 80% of all cardiovascular disease cases occur in developing countries (Yusuf, Vaz et al. 2004), causing more than 19% of deaths. This is more than war and malaria combined (Ribeiro, Jacobsen et al. 2008). In Western countries the population primarily suffers from aging related degenerative syndromes, but the population of the developing world suffers from non-ischemic cardiovascular pathologies characterized by fibrosis, inflammation, and immune reactions. The demographic most affected by valve disease in the developing world are children and young adults (Dajani and Taubert 1992; Mayosi 2007; Sani, Karaye et al. 2007; Mocumbi, Ferreira et al. 2008). In most of the developing world heart valve disease is the single largest cause of hospital admissions for children and young adults (Dajani and Taubert 1992). Recent epidemiological studies suggest that the incidence of valve disease in developing countries may be grossly underestimated (Marijon, Ou et al. 2007). Numerous cases of valve related pathologies have been documented with no known cause. Infant mortality rates remain unacceptably high in developing countries, and the proportion of death due to CHD is over 15-fold higher than in the US (Rosano, Botto et al. 2000). These statistics indicate tremendous national and global burden of heart valve disease.

#### **Rheumatic Valve Disease**

Rheumatic valve disease is one example of a non-ischemic cardiovascular pathology, characterized by fibrosis, inflammation, and immune reactions. There are more than 15 million documented cases and 282,000 deaths from rheumatic valve disease worldwide each year, comparable to all cardiovascular related deaths in the US (Carapetis, Steer

et al. 2005). Rheumatic fever may develop after a non-treated throat infection by the gram-positive bacteria *Streptococcus pyogenes* in susceptible children and teenagers. Carditis (inflammation of the heart), which is the most serious rheumatic fever complication, occurs about 20 days after the infection in 40–50% of patients and can lead to valvular heart disease, heart failure, or death (Veinot 2006). Valve complications are the result of an autoimmune reaction induced by the molecular mimicry to human tissues of streptococcal M proteins and group A carbohydrate. The resulting valve pathologies include neovascularization, chronic inflammation, commissural fusion, thickening, calcification, and thickened and shortened chordae in the atrioventricular valves.

### **1.3 Treatment of Valve Disease**

Heart valves, especially aortic valves, are critical for ensuring unidirectional blood flow through the heart. 90% of patients with severe aortic valve stenosis have a life expectancy of less than 10 years unless treated, and 50% of these patients with heart failure will die within 1 year (Carabello and Paulus 2009). Prosthetic replacement is virtually the only clinical therapy for aortic valve disease. A small subset of patients undergo aortic valve repair (valvuloplasty), but this almost always involves replacing the leaflets and/or root with autologous or allogeneic tissue components (Cheng, Dagum et al. 2007).

#### **1.3.1 Valve Replacement**

Non-living prosthetics are the clinical standard for heart valve replacement. Living valve replacement of the aortic valve with the pulmonary valve in the Ross procedure is being explored and requires the replacement of the pulmonary valve with a non-living prosthetic. Non-living replacement valves can be divided into two classes: mechanical and bio-prosthetic/treated tissue.

### Mechanical Prosthetic Valves

Mechanical valves are composed of specialized metals and ceramics. They are manufactured in several forms but generally are built with pyrolytic carbon coated metal surfaces. These designs are structurally durable, but suffer from two limitations. First, they contain complex hinge geometries and components that must remain inside the flow zone of the outflow tract. This results in greater than physiological shear stresses that induce platelet lysis and protein aggregation on the mechanical valve surfaces. Despite 40 years of design iteration, no mechanical valve design has overcome this problem (Zilla, Brink et al. 2008). This requires that a patient with a mechanical valve prosthetic must manage treatment with anticoagulant drugs for the rest of their life. This is associated with severe occupational and lifestyle restrictions. Even with these treatments, mechanical prosthetic valve recipients suffer a 2–5% annually cumulative risk of serious bleeding events (hemorrhage, stroke, and infarction)(Grunkemeier, Li et al. 2000).

### Bio-prosthetic Valves

Tissue valves include xenogenic (porcine and bovine) and allogenic (homograft) valves. These are manufactured either in a stented configuration, which contains a synthetic sewing ring and struts to support the leaflets, or in a stentless configuration that includes the entire root. These valves are not subject to the hemocompatibility concerns of mechanical valves and deliver more physiological hemodynamics, but instead risk structural degeneration because they contain no living cells. Numerous clinical studies have evaluated the efficacy of prosthetic valve replacements, but only a few have been comparative and randomized (Hammermeister, Sethi et al. 2000). In general bio-prosthetic and homograft valves are the conduit of choice for patients over the age of 60–65 that are relatively physically inactive (Rahimtoola 2010). Mechanical valves, in contrast, are often chosen for patients with higher physical activity levels, those younger

than 60, and for those which blood thinner medication can be tolerated. If the prosthetic is properly chosen and sized to the patient, clinicians are pushing the age barrier for bio-prosthetic valves younger (because prostheses may be “exchanged” with less risk) and pushing the age barrier for mechanical valves older (because surgical morbidity is reduced). While bio-prosthetic results are acceptable for more sedentary older patients, it is unacceptable for more active, younger adults (Grunkemeier, Li et al. 1999).

### Pulmonary Autograft (The Ross Procedure)

The pulmonary autograft, or Ross procedure has received the most attention as an alternative intervention strategy to non-living prosthetic valve replacement. This surgery replaces the diseased aortic valve with the patient's own pulmonary valve, leaving the far less demanding pulmonary position to be replaced with a bio-prosthetic valve. Clinical studies to date demonstrate that the Ross procedure is superior to homograft aortic valves in adults (El-Hamamsy, Eryigit et al. 2010). The fact that this now creates a two-valve problem has led some to question the utility of the procedure for some patients (Cameron and Vricella 2007).

### **1.3.2. Grim Inadequacy of Valve Replacement for Pediatric Valve Disease**

Unfortunately, aortic valve replacement options for pediatric patients are grimly inadequate. Bio-prosthetic valves exhibit exhibiting excellent hemocompatibility and reasonable durability for patients over 65, but they degenerate and calcify within 5 years or faster in children (Schoen 2006). In infants and children, homograft tissue valves rapidly fail due to what appears to be an induced immune response(Rajani, Mee et al. 1998). Meanwhile, mechanical valves are extremely durable, and are the only valves that are durable enough for children, but they necessitate lifelong anti-thrombotic medication that incurs a 5% annually cumulative risk of bleeding events (Vricella, Williams et al. 2005). Infants and young children requiring valve replacement are

especially difficult to treat because their conduits are extremely small (10–15 mm diameter), yet will grow substantially over time (5–10 mm in diameter). This therefore necessitates implantation of a much larger conduit than ideal and/or repeat operations to resize the prosthesis (Lupinetti, Warner et al. 1997; Alsoufi, Al-Halees et al. 2009). 40% of growing children with prosthetic valves require repeat open-heart surgeries to resize the valve (Karamlou, Jang et al. 2005). The pulmonary autograft, or Ross procedure, provides a living replacement for the aortic position while a prosthetic valve replaces the much less demanding pulmonary position (Ross 1967). While the autograft has been effective for adults in comparison to homografts (El-Hamamsy, Eryigit et al. 2010), clinical results suggest that up to 40% of pulmonary autografts in children may dilate pathologically instead of grow (Koul, Lindholm et al. 2002; Frigiola, Varrica et al. 2010), Consequently, a second prosthetic valve replacement is required.

These limitations altogether indicate the need for valve replacements more suitable for growing children, and they also motivate the need to pursue tissue engineering strategies to create living aortic valves.

#### ***1.4 Aortic and Pulmonary Valve Tissue Engineering***

Tissue engineering is the process by which *de novo* living tissue is fabricated to replace dysfunctional tissue. A living cellular component enables the possibility for biological integration, adaptation, remodeling, and growth. Tissue engineering has great potential for real benefit for patients with aortic valve disease, particularly for children requiring valve growth and younger patients who cannot tolerate the debilitating side effects of current non-living prosthetics (Karamlou, Jang et al. 2005; Yacoub and Takkenberg 2005). This population is relatively small in Western nations, largely confined to congenital valve malformations underlying the disease (1-2% of all live births) (Roberts and Ko 2005; Hinton and Yutzey 2011). However, due to the prevalence of rheumatic

fever in the developing world, millions of young people could benefit from a tissue engineered conduit (Carapetis 2008; Zilla, Brink et al. 2008). In many ways, the pulmonary autograft represents proof of principle for clinical effectiveness of tissue engineered aortic valves (TEHV) (Ross 1967; Koul, Lindholm et al. 2002; El-Hamamsy, Eryigit et al. 2010; Frigiola, Varrica et al. 2010), but since (1) it is not an aortic valve and (2) does not remove the need for a prosthetic valve replacement, a fabricated living valve is still needed.

#### **1.4.1 Design Criteria of a Tissue Engineered Heart Valve (TEHV)**

The basic characteristics of a replacement heart valve were expressed in 1962 by Dr. Dwight Harken and extended by Sacks and Schoen for tissue engineered valves (Sacks, Schoen et al. 2009): 1) it must be non-obstructive; 2) closure must be prompt and complete; 3) it must be non-thrombogenic and non-immunogenic; 4) it must accommodate the somatic growth of the recipient; and 5) it must last the lifetime of the patient. The fifth requirement means the valve must be durable enough to endure millions of load cycles and capable of ongoing remodeling. The natural engineering of the native aortic valve is ideal for its long-term function, which suggests key design criteria for a TEHV. We believe the most important criterion is to precisely mimic the natural anatomic 3D geometry, which is critical for enabling efficient conduit hemodynamics and coronary flow (Bellhouse, Bellhouse et al. 1968; Thubrikar, Bosher et al. 1979; Thubrikar, Nolan et al. 1980). A very close second is replicating the regionally heterogeneous tissue compliance of the root and cusp (Stephens, Durst et al. ; Sauren, van Hout et al. 1983; Christie 1992; Billiar and Sacks 2000). The cusps need to be sufficiently compliant so as to not impede blood ejection (risking stenosis) while the root wall needs to be sufficiently stiff to not pathologically dilate (risking aneurysm) (Sacks, Schoen et al. 2009). While a prosthetic valve must function immediately upon implantation, it is also important not to replace diseased tissue with “disease prone”

tissue. Secondary characteristics include mechanical strength (so that it won't fail in elevated blood pressure), ease of biological functionalization (to encourage cell engraftment and differentiation), ease of reliable fabrication, cost, and the requirement for human tissue material components (Schoen 2008; Sacks, Schoen et al. 2009). Other design choices befall every TEHV strategy. These include: whether they should be "off the shelf" or custom-made for each patient (implying storage and/or transportation logistics), first processed *in vitro* (e.g. to make stronger or better cellularized tissue) or implanted directly, what cell source to use, and whether design should be affected by demographics (age, gender, race) or "one size fits all". Some of these decisions will be more heavily influenced by market forces (e.g. what can be sold and/or reimbursed by insurance) than science, but in this review I focus only on the scientific aspects.

#### **1.4.2 Design Path for Tissue Engineered Heart Valves**

The current strategy for TEHV is to aim first for an engineered pulmonary replacement in concert with the Ross procedure before progressing to aortic valves. The biomechanically weaker pulmonary valve is anatomically and micro-structurally similar to the aortic valve, which presents overlapping but more attainable benchmarks. Conduits are first evaluated *in vitro* for biological and biomechanical fidelity, often including *in vitro* hemodynamic simulation using bioreactors (Sutherland, Perry et al. 2005; Flanagan, Sachweh et al. 2009; Gottlieb, Kunal et al. 2010; Ramaswamy, Gottlieb et al. 2010). Next they are transferred to animal models for pre-clinical testing. Novel biomaterials are implanted inside small animal models (rat, rabbit) to evaluate biocompatibility and calcification potential (Tedder, Liao et al. 2009; Wang, McGoron et al. 2010). The sheep is the only FDA approved large animal model for heart valve replacement evaluation. Sheep aged 10-100 weeks have quantitatively similar cardiac sizes and outputs as humans between 1 and 20 years old (Chanda, Kuribayashi et al.

1997; de Simone, Devereux et al. 1997), a high propensity for calcifying implanted tissue, but tolerate well invasive cardiothoracic surgery (Chanda, Kuribayashi et al. 1997; Hong, Maish et al. 2000; Meuris, Ozaki et al. 2001; Meuris, Ozaki et al. 2003). Sheep however spontaneously endothelialize cardiovascular grafts, which may artificially improve performance because humans do not endothelialize grafts so readily (Ouyang, Salerno et al. 1998; Simon, Kasimir et al. 2003; Padera R Fi J r 2008). The pig also has similar cardiac sizes and outputs, but poorly endothelializes grafts and tolerates poorly invasive surgery. These features suggest pig to be a more human-like animal model for evaluating valves, but the technical challenges create too much risk for experimental variability and likelihood for prohibitive costs. Once proven in the sheep, TEHV advance to human trials as pulmonary replacements in adult Ross procedures that don't require growth. Finally, growing children implantation studies would be conducted. Due to the significant number of expensive steps involved for a relatively small affluent patient population, it is doubtful that industry will carry such a project forward without significant academic advancement and/or financial incentives (Administration October 2004).

### **1.4.3 Tissue Engineered Heart Valve Approaches**

There are six main approaches for valve tissue engineering: decellularization of aortic valve scaffolds, shaping and seeding of scaffolds made of biodegradable polymers, shaping biological protein hydrogels that have encapsulated cells, hybrid or layered decellularized tissue/polymer scaffolds, *in vivo* engineered valve shaped tissues, and 3D printing of valves. Each approach has advantages and limitations with respect to the above design criteria, which are summarized in Table 1.1.

**Table 1.1 Comparison of TEHV Approaches**

TEHV Type	Ability to Mimic Native Geometry	Fabrication	Regional Heterogeneity	Mechanical Strength of Tissue	Secondary	Reference
Decell/Re cell	Excellent since the native tissue geometry is preserved	Detergent Treatment  Limited fabrication flexibility because the size and shape determined by existing porcine or human valve	ECM heterogeneous structure remains  Limited cellular heterogeneity	Mechanical properties vary dependent on detergent protocol  Change in mechanical properties more pronounced for enzyme than detergent treated.	Less durable than native valve Slight Changes in transvalvular gradient, valve resistance, EOA, stroke work loss depending on detergent and enzyme used	(Simon, Kasimir et al. 2003), (Rieder, Seebacher et al. 2005), (Liao, Joyce et al. 2008), (Bottio, Tarzia et al.), (Dohmen, Lembcke et al. 2002), (Miller, Edwards et al. 2006), (Sayk, Bos et al. 2005), (Erdbrugger, Konertz et al. 2006)
Synthetic polymer	Simplified Geometry (symmetric, sinuses)	Injection Molding - easy to repeat the same shape  Or Sutured by hand	Homogeneous material	Material stiffness is greater than native valve  Burst strength decreases with degradation	Progressive valve insufficiency  Decreasing flexibility and motion of leaflets	(Sutherland, Perry et al. 2005), (Gottlieb, Kunal et al.), (Ramaswamy, Gottlieb et al. 2010)

**Table 1.1 Continued**

TEHV Type	Ability to Mimic Native Geometry	Fabrication	Regional Heterogeneity	Mechanical Strength of Tissue	Secondary	Reference
Biological polymer	Simplified Geometry (symmetric, sinuses)	Molding - easy to repeat the same shape	Homogeneous material	Ultimate tensile strength and tensile modulus of the leaflets in the commissural direction were 0.53 and 2.34 MPa,	Valve insufficiency observed  Leaflet shortening/shrinkage	(Flanagan, Sachweh et al. 2009), (Ahmann, Weinbaum et al.), (Robinson, Johnson et al. 2007; Syedain, Bradee et al. 2013)
<i>In-vivo</i> -engineered	Simplified 3D printed mold geometry (symmetric, sinuses)	Molding, implantation, connective tissue capsule formation	Single tissue type  No valve cells	Tensile strength less than native valve.  Elastic modulus leaflets similar to radial direction in native valve	Tissue formed thicker for larger molds. Molded cusps and sinuses.	(Hayashida, Kanda et al. 2007), (Yamanami, Yahata et al. ; Nakayama, Takewa et al. 2014; Sumikura, Nakayama et al. 2014)
Layered /Hybrid/coated	Excellent, but need to create a new mold for different implants	Molding and suturing sinus w/ cusps into valve root  Labor intensive, limit to how many different regions can be incorporated	Layered heterogeneity, multiple material and cell types.	Stiffer compared to native		(Tedder, Simionescu et al. 2010), (Stamm, Khosravi et al. 2004)

**Table 1.1 Continued**

TEHV Type	Ability to Mimic Native Geometry	Fabrication	Regional Heterogeneity	Mechanical Strength of Tissue	Secondary	Reference
3D Printing	Excellent, able to replicate native geometry or simplified	Low cost prototyping	Leaflets can be printed with compliant, flexible materials while the root can be printed with stiffer materials	Multiple cell types and materials can be printed into the structure		(Ballyns, Cohen et al. ; Cohen, Malone et al. 2006; Hockaday, Kang et al. 2012; Duan, Kapetanovic et al. 2014)

#### **1.4.4 Decellularized Valves**

The best TEHV scaffold theoretically would be the native aortic valve itself since it contains all of the structural and mechanical heterogeneity required. Since cells contain high lipid content in their membranes, valves can be washed and/or perfused with detergents to lyse and clear these cellular components. In theory, all that would remain is a (relatively) undisturbed extracellular matrix structure. Furthermore, removing cells may significantly reduce the immunogenicity of the tissue, raising the possibility that non-crosslinked xenogenic valve tissue could be used in humans. Research over the past 15 years has focused on establishing optimized decellularization protocols (O'Brien, Goldstein et al. 1999; Simon, Kasimir et al. 2003; Schmidt, Stock et al. 2007). These generally involve anionic, ionic, and/or hypotonic detergents (e.g. SDS, Triton-X, EDTA) (Rieder, Kasimir et al. 2004), enzymes (e.g. trypsin) (Steinhoff, Stock et al. 2000), and nucleases (DNase, RNase), but constituent doses and perfusion times can be varied (e.g. TRI-DOC and TRI-COL) (Rieder, Kasimir et al. 2004). Results to date have identified the following insights. First, Cusp tissue decellularizes much more readily than the root, likely because the root wall is significantly thicker and more densely populated. While decellularization largely preserves the matrix ultrastructure, collagen crimp patterns, fiber distributions, and glycosaminoglycan profiles can be changed (Naso, Gandaglia et al.). This results in altered biomechanical function, but can be either stiffer or more compliant depending on the protocol applied (Liao, Joyce et al. 2008) (Bottio, Tarzia et al.). This creates a difficult balance in completely removing cells while preserving tissue biomechanics. Any remnant cellular debris elicits a strong immune response and provides nucleation sites for calcification (Naso, Gandaglia et al.) (Simon, Kasimir et al. 2003). While post-decellularization crosslinking of the tissue via glutaraldehyde can reduce this immunogenicity, it is not completely prevented and even

completely decellularized xenogenic matrix constituents may induce an immune response (Rieder, Seebacher et al. 2005). Decellularized valves have advanced the furthest clinically of all TEHV approaches. Sheep pulmonary implantation studies demonstrated decellularized allografts can function long-term and upon explant appear to be repopulated in as little as 3 months (Erdbrugger, Konertz et al. 2006).

The Synergraft valve by Cryolife is a decellularized pulmonary valve homograft that has been implanted in humans. Adult clinical trials have been very encouraging, showing that this valve functions comparable to homografts (Konuma, Devaney et al. 2009). Explanted valves however showed minimal *in vivo* recellularization (Sayk, Bos et al. 2005; Miller, Edwards et al. 2006), questioning the ability of these conduits to remodel. This approach unfortunately proved disastrous in children, as rapid and massive inflammatory reactions caused deaths in 3 out of 4 patients (Simon, Kasimir et al. 2003). More recent strategies have focused on recellularizing these decellularized scaffolds to improve long-term biointegration (the “Decell-Recell” approach). Scaffolds are either coated with bioactive substances to encourage repopulation *in vivo* (Tedder, Liao et al. 2009), or populated with autologous cells *in vitro* before implantation (Dohmen, Lembcke et al. 2002; Tedder, Simionescu et al. 2010). Precoating with adhesive proteins (Hayman, Pierschbacher et al. 1985; Seeger and Klingman 1985; Burdick and Anseth 2002) or cell surface antibodies (Ye, Zhao et al. 2009) have shown enhanced cellularization *in vitro* and in animals. More recently, less stringent chemical crosslinking agents and porosity modulating protocols have been developed to enhance recellularization and matrix integrity following decellularization (Sierad, Simionescu et al. ; Tedder, Liao et al. 2009). While encouraging, a major limitation with the decell or decell-recell approach is that it still requires a human valve as starting material, which are of limited supply (Jashari, Goffin et al. 2010).

#### **1.4.5 Biodegradable Synthetic Polymer TEHV**

A widely applied tissue engineering strategy has been to fabricate *de novo* scaffolds using synthetic biodegradable polymers. These have the advantages of limitless supply, broad tailoring of material synthesis and characterization, large variety, ease of shaping, and compatibility with many manufacturing processes (stereolithography, injection molding). The vast majority are organic solvent based acidic polymers that degrade by hydrolysis (e.g. PGA, PGLA, PLLA, P4HB, PHA) (Sodian, Hoerstrup et al. 2000; Schmidt, Stock et al. 2007; Ramaswamy, Gottlieb et al. 2010). Mechanical strength and rigidity will therefore decrease over time. While degradation can be prescribed somewhat through polymer blends, it results in an uncontrolled “race” between cell mediated tissue synthesis and material erosion. Scaffolds can be shaped (by hand or with molds) into valved conduits, but cells cannot be seeded until after all cytotoxic solvents are removed (Gottlieb, Kunal et al. ; Sodian, Hoerstrup et al. 2000). An additional concern is that the end products from the degrading acidic polymers change local pH, causing undesired cell death and differentiation (Gunatillake and Adhikari 2003).

Biodegradable polymer TEHV have been iterated over the past 20 years by John Mayer and his protégés (Shinoka, Ma et al. 1996; Sodian, Sperling et al. 1999; Sodian, Hoerstrup et al. 2000; Sutherland, Perry et al. 2005). Early valve conduits were fabricated with multiple biodegradable materials (Shinoka, Ma et al. 1996; Sodian, Sperling et al. 1999). The porosity, degradation time, and cell-polymer interaction were different between the materials. One of the materials, a non-porous polyhydroxyalkanoate (PHO) film was ill suited to use in the scaffold composite, and this led to lack of tissue ingrowth as well as scar tissue formation in some areas (Sodian, Sperling et al. 1999). As a result the group shifted to using single material porous scaffolds (Sodian, Hoerstrup et al. 2000). In their longest animal trial to date,

composite biodegradable polymer components were constructed into valves with sinuses, seeded with mesenchymal stem cells, cultured for 4 weeks, and then implanted into a sheep model for up to 20 weeks (Sutherland, Perry et al. 2005). *In vivo* monitoring showed leaflet coaptation, and explanted valves showed near-native trilaminar matrix striation with both endothelial-like and interstitial-like cell phenotypes. Persistent elevated transvalvular pressure gradients suggest the cusps are yet too stiff. More recently, Hoerstrup and colleagues have expanded the capabilities of biodegradable polymer TEHV by creating a transapical delivery system and identifying new cell sources (Schmidt, Achermann et al. 2008; Schmidt, Dijkman et al. 2010). Amniotic fluid derived cells were isolated beads and differentiated and then used for the fabrication of valve leaflets. Sodian et al explored the use of human umbilical cord-derived progenitor cells for tissue-engineering valves (Sodian, Schaefermeier et al. 2010). Public and private tissue banks (more than 30 in the US and on 6 continents) store amniotic fluid derived cells and umbilical cord blood cells (Verter Copyright 2000 - 2010 ). The rationale of the tissue banking is to use the cells in stem cell transplantation treatments or as an autologous cell source for possible treatments of disease.

#### **1.4.6 Biological Protein Based TEHV**

Unlike biodegradable polymers, biological protein based scaffolds are inherently biocompatible and degrade through enzymolysis, which enables cell-controlled tissue remodeling. The most commonly employed proteins are type I collagen and fibrin. The former spontaneously forms a fiber network at neutral pH, while polymerization of the latter is controlled by thrombin analogs (Flanagan, Sachweh et al. 2009). *In-vitro* studies have demonstrated that almost all mesenchymal cells including VIC thrive within and rapidly compact these protein hydrogels (Ahmann, Weinbaum et al. ; Butcher and Nerem 2004; O'Cearbhaill, Murphy et al. 2010). Most biological hydrogels are created at less than 10% of native densities, resulting in significantly weaker matrices. Denser

protein scaffolds can achieve greater mechanical strength but have limited cell infiltration. Completely biological TEHV have been created using fibrin and collagen hydrogels created 3D molds with exaggerated shapes to ensure desired final geometry. *In vitro* studies show these tissues do remodel and strengthen, achieving anisotropic fiber structures similar to native valves, although much weaker (Robinson, Johnson et al. 2007). In a first sheep implant study, fibrinogen encapsulating autologous arterial cells was injection molded into valve shapes, mechanically conditioned *in vitro* for 28 days before 3 month implantation (Flanagan, Sachweh et al. 2009). Explanted valves showed almost no cusp tissue, suggesting severe tissue contraction. Prediction of remodeling and strengthening is therefore a key requirement for the success of the biological protein based TEHV (Ahmann, Weinbaum et al.). Furthermore, these results suggest that we do not yet know how the body interprets an engineered fibrin scaffold that resembles wound-like granulation matrix. Likewise, until a safe recombinant human or xenogenic collagen supply can be obtained, it is unlikely that a collagen based valve will be possible in the near future.

#### **1.4.7 *In-vivo-engineered* TEHV**

*In-vivo* tissue engineering involves co-opting the natural foreign body response to synthesize autologous tissue around an implant material. The initial proof of concept was established by Campell and colleagues, who created blood vessels by inserting silicone tubing into peritoneal cavity of dogs (Chue, Campbell et al. 2004). They found elastin-rich medial wall architecture with mesothelial-derived endothelial-like and smooth muscle-like cell phenotypes. This strategy was recently extended to valved conduits (Yamanami, Yahata et al. ; Hayashida, Kanda et al. 2007). A silicone and polyurethane mold was implanted into the dorsal subcutaneous space of a rabbit. Connective tissue formed around the valve shaped mold and leaflets were cut into the tissue after removal from the rabbit. The *in-vivo-engineered* valve was tested in an *in*

*vitro* flow loading circuit and opening and closure of the leaflets without regurgitation was observed. Tensile strength of the tissue was less than the native valve, but the modulus matched the modulus of the native valve leaflets stressed in the radial direction (Yamanami, Yahata et al.). Yamanami and colleagues recently established proof of principle of this approach in a beagle model (Yamanami, Yahata et al. 2010). An anatomical mold assembly implanted in the dorsal subcutaneous space developed native-like geometry and burst strength. Echocardiographic follow up over 84 days showed effective cusp kinematics. Explanted valves contained endothelial and medial cells, supporting biointegration. Recently additional work demonstrated ‘biovalves’ in a pulse duplicator system and in a goat animal model (Nakayama, Takewa et al. 2014; Sumikura, Nakayama et al. 2014). Using a 3D printed mold that provided the construct with valve sinuses of native size and control of cusp aperture Nakayama et al created entirely autologous valves (no additional polymer scaffold) that were predominately fibrous collagen. They found that the connective tissue formed around the mold even prior to implantation had heterogeneous mechanical properties between the leaflet and the root, and they suspect that capsule contraction around the different parts of the mold is responsible. Although biaxial mechanics and the physiological strain behavior of the material has yet to be evaluated, the maximum elastic modulus properties of these engineered tissues match (leaflet) or surpass (root) native tissue. The in-vivo-engineered valves were evaluated before and after implantation in an apico-aortic bypass. In apico-aortic bypass, a conduit is inserted into the apex of the heart so that part of the outflow of the left ventricle goes through the native aortic valve and part goes through a bypass engineered valve. Under these hemodynamic conditions Nakayama et al found minimal stenosis and regurgitation of the in-vivo-engineered TEHV after 1 month. Histological evaluation of remodeling in the valves indicates that cell ingrowth is minimal and suggests slight thinning of the leaflet and root tissue. Population of cells within the root and leaflet will affect long term remodeling and this could present a

challenge for this particular TEHV strategy. Earlier studies of in-vivo-engineered TEHV did find some cell ingrowth into these tissues although it appears much less in the leaflet compared to the root. Additionally there was evidence of differentiation/distinct cell phenotype between the cells populating the root and leaflet structures. However, the low cellularity indicates that these valves may be more useful for adult implantation rather than pediatric valve replacement. Higher levels of cellularity and remodeling may be required to enable growth and functional development of valve tissue. It is suspected that during development cardiac tissue adapts to changing mechanical loads and that cells populating the valve activate and remodel matrix as needed to deal with increasing hemodynamic demand(Aikawa, Whittaker et al. 2006). Fetal and pediatric valve tissue has much higher cell density and the cells are more proliferative and activated than in adult valves. More study will be needed to determine if a nearly quiescent valve dominated by a single ECM component will function long term in the adult and if it can adapt with a growing child.

#### **1.4.8 Hybrid TEHV Manufacturing Strategies**

Several TEHV strategies have combined features from the aforementioned categories for enhanced control of the fabrication process. Several examples are presented. Tedder and colleagues recently created a composite TEHV using stem cell seeded acellular starter matrices adhered with a biological adhesive and vacuum pressed into a valve shape (Tedder, Simionescu et al. 2010). This strategy approaches a completely biological valve, but is very labor intensive. Motor controlled electrospinning has also been used to create TEHV with prescribed polymer fiber architectures (Courtney, Sacks et al. 2006). Cells can also be co-sprayed into the fiber mesh (Stankus, Guan et al. 2006). The root and cusps however must be made separately and recombined (Sutherland, Perry et al. 2005). One failure mode for a TEHV is leaflet tissue contraction and subsequent valve insufficiency. The progressive contraction of the leaflet tissue is

attributed to cell driven remodeling by populating cells, and one strategy to address this mode of failure is to remove transplanted cells from the TEHV(Dijkman, Driessen-Mol et al. 2012; Syedain, Bradee et al. 2013; Syedain, Meier et al. 2013)). The hypothesis is that decellularizing the TEHV of contractile phenotypes (which were needed for the production of the tissue) and then recellularization the TEHV with non-contractile phenotypes will eliminate contraction of the leaflets (Syedain, Meier et al. 2013). Syedain et al has combined a biological polymer hydrogel molding technique with a decellularization strategy. They harness the cell remodeling and collagen production capabilities of encapsulated dermal fibroblasts in a fibrin hydrogel molded into a valve shape. They have demonstrated that fibroblasts reorganize and deposit addition matrix so that the resultant tissue is mechanically robust enough to be decellularized and function short term under simulated in-vitro pulmonary conditions (Syedain, Bradee et al. 2013; Syedain, Meier et al. 2013). Dijkman et al has used a similar strategy except they used a non-woven polymeric mesh shaped into leaflets held into a stented ring seeded with vascular derived (vein) myofibroblasts (Dijkman, Driessen-Mol et al. 2012). Both Dijkman et al and Syedain et al have reseeded their valves with bone marrow mesenchymal stem cells. This strategy has yet to be evaluated in-vivo long term.

Possible challenges that this TEHV strategy may face are related to the growth and the deliberate/intended engineering of the TEHV as quiescent and/or minimally populated with cells in order to preserve the geometry and prevent tissue contraction. The strategy depends on cell repopulation of the decellularized tissue with a non-contractile cell type. Recellularization been convincingly demonstrated at the surface of the tissues and into the interior of leaflets tissue with bone marrow mesenchymal stem cells which appear to be less contractile than the fibroblasts(Dijkman, Driessen-Mol et al. 2012; Syedain, Bradee et al. 2013). However, although the contractile effects may not be as immediately apparent, MSC are functionally capable of remodeling and contraction of ECM proteins particularly collagen (Awad, Butler et al. 2000; Nirmalanandhan, Levy et

al. 2006) and the valve leaflets may still contract long term. Contraction of collagen structure is dependent on both cell density and the matrix density(Nirmalanandhan, Levy et al. 2006), and controlling distribution and density of cells within in the tissue can be difficult using an outside-in seeding technique and it can depend on cell type (Colazzo, Sarathchandra et al. 2011). Additionally if these decell-recell strategies do successfully produce quiescent valve tissue, they may be suitable only for short term adult valve replacement and may be inappropriate for the adaptive and growing needs of pediatrics. The native pediatric valve remodels in response to changing hemodynamic loads(Aikawa, Whittaker et al. 2006) and the adult aortic valve responds to the cyclic stresses of normal cardiac function through constant synthesis and renewal of the valve interstitial ECM(Schneider and Deck 1981). This is part of what gives native valve tissue its durability. It has also been shown that cell activity is different depending on the location within the valve, and region differences in ECM synthesis may be critical for balanced tissue maintenance (Merryman, Youn et al. 2006).

Direct 3D tissue printing is a rapid prototyping technique where three dimensional structures are generated by extruding sequential layers of materials according to computer aided design (CAD) files (Cohen, Malone et al. 2006; Ballyns, Gleghorn et al. 2008; Ballyns and Bonassar 2009). Rapid prototyping has been used previously to create anatomical molds from which to create TEHV scaffolds (Sodian, Loebe et al. 2002; Nakayama, Takewa et al. 2014). More recently, entire valved conduits were 3D printed at 100% using poly (ethylene glycol) diacrylate (PEG-DA) and layer by layer photo-crosslinking with ultraviolet light (Filho AL 2009). Using multiple deposition syringes with different biomaterial formulations, it is possible to deposit valve and root specific microenvironments while maintaining anatomical geometry (Hockaday, Kang et al. 2012; Duan, Hockaday et al. 2013; Duan, Kapetanovic et al. 2014).

#### 1.4.9 Cell Sources for TEHV

The success of TEHV strategies depend on effective remodeling and maintenance by resident cells. Early studies demonstrated that allogenic cell sources cause an acute inflammatory response even in the presence of immunosuppressant treatment (Shinoka, Breuer et al. 1995). Subsequent strategies have focused on autologous differentiated cells and stem cells as sources for populating TEHV. Marker expression studies indicate that VIC exhibit phenotypes that are similar between the four valves (aortic, pulmonary, mitral, and tricuspid), but have significantly different expression profiles compared to other sources (arterial smooth muscle, vein, skin, pericardium) (Messier, Bass et al. 1994; Taylor, Allen et al. 2000; Maish, Hoffman-Kim et al. 2003; Taylor, Batten et al. 2003). Maish *et al* proposed tricuspid valve biopsy as a method for obtaining autologous VIC and VEC for and aortic TEHV, and their supporting study in sheep demonstrated that tricuspid valve cells could be isolated, cultured, and the tricuspid valve could remain functional (Maish, Hoffman-Kim et al. 2003). Unfortunately, the risk of operative morbidity or damage to the tricuspid valve has dampened the acceptance of the procedure. VIC phenotype appears to fall between vascular smooth muscle cells and skin fibroblasts, and both of these cell types have been explored as potential TEHV cell sources (Shinoka, Breuer et al. 1995; Hoffman-Kim, Maish et al. 2005). In engineered leaflets vascular smooth muscle cells isolated from veins and arteries performed better than dermal fibroblasts (Shinoka, ShumTim et al. 1997).

Autologous stem cells are being explored as a source of cells for TEHV, to see if they can be differentiated to duplicate the phenotype and function of native valve cells. Studies using *in vitro* bioreactors and implantation into an animal model have shown that bone marrow derived and circulating progenitors have the capacity to form both endothelial-like and interstitial-like cells when seeded on valve scaffolds (Perry, Kaushal et al. 2003; Sutherland, Perry et al. 2005; Ramaswamy, Gottlieb et al. 2010;

Sales, Mettler et al. 2010). Additionally, preliminary experiments with adipose derived mesenchymal stem cells (ADSC) indicate they could be suitable for TEHV (Colazzo, Chester et al. 2010; Colazzo, Sarathchandra et al. 2011). ADSC can be isolated in comparatively high numbers, can form endothelial-like cells (Colazzo, Chester et al. 2010), and have been shown in a partial tissue bioreactor study to have the ability to synthesize and process valve ECM components and are responsive to mechanical stress (Colazzo, Sarathchandra et al. 2011). Hoerstrup and colleagues have developed protocols and have carried out feasibility studies for several stem cell sources unique for pediatric applications. These cell sources include amniotic fluid, placenta, umbilical cord blood, and chorionic villi (Schmidt, Breyman et al. 2004; Schmidt, Mol et al. 2006; Schmidt, Mol et al. 2006; Schmidt, Achermann et al. 2008; Schmidt, Dijkman et al. 2010). Autologous pediatric stem cells could be procured prenatally or perinatally and used to fabricate a TEHV or stored in a cell bank for future use (Weber, Zeisberger et al. 2011; Weber, Emmert et al. 2012). There is already some existing infrastructure for tissue banking with public and private tissue banks that store amniotic fluid derived cells and umbilical cord blood cells (Verter Copyright 2000 - 2010 ). More research is necessary to determine if stem cell sources can adequately mimic native valve phenotypes and if they maintain that phenotype long term. Stem cell multi-lineage potential and plasticity may require that the biomaterials and the culture conditions be optimized for valve cell differentiation. A recent study highlights this, as stem cells can shift towards cartilage and osteogenic lineages which could predispose TEHV to calcification (Emani, Mayer et al. 2011).

### ***1.5 Need for Improved Remodeling and Heterogeneity in TEHV***

Classical TEHV strategies have made two key discoveries. First, *in-vivo* dynamic culture prior to implantation improves the performance of the tissue engineered valve. Second, autologous stem cells can differentiate into both endothelial-like and interstitial-like cell

phenotypes (Shinoka, Ma et al. 1996; Hoerstrup, Sodian et al. 2000; Stock, Nagashima et al. 2000; Sutherland, Perry et al. 2005; Schmidt, Mol et al. 2006; Sales, Mettler et al. 2010). However, the persistent problem for synthetic polymeric TEHV is that the material has been too stiff for the leaflets or the leaflets have stiffened over time resulting in stenotic function. For autologous biological polymeric valves, tissue contraction of the leaflets resulted in valve insufficiency. These classical TEHV strategies are limited by their fabrication strategy and materials. Using one material means that the even superficial regional mechanical differences, such as compliant leaflets and the stiff root, are neglected and the microenvironment limits heterogeneous differentiation of seeded cells. In native aortic valve there are four main structures of the valve (Figure 1.1A). The relatively stiff root to which the leaflets are attached connects to the aorta. Three thin flexible leaflets open completely when blood is ejected from the ventricle, and close to keep blood from flowing back into the ventricle. The three sinuses are pocket/parachutes structures shaped out of the root and leaflets. Vortexices form in these sinuses so that the leaflets efficiently close. The coronary ostia which lead to the coronary arteries provide oxygenated blood to the heart. In native valve tissue within each of the four main structures there is a heterogeneous distribution of mechanical properties, cell phenotypes, and extracellular matrix (ECM) proteins and fiber structure (Butcher, Mahler et al. 2011) (Figure 1.1D). For instance, the leaflets have a layered structure, with the fibrosa, spongiosa, and ventricularis having different flexure and stiffness properties (Courtney, Sacks et al. 2006). The heterogeneity and asymmetric shape of the valve affects its ability distribute load, and as a result the strain response of the valve to load during the different phases of cardiac cycle is non-uniform (Dagum, Green et al. 1999) (Figure 1.1C) . The root is populated by contractile smooth muscle cells, while the leaflets contain fibroblastic “interstitial” cells (Butcher, Mahler et al. 2011) (Figure 1.1B). The phenotype of these cells is highly sensitive to

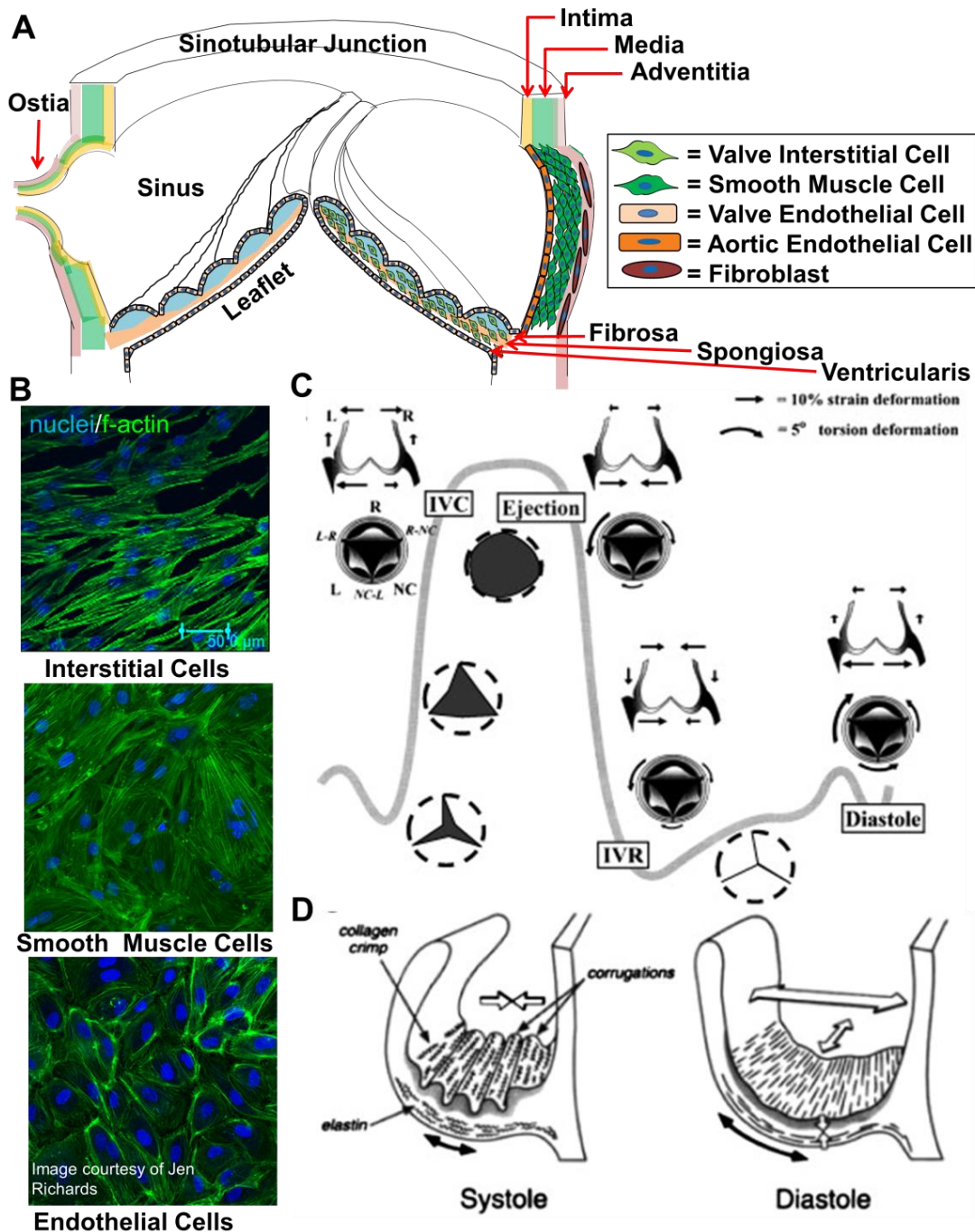


**Figure 1.1 Aortic valve complex structure and function.**

A) The heart's aortic valve has a layered fiber and multi-cellular structure within the root and leaflets. It also has a complex shape important for hemodynamic function. (B) AVIC, ASSMC, and VEC cells drive regional cellular response to load. (C) The root and cusps undergo dynamic anisotropic deformation with each heartbeat. (Dagum, Green et al. 1999) (D) Role of elastin and collagen microstructure in mediating valve cusp deformation (Schoen 1997). (Figure modified from (Sutherland, Perry et al. 2005; Butcher, Mahler et al. 2011)).

intrinsic microenvironment cues and extrinsic mechanical stimulation (Butcher and Nerem 2004; Butcher, Penrod et al. 2004; Butcher and Nerem 2006). A tissue engineered heart valve will require this balanced heterogeneity in order to have sufficient durability and healthy remodeling upon implantation.

The field has been shifting focus towards hybrid TEHV strategies which have focused on mimicking complex shape and heterogeneity (Sutherland, Perry et al. 2005; Stankus, Guan et al. 2006; Tedder, Simionescu et al. 2010) (Figure 1.2). While these studies are promising, molding and/or shaping/suturing/gluing scaffolds by hand has fundamental limits. For the field of TEHV to move forward fabrication strategies need to be identified to incorporate heterogeneity, better control scaffold remodeling, and better control differentiation of seeded cells within TEHVs.

### ***1.6 Organization of the Dissertation***

The objective of this work is to develop a strategy to fabricate and condition multiple material heart valve scaffolds with fine geometric control and internal heterogeneity to guide scaffold remodeling and differentiation of 3D printed cells.

In Chapter 2, 3D printing enabled advances and remaining unaddressed needs in soft tissue engineering are reviewed

In Chapter 3, a study is presented that demonstrates 3D printing and photo-crosslinking hydrogels can be used to rapidly fabricate anatomical scaffolds exhibiting mechanical heterogeneity and cytocompatibility. This manufacturing process was demonstrated with PEG-DA and a Fab@Home™ printing platform, but the findings indicate that this method could be adapted for use with other photocrosslinkable polymers. The findings

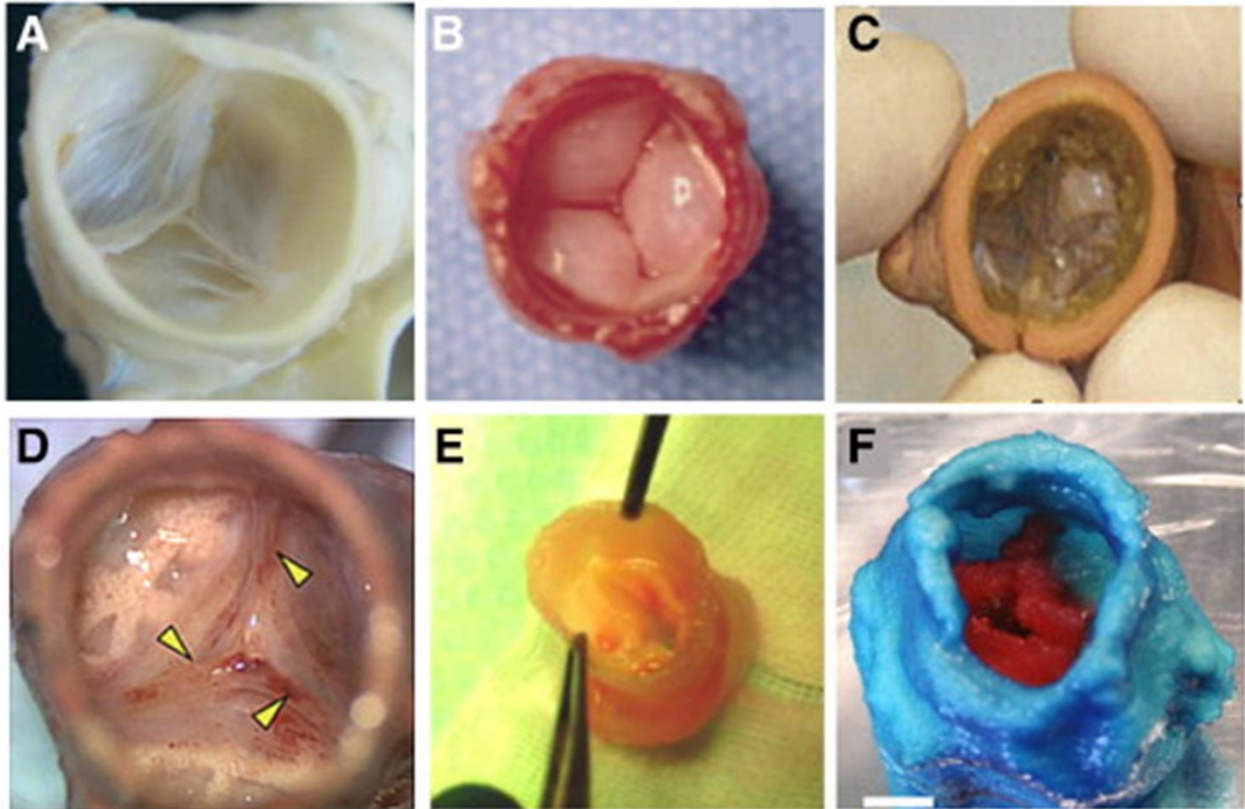


**Figure 1.2 Recent hybrid TEHV strategies to achieve improved anatomical and microstructural heterogeneity.**

(A) Biomatrix/polymer composite valve synthesized by impregnating biodegradable poly(hydroxybutrate) into decellularized porcine aortic valve. (B) Tissue engineered semilunar heart valve synthesized using polyglycolic acid (PGA) and poly-L-lactic acid (PLLA) fiber. (C) Valve constructs generated by molding collagen layers that were assembled by bio-adhesive. (D) Valve conduit created by implanting a mold that encapsulates the tissue in vivo. (E) Fibrin-based valve with autologous cells. (F) Heterogeneous PEG-DA scaffold valves fabricated via 3D tissue printing. (Review figure from (Butcher, Mahler et al. 2011)).

presented in this chapter are encouraging steps toward improved valve scaffold designs for both adult and pediatric valve disease.

In Chapter 4, a study is presented that explores variables associated with photocrosslinking hydrogels and their effects on viability for a 3D printable MEGEL:PEGDA 3350 mixture containing valve cells or mesenchymal stem cells. Contrary to numerous 2D cytotoxicity studies, the findings presented in this chapter indicate that in a 3D hydrogel culture environment and fabrication setting, Irgacure 2959 can produce more viable encapsulated cells than VA086 in a higher stiffness hydrogel. Intracellular oxidative stress was not significantly greater in hydrogel conditions of more Irgacure 2959 photoinitiator radicals. Normalized oxidative stress ratios suggest that increasing VA086 radicals induced higher intracellular oxidative stress. These findings demonstrate that suppression of intracellular oxidative stress using catalase pretreatment does not disrupt hydrogel crosslinking but it does not rescue cell viability from photoinitiator damage.

In Chapter 5, methods to generate geometries exhibiting heterogeneous distribution of printable materials and living cells throughout a fabricated shape are presented. These algorithms provide a tool for 3D printing heterogeneous, anatomically relevant tissue engineered constructs. Using the first algorithm demonstrated, the target print image is generated through processing any image into printable vector format. A second algorithm that generates spatially heterogeneous gradients with multiple materials in arbitrary directions in 2D and 3D is presented. Finally a combination algorithm that separates intrinsic tissue heterogeneity present in medical imaging scans of anatomical tissue into printable format files is described. The fabrication of the files generated by these algorithms was demonstrated using the Fab@Home™ platform by printing heterogeneous hydrogel scaffolds. We also present a method to quantify the fidelity of

heterogeneous layers, and to quantify the degree of cell mixing and blending of different materials within the layer.

In Chapter 6, a brief review of heart valve bioreactors is presented.

In Chapter 7, a dynamic conditioning system specifically for the culture of 3D bioprinted and *ex-vivo* native tissue heart valves is presented. The custom water driven diaphragm-type bioreactor was engineered with a conditioning chamber specifically designed for ultrasound monitoring of valve root wall and leaflet motion and tissue strain. The parameters of the flexible control and water driven flow loop system can be scaled or throttled to enable dynamic culture of aortic and pulmonary valves at adult or pediatric stroke volume and flow rates. Additionally the system can be scaled for parallel conditioning in multiple reactor chambers containing individual valves. Physiological systolic and diastolic loading conditions can be achieved or diastolic only loading conditions can be induced with the control setup. The results presented in this chapter will enable exploration into the optimal conditions and loading regimes needed to drive remodeling and tissue development in 3D printed hydrogel valves. 3D bioprinted heart valves composed of methacrylated gelatin, methacrylated hyaluronic acid, and PEGDA were cultured up to 14 days under static and dynamic conditions to validate the system and to induce remodeling in bioprinted valves.

In Chapter 8, concluding summaries and future recommendations are presented.

## REFERENCES

- Administration, F. a. D. (October 2004). Report to Congress: Barriers to the Availability of Medical Devices Intended for the Treatment or Diagnosis of Diseases and Conditions that Affect Children. U. S. D. o. H. a. H. Services.
- Ahmann, K. A., J. S. Weinbaum, et al. "Fibrin degradation enhances vascular smooth muscle cell proliferation and matrix deposition in fibrin-based tissue constructs fabricated *in vitro*." Tissue Eng Part A **16**(10): 3261-3270.
- Aikawa, E., P. Whittaker, et al. (2006). "Human semilunar cardiac valve remodeling by activated cells from fetus to adult: implications for postnatal adaptation, pathology, and tissue engineering." Circulation **113**(10): 1344-1352.
- Alsoufi, B., Z. Al-Halees, et al. (2009). "Mechanical valves versus the Ross procedure for aortic valve replacement in children: propensity-adjusted comparison of long-term outcomes." J Thorac Cardiovasc Surg **137**(2): 362-370 e369.
- Ballyns, J. J. and L. J. Bonassar (2009). "Image-guided tissue engineering." J Cell Mol Med **13**(8A): 1428-1436.
- Ballyns, J. J., D. L. Cohen, et al. "An optical method for evaluation of geometric fidelity for anatomically shaped tissue-engineered constructs." Tissue Eng Part C Methods **16**(4): 693-703.
- Ballyns, J. J., J. P. Gleghorn, et al. (2008). "Image-guided tissue engineering of anatomically shaped implants via MRI and micro-CT using injection molding." Tissue Eng Part A **14**(7): 1195-1202.
- Bellhouse, B. J., F. H. Bellhouse, et al. (1968). "Fluid mechanics of the aortic root with application to coronary flow." Nature **219**(5158): 1059-1061.
- Billiar, K. L. and M. S. Sacks (2000). "Biaxial mechanical properties of the native and glutaraldehyde-treated aortic valve cusp: Part II--A structural constitutive model." J Biomech Eng **122**(4): 327-335.
- Bottio, T., V. Tarzia, et al. "The changing hydrodynamic performance of the decellularized intact porcine aortic root: considerations on in-vitro testing." J Heart Valve Dis **19**(4): 485-491.
- Burdick, J. A. and K. S. Anseth (2002). "Photoencapsulation of osteoblasts in injectable RGD-modified PEG hydrogels for bone tissue engineering." Biomaterials **23**(22): 4315-4323.
- Butcher, J. T., G. J. Mahler, et al. (2011). "Aortic valve disease and treatment: the need for naturally engineered solutions." Adv Drug Deliv Rev **63**(4-5): 242-268.
- Butcher, J. T. and R. M. Nerem (2004). "Porcine aortic valve interstitial cells in three-dimensional culture: comparison of phenotype with aortic smooth muscle cells." J Heart Valve Dis **13**(3): 478-485; discussion 485-476.
- Butcher, J. T. and R. M. Nerem (2006). "Valvular endothelial cells regulate the phenotype of interstitial cells in co-culture: effects of steady shear stress." Tissue Eng **12**(4): 905-915.
- Butcher, J. T., A. M. Penrod, et al. (2004). "Unique morphology and focal adhesion development of valvular endothelial cells in static and fluid flow environments." Arterioscler Thromb Vasc Biol **24**(8): 1429-1434.

- Butcher, J. T., C. A. Simmons, et al. (2008). "Review - Mechanobiology of the aortic heart valve." Journal of Heart Valve Disease **17**: 62-73.
- Cameron, D. E. and L. A. Vricella (2007). "What is the proper place of the Ross procedure in our modern armamentarium?" Curr Cardiol Rep **9**(2): 93-98.
- Carabello, B. A. and W. J. Paulus (2009). "Aortic stenosis." Lancet **373**(9667): 956-966.
- Carapetis, J. R. (2008). "Rheumatic heart disease in Asia." Circulation **118**(25): 2748-2753.
- Carapetis, J. R., A. C. Steer, et al. (2005). "The global burden of group A streptococcal diseases." Lancet Infect Dis **5**(11): 685-694.
- Chanda, J., R. Kuribayashi, et al. (1997). "Valved conduit in the descending thoracic aorta in juvenile sheep: a useful, cost-effective model for accelerated calcification study in systemic circulation." Biomaterials **18**(19): 1317-1321.
- Cheng, A., P. Dagum, et al. (2007). "Aortic root dynamics and surgery: from craft to science." Philos Trans R Soc Lond B Biol Sci **362**(1484): 1407-1419.
- Christie, G. W. (1992). "Anatomy of aortic heart valve leaflets: the influence of glutaraldehyde fixation on function." Eur J Cardiothorac Surg **6 Suppl 1**: S25-32; discussion S33.
- Chue, W. L., G. R. Campbell, et al. (2004). "Dog peritoneal and pleural cavities as bioreactors to grow autologous vascular grafts." J Vasc Surg **39**(4): 859-867.
- Clark, E. B. (1996). "Pathogenetic mechanisms of congenital cardiovascular malformations revisited." Semin Perinatol **20**(6): 465-472.
- Cohen, D. L., E. Malone, et al. (2006). "Direct freeform fabrication of seeded hydrogels in arbitrary geometries." Tissue Eng **12**(5): 1325-1335.
- Colazzo, F., A. H. Chester, et al. (2010). "Induction of mesenchymal to endothelial transformation of adipose-derived stem cells." Journal of Heart Valve Disease **19**: 736-744.
- Colazzo, F., P. Sarathchandra, et al. (2011). "Extracellular matrix production by adipose-derived stem cells: Implications for heart valve tissue engineering." Biomaterials **32**: 119-127.
- Colvee, E. and J. M. Hurlle (1983). "Malformations of the semilunar valves produced in chick embryos by mechanical interference with cardiogenesis. An experimental approach to the role of hemodynamics in valvular development." Anat Embryol (Berl) **168**(1): 59-71.
- Courtney, T., M. S. Sacks, et al. (2006). "Design and analysis of tissue engineering scaffolds that mimic soft tissue mechanical anisotropy." Biomaterials **27**(19): 3631-3638.
- Dagum, P., G. R. Green, et al. (1999). "Deformational dynamics of the aortic root: modes and physiologic determinants." Circulation **100**(19 Suppl): II54-62.
- Dajani, A. S. and K. A. Taubert (1992). "Re: Letter to the editor by Dr. Steven M. Pollack and author's response from Drs. Thomas J. Pallasch and Jorgen Slots. Committee on Rheumatic Fever, Endocarditis, and Kawasaki Disease of the American Heart Association." J Periodontol **63**(5): 488.
- de Simone, G., R. B. Devereux, et al. (1997). "Stroke volume and cardiac output in normotensive children and adults. Assessment of relations with body size and impact of overweight." Circulation **95**(7): 1837-1843.

- Dohmen, P. M., A. Lembcke, et al. (2002). "Ross operation with a tissue-engineered heart valve." Ann Thorac Surg **74**(5): 1438-1442.
- Duan, B., L. A. Hockaday, et al. (2013). "3D bioprinting of heterogeneous aortic valve conduits with alginate/gelatin hydrogels." J Biomed Mater Res A **101**(5): 1255-1264.
- Duan, B., E. Kapetanovic, et al. (2014). "Three-dimensional printed trileaflet valve conduits using biological hydrogels and human valve interstitial cells." Acta Biomater **10**(5): 1836-1846.
- El-Hamamsy, I., Z. Eryigit, et al. (2010). "Long-term outcomes after autograft versus homograft aortic root replacement in adults with aortic valve disease: a randomised controlled trial." Lancet **376**(9740): 524-531.
- Emani, S., J. E. Mayer, et al. (2011). "Gene regulation of extracellular matrix remodeling in human bone marrow stem cell-seeded tissue-engineered grafts." Tissue Engineering Part A **17**: 2379-2388.
- Erdbrugger, W., W. Konertz, et al. (2006). "Decellularized xenogenic heart valves reveal remodeling and growth potential *in vivo* ." Tissue Eng **12**(8): 2059-2068.
- Filho AL, C. P., Noritomi PY, Silva JVL, Colangelo NW, Kang H, Lipson H, Butcher JT, Malone E, Neto PI. ( 2009). "Construction and Adaptation of an Open Source Rapid Prototyping Machine for Biomedical Research Purposes - a Multinational Collaborative Development." Advanced Research in Virtual and Rapid Prototyping.
- Flanagan, T. C., C. Cornelissen, et al. (2007). "The *in vitro* development of autologous fibrin-based tissue-engineered heart valves through optimised dynamic conditioning." Biomaterials **28**(23): 3388-3397.
- Flanagan, T. C., J. S. Sachweh, et al. (2009). "*In vivo* remodeling and structural characterization of fibrin-based tissue-engineered heart valves in the adult sheep model." Tissue Eng Part A **15**(10): 2965-2976.
- Frigiola, A., A. Varrica, et al. (2010). "Neo-aortic Valve and Root Complex Evolution After Ross Operation in Infants, Children, and Adolescents." Ann Thorac Surg **90**(4): 1278-1285.
- Gandaglia, A., A. Bagno, et al. (2011). "Cells, scaffolds and bioreactors for tissue-engineered heart valves: a journey from basic concepts to contemporary developmental innovations " European Journal of Cardio-thoracic Surgery **39**: 523-531.
- Glen, S., J. Burns, et al. (2004). "Prevalence and development of additional cardiac abnormalities in 1448 patients with congenital ventricular septal defects." Heart **90**(11): 1321-1325.
- Gottlieb, D., T. Kunal, et al. "*In vivo* monitoring of function of autologous engineered pulmonary valve." J Thorac Cardiovasc Surg **139**(3): 723-731.
- Gottlieb, D., T. Kunal, et al. (2010). "*In vivo* monitoring of function of autologous engineered pulmonary valve." J Thorac Cardiovasc Surg **139**(3): 723-731.
- Grunkemeier, G. L., H. H. Li, et al. (2000). "Long-term performance of heart valve prostheses." Curr Probl Cardiol **25**(2): 73-154.
- Grunkemeier, G. L., H. H. Li, et al. (1999). "Heart valve replacement: a statistical review of 35 years' results." J Heart Valve Dis **8**(5): 466-470; discussion 470-461.
- Gunatillake, P. A. and R. Adhikari (2003). "Biodegradable synthetic polymers for tissue engineering." Eur Cell Mater **5**: 1-16; discussion 16.

- Hammermeister, K., G. K. Sethi, et al. (2000). "Outcomes 15 years after valve replacement with a mechanical versus a bio-prosthetic valve: final report of the Veterans Affairs randomized trial." J Am Coll Cardiol **36**(4): 1152-1158.
- Hayashida, K., K. Kanda, et al. (2007). "Development of an *in vivo* tissue-engineered, autologous heart valve (the biovalve): preparation of a prototype model." J Thorac Cardiovasc Surg **134**(1): 152-159.
- Hayman, E. G., M. D. Pierschbacher, et al. (1985). "Vitronectin--a major cell attachment-promoting protein in fetal bovine serum." Exp Cell Res **160**(2): 245-258.
- Hinton, R. B. and K. E. Yutzey (2011). "Heart Valve Structure and Function in Development and Disease." Annual Review of Physiology **73**(1): null.
- Hockaday, L. A., K. H. Kang, et al. (2012). "Rapid 3D printing of anatomically accurate and mechanically heterogeneous aortic valve hydrogel scaffolds." Biofabrication **4**(3): 035005.
- Hoffman-Kim, D., M. S. Maish, et al. (2005). "Comparison of three myofibroblast cell sources for the tissue engineering of cardiac valves." Tissue Engineering **11**: 288-301.
- Hoffman, J. I. (1995). "Incidence of congenital heart disease: II. Prenatal incidence." Pediatr Cardiol **16**(4): 155-165.
- Hoffman, J. I. and S. Kaplan (2002). "The incidence of congenital heart disease." J Am Coll Cardiol **39**(12): 1890-1900.
- Hong, T., M. S. Maish, et al. (2000). "Reproducible echocardiography in juvenile sheep and its application in the evaluation of a pulmonary valve homograft implant." Contemp Top Lab Anim Sci **39**(5): 20-25.
- Ilbawi, A. M., D. E. Spicer, et al. (2007). "Morphologic study of the ascending aorta and aortic arch in hypoplastic left hearts: surgical implications." J Thorac Cardiovasc Surg **134**(1): 99-105.
- Jashari, R., Y. Goffin, et al. (2010). "European homograft bank: twenty years of cardiovascular tissue banking and collaboration with transplant coordination in Europe." Transplant Proc **42**(1): 183-189.
- Karamlou, T., K. Jang, et al. (2005). "Outcomes and associated risk factors for aortic valve replacement in 160 children: a competing-risks analysis." Circulation **112**(22): 3462-3469.
- Konstantinov, I. E., T. Karamlou, et al. (2006). "Truncus arteriosus associated with interrupted aortic arch in 50 neonates: a Congenital Heart Surgeons Society study." Ann Thorac Surg **81**(1): 214-222.
- Konuma, T., E. J. Devaney, et al. (2009). "Performance of CryoValve SG decellularized pulmonary allografts compared with standard cryopreserved allografts." Ann Thorac Surg **88**(3): 849-854; discussion 554-845.
- Kosaki, K., A. Mendoza, et al. (1996). "Cervical flexion: its contribution to normal and abnormal cardiac morphogenesis." Teratology **54**(3): 135-144.
- Koul, B., C. J. Lindholm, et al. (2002). "Ross operation for bicuspid aortic valve disease in adults: is it a valid surgical option?" Scand Cardiovasc J **36**(1): 48-52.
- Liao, J., E. M. Joyce, et al. (2008). "Effects of decellularization on the mechanical and structural properties of the porcine aortic valve leaflet." Biomaterials **29**(8): 1065-1074.

- Lupinetti, F. M., J. Warner, et al. (1997). "Comparison of human tissues and mechanical prostheses for aortic valve replacement in children." Circulation **96**(1): 321-325.
- Maish, M. S., D. Hoffman-Kim, et al. (2003). "Tricuspid valve biopsy: A potential source of cardiac myofibroblast cells for tissue-engineered cardiac valves." Journal of Heart Valve Disease **12**: 264-269.
- Marijon, E., P. Ou, et al. (2007). "Prevalence of rheumatic heart disease detected by echocardiographic screening." N Engl J Med **357**(5): 470-476.
- Mayosi, B. M. (2007). "Contemporary trends in the epidemiology and management of cardiomyopathy and pericarditis in sub-Saharan Africa." Heart **93**(10): 1176-1183.
- McBride, K. L., L. Marengo, et al. (2005). "Epidemiology of noncomplex left ventricular outflow tract obstruction malformations (aortic valve stenosis, coarctation of the aorta, hypoplastic left heart syndrome) in Texas, 1999-2001." Birth Defects Res A Clin Mol Teratol **73**(8): 555-561.
- Messier, R. H., B. L. Bass, et al. (1994). "Dual structural and functional phenotypes of the porcine aortic-valve interstitial population-Characteristics of the leaflet myofibroblast." Journal of Surgical Research **57**: 1-21.
- Meuris, B., S. Ozaki, et al. (2001). "Influence of species, environmental factors, and tissue cellularity on calcification of porcine aortic wall tissue." Semin Thorac Cardiovasc Surg **13**(4 Suppl 1): 99-105.
- Meuris, B., S. Ozaki, et al. (2003). "Bio-prosthetic tissue calcification: influence of blood contact and arterial pressure. an experimental study in rats and sheep." J Heart Valve Dis **12**(3): 392-399; discussion 399.
- Miller, D. V., W. D. Edwards, et al. (2006). "Endothelial and smooth muscle cell populations in a decellularized cryopreserved aortic homograft (SynerGraft) 2 years after implantation." J Thorac Cardiovasc Surg **132**(1): 175-176.
- Mocumbi, A. O., M. B. Ferreira, et al. (2008). "A population study of endomyocardial fibrosis in a rural area of Mozambique." N Engl J Med **359**(1): 43-49.
- Nakayama, Y., Y. Takewa, et al. (2014). "In-body tissue-engineered aortic valve (Biovalve type VII) architecture based on 3D printer molding." Journal of Biomedical Materials Research Part B: Applied Biomaterials: n/a-n/a.
- Naso, F., A. Gandaglia, et al. "Differential distribution of structural components and hydration in aortic and pulmonary heart valve conduits: Impact of detergent-based cell removal." Acta Biomater **6**(12): 4675-4688.
- O'Brien, M. F., S. Goldstein, et al. (1999). "The SynerGraft valve: a new acellular (nongluteraldehyde-fixed) tissue heart valve for autologous recellularization first experimental studies before clinical implantation." Semin Thorac Cardiovasc Surg **11**(4 Suppl 1): 194-200.
- O'Cearbhaill, E. D., M. Murphy, et al. (2010). "Behavior of human mesenchymal stem cells in fibrin-based vascular tissue engineering constructs." Ann Biomed Eng **38**(3): 649-657.
- Ouyang, D. W., C. T. Salerno, et al. (1998). "Long-term evaluation of orthotopically implanted stentless bio-prosthetic aortic valves in juvenile sheep." J Invest Surg **11**(3): 175-183.

- Owens, S. T., C. Gomez-Fifer, et al. (2006). "Thrombus formation in the native aortic root in patients with hypoplastic left heart syndrome." Pediatr Cardiol **27**(3): 385-387.
- Padera R Fi J r , S. F. J., Ed. (2008). Pathology of Cardiac Surgery. Cardiac Surgery in the Adult. . New York, McGraw-Hill.
- Perry, T. E., S. Kaushal, et al. (2003). "Bone marrow as a cell source for tissue engineering heart valves." Annals of Thoracic Surgery **75**: 761-767.
- Rahimtoola, S. H. (2010). "Choice of prosthetic heart valve in adults an update." J Am Coll Cardiol **55**(22): 2413-2426.
- Rajani, B., R. B. Mee, et al. (1998). "Evidence for rejection of homograft cardiac valves in infants." J Thorac Cardiovasc Surg **115**(1): 111-117.
- Ramaswamy, S., D. Gottlieb, et al. (2010). "The role of organ level conditioning on the promotion of engineered heart valve tissue development in-vitro using mesenchymal stem cells." Biomaterials **31**: 1114-1125.
- Ramaswamy, S., D. Gottlieb, et al. (2010). "The role of organ level conditioning on the promotion of engineered heart valve tissue development in-vitro using mesenchymal stem cells." Biomaterials **31**(6): 1114-1125.
- Ribeiro, P. S., K. H. Jacobsen, et al. (2008). "Priorities for women's health from the Global Burden of Disease study." Int J Gynaecol Obstet **102**(1): 82-90.
- Rieder, E., M. T. Kasimir, et al. (2004). "Decellularization protocols of porcine heart valves differ importantly in efficiency of cell removal and susceptibility of the matrix to recellularization with human vascular cells." J Thorac Cardiovasc Surg **127**(2): 399-405.
- Rieder, E., G. Seebacher, et al. (2005). "Tissue engineering of heart valves: decellularized porcine and human valve scaffolds differ importantly in residual potential to attract monocytic cells." Circulation **111**(21): 2792-2797.
- Roberts, W. C. and J. M. Ko (2005). "Frequency by decades of unicuspid, bicuspid, and tricuspid aortic valves in adults having isolated aortic valve replacement for aortic stenosis, with or without associated aortic regurgitation." Circulation **111**(7): 920-925.
- Robinson, P. S., S. L. Johnson, et al. (2007). "Functional Tissue-Engineered Valves from Cell-Remodeled Fibrin with Commissural Alignment of Cell-Produced Collagen." Tissue Eng.
- Robinson, P. S., S. L. Johnson, et al. (2008). "Functional tissue-engineered valves from cell-remodeled fibrin with commissural alignment of cell-produced collagen." Tissue Eng Part A **14**(1): 83-95.
- Rosano, A., L. D. Botto, et al. (2000). "Infant mortality and congenital anomalies from 1950 to 1994: an international perspective." J Epidemiol Community Health **54**(9): 660-666.
- Ross, D. N. (1967). "Replacement of aortic and mitral valves with a pulmonary autograft." Lancet **2**(7523): 956-958.
- Sacks, M. S., F. J. Schoen, et al. (2009). "Bioengineering challenges for heart valve tissue engineering." Annu Rev Biomed Eng **11**: 289-313.
- Sales, V. L., B. A. Mettler, et al. (2010). "Endothelial progenitor cells as a sole source for ex vivo seeding of tissue-engineered heart valves." Tissue Engineering Part A **16**: 257-267.

- Sani, M. U., K. M. Karaye, et al. (2007). "Prevalence and pattern of rheumatic heart disease in the Nigerian savannah: an echocardiographic study." Cardiovasc J Afr **18**(5): 295-299.
- Sauren, A. A., M. C. van Hout, et al. (1983). "The mechanical properties of porcine aortic valve tissues." J Biomech **16**(5): 327-337.
- Sayk, F., I. Bos, et al. (2005). "Histopathologic findings in a novel decellularized pulmonary homograft: an autopsy study." Ann Thorac Surg **79**(5): 1755-1758.
- Schmidt, D., J. Achermann, et al. (2008). "Cryopreserved amniotic fluid-derived cells: A life-long autologous fetal stem cell source for heart valve tissue engineering." Journal of Heart Valve Disease **17**: 446-455.
- Schmidt, D., J. Achermann, et al. (2008). "Cryopreserved amniotic fluid-derived cells: a lifelong autologous fetal stem cell source for heart valve tissue engineering." J Heart Valve Dis **17**(4): 446-455; discussion 455.
- Schmidt, D., C. Breymann, et al. (2004). "Umbilical cord blood derived endothelial progenitor cells for tissue engineering of vascular grafts." Annals of Thoracic Surgery **78**: 2094-2098.
- Schmidt, D., P. E. Dijkman, et al. (2010). "Minimally-invasive implantation of living tissue engineered heart valves: a comprehensive approach from autologous vascular cells to stem cells." J Am Coll Cardiol **56**(6): 510-520.
- Schmidt, D., A. Mol, et al. (2006). "Living autologous heart valves engineered from human prenatally harvested progenitors." Circulation **114**: I125-I131.
- Schmidt, D., A. Mol, et al. (2006). "Engineering of biologically active living heart valve leaflets using human umbilical cord-derived progenitor cells." Tissue Engineering **12**: 3223-3232.
- Schmidt, D., U. A. Stock, et al. (2007). "Tissue engineering of heart valves using decellularized xenogeneic or polymeric starter matrices." Philos Trans R Soc Lond B Biol Sci **362**(1484): 1505-1512.
- Schoen, F. J. (2006). "New frontiers in the pathology and therapy of heart valve disease: 2006 Society for Cardiovascular Pathology, Distinguished Achievement Award Lecture, United States-Canadian Academy of Pathology, Atlanta, GA, February 12, 2006." Cardiovasc Pathol **15**(5): 271-279.
- Schoen, F. J. (2008). "Evolving concepts of cardiac valve dynamics: the continuum of development, functional structure, pathobiology, and tissue engineering." Circulation **118**(18): 1864-1880.
- Seeger, J. M. and N. Klingman (1985). "Improved endothelial cell seeding with cultured cells and fibronectin-coated grafts." J Surg Res **38**(6): 641-647.
- Shinoka, T., C. K. Breuer, et al. (1995). "Tissue engineering heart valves: valve leaflet replacement study in a lamb model." Annals of Thoracic and Surgery **60**: S513-516.
- Shinoka, T., P. X. Ma, et al. (1996). "Tissue-engineered heart valves. Autologous valve leaflet replacement study in a lamb model." Circulation **94**(9 Suppl): I1164-1168.
- Shinoka, T., D. ShumTim, et al. (1997). "Tissue-engineered heart valve leaflets - Does cell origin affect outcome?" Circulation **96**: 102-107.
- Sierad, L., A. Simionescu, et al. "Design and Testing of a Pulsatile Conditioning System for Dynamic Endothelialization of Polyphenol-Stabilized Tissue Engineered Heart Valves." Cardiovascular Engineering and Technology **1**(2): 138.

- Simon, P., M. T. Kasimir, et al. (2003). "Early failure of the tissue engineered porcine heart valve SYNERGRAFT in pediatric patients." Eur J Cardiothorac Surg **23**(6): 1002-1006; discussion 1006.
- Sodian, R., S. P. Hoerstrup, et al. (2000). "Early *in vivo* experience with tissue-engineered trileaflet heart valves." Circulation **102**(19 Suppl 3): III22-29.
- Sodian, R., S. P. Hoerstrup, et al. (2000). "Evaluation of biodegradable, three-dimensional matrices for tissue engineering of heart valves." Asaio J **46**(1): 107-110.
- Sodian, R., M. Loebe, et al. (2002). "Application of stereolithography for scaffold fabrication for tissue engineered heart valves." Asaio J **48**(1): 12-16.
- Sodian, R., P. Schaefermeier, et al. (2010). "Use of human umbilical cord blood-derived progenitor cells for tissue-engineered heart valves." Ann Thorac Surg **89**(3): 819-828.
- Sodian, R., J. S. Sperling, et al. (1999). "Tissue engineering of a trileaflet heart valve-early *in vitro* experiences with a combined polymer." Tissue Eng **5**(5): 489-494.
- Stamm, C., A. Khosravi, et al. (2004). "Biomatrix/polymer composite material for heart valve tissue engineering." Ann Thorac Surg **78**(6): 2084-2092; discussion 2092-2083.
- Stankus, J. J., J. Guan, et al. (2006). "Microintegrating smooth muscle cells into a biodegradable, elastomeric fiber matrix." Biomaterials **27**(5): 735-744.
- Steinhoff, G., U. Stock, et al. (2000). "Tissue engineering of pulmonary heart valves on allogenic acellular matrix conduits: *in vivo* restoration of valve tissue." Circulation **102**(19 Suppl 3): III50-55.
- Stephens, E. H., C. A. Durst, et al. "Mitral valvular interstitial cell responses to substrate stiffness depend on age and anatomic region." Acta Biomater **7**(1): 75-82.
- Sumikura, H., Y. Nakayama, et al. (2014). "*In vitro* evaluation of a novel autologous aortic valve (biovalve) with a pulsatile circulation circuit." Artif Organs **38**(4): 282-289.
- Sutherland, F. W., T. E. Perry, et al. (2005). "From stem cells to viable autologous semilunar heart valve." Circulation **111**(21): 2783-2791.
- Sutherland, F. W. H., T. E. Perry, et al. (2005). "From stem cells to viable autologous semilunar heart valve." Circulation **111**: 2783-2791.
- Syedain, Z. H., A. R. Bradee, et al. (2013). "Decellularized tissue-engineered heart valve leaflets with recellularization potential." Tissue Eng Part A **19**(5-6): 759-769.
- Syedain, Z. H., L. A. Meier, et al. (2013). "Tubular heart valves from decellularized engineered tissue." Ann Biomed Eng **41**(12): 2645-2654.
- Tanner, K., N. Sabrine, et al. (2005). "Cardiovascular malformations among preterm infants." Pediatrics **116**(6): e833-838.
- Taylor, P. A., P. Batten, et al. (2003). "The cardiac valve interstitial cell." International Journal of Biochemistry & Cell Biology **35**: 113-118.
- Taylor, P. M., S. P. Allen, et al. (2000). "Phenotypic and functional characterization of interstitial cells from human heart valves, pericardium and skin." Journal of Heart Valve Disease **9**: 150-158.
- Tedder, M. E., J. Liao, et al. (2009). "Stabilized collagen scaffolds for heart valve tissue engineering." Tissue Eng Part A **15**(6): 1257-1268.

- Tedder, M. E., A. Simionescu, et al. (2010). "Assembly and Testing of Stem Cell-Seeded Layered Collagen Constructs for Heart Valve Tissue Engineering." Tissue Eng Part A.
- Thubrikar, M., L. P. Boshier, et al. (1979). "The mechanism of opening of the aortic valve." J Thorac Cardiovasc Surg **77**(6): 863-870.
- Thubrikar, M., S. P. Nolan, et al. (1980). "The cyclic changes and structure of the base of the aortic valve." Am Heart J **99**(2): 217-224.
- Veinot, J. P. (2006). "Pathology of inflammatory native valvular heart disease." Cardiovasc Pathol **15**(5): 243-251.
- Verter, F. (Copyright 2000 - 2010 December 7, 2010). "Parent's Guide to Cord Blood Foundation - With Emphasis on how to Evaluate Bank Services." from <http://parentsguidecordblood.org/content/usa/banklists/index.shtml?navid=14>.
- Vricella, L. A., J. A. Williams, et al. (2005). "Early experience with valve-sparing aortic root replacement in children." Ann Thorac Surg **80**(5): 1622-1626; discussion 1626-1627.
- Wang, Q., A. J. McGoron, et al. (2010). "A novel small animal model for biocompatibility assessment of polymeric materials for use in prosthetic heart valves." J Biomed Mater Res A **93**(2): 442-453.
- Weber, B., M. Y. Emmert, et al. (2012). "Prenatally engineered autologous amniotic fluid stem cell-based heart valves in the fetal circulation." Biomaterials **33**: 4031-4043.
- Weber, B., S. M. Zeisberger, et al. (2011). "Prenatally harvested cells for cardiovascular tissue engineering: Fabrication of autologous implants prior to birth." Placenta **32**: S316-S319.
- Yacoub, M. H. and J. J. Takkenberg (2005). "Will heart valve tissue engineering change the world?" Nat Clin Pract Cardiovasc Med **2**(2): 60-61.
- Yamanami, M., Y. Yahata, et al. "Preparation of in-vivo tissue-engineered valved conduit with the sinus of Valsalva (type IV biovalve)." J Artif Organs **13**(2): 106-112.
- Yamanami, M., Y. Yahata, et al. (2010). "Preparation of in-vivo tissue-engineered valved conduit with the sinus of Valsalva (type IV biovalve)." J Artif Organs **13**(2): 106-112.
- Ye, X., Q. Zhao, et al. (2009). "Enhancement of mesenchymal stem cell attachment to decellularized porcine aortic valve scaffold by *in vitro* coating with antibody against CD90: a preliminary study on antibody-modified tissue-engineered heart valve." Tissue Eng Part A **15**(1): 1-11.
- Yusuf, S., M. Vaz, et al. (2004). "Tackling the challenge of cardiovascular disease burden in developing countries." Am Heart J **148**(1): 1-4.
- Zilla, P., J. Brink, et al. (2008). "Prosthetic heart valves: catering for the few." Biomaterials **29**(4): 385-406.

## CHAPTER 2

### APPLICATIONS OF 3D PRINTING TO ENGINEERING SOFT AND HETEROGENEOUS TISSUES

#### **2.1 3D Printing Fabrication Systems**

3D printing is a technology that is finding application in the automotive, aviation, manufacturing, jewelry, do-it yourself, food, and medical industries. The beginnings of the technology were in 1976 with the invention of the inkjet printer and then in 1984 with the invention of stereolithography (SLA) to create solid three dimensional objects from digital information. The application of 3D printing to tissue engineering (TE) within the last two decades has been heavily exploratory – investigators testing the limits and utility of new and modified 3D printers, using new materials and schemes to incorporate living cells, and applying the technology to mimic different tissue systems for regenerative medicine, modeling, and diagnostics.

3D printing, solid freeform fabrication (SFF), and additive manufacturing are general terms to describe techniques that build three dimensional objects in layers through sequential delivery of energy and/or material (Billiet, Vandenhoute et al. 2012). 3D printing is being explored for tissue engineering due to the flexibility, ease of patient specific geometry, and multiple material control.

In this chapter, recent progress and remaining unaddressed needs for utilizing 3D printing for engineering replacement and regenerative tissues, and engineering support devices for *in vitro* culture and loading of engineered tissue are reviewed.

### ***2.1.1 3D printing to create living tissue - encapsulation and direct cell printing vs post fabrication cell seeding of scaffolds***

The challenge of tissue engineering is characterizing and then translating understanding of native tissue and cell biology into an application format to engineer models that recapitulate organ and tissue function. Towards this goal, investigators are working on multiple fronts to identify biological mechanisms, evaluating and inventing new materials, and improving fabrication and culture technologies. With numerous studies indicating that cell-cell interactions and cell-material interactions in the 3D microenvironment in native tissue is fundamentally different than in 2D (Muller, Davenport et al. 2009; Bellis, Bernabe et al. 2013; Chitcholtan, Asselin et al. 2013), the emphasis and how cell biology is investigated is shifting from 2D culture models to 3D culture models (Lund, Yener et al. 2009; Baker and Chen 2012; Santos, Hernandez et al. 2012). 3D printing is of interest as a tool, both because it enables mechanistic and biological investigation in 3D at multiple scales from cell (Lee, Moon et al. 2008; Torgersen, Ovsianikov et al. 2012) to tissue (Chang, Boland et al. 2011; Fedorovich, Alblas et al. 2011); but, also because it could translate into a means for fabricating living tissue at a scale suitable for clinical use (Koch, Deiwick et al. 2012; Luangphakdy, Walker et al. 2013). Two strategies feature prominently in TE for how to mimic native tissue – the first is to use a 3D biomaterial scaffold to mimic extracellular matrix as a necessary guide and support template for cells, the second is to position cells and allow them to self-organize through cell-cell interactions and to create their own matrix (Leong, Cheah et al. 2003; Norotte, Marga et al. 2009; Marga, Jakab et al. 2012). The strategy selection, scaffold or scaffold-free, and the tissue-target influences the choice of 3D printing fabrication process and the materials.

Specific requirements for tissue engineering constructs will change depending on the tissue target and the intended application, but there are four critical categories to

consider - 1) biological requirements, 2) mechanical requirements, 3) transport requirements, and 4) geometric requirements (Butscher, Bohner et al. 2011; Billiet, Vandenhoute et al. 2012; Derby 2012). For example, a tissue engineered heart valve intended for implantation might need an active population of remodeling interstitial-like cells that function with the endothelial cells to maintain valve function. A tissue engineered heart valve would also be required to function mechanically the moment it is implanted; however transport is less of a problem for heart valves compared to other tissues because the valves are in contact with circulating blood in the heart, and the valve has a complex non-self-supporting geometry (Butcher, Simmons et al. 2008; Gandaglia, Bagno et al. 2011; Hockaday, Kang et al. 2012).

Materials that are compatible for a specific 3D printer may not fit the needs for engineering a specific tissue or strategy. In direct cell printing or in bioprinting, cells are incorporated into the tissue engineered construct during the printing process, and in the process they are exposed to the fabrication conditions. Determining the effect of the fabrication conditions during 3D printing on deposited cells – mixing (Cohen, Lo et al. 2011), extrusion (Kang, Hockaday et al. 2013), light exposure on cell integrity (Cui, Breitenkamp et al. 2012), viability, function, and differentiation capability– is a critical step for 3D printing. Different cell types have different responses to fabrication conditions, including sensitivity to photoinitiator (Williams, Malik et al. 2005). By contrast in a strategy where only the scaffold is 3D printed and then cell seeded post-fabrication, the fabrication conditions do not have to be cell permissive as long as the end result scaffold is. This allows a wider range of scaffold materials and printing processes, but it also depends on cell infiltration and integration from the surface of the scaffold in which limits control over cell spatial organization within the engineered tissue.

### **2.1.2 3D Printing devices to grow engineered tissue: 3D printing in molds and support structures/devices for culture and mechanical loading**

Both indirect and direct rapid prototyping methods have been used for tissue engineering (Ballyns, Cohen et al. 2010). For indirect rapid prototyping, the scaffold and/or cells are processed out of a rapid prototyping mold (Tan, Chua et al. 2013) and for direct rapid prototyping the scaffold and/or cells are directly processed by the rapid prototyping machine (Yeong, Chua et al. 2004). Indirect rapid prototyping has been used to make high fidelity injection molds of patient-specific anatomy for tissue engineered constructs (Ballyns, Gleghorn et al. 2008; Wilson, van Blitterswijk et al. 2011). Another utilization of 3D printing is to produce support devices for culture and mechanical loading of the engineered tissue. Many tissue engineering strategies depend on an *in vitro* culture phase in order to control cell phenotype, to promote extracellular matrix (ECM) deposition, and to strengthen the tissue prior to implantation. To mimic physiologic loading conditions, which may be nearly as complex as the native tissue, support structures/devices that mimic proximal or impacting tissues have recently been built using 3D printing. Ballyns et al created an *in vitro* knee bioreactor to dynamically load TE-menisci with patient specific geometry during culture (Ballyns and Bonassar 2011). A similar loaded organ culture device was made for intervertebral disks, but the parts were machined (Haglund, Moir et al. 2011). Several authors have discussed the unaddressed need for more 3D printable materials, usually in the context for direct fabrication of the engineered tissue; but, more materials for fabricating support and culture devices, screened for biocompatibility and long term contact with culture media, would help advance bioreactor technology.

### **2.2 Recent progress in TE for soft tissue**

For soft tissue TE 3D printing has been utilized for developing tissue engineered skin, cartilage, myocardium, heart valves, blood vessels and vasculature, scaffolds for brain

injury and neural sheets. 3D printing because of its multi-material capability and geometric control, has enabled direct rapid prototyping of multi-level and multi-cell type structure into engineered soft tissue, been used to demonstrate the potential for in-situ printing into non-uniform wounds, and has been used in strategies that have advanced to in-vivo animal models and clinical trials.

### **2.2.1 Skin tissue engineering: Advances in multi-level structure, in-situ printing into contoured wounds, *in vivo* animal model**

Skin is the largest organ in the body, it provides critical barrier functions, and it is densely innervated to perceive and discern between pain, temperature and touch (Groeber, Holeiter et al. 2011). Treatment of burns is an area of need where TE could be beneficial as the gold standard for deep burns- autologous split-thickness skin grafts can be of limited use for patients who have few unburned areas left on their body (Boettcher-Haberzeth, Biedermann et al. 2010). The ultimate goal for tissue engineered skin is a construct featuring both the epidermis and dermis that improves healing quality and avoids scar formation (MacNeil and 2007 2007). Skin is a complex 3D tissue, with several cell types arranged/organized within distinct microenvironments for specific functions (Michael, Sorg et al. 2013). This complexity is what has motivated the use of 3D printing for tissue engineering skin, for control of heterogeneity, pattern, and cell density.

Both nozzle-based and printer-based 3D printing approaches have been used for skin tissue engineering. In one example study, Koch et al used a laser based direct-write printing technique to print fibroblasts and keratinocytes into 3D cell-hydrogel structures (Koch, Deiwick et al. 2012). Although Koch et al. demonstrated using red and green labeled cells that they could fabricate more complex geometry grid-layered patterns, they specifically focused their study on tissue formation and intercellular junctions within

the tissue constructs and used a simplified geometry. In a subsequent *in vivo* study the 3D printed bi-layer skin equivalents were implanted into full thickness wounds in the dorsal skin fold of mice for 11 days (Michael, Sorg et al. 2013). The printed skin implants form a tissue similar to native skin and appear to integrate into the wound accompanied by capillary and blood vessel formation in the matriderm layer. However, native skin characteristic rete ridge structures are absent in the TE skin, during remodeling the TE skin thinned, and vascularization of the TE skin was incomplete. Michael et al anticipates that rete ridge structures could be printed in and that adding endothelial cells into the printed constructs will improve vascularization based on work showing endothelial cells in combination with fibroblasts and/or keratinocytes in biomaterial scaffolds or decellulized dermis form capillary like tubules in the dermis (Black, Hudon et al. 1999; Schechner, Crane et al. 2003).

Using a nozzle-based 3D printing system to print collagen, gelatin, and fibroblasts, Lee et al demonstrated that cells and micro channels could be printed into cellularized scaffolds and that cell viability was improved with perfusion (Lee, Lee et al. 2010). The gelatin was used as a sacrificial material to form channels in the collagen. In a study by the same group, TE skin with stratified keratinocytes and fibroblasts was 3D printed into a contoured wound model using a nozzle-based 3D printer and nebulized mist of crosslinking agent (Lee, Debasitis et al. 2009). A collagen layer was deposited, partially crosslinked with mist, cells were deposited into the collagen layer, additional crosslinker was applied, and then the next layer was deposited. This nebulized crosslinker approach enabled print and build on a non-uniform surface without a bath or supporting frame.

These TE skin studies have demonstrated the ability to control cell density, spatial distribution of multiple materials and cell types, and geometric complexity with 3D

printing. Additionally, TE skin has reached the *in vivo* animal model stage. Key advances include creation of densely cellularized tissue with cell-cell junctions, multicellularity with keratinocyte and fibroblast layers which may be critical for the ability to recruit vasculature and for ECM production (compared to acellular controls or single cell type TE skin studies), incorporation of perfusion channels to augment capillary self-assembly and/or invasion from surrounding tissue, and filling of a non-level wound model which indicates feasibility for in situ treatment of burn wounds.

A critical feature of the laser induced forward transfer printing technique for laser assisted bioprinting is that it is not yet automated and is dependent on coating and loading of glass slides. By contrast, nozzle based printing system used by Lee et al is a semi-automated system that allows for fast switching of materials (Lee, Debasitis et al. 2009; Lee, Lee et al. 2010). However, even with a non-automated process, Koch et al demonstrated spatial capabilities of this type of 3D printing higher than what were immediately needed for the biological/mechanistic investigation for which they used a simplified structure (Koch, Deiwick et al. 2012; Michael, Sorg et al. 2013) that was subsequently used in an *in vivo* mouse study. Printing studies assessing the capabilities of a given 3D printer in terms of viability/impact on cells and geometry are generally followed by biological/mechanistic investigations of biomaterial and cell combinations and geometries. Identifying to what degree and which aspects of a native tissue to mimic for TE, is an iterative process based on what works *in vitro* and then *in vivo*. TE skin studies have already demonstrated that 3D printing enable multi-material and multi-cell spatial control, but the next step with the technology is to incorporate additional complexity with additional cell types into TE skin, such as peripheral nerve cells, Schwann cells, melanocytes, and endothelial cells.

## **2.2.2 Cartilage tissue engineering – advances in ear, intervertebral disc, and meniscus TE and hybrid technologies for engineering cartilage**

3D printing has been used extensively for cartilage tissue engineering. While direct cell-scaffold 3D printing has been used for cartilage TE to demonstrate that multiple regions of mechanical properties and/or cells can be deposited within cartilage structures, indirect rapid prototyping of tissue using 3D printed molds for tissue-injection molding has been used to create implants that have progressed to *in vivo* animal testing. Load bearing and non-load bearing tissue engineered cartilage has been fabricated into specific structures including the ear auricle and knee menisci using 3D printing.

### Ear TE and non-load bearing cartilage

The ear is a complex structure with several different tissue types within it. At the most basic level it contains skin, bone, cartilage, and nerve tissue. The pinna or auricle of the outer ear collects sound and directs it to the outer ear canal and is composed of cartilage and skin, and the ear drum aka tympanic membrane vibrates when sound waves reach it. The Eustachian tube connects the middle ear to the back of the nose and it equalizes pressure between the inner ear and the outside (Ciorba and Martini 2006; Swarts, Alper et al. 2013). The three tiny bones of the ossicular chain - the hammer, then anvil, and the stirrup - transfer vibrations from the ear drum to the cochlea. The cochlea is a spiral shaped, fluid filled inner ear structure lined with cilia that move when vibrated and cause a nerve impulse to form. Investigators are interested in applying TE for replacement/treatment of several of these tissues/parts including: the tympanic membrane (Teh, Marano et al. 2013); the inner ear cells (Devarajan, Forrest et al. 2013); the Eustachian tube (Kanemaru, Umeda et al. 2013); the ossicular chain (D'Alessandro, Danti et al. 2012) and the auricular cartilage (Liu, Zhang et al. 2010; Mannoor, Jiang et al. 2013; Nimeskern, Martinez Avila et al. 2013;

Nimeskern, van Osch et al. 2013; Reiffel, Kafka et al. 2013; Sterodimas and de Faria 2013; Xue, Feng et al. 2013).

Both direct and indirect rapid prototyping 3D printing techniques have been used for ear TE, primarily to engineer auricular cartilage. Microtia is a congenital deformity where the auricle of the ear is underdeveloped. The gold standard treatment is to sculpt autologous costal cartilage from the anterior ends of the ribs into the shape of the auricle, and implant it under the periauricular skin (Reiffel, Kafka et al. 2013). However, limitations to this treatment include limited donor site supply, donor site morbidity, inherent difficulty in sculpting an anatomically accurate patient specific auricular shape, and auricular cartilage differs biomechanically from costal cartilage. While auricular cartilage is not load bearing in the same sense that joint cartilage is, it is elastic and experiences tension, bending, and compression.

Auricle-TE has moved from merely coating a frame scaffold shaped like an ear to engineering underlying cartilage. To create an auricle frame coated with skin cells, Cai et al used FDM to print acrylonitrile butadiene styrene (ABS) plastic shaped like the ear auricle, coated it with fibronectin, seeded fibroblasts onto the structure, and then after two weeks of static culture seeded keratinocytes on top of the fibroblasts (Cai, Azangwe et al. 2005). Studies focused on TE cartilage for the ear have used both direct rapid prototyping 3D printing of cartilage (Mannoor, Jiang et al. 2013) and indirect rapid prototyping 3D printing of molds for cartilage (Liu, Zhang et al. 2010; Reiffel, Kafka et al. 2013). Mannoor et al 3D printed bionic ears using an extrusion nozzle-based Fab@Home printer, using alginate and chondrocytes for the auricle and silver nanoparticle infused silicone to form cochlea-shaped electrodes (Mannoor, Jiang et al. 2013). After the TE-auricle/Ag-cochlea was cultured in-vitro for up to 10 weeks, the chondrocytes were viable throughout the auricle and in contact with the Ag-cochlea and

the histology staining of the tissue was consistent with the development of new cartilage. They also performed an electrical and sound test to demonstrate that the bionic ears could hear/listen. For indirect fabrication, Reiffel et al used 3D printed 7-part molds to mold patient-specific auricle TE-cartilage using collagen and bovine auricular chondrocytes (Reiffel, Kafka et al. 2013). They found that auricle constructs implanted into the subcutaneous pockets of rats for up to 3 months showed significant differences between cellular constructs and acellular constructs. Cellular constructs demonstrated marked cartilage deposition and elastin content, while the acellular constructs only showed invasion of mononuclear cells and capsule formation around the constructs.

One critical consideration for fabrication strategy is sufficiency and necessity. Reiffel et al found that treatment of the cartilage and the auricle structure as a single material/structure produced excellent in-vivo results, and the tissue injection molding strategy is generally less demanding in terms of material used to make the TE-construct (for example viscosity appropriate for deposition or speed of crosslinking for layer build and working time) compared to direct cell-scaffold 3D printing (Reiffel, Kafka et al. 2013). For the outer ear tissue, injection molds may be the extent of the need for 3D printing. However, while indirect rapid prototyping may prove sufficient for creation of effective TE auricles, the level of complexity needed for the inner and middle ear structures may require direct 3D printing (Mannoor, Jiang et al. 2013).

### Meniscus

The meniscus is a load bearing cartilage structure in the knee. For meniscus injury, the most common treatment is partial or total removal of the injured tissue. Investigators have been pursuing TE strategies to repair or 'patch' defects and tears in the meniscus, treatment with growth factors to stimulate growth and healing, and whole TE-menisci for replacement (Haddad, Pakravan et al. 2013). Clinical use of cadaveric menisci is

problematic due to scarcity of donor tissue, risk of disease transmission, and difficulties in matching native joint anatomical shape. The size and the shape of the native meniscus are critical for distribution of pressure across the joint. Both indirect and direct rapid prototyping 3D printing has been used for meniscus tissue engineering. 3D printing has enabled advances in whole meniscus tissue engineering for replicating the characteristic meniscus shape.

Cohen et al directly printed menisci constructs in alginate with chondrocytes and demonstrated 1 week viability and sterility using the Fab@Home extrusion nozzle-based system (Cohen, Malone et al. 2006). Ballyns et al having used MRI and FDM in ABS to generate a 3D printed mold of a knee meniscus, used tissue-injection molding to make TE-cartilage menisci constructs that retained their shape throughout 8 weeks of static culture, showed viability throughout, but did not achieve the mechanics or ECM content of native menisci (Ballyns, Gleghorn et al. 2008). In a subsequent study, Ballyns et al investigated the effects of dynamic loading during in-vitro culture using platens designed to replicate anatomic loading that were 3D printed in ABS plastic (Ballyns and Bonassar 2011). They also evaluated shape fidelity for directly 3D printed alginate hydrogel menisci compared to injection molded menisci for uCT and MRI generated geometries (Ballyns, Cohen et al. 2010). Less deviation from the target geometry was observed for injection molding compared to 3D printing using the Fab@Home, and it could be argued that if a single starting composition is used for a tissue construct, such as the meniscus, indirect fabrication is a more practical strategy. However, optimized printing and handling of different materials for a given 3D printing system can improve the quality and fidelity of printed constructs (Cohen, Lo et al. 2011; Kang, Hockaday et al. 2013).

### **2.2.3 Cardiovascular tissue engineering**

Cardiovascular disease is the leading cause of death worldwide (Yusuf, Reddy et al. 2001; Labarthe and Dunbar 2012). Cardiovascular tissue is a critical target for tissue engineering and regenerative medicine. 3D printing has been used in strategies to create engineered tissue for myocardium repair/regeneration, heart valve replacement, and blood vessels.

#### Myocardium

The central pathology for congestive heart failure, the loss of cardiomyocytes and the subsequent loss of myocardial contractile function is unaddressed by current clinical strategies (Zimmermann, Schneiderbanger et al. 2002). When injury or ischemia occurs, the heart forms scar tissue rather than regenerating cardiomyocytes. Using cell transplantation therapy with direct cell injection has shown improved ventricular function in injured hearts (Gaetani, Barile et al. 2009). The strategy for a tissue engineered myocardium patch is to increase the efficiency of cell delivery, provide mechanical support to the diseased myocardium, and provide appropriate microenvironment to transplanted cells.

Gaetani et al used an extrusion based 3D printer, the BioScaffolder system, to print RGD-modified alginate hydrogel and encapsulated human fetal cardiomyocyte progenitor cells into porous patches (Gaetani, Doevendans et al. 2012). They showed that human fetal cardiomyocyte progenitor cell viability could be maintained if a pore structure was incorporated into the patch, and the printing and static culture conditions did not block the proliferation rate of encapsulated cells or change the cardiac commitment of the cells. This study demonstrated the utility of controlling the internal pore structure for TE-myocardium patches. They also anticipated that additional cell

types and multi-cellular could be implemented into the patches, because injection cell therapies found that non-cardiomyocyte also improved ventricular function.

### Heart Valves

Heart valves ensure one way blood flow through the cardiovascular system. Critically diseased or defective heart valves require replacement, and tissue engineering has the potential to address the limitations of non-living prosthetics and to grow, remodel, and integrate with the patient, which is of particular relevance to pediatrics (Butcher, Mahler et al. 2011). Direct rapid prototyping 3D printing is being explored for aortic heart valve tissue engineering due to the complex 3D geometry and heterogeneity that is critical for valve function (Hockaday, Kang et al. 2012; Duan, Hockaday et al. 2013). 3D printed tissue engineered heart valves have multiple cells and material properties directly incorporated into TE constructs in addition to complex anatomical shape and have progressed to *in vitro* static culture.

Hockaday et al used an extrusion nozzle-based Fab@Home 3D printer to fabricate aortic valve shaped polyethylene-glycol diacrylate (PEG-DA)/alginate scaffolds with two different mechanical properties in the leaflets and root structures and then post fabrication seeded aortic valve interstitial cells into them (Hockaday, Kang et al. 2012). A high degree of scaffold shape fidelity was achieved although it was affected by hydrogel swelling, and cells when seeded onto the scaffold had cell viability. However, cell infiltration into the scaffold was minimal and only a single cell type was used. In a subsequent study, Duan et al directly 3D printed aortic smooth muscle cells and valve interstitial cells into the valve root and leaflet using a gelatin and alginate hydrogel combination (Duan, Hockaday et al. 2013). Cellularized valve constructs were cultured up to 7 days and expressed regional valve markers.

### Blood Vessels and Microvasculature 3D Printing

Large blood vessels, branched vessel networks within organs, and microvasculature are TE targets. Large blood vessels have been engineered with some success using a self-assembly strategy by rolling and fusing cell sheets into tube structures and then conditioning in a bioreactor prior to implantation. This strategy of engineering vascular grafts has reached clinical testing (L'Heureux, Paquet et al. 1998; McAllister, Maruszewski et al. 2009). 3D printing has been explored for more complex geometries than these simple tube structures. 3D extrusion printing, both cell-laden hydrogel direct printing and scaffold-free cell aggregate printing, has been used to print tubular and/or branched vessel structures that have been cultured *in vitro* (Norotte, Marga et al. 2009; Skardal, Zhang et al. 2010; Xu, Chai et al. 2012).

A critical need for tissue engineering thick tissues and full scale organs. is engineering a functional vasculature into the tissue for transport of nutrients, oxygen, and waste products. 3D printing has enabled significant progress towards filling the need for complex branching and variable vessel size within a network that all lies within another tissue. Cui et al used a modified HP Deskjet 500 thermal inkjet printer to fabricate grid-like TE-microvasculature structures (Cui and Boland 2009). Human microvascular endothelial cells were mixed with thrombin and calcium ions and loaded into inkjet cartridges and then deposited drop by drop into a layer of fibrinogen, to form cellularized fibrin grid structures. The cells proliferated and formed a confluent lining inside the fibrin channel after 21 days *in vitro* culture. The integrity of the vasculature was tested using red fluorescently tagged dextran molecules. After 14 days culture red dye could leak through the endothelial cells, but by 21 days dextran could be excluded from the printed structures due to improvement in the endothelial cell lining.

Miller et al used 3D printing for a 3D sacrificial molding technique to generate a network of TE microvasculature within a monolithic tissue (Miller, Stevens et al. 2012). Using a thermal extrusion and drawing 3D printer a rigid open lattice of carbohydrate glass filaments was printed, the filament structure was coated with poly(D-lactide-co-glycolide), and then a suspension of cells and precursor was poured to encapsulate the lattice and crosslinked. The coating on the filament structure enabled dissolved carbohydrates of the glass to flow out of the channels not through the bulk of the TE construct. Critical advancements for this technology included getting the glass to have appropriate mechanical and temperature handling, but also to be transparent and compatible with photopolymerization. Miller et al demonstrated the technology with cellularized agarose, alginate, PEG, fibrin, and Matrigel tissue constructs. With this 3D printing strategy it is possible to make multilayered vascular network structures within the interior of a tissue, control variation in filament/vessel size, and create perfusable gradients. Endothelial cells were seeded/perfused into the channels of tissue constructs after the glass filaments were dissolved and removed, and they formed a continuous lumen during culture. Additionally, single and multicellular sprouts formed from patterned vasculature into the surrounding gel/cells. A significant part of Miller et al's study demonstrated that the microvasculature enabled preservation of viability and function for densely seeded tissues, and they tested up to 40 million cells/ml in their constructs (native tissue approximately 10-500 million cells/ml). This is significant for engineering any tissue that is vascularized, and Miller et al demonstrated the carbohydrate glass printing technology with liver and kidney cells, both critical soft tissue engineering targets. While strategies for engineering functional vascular networks could advance TE for tissue engineered skin and thin myocardial patches, for high density and higher order complex tissues such as liver and kidney inherent vascularization is probably essential.

## **2.2.4 3D printing for Higher Order Complex Tissue**

Characterization of the biology, function, and organization of tissues and resident cells is incomplete and ongoing for even seemingly simple tissue systems. However, the challenges for tissue engineering become compounded as tissue complexity and multifunctionality increase. 3D printing has been applied to engineering higher order complex tissues ultimately for the purpose of regenerative medicine, and it has also been used to better understand cell-material interactions and tissue development. 3D printing has enabled advances in liver tissue engineering, neural tissue engineering, heterogeneous soft and hard tissues, and mechanistic studies.

### Liver 3D Printing Advances

Acute and chronic liver failure is a major problem in human health and due to the limited number of donors, low survival rate after transplantation, and high cost of liver transplantation operations liver tissue engineering is a significant target for regenerative medicine (Wang, Yan et al. 2007). On the spectrum of tissue within the body, the liver is an ambitious engineering target. The liver is an intricate tissue with multiple functions including biosynthesis, biotransformation, and excretion. It has complex branched vasculature and bile ductular systems in addition to a variety of cell types, matrices, and regulatory factors. 3D printing has enabled some advances in liver tissue engineering by identifying some fabrication and construct conditions affecting hepatocyte viability. Investigators have found that 3D structure is important to hepatocyte stability. Wang et al 3D printed gelatin and hepatocytes into porous stacked grid structures using an extrusion based printer, where the temperature-based solidification of gelatin enabled for build of a many layered structure (38 layers) which could be post-fabrication crosslinked with glutaraldehyde to stabilize the structure (Wang, Yan et al. 2006). Wang et al found that hepatocytes survive within 3D matrix structures but die when the structures break down. Although the hepatocyte constructs had high viability for more

than 2 months, monitoring enzyme activity indicated that necrosis was occurring in constructs during the whole culture period. The study demonstrated that some liver specific functions, albumin and urea synthesis, were maintained by the hepatocytes in these printed constructs.

### Neural 3D Printing Advances

3D printing has been applied for peripheral nerve repair TE, tissue engineered neural sheets, scaffold strategies to help with traumatic brain injury, and testing nervous system cell-material interactions. Advances in scaffold-free printing where a support cell is used to make Schwann cell aggregates printable has enabled functional neuron bridging that has advanced to *in vivo* testing. *In vitro* studies have shown that neurons can retain their electrophysiological characteristics after printing, and multicellular and multi-material constructs can be printed out of astrocytes and neurons with a high degree of spatial control.

Scaffold-free printing with cell aggregates using an extrusion based printer has been used to make TE grafts designed to bridge severed nerves, which have progressed to *in vivo* animal model testing. Initially Schwann cell-only constructs were attempted, however Marga et al found that Schwann cells had insufficient cell-cell adhesion to make printable bio-ink/cell aggregates (Marga, Jakab et al. 2012). An addition of different cell type can be used to modulate the scaffold-free bio-inks. Bone marrow derived mesenchymal stem cells were sufficiently cell-cell adhesive to be printable, had previously been shown to transdifferentiate into Schwann cells, and had previously been used to support nerve regeneration, so Marga et al combined Schwann cells with bone marrow derived stem cells to form cell aggregates which were printed into multichannel tube structures. After 7 days *in vitro* culture the multichannel construct was implanted as a nerve graft to bridge the sciatic nerve in rats, and after 3 weeks 40% of

the axons present in the sciatic nerve stump had reached the other side through the graft. Scaffold extrusion based 3D printing has been used to fabricate gelatin and hyaluronan into 3D open channel scaffolds without cells as a temporary support for brain trauma injury which have been implanted into rats (Zhang, Yan et al. 2007).

Direct cell and scaffold printing has also been used for neural TE. Xu et al. used inkjet printing to print thrombin/CaCl<sub>2</sub>/cells into fibrinogen to form 3D neural sheet constructs (Xu, Gregory et al. 2006). Rat primary embryonic hippocampal and cortical neurons were printed into patterns and 3D fibrin/cell structures using a thermal nozzle inkjet printing process and then evaluated the functionality of printed cells using immunostaining and a patch clamp setup. The results supported that in addition to tolerating inkjet printing fabrication conditions (90% viability), neurons could maintain their neuronal phenotype and were able to regrow both axonal and dendritic processes after printing and could retain their electrophysiological properties. The speed of the inkjet printing technique may be a critical condition to avoid detrimental neuron response to heat shock and the effects of shear stress by the nozzles.

Lee et al used the same nozzle-based 3D printer and nebulized mist crosslinking strategy they used for skin printing and applied it to neural TE (Lee, Pinckney et al. 2009). Neurons and astrocytes were directly printed into single layer and multi-layer collagen constructs with cross and ring geometries. Single cell type and multi-cell type constructs were printed during the study and cultured *in vitro* for up to 15 days. They demonstrated that a high degree of spatial control within the constructs could be obtained and that neurons and astrocytes had similar viability between control and printed cells. They also observed that adjusting printed cell density could improve connectivity and growth and neurite outgrowth was dependent on collagen gel concentration. The same printing technology was used to print cells from a neonatal

derived cerebellum cell line into a composite collagen and vascular endothelial growth factor (VEGF) releasing fibrin construct (Lee, Polio et al. 2010). The study demonstrated that multiple hydrogel types (pH sensitive and enzymatically crosslinked) could be printed into constructs for neural TE, and VEGF releasing fibrin promoted migration and proliferation of cerebellum cells encapsulated in adjacent collagen regions. Findings from 3D printed *in vitro* models and the testing of materials and cells under simplified or controlled conditions have contributed to the knowledge base of TE. The advantage of doing *in vitro* studies with 3D printing is that the results have the potential to be directly applicable because of the pairing of basic science with the means of fabrication.

### Heterogeneous Tissue Engineering

3D printing technologies are capable of printing multiple cell types and materials into TE scaffolds, but only a few strategies have advanced to evaluating the consequences of heterogeneity and multi-cellularity *in vivo*. Recent work by Fedorovich et al has focused on evaluation of heterogeneous, multi-cell type functionality and development/differentiation within printed TE constructs *in vitro* and *in vivo*. They have printed bone and cartilage combination constructs and implanted into mice ultimately intended for treatment of osteochondral defects (Fedorovich, Schuurman et al. 2012). Another separate study has implanted printed bone and blood vessel combination constructs to enable functional blood supply for engineered bone (Fedorovich, Wijnberg et al. 2011). For these studies a Bioscaffolder pneumatic dispensing printer system was used in a direct cell and scaffold fabrication strategy to extrude cell-laden hydrogels into chessboard structures and into multilayered tube-within-cube structures that were crosslinked post fabrication in calcium chloride solution.

For osteochondral constructs, bone marrow derived mesenchymal stem cells and osteoinductive biphasic calcium phosphate particles were mixed into one alginate

solution and articular chondrocytes were mixed into another alginate solution and printed into constructs with different alginate/cell regions. For osteo-endothelial constructs, both matrigel and alginate solutions were used to print bone marrow derived mesenchymal stem cells and endothelial progenitor cells.

These studies demonstrated that heterogeneous printing resulted in heterogeneous tissue formation during *in vivo* culture. ECM produced by the cells corresponded to the deposited cell type, and the scaffold mixture or hydrogel type could be used to direct and influence matrix production of encapsulated cells. Depending on the encapsulating scaffold material, cells maintained the original printed organization or migrated out of the pattern to different degrees. New blood vessel formation and ingrowth was enabled by the presence of endothelial progenitor cells. While the scaffolds printed by Fedorovich (Fedorovich, Schuurman et al. 2012) are centimeter scale tissue constructs, the indications of a formation/recruitment of functional vascular network and blood supply is promising for the possibility of larger scale constructs.

### 3D Printing Mechanistic Studies and Tools for Engineering Complexity into Soft Tissue

Wang et al highlights obstacles hindering progress in bioartificial liver manufacturing using rapid prototyping technologies in terms of biological, biomaterial, and engineering challenges (Wang, Yan et al. 2007). Some of these obstacles/challenges are not unique to liver TE, but are challenges for the entire field of tissue engineering. One question that Wang et al raises is how can different time scales for maturation of different tissues and cell types be accommodated to ensure all cell types are functional? Depending on the fabrication and culture strategy, cell induction during *in vitro* culture, cell induction prior to assembly/printing, signals and mechanics directly incorporated into the matrix, or sequential release of signaling and growth factors may be necessary to engineer functional complex tissues.

There have been significant advances in hydrogel biomaterials research that could enable a high degree of control within the 3D matrix. Tibbet and Anseth describe these as technologies for 4D biology - 3D cell laden matrices that change or can be controlled over time (Tibbitt and Anseth 2012). Photodegradable/photoreleasible attachment peptides (Kloxin, Tibbitt et al. 2010), photocontrolled nanoparticles for triggered release of proteins (Azagarsamy, Alge et al. 2012), photodegradable mechanics and on demand pendant functionality release (Kloxin, Kasko et al. 2009), two photon immobilization of growth factors within hydrogels (Wylie, Ahsan et al. 2011), and mRNA transfection of mesenchymal stem cells prior to encapsulation in hydrogels (Mariner, Johannesen et al. 2012) are examples of tools that could be used with 3D printing to control the timing of development and maturation of 3D printed tissues with high spatial precision. Some of the fabrication strategies used to demonstrate these biomaterial technologies such as  $\mu$ SLA and 2-photon polymerization have already been used for 3D printing fabrication of tissue constructs (example cartilage) (Lee, Kang et al. 2008; Lee, Rhie et al. 2008) and for mechanistic studies to test how geometry and microenvironment direct cell morphogenesis or regeneration (Kloxin, Lewis et al. 2012). While the application of 3D printing to complex higher order tissue has been limited, as the knowledge base of biological mechanism and the number of possible materials compatible with 3D printing fabrication expand, tissue-level scale engineering of these types of tissue becomes more feasible.

## REFERENCES

- Azagarsamy, M. A., D. L. Alge, et al. (2012). "Photocontrolled nanoparticles for on-demand release of proteins." Biomacromolecules **13**: 2219-2224.
- Baker, B. M. and C. S. Chen (2012). "Deconstructing the third dimension - how 3D culture microenvironments alter cellular cues." Journal of Cell Science **125**: 3015-3024.
- Ballyns, J. J. and L. J. Bonassar (2011). "Dynamic compressive loading of image-guided tissue engineered meniscal constructs." Journal of Biomechanics **44**: 509-516.
- Ballyns, J. J., D. L. Cohen, et al. (2010). "An optical method for evaluation of geometric fidelity for anatomically shaped tissue-engineered constructs " Tissue Engineering Part C-Method **16**: 693-703.
- Ballyns, J. J., J. P. Gleghorn, et al. (2008). "Image-guided tissue engineering of anatomically shaped implants via MRI and micro-CT using injection molding " Tissue Engineering Part A **14**: 1195-1202.
- Bellis, A. D., B. P. Bernabe, et al. (2013). "Dynamic transcription factor activity profiling in 2D and 3D cell cultures." Biotechnology and Bioengineering **110**: 563-572.
- Billiet, T., M. Vandenhoute, et al. (2012). "A review of trends and limitations in hydrogel-rapid prototyping for tissue engineering." Biomaterials **33**: 6020-6041.
- Black, A. F., V. Hudon, et al. (1999). "A novel approach for studying angiogenesis: A human skin equivalent with a capillary-like network." Cell Biology and Toxicology **15**: 81-90.
- Boettcher-Haberzeth, S., T. Biedermann, et al. (2010). "Tissue engineering of skin." Burns **36**: 450-460.
- Butcher, J. T., G. J. Mahler, et al. (2011). "Aortic valve disease and treatment: The need for naturally engineered solutions." Advanced Drug Delivery Reviews **63**: 242-268.
- Butcher, J. T., C. A. Simmons, et al. (2008). "Review - Mechanobiology of the aortic heart valve." Journal of Heart Valve Disease **17**: 62-73.
- Butscher, A., M. Bohner, et al. (2011). "Structural and material approaches to bone tissue engineering in powder-based three-dimensional printing." Acta Biomaterialia **7**: 907-920.
- Cai, H., G. Azangwe, et al. (2005). "Skin cell culture on an ear-shaped scaffold created by fused deposition modelling." Bio-medical Materials and Engineering **15**: 375-380.
- Chang, C. C., E. D. Boland, et al. (2011). "Direct-write bioprinting three-dimensional biohybrid systems for future regenerative therapies." Journal of Biomedical Materials Research Part B-Applied Biomaterials **98B**: 160-170.
- Chitcholtan, K., E. Asselin, et al. (2013). "Differences in growth properties of endometrial cancer in three dimensional (3D) culture and 2D cell monolayer." Experimental Cell Research **319**: 75-87.
- Ciorba, A. and A. Martini (2006). "Tissue engineering and cartilage regeneration for auricular reconstruction." International Journal of Pediatric Otorhinolaryngology **70**: 1507-1515.

- Cohen, D. L., W. Lo, et al. (2011). "Increased mixing improves hydrogel homogeneity and quality of three-dimensional printed constructs " Tissue Engineering Part C-Method **17**: 239-248.
- Cohen, D. L., E. Malone, et al. (2006). "Direct freeform fabrication of seeded hydrogels in arbitrary geometries." Tissue Engineering **12**: 1325-1335.
- Cui, X. F. and T. Boland (2009). "Human microvasculature fabrication using thermal inkjet printing technology." Biomaterials **30**: 6221-6227.
- Cui, X. F., K. Breitenkamp, et al. (2012). "Direct human cartilage repair using three-dimensional bioprinting technology." Tissue engineering Part A **18**: 1304-1312.
- D'Alessandro, D., S. Danti, et al. (2012). "Histologic characterization of human ear ossicles for the development of tissue-engineered replacements " Otology & Neurotology **33**: 1458-1468.
- Derby, B. (2012). "Printing and prototyping of tissues and scaffolds " Science **338**: 921-926.
- Devarajan, K., M. L. Forrest, et al. (2013). "Adenovector-mediated gene delivery to human umbilical cord mesenchymal stromal cells induces inner ear cell phenotype." Cellular Reprogramming **15**: 43-54.
- Duan, B., L. A. Hockaday, et al. (2013). "3D bioprinting of heterogeneous aortic valve conduits with alginate/gelatin hydrogels." Journal of Biomedical Materials Research Part A **101A**: 1255-1264.
- Fedorovich, N. E., J. Alblas, et al. (2011). "Organ printing: the future of bone regeneration?" Trends in Biotechnology **29**: 601-606.
- Fedorovich, N. E., W. Schuurman, et al. (2012). "Biofabrication of osteochondral tissue equivalents by printing topologically defined, cell-laden hydrogel scaffolds." Tissue Engineering Part C-Methods **18**: 33-44.
- Fedorovich, N. E., H. M. Wijnberg, et al. (2011). "Distinct tissue formation by heterogeneous printing of osteo- and endothelial progenitor cells " Tissue Engineering Part A **17**: 2113-2121.
- Gaetani, R., L. Barile, et al. (2009). "New perspectives to repair a broken heart." Cardiovascular & Hematological Agents in Medicinal Chemistry **7**: 91-107.
- Gaetani, R., P. A. Doevendans, et al. (2012). "Cardiac tissue engineering using tissue printing technology and human cardiac progenitor cells." Biomaterials **33**: 1782-1790.
- Gandaglia, A., A. Bagno, et al. (2011). "Cells, scaffolds and bioreactors for tissue-engineered heart valves: a journey from basic concepts to contemporary developmental innovations " European Journal of Cardio-thoracic Surgery **39**: 523-531.
- Groeber, F., M. Holeiter, et al. (2011). "Skin tissue engineering - *In vivo* and *in vitro* applications." Advanced Drug Delivery Reviews **63**: 352-366.
- Haddad, B., A. H. Pakravan, et al. (2013). "A systematic review of tissue engineered meniscus: Cell-based preclinical models " Current Stem Cell Research & Therapy **8**: 222-231.
- Haglund, L., J. Moir, et al. (2011). "Development of a bioreactor for axially loaded intervertebral disc organ culture " Tissue Engineering Part C-Method **17**: 1011-1019.

- Hockaday, L. A., K. H. Kang, et al. (2012). "Rapid 3D printing of anatomically accurate and mechanically heterogeneous aortic valve hydrogel scaffolds." Biofabrication **4**(3): 035005.
- Hockaday, L. A., K. H. Kang, et al. (2012). "Rapid 3D printing of anatomically accurate and mechanically heterogeneous aortic valve hydrogel scaffolds." Biofabrication **4**: 035005.
- Kanemaru, S., H. Umeda, et al. (2013). "Improvement of eustachian tube function by tissue-engineered regeneration of mastoid air cells." Laryngoscope **123**: 472-476.
- Kang, K. H., L. A. Hockaday, et al. (2013). "Quantitative optimization of solid freeform deposition of aqueous hydrogels." Biofabrication **5**: 035001.
- Kloxin, A. M., A. M. Kasko, et al. (2009). "Photodegradable hydrogels for dynamic tuning of physical and chemical properties." Science **324**: 59-63.
- Kloxin, A. M., K. J. R. Lewis, et al. (2012). "Responsive culture platform to examine the influence of microenvironmental geometry on cell function in 3D." Integrative Biology **4**: 1540-1549.
- Kloxin, A. M., M. W. Tibbitt, et al. (2010). "Synthesis of photodegradable hydrogels as dynamically tunable cell culture platforms." Nature Protocols **5**: 1867-1887.
- Koch, L., A. Deiwick, et al. (2012). "Skin tissue generation by laser cell printing." Biotechnology and Bioengineering **109**: 1855-1863.
- L'Heureux, N., S. Paquet, et al. (1998). "A completely biological tissue-engineered human blood vessel." Faseb Journal **12**: 47-56.
- Labarthe, D. R. and S. B. Dunbar (2012). "Global cardiovascular health promotion and disease prevention 2011 and beyond." Circulation **125**: 2667-2676.
- Lee, S. H., J. J. Moon, et al. (2008). "Three-dimensional micropatterning of bioactive hydrogels via two-photon laser scanning photolithography for guided 3D cell migration." Biomaterials **29**: 2962-2968.
- Lee, S. J., H. W. Kang, et al. (2008). "Application of microstereolithography in the development of three-dimensional cartilage regeneration scaffolds." Biomedical Microdevices **10**: 233-241.
- Lee, S. J., J. W. Rhie, et al. (2008). "Development of three-dimensional alginate encapsulated chondrocyte hybrid scaffold using microstereolithography." Journal of Manufacturing Science and Engineering-Transactions of the ASME **130**: 021007.
- Lee, W., J. C. Debasitis, et al. (2009). "Multi-layered culture of human skin fibroblasts and keratinocytes through three-dimensional freeform fabrication." Biomaterials **30**: 1587-1595.
- Lee, W., V. Lee, et al. (2010). "On-demand three-dimensional freeform fabrication of multi-layered hydrogel scaffold with fluidic channels." Biotechnology and Bioengineering **105**: 1178-1186.
- Lee, W., J. Pinckney, et al. (2009). "Three-dimensional bioprinting of rat embryonic neural cells." Neuroreport **20**: 798-803.
- Lee, Y. B., S. Polio, et al. (2010). "Bio-printing of collagen and VEGF-releasing fibrin gel scaffolds for neural stem cell culture." Experimental Neurology **223**: 645-652.

- Leong, K. F., C. M. Cheah, et al. (2003). "Solid freeform fabrication of three-dimensional scaffolds for engineering replacement tissues and organs." Biomaterials **24**: 2363-2378.
- Liu, Y., L. Zhang, et al. (2010). "*In vitro* engineering of human ear-shaped cartilage assisted with CAD/CAM technology." Biomaterials **31**: 2176-2183.
- Luangphakdy, V., E. Walker, et al. (2013). "Evaluation of osteoconductive scaffolds in the canine femoral multi-defect model " Tissue Engineering Part A **19**: 634-648.
- Lund, A. W., B. Yener, et al. (2009). "The natural and engineered 3D microenvironment as a regulatory cue during stem cell fate determination." Tissue Engineering Part B-Reviews **15**: 371-380.
- MacNeil, S. and S. N. V. I. P. D. n. P. F. 2007 (2007). "Progress and opportunities for tissue-engineered skin." Nature **445**: 874-880.
- Mannoor, M. S., Z. W. Jiang, et al. (2013). "3D printed bionic ears." Nano Letters **13**: 2634–2639.
- Marga, F., K. Jakab, et al. (2012). "Toward engineering functional organ modules by additive manufacturing." Biofabrication **4**: 022001.
- Mariner, P. D., E. Johannesen, et al. (2012). "Manipulation of miRNA activity accelerates osteogenic differentiation of hMSCs in engineered 3D scaffolds." Journal of Tissue Engineering and Regenerative Medicine **6**: 314-324.
- McAllister, T. N., M. Maruszewski, et al. (2009). "Effectiveness of haemodialysis access with an autologous tissue-engineered vascular graft: a multicentre cohort study." Lancet **373**: 1440-1446.
- Michael, S., H. Sorg, et al. (2013). "Tissue engineered skin substitutes created by laser-assisted bioprinting form skin-like structures in the dorsal skin fold chamber in mice " Plos One **8**: e57741.
- Miller, J. S., K. R. Stevens, et al. (2012). "Rapid casting of patterned vascular networks for perfusable engineered three-dimensional tissues." Nature Materials **11**: 768-774.
- Muller, A. M., M. Davenport, et al. (2009). "Platelet lysate as a serum substitute for 2D static and 3D perfusion culture of stromal vascular fraction cells from human adipose tissue." Tissue Engineering Part C **15**: 869-875.
- Nimeskern, L., H. Martinez Avila, et al. (2013). "Mechanical evaluation of bacterial nanocellulose as an implant material for ear cartilage replacement." Journal of Mechanical Behavior of Biomedical Materials **22**: 12-21.
- Nimeskern, L., G. J. van Osch, et al. (2013). "Quantitative evaluation of mechanical properties in tissue-engineered auricular cartilage." Tissue Engineering Part B-Reviews: DOI: 10.1089/ten.teb.2013.0117.
- Norotte, C., F. S. Marga, et al. (2009). "Scaffold-free vascular tissue engineering using bioprinting." Biomaterials **30**: 5910-5917.
- Reiffel, A. J., C. Kafka, et al. (2013). "High-fidelity tissue engineering of patient-specific auricles for reconstruction of pediatric microtia and other auricular deformities." Plos One **8**: e56506.
- Santos, E., R. M. Hernandez, et al. (2012). "Novel advances in the design of three-dimensional bio-scaffolds to control cell fate: translation from 2D to 3D." Trends in Biotechnology **30**: 331-341.

- Schechner, J. S., S. K. Crane, et al. (2003). "Engraftment of a vascularized human skin equivalent." Faseb Journal **17**: 2250-2256.
- Skardal, A., J. X. Zhang, et al. (2010). "Photocrosslinkable hyaluronan-gelatin hydrogels for two-step bioprinting." Tissue engineering Part A **16**: 2675-2685.
- Sterodimas, A. and J. de Faria (2013). "Human auricular tissue engineering in an immunocompetent animal model " Aesthetic Surgery Journal **33**: 283-289.
- Swartz, J. D., C. M. Alper, et al. (2013). "Panel 2: Eustachian tube, middle ear, and mastoid-anatomy, physiology, pathophysiology, and pathogenesis " Otolaryngology-Head and Neck Surgery **148**: E26-E36.
- Tan, J. Y., C. K. Chua, et al. (2013). "Fabrication of channeled scaffolds with ordered array of micro-pores through microsphere leaching and indirect Rapid Prototyping technique " Biomedical Microdevices **15**: 83-96.
- Teh, B. M., R. J. Marano, et al. (2013). "Tissue engineering of the tympanic membrane." Tissue Engineering Part B-Reviews **19**: 116-132.
- Tibbitt, M. W. and K. S. Anseth (2012). "Dynamic microenvironments: The fourth dimension " Science Translational Medicine **4**: 160ps124.
- Torgersen, J., A. Ovsianikov, et al. (2012). "Photo-sensitive hydrogels for three-dimensional laser microfabrication in the presence of whole organisms." Journal of Biomedical Optics **17**: 105008.
- Wang, X. H., Y. N. Yan, et al. (2006). "Generation of three-dimensional hepatocyte/gelatin structures with rapid prototyping system." Tissue Engineering **12**: 83-90.
- Wang, X. H., Y. N. Yan, et al. (2007). "Rapid prototyping as a tool for manufacturing bioartificial livers." Trends in Biotechnology **25**: 505-513.
- Williams, C. G., A. N. Malik, et al. (2005). "Variable cytocompatibility of six cell lines with photoinitiators used for polymerizing hydrogels and cell encapsulation." Biomaterials **26**(11): 1211-1218.
- Wilson, C. E., C. A. van Blitterswijk, et al. (2011). "Scaffolds with a standardized macro-architecture fabricated from several calcium phosphate ceramics using an indirect rapid prototyping technique " Journal of Materials Science-Materials in Medicine **22**: 97-105.
- Wylie, R. G., S. Ahsan, et al. (2011). "Spatially controlled simultaneous patterning of multiple growth factors in three-dimensional hydrogels." Nature Materials **10**: 799-806.
- Xu, C. X., W. X. Chai, et al. (2012). "Scaffold-free inkjet printing of three-dimensional zigzag cellular tubes." Biotechnology and Bioengineering **109**: 3152-3160.
- Xu, T., C. A. Gregory, et al. (2006). "Viability and electrophysiology of neural cell structures generated by the inkjet printing method." Biomaterials **27**: 3580-3588.
- Xue, J. X., B. Feng, et al. (2013). "Engineering ear-shaped cartilage using electrospun fibrous membranes of gelatin/polycaprolactone." Biomaterials **34**: 2624-2631.
- Yeong, W. Y., C. K. Chua, et al. (2004). "Rapid prototyping in tissue engineering: challenges and potential " Trends in Biotechnology **22**: 643-652.
- Yusuf, S., S. Reddy, et al. (2001). "Global burden of cardiovascular diseases - Part I: General considerations, the epidemiologic transition, risk factors, and impact of urbanization." Circulation **104**: 2746-2753.

Zhang, T., Y. N. Yan, et al. (2007). "Three-dimensional gelatin and gelatin/hyaluronan hydrogel structures for traumatic brain injury." Journal of Bioactive and Compatible Polymers **22**: 19-29.

Zimmermann, W. H., K. Schneiderbanger, et al. (2002). "Tissue engineering of a differentiated cardiac muscle construct." Circulation Research **90**: 223-230.

## CHAPTER 3

### RAPID 3D PRINTING OF ANATOMICALLY ACCURATE AND MECHANICALLY HETEROGENEOUS AORTIC VALVE HYDROGEL SCAFFOLDS

This chapter was published in *Biofabrication* (Hockaday, Kang et al. 2012).

#### **3.1 Abstract**

The aortic valve exhibits complex three-dimensional (3D) anatomy and heterogeneity essential for long-term efficient biomechanical function. These are, however, challenging to mimic in *de novo* engineered living tissue valve strategies. We present a novel simultaneous 3D-printing/photo-crosslinking technique for rapidly engineering complex, heterogeneous aortic valve scaffolds. Native anatomic and axisymmetric aortic valve geometries (root wall and tri-leaflets) with 12 to 22 mm inner diameters (ID) were 3D printed with poly-ethylene glycol-diacrylate (PEG-DA) hydrogels (700 or 8000 MW) supplemented with alginate. 3D printing geometric accuracy was quantified and compared using  $\mu$ CT. Porcine aortic valve interstitial cells (PAVIC) seeded scaffolds were cultured for up to 21 days. Results showed that blended PEG-DA scaffolds could achieve over 10-fold range in elastic modulus ( $5.3\pm 0.9$  to  $74.6\pm 1.5$  kPa). 3D printing times for valve conduits with mechanically contrasting hydrogels were optimized to 14 to 45 minutes, increasing linearly with conduit diameter. Larger printed valves had greater shape fidelity ( $93.3\pm 2.6$ ,  $85.1\pm 2.0$ , and  $73.3\pm 5.2\%$  for 22, 17, and 12 mm ID porcine valves;  $89.1\pm 4.0$ ,  $84.1\pm 5.6$ , and  $66.6\pm 5.2\%$  for simplified valves). PAVIC seeded scaffolds maintained near 100% viability over 21 days. These results demonstrate that 3D hydrogel printing with controlled photo-crosslinking can rapidly fabricate anatomical heterogeneous valve conduits that support cell engraftment.

### **3.1 Introduction**

Aortic valve disease (AVD) is a serious and increasing clinical burden that affects patients at all stages and walks of life. In particular, congenital heart valve defects, which affect 1-2% of all live births in the United States, predispose the valve to premature failure and can be fatal if left untreated (Hoffman and Kaplan 2002). AVD is most commonly treated with surgical replacement of the defective valve. Tissue engineering has the potential to address current limitations of non-living prosthetics and donor supply shortage of allografts by providing living tissues that can grow, remodel, and integrate with the patient (Butcher, Mahler et al. 2011).

A major criterion for a tissue engineered heart valve is that the engineered valve must mimic the physiological function of the native valve. Several studies highlight that the natural geometry of the root, cusps, and sinus wall is critical for enabling efficient hemodynamics and coronary flow (Bellhouse, Bellhouse et al. 1968; Vesely 2000). Geometry is also important for tissue durability, where the intrinsic asymmetry of the root prevents cusp deterioration by minimizing the transvalvular pressure and stress on the cusps (Dagum, Green et al. 1999). In addition to geometry, spatial and mechanical heterogeneity is also critical for function. During the majority of their *in vivo* strain range (<20%), valve leaflets are very extensible and compliant, which permits rapid and efficient opening (modulus ~54 kPa aortic leaflet radial direction and the pulmonary leaflets are less stiff (Mavrilas and Missirlis 1991; Christie and Barratt-Boyes 1995)). The sinus root wall however is significantly more rigid (aortic root modulus ~ 140-180 kPa and pulmonary root modulus ~50-85 kPa (Matthews, Azadani et al. 2010; Butcher, Mahler et al. 2011; Azadani, Chitsaz et al. 2012)), which helps maintain an open lumen under demanding hemodynamic loads (Sacks, Schoen et al. 2009). Tissue engineers have fabricated mechanically heterogeneous tissues, but specific benchmarks for valve engineering are unmet. An improved tissue engineering fabrication strategy should 1)

effectively replicate native valve geometry and 2) effectively replicate regional mechanical heterogeneity.

Traditional *de novo* valve scaffold engineering involves manually shaping valve root and leaflet geometries out of polymer scaffold and seeding them with cells. A number of synthetic (poly-glycolic acid, polylactic acid, poly-4-hydroxybutyrate, polyhydroxyalkanoate) (Sodian, Hoerstrup et al. 2000; Sutherland, Perry et al. 2005; Balguid, Mol et al. 2009; Gottlieb, Kunal et al. 2010; Ramaswamy, Gottlieb et al. 2010; Sales, Mettler et al. 2010; Schmidt, Dijkman et al. 2010; Sodian, Schaefermeier et al. 2010; Eckert, Mikulis et al. 2011; van Geemen, Driessen-Mol et al. 2012) and biological polymeric (collagen I, fibrin) (Neidert and Tranquillo 2006; Robinson, Johnson et al. 2007; Flanagan, Sachweh et al. 2009) scaffolds have been created, mechanically conditioned *in vitro*, and tested in animal models. In the longest such trial to date (8 months within a growing sheep model), engineered valves (leaflet + conduit) were still functional but mildly stenotic, suggesting that the leaflets lacked sufficient compliance (Sutherland, Perry et al. 2005). While the exact cause is unknown, forming the root and leaflets with the same scaffold material mesh may have created root walls that are too compliant and/or cusps that are too stiff, both of which are characteristics of valve pathology (Butcher, Simmons et al. 2008). Incorporation of heterogeneity into tissue engineered valves with different root versus leaflet materials has been achieved, but this required the different parts to be fabricated sequentially and then joined with sutures manually (Shinoka, Ma et al. 1996; Sodian, Sperling et al. 1999).

Automated manufacturing technology has the potential to fabricate tissue-engineered scaffolds more rapidly with higher anatomical precision. Stereolithographic 3D printing and extrusion based 3D printing have both been used to fabricate scaffolds on the scale of heart valves. Schaefermeier et al. used stereolithography to fabricate a silicone

aortic valve replica based on X-ray computed tomography (CT) scans and then used the replica to mold a PGA valve scaffold (Sodian, Loebe et al. 2002; Schaefermeier, Szymanski et al. 2009). Extrusion based 3D printing has been employed to engineer hard tissue scaffolds such as knee menisci and intervertebral disks complete with encapsulated cells (Cohen, Malone et al. 2006; Ballyns, Cohen et al. 2010). This process can rapidly recreate 3D computer aided design (CAD) models by slicing them into layers and building the layers upward using deposition tools that can extrude a wide range of materials. Adapting 3D printing technology to fabricate soft tissue heart valve scaffolds, however, requires overcoming the additional challenges of 1) adapting highly extensible elastomeric cell-friendly materials for 3D printing, and 2) printing complex soft tissues with overhanging structures and both internal and external geometric features.

Hydrogels can be designed to mimic mechanical and biological properties of soft tissue, and can be controlled for direct 3D printing. By modifying polymer precursors hydrogels can have tunable mechanics, provide attachment and signals to cells, have custom degradability, and be modified to allow for photo and chemical crosslinking (Benton, Fairbanks et al. 2009; Huebsch, Arany et al. 2010; Kloxin, Kloxin et al. 2010; Pedron, Kasko et al. 2010; Chandler, Berglund et al. 2011; Hutson, Nichol et al. 2011). The technology exists to rapidly 3D print clinically sized, geometrically complex constructs with hydrogels (Arcaute, Mann et al. 2006; Ballyns, Cohen et al. 2010; Fedorovich, Schuurman et al. 2012), but it has not been utilized for engineering heart valves. 3D printing clinically sized tissues (>10 mm) with high anatomical precision has been primarily demonstrated for hard tissues such as bone and cartilage (Hollister 2005; Ballyns, Cohen et al. 2010; Cipitria, Lange et al. 2012). Clinically sized soft tissues are a small minority of the 3D printing literature, dominated by vascular conduits and networks that don't exhibit external geometric complexity or non-self-supporting geometries (Skardal, Zhang et al. 2010; Xu, Chai et al. 2012). Micro-scale 3D printed tissues have

been fabricated with very fine precision using hydrogels, but have been limited to tissues ~5 mm tall or less (Liu and Bhatia 2002; Chan, Zorlutuna et al. 2010; Gauvin, Chen et al. 2012). This leads us to investigate utility of extrusion based 3D hydrogel printing for enabling rapid soft tissue hydrogel fabrication at clinically necessary sizes (>10 mm) with high spatial precision.

In this study, we implemented an on-board photo-crosslinking system to enable simultaneous 3D extrusion printing and curing of hydrogels in complex aortic valve geometries. We additionally compare 3D printed geometry accuracy for native and axisymmetric valve anatomy using micro-CT. Cell viability and spreading of PAVIC cultured on 3D printed scaffolds were assessed over 21 days.

## **3.2 Materials and Methods**

### **3.2.1 Base hydrogel formulation**

Poly(ethylene glycol)-diacrylate (PEG-DA) was used as the base polymer precursor for this study. Many tissue engineering applications have used PEG-DA as a scaffold component because it is a biocompatible, photo-crosslinkable elastomer whose mechanical properties can be easily modified (Peyton, Raub et al. 2006; Guo and Chu 2007). 700 and 8000MW PEG-DA precursors were chosen for this study because their differences in molecular weight have been shown by others to correlate with hydrogel stiffness (Hahn, McHale et al. 2007; Huebsch, Arany et al. 2010; Browning, Wilems et al. 2011; Hutson, Nichol et al. 2011). PEG-DA undergoes slow hydrolytic degradation *in vivo*, and it can also be functionalized and combined with other precursors to encourage cell attachment (Peyton, Raub et al. 2006; Hutson, Nichol et al. 2011; Browning and Cosgriff-Hernandez 2012). Several studies employing stereolithography printing have demonstrated that photopolymerizing layered hydrogels using ultraviolet (UV) irradiation can yield 3D structures (Dhariwala, Hunt et al. 2004; Arcaute, Mann et

al. 2006; Chan, Zorlutuna et al. 2010). These features support the use of PEG-DA as base polymer precursor for 3D printing of valve scaffolds.

The base hydrogel solution used in this study consisted of phosphate buffered saline (PBS), photoinitiator, and PEG-DA. Photoinitiator (Irgacure 2959; Ciba Specialty Chemicals, Tarrytown, NJ) was first dissolved in PBS at 60°C. After cooling the solution to room temperature, 700 MW (Sigma Aldrich, St. Louis, MO) and/or 8000 MW PEG-DA (synthesized by the authors (Guo and Chu 2005)) were dissolved into the solution.

### **3.2.2 Mechanical testing of base hydrogel blends**

We examined the degree of biomechanical tunability in PEG-DA hydrogels by performing uniaxial ring tensile tests (Seliktar, Black et al. 2000; Seliktar, Nerem et al. 2001). Hydrogel precursor solutions were prepared by dissolving 0.1-0.2% w/v photoinitiator and 0-20:0-10% 700:8000 MW PEG-DA in PBS, where amount of photoinitiator was directly proportional to increasing PEG-DA concentration (to maintain 1% w/w precursor to polymer). For the extremes, 10% w/v 8000 MW and 20% w/v 700 MW PEG-DA hydrogels were optimal for handling (room temperature solubility and resulting robust gels). Precursor solutions were crosslinked at 365 nm UV light at 245 mW/cm<sup>2</sup> inside 4-well plates for 10 minutes (EN280L lamp; Spectroline, Westbury, NY). Rings were created from crosslinked hydrogel cylinders with an 8-mm biopsy punch and then secured in a vertical orientation between two hook fixtures within a PBS bath on the testing platform (EnduraTec 3200; Bose Electroforce, Eden Prairie, MN). Samples were loaded quasi-statically at 0.02mm/sec until failure (strain rate is 0.005/sec).

### **3.2.3 3D printing system and hydrogel modification**

Detailed specifications and mechanics of the open-source Fab@Home<sup>TM</sup> Model 1 extrusion based 3D printing (robocasting) can be found at [www.fabathome.org](http://www.fabathome.org) and in

our previous studies (Cohen, Malone et al. 2006; Malone and Lipson 2007). For this study, the printing platform was modified to carry three syringes. In addition, we built a UV-LED crosslinking module, in which four LEDs were arranged in a 2 x 2 formation and mounted directly on the syringe carriage (crosslinking energy at the printing surface was 16.5 mW/cm<sup>2</sup>/LED, (Nichia America Corporation, Wixom, MI) (Figure 3.1(A)). For sterile printing, an autoclavable bag attached with a UV transparent film with access ports for the nozzles was autoclaved. The bag was then mounted below the syringe carriage inside a laminar hood, and the precursor solutions were printed through the access ports while the UV-LED crosslinked the printed solutions through the film.

Un-modified soluble alginate (LF10/60, FMC BioPolymer, Drammen, Norway) was mixed into PEG-DA precursor formulations to temporarily increase viscosity during the printing extrusion process. While 2% w/v alginate mixed in PBS is sufficiently viscous to be extrudable (Cohen, Malone et al. 2006), pilot studies found that PEG-DA dramatically increased the solubility of alginate. We found adding 10-15% w/v alginate to a PEG-DA solution achieves suitable extrusion viscosity. In addition, PEG-DA extrusion was sensitive to the salt concentration of the buffer in a MW dependent manner. Precursor solutions made with 1x PBS and only 700 MW PEG-DA could not be printed due to phase separation, but this was overcome by changing the salt concentration (13.7 mM NaCl) but maintaining normal pH.

### **3.2.4 Measuring crosslinking time of hydrogels**

The crosslinking time required of the printed precursor solutions need to match each other in order to fabricate heterogeneous hydrogel layers. Therefore, we investigated

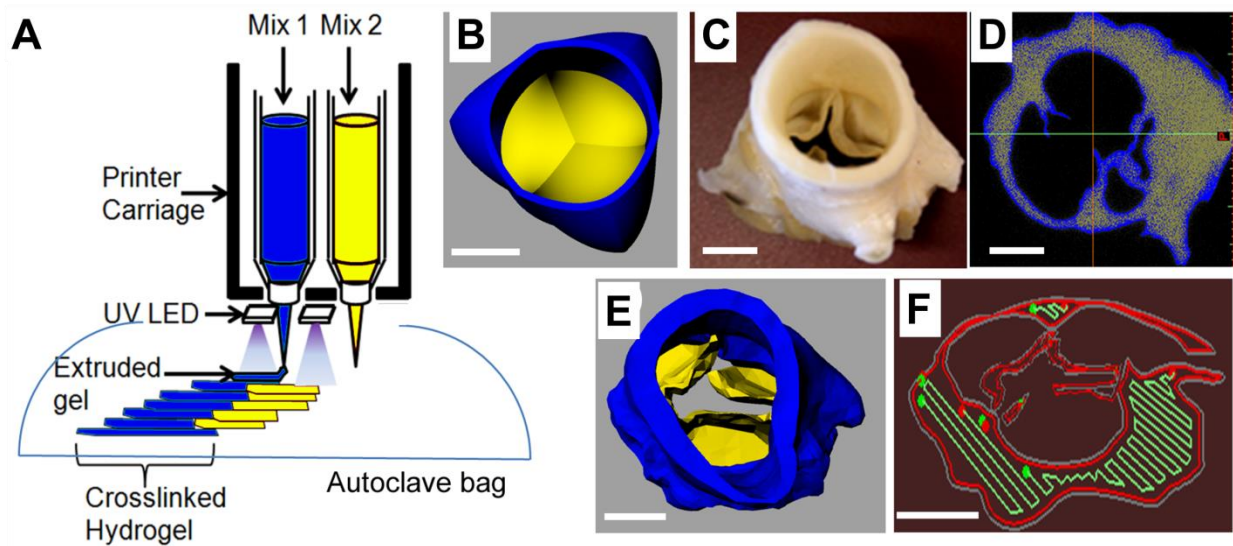


**Figure 3.1 3D Printer setup and valve geometry modeling.**

(A) Syringe tools were loaded with different hydrogels, and UV-LED array integrated into the deposition tools crosslinked hydrogels during printing. Sterile scaffolds were generated by printing inside an autoclaved bag that was mounted on the printer stage inside a laminar hood. (B) Axisymmetric valve STL file with the root and leaflet in the closed position was designed in Solidworks. (C) A fixed porcine aortic valve underwent micro-CT scan, and (D) the leaflet and root regions were thresholded based on tissue density. (E) The thresholded regions were reconstructed into printable STL geometries, (F) and the printing software sliced the geometries into layers and generated extrusion paths for each layer (red: contour, green: fill-in paths). Scale bar = 1 cm.

how crosslinking time was controlled by molecular weight PEG-DA and varying photoinitiator concentration. Hydrogel precursor solution containing 10-15% w/v alginate and 0.2-2.0% w/v Irgacure was first injected into 4-8 mm diameter, 1-mm thick disc molds made with either 700 MW or 8000 MW PEG-DA. The solutions were then exposed to 365 nm UV light from the crosslinking module. Minimum crosslinking time was defined as the point when the hydrogel gel transitioned from liquid to solid. This was the point where the hydrogel disc did not flow after the mold was removed, did not flow in response to gentle compression with a spatula, and held its shape upon being transferred into PBS (did not dissolve).

### **3.2.5. Valve geometry design**

Two aortic valve models were created for printing. The first model, an axi-symmetric aortic valve geometry including the sinus and leaflets (kind gift of Dr. Reetu Sing), was generated in SolidWorks (Waltham, MA) as shown in Figure 3.1(B). For the second model, a porcine aortic valve conduit obtained fresh at slaughter (Shirk Meats, Himrod, NY) was fixed in formalin (Figure 3.1(C)) and scanned with the leaflets in a partially open position via micro-CT at 100  $\mu\text{m}$  voxel size, 80 keV, 30 mA, 800 angles, 30 ms exposure time, 30 gain, and 20 offset (eXplore CT120; GE Healthcare, United Kingdom). The root and leaflet regions in the resulting DICOM scans were segmented via intensity thresholds (Figure 3.1(D)) and rendered into 3D geometries in stereolithography format of Standard Tessellated Language (STL) files (Mimics 12.0; Materialise, Leuven, Belgium) (Figure 3.1(E)). A separate temporary scaffold to support the ostia lumens was generated by Boolean subtraction.

### 3.2.6. Heterogeneous valve printing

Based on the mechanical testing crosslinking test results (Figure 3.2), we established a biomechanically stiff PEG-DA formulation (20%:0% 700:8000 MW) to comprise the aortic root wall and a compliant and extensible hydrogel for the leaflets formulation (5%:7.5% 700:8000 MW). Using these ratios, stiff hydrogel (13.7 mM NaCl, 1% w/v photoinitiator, 20:0% PEG-DA, 12.5% w/v alginate) and compliant hydrogel (PBS, 1% w/v photoinitiator, 5:7.5% w/v PEG-DA, 15.0% w/v alginate) precursor solutions were prepared. 1% photoinitiator concentration was chosen since it enabled both hydrogel formulations to crosslink rapidly in about 30-60 seconds, which was comparable to the print time of each layer.

Precursor solutions were loaded into the deposition syringes fitted with 0.83 mm inner diameter nozzles. After importing the STL geometries, the software generated print paths at 0.6-0.7 mm path height and 0.8-0.9 mm path width (Figure 3.1(F)) for all geometries. The aortic root was printed with the stiff hydrogel while the leaflet was printed with the compliant PEG-DA hydrogel at 0.6 and 0.4 ml/min and traversing rate of 6 and 3 mm/s, respectively. The UV crosslinking array attached on the carriage crosslinked the printed hydrogel paths as they were extruded at 16.5 mW/cm<sup>2</sup> during fabrication (Figure 3.2(E)). To print the support geometry for the overhanging ostia and leaflets, a third syringe was loaded with a non-photo-crosslinking alginate-gelatin solution. The temporary support structure printed with this formulation was able to support itself without crosslinking due to the high viscosity of the solution, but was easily removed by rinsing in aqueous buffer. To assess size dependent accuracy and volume, scalability, valve scaffolds were printed at 100, 50, and 18% of the original model.

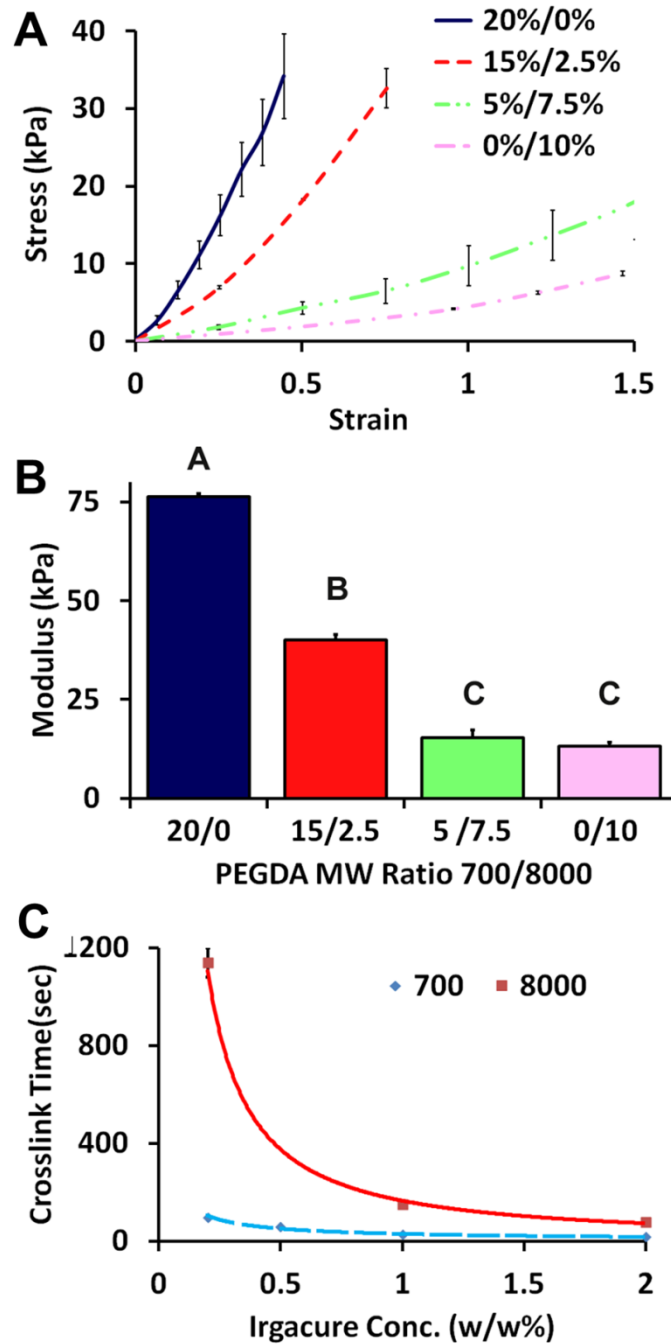


**Figure 3.2 Uniaxial tensile testing and crosslinking time testing of PEG-DA hydrogels.**

**(A)** Stress-strain profile, and **(B)** elastic modulus of hydrogels with 20:0, 15:2.5, 5:7.5, and 0:10% 700:8000 MW PEG-DA hydrogels ( $n = 3$ ). Non-matching letters are statistically different ( $p < 0.05$ ). **(C)** Crosslinking time of 700 and 8000 MW PEG-DA hydrogels with varying photoinitiator concentrations ( $n \geq 5$ ).

### **3.2.7 Shape fidelity evaluation of aortic valve scaffolds**

Shape fidelity was assessed quantitatively using micro-CT. Valve conduits were printed using 20% w/v 700 MW PEG-DA hydrogel (13.7 mM NaCl, 1% w/v photoinitiator, 12.5% w/v alginate). Conduits were scanned directly after printing via micro-CT. To test how swelling affects geometry, they were also hydrated in PBS overnight and scanned. Resulting scans were then reconstructed into STL geometries using MicroView (GE Healthcare). Surface deviations between printed and native STL models were quantified through autoregistration and heat maps in Geomagic Qualify (v9.0; Research Triangle, NC; (Ballyns, Cohen et al. 2010)). We chose  $\pm 10\%$  in diameter as the tolerance threshold for valve fabrication since greater than 10% diameter mismatch in non-living prosthetic valves has been shown to impair hemodynamic function (Pibarot and Dumesnil 2006).

Assessing the internal geometric fidelity was impossible with surface heat maps. Therefore, slice-by-slice comparison of each printed layer was also performed. Micro-CT generated virtual slices of the printed scaffolds were compared to the corresponding image-derived layers of the original valve STL files in the XY-plane (Figure 3.2(D)). The two slices were overlapped and compared using Boolean operations. For a given slice, regions printed outside the target print area were designated overprint error, and regions that were not printed within the target area were designated underprint error.

### **3.2.8 Cell viability and spreading**

Porcine aortic valve interstitial cells (PAVIC) were employed as model cell source to investigate valve scaffold biocompatibility because VIC are the main cell type that populates valve leaflets (Butcher, Simmons et al. 2008). PAVIC were isolated via collagenase digestion as previously described (Butcher, Penrod et al. 2004) and cultured with Dulbecco's Modified Eagle's Medium (DMEM; Invitrogen, Carlsbad, CA)

supplemented with 10% fetal bovine serum (FBS; Invitrogen) and 1% penicillin/streptomycin (PS; Invitrogen). Cells were used at passage 5-8.

Sterile 12 mm diameter aortic valve conduits were printed with 700 MW PEG-DA hydrogel. Conduits were rinsed in PBS overnight to leach out the non-crosslinking alginate. They were then transferred to a 50 ml conical vial containing  $20 \times 10^6$  PAVIC in 40 ml of culture media. After 24 hours of rotary seeding at 37°C, 5% CO<sub>2</sub> (day 1), valve conduits were cultured in flasks for 7 and 21 days. Media was exchanged every 48 hrs. Conduits were then stained with 4 mM calcein-AM and 2 mM ethidium homodimer (LIVE-DEAD, Invitrogen) for 30 min at 37°C and then rinsed with PBS. Conduits were cut with a razor blade and imaged using an epifluorescence stereomicroscope (SteREO Discovery.V20; Zeiss, Germany).

Since PEG-DA is virtually non-adhesive and non-adsorptive in its unmodified form (Hutson, Nichol et al. 2011), we tested whether collagen fibrillized within the PEG-DA hydrogels could provide enhanced cell activity. Collagen I was extracted from rat tail tendons (Pel-Freez Biologicals, Rogers, AR) and dissolved in sterile 0.1% acetic acid for 24 hrs prior to hydrogel preparation as previously described (Bowles, Williams et al. 2010). Low concentrations of collagen (0.1 or 0.5 mg/ml) were mixed in 3x DMEM containing 10% FBS, and 0.1M NaOH was added to neutralize pH. This solution and PEG-DA hydrogel precursor solutions were kept on ice until they were combined. The combined solution was photo-crosslinked in disc molds and then incubated at 37°C for 30 minutes to allow the collagen monomers to fibrillize. Ultrastructure of completely crosslinked PEG-DA hydrogels with and without collagen and/or alginate leaching prior to seeding was analyzed via scanning electron microscopy (SEM). Fully hydrated hydrogels were flash frozen, lyophilized, mounted on aluminum SEM stubs, and imaged (Leo 1550 FESEM Cornell Center for Materials Research, Ithaca, NY; (Benton,

DeForest et al. 2009). Image J was used to analyze mean pore area for each representative image. Hydrogel discs were then rinsed and surface-seeded with  $0.5 \times 10^6$  PAVIC/ml. Cell circularity (index of cell spreading) was quantified using ImageJ.

### **3.2.9 Statistical analysis**

Mechanical testing was conducted with  $n = 3$  rings per formulation. Crosslinking tests were conducted with  $n \geq 5$  disks per condition. Fidelity and viability assessment was performed with  $n = 3-4$  printed valve scaffolds. Measurements were indicated as mean and standard deviation unless noted otherwise. Statistical comparisons were made using 1-way analysis of variance (ANOVA) followed by Tukey modified t-tests.  $P < 0.05$  denoted significance. For SEM pore area analysis statistical comparisons were made using 2-way ANOVA with Tukey post-test,  $p < 0.05$ . 2-way factors are gel MW and treatment (unrinsed, rinsed, collagen).

## **3.3. Results**

### **3.3.1 Mechanical properties of hydrogels**

Mixing of 700 and 8000 MW PEG-DA resulted in elastomeric hydrogels with a broad range of mechanical properties. In general, hydrogels became stiffer and less extensible as the proportion of 700 MW PEG-DA increased (Figure 3.2(A, B)). 0:10% w/v (700:8000 MW) hydrogels exhibited very extensible, nearly linear elastic behavior with modulus of  $5.3 \pm 0.9$  kPa through a strain of  $1.6 \pm 0.1$ . 20:0% w/v hydrogels, on the other hand, exhibited nonlinear tensile stress-strain behavior, with an approximately 13-fold greater modulus at  $74.6 \pm 1.5$  kPa through a strain of  $0.50 \pm 0.15$ . Intermediate ratios between these extremes created stress-strain responses between the individual polymer extremes (Figure 3.2(A)). As examples, 5:7.5% w/v hydrogels exhibited modulus of  $12.7 \pm 1.6$  kPa though a strain of  $2.0 \pm 0.5$ , and 15:2.5% w/v hydrogels exhibited modulus of  $42.5 \pm 1.0$  kPa through a strain of  $0.94 \pm 0.01$ . Modulus between

5:7.5% and 0:10% w/v did not vary significantly. Collectively, these results show that PEG-DA hydrogels exhibit nonlinear elastic mechanics that can be tuned through polymer mass and molecular weight ratio.

### **3.3.2 Effect of photoinitiator concentration on hydrogel crosslinking time**

PEG-DA hydrogel crosslinking time decreased exponentially with increasing concentrations of Irgacure (Figure 3.2(C)). 700 MW PEG-DA hydrogels crosslinked 5-10 fold faster than 8000 MW hydrogels at the same Irgacure concentration, likely because of the increased availability of polymer chains and active end groups. At 0.2% w/v Irgacure, 700 MW hydrogels crosslinked in  $98 \pm 3$  s, but 8000 MW hydrogels crosslinked at  $1140 \pm 60$  s. At 2% w/v Irgacure, 700 MW hydrogels took only  $17 \pm 1$  s to crosslink, and 8000MW hydrogels took just  $78 \pm 8$  s. These results demonstrate that hydrogel crosslinking time can be tuned with photoinitiator concentration, and they further suggest that balancing photoinitiator concentration for each base material can maintain overall crosslinking kinetics.

### **3.3.3 Rapid printing of heterogeneous and scaled valve scaffolds**

Crosslinking the hydrogel during fabrication enabled the two different hydrogels formulations to fuse and integrate with each other and between printed layers. Printed valve conduits retained biomechanical heterogeneity, where the leaflets extended and bent easily while the root remained relatively rigid (Figure 3.3(B, E)). Both anatomic and axially symmetric valve scaffolds were successfully printed at 100%, 50%, and 18% of the original model volume. The valve conduits had inner diameters (ID) of 22, 17, and 12 mm (Figure 3.3(C, F)) and heights of 25, 20, and 14 mm, respectively. Gross anatomical features such as ostia, commissures, and sinuses were present at all sizes. The 12 mm ID valve conduits were fabricated in 14 minutes, the 17 mm in 30 minutes, and the 22 mm in 45 minutes. Together, these results support that 3D printing strategy

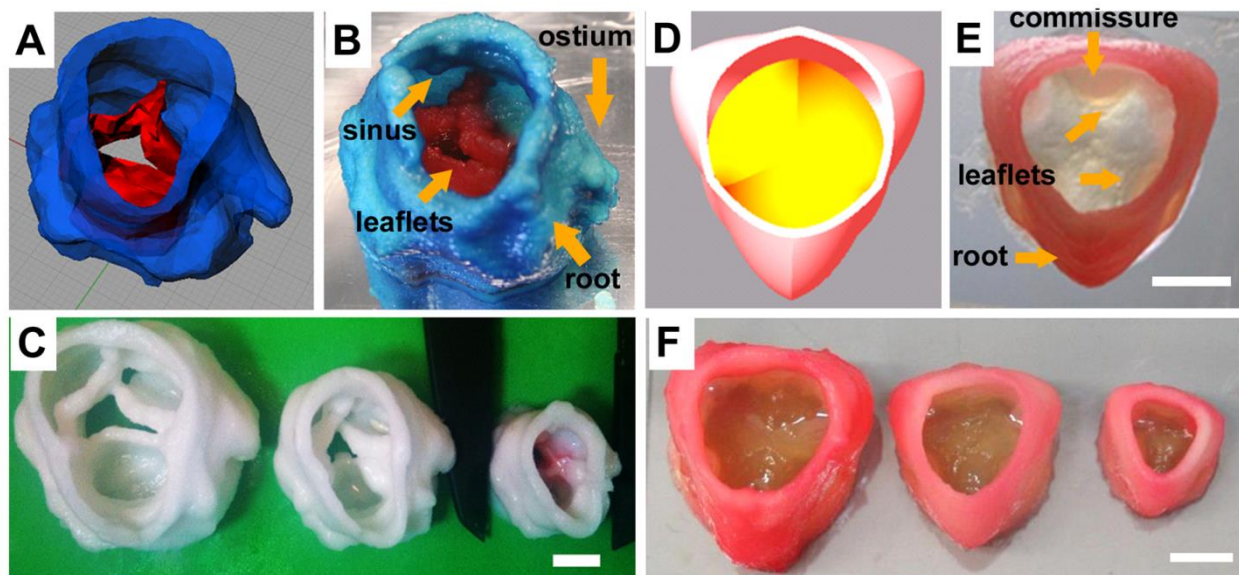


**Figure 3.3 Printing heterogeneous valve and scaled valve constructs.**

**(A)** Porcine aortic valve model was **(B)** printed, where root was formed with 700 MW PEG-DA hydrogel while the leaflets were formed with 700/8000 MW PEG-DA hydrogels. Key features such as the coronary ostium and sinuses were present **(C)** Scaffolds were printed with 700 MW PEG-DA at different scale for fidelity analysis, where the inner diameters (ID) were 22, 17, and 12 mm. **(D)** Axisymmetric valve model was **(E)** printed with two blends of hydrogels **(F)** and at 22, 17, and 12 mm ID. Scale bar = 1 cm.

can rapidly generate mechanically heterogeneous, anatomically complex valve conduits.

### 3.3.4 Shape fidelity

We further characterized their shape fidelity using surface deviation analysis through micro-CT imaging. For the 22, 17, and 12 mm ID image-derived, hydrated valve scaffolds,  $93.3 \pm 2.6$ ,  $85.1 \pm 2.0$ , and  $73.3 \pm 5.2\%$  of the points laid within the  $\pm 10\%$  diameter threshold respectively (Figure 3.4(A, C)). For the axial symmetric hydrated valve scaffolds,  $89.1 \pm 4.0$ ,  $84.1 \pm 5.6$ , and  $66.6 \pm 5.2\%$  of the points were within  $\pm 10\%$  threshold (Figure 3.4(B, C)). These results indicate that the 3D printing strategy generates scaffolds with high geometric precision, but accuracy decreased somewhat with reduced size. For the image-derived valve scaffolds, overprint error (points lying beyond  $+10\%$  threshold) predominated the underprint error (points beyond  $-10\%$  threshold, error proportion over:under was 89.0:11.0%, 90.0:10.0%, and 82.3:17.7%, for 22, 17, and 12 mm ID, respectively) throughout the root and leaflet (Figure 3.4(D) solid bars). Overprint error also predominated over the underprint error in the axially symmetric valve scaffolds (88.2:11.8, 92.7:7.3, and 94.4:5.6%, for 22, 17, and 12 mm ID in over:under ratio, respectively) (Figure 3.4(D) striped bars).

Slice-by-slice analysis to assess the internal geometric fidelity indicated that overlapping area percentage decreased as the size of the image-derived valve scaffolds decreased ( $81.7 \pm 1.9$  to  $61.9 \pm 4.3\%$  from 22 to 12 mm ID) (Figure 3.5(A)). Total overprint and underprint area percentage between fully hydrated and scaffolds scanned immediately after printing was not significantly different, but the error locations were different. Non-hydrated scaffolds contained overprinted regions on the inner walls, but hydrated valve scaffolds were underprinted on the inner walls and overprinted on the outer walls

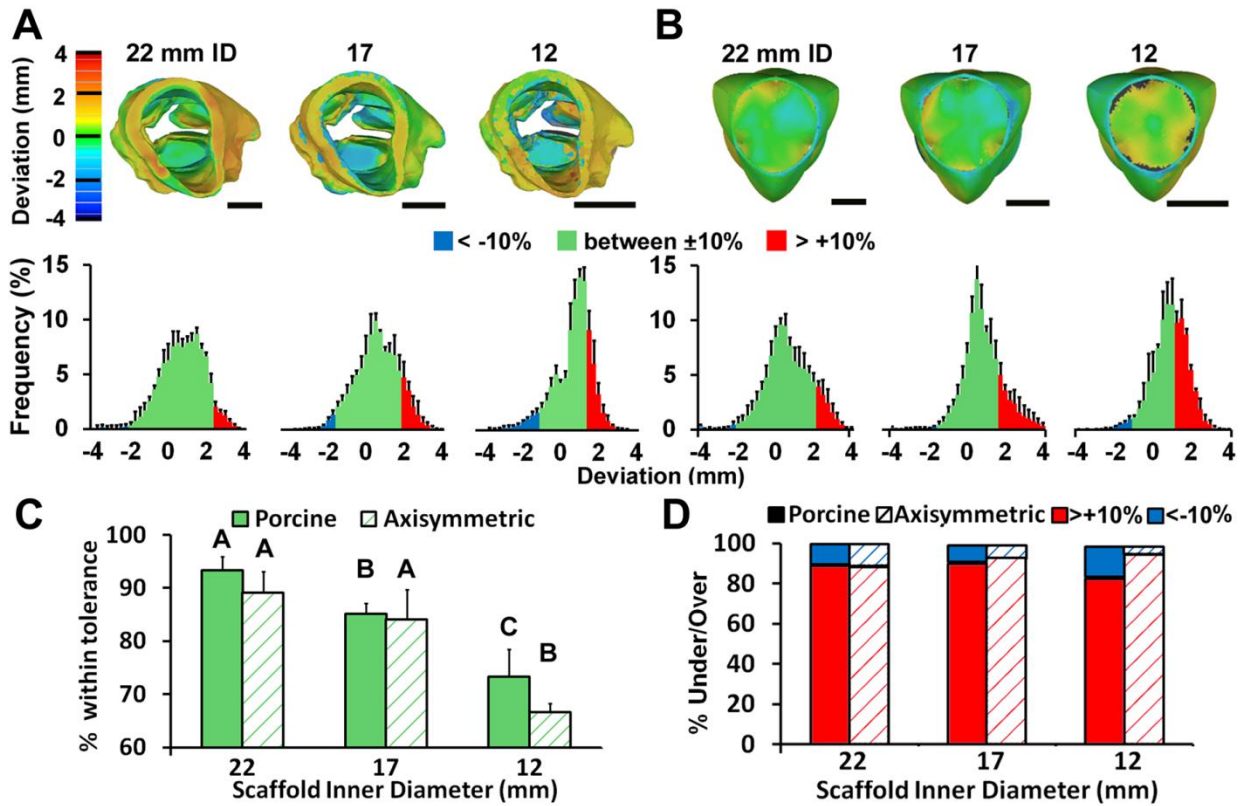


**Figure 3.4 Fidelity analysis of fully hydrated printed valve scaffold geometry compared to model geometry using  $\mu$ CT-derived STL files.**

**(A)** Heat maps and average % frequency histograms representing surface deviations between printed porcine scaffold vs. model geometries and **(B)** printed simplified scaffolds vs. model geometries. Printed valve constructs were fully hydrated in PBS (equilibrium swollen). Warmer colors indicate positive deviation while cooler colors indicate negative deviation in millimeters. % frequency histograms show the deviations that lie within  $\pm 10\%$  tolerance (green), and outside the tolerance (blue and pink).  $\pm 10\%$  tolerance is 2.2, 1.7, and 1.2 mm for the 22, 17 and 12 mm diameter scaffolds, respectively. **(C)** The percentage of surface points whose deviation falls within  $\pm 10\%$  tolerance. This percentage decreases as scaffold size decreases. Bars of the same pattern with different letters are significantly different from each other,  $P < 0.05$  **(D)** The percentage of surface points whose deviation falls outside the  $\pm 10\%$  tolerance that are above (pink) and below (blue). Scale bar = 1 cm.  $n = 2-4$ ,  $p < 0.05$ .

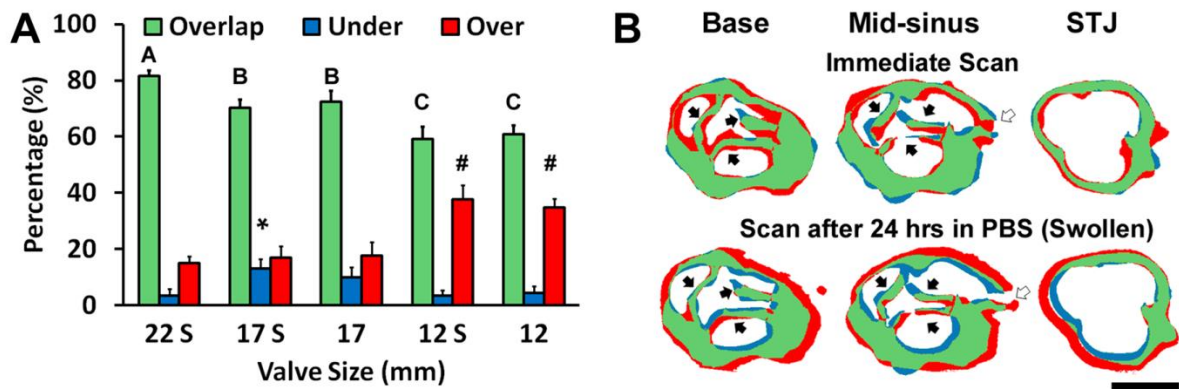


**Figure 3.5 Slice-by-slice analysis comparing  $\mu$ CT image slices of printed porcine valve scaffolds to model layers and assess internal geometric fidelity.**

**(A)** Overlap, underprint, and overprint area percentage of each printed construct. S denotes constructs that were fully hydrated in PBS (swollen), and absence of an S means constructs were scanned directly after printing. Bars of the same color with different letters or symbols are significantly different from each other,  $P < 0.05$  **(B)** Representative images of Boolean analysis of valve sections at levels of base, mid-sinus, and sino-tubule junction (STJ).  $\mu$ CT image slices of a printed scaffold are compared to slices of the native geometry used to print the scaffold. Top row: 17 mm ID valve scaffold scanned immediately after printing. Bottom: Same scaffold that was later fully hydrated. Solid arrow: leaflets; hollow arrow: ostium.  $N=3-4$ ,  $p < 0.05$

(Figure 3.5(B)). These results suggest that residual error in final shape is caused in part by outward but not inward swelling.

### **3.3.5 Alginate removal and cell cytocompatibility of hydrogel scaffolds**

PEG-DA hydrogel structure appears to be modulated by molecular weight and type of additives (alginate and collagen I) (Figure 3.6). The SEM images show that PEG-DA precursor solution + 10% w/v alginate appears to form small pores, with alginate packing the structure (Figure 3.6 (A, B)). Alginate leached out of hydrogels rinsed in an aqueous buffer (nearly 100% within 24 hours according to weight), and this was confirmed with the SEM images where PEG-DA pore size appears to increase for 700 and 8000 MW, respectively (Figure 3.6 (C, D)). We noticed that post-polymerization the alginate hydrogels were opaque and were opaque even after leaching, which suggests that a microscopic amount of alginate may persist. When PEG-DA precursor solutions with alginate were further mixed with neutralized collagen I before crosslinking (0.01% w/v collagen in total solution) and then alginate was leached out, the structures appeared more fibrous (Figure 3.6 (E, F)). Image analysis of mean pore area for each representative SEM image (A)  $6.1 \pm 1.0 \text{ } \mu\text{m}^2$ , (B)  $14.0 \pm 2.8 \text{ } \mu\text{m}^2$ , (C)  $36.6 \pm 7.4 \text{ } \mu\text{m}^2$ , (D)  $103.5 \pm 14.1 \text{ } \mu\text{m}^2$ , (E)  $103.1 \pm 21.3 \text{ } \mu\text{m}^2$ , and (F)  $154.8 \pm 36 \text{ } \mu\text{m}^2$ . The pore size was non-uniform. Pores in A, B, and C were significantly different from D, E, and F.

PAVIC seeded valve scaffolds contained cells across the entire surface of the conduits, and to a lesser degree within the root and leaflet interstitium (Figure 3.7 (A, B)). Cells were  $91.3 \pm 10.7\%$  viable at day 1. At day 7 and 21 cells were 100% viable. For PAVIC cultured on disks, cell morphology was tested on the base hydrogel formulation and with 0.1 or 0.5 mg/ml collagen I to the precursor solution (Figure 3.8). The mean circularity of PAVIC on 700 MW PEG-DA base gels decreased significantly over time ( $0.83 \pm 0.03$  to  $0.74 \pm 0.01$  between day 1 and 21) (Figure 3.8(A)). Meanwhile, PAVIC circularity in

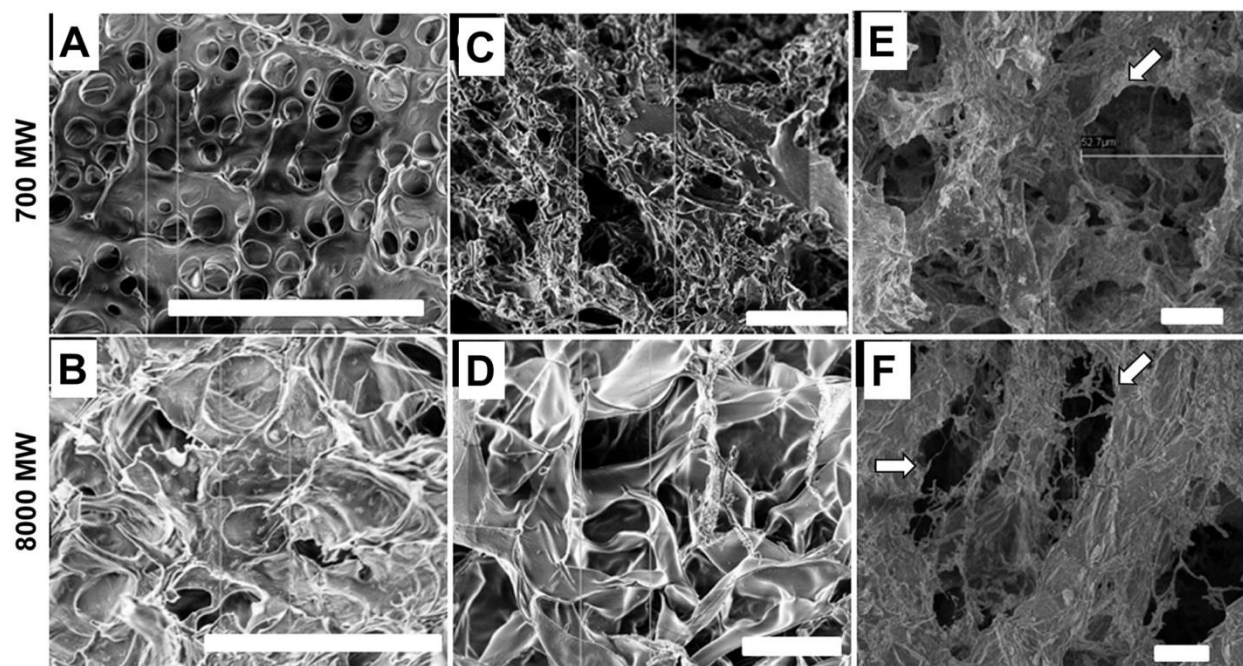


**Figure 3.6 Representative SEM imaging of hydrogels.**

Top row: 700 MW PEG-DA; bottom row: 8000 MW PEG-DA. **(A, B)** Images of PEG-DA hydrogels that were made with alginate viscosity modifier in the precursor solution. **(C, D)** Rinsed PEG-DA hydrogels made with alginate viscosity modifier **(E, F)** Rinsed PEG-DA hydrogels made with the addition of 0.1 mg/ml collagen and alginate viscosity modifier to precursor solution. Hollow arrows indicate fibrous material. Scale bar = 20  $\mu\text{m}$ .

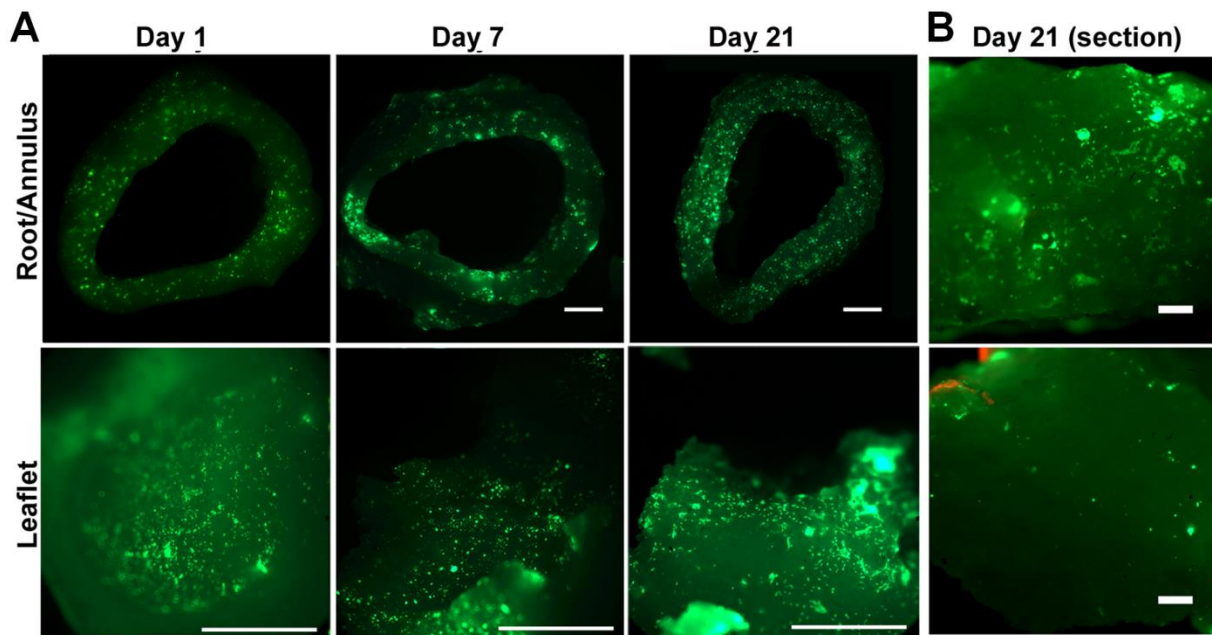


**Figure 3.7 Live/Dead imaging of PAVIC cultured on 12 mm ID printed valve constructs.**

**(A)** Live PAVIC were visible in both the root (top) and leaflets (bottom) surface for day 1, 7, and 21 (scale bar = 2 mm). **(B)** Cells were also detected in the interstitium of the root and leaflet for up to 21 days (scale bar = 100 mm).

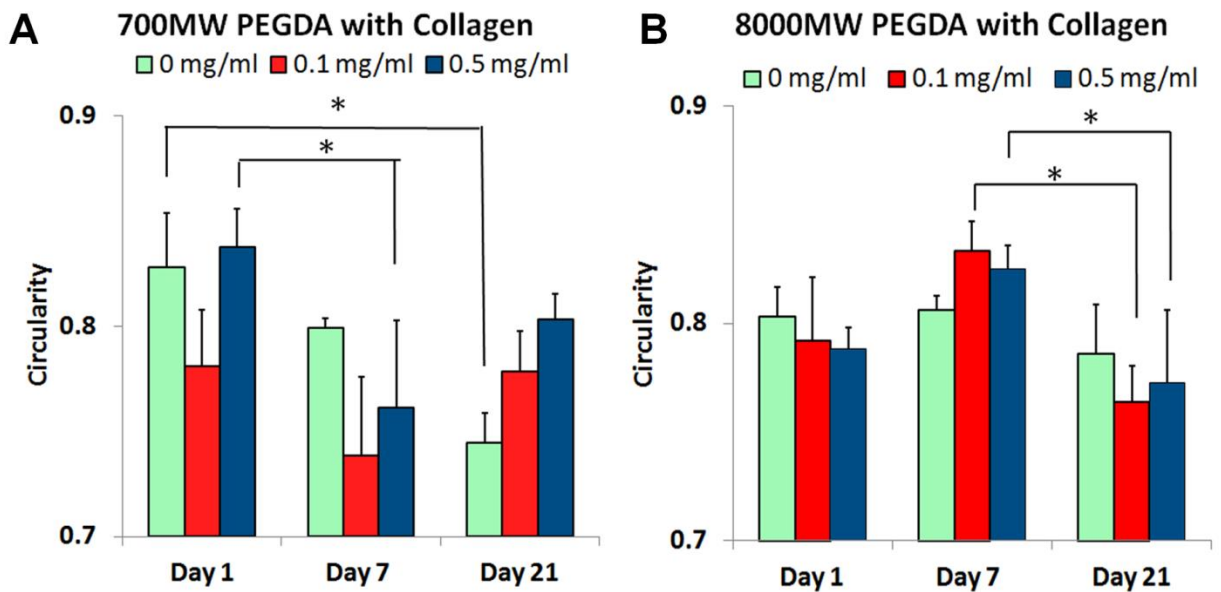


**Figure 3.8 Morphology of PAVIC cultured on PEG-DA and collagen hydrogels**  
**(A)** Circularity of PAVICs on 700 MW PEG-DA (control), + 0.1 mg/ml, and + 0.5 mg/ml collagen at 1, 7, and 21 days of culture. **(B)** Circularity of PAVIC on 8000 MW PEG-DA hydrogels with and without collagen for up to 21 days. \* indicates statistical difference with  $p < 0.05$ .

8000 MW PEG-DA hydrogels did not change significantly over time ( $0.80 \pm 0.01$ ,  $0.80 \pm 0.01$ , and  $0.79 \pm 0.02$  at day 1, 7, and 21, respectively) (Figure 3.8(B)). Circularity after addition of 0.1 or 0.5 mg/ml of type I collagen into either PEG-DA hydrogel did not change over time. These results indicated that PAVIC adhere and spread on the PEG-DA hydrogel (with alginate removed) scaffold material, but that the addition of collagen at 0.1 or 0.5 mg/ml did not improve cell spreading.

#### **4. Discussion**

Replicating mechanical heterogeneity and geometry of the native tissue has been increasingly considered critical for engineering living *de novo* aortic heart valves. We developed and implemented a 3D printing strategy combining on-board UV photocrosslinking with mechanically tunable PEG-DA hydrogels to rapidly fabricate anatomically complex, mechanically heterogeneous valve scaffolds at different sizes. These scaffolds can be seeded with valve cells, which populated the surface and reached the interstitium and remained viable to at least 21 days. The relatively rapid printing times (14-45 minutes), with no requirement for further processing post-fabrication (e.g. joining components), support that 3D printing is an efficient process for engineering anatomically precise soft tissue scaffolds.

Matching patient-specific size is integral for proper valve function. An ongoing limitation of current valve prosthetics is that the prosthetics are often too big for pediatric and young patients. The smallest manufactured mechanical valve to date spans 17 mm (St. Jude Medical Mechanical Heart Valve; St. Jude Medical Inc., Minneapolis, MN). Smaller sized mechanical prosthetic valves have higher gradients and are effectively occluded more by the mechanical leaflets that lie in the flow field (Dasi, Simon et al. 2009). We were able to print valve conduit scaffolds spanning a range of clinically relevant sizes as small as 12 mm ID, which is approximately the size of a 6 month infant aortic valve, and

up to 22 mm ID valve, which is an adult size. We also demonstrated that multiple geometries, a simplified axial symmetric geometry and a medical imaging derived geometry, can be printed using this printing technique. The capability to incorporate direct sizing and patient derived geometry into valve scaffolds suggests that 3D printing could potentially alleviate the prosthetic sizing concern. It is important to note that this study focused on valve scaffold fabrication, and determination of function will require *in vitro* flow studies that are beyond the scope of this work.

Assessing shape fidelity is important for tissue engineering. The common approach of visual inspection, mainly by identifying the presence of key features such as the coronary ostia and the sinuses (Sodian, Loebe et al. 2002), is helpful as a cursory screening process. However, it cannot pinpoint deviations or tolerances of scaffolds in detail required for scale-up manufacturing or complex patient specific applications. Calipers provide limited information on how to improve shape fidelity (Ballyns, Gleghorn et al. 2008), particularly for a complex shape such as a valve where leaflet and root tissue thickness may vary along their lengths. In this study, we used an image-based method to quantitatively assess print accuracy, which was as high as 93% that reduced somewhat as the inner diameter size decreased. This evaluation, which supplemented the visual inspections, provided a more comprehensive demonstration that the printed scaffolds exhibit geometric fidelity.

Our shape fidelity analysis suggested steps that can be taken to improve print accuracy. The same print parameters that yielded high fidelity for 22 mm ID valves produced much more overprint for 12 mm ID valves, suggesting that the print paths were too wide for filling in smaller regions of the 12 mm ID valves without overprinting. Therefore, employing smaller extrusion rate and narrower nozzle diameters (to increase print resolution) would be a scaled approach for optimizing the printing. This adjustment

would have to be balanced with an accompanying increase in print time, but the time would still likely remain to be less than 45 minutes, which was the print time for the 22 mm ID valve. The other step is to adjust for swelling. Compensating for swelling is important because hydrogels have characteristic equilibrium swelling ratio (Bryant and Anseth 2002; Ma and Elisseeff 2005). Since our scaffolds expanded outward but not inward, we suspect that surface tension on the inner walls prevented the scaffolds from swelling inward. Hydrogel scaffolds should therefore be printed thinner than the target size so that the expanded final state matches the native model. By analyzing the fidelity of the printing process layer by layer, we were also able to pinpoint anatomical features that were locally over- or underprinted. Therefore, the fidelity of the final printed shape can likely be improved by adjusting the initial print paths for each layer, but the specific changes will be dependent on the relative thicknesses of each polymer component, the curvature of the shape, and the kinetics of the extrusion process.

Ultimately, tissue engineered heart valve scaffolds must be able to support cell adhesion and migration. The 3D printed scaffolds were populated at the surface and with high viability, indicating that the printing method and resulting material were not cytotoxic. Seeded scaffolds and disks were fed and rinsed with media every 48 hours, and it is possible that cells unable to attach or dying washed away from the valve scaffolds over time. We expect that cell viability is conservatively maintained at the same levels as day 1. We measured a circularity of 0.7-0.8 for all conditions, which indicates that cells were in an elliptically spread configuration. Contrary to our expectations, the addition of collagen into the PEG-DA hydrogels did not promote further spreading. While our SEM images show a hydrogel structure that appears more fibrous upon the addition of collagen to the precursor solution, this addition did not significantly affect the cell behavior. What is interesting to note is that other studies indicate that PEG-DA is non-adsorptive (Rogers, Pagaduan et al. 2011) and alginate is

non-absorptive due to electrostatic repulsion (Rowley, Madlambayan et al. 1999). Additionally, alginate does not have groups that provide any means for mammalian cell attachment (Genes, Rowley et al. 2004), and PEG-DA alone is also reported to discourage cell attachment (Hutson, Nichol et al. 2011). We hypothesize that that a small amount of alginate must remain in the PEG-DA network and the combination roughens the scaffold surface to permit cell adhesion, similar to the microphase separation that is seen in multicomponent PEG-DA hydrogels (Zhang, Wang et al. 2011).

Controlling the mechanical heterogeneity between the root and leaflet has been a major focus in engineering valve scaffolds for ensuring proper hemodynamics and durability. We believe 3D printing can be advantageous for incorporating heterogeneity since it can establish relative differences between tissue regions using these synthetic materials with ease. The ability to rapidly fabricate scaffolds also provides a platform for studying how cells behave on heterogeneous environments, which is crucial to investigate since the modulus of the scaffold material can direct cell migration (Tayalia, Mendonca et al. 2008), spreading (Kloxin, Kloxin et al. 2010), and differentiation (Engler, Sen et al. 2006; Kloxin, Kloxin et al. 2010). The modulus numbers in this study fall within the range of values demonstrated by other studies investigating the tunability of PEG-DA hydrogel tensile mechanical properties (Hahn, McHale et al. 2007; Hou, Schoener et al. 2010; Browning, Wilems et al. 2011). Our results overall suggest that PEG-DA hydrogels can partially recreate the mechanical properties of the aortic valve and pulmonary valve. At physiological tensile strains (0.01-0.20) and low strain rates, the moduli of PEG-DA hydrogels tested here (700 MW: ~75 kPa; 8000 MW: ~5 kPa) fall within range of modulus of native leaflet tissue in the radial direction (~54 kPa (Mavrilas and Missirlis 1991)). However, they are softer than the aortic valve sinus tissue (~ 140-180 kPa (Matthews, Azadani et al. 2010; Butcher, Mahler et al. 2011; Azadani, Chitsaz et al.

2012)). The mechanical properties of the PEG-DA hydrogels more closely match pulmonary valve sinus tissue (~50-85 kPa) (Matthews, Azadani et al. 2010). With the clinical success of the Ross procedure, the pulmonary valve has been identified as a first target for tissue engineered heart valves (Butcher, Mahler et al. 2011), and duplicating those mechanics may be initially more relevant to the field. Additionally, it has been shown that cellularized PEG-DA hydrogels with the addition of moieties that allow for remodeling have improved mechanical properties with dynamic culture (Hahn, McHale et al. 2007). Therefore, this fabrication strategy for engineering valve conduits could be pursued further with the addition of a variety of moieties to PEG-DA hydrogels and dynamic conditioning.

## **5. Conclusions**

This study demonstrated that 3D printing and photo-crosslinking hydrogels can rapidly fabricate anatomical scaffolds exhibiting mechanical heterogeneity and cytocompatibility. This manufacturing process was demonstrated with PEG-DA, but we believe this method could be adapted for use with other photo-crosslinkable polymers. Further work is necessary to complete the translation of this strategy to the clinic. Continued effort must be made to understanding how cells on constructs would remodel the scaffold in simulated hemodynamic conditions. Further investigation of multiple polymer blends to be incorporated into heterogeneous valve conduits would also be required to mimic the complete low and high magnitude strain behaviors of native valve tissues. Our findings herein are encouraging steps toward improved valve scaffold designs for both adult and pediatric valve disease.

## REFERENCES

- Arcaute, K., B. K. Mann, et al. (2006). "Stereolithography of three-dimensional bioactive poly(ethylene glycol) constructs with encapsulated cells." Ann Biomed Eng **34**(9): 1429-1441.
- Azadani, A. N., S. Chitsaz, et al. (2012). "Biomechanical comparison of human pulmonary and aortic roots." Eur J Cardiothorac Surg.
- Balguid, A., A. Mol, et al. (2009). "Hypoxia induces near-native mechanical properties in engineered heart valve tissue." Circulation **119**(2): 290-297.
- Ballyns, J. J., D. L. Cohen, et al. (2010). "An optical method for evaluation of geometric fidelity for anatomically shaped tissue-engineered constructs." Tissue Eng Part C **16**(4): 693-703.
- Ballyns, J. J., D. L. Cohen, et al. (2010). "An optical method for evaluation of geometric fidelity for anatomically shaped tissue-engineered constructs." Tissue Eng Part C Methods **16**(4): 693-703.
- Ballyns, J. J., J. P. Gleghorn, et al. (2008). "Image-guided tissue engineering of anatomically shaped implants via MRI and micro-CT using injection molding." Tissue Eng Part A **14**(7): 1195-1202.
- Bellhouse, B. J., F. H. Bellhouse, et al. (1968). "Fluid mechanics of the aortic root with application to coronary flow." Nature **219**(5158): 1059-1061.
- Benton, J. A., C. A. DeForest, et al. (2009). "Photo-crosslinking of gelatin macromers to synthesize porous hydrogels that promote valvular interstitial cell function." Tissue Eng Part A **15**(11): 3221-3230.
- Benton, J. A., B. D. Fairbanks, et al. (2009). "Characterization of valvular interstitial cell function in three dimensional matrix metalloproteinase degradable PEG hydrogels." Biomaterials **30**(34): 6593-6603.
- Bowles, R. D., R. M. Williams, et al. (2010). "Self-assembly of aligned tissue-engineered annulus fibrosus and intervertebral disc composite via collagen gel contraction." Tissue Eng Part A **16**(4): 1339-1348.
- Browning, M. B. and E. Cosgriff-Hernandez (2012). "Development of a biostable replacement for PEG-DA hydrogels." Biomacromolecules **13**(3): 779-786.
- Browning, M. B., T. Wilems, et al. (2011). "Compositional control of poly(ethylene glycol) hydrogel modulus independent of mesh size." J Biomed Mater Res A **98**(2): 268-273.
- Bryant, S. J. and K. S. Anseth (2002). "Hydrogel properties influence ECM production by chondrocytes photoencapsulated in poly(ethylene glycol) hydrogels." J Biomed Mater Res **59**(1): 63-72.
- Butcher, J. T., G. J. Mahler, et al. (2011). "Aortic valve disease and treatment: the need for naturally engineered solutions." Adv Drug Deliv Rev **63**(4-5): 242-268.
- Butcher, J. T., A. M. Penrod, et al. (2004). "Unique morphology and focal adhesion development of valvular endothelial cells in static and fluid flow environments." Arterioscler Thromb Vasc Biol **24**(8): 1429-1434.
- Butcher, J. T., C. A. Simmons, et al. (2008). "Mechanobiology of the aortic heart valve." J Heart Valve Dis **17**(1): 62-73.

- Chan, V., P. Zorlutuna, et al. (2010). "Three-dimensional photopatterning of hydrogels using stereolithography for long-term cell encapsulation." Lab Chip **10**(16): 2062-2070.
- Chandler, E. M., C. M. Berglund, et al. (2011). "Stiffness of photo-crosslinked RGD-alginate gels regulates adipose progenitor cell behavior." Biotechnol Bioeng **108**(7): 1683-1692.
- Christie, G. W. and B. G. Barratt-Boyes (1995). "Mechanical properties of porcine pulmonary valve leaflets: how do they differ from aortic leaflets?" Ann Thorac Surg **60**(2 Suppl): S195-199.
- Cipitria, A., C. Lange, et al. (2012). "Porous scaffold architecture guides tissue formation." J Bone Miner Res **27**(6): 1275-1288.
- Cohen, D. L., E. Malone, et al. (2006). "Direct freeform fabrication of seeded hydrogels in arbitrary geometries." Tissue Eng **12**(5): 1325-1335.
- Dagum, P., G. R. Green, et al. (1999). "Deformational dynamics of the aortic root: modes and physiologic determinants." Circulation **100**(19 Suppl): II54-62.
- Dasi, L. P., H. A. Simon, et al. (2009). "Fluid mechanics of artificial heart valves." Clin Exp Pharmacol Physiol **36**(2): 225-237.
- Dhariwala, B., E. Hunt, et al. (2004). "Rapid prototyping of tissue-engineering constructs, using photopolymerizable hydrogels and stereolithography." Tissue Eng **10**(9-10): 1316-1322.
- Eckert, C. E., B. T. Mikulis, et al. (2011). "Three-dimensional quantitative micromorphology of pre- and post-implanted engineered heart valve tissues." Ann Biomed Eng **39**(1): 205-222.
- Engler, A. J., S. Sen, et al. (2006). "Matrix elasticity directs stem cell lineage specification." Cell **126**(4): 677-689.
- Fedorovich, N. E., W. Schuurman, et al. (2012). "Biofabrication of osteochondral tissue equivalents by printing topologically defined, cell-laden hydrogel scaffolds." Tissue Eng Part C Methods **18**(1): 33-44.
- Flanagan, T. C., J. S. Sachweh, et al. (2009). "*In vivo* remodeling and structural characterization of fibrin-based tissue-engineered heart valves in the adult sheep model." Tissue Eng Part A **15**(10): 2965-2976.
- Gauvin, R., Y. C. Chen, et al. (2012). "Microfabrication of complex porous tissue engineering scaffolds using 3D projection stereolithography." Biomaterials **33**(15): 3824-3834.
- Genes, N. G., J. A. Rowley, et al. (2004). "Effect of substrate mechanics on chondrocyte adhesion to modified alginate surfaces." Arch Biochem Biophys **422**(2): 161-167.
- Gottlieb, D., T. Kunal, et al. (2010). "*In vivo* monitoring of function of autologous engineered pulmonary valve." J Thorac Cardiovasc Surg **139**(3): 723-731.
- Guo, K. and C. C. Chu (2005). "Synthesis and characterization of novel biodegradable unsaturated poly(ester amide)/poly(ethylene glycol) diacrylate hydrogels." Journal of Polymer Science Part A: Polymer Chemistry **43**(17): 3932-3944.
- Guo, K. and C. C. Chu (2007). "Controlled release of paclitaxel from biodegradable unsaturated poly(ester amide)s/poly(ethylene glycol) diacrylate hydrogels." J Biomater Sci Polym Ed **18**(5): 489-504.

- Hahn, M. S., M. K. McHale, et al. (2007). "Physiologic pulsatile flow bioreactor conditioning of poly(ethylene glycol)-based tissue engineered vascular grafts." Ann Biomed Eng **35**(2): 190-200.
- Hockaday, L. A., K. H. Kang, et al. (2012). "Rapid 3D printing of anatomically accurate and mechanically heterogeneous aortic valve hydrogel scaffolds." Biofabrication **4**(3): 035005.
- Hoffman, J. I. and S. Kaplan (2002). "The incidence of congenital heart disease." J Am Coll Cardiol **39**(12): 1890-1900.
- Hollister, S. J. (2005). "Porous scaffold design for tissue engineering." Nat Mater **4**(7): 518-524.
- Hou, Y., C. A. Schoener, et al. (2010). "Photo-cross-linked PDMSstar-PEG hydrogels: synthesis, characterization, and potential application for tissue engineering scaffolds." Biomacromolecules **11**(3): 648-656.
- Huebsch, N., P. R. Arany, et al. (2010). "Harnessing traction-mediated manipulation of the cell/matrix interface to control stem-cell fate." Nat Mater **9**(6): 518-526.
- Hutson, C. B., J. W. Nichol, et al. (2011). "Synthesis and characterization of tunable poly(ethylene glycol): gelatin methacrylate composite hydrogels." Tissue Eng Part A **17**(13-14): 1713-1723.
- Kloxin, A. M., C. J. Kloxin, et al. (2010). "Mechanical properties of cellularly responsive hydrogels and their experimental determination." Adv Mater **22**(31): 3484-3494.
- Liu, V. A. and S. N. Bhatia (2002). "Three-Dimensional Photopatterning of Hydrogels Containing Living Cells." Biomedical Microdevices **4**(4): 257-266.
- Ma, P. X. and J. H. Elisseeff (2005). Scaffolding in tissue engineering. Boca Raton, Taylor&Francis.
- Malone, E. and H. Lipson (2007). "Fab@Home: The Personal Desktop Fabricator Kit." Rapid Prototyping J **13**: 244-255.
- Matthews, P. B., A. N. Azadani, et al. (2010). "Comparison of porcine pulmonary and aortic root material properties." Ann Thorac Surg **89**(6): 1981-1988.
- Mavrilas, D. and Y. Missirlis (1991). "An approach to the optimization of preparation of bio-prosthetic heart valves." J Biomech **24**(5): 331-339.
- Neidert, M. R. and R. T. Tranquillo (2006). "Tissue-engineered valves with commissural alignment." Tissue Eng **12**(4): 891-903.
- Pedron, S., A. M. Kasko, et al. (2010). "Effect of heparin oligomer chain length on the activation of valvular interstitial cells." Biomacromolecules **11**(6): 1692-1695.
- Peyton, S. R., C. B. Raub, et al. (2006). "The use of poly(ethylene glycol) hydrogels to investigate the impact of ECM chemistry and mechanics on smooth muscle cells." Biomaterials **27**(28): 4881-4893.
- Pibarot, P. and J. G. Dumesnil (2006). "Prosthesis-patient mismatch: definition, clinical impact, and prevention." Heart **92**(8): 1022-1029.
- Ramaswamy, S., D. Gottlieb, et al. (2010). "The role of organ level conditioning on the promotion of engineered heart valve tissue development in-vitro using mesenchymal stem cells." Biomaterials **31**(6): 1114-1125.
- Robinson, P. S., S. L. Johnson, et al. (2007). "Functional Tissue-Engineered Valves from Cell-Remodeled Fibrin with Commissural Alignment of Cell-Produced Collagen." Tissue Eng.

- Rogers, C. I., J. V. Pagaduan, et al. (2011). "Single-monomer formulation of polymerized polyethylene glycol diacrylate as a nonadsorptive material for microfluidics." Anal Chem **83**(16): 6418-6425.
- Rowley, J. A., G. Madlambayan, et al. (1999). "Alginate hydrogels as synthetic extracellular matrix materials." Biomaterials **20**(1): 45-53.
- Sacks, M. S., F. J. Schoen, et al. (2009). "Bioengineering challenges for heart valve tissue engineering." Annu Rev Biomed Eng **11**: 289-313.
- Sales, V. L., B. A. Mettler, et al. (2010). "Endothelial progenitor cells as a sole source for ex vivo seeding of tissue-engineered heart valves." Tissue Eng Part A **16**(1): 257-267.
- Schaefermeier, P. K., D. Szymanski, et al. (2009). "Design and fabrication of three-dimensional scaffolds for tissue engineering of human heart valves." Eur Surg Res **42**(1): 49-53.
- Schmidt, D., P. E. Dijkman, et al. (2010). "Minimally-invasive implantation of living tissue engineered heart valves: a comprehensive approach from autologous vascular cells to stem cells." J Am Coll Cardiol **56**(6): 510-520.
- Seliktar, D., R. A. Black, et al. (2000). "Dynamic mechanical conditioning of collagen-gel blood vessel constructs induces remodeling *in vitro*." Ann Biomed Eng **28**(4): 351-362.
- Seliktar, D., R. M. Nerem, et al. (2001). "The role of matrix metalloproteinase-2 in the remodeling of cell-seeded vascular constructs subjected to cyclic strain." Ann Biomed Eng **29**(11): 923-934.
- Shinoka, T., P. X. Ma, et al. (1996). "Tissue-engineered heart valves. Autologous valve leaflet replacement study in a lamb model." Circulation **94**(9 Suppl): II164-168.
- Skardal, A., J. Zhang, et al. (2010). "Photocrosslinkable hyaluronan-gelatin hydrogels for two-step bioprinting." Tissue Eng Part A **16**(8): 2675-2685.
- Sodian, R., S. P. Hoerstrup, et al. (2000). "Early *in vivo* experience with tissue-engineered trileaflet heart valves." Circulation **102**(19 Suppl 3): III22-29.
- Sodian, R., M. Loebe, et al. (2002). "Application of stereolithography for scaffold fabrication for tissue engineered heart valves." ASAIO J **48**(1): 12-16.
- Sodian, R., P. Schaefermeier, et al. (2010). "Use of human umbilical cord blood-derived progenitor cells for tissue-engineered heart valves." Ann Thorac Surg **89**(3): 819-828.
- Sodian, R., J. S. Sperling, et al. (1999). "Tissue engineering of a trileaflet heart valve-early *in vitro* experiences with a combined polymer." Tissue Eng **5**(5): 489-494.
- Sutherland, F. W., T. E. Perry, et al. (2005). "From stem cells to viable autologous semilunar heart valve." Circulation **111**(21): 2783-2791.
- Tayalia, P., C. R. Mendonca, et al. (2008). "3D Cell-Migration Studies using Two-Photon Engineered Polymer Scaffolds." Advanced Materials **20**(23): 4494-4498.
- van Geemen, D., A. Driessen-Mol, et al. (2012). "Variation in tissue outcome of ovine and human engineered heart valve constructs: relevance for tissue engineering." Regen Med **7**(1): 59-70.
- Vesely, I. (2000). "Aortic root dilation prior to valve opening explained by passive hemodynamics." J Heart Valve Dis **9**(1): 16-20.
- Xu, C., W. Chai, et al. (2012). "Scaffold-free inkjet printing of three-dimensional zigzag cellular tubes." Biotechnology and Bioengineering: n/a-n/a.

Zhang, H., L. Wang, et al. (2011). "Controllable properties and microstructure of hydrogels based on crosslinked poly(ethylene glycol) diacrylates with different molecular weights." Journal of Applied Polymer Science **121**(1): 531-540.

## CHAPTER 4

### PHOTO-ENCAPSULATION AND VIABILITY OPTIMIZATION OF VALVE CELLS AND MESENCHYMAL STEM CELL FOR DIRECT 3D PRINTING

#### **4.1 Summary**

This study further explores variables associated with photo-crosslinking hydrogels and relationships previously demonstrated or suspected by other investigators, for a printable MEGEL:PEG-DA 3350 mixture containing valve cells or mesenchymal stem cells. Contrary to numerous 2D cytotoxicity studies, we demonstrate that in a 3D hydrogel culture environment and fabrication setting, Irgacure 2959 can produce more viable encapsulated cells than VA086 in a higher stiffness hydrogel. Intracellular oxidative stress was not significantly greater in hydrogel conditions of more Irgacure 2959 photoinitiator radicals. Normalized oxidative stress ratios suggest that increasing VA086 radicals induced higher Intracellular oxidative stress. Suppression of intracellular oxidative stress using catalase pretreatment does not disrupt hydrogel crosslinking but it does not rescue cell viability.

#### **4.2 Introduction**

Numerous studies indicate that cell-cell interactions and cell-material interactions in the 3D microenvironment in native tissue are fundamentally different than in 2D (Muller, Davenport et al. 2009; Bellis, Bernabe et al. 2013; Chitcholtan, Asselin et al. 2013). As a result, the emphasis of how cell biology is investigated is shifting from 2D culture models to 3D culture models (Lund, Yener et al. 2009; Baker and Chen 2012; Santos, Hernandez et al. 2012). 3D printing is of interest as a tool both because it enables

mechanistic and biological investigation in 3D at multiple scales, such as at the cell level (Lee, Moon et al. 2008; Torgersen, Ovsianikov et al. 2012) and the tissue level (Chang, Boland et al. 2011; Fedorovich, Alblas et al. 2011)), and because it could translate into a means for fabricating living tissue at a scale suitable for clinical use (Koch, Deiwick et al. 2012; Luangphakdy, Walker et al. 2013). In our first study (described in Chapter 3) where we 3D printed hydrogel valve constructs, the hydrogel constructs were post-fabrication seeded with PAVIC (Hockaday, Kang et al. 2012). We demonstrated that by using photo-crosslinking we could achieve a high degree of geometric control and shape fidelity. However, the cellularity of these constructs is limited to the surface of the scaffolds. In a subsequent study we directly printed cells into valve constructs but used a chemical/ionic crosslinker to solidify the hydrogel (Duan, Hockaday et al. 2013). We did not have the same level of geometric control with this crosslinking strategy. In order to fully utilize the geometric control of the Fab@Home™ 3D printer to incorporate heterogeneity and to deposit multiple cell types throughout the valve construct, optimal conditions for direct cell printing and photo-crosslinking were investigated.

In this study, poly-(ethylene glycol)diacrylate (PEG-DA) and methacrylated gelatin (MeGel) photo-crosslinkable hydrogel precursors (Benton, DeForest et al. 2009; Hutson, Nichol et al. 2011) were combined with non-photo-crosslinking alginate to make a solution suitable for extrusion 3D printing. PEG-based hydrogels have been used to study heart valve interstitial cells response to mechanical properties in both 2D and encapsulate 3D in-vitro studies (Kloxin, Benton et al. 2010; Durst, Cuchiara et al. 2011). This vast potential for mechanical and/or molecular customization, coupled with

their relatively low cost, suggests PEG-DA could be an ideal material component for clinically relevant scale 3D tissue printing. Gelatin is synthesized by partial breakdown of collagen, but it retains some bioactive features of collagen, particularly cell attachment/binding domains (Benton, DeForest et al. 2009). Gelatin can be modified for photo-crosslinking by incorporating double bond pendent groups on the gelatin chains, to make methacrylated gelatin. Methacrylated gelatin (MeGel) hydrogels are enzymatically degradable and have been used to encapsulate valve interstitial cells (Benton, DeForest et al. 2009), and with the addition of PEG-DA the degradation properties are modifiable (Hutson, Nichol et al. 2011). Irgacure 2959 and VA086 photoinitiators have previously been used with live cells in 3D hydrogels (Rouillard, Berglund et al. 2010; Hutson, Nichol et al. 2011). Irgacure 2959 and VA086 were tested in this study for their ability to photo-crosslink MEGEL/PEG-DA precursor solution and for their effect on encapsulated cells.

In a healthy cell of an aerobic organism reactive oxygen species (ROS) are produced at a controlled rate, but in a cell subjected to oxidative stress there is an imbalance between production of ROS and the cell's ability to scavenge and manage them (Molecular Probes Handbook;(Abramov, Scorziello et al. 2007; Mallajosyula, Kaur et al. 2008; Quintanilla, Matthews-Roberson et al. 2009; Wang, Su et al. 2009). As a result oxidative stress and ROS can cause alterations in membrane lipids, proteins, and nucleic acids. The free radicals produced by Irgacure 2959 photo-initiation are membrane impermeable and are suspected to cause damage by lipid peroxidation (Lampe, Namba et al. 2009). Less is known about VA086 radicals, but as a photoinitiator it is considered

less cytotoxic than Irgacure 2959 (Chandler, Berglund et al. 2011; Rouillard, Berglund et al. 2011; Occhetta, Sadr et al. 2013). Fedorovich et al tested the effects of Irgacure 2959 photo-initiation on bone marrow mesenchymal stem cells in both 2D and in encapsulating hydrogels. They found that cell viability, cell cycle, and cell proliferation are negatively affected by Irgacure 2959 photoinitiation/radicals and that DNA damage occurs inside the cell (indicated by positive staining of p53 binding protein 1). DNA damage in the nucleus suggests that oxidative stress may propagate into the cell. In their 3D hydrogels, they observed significantly less DNA damage in the 3D conditions than in the 2D conditions (10% compared to 66% of cells) and at the concentrations and energies they used (0.05-0.1% w/v Irgacure, 6 mW/cm<sup>2</sup>) photo-polymerization in a 3D hydrogel precursor environment did not negatively influence cell survival or osteogenic differentiation (Fedorovich, Oudshoorn et al. 2009). They also did not observe differences between Irgacure concentration conditions in 3D. They conclude from this protective effect that in the 3D hydrogel environment that photoinitiator radicals preferentially react with target polymer precursors and that reactive species are therefore unavailable to damage cellular components. Rouillard et al working at a lower concentration of Irgacure 2959 (0.03% w/v) in alginate hydrogels observed that Irgacure 2959 had a detrimental effect on chondrocyte viability (below 70%) (Rouillard, Berglund et al. 2011). The difference between these two studies (Irgacure effects viability in one, Irgacure does not affect viability in the other) suggests that the protective effect of a 3D hydrogel photo-crosslinking system could be related to the encapsulating hydrogel material (methacrylated alginate verses the methacrylated hyaluronic acid and methacrylated hyperbranched polyglycerol) or that the two cell types have different

sensitivities to the Irgacure radicals in photo-crosslinking conditions. Others have observed cell-specific differences in response to photoinitiator radicals (Williams, Malik et al. 2005) and different amounts/expression of intracellular and membrane components can engender protection against oxidative stress (Manevich, Sweitzer et al. 2002; Singh, Brocker et al. 2013). Identifying what causes cell-type specific viability differences in hydrogels could lead to a strategy to combat photo-crosslinking damage in more sensitive cells. This would enable a broader use of photo-crosslinking in tissue engineering.

In this study we quantify the different viability response of valve interstitial cells, valve smooth muscle cells, and adipose derived mesenchymal stem cells to photo-crosslinking encapsulation conditions in Methacrylated Gelatin/PEG-DA hydrogels with Irgacure 2959 and VA086 photoinitiators. To investigate the role intracellular oxidative stress in cell-specific vulnerability to photo-crosslinking conditions, encapsulated cells were loaded with DCF, a general oxidative stress indicator, prior to encapsulation. We also tested catalase treatment for its ability to rescue photo-encapsulated cells from photoinitiator induced damage.

### ***4.3 Materials and Methods***

#### **4.3.1 Synthesis of Polymer Precursors**

Methacrylated gelatin (MEGEL) was synthesized as previously described (Nichol, Koshy et al. 2010; Duan, Hockaday et al. 2013; Duan, Kapetanovic et al. 2014). Briefly, gelatin from bovine skin (Sigma) was dissolved at 10% w/v into distilled water at 40 °C and then methacrylic anhydride (MA, Sigma) (1:5 v/v to gelatin solution) was added

drop by drop under stirred conditions at 40 °C for 1 hour. Polyethylene glycol diacrylate molecular weight 3350 was synthesized as previously described (PEG-DA 3350) (Cruise, Scharp et al. 1998; Guo, Chu et al. 2005). Poly(ethylene glycol) (PEG, Sigma) was dissolved in benzene (1.5 mmol of PEG in 150 ml of benzene) and heated to 45 °C with continuous stirring until completely dissolved. The solution was cooled to room temperature and triethylamine was added at 8 fold molar concentration (based on PEG diol end groups) to the PEG solution (12 mmol). Acryloyl chloride (Sigma) at eightfold molar excess concentration was weighed out then diluted using benzene (1:40 acryloyl chloride to benzene) and added drop wise to the PEG solution through a drop funnel under an ice bath. The mixture was stirred overnight, and then the reaction stopped. The insoluble triethylamine was removed by filtration. PEG-DA was precipitated from the solution by the addition of petroleum ester (Sigma). The PEG-DA precipitate was collected using a funnel, re-dissolved in 20 ml of benzene, and again precipitated by adding petroleum ester. The precipitation process was repeated several times.

After synthesis the MEGEL and PEG-DA products were dissolved in distilled water and transferred and sealed into dialysis tubing with a molecular weight cut off of 1000 Da. The polymers were dialyzed against distilled water for 5-7 days in 5 gallon containers with frequent water changes. The polymer product was then frozen at -20C and then lyophilized. Lyophilized polymers were stored at -20°C.

#### **4.3.2 Preparation of Sterile Polymer Precursor Solution**

Polymer precursor solution was prepared the same way for mechanical comparisons and for cell encapsulation for viability assessment and printing. Polymer solutions were prepared in a biosafety cabinet. Hydrogel precursor solutions were made 20% w/v

polymer to solution, MEGEL:PEG-DA 3350 1:1. Polymer precursors were weighed out dry and then sterilized for 1 hour using germicidal UV and then transferred into sterile 50-ml conical tubes. Photoinitiators 2,2'-Azobis[2-methyl-N-(2-hydroxyethyl)propionamide] (VA-086, Wako Chemicals) and 2-hydroxy-1(4-(hydroxyethoxy)phenyl)-2-methyl-1-propanone (Irgacure 2959, BASF Corporation, Newport, DE) were weighed out and dissolved in 70% ethanol to make stock solutions of 0.1g VA086/ml of ethanol solution and 0.015g Irgacure/ml of ethanol solution which were then sterile filtered (Chandler, Berglund et al. 2011; Rouillard, Berglund et al. 2011). Stock solutions were stored at room temperature and used within 1 week. Photoinitiator stock solution was added to sterilized polymers to give a final concentration of 0.25-1.0% w/v VA086 or 0.025-0.1% w/v Irgacure. The remaining solution volume was valve cell culture media. Polymer precursors, photoinitiator solution, and media were combined in conical tube, the tube cap was wrapped with parafilm, and the tube placed into water bath at 37°C to dissolve.

#### **4.3.3 Light Meter Measurements and Light Sources for Photo-crosslinking**

365 nm UV light intensity was measured at different distances from several light sources with a UVX Radiometer UVP and sensor model UVX-36 Serial Number E 23832. The meter reached its maximum at 20 mW/cm<sup>2</sup> so the distance from the sensor and the intensity was measured and then a power fit to the data was used to extrapolate the intensity at the printing surface for the higher intensity light sources.

Three light sources were measured - a lamp, a low power LED array, and a high power LED array. The lamp used was a Spectroline Lamp 365nm EN280L with a single bulb.

The 365nm LED arrays were built to mount on the syringe carriage. The low power LED array, previously used for printing valve scaffolds [Biofabrication 2012], was built with 4 NCSU033A LEDs (Nichia America Corporation, Wixom, MI). Note: NCSU033A LEDs have since been discontinued and the equivalent is NCSU033B LEDs. The circuit was built with 50  $\Omega$ , 33  $\Omega$ , or 25  $\Omega$  limiting resistances per LED (calculated 248 mA, 375 mA, and 496 mA forward current per LED and radiant flux at LED 154 mW, 233 mW, and 307mW for each limiting resistance). The high power LED array, was built with 4 NC4U133A LEDs (Nichia) and 60  $\Omega$  limiting resistances (calculated 350 mA forward current per LED and radiant flux 868 mW). An ice water cooled copper heatsink was built into the high powered LED array to keep the LEDs cool.

#### **4.3.4 Mechanical Testing of Hydrogel Disks**

Mechanical properties of crosslinked hydrogels were tested to determine working ranges for fabrication. Hydrogel precursor solution was crosslinked into disks and rinsed for mechanical testing and swelling tests. Precursor solution was pipetted into a syringe, 7.5% w/v Protanal LF 10/60 sodium alginate (alginate, FMC Biopolymer now changed name to FMC Health and Nutrition) was added as a viscosity modifier and stirred in with a spatula. The syringe stopper was reinserted, the bubbles squeezed out, and the viscous precursor solution was mixed back and forth between two syringes connected by a Luer adapter to fully homogenize. The solution was extruded into silicon rubber 8 mm diameter disk molds in a petri dish and leveled with a coverslip (coverslip used to scrape excess off). The solution filled molds were positioned under either the lamp (2.7 cm from source) or high power LED array mounted on the printer syringe carriage (at print surface 1.2 cm from source) and crosslinked for 3, 5, and 7 min minutes. The

gaskets were peeled off the petri dish, and 1X phosphate buffered saline (PBS, VWR International, Radnor PA) was added to the petri dish with the crosslinked hydrogel disks. The hydrogels in PBS were placed on rocker/rotator at room temperature, and PBS was exchanged after 1 hour and 24 hours to rinse out the alginate viscosity modifier. Disks were mechanically tested or evaluated in swelling tests.

Uniaxial confined compression testing was performed on hydrated and rinsed disks within 48 hours on a mechanical testing platform (EnduraTec 3200; Bose Electroforce, Eden Prairie, MN). Samples were ramp loaded quasi-statically at 0.01mm/sec to 30% strain. Modulus ( $E_{5\text{to}15}$ ) was calculated from the 5 to 15% strain portion of the stress strain curve. Sample size was n=3 to n=14. The Student's t-test was applied to the data set.

PBS hydrated and rinsed disks were weighed to determine the equilibrium swollen mass, then lyophilized for 48 hours, and then weighed to obtain the dry polymer mass for each sample. The hydrogel swelling ratio based on mass was calculated (Baier Leach, Bivens et al. 2003) with the relationship:

$$\text{Swelling Ratio (SR)} = \frac{\text{Wet Weight of Swollen Hydrogel Disk}}{\text{Dry Weight of Hydrogel}}$$

Sample size was n=5 to n=8.

#### **4.3.5 Heart Valve and Mesenchymal Cell Culture**

Direct cell printing encapsulation conditions were tested with both primary aortic valve cells and adipose derived mesenchymal stem cells (ADMSC). Valve interstitial cells

(VIC) are the main cell type that populates valve leaflets (Butcher, Simmons et al. 2008) and valve sinus smooth muscle cells (SSMC) populate the root wall of the valve. Primary valve cells have been used to study mechanistic and remodeling behavior as well as to establish tissue engineering targets (Stephens, Durst et al. 2011; Gould, Chin et al. 2012; Duan, Hockaday et al. 2013; Gould and Anseth 2013). Heart valves are non-sacrificial, and for the purposes of tissue engineering a heart valve a cell source other than primary valve cells is needed. A recent study profiled ECM gene expression of ADMSC and VICs in response to strain. They found that the two cell types have the capacity to synthesize and remodel the surrounding matrix and the two cell types have comparable response to mechanical stimulus (Latif, Sarathchandra et al. 2007; Colazzo, Sarathchandra et al. 2011). ADMSC can be differentiated towards osteogenic, adipogenic, myogenic, chondrogenic, neurogenic, endothelial, and smooth muscle cell lineages (Colazzo, Chester et al. 2010; Wang, Yin et al. 2010). ADMSC have demonstrated similar phenotypic and functional characteristics to bone marrow mesenchymal stem cells (BMMSC), which are more established in the literature, but ADMSC isolation is less invasive (Bunnell, Flaatt et al. 2008); (Colazzo, Chester et al. 2010). In addition, adipose tissue is present in infants, children, and adults (Kuzawa 1998). These characteristics suggest ADMSC are a potentially feasible cell source for TEHV that could be applicable to all three age groups.

Porcine aortic valve interstitial cells (PAVIC) were isolated via collagenase digestion as previously described (Butcher and Nerem 2004; Butcher, Penrod et al. 2004; Richards, El-Hamamsy et al. 2013). PAVIC were cultured with Dulbecco's Modified Eagle's

Medium (DMEM; Invitrogen, Carlsbad, CA) supplemented with 10% fetal bovine serum (FBS; Invitrogen) and 1% penicillin/streptomycin (PS; Invitrogen). Cells were fed every 2-3 days and were used at passage number 4-8.

Human aortic valve interstitial cells (HAVIC) and human aortic sinus smooth muscle cells (HASSMC) were isolated from the aortic valve of the donor heart of a 12-year old patient undergoing cardiac transplant for a myocardial contractility mutation that is not present in valves (Duan, Kapetanovic et al. 2014). Human cells were isolated using the same procedure as previously used for porcine cells (Butcher and Nerem 2004), except that the collagenase used to digest the endothelial cell denuded leaflet and root tissue was made with MCDB 131 medium (Sigma) instead of DMEM and the HASSMC were isolated from biopsy punches taken below the sinotubule junction. The valve leaflets were inspected and contained no calcific deposits or thickened lesions. Tissue was procured with consent as approved by the Institutional Review Board of Weill-Cornell Medical College in New York City. Cells were cultured in MCDB131 medium supplemented with 10% FBS, 1% PS, 0.25 µg/L recombinant human fibroblast growth factor basic (rhFGF-2; Invitrogen) and 5 µg/L recombinant human epidermal growth factor (rhEGF; Invitrogen). Cells were fed every 2-3 days and used at passage number 4-8.

Cryopreserved HADMSC were purchased (Cat #:PT-5006, Lot#0F4505) Lonza, Walkersville). HADMSC were isolated from a 52 year old female donor and cryopreserved December 6, 2010. Greater than 90% of the cells were positive for

CD13, CD29, CD44, CD73, CD90, CD105, and CD166. Less than 5% of cells were positive for CD14, CD31, and CD45. (Note: According to the certificate of analysis for HADMSC 23 hour doubling time). HADMSC were thawed and cultured using Dulbecco's Modified Eagle Medium: Nutrient Mixture F-12 (F12:DMEM, Invitrogen) supplemented with 10% FBS, 1% PS. HADMSC were passaged at just sub-confluent (~90%) and fed every 3-4 days. Cells were used at passage number 4-8.

PAVIC, HAVIC, HASSMC, and HADMSC were expanded and maintained in flasks with DMEM, MCDB 131, MCDB 131, and F12/DMEM media respectively.

#### **4.3.6 Encapsulation and Handling for Disk Experiments and *In vitro* Culture**

To test how variations in photoinitiator type, photoinitiator concentration, and intensity of UV light exposure effect printed cells, cells were encapsulated in precursor solution, extruded into disk molds, and crosslinked with either lamp or the high power LED array. For encapsulation studies porcine cells were cultured in DMEM, and all human cells were cultured in MCDB131 media. Cells were rinsed with PBS, trypsinized from flasks that were 80-95% confluent, trypsin was inactivated with supplemented media, and cells were counted. Cells were spun down into a pellet (1000 RPM, 5 min). Cells were suspend in a small amount of media and then resuspended in warmed 37°C precursor solution so that the concentration was 2.5 million cells/ml of precursor solution. Precursor solution was pipetted into syringes connected by Luer adapter with the stopper/piston removed from one side. 7.5% w/v alginate powder was added and stirred in with a sterile spatula. The syringe piston was reinserted, the bubbles squeezed out, and the viscous precursor solution was mixed back and forth between the two syringes

to fully homogenize. Syringes were kept in the incubator at 37°C until ready to crosslink to keep precursor gel warm. If the solution is allowed to cool, the MEGEL component solidifies and the photo-crosslinking does not work or is only partial. The Luer adapter was detached and the syringe was used to extrude precursor gel into 8 mm diameter, 1-mm thick gasket molds in a petri dish. The gel was leveled with a sterile coverslip. Filled molds were positioned under the lamp or HLED array and were exposed to UV light for 5 minutes. 20 ml of media was applied to submerge, hydrate, and loosen the hydrogel disks and the gasket was peeled/removed before the petri dish was placed in the incubator. After 1 hour incubation in the media, the hydrogel disks were transferred to 6-well plates containing fresh media. Plates were placed on a rocker in a walk in incubator set at 37°C and 5% CO<sub>2</sub>. Media was exchanged after 24 hrs and then hydrogels were fed every 48 hours

#### **4.3.7 LIVE/DEAD Staining**

Encapsulated cells were stained with LIVE/DEAD Viability and Cytotoxicity Kit (Invitrogen) to determine viability of cells after 1 day, 3 day, 4 day, and 7 day culture. Green fluorescent calcein-AM (LIVE) staining indicates intracellular esterase activity and red fluorescent ethidium homodimer-1 (DEAD) indicates loss of plasma membrane integrity. Dye working solution was prepared at a concentration of 4 μM DEAD and 2 μM LIVE in PBS warmed to 37°C. Media was aspirated from wells containing gel disks and dye working solution was applied directly to gels. Working solution submerged gels were incubated for 30 minutes at 37°C. Dye solution was aspirated and gels were rinsed with warmed PBS. PBS was aspirated and warmed culture media was added to wells. LIVE/DEAD stained disks were imaged using an epifluorescence

stereomicroscope (SteREO Discovery.V20; Zeiss, Germany). 3-4 disks per condition were imaged and 3 images per sample were averaged. Images for analysis were taken using the 1X objective and 150X magnification and analyzed using Image J.

#### **4.3.8 Metabolic Activity Assessment**

3-[4,5-dimethylthiazol-2-yl]-2,5- diphenyltetrazolium bromide; thiazolyl blue (MTT, Sigma-Aldrich) was used to assess metabolic activity of encapsulated cells after 1 day, 3 day, 4 day, and 7 day culture (Duan, Wang et al. 2010). MTT is yellow in solution and then is converted to a dark blue water insoluble MTT formazan by mitochondrial dehydrogenase of living metabolically active cells (Carmichael, DeGraff et al. 1987). Cells that are actively proliferating have an increased metabolic activity while cells that have been exposed to toxins will have decreased metabolic activity. MTT assay does not distinguish between cytostatic (growth inhibitory) and cytotoxic (lethal) effects of a treatment. Hydrogel disks seeded with encapsulated cells were cultured for 1, 3, 4, and 7 days and then stained with MTT. MTT solution was prepared at a concentration of 5 mg MTT powder/ml in PBS and sterile filtered before use. Cultured disks were rinsed with PBS and transferred to a 24-well plate with each well containing 1 ml of media. 1/10 media volume of MTT solution (0.1 ml) was added to each well and incubated for 4 hours at 37°C. Disks were transferred to a 48 well plate containing 500 µl of dimethyl sulfoxide (DMSO, Sigma-Aldrich) per well and pulverized using forceps to break up the gel and completely dissolve the formazan. 100 µl aliquots of solution were pipetted into a 96-well plate and the absorbance of the solution was analyzed using a multi-detection microplate reader (BioTek Synergy HT) at 570 nm. 3-4 disks per condition were analyzed.

#### **4.3.9 Doubling Time Assay**

Sensitivity to photoinitiator conditions and degree of oxidative damage can depend on cell type and proliferation rate (Williams, Malik et al. 2005). Growth kinetics were assessed for all 4 cell types: PAVIC, HAVIC, HASSMC, and HADMSC (Williams, Malik et al. 2005). Cells were plated at an initial cell density of 2500 cells/cm<sup>2</sup> in 24-well plates and cell medium (MCDB for human, DMEM for porcine). Media was changed every other day and cells were trypsinized from 4 individual wells per cell every other day for 10 days and counted with a hemocytometer. The number of cells for each day for each cell type was calculated as a mean of the 4 wells. Population doubling times ( $P_D$ ) were calculated by dividing the length of log phase of growth by the results of the equation  $P=3.32(\log_{10}N_1-\log_{10}N_0)$ .  $N_1$ =number of cells at end of log phase,  $N_0$ =number of cells at beginning of log phase,  $P$ = number of population doublings.

#### **4.3.10 General Oxidative Stress**

Cells were labeled with a general oxidative stress indicator and exposed to photo-encapsulation conditions to determine if oxidative stress could explain viability differences between human cell types and conditions. Two chloromethyl derivative dyes were used to investigate oxidative stress in encapsulated and printed cells: 5-(and-6)-chloromethyl-2',7'-dichlorodihydrofluorescein diacetate, acetyl ester CM-H<sub>2</sub>DCFDA (DCF, Invitrogen) and CellTracker Red CMTPX (CTR, Invitrogen). DCF was used to indicate general oxidative stress in encapsulated cells. CTR was used to tag all cells being encapsulated to determine what fraction of cells were fluorescing positive for oxidative stress with DCF. DCF passively diffuses into a cell where its acetate groups are cleaved by intracellular esterases and its thiol-reactive group reacts with intracellular

glutathione and thiols (Kirkland and Franklin 2001; Kirkland, Saavedra et al. 2007). Oxidation of this product results in a fluorescent adduct that is trapped inside the cell. DCF is oxidized by cellular hydrogen peroxide, hydroxyl radicals, and radicals downstream from hydrogen peroxide. DCF is itself insensitive to oxidation by superoxide ( $O_2^-$ ) (Kirkland and Franklin 2001) or singlet molecular oxygen ( $O_2^*$ ) (Bilski, Belanger et al. 2002), but it can be considered an indirect indicator of these. It reacts with the downstream products of  $O_2^*$  reaction with cellular substrates that produce peroxy products and peroxy radicals, and it reacts with the hydrogen peroxide produced by dismutation of  $O_2^-$  (Kirkland and Franklin 2001; Bilski, Belanger et al. 2002). CTR passes freely through the cell membrane where upon it is converted into cell membrane impermeant fluorescent dye which is retained for several days and multiple cell divisions. Celltracker Red does not require enzymatic cleavage to be fluorescent.

For oxidative stress studies, cells were pre-loaded with DCF and CTR prior to encapsulation. After cells were trypsinized and spun down, cells were suspended in DCF/CTR working solution at a concentration of 0.5 million cells/ml of working solution. Working solution concentration was 10  $\mu$ M DCF and 7  $\mu$ M CTR in Hank's Balanced Salt Solution (HBSS, Gibco Invitrogen(Johnson 2010)). DCF working solution concentration and incubation time was previously described (except in media instead of HBSS)(Kirkland, Saavedra et al. 2007). Cells were incubated in working solution for 20 minutes at 37°C, spun down (1000 RPM, 5min), rinsed and re-suspended with HBSS, spun down, and then encapsulated in polymer precursor solution made with either 0.1% w/v Irgacure or 1.0% VA086 (same encapsulation procedure at above). Precursor

solution was mixed with alginate, extruded into disks, and exposed to UV light using the lamp or the high powered LED array for 5 minutes. MCDB media was applied to hydrogel disks to hydrate and loosen from the petri dish and gaskets. 1 ml of HBSS was pipetted into each well of a black bottom 48 well plate and the hydrogel disks were transferred into the wells. Cell suspension controls of loaded cells suspended in HBSS were also pipetted into wells. The plate was scanned immediately on the plate reader for fluorescence intensity of DCF using an area scan of each well (Ex/Em 485/528).

Hydrogel disks were transferred back into media and incubated at 37°C and imaged using confocal laser scanning microscopy (25X H<sub>2</sub>O objective, LSM 710, Carl Zeiss).

n=4 for all conditions. Images were evaluated using image J. Number of red fluorescent cells (cell tracker) and green fluorescent cells (DCF) were counted and then percent of cells experiencing oxidative stress was calculated (DCF cell count/Cell tracker cell count \*100) .

#### **4.3.11 Catalase Treatment of Cells**

Cells were treated with catalase prior to encapsulation to determine if oxidative stress could explain viability differences between cell types and conditions and if reduction in oxidative stress could improve viability in encapsulated conditions. Cells were incubated in catalase isolated from bovine liver (Sigma-Aldrich) solution 1000 units/ml of HBSS. This dosage is in the range of what has previously been used with live cells (Hela cells, smooth muscle cells)(Sakata, Miyamoto et al. 1998; Sakai, Liu et al. 2013) Catalase is an enzyme that catalyzes the decomposition of hydrogen peroxide into water and oxygen. For testing the effect of catalase on oxidative stress, catalase was

added to the DCF/CTR/HBSS working solution and incubated with cells for 20 minutes prior to encapsulation. Samples were assessed using the plate reader and confocal imaging. For testing the effect of catalase on day 3 viability, cells were incubated in catalase/HBSS solution for 20 minutes prior to encapsulation.

Oxidative stress ratio was calculated from the average of relative fluorescence values of HBSS treated cell laden hydrogels relative fluorescence divided by catalase treated cell laden hydrogels relative fluorescence of a given photoinitiator and light source condition.

$$\text{Oxidative Stress Ratio} = \frac{\text{Average HBSS Relative DCF Fluorescence}}{\text{Average Catalase Relative DCF Fluorescence}}$$

As a cell suspension control, cells DCF and cell tracker loaded and resuspended were then benchtop incubated in media while the hydrogel disks were printed and photo-crosslinked. The cells were then spun down and then suspended in HBSS. Relative fluorescence data was collected using the plate reader and then the HBSS suspended cells were imaged with the confocal microscope.

#### **4.3.12 Statistics**

JMP PRO was used to make statistical comparisons. The Student's t-test was applied to the data sets. Standard error of the mean was calculated and is displayed on graphs. Fit least squares regression analysis was done on the day 3 lamp viability results to compare slopes.

## **4.4 Results**

### **4.4.1 Range of Light Intensities for Photo-crosslinking During Printing**

Strategies for photo-crosslinking include both crosslinking during the fabrication, directly after material is extruded from the syringe tips (example: mounted LEDs configuration shown in Figure 4.1A, 1D), or crosslinking post fabrication of the whole scaffold (example: bench top lamp configuration shown in Figure 4.1B). It is important to consider that the energy delivery is not constant with a mounted light source that photo-crosslinks material as it is being printed. There is a range of light intensity on the extruded hydrogel during the course of printing since the distance between the light source and construct changes. During the course of printing the syringes trace out the print paths and the stage moves up and down when it initiates a new path, and as the scaffold builds up in layers the stage moves down. In this printing platform the minimum crosslinking time and light exposure required to solidify a hydrogel are critical variables that set the fabrication time of a construct as well as determines the feasibility of using a particular polymer combination for direct bio-printing of cells. Light sources were first characterized to establish working ranges in subsequent experiments that cells will tolerate for printing. The 365 nm light intensity of the low power LEDs (Figure 4.1A), previously used in a 4 LED array to print PEG-DA hydrogel aortic valve constructs (Hockaday, Kang et al. 2012), fell between the Spectroline lamp (Figure 4.1B) and the high powered LED array (Figure 4.1C, Figure 4.1E, Table 4.1). The array circuit resistance is used to set the forward current through each LED and thus the radiant flux. The measured and extrapolated intensity at the printing surface with a single low power LED (the other 3 LEDs were masked for the measurement) increases as the resistance

**Figure 4.1 UV light intensity vs distance for different sources used for crosslinking printed hydrogels.**

**(A)** Low Power 4 Nichia LED Array (NCSU033A LEDs Biofabrication 2012) **(B)** Spectroline Lamp 365 nm EN280L single bulb,  $2.0 \text{ mW/cm}^2$  **(C)** Underside view of High Powered 4 LED Array and circulation heat sink,  $136 \text{ mW/cm}^2$ , 60 Ohm resistance per LED, Nichia 365 nmUV LED NC4U133A **(D)** Side view of High Powered LED array at printing distance with tip in contact with printing surface. **(E)** Intensity measured with radiometer. Power fit data and extrapolated to generate intensity estimates at print surface (Table 4.1). Plotted are the intensity vs distance for the light meter sensor centered under the high powered LED array mounted on the syringe carriage (C 4 HLED), sensor under the right syringe tip (RT 4 HLED), sensor under the left syringe tip (LT 4 HLED), sensor under single high power LED (HLED), sensor under single low power LED with resistance set at 25 Ohms (LLED 25 Ohm), under single low power LED with resistance set at 33 Ohms (LLED 33 Ohm), single low power LED with resistance set at 55 Ohms (LLED 55 Ohm), and sensor under the Spectroline lamp.

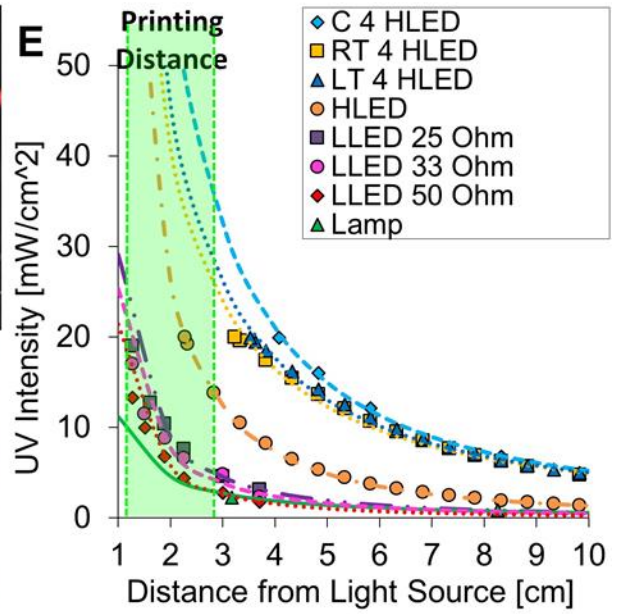
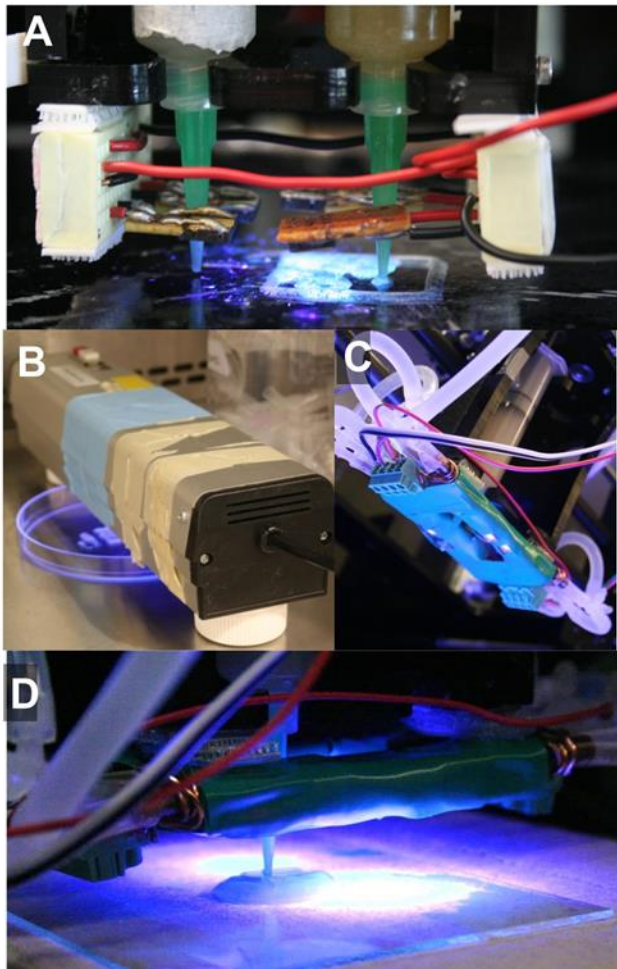


Table 4.1 Extrapolation of light source measurements and intensity at printing and crosslinking surface.

Light Source	Power Fit	R <sup>2</sup>	Intensity at Printing/ Crosslinking Surface [mW/cm <sup>2</sup> ]	Distance from Source [cm]	Energy [J] to 8 mm disk		
					3 min	5min	7min
Sensor Centered between syringe Tips, 4 HLEDS	$y=175.61*(x)^{-1.531}$	0.9987	136	1.2	12.30	20.51	28.71
Sensor Under Right Syringe Tip, 4 HLEDS	$y=101.78*(x)^{-1.312}$	0.9887	82	1.2	7.42	12.37	17.31
Sensor under left syringe tips 4HLEDS	$y=118.65*(x)^{-1.371}$	0.9953	94	1.2	8.50	14.17	19.84
Single HLED (60 Ohm)	$y=93.868*x^{-1.834}$	0.9993	67	1.2	6.08	10.13	14.18
Single LLED (25 Ohm)	$y=29.102*x^{-1.686}$	0.9976	21	1.2	1.94	3.23	4.52
Single LLED (33 Ohm)	$y = 25.365*x^{-1.699}$	0.9663	19	1.2	1.68	2.81	3.93
Single LLED (50 Ohm)	$y=21.38*x^{-1.878}$	0.9978	15	1.2	1.37	2.29	3.20
Lamp	$y=11.194*x^{-1.281}$	0.976	2	2.7	0.18	0.30	0.42

decreases (Table 4.1). The high power LED array was positioned on the carriage so that the LED array was centered between the two syringe tips. On the Model 1 Fab@Home printer, the syringe tips are 29 mm apart, and the intensity at the center between the two tips was  $136 \text{ mW/cm}^2$ . At 14.5 mm off center, where the right or left syringe tip make contact with the printing stage, the intensity is roughly 2/3 that of centered intensity. The lowest and highest intensities tested were used for the subsequent photo-crosslinking experiments ( $2 \text{ mW/cm}^2$  and  $136 \text{ mW/cm}^2$ ).

#### ***4.4.2 Mechanical Testing Photo-crosslinked Hydrogel Disks***

Modulus ( $E_{5\text{to}15}$ ) and swelling ratio of photo-crosslinked MEGEL:PEG-DA hydrogels were affected by the photoinitiator type (Figure 4.2), the photoinitiator concentration, the light source intensity, and exposure time (Figure 4.3). Hydrogels could be tuned to three significantly different moduli. For this study a hydrogel was considered crosslinked when it could be transferred into media or PBS and it did not dissolve at either room temperature or  $37^\circ\text{C}$ . Properties of the polymer precursor solution; viscosity; temperature sensitivity; polymer concentration and availability of double bonds; photoinitiator concentration; photoinitiator efficiency in producing free radicals; and type of free radical produced can all effect the minimum crosslinking time if the precursor solution crosslinks at all, and can also effect the resulting mechanical properties (Hockaday, Kang et al. 2012). A single polymer combination and concentration was used in this study to keep the availability of double bonds, the density, and the viscosity of the solution constant. The solutions were kept as close to  $37^\circ\text{C}$  as possible during handling and staging. The MEGEL:PEG-DA solutions will solidify as the temperature drops from  $37^\circ\text{C}$  to room temperature ( $25^\circ\text{C}$ ) because of the gelatin component. If the solution is allowed to cool, it will not photo-crosslink and the gel will dissolve when transferred into PBS or Media.

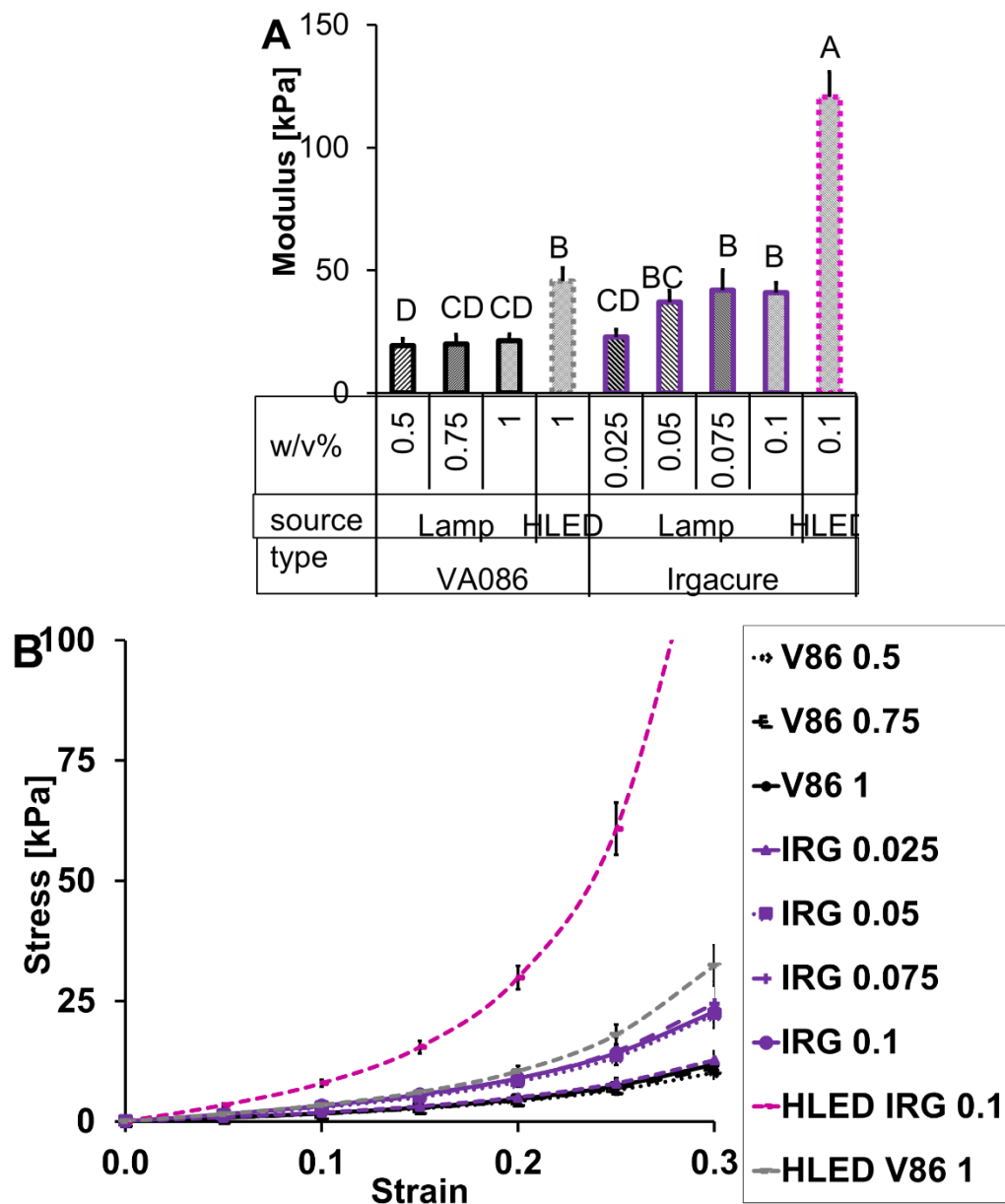


**Figure 4.2 Concentration and intensity study of mechanical properties of crosslinked hydrogels.**

**(A)** Young's modulus of hydrogels made with variable photoinitiator type and concentration and light source during crosslinking. All the precursor solutions in these conditions were photocrosslinked under either the lamp or high LED array (HLED) for 5 minutes.  $p < 0.05$  non-matching letters, testing effect of photoinitiator type and concentration and light power, Student's t-test and standard error of the mean used. **(B)** Stress versus strain for hydrogels in A.

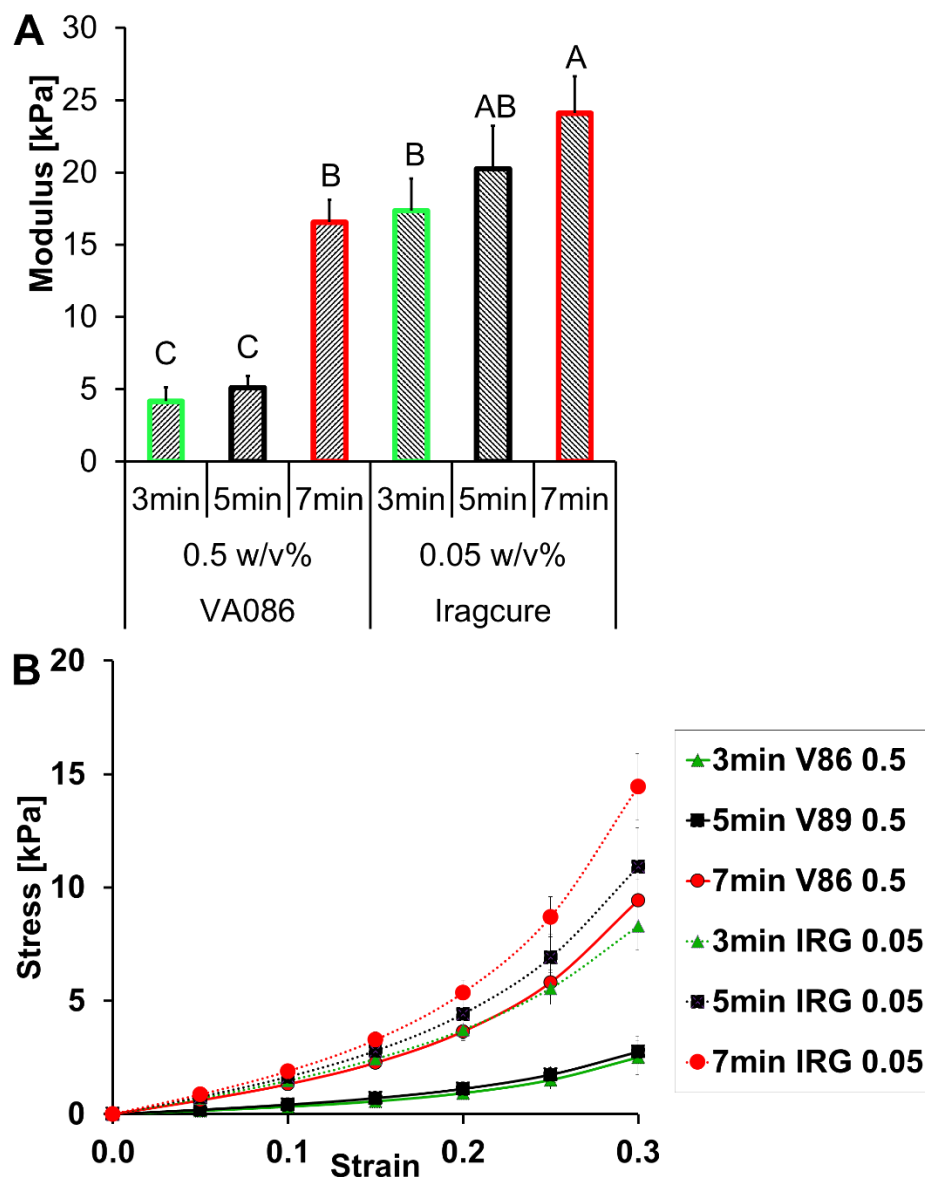


**Figure 4.3** Time study of mechanical properties of crosslinked hydrogels.

**(A)** Young's Modulus of hydrogels made with variable crosslinking time. Standard error of the mean,  $p < 0.05$  non-matching letters, testing effect of photoinitiator type and crosslinking time. **(B)** Stress versus strain for hydrogels in A.

$E_{5to15}$  of hydrogels made with VA086 and photo-crosslinked for 5 minutes with the low intensity light source ( $2 \text{ mW/cm}^2$ ) was not significantly affected by increasing the photoinitiator concentration except below a certain photoinitiator concentration, a robust gel did not form (Figure 4.2-12A) (For 0.5,0.75,1.0% w/v  $E_{5to15}$  was  $19.3\pm 2.7$ ,  $20.0\pm 3.9$ , and  $21.3\pm 2.7$  kPa respectively, NSD). Only a small fraction of hydrogel disk batches made with 0.25% w/v VA086 did not dissolve when transferred into PBS or media. Crosslinking for 0.5% w/v VA086 was inconsistent, but almost 100% for 0.75% w/v VA086.  $E_{5to15}$  of hydrogels made with Irgacure 2959, and photo-crosslinked for 5 min with the low intensity light source ( $2 \text{ mW/cm}^2$ ), was affected by increasing the photoinitiator concentration (For 0.025,0.05,0.075,0.1% w/v  $E_{5to15}$   $22.8\pm 3.1$ ,  $37.1\pm 4.8$ ,  $42.0\pm 8.2$ ,  $40.9\pm 4.1$  kPa respectively, but only 0.1 and 0.025% w/v were significantly different). Increasing the light intensity that precursor solution was exposed to for 5 minutes of crosslinking (centered under high powered LED  $136 \text{ mW/cm}^2$ ) significantly increased the  $E_{5to15}$  for hydrogels made with both photoinitiator types. For 1.0% w/v VA086 gels increasing the light source intensity increased the  $E_{5to15}$  from  $21.3\pm 2.7$  kPa to  $45.7\pm 5.2$  kPa. For 0.1% w/v Irgacure gels increasing the light source intensity increased the  $E_{5to15}$  from  $40.9\pm 4.1$  kPa to  $120.7\pm 10.2$  kPa.  $E_{5to15}$  of hydrogels made with VA086 and Irgacure, and photo-crosslinked with the low intensity light source ( $2 \text{ mW/cm}^2$ ) were affected by the amount of exposure time. For hydrogels made with 0.05% w/v Irgacure and photo-crosslinked at 3, 5, 7 min during the timing experiment,  $E_{5to15}$  was  $17.4\pm 2.2$ ,  $20.3\pm 7.8$ , and  $24.1\pm 2.6$  kPa (Figure 4.3). For hydrogels made during the timing experiment made with 0.5% w/v VA086 photo-crosslinked at 3, 5, 7 min,  $E_{5to15}$  was  $4.2\pm 1.0$ ,  $5.1\pm 1.8$ ,  $16.6\pm 1.5$  kPa respectively. During hydrogel

compression the stress response to strain is non-linear (Figure 4.2B and 3B), and changing the photoinitiator and light source intensity produces hydrogels that fall into 3 different stiffness.

Hydrogel swelling ratio was affected by both the light intensity used for crosslinking and the photoinitiator concentration (Figure 4.4A). 1.0% w/v VA086 hydrogels and 0.1% w/v Irgacure hydrogels photo-crosslinked for 5 min were significantly less swollen when crosslinked at the higher intensity. SR was  $19.9 \pm 0.3$  ( $2 \text{ mW/cm}^2$ ) compared to  $10.5 \pm 0.4$  ( $136 \text{ mW/cm}^2$ ) for VA086 hydrogels, and SR was  $13.2 \pm 1.2$  ( $2 \text{ mW/cm}^2$ ) compared to  $10.2 \pm 0.7$  ( $136 \text{ mW/cm}^2$ ). However, for the low photoinitiator Irgacure hydrogels (0.025% w/v), increasing the intensity of light source did not significantly affect the swelling ratio,  $26.3 \pm 1.8$  at  $2 \text{ mW/cm}^2$ , compared to  $24.0 \pm 1.1$  at  $136 \text{ mW/cm}^2$ . Increasing the photoinitiator concentration affected the swelling ratio for both VA086 hydrogels and Irgacure hydrogels. In general decreasing swelling ratio indicates increased levels of crosslinking (Leach and Schmidt 2005), and increased modulus indicates increased levels of crosslinking. Plotting the modulus against the swelling ratio (Figure 4.4B) confirms the trend that as swelling ratio decreases the modulus increases.

These results indicate that there are saturation points in the polymer precursor solution terms of the photoinitiator ranges being tested. The modulus data suggests that once a certain point is reached there are diminishing returns for increasing photoinitiator concentration when using a particular light source. Increasing the light intensity to

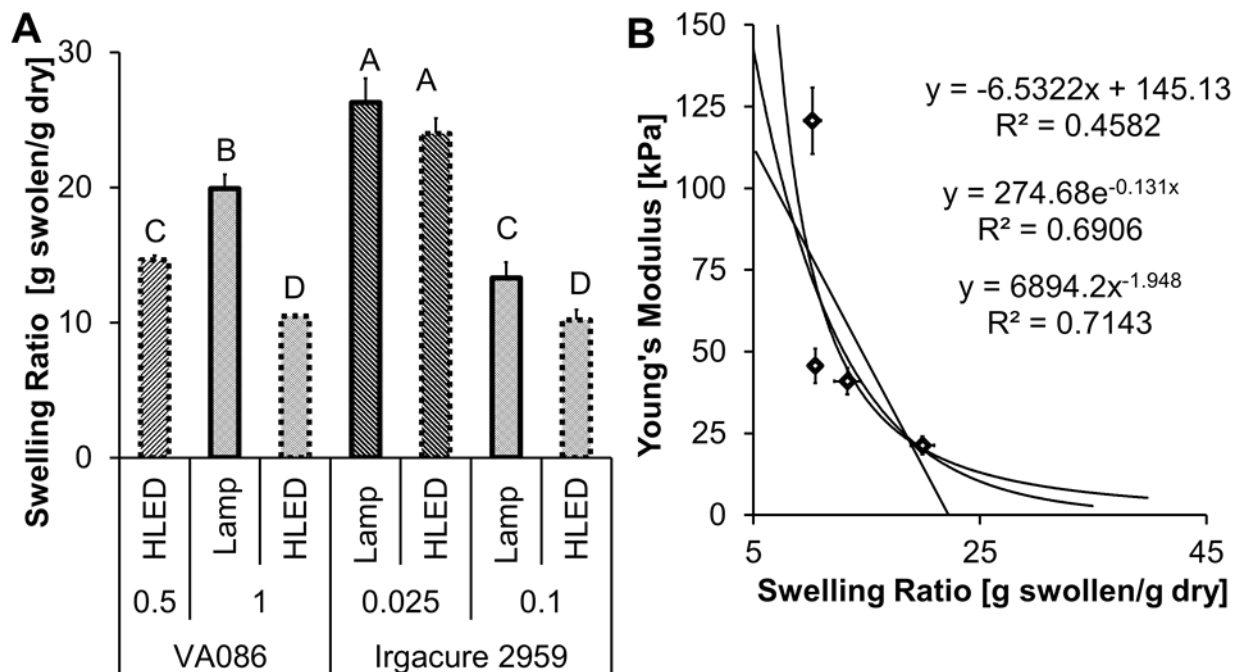


**Figure 4.4 Swelling properties of crosslinked hydrogels.**

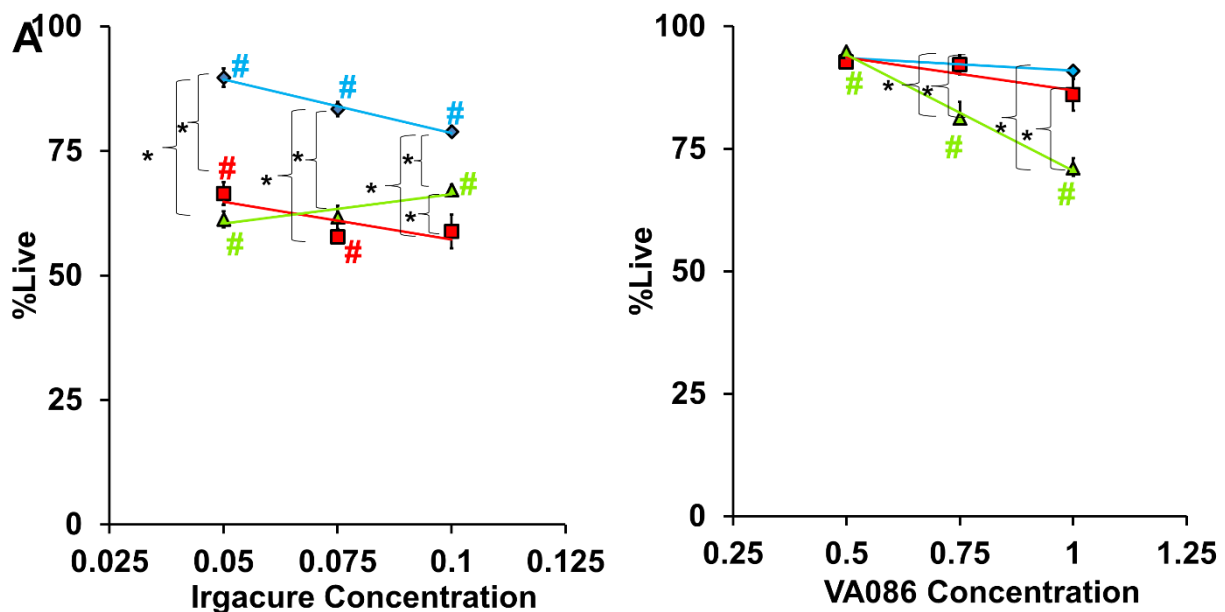
(A) Weight based swelling ratio (swollen weight divided by dry weight) of crosslinked hydrogels made with variable photoinitiator type and concentration and light source during crosslinking.  $p < 0.05$  non-matching letters, testing effect of photoinitiator type and concentration and light power, standard error of the mean shown by error bars.

(B) Young's modulus verses swelling ratio of hydrogels. (VA086 1.0 Lamp, VA086 1.0 HLED, Irgacure 0.1 lamp, Irgacure 0.1 HLED). Standard error of the mean shown by error bars.

**136mW/cm<sup>2</sup> does increase the stiffness of the gel for each photoinitiator, but VA086 hydrogel modulus does not reach the magnitude of Irgacure hydrogel modulus.**

#### **4.4.3 Encapsulated Valve and Mesenchymal Cell Viability**

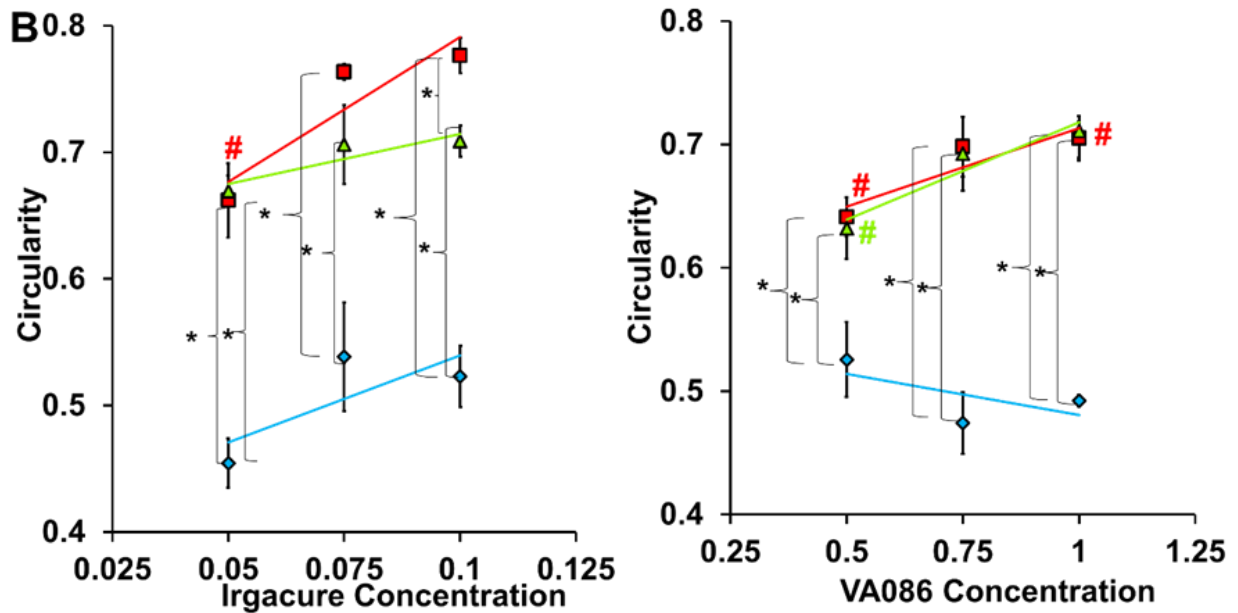
Encapsulated valve cells had significantly less viability and rounded morphology compared to mesenchymal stem cells in photo-crosslinked MEGEL:PEG-DA hydrogels. HADMSC, HAVIC, and HASSMC survival were all affected by photoinitiator concentration in the photo-crosslinked hydrogels (Figure 4.5A). Irgacure has a more detrimental effect on encapsulated cells than VA086 concentrations tested. HADMSC encapsulated viability in Irgacure hydrogels prepared with 0.05% w/v was significantly higher than both 0.075 and 0.1 % w/v (89.7±1.9 compared to 83.4±1.5 and 78.9±1.1 %live cells). VA086 hydrogels HADMSC cultured to day 4 had no significant difference in viability with photoinitiator concentration (percent live for 0.05, 0.075, and 0.1 % w/v was 93.4±0.8, 92.5±1.6, and 90.9±0.9). HAVIC encapsulated viability in hydrogels prepared with 0.05% w/v Irgacure was significantly higher than 0.075% w/v (66.4±2.3 compared to 57.7±0.6). VA086 hydrogels HAVIC cultured to day 3 had no significant difference in viability with photoinitiator concentration (percent live was 0.05, 0.075, and 0.1 % w/v, 92.7±0.9, 92.1±2.0, and 86.0±3.3). HASSMC encapsulated viability in hydrogels prepared with Irgacure did not follow the same trend as HADMSC and HAVIC (0.05, 0.075, and 0.1% w/v hydrogels had 61.2±1.6, 61.7±2.4, and 67.2±1.1 percent viability at day 3 culture). In VA086 hydrogels HASSMC cultured to day 3 had a significant decreasing trend in viability with increasing photoinitiator concentration (percent live was 0.05, 0.075, and 0.1 % w/v, 94.8±0.4, 81.2±3.3, and 71.1±2.0). In



		IRGACURE	VA086
HADMSC	 	$y = -216.64x + 100.24$	$y = -5.0106x + 96.004$
		$R^2 = 0.991$	$R^2 = 0.9777$
HAVIC	 	$y = -152.04x + 72.395$	$y = -13.335x + 100.3$
		$R^2 = 0.6464$	$R^2 = 0.8108$
HASSMC	 	$y = 118.4x + 54.503$	$y = -47.483x + 117.97$
		$R^2 = 0.8085$	$R^2 = 0.993$

**Figure 4.5 (A) Viability of encapsulated HADMSC, HAVIC, HASSMC stained at day 3 of culture.**

Percentage of live of cells encapsulated in hydrogel discs and cultured for 3-4days. Gels made with increasing Irgacure 2959 and VA086 concentration. Standard error of the mean used.\* $p < 0.05$  within groups (effect of cell type), #  $p < 0.05$  between groups (effect of photoinitiator concentration) Lamp 2  $mW/cm^2$  crosslinking.



		IRGACURE	VA086
HADMSC	 	$y = 1.3683x + 0.4027$	$y = -0.0667x + 0.5474$
		$R^2 = 0.5869$	$R^2 = 0.4063$
HAVIC	 	$y = 2.2883x + 0.5623$	$y = 0.1277x + 0.5857$
		$R^2 = 0.8335$	$R^2 = 0.8299$
HASSMC	 	$y = 0.7892x + 0.6355$	$y = 0.1575x + 0.5604$
		$R^2 = 0.7981$	$R^2 = 0.9125$

**Figure 4.5 (B) Circularity of viable encapsulated HADMSC, HAVIC, HASSMC stained at day 3 of culture.**

Circularity of live of cells encapsulated in hydrogel discs and cultured or 3-4 days. Increasing Irgacure 2959 and VA086 concentration. 1 is a perfect circle. Standard error of the mean used,  $p < 0.05$  within groups (effect of cell type), #  $p < 0.05$  between groups (effect of photoinitiator concentration).

hydrogels prepared with Irgacure HADMSC viability is higher than both HAVIC and HASSMC. At 0.1 % w/v viability is significantly different between HADMSC, HAVIC, and HASSMC. In hydrogels prepared with VA086 at 0.5% w/v there is no significant difference in viability between the 3 cell types. Increasing the VA086 concentration caused the percentage of live HASSMC to decrease but did not affect the HADMSC and HAVIC viability which remained the same.

ANCOVA (analysis of covariance) for the day 3&4 viability data trends:

Least squares fit of the Irgacure concentration and cell type interaction data with the JMP full factorial macro showed the HASSMC/IRG slope was significantly different from the HAVIC and HADMSC slopes ( $p < 0.0005$ ). HADMSC/IRG and HAVIC/IRG slopes were not different ( $p = 0.4498$ ) and ANCOVA showed that the groups are significantly different (least square mean HADMSC  $83.99 \pm 1.20$  and HAVIC  $60.99 \pm 1.20$ ). The least squares fit of the data from testing the VA086 concentration and cell type interaction showed the HASSMC/VA086 slope was significantly different from the HAVIC and HADMSC slopes ( $p < 0.0001$ ) but the HADMSC/IRG and HAVIC/IRG slopes were not different ( $p = 0.2386$ ). ANCOVA showed that the groups are not significantly different (least squares means HADMSC  $92.24 \pm 1.00$  and HAVIC  $90.13 \pm 1.04$ ).

#### **4.4.4 Encapsulated Valve and Mesenchymal Cell Morphology**

Encapsulated HADMSC had significantly more spread morphology compared to HAVIC and HASSMC at all photoinitiator concentrations tested, at day 3 and 4 (Figure 4.5B) and day 1 and day 7 of culture (Figures 4.6 - 4.11) . HADMSC cultured in Irgacure and VA086 hydrogels cultured to day 3 and day 4 did not have any significant difference in circularity with increasing photoinitiator concentration For 0.05, 0.075, 0.1% w/v

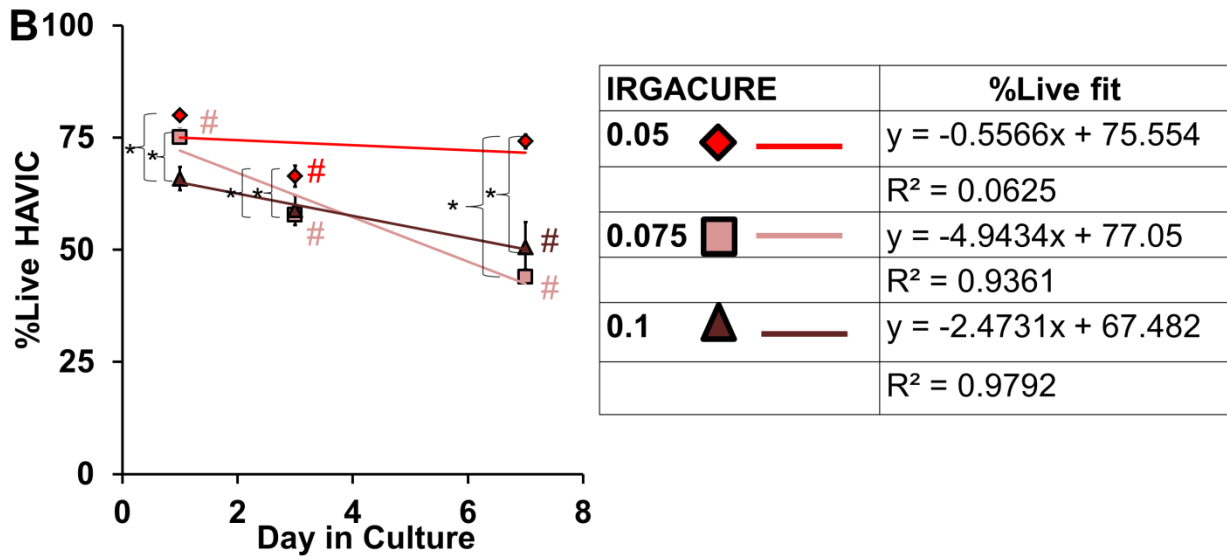
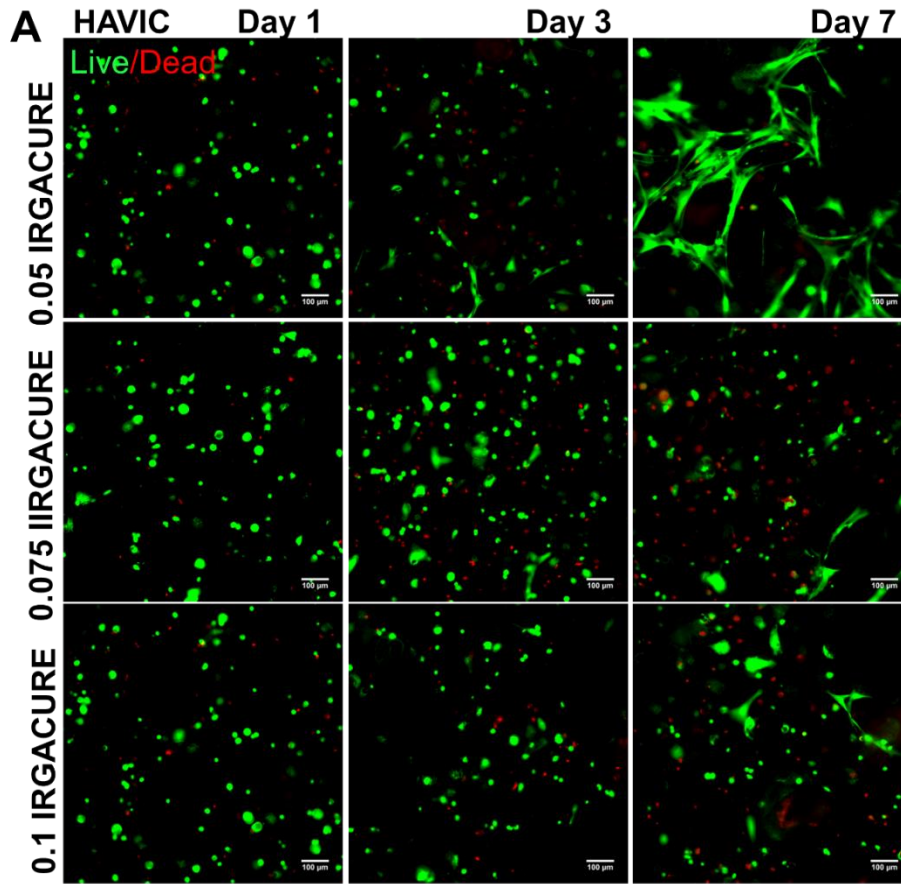


**Figure 4.6 Viability in HAVIC/Iraacure hydrogels.**

(A) Representative images of Live/Dead stained HAVIC gels crosslinked at 2 mW/cm<sup>2</sup> after up to Day 7 culture. (B) Percentage of live HAVIC encapsulated in hydrogel discs and then stained at 1, 3, 7 days culture time. Increasing Irgacure concentration. SEM, \*p<0.05 within groups (effect of photoinitiator concentration), #p<0.05 between groups (effect of day in culture).

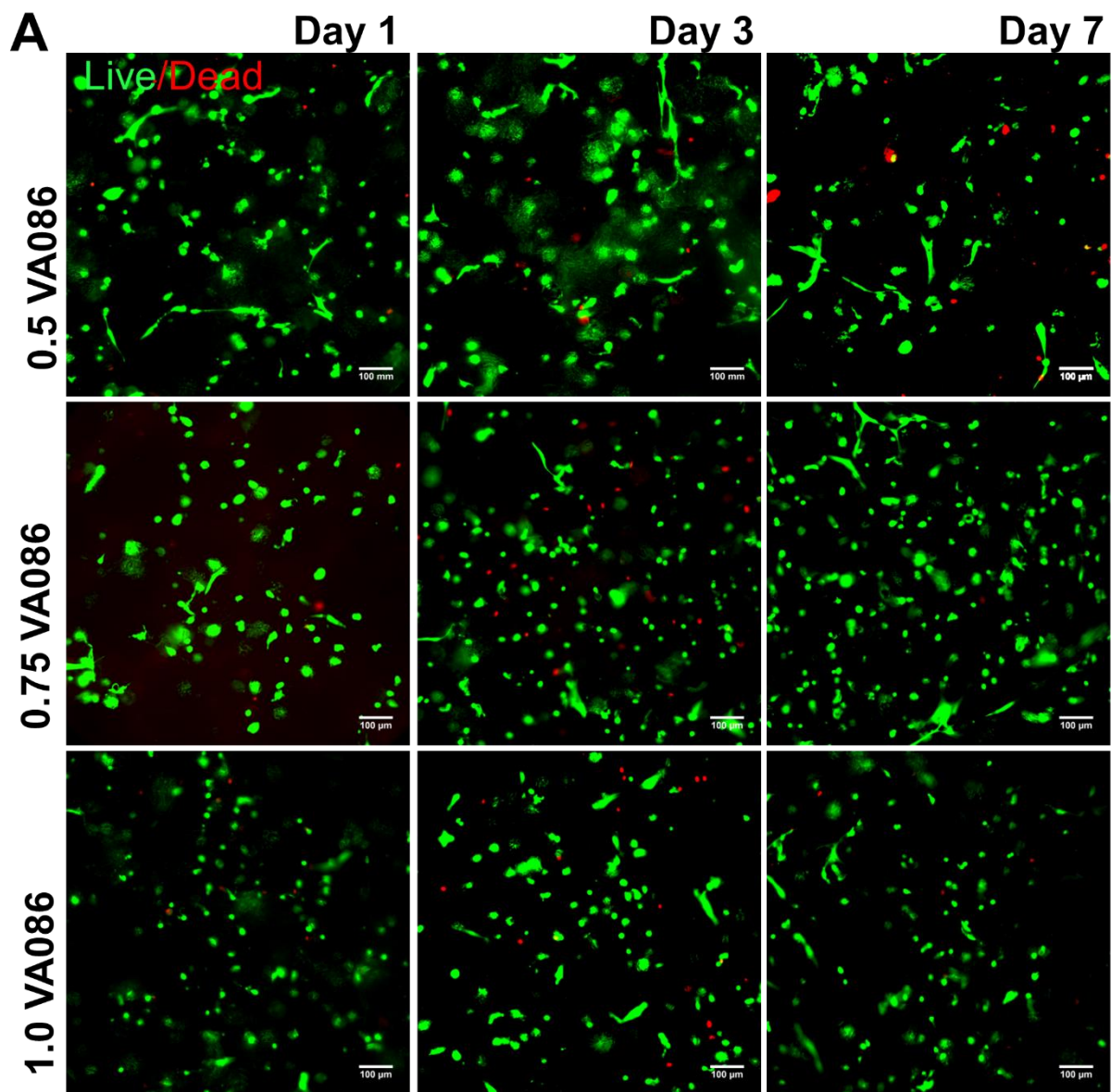
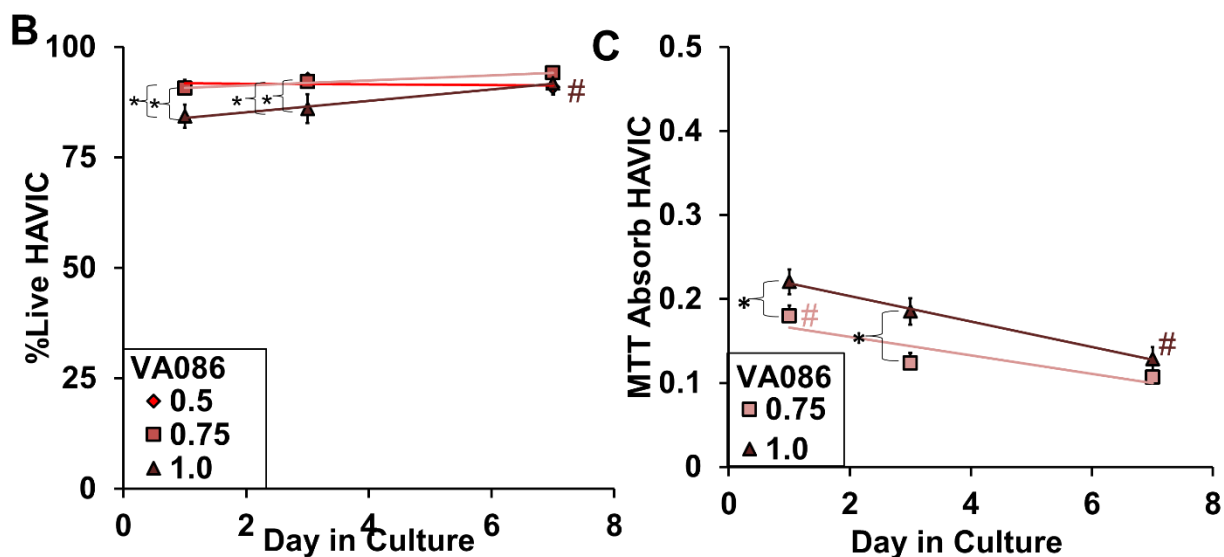


**Figure 4.7 (A) Viability in HAVIC/VA086 hydrogels.**

Representative images of Live/Dead stained HAVIC gels crosslinked at  $2 \text{ mW/cm}^2$  after up to Day 7 culture.



VA086	% Live fit
0.5	$y = -0.07x + 91.819$ $R^2 = 0.0467$
0.75	$y = 0.568x + 90.213$ $R^2 = 0.9849$
1.0	$y = 1.2781x + 82.697$ $R^2 = 0.9877$

VA086	MTT fit
0.5	$y = -0.0111x + 0.1771$ $R^2 = 0.7766$
1.0	$y = -0.0152x + 0.2336$ $R^2 = 0.9968$

**Figure 4.7 (B) and (C) Viability in HAVIC/VA086 hydrogels.**

**(B)** Percentage of live HAVIC encapsulated in hydrogel discs and then stained at 1, 3, and 7 day culture time. Increasing VA086 concentration. **(C)** MTT plate reader absorbance of HAVIC encapsulated in hydrogel discs and then stained at 1, 3, and 7 day culture time at two VA086 concentrations. SEM, \* $p < 0.05$  within groups (effect of photoinitiator concentration), # $p < 0.05$  between groups (effect of day in culture).

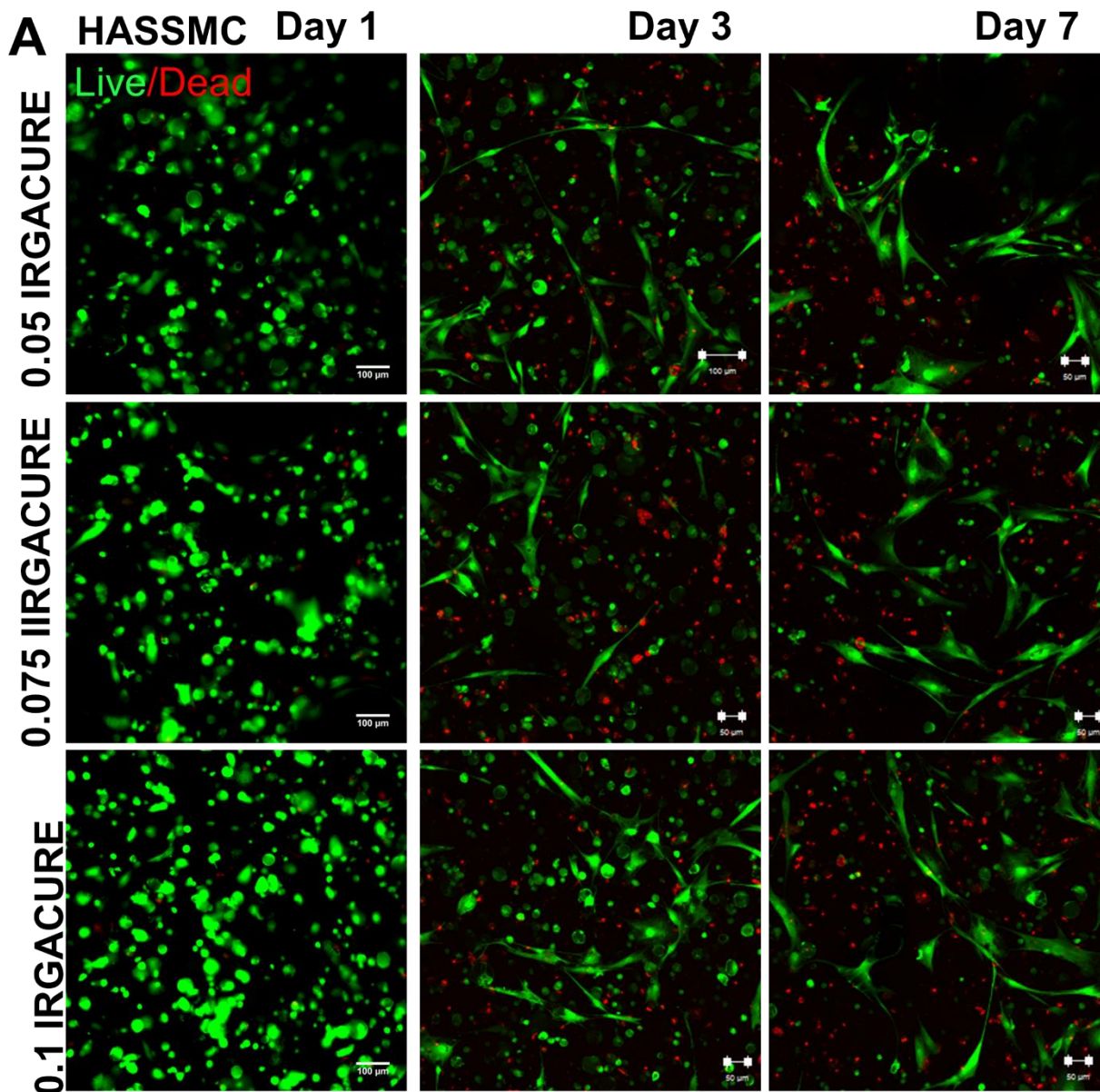
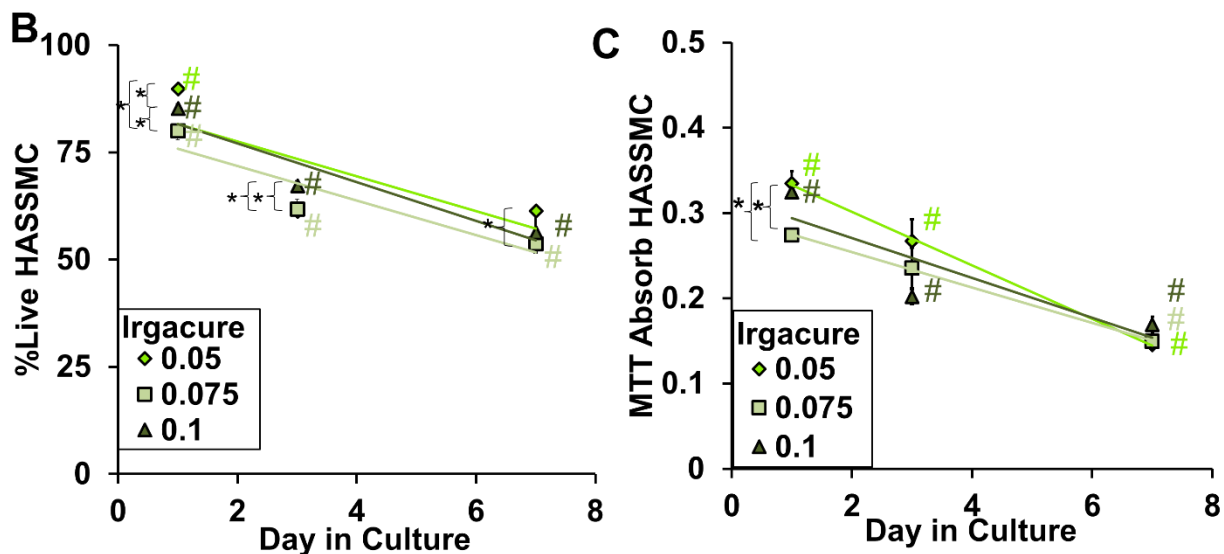


**Figure 4.8 20(A) Viability in HASSMC/Irgacure hydrogels.**

Representative images of Live/Dead stained HASSMC gels crosslinked at  $2 \text{ mW/cm}^2$  after up to Day 7 culture.



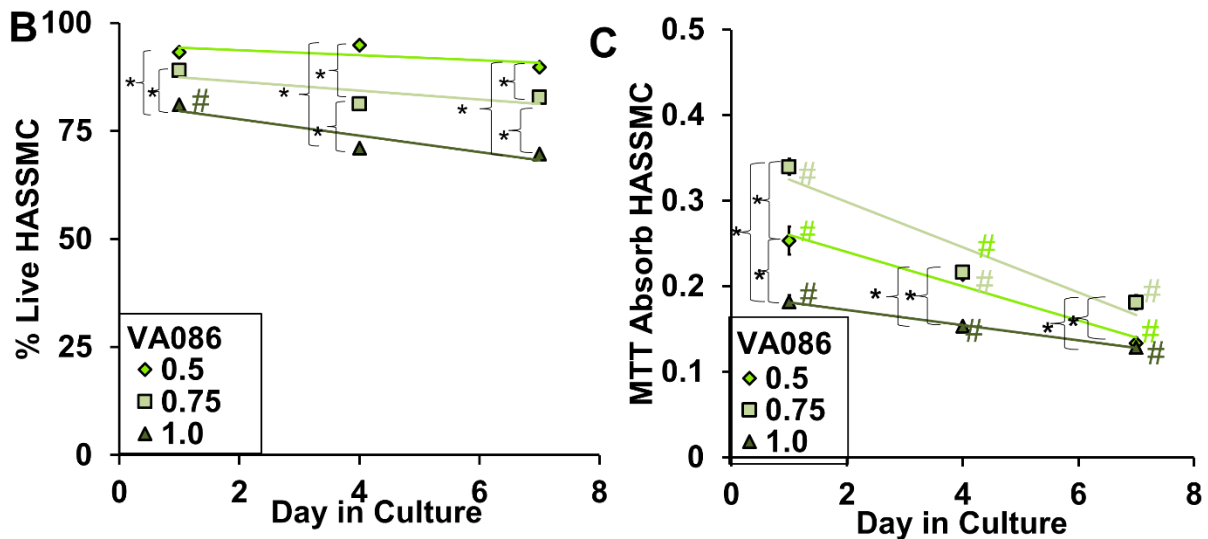
IRGACURE	%Live fit
0.05 <span style="color: green;">◆</span>	$y = -4.0648x + 85.667$ $R^2 = 0.5705$
0.075 <span style="color: grey;">■</span>	$y = -4.0415x + 79.926$ $R^2 = 0.8412$
0.1 <span style="color: black;">▲</span>	$y = -4.5182x + 86.114$ $R^2 = 0.8941$

IRGACURE	MTT fit
0.05 <span style="color: green;">◆</span>	$y = -0.0314x + 0.3642$ $R^2 = 0.9992$
0.075 <span style="color: grey;">■</span>	$y = -0.0208x + 0.296$ $R^2 = 0.9993$
0.1 <span style="color: black;">▲</span>	$y = -0.0234x + 0.3175$ $R^2 = 0.7605$

**Figure 4.8 21(B) and (C)**

(B) Percentage of live HASSMC encapsulated in hydrogel discs and then stained at 1, 3, and 7 day culture time. Increasing Irgacure concentration. (C) MTT plate reader absorbance of HASSMC encapsulated in Irgacure hydrogel discs and then stained at 1, 3, and 7 day culture time for increasing Irgacure concentrations. SEM, \*p<0.05 within groups (effect of photoinitiator concentration), # p<0.05 between groups (effect of day in culture).





VA086	%Live fit
0.5 <span style="color: green;">◆</span>	$y = -0.5794x + 94.89$ $R^2 = 0.4465$
0.75 <span style="color: lightgreen;">■</span>	$y = -1.0312x + 88.44$ $R^2 = 0.5701$
1.0 <span style="color: darkgreen;">▲</span>	$y = -1.9097x + 81.574$ $R^2 = 0.8416$

VA086	MTT fit
0.5 <span style="color: green;">◆</span>	$y = -0.02x + 0.2801$ $R^2 = 0.9633$
0.75 <span style="color: lightgreen;">■</span>	$y = -0.0264x + 0.3511$ $R^2 = 0.9067$
1.0 <span style="color: darkgreen;">▲</span>	$y = -0.0089x + 0.1901$ $R^2 = 0.9984$

**Figure 4.9 (B) and (C) Viability in HASSMC/VA086 hydrogels.**

**(B)** Percentage of live HASSMC encapsulated in hydrogel discs and then stained at 1, 3, 7 day culture time. Increasing VA086 concentration. **(C)** MTT plate reader absorbance of HASSMC encapsulated in VA086 hydrogel discs and then stained at 1, 3, 7 day culture time for increasing VA086 concentrations. SEM, \* $p < 0.05$  within groups (effect of photoinitiator concentration), # $p < 0.05$  between groups (effect of day in culture).

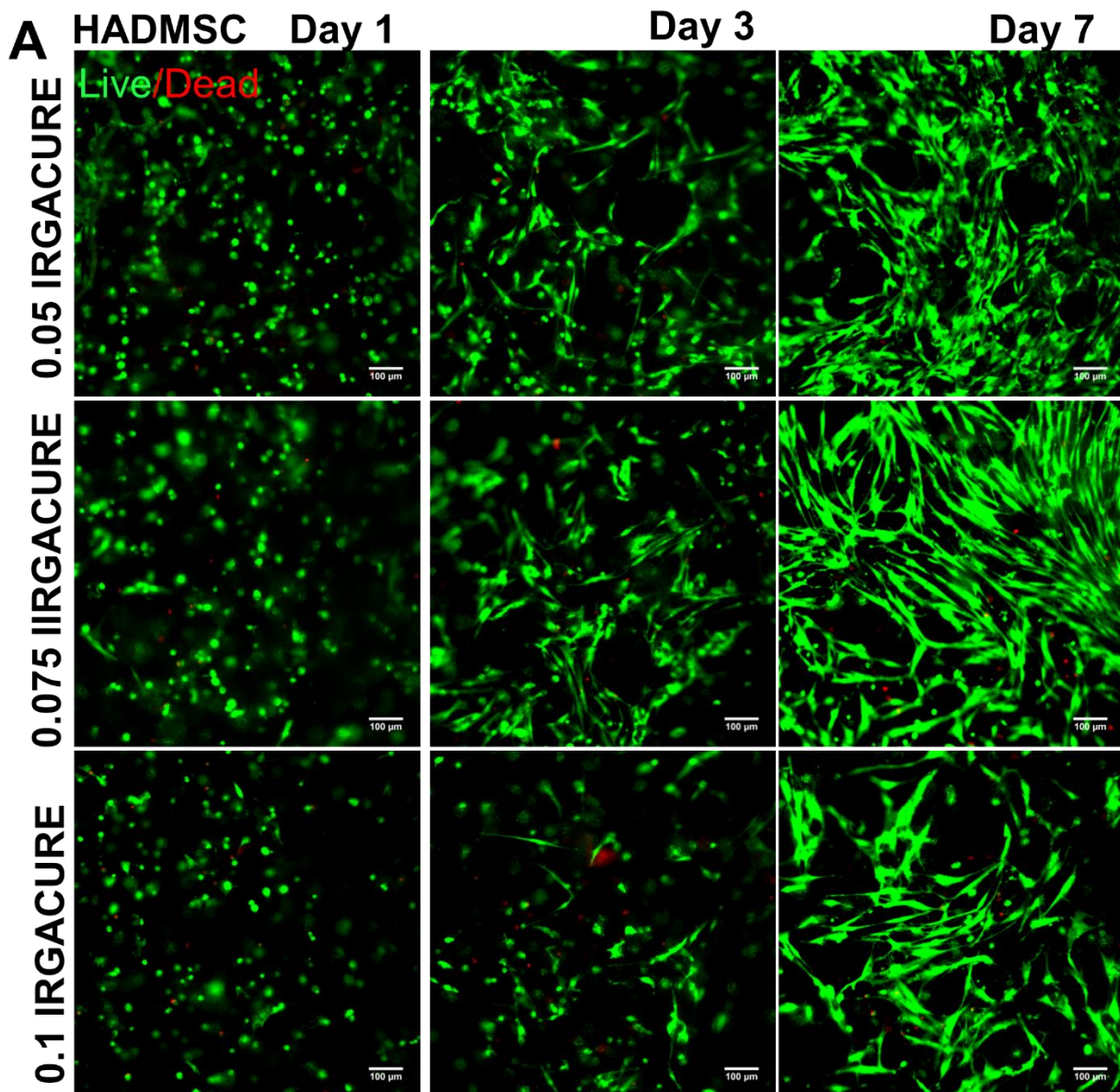
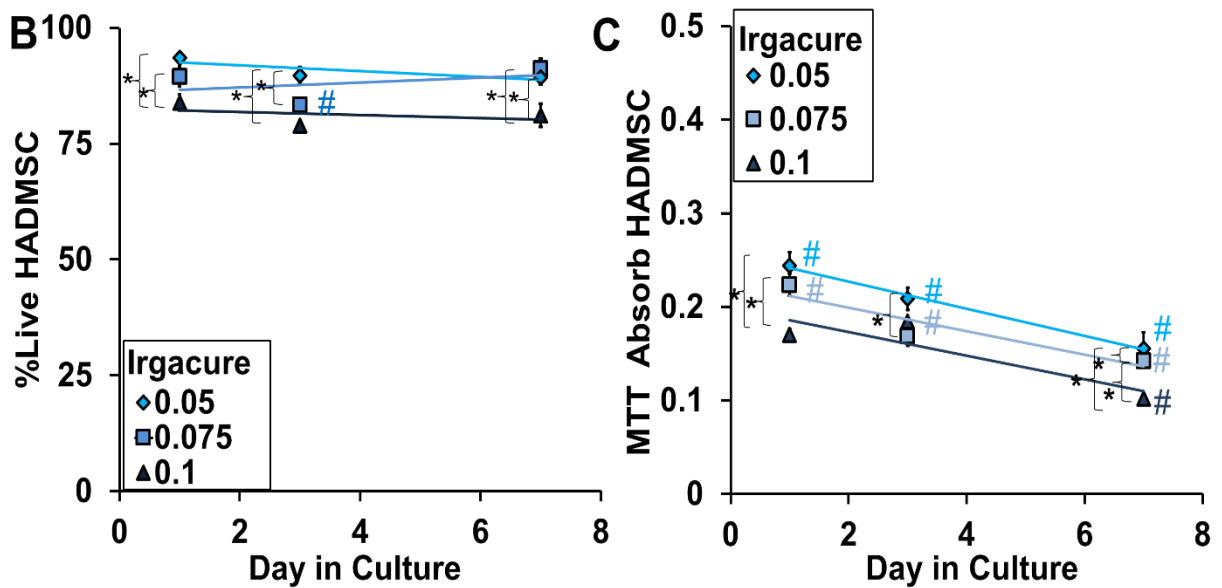


**Figure 4.10 (A) Viability in HADMSC/Irgacure hydrogel.**

Representative images of Live/Dead stained HADMSC gels crosslinked at  $2 \text{ mW/cm}^2$  after up to Day 7 culture.



IRGACURE	%Live fit
0.05 <span style="color: blue;">◆</span> <span style="color: blue;">—</span>	$y = -0.6299x + 93.162$ $R^2 = 0.6594$
0.075 <span style="color: blue;">■</span> <span style="color: blue;">—</span>	$y = 0.5247x + 86.094$ $R^2 = 0.1531$
0.1 <span style="color: black;">▲</span> <span style="color: black;">—</span>	$y = -0.3201x + 82.459$ $R^2 = 0.1513$

IRGACURE	MTT fit
0.05 <span style="color: blue;">◆</span> <span style="color: blue;">—</span>	$y = -0.0146x + 0.2562$ $R^2 = 0.9939$
0.075 <span style="color: blue;">■</span> <span style="color: blue;">—</span>	$y = -0.0125x + 0.2241$ $R^2 = 0.8556$
0.1 <span style="color: black;">▲</span> <span style="color: black;">—</span>	$y = -0.0126x + 0.1985$ $R^2 = 0.7768$

**Figure 4.10 (B) and (C) Viability in HADMSC/Irgacure hydrogel.**

**(B)** Percentage of live HADMSC encapsulated in hydrogel discs and then stained at 1, 3, and 7 day culture time. Increasing Irgacure concentration. **(C)** MTT plate reader absorbance of HADMSC encapsulated in Irgacure hydrogel discs and then stained at 1,3, and 7 day culture time for increasing Irgacure concentrations. SEM, \* $p < 0.05$  within groups (effect of photoinitiator concentration), # $p < 0.05$  between groups (effect of day in culture).

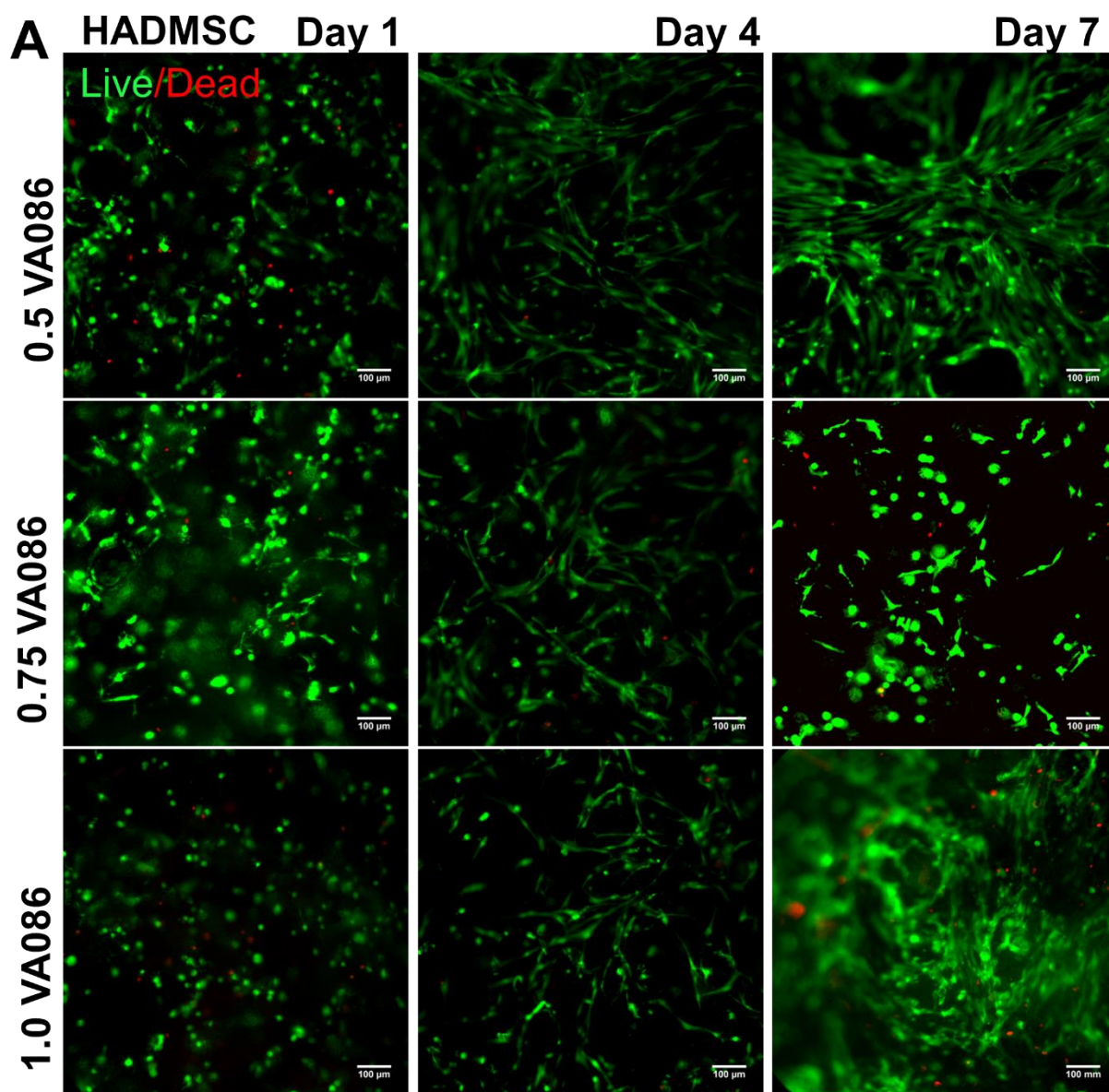
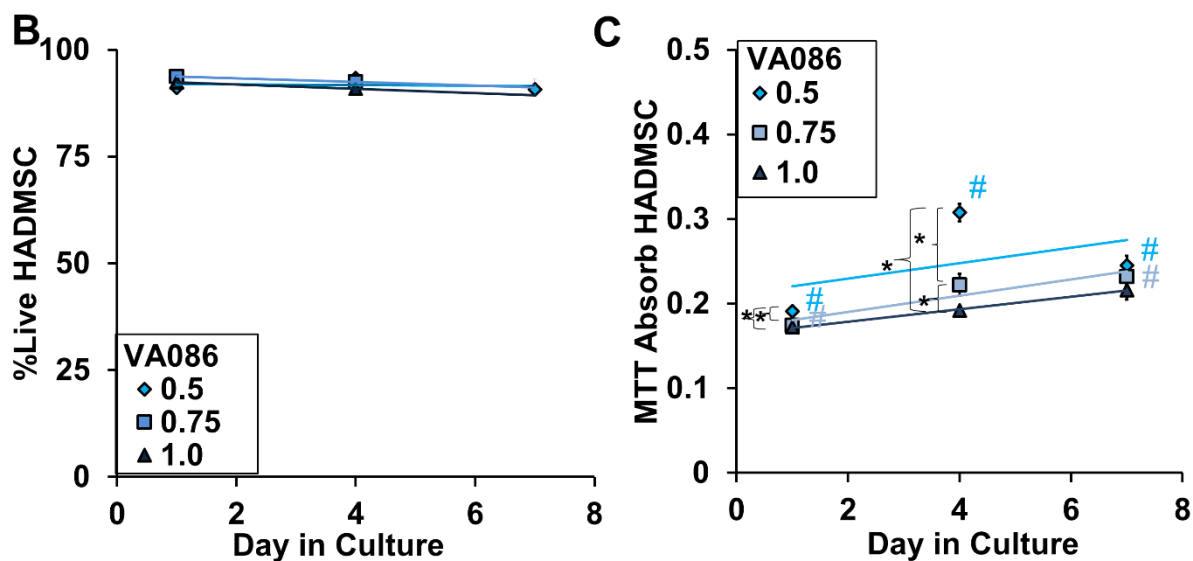


**Figure 4.11 (A) Viability in HADMSC/VA086 hydrogel.**

Representative images of Live/Dead stained HADMSC gels crosslinked at  $2 \text{ mW/cm}^2$  after up to Day 7 culture.



VA086	%Live fit
0.5	$y = -0.0695x + 92.009$ $R^2 = 0.0207$
0.75	$y = -0.4315x + 94.191$ $R^2 = 1$
1.0	$y = -0.5047x + 92.903$ $R^2 = 1$

VA086	MTT fit
0.5	$y = 0.0091x + 0.2116$ $R^2 = 0.2159$
0.75	$y = 0.0096x + 0.171$ $R^2 = 0.8724$
1.0	$y = 0.0073x + 0.1641$ $R^2 = 0.9966$

**Figure 4.11 (B) and (C) Viability in HADMSC/VA086 hydrogel.**

**(B)** Percentage of live HADMSC encapsulated in hydrogel discs and then stained at 1, 3, and 7 day culture time. Increasing VA086 concentration. **(C)** MTT plate reader absorbance of HADMSC encapsulated in VA086 hydrogel discs and then stained at 1, 3, and 7 day culture time for increasing VA086 concentrations. SEM, \* $p < 0.05$  within groups (effect of photoinitiator concentration), # $p < 0.05$  between groups (effect of day in culture).

Irgacure, the circularity was  $0.45\pm 0.02$ ,  $0.54\pm 0.04$ ,  $0.52\pm 0.02$  respectively. For 0.5, 0.75, 1.0% w/v VA086, the circularity was  $0.53\pm 0.03$ ,  $0.47\pm 0.03$ ,  $0.49\pm 0.01$  NS respectively (Figure 4.5B). HAVIC cultured in Irgacure and VA086 hydrogels cultured to day 3 became more rounded (increase in circularity) with increasing photoinitiator concentration. For 0.05, 0.075, 0.1% w/v Irgacure, the circularity was  $0.66\pm 0.03$ ,  $0.76\pm 0.01$ ,  $0.78\pm 0.01$  respectively. For 0.5, 0.75, 1.0% w/v VA086, the circularity was  $0.64\pm 0.02$ ,  $0.70\pm 0.03$ ,  $0.71\pm 0.02$  respectively. HASSMC cultured in Irgacure hydrogels cultured to day 3 had no significant difference in circularity with the photoinitiator concentrations tested. For 0.05, 0.075, 0.1% w/v Irgacure, the circularity was  $0.67\pm 0.01$ ,  $0.71\pm 0.03$ ,  $0.71\pm 0.01$ , NS respectively. (Figure 4.5B). HASSMC cultured in VA086 hydrogels cultured to day 4 became more rounded with increasing photoinitiator concentration (0.5, 0.75, 1.0% w/v VA086 circularity was  $0.63\pm 0.01$ ,  $0.69\pm 0.01$ ,  $0.71\pm 0.01$  respectively).

ANCOVA (analysis of covariance) for the day 3&4 circularity data trends:

Least squares of the Irgacure concentration and cell type interaction circularity data with the JMP full factorial macro showed the HASSMC/IRG, HAVIC/IRG, and HADMSC/IRG slopes were not significantly different ( $p=0.3300$ ). Subsequent ANCOVA and Student's-t test indicated that HADMSC were significantly different from HASSMC and HAVIC which were not different from each other (least squares means  $0.51\pm 0.01$ ,  $0.69\pm 0.01$ ,  $0.73\pm 0.01$  respectively). Least squares fit of the VA086 concentration and cell type interaction circularity data showed the HADMSC/IRG slope was significantly different from the HASSMC/IRG and HAVIC/IRG slopes ( $p=0.0081$ ) and the HASSMC/IRG and HAVIC/IRG slopes were not different from each other ( $p=0.6083$ ). Subsequent

ANCOVA and Student's t-test of the HAVIC and HASSMC data, indicated no significant difference (least squares means  $0.68\pm 0.01$ ,  $0.68\pm 0.01$  respectively).

#### **4.4.5 Cell Viability at Day 1, 3, 4, and 7 Culture**

Over the course of 7 days of culture, in general the viability of encapsulated HAVIC and HASSMC decreased the longer hydrogel disks made with Irgacure were cultured, while the percentage of live HADMSC was maintained (Figure 4.6, 4.8, and 4.10). In general HAVIC, HASSMC, HADMSC viability is maintained in hydrogels prepared with VA086 (Figure 4.7, 4.9, and 4.11). HAVIC viability was less in Irgacure hydrogels compared to VA086 hydrogels, and photoinitiator concentration affected the viability over time (Figure 4.6 and 4.7). HAVIC percent viability in lower Irgacure hydrogels (0.05 % w/v had a dip in viability on day 3 (day 1, 3, and 7 viability  $79.1\pm 0.1$ ,  $66.4\pm 2.3$ ,  $74.1\pm 1.56$  respectively, Figure 4.6B). Viability of encapsulated HAVIC decreased with increasing day in culture for hydrogels made with higher Irgacure concentration (0.075% w/v: day 1, 3, and 7 viability  $75.1\pm 2.0$ ,  $57.7\pm 0.6$ ,  $43.9\pm 1.9$  respectively; 0.1% w/v: day 1, 3, and 7 viability  $65.8\pm 2.6$ ,  $58.8\pm 3.4$ ,  $50.6\pm 5.6$  respectively; Figure 4.6B)). Least squares fit analysis in JMP indicated the slopes are significantly different. HAVIC viability in 0.5 and 0.75% w/v VA086 hydrogels was not significantly different between day 1, 3, and 7 of culture or between photoinitiator concentrations (0.5% w/v: day 1, 3, and 7 viability  $91.0\pm 1.5$ ,  $92.7\pm 0.9$ ,  $91.0\pm 1.7$  respectively; 0.75% w/v: day 1, 3, and 7 viability  $90.6\pm 1.3$ ,  $92.2\pm 2.0$ ,  $94.1\pm 0.8$ ; Figure 4.7B respectively). Percentage of live encapsulated HAVIC in in 1.0% w/v VA086 hydrogels initially was lower than in 0.5 and 0.75% w/v VA086 hydrogels but it increased with time in culture (1.0% w/v: day 1, 3, and 7 viability  $84.3\pm 2.7$ ,  $86.0\pm 3.3$ ,  $91.8\pm 1.9$  respectively).

HASSMC viability was less in Irgacure hydrogels compared to VA086 hydrogels. Photoinitiator concentration affected the viability over time for Irgacure and VA086 hydrogels (Figure 4.8 and 4.9).

HASSMC viability decreased in Irgacure hydrogels as the time in culture increased (0.05% w/v: day 1, 3, and 7 viability  $89.7 \pm 1.1$ ,  $61.3 \pm 1.6$ ,  $61.3 \pm 0.8$  respectively; 0.075% w/v: day 1, 3, and 7 viability  $79.9 \pm 1.2$ ,  $61.7 \pm 2.4$ ,  $53.7 \pm 0.1$  respectively; 0.1% w/v: day 1, 3, and 7 viability  $85.1 \pm 1.0$ ,  $67.2 \pm 1.1$ ,  $56.3 \pm 4.6$  respectively; Figure 4.8B). The encapsulated cells follow the same decreasing viability trend for all three Irgacure concentrations. Least squares fit analysis in JMP indicated the slopes are not significantly different. There were significant differences in viability between photoinitiator concentrations at day 1,3, and 7. HASSMC viability decreased in VA086 hydrogels as the day in culture increased only in the highest photoinitiator concentration (1.0%, Figure 4.9B, day 1, 3, and 7 viability  $81.1 \pm 1.6$ ,  $71.1 \pm 2.0$ ,  $69.6 \pm 1.2$  respectively) and for the lower photoinitiator concentrations (0.5 and 0.75% w/v) the viability was not significantly different between the different days (0.5% w/v: day 1, 3, and 7 viability  $93.2 \pm 0.6$ ,  $94.8 \pm 0.4$ ,  $89.7 \pm 2.3$ ; 0.75% w/v respectively; day 1, 3, and 7 viability  $89.0 \pm 1.2$ ,  $81.2 \pm 3.3$ ,  $82.8 \pm 4.5$  respectively). For day 1, 4, and 7 culture times, percent viability decreased with increasing photoinitiator concentration

HADMSC viability did not vary significantly between days for 1,3, and 7 day culture for Irgacure hydrogels except for one condition (Figure 4.10B; 0.05% w/v: day 1, 3, and 7

viability  $93.6\pm 0.4$ ,  $89.7\pm 1.9$ ,  $89.3\pm 1.5$ ; 0.075% w/v respectively; day 1, 3, and 7 viability  $89.5\pm 2.2$ ,  $83.4\pm 1.5$ ,  $91.2\pm 2.1$  respectively; 0.1% w/v: day 1, 3, and 7 viability  $83.9\pm 1.7$ ,  $88.9\pm 1.1$ ,  $81.2\pm 2.5$  respectively). In the 0.075% Irgacure hydrogel the viability of HADMSC was less on day 3 than on day 1 and day 7. There were significant viability differences between photoinitiator concentration conditions. On day 1 and 7 0.05% w/v and 0.075% w/v had higher viability than 0.1% w/v hydrogels. On day 3 HADMSC viability was significantly different between 0.05% w/v hydrogels and the 0.075 and 0.1% Irgacure hydrogels. Percent viability for HADMSC in VA086 hydrogels was not significantly different between day 1, 4, and 7 of culture or between photoinitiator concentrations (Figure 4.11B; 0.5% w/v: day 1, 4, and 7 viability  $91.1\pm 1.1$ ,  $93.4\pm 0.8$ ,  $90.7\pm 2.4$ ; 0.75% w/v respectively; day 1, 4 viability  $93.8\pm 0.9$ ,  $92.5\pm 1.6$  respectively; 1.0% w/v: day 1, 4 viability  $92.4\pm 1.2$ ,  $90.9\pm 0.9$  respectively).

These results indicate that compared to VA086, Irgacure by weight has a more detrimental effect on cell viability for both primary valve cells and adipose derived stem cells. As time in culture increases, viability of HASSMC and HAVIC decreases. As time in culture increases the viability of HADMSC is generally maintained except at the highest Irgacure concentration where it also decreases.

#### **4.4.6 Metabolic Activity of Encapsulated Cells in 3D Culture**

MTT absorbance decreased with increasing time in culture for HASSMC and HADMSC in Irgacure hydrogels (Figure 4.8C, 4.10C). In VA086 hydrogels, MTT absorbance decreased with increasing day in culture for HAVIC and HASSMC and increased with increasing time in culture for HADMSC. MTT absorbance of HAVIC hydrogels was

significantly different between 0.75 and 1.0% w/v VA086 conditions at day 1 and day 3 (Figure 4.7C; 0.75% w/v: day 1, 4, and 7 absorbance  $0.180\pm 0.012$ ,  $0.123\pm 0.012$ ,  $0.107\pm 0.007$  respectively; 1.0% w/v: day 1, 4 absorbance  $0.220\pm 0.015$ ,  $0.185\pm 0.016$ ,  $0.129\pm 0.014$  respectively). MTT absorbance of HASSMC Irgacure hydrogels decreased with increasing time in culture, and only at day 1 of culture was there a significant difference between photoinitiator concentrations (Figure 4.8C, 0.05% w/v: day 1, 3, and 7 absorbance  $0.335\pm 0.014$ ,  $0.267\pm 0.026$ ,  $0.150\pm 0.009$  respectively; 0.075% w/v: day 1, 3, and 7 absorbance  $0.273\pm 0.006$ ,  $0.235\pm 0.024$ ,  $0.150\pm 0.009$  respectively; 0.1% w/v: day 1, 3, and 7 absorbance  $0.324\pm 0.008$ ,  $0.202\pm 0.009$ ,  $0.169\pm 0.010$  respectively). MTT absorbance of HASSMC VA086 hydrogels decreased with increasing time in culture (Figure 4.9C). At day 1 of culture photoinitiator condition 0.75% w/v had greater MTT absorbance than 0.5 which was greater than 1.0% w/v conditions (0.5, 0.75, and 1.0% w/v:  $0.253\pm 0.016$ ,  $0.339\pm 0.009$ ,  $0.181\pm 0.007$  respectively), at day 4 of culture photoinitiator conditions 0.5% w/v and 0.75w/v% MTT absorbance were higher than 1.0% w/v condition (0.5, 0.75, and 1.0% w/v:  $0.214\pm 0.005$ ,  $0.216\pm 0.005$ ,  $0.153\pm 0.005$  respectively), and at day 7 of culture photoinitiator condition 0.75% w/v had a higher MTT absorbance than both 0.5% w/v and 1.0% w/v conditions (0.5, 0.75, and 1.0% w/v:  $0.133\pm 0.007$ ,  $0.181\pm 0.008$ ,  $0.128\pm 0.006$  respectively).

MTT absorbance of HADMSC Irgacure samples decreased with increasing time in culture (Figure 4.10C). At day 1 of culture MTT absorbance decreased with increasing Irgacure concentration (0.05, 0.075, and 0.1% w/v:  $0.244\pm 0.014$ ,  $0.224\pm 0.012$ ,  $0.170\pm 0.006$  respectively), at day 3 of culture absorbance was higher for the 0.05

condition than 0.075 and 0.1 conditions (0.05, 0.075, and 0.1% w/v:0.209±0.012, 0.169±0.010, 0.184±0.005 respectively), and at day 7 in culture MTT absorbance decreases with increasing Irgacure concentration (0.05, 0.075, and 0.1% w/v:0.156±0.017, 0.142±0.007, 0.102±0.003 respectively). MTT absorbance of HADMSC VA086 samples increased with increasing time in culture (Figure 4.11C). At day 1 0.5% w/v condition, MTT absorbance was higher than 0.75 and 1.0 % w/v conditions (0.5, 0.75, and 1.0% w/v:0.191±0.005, 0.174±0.003, 0.172±0.003 respectively), at day 4 of culture MTT absorbance decreased with increasing VA086 photoinitiator concentration (0.5, 0.75, and 1.0% w/v:0.308±0.011, 0.222±0.013, 0.182±0.005 respectively), at day 7 of culture MTT absorbance decreased with increasing VA086 photoinitiator concentration (0.5, 0.75, and 1.0% w/v:0.245±0.011, 0.232±0.010, 0.216±0.011 respectively).

These results indicate that over the course of 7 days the metabolism of the cell laded hydrogel decreases in all but the HADMSC populated VA086 hydrogels. Hydrogel and cell erosion was observed for the low concentration VA086 hydrogels which could affect MTT results.

#### **4.4.7 Doubling Time Compared to 3D Survival**

Williams et al found that rapidly proliferating cells had higher sensitivity to photoinitiator toxicity (Williams, Malik et al. 2005) and hypothesized that cell doubling time could be a predictor of survival during photo-encapsulation in hydrogels. To test if doubling time could predict/explain cell type survival in photo-crosslinked hydrogels, 2D proliferation was assessed. In addition to the HAVIC, HASSMC, and HADMSC a 4th cell type was

included for the 2D doubling time test. Porcine Aortic Valve Interstitial Cells (PAVIC) are known in the lab for being robust in 2D culture and are often utilized as a model cell type due to the similarity between the porcine and human cardiovascular systems (Swindle, Makin et al. 2012). HAVIC 2D doubling time on tissue culture plastic was significantly slower than the PAVIC and HADMSC doubling time (Figure 4.12A) (HAVIC, HASSMC, HADMSC, PAVIC doubling times  $65.5 \pm 6.4$ ,  $46.3 \pm 2.4$  hrs,  $37.7 \pm 4.2$  hrs, and  $33.2 \pm 1.8$  respectively). HADMSC tolerated encapsulation and photo-crosslinking conditions the best and PAVIC tolerated the conditions the least (Figure 4.12B). Human valve cell viability fell between the two extremes and the percentage of cells alive in the hydrogels prepared with 0.05% w/v and 0.1% w/v Irgacure and photo-crosslinked with the lamp for 5 minutes after 3 and 4 days culture was not significantly different between HAVIC and HASSMC or between the two Irgacure concentrations (HAVIC 0.05% w/v:  $65.8 \pm 2.6$  %live; HAVIC 0.1% w/v:  $58.8 \pm 3.3$  %live; HASSMC 0.05% w/v:  $61.3 \pm 1.6$  %live; HASSMC 0.1% w/v:  $67.2 \pm 1.1$  %live). HADMSC viability was significantly higher than all the other cell types and was sensitive to Irgacure concentration (HADMSC 0.05% w/v:  $89.7 \pm 1.9$  %live; HADMSC 0.1% w/v:  $78.9 \pm 1.1$  %live). PAVIC viability was significantly lower than all the other cell types and was also sensitive to Irgacure concentration (PAVIC 0.05% w/v:  $46.0 \pm 9.7$  %live; PAVIC 0.1% w/v:  $38.9 \pm 4.2$  %live). The PAVIC sensitivity to encapsulation conditions was also observed in VA086 hydrogels (Figure 4.12C). The percentage of PAVIC alive in the hydrogels prepared with 0.5% VA086 and photo-crosslinked with the lamp for 5 minutes after 3 and 4 days of culture was significantly less than it was for the other 3 cell types (PAVIC 0.5% w/v:  $62.7 \pm 6.8$  %live; HADMSC 0.5% w/v:  $93.4 \pm 0.8$  %live ; HAVIC 0.5% w/v:  $92.7 \pm 0.9$  %live, HASSMC 0.5% w/v:  $94.8 \pm 0.3$ ).

3D viability did not appear to correlate with 2D doubling time for either Irgacure or VA086 hydrogels (Figure 4.12 D and E). HADMSC and PAVIC have similar doubling time, but have the most pronounced survival differences in 3D.

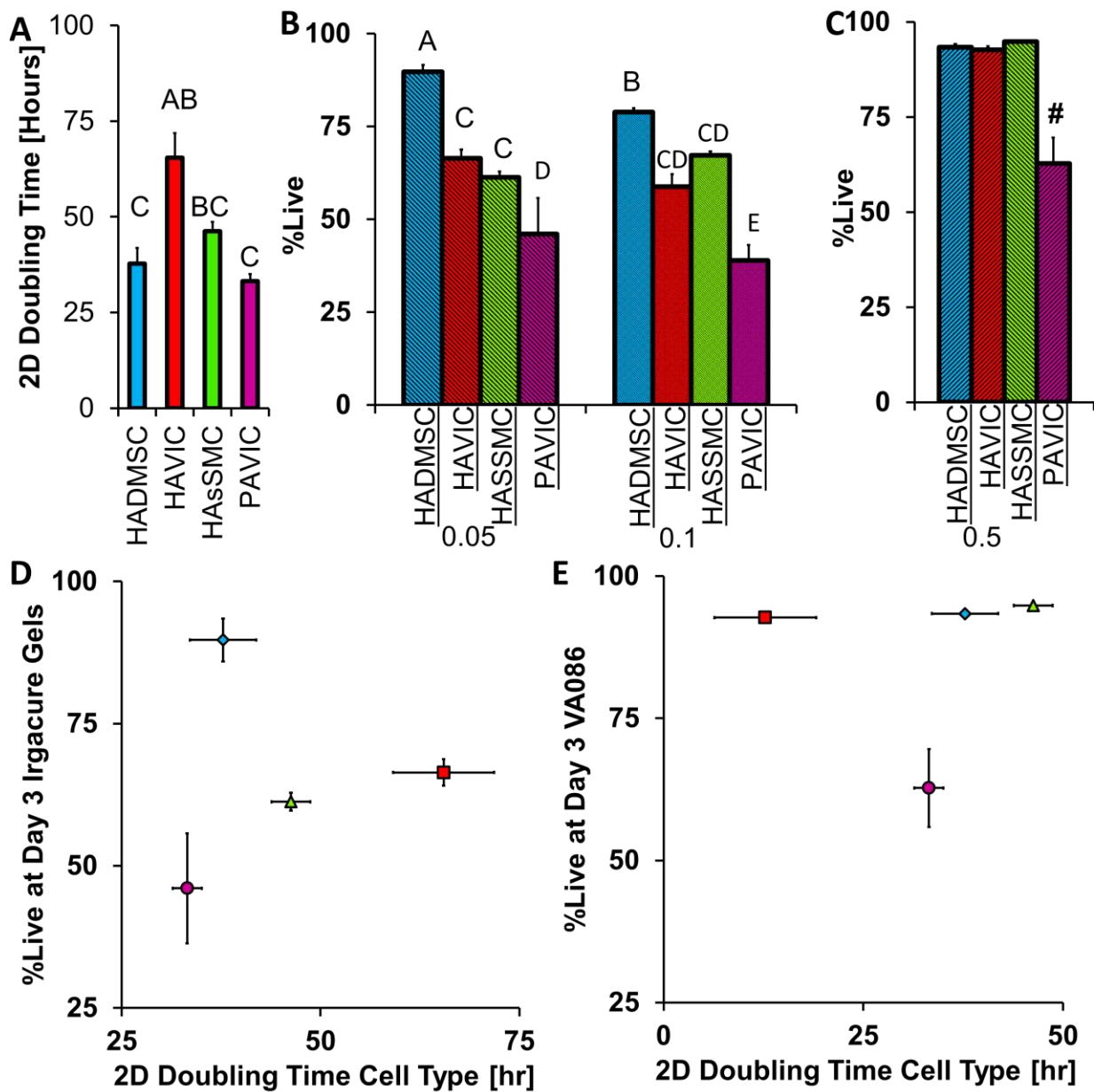


**Figure 4.12 Cell type 2D doubling time and 3D hydrogel viability.**

**(A)** 2D doubling time of 4 different cell types.  $p < 0.05$  non-matching letters. **(B)** Live/dead viability of 4 different cell types encapsulated in Irgacure gels made with two photoinitiator concentrations cultured to day 3 and 4.  $p < 0.05$  non-matching letters. **(C)** Live/dead viability of 4 different cell types encapsulated in VA086 gels. Standard error of the mean was used. # $p < 0.05$ . **(D)** Viability versus 2D doubling time plot for 0.05% w/v Irgacure hydrogels. **(E)** Viability versus 2D doubling time plot for 0.5% w/v VA086 hydrogels.

#### **4.4.8 Percentage of Encapsulated Cells Experiencing General Oxidative Stress (DCF) with and without Catalase Treatment**

Hydrogels prepared at the highest photoinitiator concentrations tested in this study, Irgacure 0.1% w/v and VA086 1.0% w/v, had the most pronounced differences in encapsulated cell viability between cell-type (Figure 4.5). DCF fluorescence indicates that general oxidative stress was induced in HADMSC, HAVIC, and HASSMC by these encapsulation conditions (Figure 4.13). In a given condition not all cells fluoresced green (positive for oxidative stress) and to the same degree and intensity (Figure 4.13 - 4.17). Figure 4.18 summarizes the percentage of cells with positive DCF fluorescence and the relative DCF fluorescence intensity of encapsulated cells. The graph y-axes of 4.18A and 4.18C are percent of encapsulated cells that are DCF positive. Figure 4.18B and 4.18D graph y-axes are the relative fluorescence of DCF in encapsulated cells. Magnitude for B and D axes is different to include the range of the HLED/VA086 condition. (The HLED/VA086 condition fluorescence signal is more intense due to the higher buoyancy of the hydrogels, which is explained in more detail in the HLED section).

#### Lamp Tests

For cells treated with HBSS control solution prior to encapsulation and then lamp photocrosslinking for 5 minutes there was no significant percentage difference of cells showing oxidative stress between cell types in each photoinitiator condition (Figure 4.18A) (Irgacure 0.1% w/v: HADMSC  $58.82 \pm 7.31$ , HAVIC  $58.18 \pm 11.66$ , HASSMC  $72.38 \pm 6.68$ ; VA086: HADMSC  $41.59 \pm 12.28$ , HAVIC  $39.46.18 \pm 10.86$ , HASSMC  $38.27 \pm 8.69$ ). Between photoinitiator types only HASSMC had a significantly different

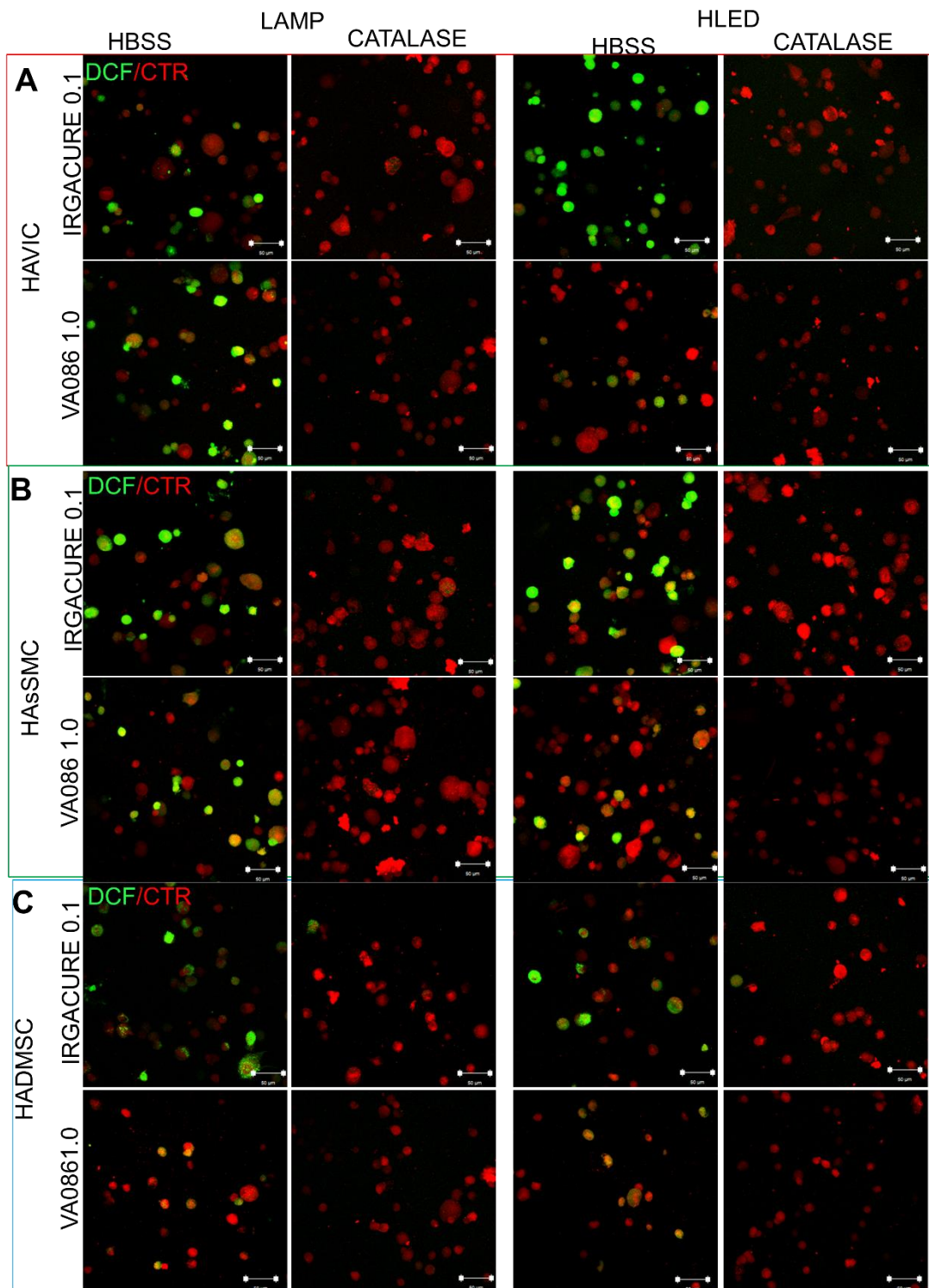


**Figure 4.13** Representative images of encapsulated DCF/CTR labeled HBSS and catalase treated cells taken directly after crosslinking of hydrogel.

**(A)** HAVIC **(B)** HASSMC **(C)** HADMSC. Green is the DCF indicating oxidative stress and red is cell tracker red staining the cytoplasm.

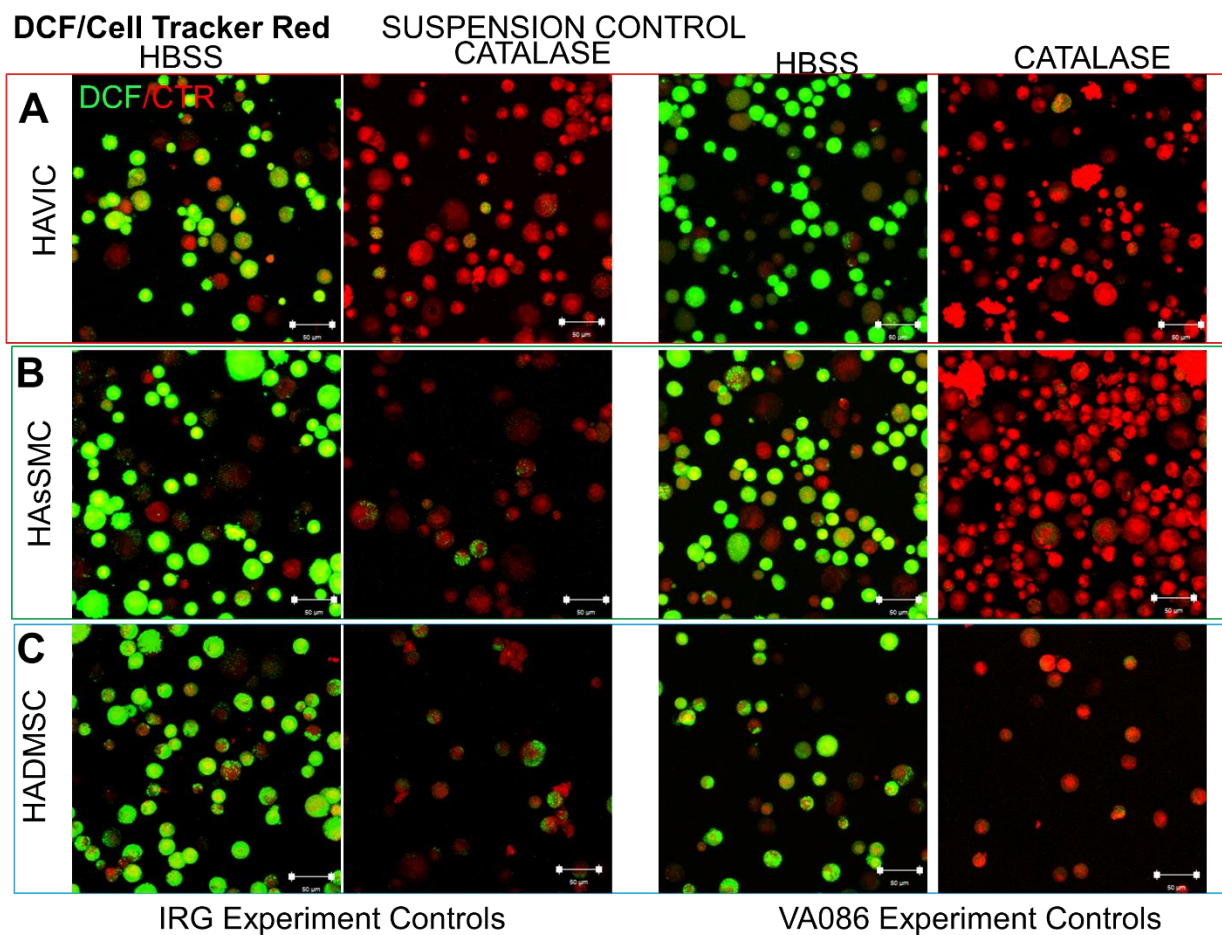


**Figure 4.14** Representative images of HBSS and catalase treated cells labeled with DCF/DTR suspended in HBSS and benchtop incubated during encapsulation handling.

**(A)** HAVIC **(B)** HASSMC **(C)** HADMSC. Green is the DCF indicating oxidative stress and red is cell tracker red staining the cytoplasm.

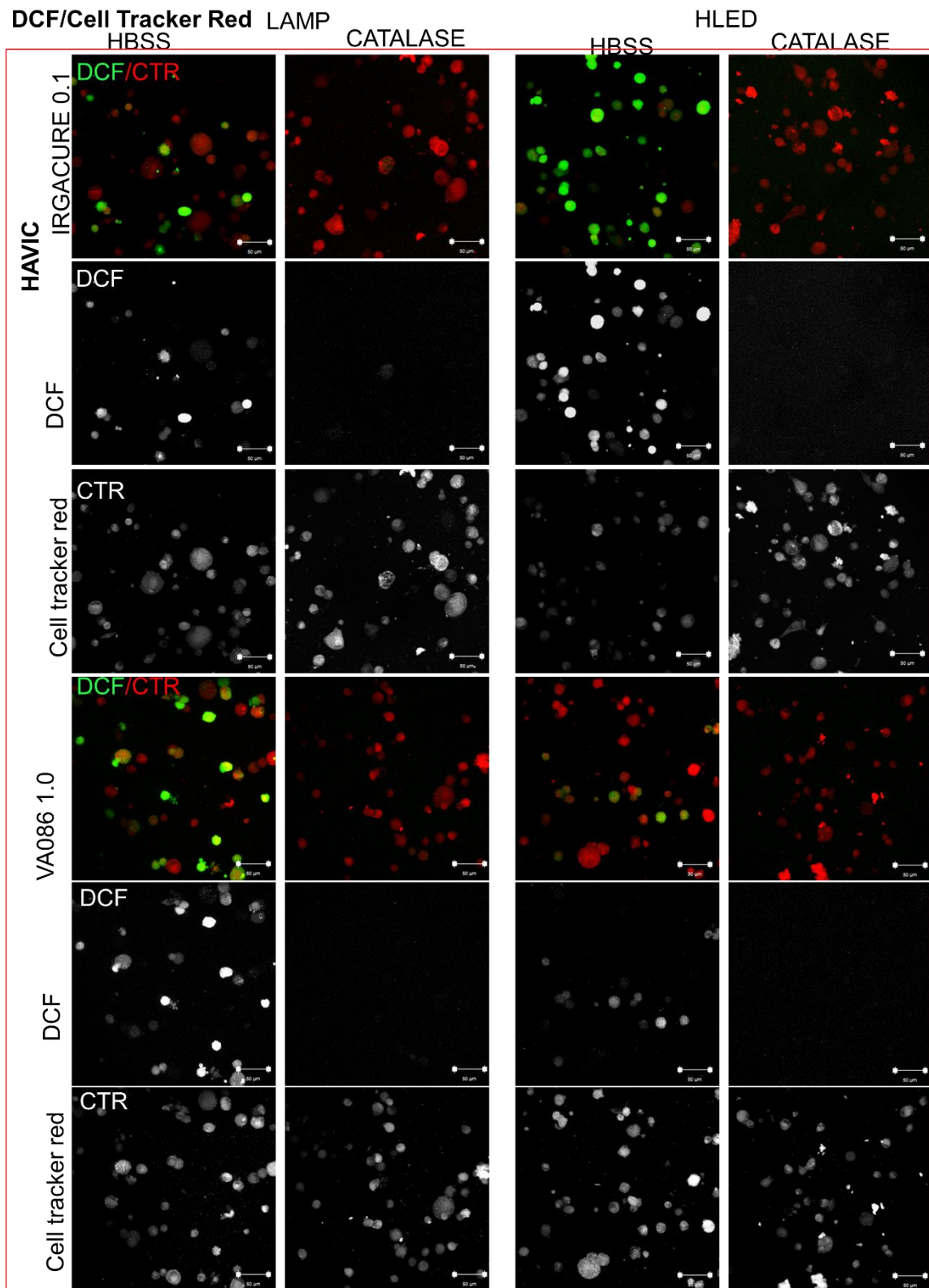


**Figure 4.15** Split channels of representative images of encapsulated DCF/DTR labeled HAVIC taken directly after crosslinking of hydrogel.

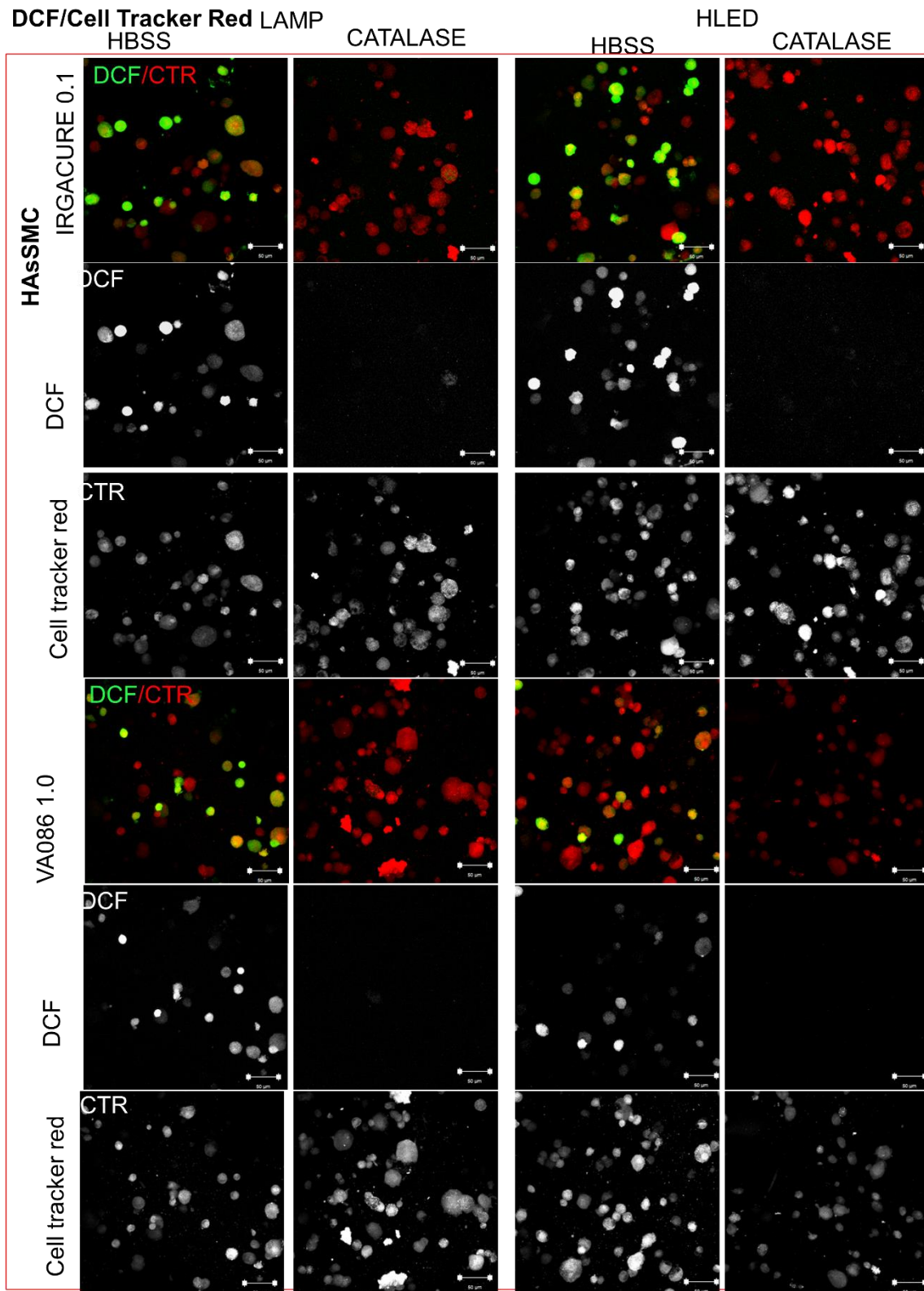


**Figure 4.16** Split channels of representative images of encapsulated DCF/DTR labeled HAsSMC cells taken directly after crosslinking of hydrogel.

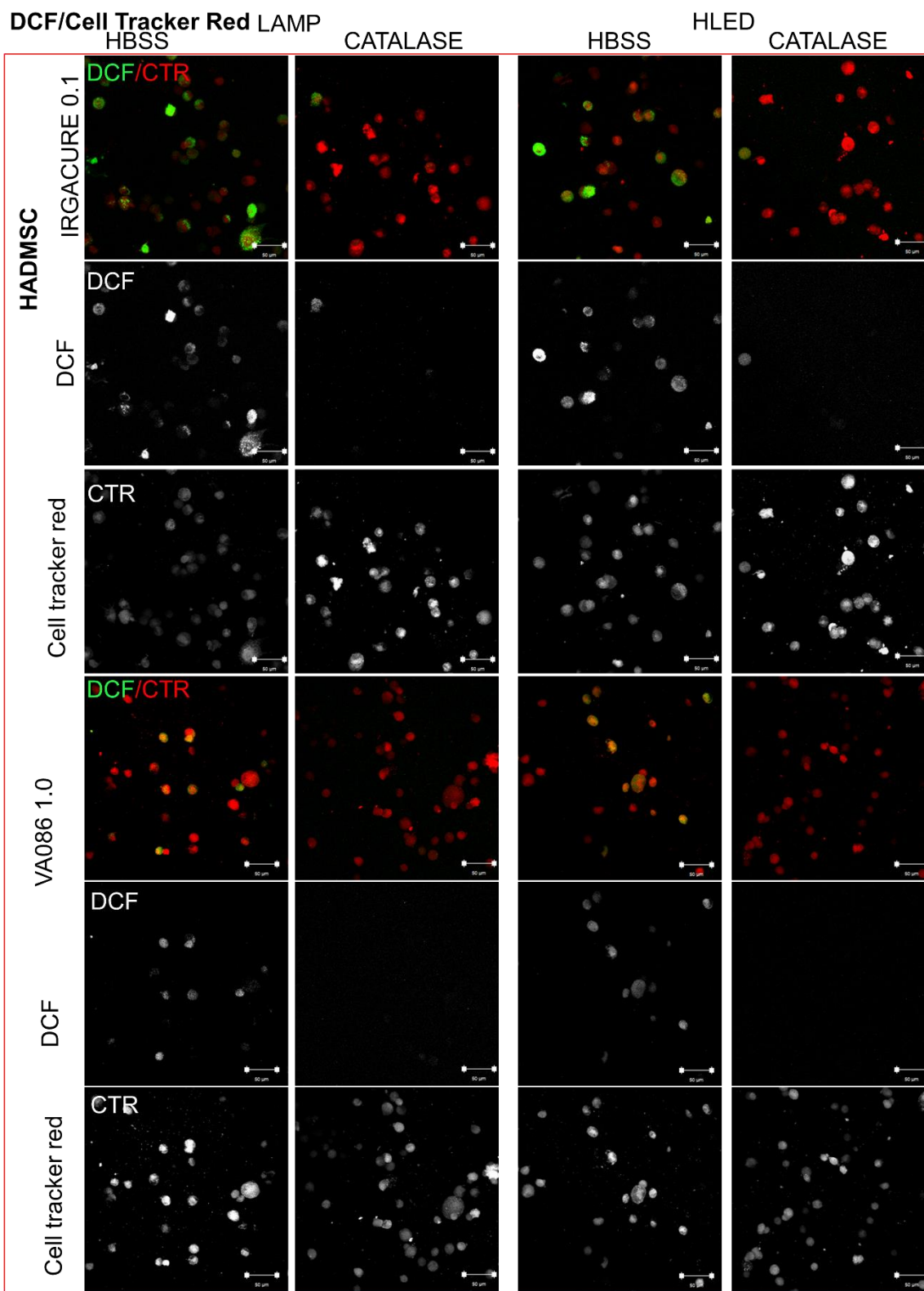


**Figure 4.17** Split channels of representative images of encapsulated DCF/DTR labeled HADMSC cells taken directly after crosslinking of hydrogel.

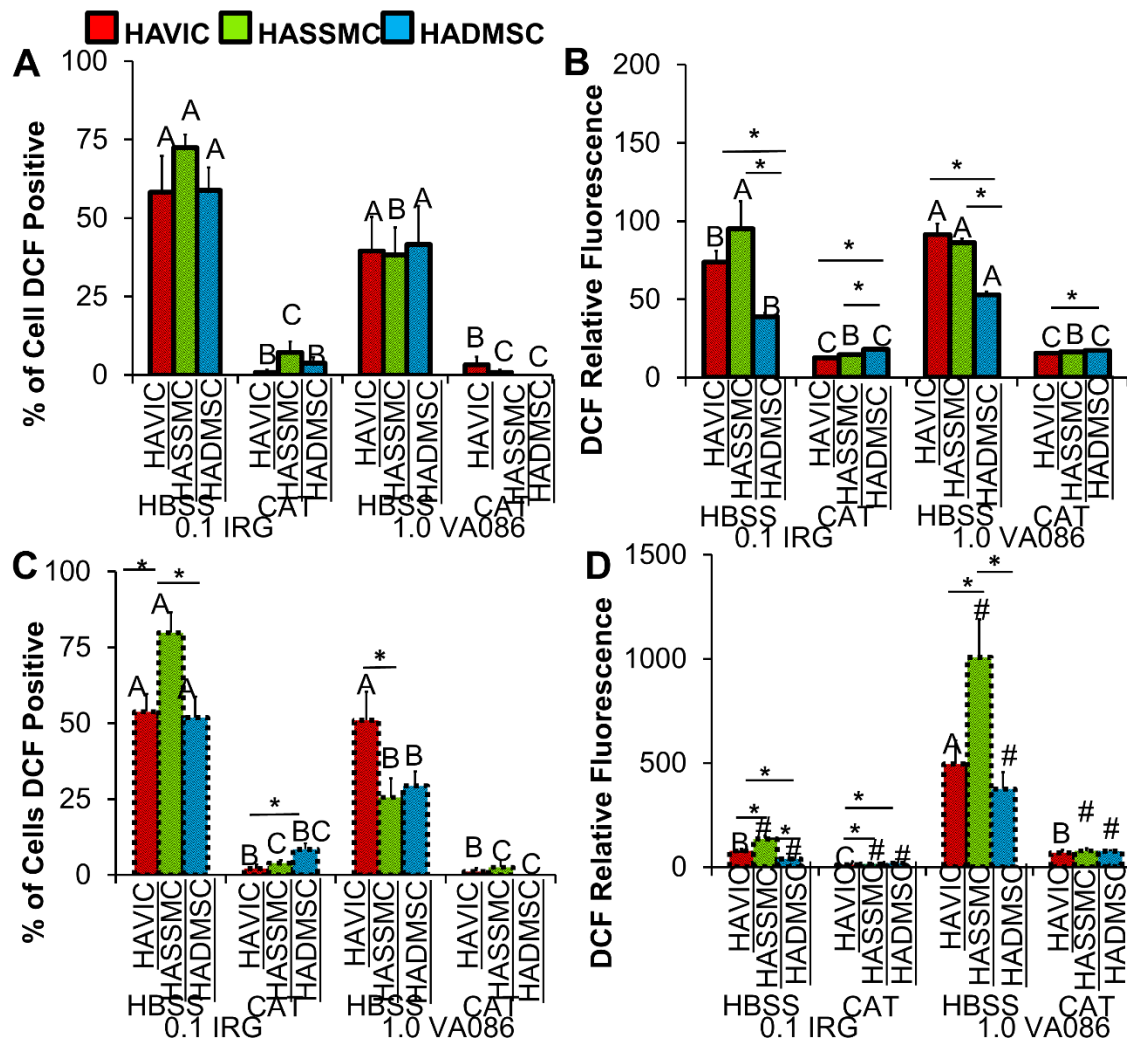


**Figure 4.18 Oxidative stress differences between cell type: HAVIC, HASSMC, and HADMSC treated with catalase or HBSS (control) before encapsulation and light exposure.**

**(A)** Percent of encapsulated cells that are DCF positive and experiencing general oxidative stress after photo-crosslinking with lamp. Non matching letters  $p < 0.05$  testing between groups (effect of photoinitiator and treatment),  $*p < 0.05$  testing within groups (effect of cell type). **(B)** Relative fluorescence of general oxidative stress indicator in encapsulated HAVIC, HASSMC, and HADMSC samples crosslinked with lamp. Non matching letters  $p < 0.05$  testing between groups (effect of photoinitiator and treatment),  $*p < 0.05$  testing within groups (effect of cell type). All error bars are standard error of the mean. **(C)** Percent of encapsulated cells DCF positive after photo-crosslinking with high powered LED. Non matching letters  $p < 0.05$  testing between groups (effect of photoinitiator and treatment),  $*p < 0.05$  testing within groups (effect of cell type). **(D)** Relative fluorescence of general oxidative stress indicator in encapsulated HAVIC, HASSMC, and HADMSC samples crosslinked with high power LED. Non matching letters  $p < 0.05$  testing between groups (effect of photoinitiator and treatment),  $*p < 0.05$  testing within groups (effect of cell type).

percentage of cells showing oxidative stress between Irgacure and VA086 hydrogels, and Irgacure induced a higher percentage (Figure 4.18A) (Irgacure 0.1% w/v: 72.38±6.68; VA086: HASSMC 38.27±8.69). Catalase decreased the percentage of cells displaying an oxidative stress response in all 3 cell types. For cells treated with catalase solution prior to encapsulation and then lamp photo-crosslinking for 5 minutes there was no significant percentage difference of cells showing oxidative stress between cell types in each photoinitiator condition (Irgacure 0.1% w/v: HADMSC 3.80±1.80, HAVIC 0.82±0.82, HASSMC 7.18±3.45; VA086: HADMSC 0.0±0.0, HAVIC 3.24±2.50, HASSMC 0.78±0.78). Between photoinitiator types only catalase treated HADMSC had a significantly different percentage of cells showing oxidative stress between Irgacure and VA086 hydrogels, and Irgacure induced a higher percentage (Irgacure 0.1% w/v: 34.10±10.88, VA086 0.5% w/v: 0.0±0.0).

### HLED Test

Additionally, the effect of increasing the photo-crosslinking light intensity was tested. Within cell type, the percent of cells experiencing oxidative stress induced by the high power LED array compared to the lamp was not significantly different (Figure 4.19, Figure 4.20, and Figure 4.21 showing lamp and LED comparisons). For cells treated with HBSS control solution prior to encapsulation and then HLED array photo-crosslinking for 5 minutes there was a significant percentage difference of cells showing oxidative stress between cell types in each photoinitiator condition (Figure 4.18C). In 0.1% Irgacure hydrogels HASSMC had a higher percentage of cells experiencing oxidative stress than both HAVIC and HADMSC (HADMSC 51.79±6.93, HAVIC 53.76±5.82, HASSMC 79.86±6.68) and in 1.0% VA086 hydrogels HAVIC had a higher percentage of cells experiencing oxidative stress than HASSMC (HADMSC 29.27±4.82, HAVIC 50.98±9.45, HASSMC 25.47±6.27). Between photoinitiator types the percentage of HASSMC and HADMSC displaying oxidative stress was higher in

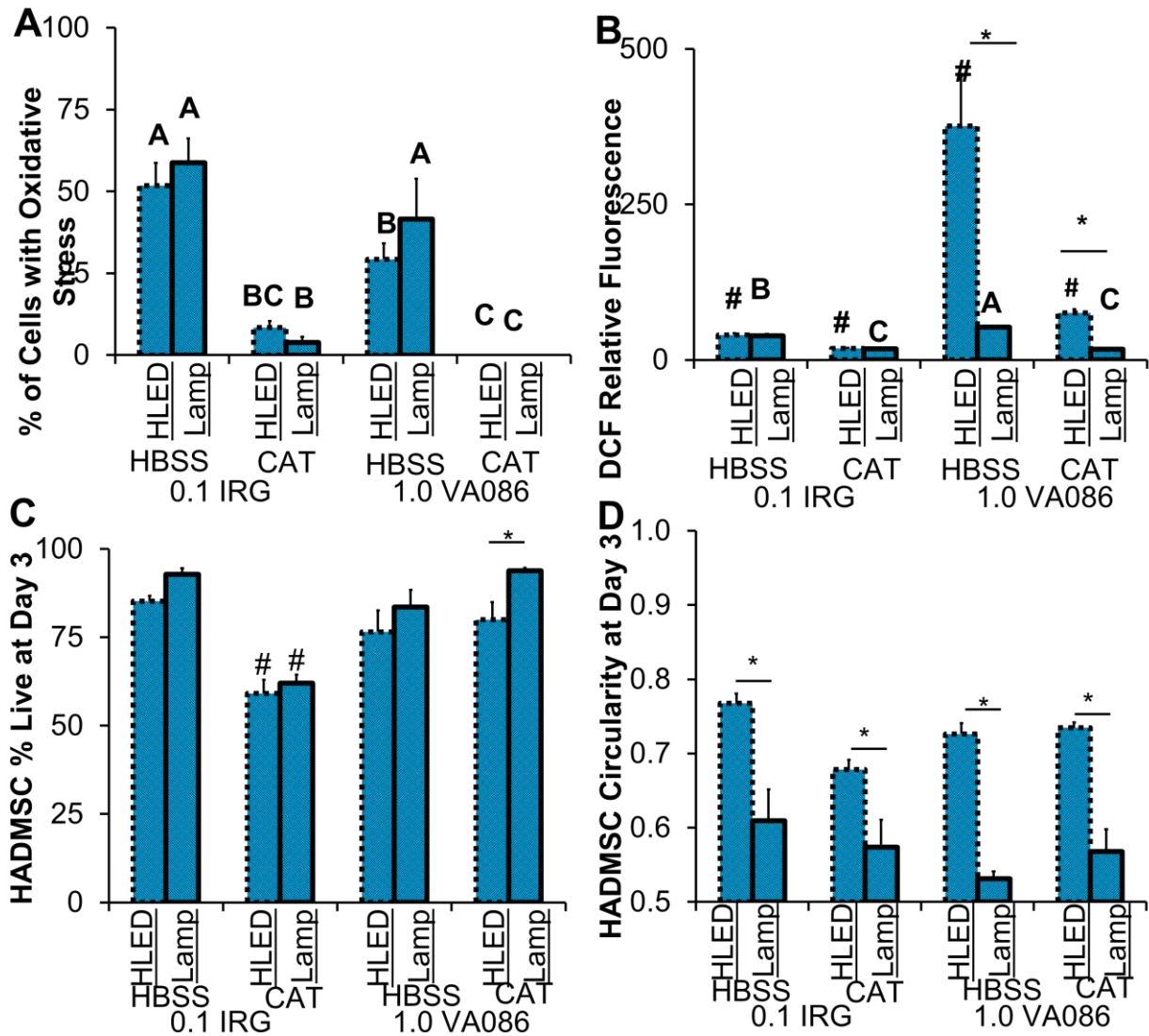


**Figure 4.19 Oxidative stress and effect of catalase loading for HADMSC as a function of light source intensity.**

Percent of HADMSC experiencing general oxidative stress after photo-crosslinking. Non matching letters  $p < 0.05$  testing between groups (effect of photoinitiator and treatment), \* $p < 0.05$  testing within groups (effect of light source). No significant difference within groups (no effect of light source). **(B)** Relative fluorescence of general oxidative stress indicator in encapsulated HADMSC samples. Non matching letters  $p < 0.05$  testing between groups (effect of photoinitiator and treatment), \* $p < 0.05$  testing within groups (effect of light source). **(C)** Percent live treated and encapsulated HADMSC after 3 days culture. Non matching letters and # $p < 0.05$  testing between groups (effect of photoinitiator and treatment), \* $p < 0.05$  testing within groups (effect of light source). **(D)** Circularity of HADMSC after 3 days culture. # $p < 0.05$  testing between groups (effect of photoinitiator and treatment), \* $p < 0.05$  testing within groups (effect of light source). All error bars are standard error of the mean.

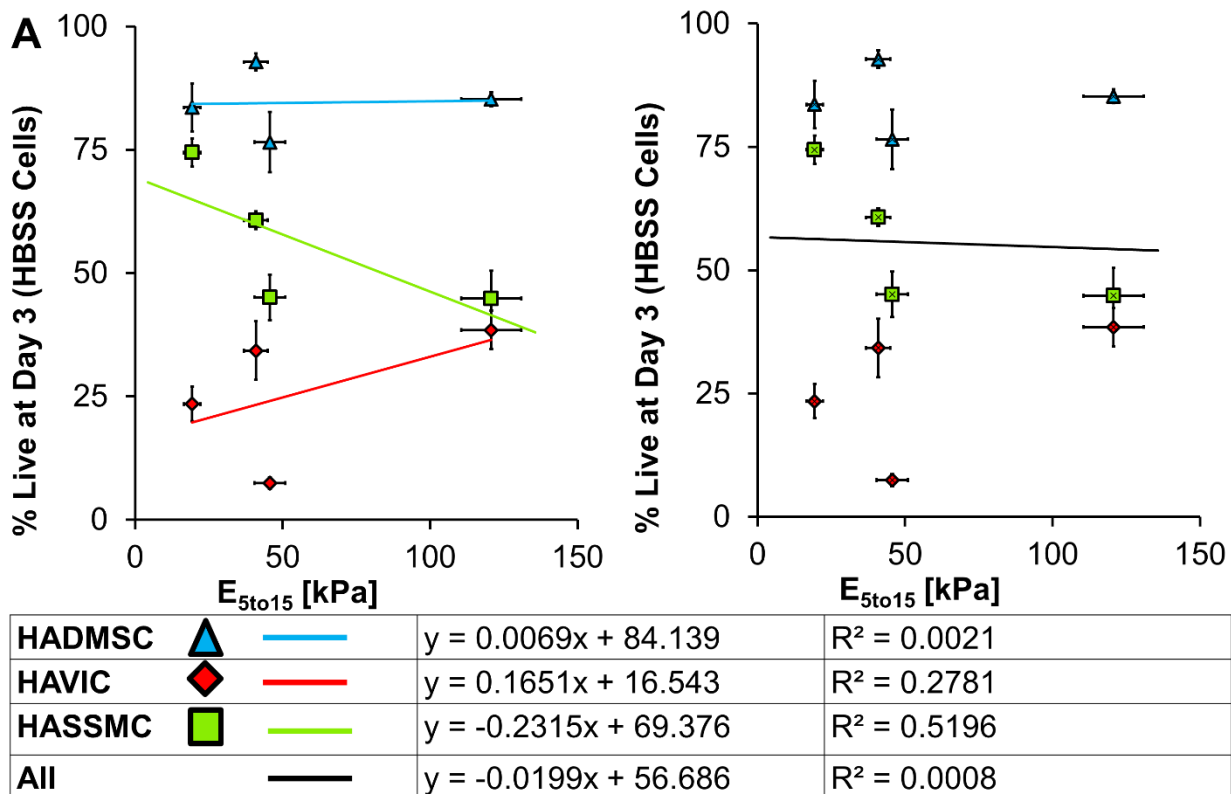


**Figure 4.20 (A) Viability and circularity of HBSS treated control cells verses encapsulating hydrogel modulus.**

Percent Live/Dead at day 3 verses modulus (calculated between 5 and 15% strain). Each cell type and data from both photoinitiators linear fit (red HAVIC line, green HASSMC line, blue HADMSC line). All cell types and data from both photoinitiator linear fit (black line).

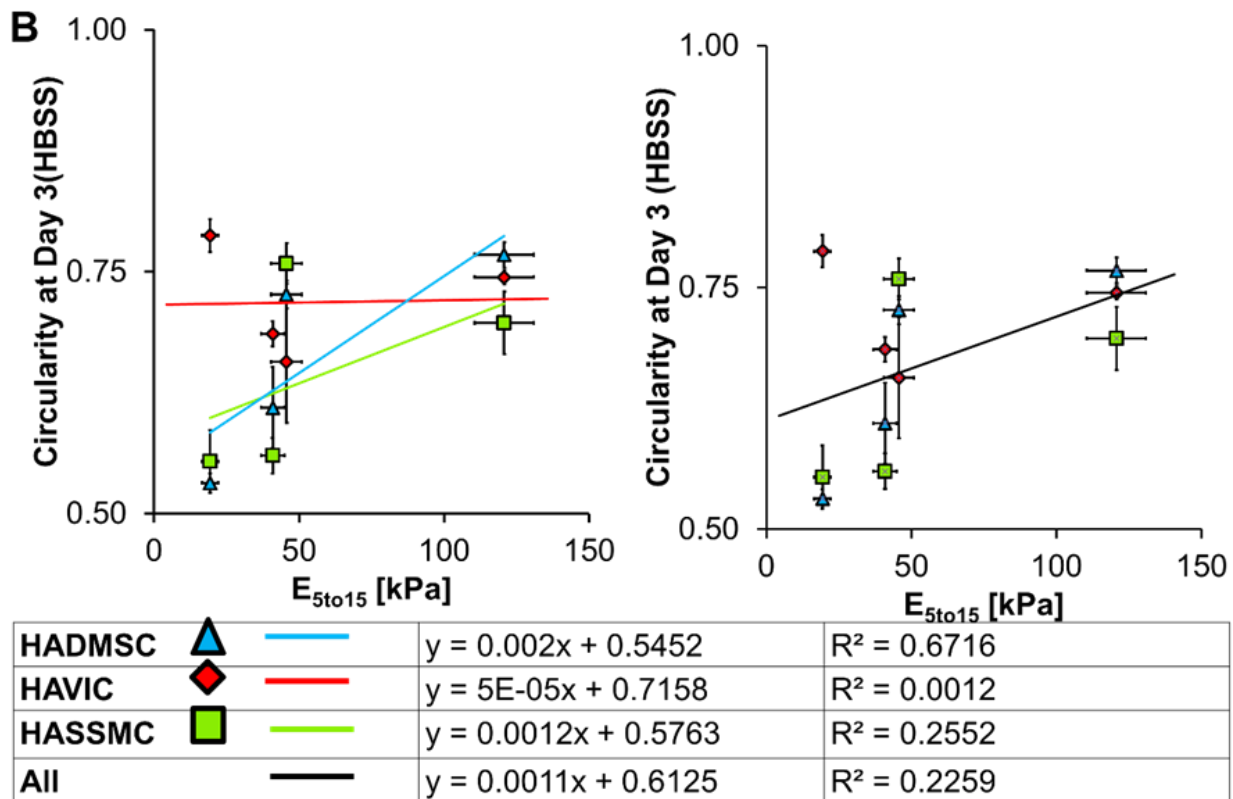
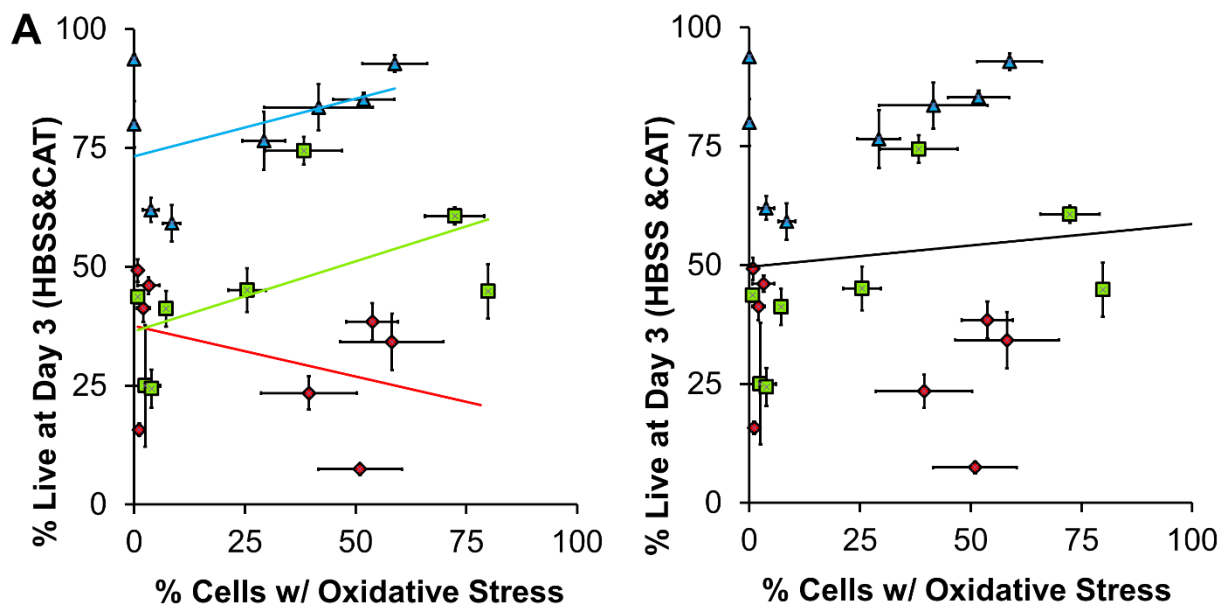


**Figure 4.20 (B) Viability and circularity of HBSS treated control cells verses encapsulating hydrogel modulus.**

Circularity of live cells at day 3 verses modulus Each cell type and data from both photoinitiators linear fit (red HAVIC line, green HASSMC line, blue HADMSC line). All cell types and data from both photoinitiator linear fit (black line).



HADMSC			$y = 0.2412x + 73.282$	$R^2 = 0.2072$
HAVIC			$y = -0.2121x + 37.554$	$R^2 = 0.142$
HASSMC			$y = 0.2946x + 36.422$	$R^2 = 0.3187$
All			$y = 0.0905x + 49.618$	$R^2 = 0.0094$

**Figure 4.21(A) Viability and morphology verses percentage of cells experiencing oxidative stress for catalase treated and HBSS controls cells in Irgacure and VA086 encapsulation conditions.**

Percent Live/Dead at day 3 verses percent of cells positively stained oxidative stress after crosslinking of treated cells.

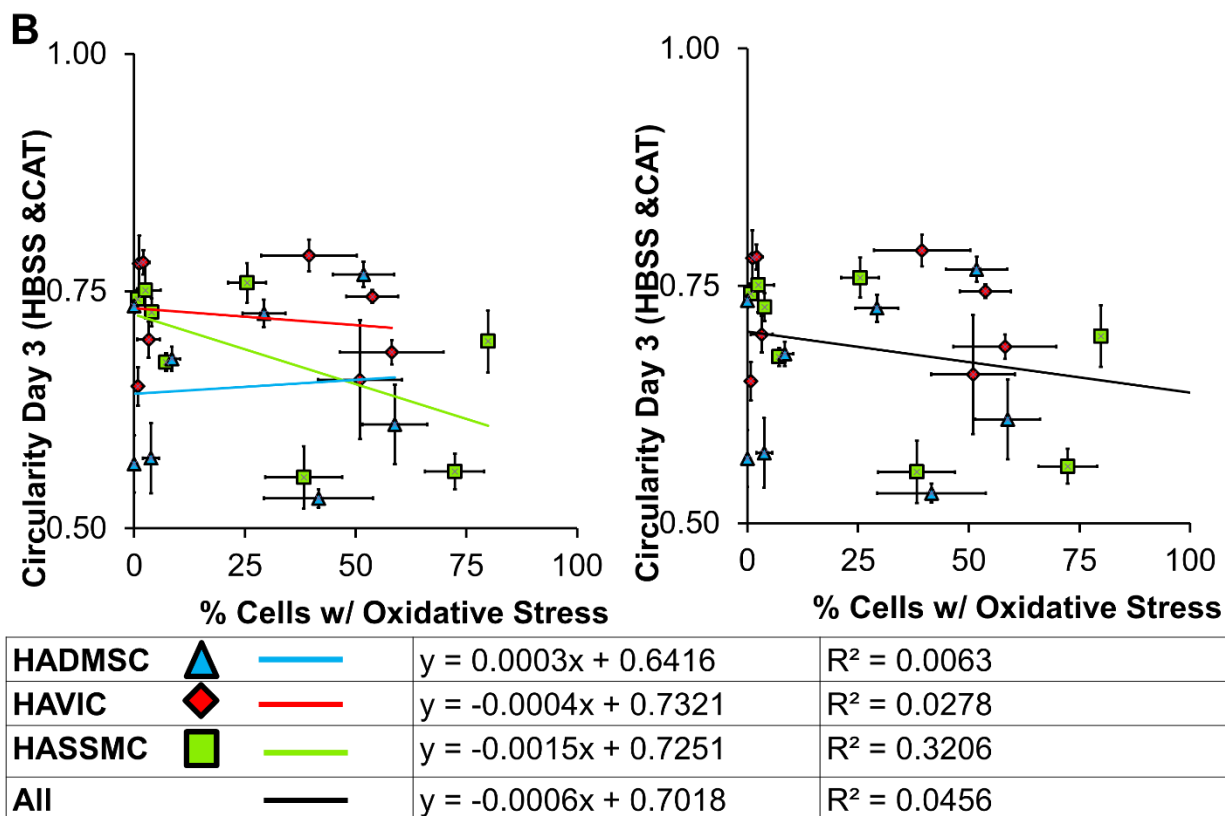


**Figure 4.21 (B) Viability and morphology verses percentage of cells experiencing oxidative stress for catalase treated and HBSS controls cells in Irgacure and VA086 encapsulation conditions.**

Circularity of live cells at day 3 verses percent of cells positively stained for oxidative stress verses. Each cell type and data from both photoinitiators and light sources linear fit (red HAVIC line, green HASSMC line, blue HADMSC line). All cell types and data from both photoinitiator types and light sources linear fit (black line).

Irgacure compared to VA086 hydrogels, but there was no significant difference for HAVIC. Catalase decreased the percentage of cells displaying an oxidative stress response in all 3 cell types (Irgacure 0.1% w/v: HADMSC 8.46±1.94, HAVIC 2.06±1.41, HASSMC 3.90±0.93; VA086 1.0% w/v: HADMSC 0.0±0.0, HAVIC 1.14±1.14, HASSMC 2.50±2.50). For cells treated with catalase solution prior to encapsulation and then HLED array photo-crosslinking for 5 minutes between cell types in each photoinitiator condition only HADMSC when compared to HAVIC in Irgacure hydrogel had a significantly higher percentage of cells showing oxidative stress. Between photoinitiator types none of the catalase treated cell types had a significantly different percentage of cells showing oxidative stress between Irgacure and VA086 hydrogels.

These results indicate that catalase treatment prior to encapsulation dramatically decreases the number of cells experiencing intracellular general oxidative stress. The percentage of cells positive for oxidative stress is higher for Irgacure 0.1% w/v conditions compared to VA086 1.0% w/v conditions between photoinitiator types for HASSMC at the lower light intensity and for HASSMC and HADMSC at the greater light intensity. Between cell types, percentage of cells experiencing oxidative stress are evident at the higher light intensity, where HASSMC experience more oxidative stress compared to HAVIC and HADMSC in Irgacure hydrogels and HAVIC experience more oxidative stress compared to HASSMC and HADMSC in VA086 hydrogels.

#### **4.4.9 Relative Fluorescence of Hydrogels Loaded with DCF Tagged Cells**

The plate reader was used to get a quantitative measurement of the relative fluorescence of an entire encapsulated cell-hydrogel disk. Relative fluorescence was measured directly after photo-crosslinking. From the confocal images it is possible to see that in a given condition not all cells fluoresced green (positive for oxidative stress)

and to the same degree and intensity (Figure 4.13 and Figure 4.14). The plate reader area scan of the entire gel was performed to quantitatively capture the intensity differences of the positively stained cells.

### Lamp Tests

For cells treated with HBSS control solution prior to encapsulation and then lamp photo-crosslinking for 5 minutes there were significant differences in oxidative stress fluorescence (DCF) between cell types in each photoinitiator condition (Figure 4.18B). HADMSC hydrogels were significantly less fluorescent than HAVIC and HASSMC (Irgacure 0.1% w/v: HADMSC  $38.96 \pm 2.39$ , HAVIC  $73.85 \pm 7.24$ , HASSMC  $135.88 \pm 14.79$ ; VA086 1.0% w/v: HADMSC  $52.90 \pm 2.08$ , HAVIC  $91.40 \pm 7.09$ , HASSMC  $86.29 \pm 2.67$ ). Between photoinitiator types HAVIC and HADMSC hydrogels had significantly different oxidative stress fluorescence between Irgacure and VA086 hydrogels. HAVIC VA086 hydrogels had higher fluorescence than Irgacure hydrogels, and HADMSC VA086 hydrogels had higher fluorescence than Irgacure hydrogels. Catalase decreased the relative fluorescence oxidative stress response in all 3 cell types. For cells treated with catalase solution prior to encapsulation and then lamp photo-crosslinking for 5 minutes there were significant differences of relative fluorescence between cell types in each photoinitiator condition (Irgacure 0.1% w/v: HADMSC  $17.92 \pm 1.03$ , HAVIC  $12.75 \pm 0.39$ , HASSMC  $14.65 \pm 0.16$ ; VA086 1.0% w/v: HADMSC  $17.27 \pm 0.27$ , HAVIC  $15.50 \pm 0.19$ , HASSMC  $16.42 \pm 0.66$ ). Interestingly, in the catalase condition the HADMSC hydrogels have higher relative fluorescence than the valve cells. Between photoinitiator types there was no significant difference in relative fluorescence oxidative stress between Irgacure and VA086 hydrogels.

### HLED Tests

In general increasing the photo-crosslinking light intensity increased the relative fluorescence of cell-hydrogels in VA086 conditions and not Irgacure conditions. There was not a significant difference in Irgacure hydrogel fluorescence between the high power LED array compared to the lamp, with the sole exception of catalase treated HASSMC (Figure 4.22B). The relative fluorescence measurement induced by the high power LED array compared to the lamp was significantly higher in all VA086 conditions (Figure 4.18D, Figure 4.19B, Figure 4.22B and Figure 4.23B, showing lamp and HLED comparisons) (HLED VA086 1.0% w/v: HADMSC  $375.90 \pm 80.21$ , HAVIC  $495.42 \pm 113.35$ , HASSMC  $1007.81 \pm 182.18$ ). However, the relative fluorescence signal for the VA086 cell-hydrogels may be artificially high. The VA086 photoinitiator foams the hydrogel during photo-crosslinking, and it is dramatic/pronounced in the HLED array crosslinked hydrogels. The oxidative stress measurements were taken quickly after photo-crosslinking (within 1 hour with the peeling, media rinse, and transfer of disks into HBSS filled black-bottom well plates steps), and the gels likely did not have sufficient time to equilibrate with the surrounding solution. The HLED/VA086 cell-hydrogel disks were noticeably more buoyant than the other conditions in the well plates. The read height setting on the multi-plate reader is the same for all the wells, and the top-read scan would place the floating gels closer to the excitation light source and the detector (Figure 4.24A). Therefore the relative fluorescence measurements of the VA086/HLED conditions should not be compared to the VA086/Lamp, Irgacure/Lamp, and Irgacure/HLED conditions. Treatments and cell type within the VA086/HLED condition can be compared for this experiment. For cells treated with HBSS control solution prior to encapsulation and then HLED array photo-crosslinking for 5 minutes there were

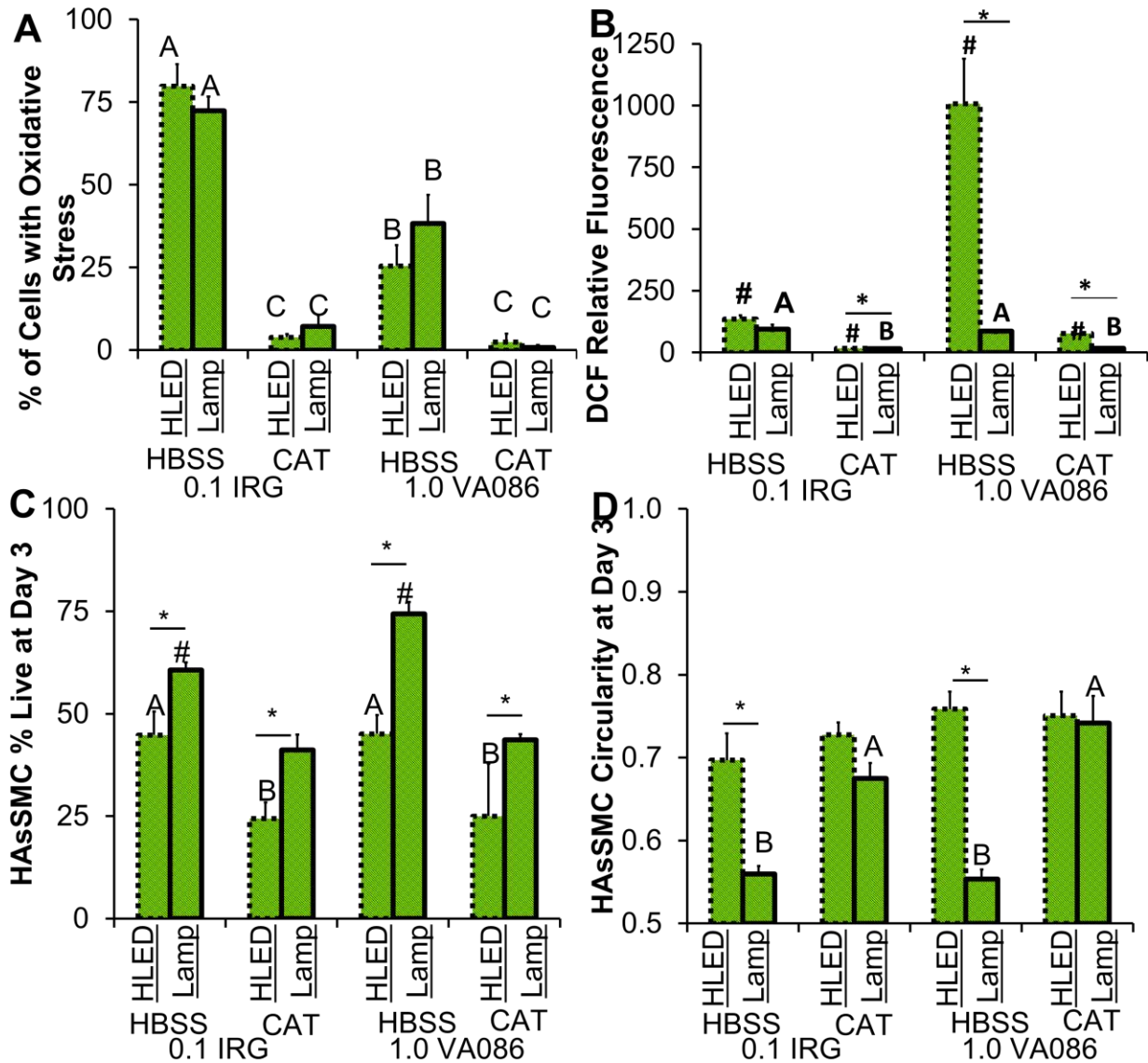


**Figure 4.22 Oxidative stress and effect of catalase loading for HASSMC as a function of light source intensity.**

**(A)** Percent of HASSMC experiencing general oxidative stress after photocrosslinking. Non matching letters  $p < 0.05$  testing between groups (effect of photoinitiator and treatment),  $*p < 0.05$  testing within groups (effect of light source). No significant difference within groups (no effect of light source). **(B)** Relative fluorescence of general oxidative stress indicator in encapsulated HASSMC samples. Non matching letters  $p < 0.05$  testing between groups (effect of photoinitiator and treatment),  $*p < 0.05$  testing within groups (effect of light source). **(C)** Percent live treated and encapsulated HASSMC after 3 days culture. Non matching letters and #  $p < 0.05$  testing between groups (effect of photoinitiator and treatment),  $*p < 0.05$  testing within groups (effect of light source). **(D)** Circularity of HASSMC after 3 days culture. #  $p < 0.05$  testing between groups (effect of photoinitiator and treatment),  $*p < 0.05$  testing within groups (effect of light source). All error bars are standard error of the mean.

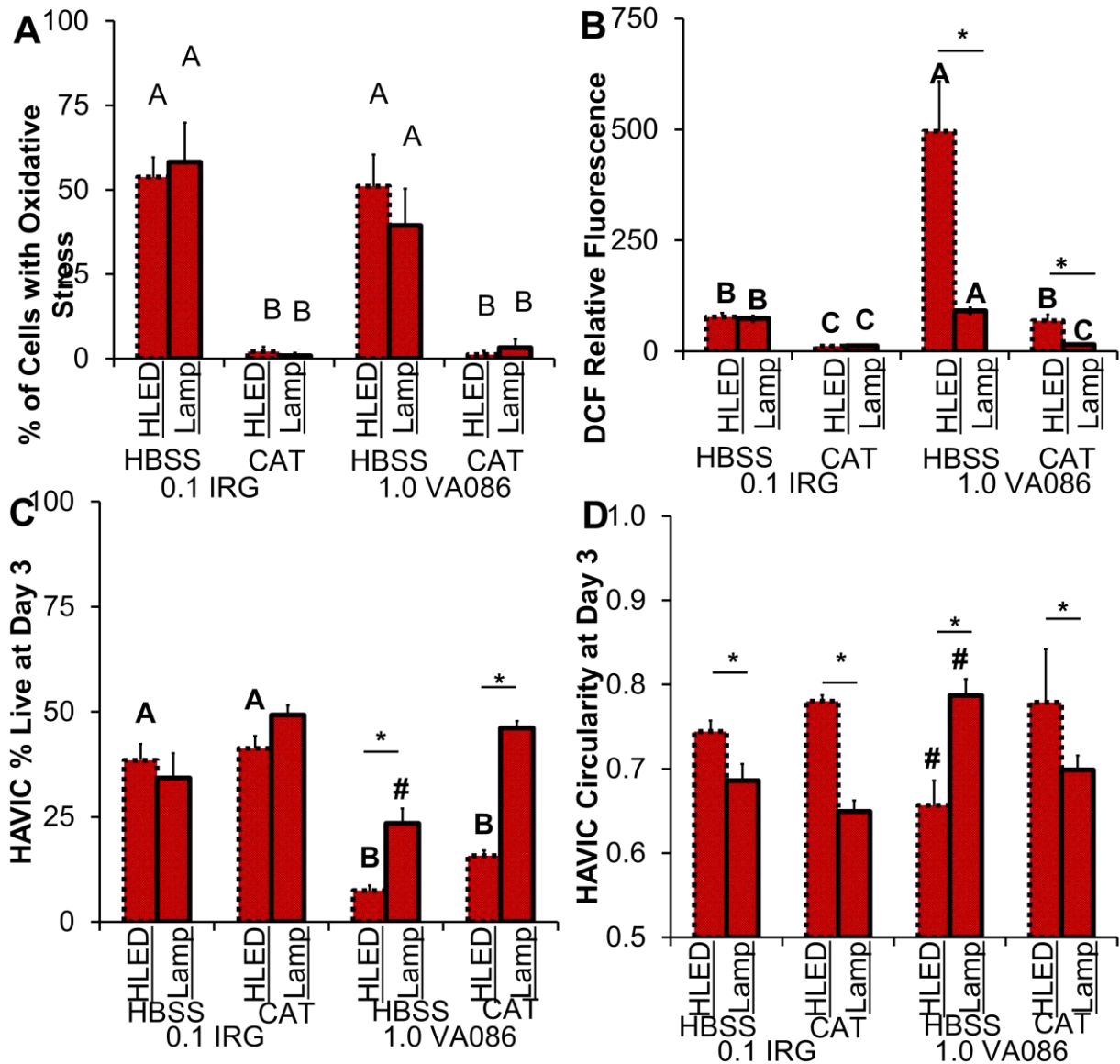


**Figure 4.23 Oxidative stress and effect of catalase loading for HAVIC as a function of light source intensity.**

**(A)** Percent of HAVIC experiencing general oxidative stress after photo-crosslinking. Non matching letters  $p < 0.05$  testing between groups (effect of photoinitiator and treatment), \* $p < 0.05$  testing within groups (effect of light source). No significant difference within groups (no effect of light source). **(B)** Relative fluorescence of general oxidative stress indicator in encapsulated HAVIC samples. Non matching letters  $p < 0.05$  testing between groups (effect of photoinitiator and treatment), \* $p < 0.05$  testing within groups (effect of light source). **(C)** Percent live treated and encapsulated HAVIC after 3 days culture. Non matching letters and # $p < 0.05$  testing between groups (effect of photoinitiator and treatment), \* $p < 0.05$  testing within groups (effect of light source). **(D)** Circularity of HAVIC after 3 days culture. #  $p < 0.05$  testing between groups (effect of photoinitiator and treatment), \* $p < 0.05$  testing within groups (effect of light source). All error bars are standard error of the mean.

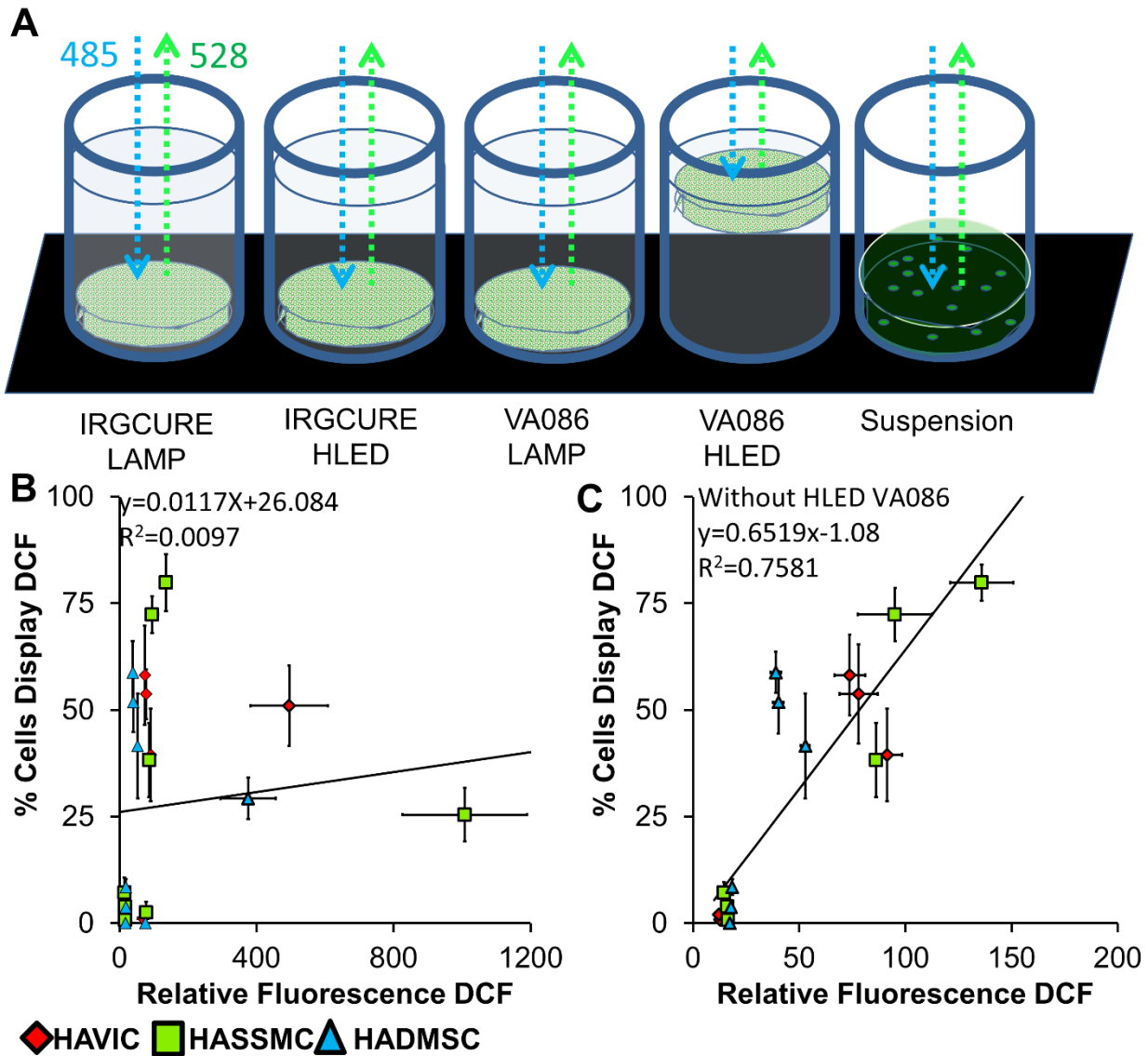


**Figure 4.24 Linear fit of percent of encapsulated cells experiencing general oxidative stress versus relative fluorescence of general oxidative stress indicator in encapsulated cell-hydrogels.**

**(A)** Diagram of how foaming in VA086 hydrogels crosslinked with HLED array would cause higher signal in the multi-well plate reader set on top read. **(B)** Linear fit of percentage of cells displaying oxidative stress in confocal images versus relative fluorescence of cell-hydrogel disks for all 24 conditions. 3 cell types, 2 light sources, 2 cell treatments (HBSS and Catalase), 2 photoinitiator conditions. All error bars are standard error of the mean. **(C)** Excluding HLED/VA086 data and refit percentage of cells displaying oxidative stress in confocal images versus relative fluorescence of cell-hydrogel disk.

significant differences in oxidative stress fluorescence (DCF) between cell types in each photoinitiator condition (Figure 4.18D) (Irgacure 0.1% w/v: HADMSC 40.24±2.45, HAVIC 78.00±9.05, HASSMC 135.88±14.79; VA086 1.0% w/v: HADMSC 375.90±80.21, HAVIC 495.42±113.35, HASSMC 1007.81±182.18). HADMSC hydrogels were less fluorescent than HAVIC and HASSMC, and HASSMC hydrogels were more fluorescent than HAVIC. Catalase decreased the relative fluorescence oxidative stress (response in all 3 cell types (Irgacure 0.1% w/v: HADMSC 40.24±2.45, HAVIC 78.00±9.05, HASSMC 135.88±14.79; VA086 1.0% w/v: HADMSC 375.90±80.21, HAVIC 495.42±113.35, HASSMC 1007.81±182.18). For cells treated with catalase solution prior to encapsulation and then HLED array photo-crosslinking for 5 minutes there were significant differences of relative fluorescence between cell types in the Irgacure condition (Figure 4.18D). In the Irgacure catalase condition the HAVIC hydrogels have lower relative fluorescence than the HASSMC and the HADMSC.

When percent of encapsulated cells experiencing general oxidative stress were plotted against relative fluorescence of general oxidative stress indicator in encapsulated cell-hydrogels for all cell types and conditions there was very little correlation  $R^2=0.0097$  (Figure 4.24B). However, when the HLED VA086 condition was excluded the percentage of cells experiencing general oxidative stress and the intensity of the oxidative stress correlate,  $R^2=0.7581$ .

These results indicate that there are differences in oxidative stress between cell type, and in general oxidative stress is greater in HASSMC and HAVIC compared to HADMSC in 3D hydrogel photo-crosslinking conditions. These results indicate the VA086 1.0% w/v condition induces a higher degrees of oxidative stress in HAVIC and

HADMSC than the Irgacure 0.1% w/v condition (2 mW/cm<sup>2</sup> crosslinking). These results indicate that catalase treatment prior to encapsulation dramatically decreases intracellular general oxidative stress.

#### **4.4.10 Cell Suspension Relative DCF Fluorescence After Bench Top Incubation**

HAVIC, HASSMC, and HADMSC experience oxidative stress after the handling steps prior to encapsulation and bench top incubation (Figure 4.25). Cells tagged with DCF dye and cell tracker dye that were subjected to HBSS and catalase treatment and all the same handling and spin down steps as encapsulated cells but were not encapsulated experienced oxidative stress detectable by both confocal microscopy (Figure 4.14, Figure 4.25A) and the plate reader (Figure 4.25B). The percentage of cells stained positive for oxidative stress in these suspension controls was not significantly different between cell types (HAVIC 78.8±2.8, HASSMC 73.2±4.2, HADMSC 84.9±4.8). Catalase decreased the percentage of cells fluorescing positive for oxidative stress more in the HAVIC and HASSMC than in the HADMSC (HAVIC 13.4±4.2, HASSMC 17.1±4.1, HADMSC 68.9±9.8). DCF relative fluorescence was significantly different between cell types for the HBSS conditions. Fluorescence intensity was highest in HASSMC (104.1±19.1), then the HAVIC (71.9±8.0), and then the HADMSC (38.1±7.1). Treatment with catalase reduced the fluorescence to the same intensity as the no cell hydrogel and HBSS controls (HAVIC 6.91±0.28, HASSMC 10.4±0.5, HADMSC 14.1±3.4, No cell hydrogel 9.35±0.34, HBSS 10.4±1.4)

#### **4.4.11 Effect of Catalase Treatment on Cell Viability and Morphology**

Catalase treatment did not improve 3 day encapsulated cell viability.

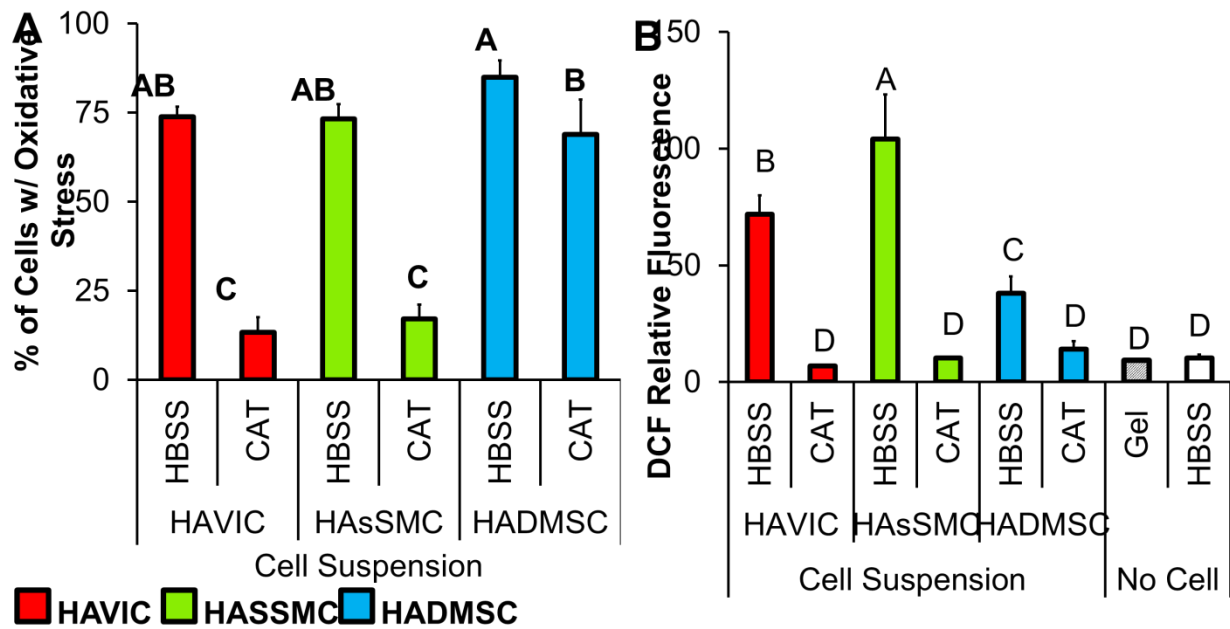


**Figure 4.25 General oxidative stress cell suspension controls for HAVIC, HASSMC, HADMSC.**

**(A)** Percent of encapsulated cells experiencing general oxidative stress after HBSS and catalase treatment and bench top incubation. Non matching letters  $p < 0.05$  (effect of cell type and treatment). **(B)** Relative fluorescence of general oxidative stress indicator in cells experiencing general oxidative stress after HBSS and catalase treatment and bench top incubation and no cell controls. Non matching letters  $p < 0.05$  (effect of cell type and treatment). All error bars are standard error of the mean.

### Lamp Tests

Catalase treatment had a detrimental effect on HASSMC 3 day encapsulated viability, a beneficial effect on HAVIC in VA086 hydrogels, and a detrimental effect on HADMSC in Irgacure hydrogels (Figure 4.26 and 4.27A). Cells treated with HBSS control solution compared to catalase treated cells prior to encapsulation and then lamp photocrosslinking for 5 minutes had a significantly higher percentage of live cells for HASSMC in both photoinitiator conditions (Irgacure:  $60.7 \pm 1.8$  compared to  $41.3 \pm 3.0$  %live, VA086:  $74.4 \pm 2.9$  compared to  $43.7 \pm 1.4$  %live). Catalase treatment of HAVIC did not significantly affect encapsulated viability in Irgacure gels crosslinked with the lamp (NS, Irgacure:  $34.2 \pm 5.9$  for HBSS compared to  $49.2 \pm 2.4$  %live for catalase treated). Catalase treatment of HAVIC improved encapsulated viability in VA086 gels crosslinked with lamp (VA086:  $23.4 \pm 3.5$  for HBSS compared to  $46.1 \pm 1.8$  %live for catalase treated). Catalase treatment did not affect HADMSC viability in VA086 hydrogels and it was detrimental in Irgacure hydrogels crosslinked with the lamp light source (Irgacure:  $92.8 \pm 1.7$  compared to  $62.0 \pm 2.5$  %live, VA086:  $83.6 \pm 4.8$  compared to  $93.7 \pm 0.9$  %live). In all HBSS conditions HADMSC and HASSMC viability is greater than HAVIC viability, but with catalase treatment HAVIC viability is greater than HASSMC.

Circularity increased and morphology became less spread for HASSMC in both Irgacure and VA086 hydrogels with catalase treatment (Figure 4.27B; Irgacure: HBSS  $0.559 \pm 0.018$  compared to catalase treated  $0.661 \pm 0.009$ ; VA086:  $0.554 \pm 0.033$  compared to  $0.742 \pm 0.011$ ). HAVIC circularity remained the same in Irgacure hydrogels and increased in VA086 hydrogels with the application of catalase treatment (Irgacure:

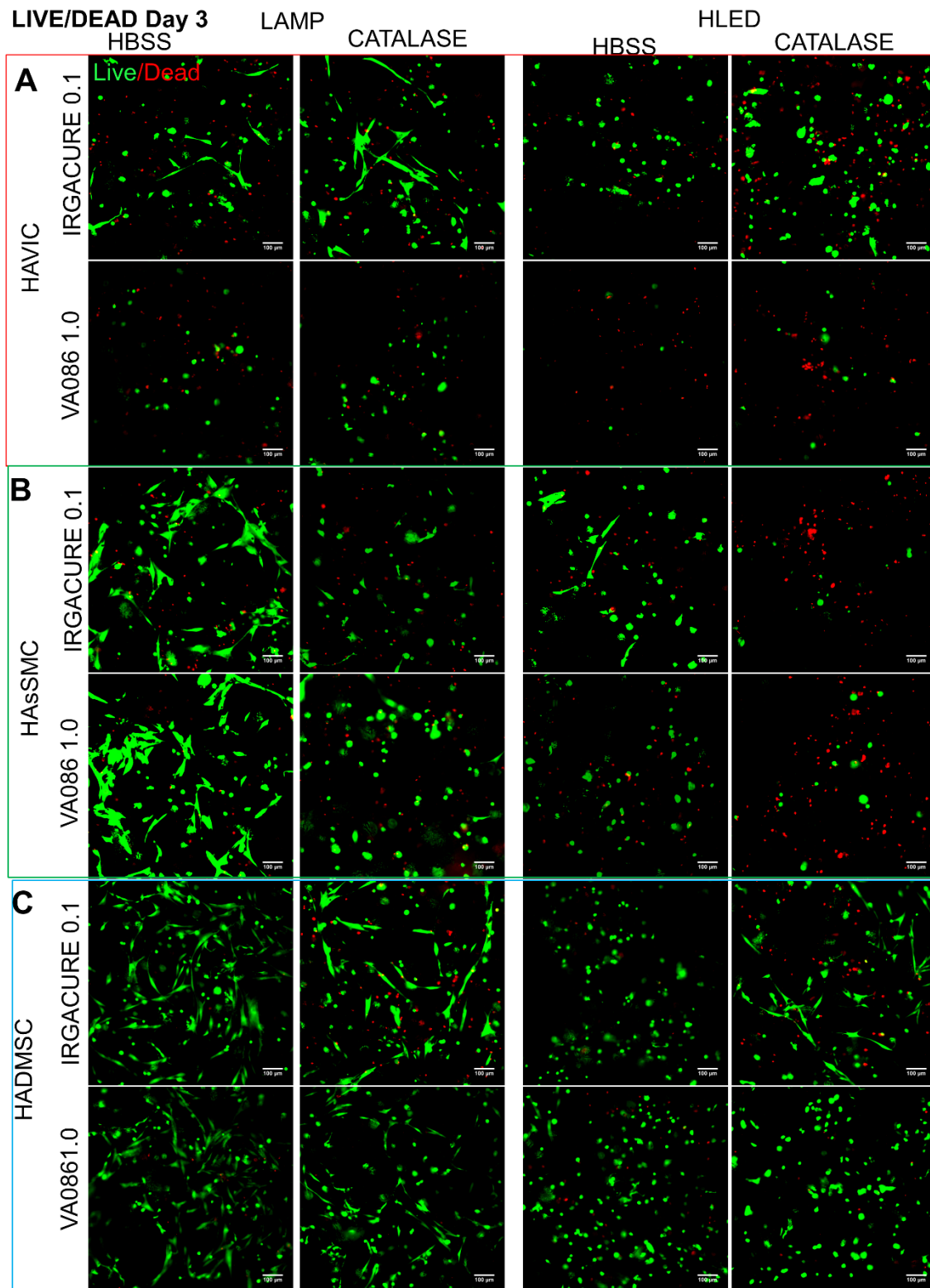
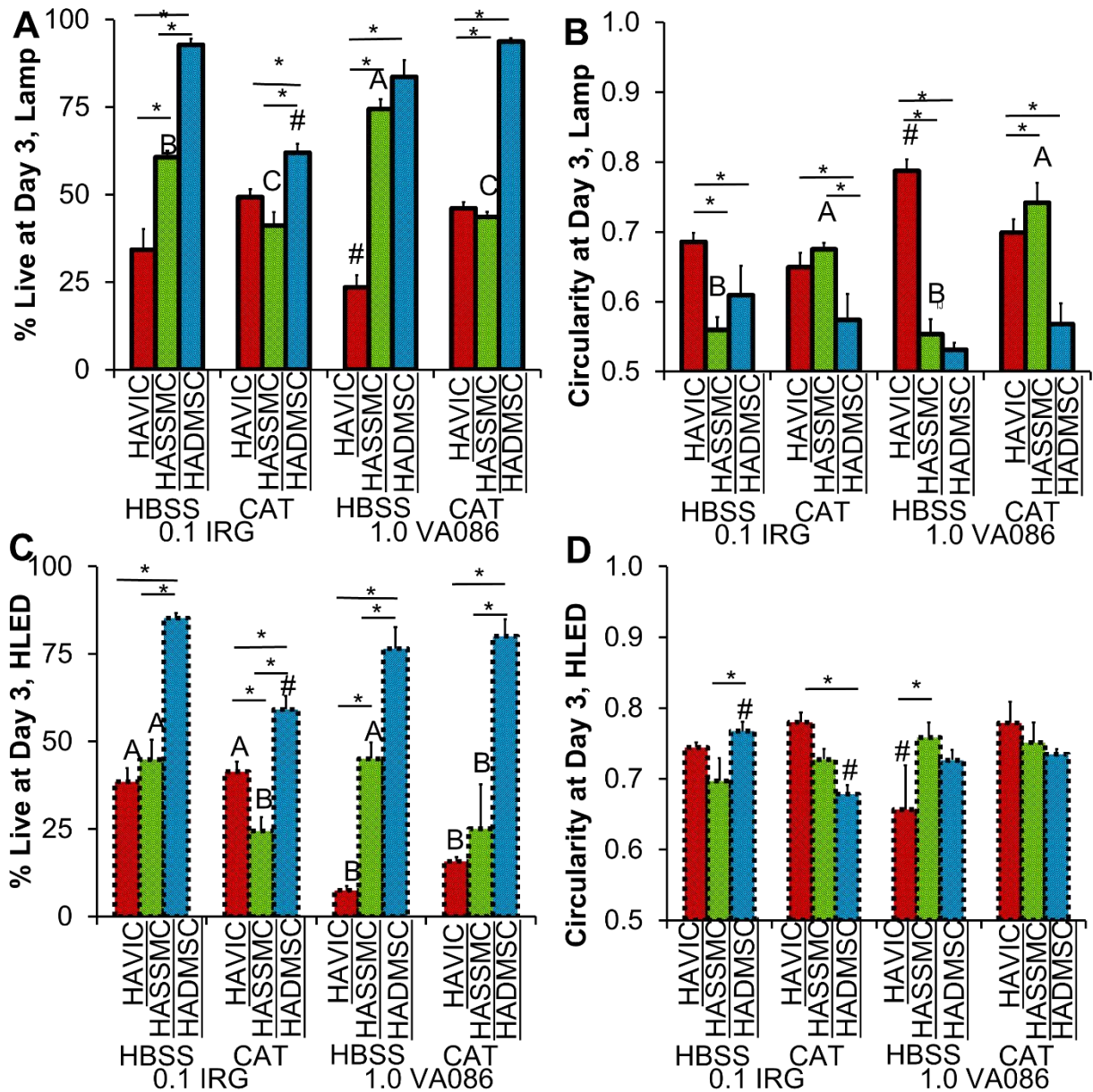


Figure 4.26 Representative images of Day 3 encapsulated, HBSS and catalase treated cells stained with Live/Dead.

(A) HAVIC (B) HASSMC (C) HADMSC



**Figure 4.27 Effect of catalase loading on cell viability and circularity.**

Differences between cell type. HAVIC, HASSMC, and HADMSC treated with catalase or HBSS (control) before encapsulation and light exposure. **(A)** Percentage of live of cells encapsulated in hydrogel discs and cultured for 3 day after photo-crosslinking with lamp **(B)** Circularity of live of cells encapsulated in hydrogel discs and cultured for 3 days after photo-crosslinking with lamp. **(C)** Percentage of live cells encapsulated in hydrogel discs and cultured for 3 day after photo-crosslinking with high powered LED. **(D)** Circularity of live of cells encapsulated in hydrogel discs and cultured for 3 days after photo-crosslinking with high powered LED. Non matching letters and # $p < 0.05$  testing between groups (effect of photoinitiator and treatment), \* $p < 0.05$  testing within groups (effect of cell type).

HBSS  $0.686 \pm 0.013$  compared to catalase treated  $0.650 \pm 0.020$ ; VA086:  $0.787 \pm 0.17$  compared to  $0.699 \pm 0.019$ ). HADMSC circularity remained the same in Irgacure and VA086 hydrogels with the application of catalase treatment (not significantly different; Irgacure: HBSS  $0.609 \pm 0.042$  compared to catalase treated  $0.574 \pm 0.037$ ; VA086:  $0.532 \pm 0.010$  compared to  $0.568 \pm 0.030$ ).

### HLED Tests

For cells treated with HBSS control solution prior to encapsulation and then HLED array photo-crosslinking for 5 minutes there were significant differences in live/dead viability between cell types in each photoinitiator condition. HADMSC hydrogels had higher viability compared to HAVIC and HASSMC (Figure 4.27C) and generally followed the trend HADMSC > HASSMC > HAVIC. For cells treated with catalase solution prior to encapsulation and then HLED array photo-crosslinking for 5 minutes there were significant differences in each photoinitiator condition (Figure 4.27C). In hydrogels prepared with Irgacure catalase treatment decreased HASSMC and HADMSC viability in Irgacure hydrogels and did not affect HAVIC viability (HASSMC: in HBSS  $44.8 \pm 5.7$  compared to catalase  $24.4 \pm 3.8$  percent live; HADMSC: in HBSS  $85.2 \pm 1.4$  compared to catalase  $59.2 \pm 2.5$  percent live; and HAVIC: in HBSS  $38.5 \pm 3.9$  compared to catalase  $41.3 \pm 3.0$  percent live). In hydrogels prepared with VA086, catalase treatment decreased HASSMC viability, but did not affect HADMSC or HAVIC viability (HASSMC: in HBSS  $45.1 \pm 4.6$  compared to catalase  $25.0 \pm 12.8$  %live; HADMSC: in HBSS  $76.5 \pm 6.1$  compared to catalase  $80.0 \pm 4.9$  %live; and HAVIC: in HBSS  $7.44 \pm 1.2$  compared to catalase  $15.8 \pm 1.3$  %live).

Circularity remained the same with catalase treatment for encapsulated HASSMC in both Irgacure and VA086 hydrogels crosslinked with HLED array (Figure 4.27D,

Irgacure: HBSS  $0.697\pm 0.032$  compared to catalase treated  $0.728\pm 0.015$ ; VA086: HBSS  $0.759\pm 0.021$  compared to catalase treated  $0.751\pm 0.028$ ). HAVIC circularity remained the same in Irgacure hydrogels and VA086 hydrogels with the application of catalase treatment (Irgacure: HBSS  $0.657\pm 0.063$  compared to catalase treated  $0.779\pm 0.029$ ; VA086: HBSS  $0.759\pm 0.021$  compared to catalase treated  $0.751\pm 0.029$ ). HADMSC circularity decreased in Irgacure hydrogels with the application of catalase treatment and circularity remained the same in VA086 hydrogels with the application of catalase treatment (Irgacure: HBSS  $0.767\pm 0.013$  compared to catalase treated  $0.678\pm 0.013$ ; VA086: HBSS  $0.726\pm 0.014$  compared to catalase treated  $0.735\pm 0.008$ ).

#### **4.4.12 Light Source Intensity Comparisons**

Increasing the light source intensity from  $2 \text{ mW/cm}^2$  to  $136 \text{ mW/cm}^2$  has a detrimental effect on encapsulated cell viability in VA086 hydrogels for HAVIC, HASSMC, and HADMSC (Figure 4.19C, Figure 4.22C, and Figure 4.23C show the pair comparisons).

The reduction in viability for 1.0% w/v VA086 hydrogels crosslinked with  $2 \text{ mW/cm}^2$  and  $136 \text{ mW/cm}^2$  was HAVIC:  $23.4\pm 3.4$  to  $7.43\pm 1.2$ , HASSMC:  $74.4\pm 2.9$ , to  $45.1\pm 4.6$  HADMSC:  $83.5\pm 4.8$  to  $76.5\pm 6.1$  percent viability, which corresponded to a mechanical bump of  $19.3\pm 2.8$ ,  $45.6\pm 5.2$  kPa.

The light source intensity does not significantly affect encapsulated HAVIC or HADMSC viability in Irgacure hydrogels (Figure 4.19C and Figure 4.23C). However, increasing light source intensity has a detrimental effect on encapsulated HASSMC viability in Irgacure hydrogels (Figure 4.22C). The percent viability for 0.1% w/v Irgacure hydrogels crosslinked with  $2 \text{ mW/cm}^2$  to  $136 \text{ mW/cm}^2$  was HAVIC:  $49.2\pm 2.4$  to  $41.3\pm 3.0$

NSD, HASSMC:  $62.0 \pm 1.8$ , to  $44.8 \pm 5.7$ , HADMSC:  $92.7 \pm 1.7$  to  $85.2 \pm 1.4$  NSD corresponded to a mechanical bump of  $40.9 \pm 4.1$ ,  $120.7 \pm 10.2$  kPa.

Increasing light source intensity increases encapsulated HADMSC circularity in VA086 and Irgacure hydrogels (Figure 4.19D, shows the pair comparisons). The effect of light source intensity on encapsulated HAVIC and HASSMC follows a less regular pattern (Figure 4.23D and Figure 4.22D). In Irgacure hydrogels, increasing light source intensity increases both HAVIC and HASSMC circularity, but not significantly in the HASSMC catalase treated condition. In VA086 hydrogels, increasing light source intensity decreases the HAVIC circularity in the HBSS condition but decreases the HAVIC circularity in the catalase treated condition. In VA086 hydrogels increasing light source intensity decreases the HASSMC circularity in the HBSS condition, but the circularity in the catalase treated condition remained the same (Figure 4.22D).

#### **4.4.13 Effect of Handling Buffer and Incubation on Encapsulated Cell Viability**

There were differences in viability that resulted from using the oxidative stress assay encapsulation protocol compared to the standard encapsulation protocol (HBSS verses PBS) (Figure 4.28 compares HBSS data to Figure 4.5 PBS data). HBSS was used instead of PBS for the oxidative stress experiments for the handling buffer and a 20 minute incubation time with the DCF and cell tracker working solution. The addition into the encapsulation protocol of a 20 minute incubation in HBSS significantly decreases HAVIC viability in Irgacure and VA086 hydrogels (Figure 4.28A; Irgacure: PBS  $58.8 \pm 3.4$  vs HBSS  $34.2 \pm 5.9$ ; VA086: PBS  $86.0 \pm 3.2$  vs HBSS  $23.4 \pm 3.5$ ). The addition of the 20 minute incubation in HBSS it is not detrimental to the HADMSC (Figure 4.28C, Irgacure:

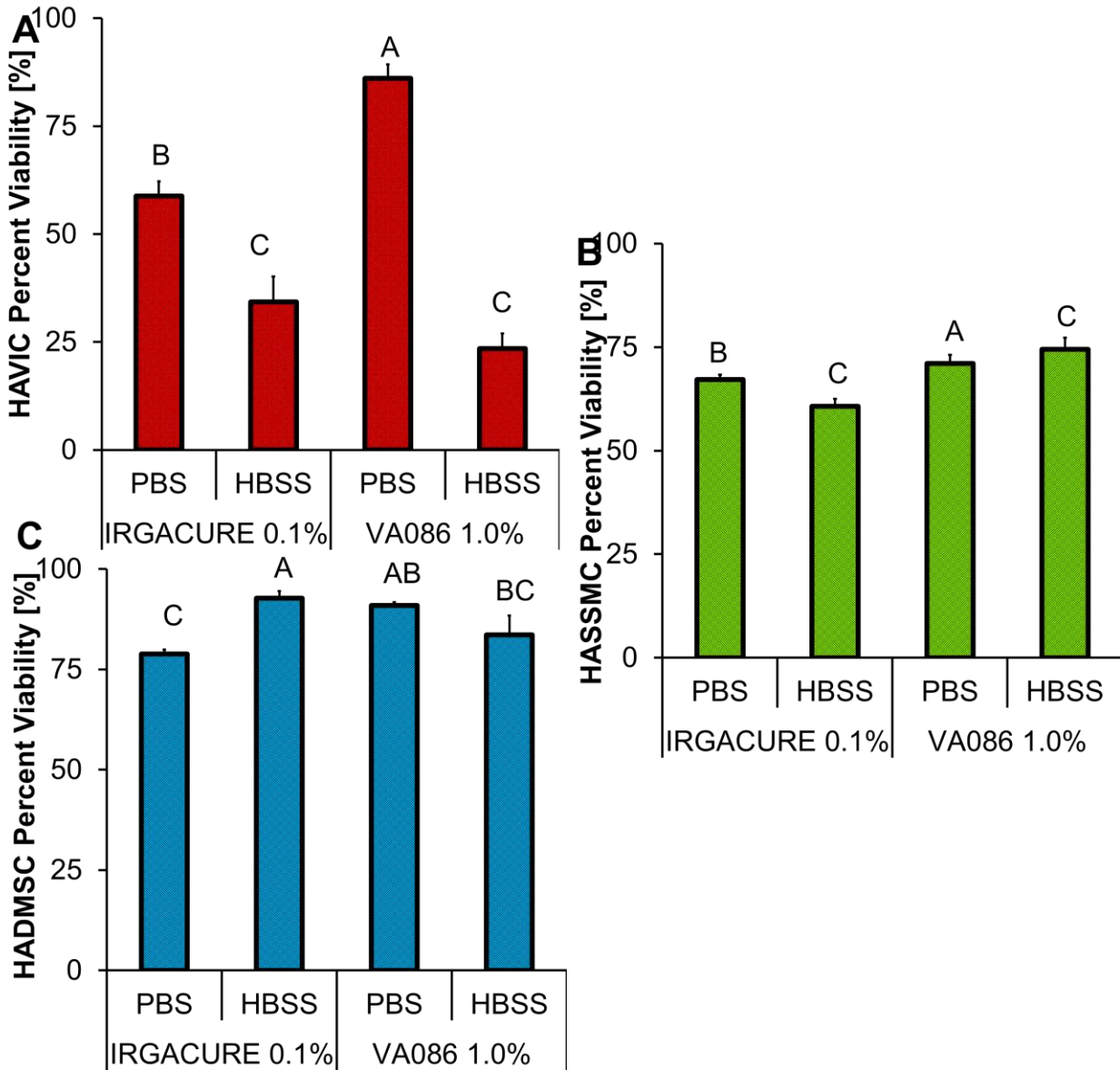


**Figure 4.28 Handling buffer and extended incubation effect on 3 day viability.**

Percentage of live (A) HAVIC (B), HASSMC(C) HADMSC. Handled in either PBS or HBSS and then encapsulated in hydrogel discs and cultured for 3 day after photocrosslinking with lamp for 5minutes. Non-matching letters and #  $p < 0.05$  testing between groups (effect of photoinitiator and handling buffer) . Note: Handling time for HBSS was longer as there was a 20 minute incubation for the oxidative stress experiments.

PBS 78.9±1.1 vs HBSS 92.8±1.7; VA086: PBS 90.8±0.9 vs HBSS 83.5±4.8), and it affects HASSMC only in Irgacure hydrogels (Figure 4.28B Irgacure: PBS 78.9±1.1 vs HBSS 92.8±1.7; VA086: PBS 90.8±0.9 vs HBSS 83.5±4.8).

#### **4.4.14 Linear Regression Analysis of Viability, Circularity, Oxidative Stress, Modulus**

The viability of HBSS treated encapsulated cells was plotted against  $E_{5to15}$  and a linear fit applied to data from each cell type and then to the entire data set (Figure 4.20A). For HAVIC, HASSMC, and HADMSC data the linear fit  $R^2$  values were 0.278, 0.520, and 0.002 respectively. For the combined data set the linear fit  $R^2$  value was 0.0008. HASSMC viability shows decrease with increasing hydrogel stiffness, but for HADMSC we find no relationship between the viability and the hydrogel stiffness. Independent of cell type, we find no relationship between viability and hydrogel stiffness.

The circularity of HBSS treated encapsulated cells was plotted against  $E_{5to15}$  and a linear fit applied to data from each cell type and then to the entire data set (Figure 4.20B). For HAVIC, HASSMC, and HADMSC data the linear fit  $R^2$  values were 0.001, 0.255, and 0.672 respectively. For the combined data set the linear fit  $R^2$  value was 0.226. Cells become more round with increasing hydrogel stiffness, but in the conditions tested this appears not to be true for HAVIC. Low HAVIC viability may be affecting this measurement.

The viability of HBSS and catalase treated encapsulated cells was plotted against percent cells positive for oxidative stress and a linear fit applied to data from each cell type and then to the entire data set (Figure 4.21A). For HAVIC, HASSMC, and HADMSC data, the linear fit  $R^2$  values were 0.142, 0.319, and 0.207 respectively. For the combined data set the linear fit  $R^2$  value was 0.009. Weak relationships show

HADMSC and HASSMC viability increase with increasing percentage of cells experiencing oxidative stress. Also, HAVIC viability decreases with increasing oxidative stress (weakly). However, independent of cell type the linear regression shows there is no relationship between the percentage of live cells versus percentage of cells experiencing oxidative stress.

The circularity of HBSS and catalase treated encapsulated cells was plotted against percent cells positive for oxidative stress and a linear fit applied to data from each cell type and then to the entire data set (Figure 4.21B). For HAVIC, HASSMC, and HADMSC data the linear fit  $R^2$  values were 0.028, 0.321, and 0.006 respectively. For the combined data set the linear fit  $R^2$  value was 0.046. HASSMC circularity appears to decrease with increasing oxidative stress. Independent of cell type the linear regression shows there is not a relationship between circularity and percentage of cells positive for oxidative stress.

The percentage of HBSS treated and encapsulated cells positive for oxidative stress was plotted against  $E_{51015}$  and a linear fit applied to data from each cell type and then to the entire data set (Figure 4.29). For HAVIC, HASSMC, and HADMSC data the linear fit  $R^2$  values were 0.218, 0.424, and 0.092 respectively. For the combined data set the linear fit  $R^2$  value was 0.211.

Percentage of cells experiencing oxidative stress correlates weakly with  $E_{51015}$  independent of cell type and the percentage of cells experiencing oxidative stress

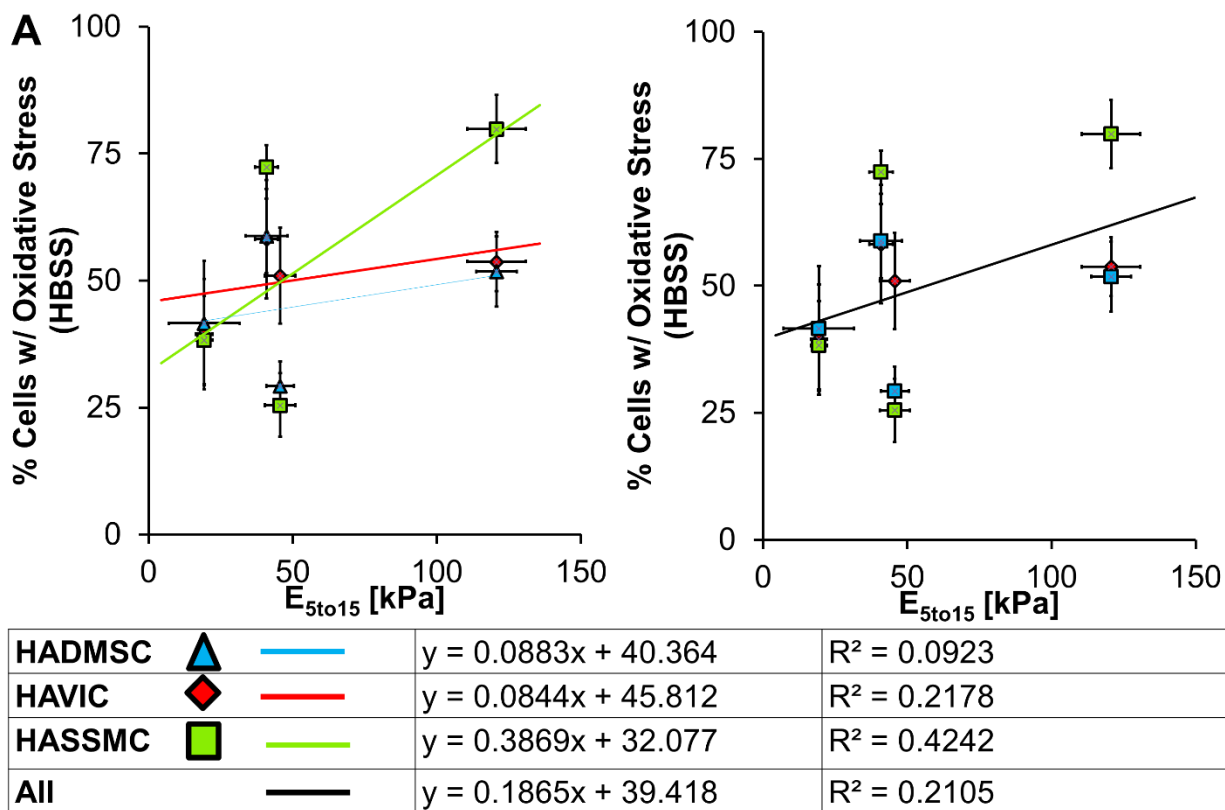


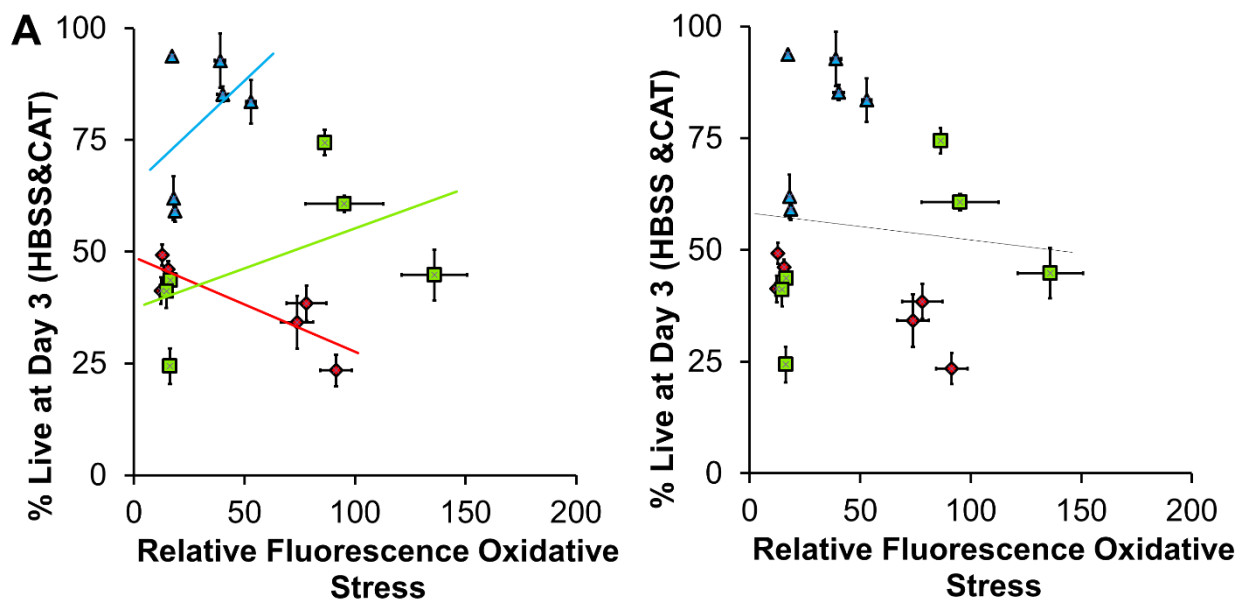
**Figure 4.29 Percentage of cells stained positive for oxidative stress verses modulus for HBSS control cells in Irgacure and VA086 encapsulation conditions.**

Percent of cells positively stained for oxidative stress after crosslinking of treated cells. Each cell type and data from both photoinitiators and light sources linear fit (red HAVIC line, green HASSMC line, blue HADMSC line) All cell types and data from both photoinitiator types and light sources linear fit (black line).

increases with hydrogel stiffness. Percentage of cells experiencing oxidative stress correlates more strongly with  $E_{5to15}$  for HASSMC than for HAVIC and HADMSC.

Percentage of live cells at day 3 in culture that had been treated with HBSS and catalase and encapsulated was plotted against oxidative stress relative fluorescence and a linear fit applied to data from each cell type and then to the entire data set (Figure 4.30A). The HLED/VA086 condition was excluded for this plot. For HAVIC, HASSMC, and HADMSC data the linear fit  $R^2$  values were 0.7423, 0.2923, and 0.2179 respectively. For the combined data set the linear fit  $R^2$  value was 0.0102. Reduction of oxidative stress does not improve the viability of HADMSC and HASSMC, in fact for those cell types percentage of live cells appears to increase as oxidative stress ratio increases for individual cell types. HAVIC viability decreases as oxidative stress increases. Independent of cell type, percentage of live cells is not related to oxidative stress intensity when both HBSS and catalase treatments are considered.

When just the HBSS treated cells are considered, and percentage of live cells at day 3 in culture was plotted against oxidative stress relative fluorescence and a linear fit applied to data from each cell type and then to the entire data set (Figure 4.30B), there is a stronger correlation between cell viability and oxidative stress. The HLED/VA086 condition was excluded for this plot. For HAVIC, HASSMC, and HADMSC data the linear fit  $R^2$  values were 0.7605, 0.9048, and 0.4943 respectively. For the combined data set the linear fit  $R^2$  value was 0.4049.



HADMSC			$y = 0.468x + 64.916$	$R^2 = 0.2179$
HAVIC			$y = -0.2118x + 48.812$	$R^2 = 0.7423$
HASSMC			$y = 0.1794x + 37.287$	$R^2 = 0.2923$
All			$y = -0.0596x + 58.228$	$R^2 = 0.0102$

**Figure 4.30 (A) Viability verses relative fluorescence excluding VA086/HLED condition.**

Live/dead viability verses oxidative stress relative fluorescence for HBSS and catalase treated cells conditions. Each cell type treated with HBSS and catalase data from 3 encapsulation conditions (lamp Irgacure and VA086, and HLED Irgacure) linear fit (red HAVIC line, green HASSMC line, blue HADMSC line). Data from all HBSS and catalase treated cells in 3 conditions linear fit (black line).

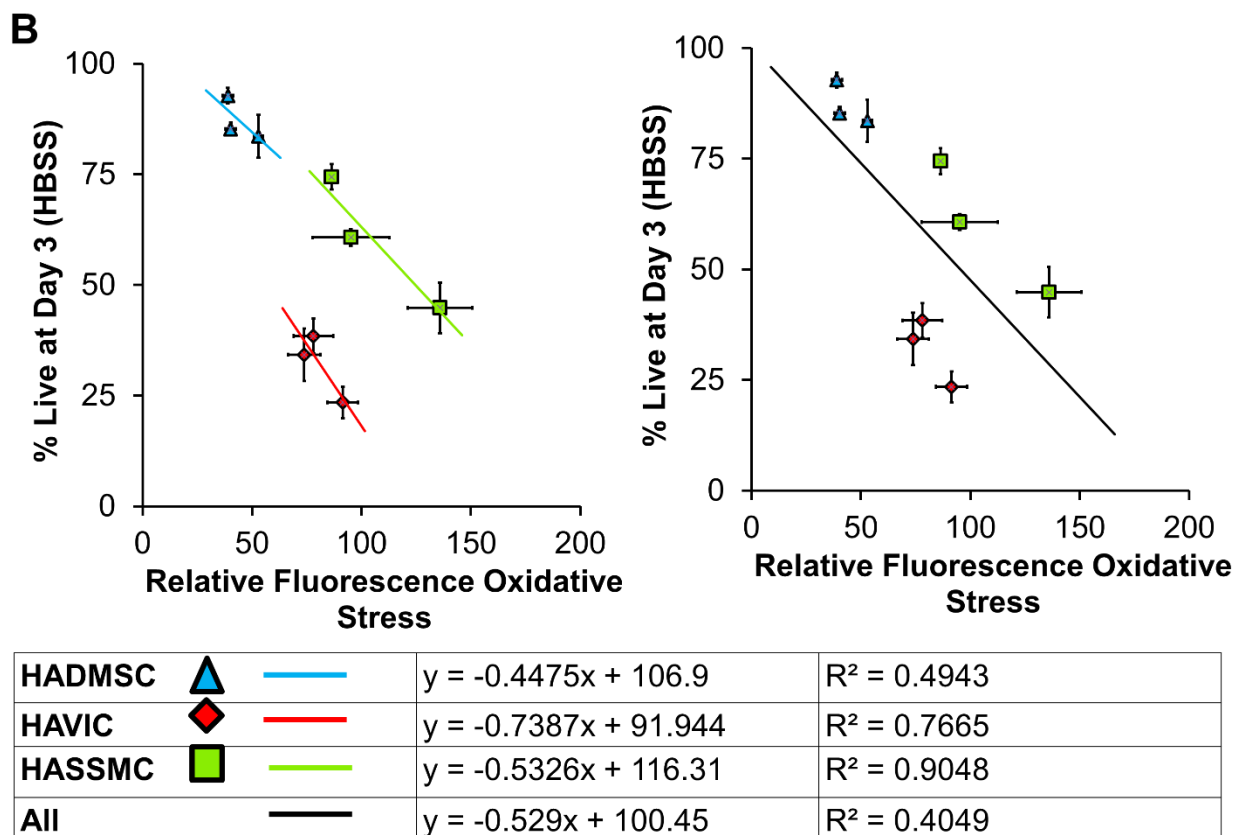


**Figure 4.30 (B) Viability versus relative fluorescence excluding VA086/HLED condition.**

Live/dead viability versus relative fluorescence of HBSS and catalase treated cells. in encapsulation conditions. Each cell type treated with HBSS and data from both photoinitiator conditions and light source conditions linear fit (red HAVIC line, green HASSMC line, blue HADMSC line). Data from all HBSS treated cells in 4 conditions linear fit (black line).

For the HBSS conditions HAVIC, HASSMC, and HADMSC viability decreases as oxidative stress relative fluorescence increases for all three cell types and independent of cell type.

Oxidative stress ratio was plotted to normalize the artificially high HLED/VA086 relative DCF fluorescence values. The oxidative stress ratio was the ratio of the HBSS control DCF fluorescence average divided by the catalase treated DCF fluorescence average for a given photo-crosslinking condition and cell type. The incorporation of the HLED/VA086 data using the oxidative stress ratio produces fits that generally follow the same trends seen with the relative fluorescence data of the other three conditions.

Oxidative stress ratio was calculated for 3D conditions and bench top incubation cell suspensions (Figure 4.31A). Oxidative stress ratio is higher for nearly all HAVIC and HASSMC conditions than for HADMSC (HLED/IRG, HLED/VA086, Lamp/IRG, Lamp/VA086, and Bench top for HAVIC:6.40, 5.79, 7.21, 5.9,10.41; HASSMC:8.37, 6.49, 12.97,5.25,10.01; HADMSC:2.17,2.17,4.98,3.06,2.70 respectively).

Percentage of live cells that had been treated with HBSS and encapsulated at day 3 was plotted against oxidative stress ratio and a linear fit applied to data from each cell type and then to the entire data set (Figure 4.31B). For HAVIC, HASSMC, and HADMSC data the linear fit  $R^2$  values were 0.490, 0.651, and 0.775 respectively. For the combined data set the linear fit  $R^2$  value was 0.355. For the combined data set a natural log fit was better than a linear fit, and the  $R^2$  value was 0.504. The percentage of live cells decreases as oxidative stress ratio increases for individual cell types and independent of cell type.

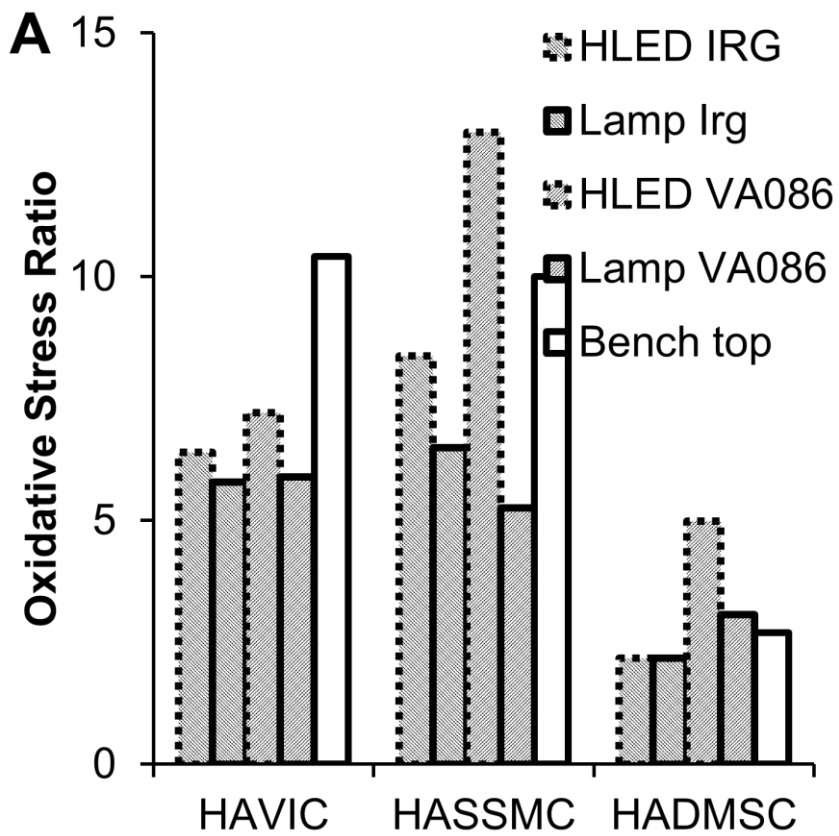


**Figure 4.31 (A) Oxidative stress ratio for HBSS treated cells.**

Oxidative stress ratio for HBSS treated cells for 4 encapsulation conditions and the bench top incubated cell suspension.

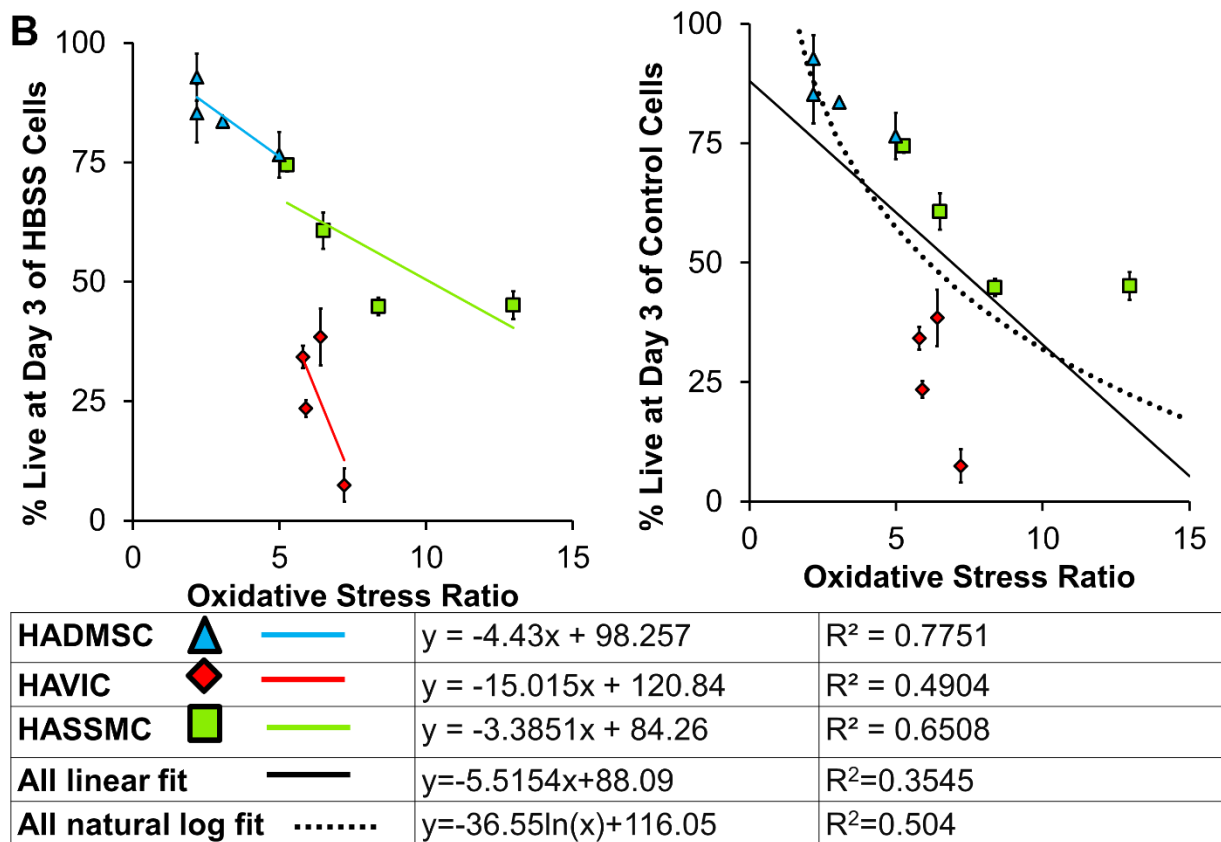


**Figure 4.31 (B) Viability verses oxidative stress ratio for HBSS treated cells.**

Live/dead viability verses relative fluorescence of HBSS and catalase treated cells. In encapsulation conditions. Each cell type treated with HBSS and data from both photoinitiator conditions and light source conditions linear fit (red HAVIC line, green HASSMC line, blue HADMSC line). Data from all HBSS treated cells in 4 conditions linear fit (black line).

The percentage of HBSS treated and encapsulated cells positive for oxidative stress was plotted against  $E_{5to15}$  (excluding the VA086 HLED condition) and a linear fit applied to data from each cell type and then to the entire data set (Figure 4.32A). For HAVIC, HASSMC, and HADMSC data the linear fit  $R^2$  values were 0.229, 0.999, and 0.361 respectively. For the combined data set the linear fit  $R^2$  value was 0.027. Relative fluorescence correlates with modulus to some degree for each cell type; but, the relative fluorescence decreases with increasing stiffness for HAVIC and HADMSC while the relative fluorescence increases with increasing hydrogel stiffness for HASSMC. Independent of cell type, there is not a relationship between relative fluorescence oxidative stress and  $E_{5to15}$ .

The oxidative stress ratio was plotted against  $E_{5to15}$  (excluding the VA086 HLED condition) and a linear fit applied to data from each cell type and then to the entire data set (Figure 4.32B). For HAVIC, HASSMC, and HADMSC data the linear fit  $R^2$  values were 0.871, 0.960, and 0.442 respectively. For the combined data set the linear fit  $R^2$  value was 0.041. Oxidative stress ratio is related to with modulus for each cell type. Oxidative stress ratio increases with stiffness for HAVIC and HASSMC while the oxidative stress ratio slightly decreases with increasing hydrogel stiffness for HADMSC. Independent of cell type, linear regression shows there is not a relationship between oxidative stress ratio and hydrogel stiffness.

These studies with DCF indicate that general oxidative stress is higher in photocrosslinking conditions that induce lower cell viability. Elimination of that oxidative

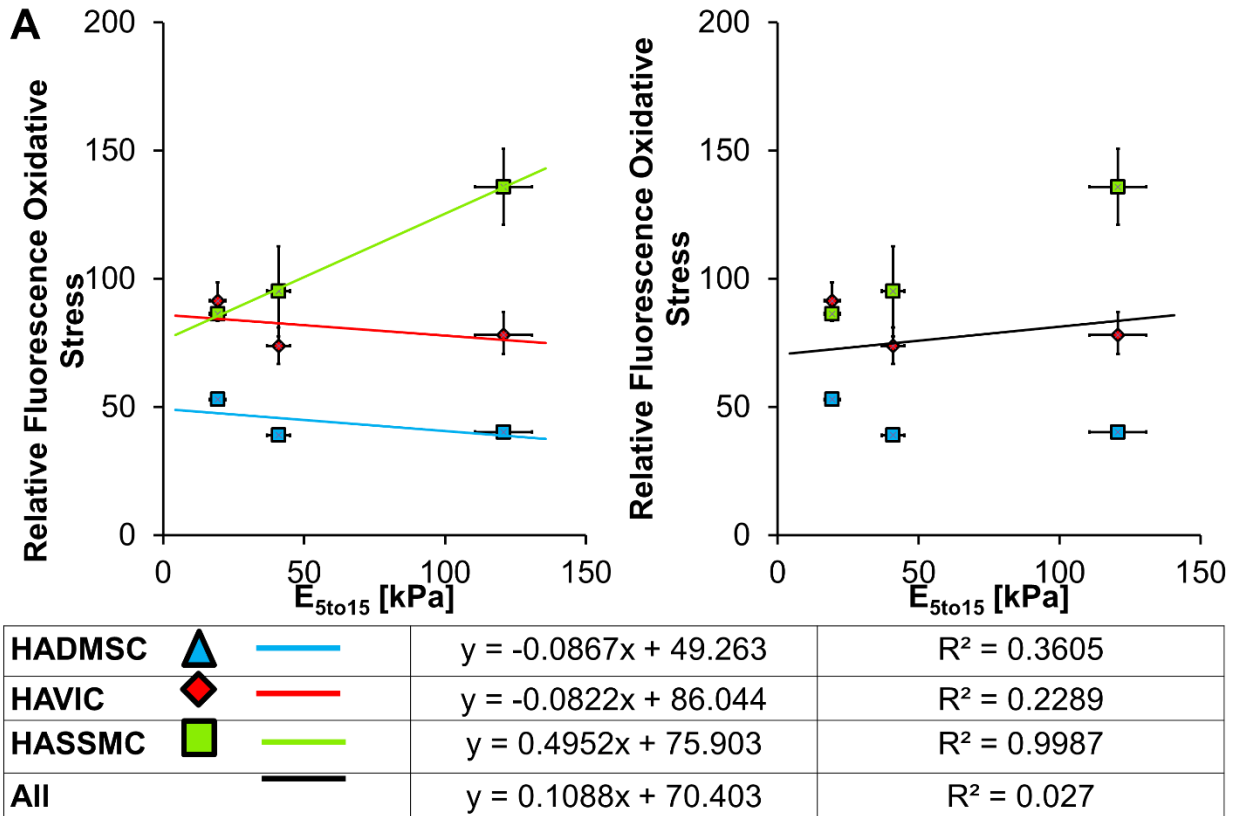


**Figure 4.32 (A) Relative fluorescence intensity of oxidative stress versus modulus for HBSS control cells in encapsulation conditions, excluding HLED VA086 condition.**

Relative fluorescence intensity of oxidative stress versus modulus.

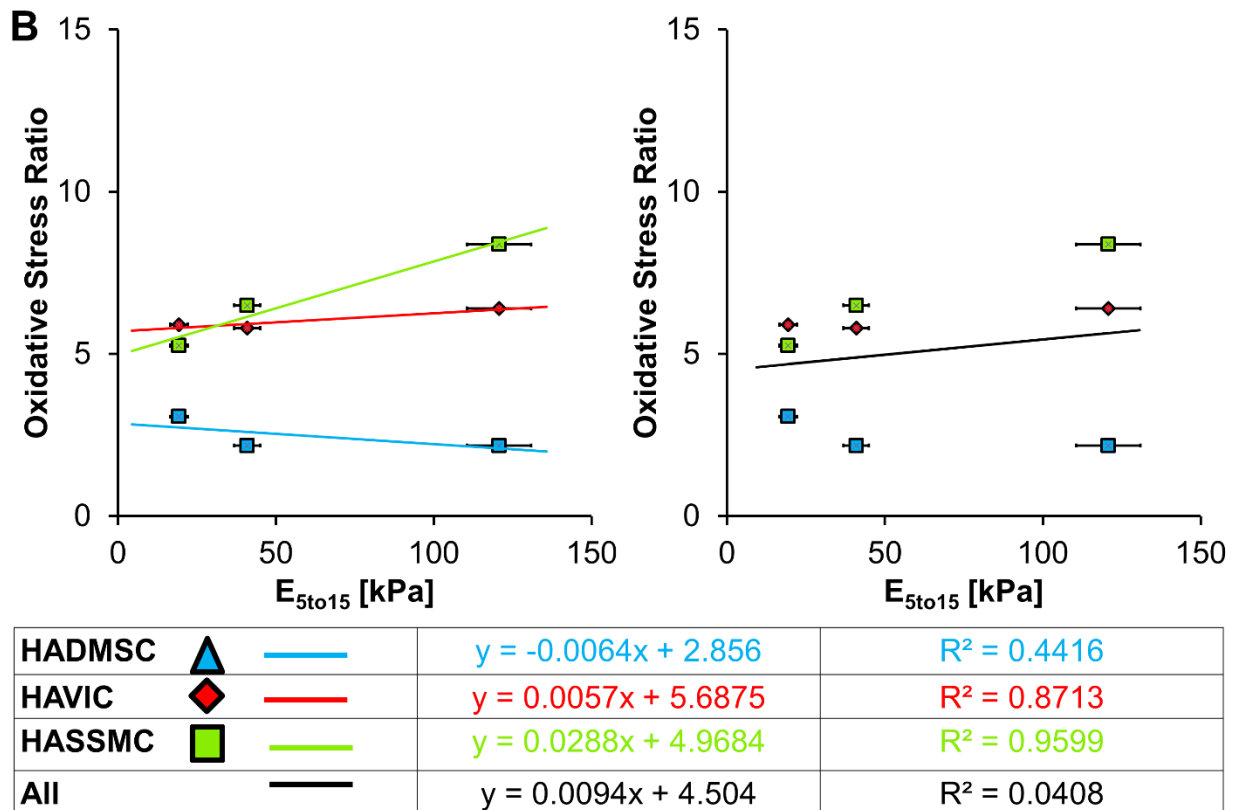


**Figure 4.32 (B) Relative fluorescence intensity of oxidative stress verses modulus for HBSS control cells in encapsulation conditions, excluding HLED VA086 condition.**

Ratio of HBSS to catalase treated cells relative fluorescence verses modulus. Each cell type and data from lamp crosslinked Irgacure and VA086 conditions and HLED array crosslinked Irgacure conditions (red HAVIC line, green HASSMC line, and blue HADMSC line). Data from 3 conditions and 3 cell types with linear fit (black line).

stress does not increase cell viability, which suggests that intracellular oxidative stress is not a primary mode or symptom of damage caused by photocrosslinking conditions.

#### **4.5 Discussion**

MEGEL and PEG-DA 3350 when combined with alginate viscosity modifier and either Irgacure 2959 or VA086 photoinitiator and maintained at 37°C is a 3D printable and photo-crosslinkable precursor mixture that was used for encapsulated bioprinting/direct extrusion cell printing. A range of photoinitiator concentrations, 0.05 to 0.1% w/v Irgacure and 0.5 to 1.0% w/v VA086, and light source intensities, 2 mW/cm<sup>2</sup> to 136mW/cm<sup>2</sup> at printing surface, produced crosslinked hydrogels that were robust enough for handling and culture for at least 1 week with encapsulated cells. Hydrogel stiffness and swelling ratio were tunable using photoinitiator type, photoinitiator concentration, UV light source intensity, and UV exposure time. The range of encapsulation conditions (photoinitiator concentrations, light source intensities, and hydrogel mechanical properties) tested were tolerated to different degrees by HADMSC, HAVIC, HASSMC, and PAVIC. The viability of encapsulated HADMSC was always higher than the other three cell types, except at the lowest concentration of VA086 and the lowest light intensity tested where HAVIC and HASSMC viability was the same as HADMSC. Other groups have observed cell specific sensitivity to photoinitiator toxicity and different toxicity of various photoinitiators (Atsumi, Murata et al. 1998; Bryant, Nuttelman et al. 2000; Williams, Malik et al. 2005; Rouillard, Berglund et al. 2011; Occhetta, Sadr et al. 2013). Williams et al tested 6 different cell lines and found cell-specific sensitivities to Irgacure 2959 radical toxicity, and demonstrated that cell proliferation rate in 2D could predict vulnerability to free radical damage in 3D. However,

in the present study 2D doubling time for HADMSC, HAVIC, HASSMC, and PAVIC did not correlate with viability in 3D.

Many studies using photo-crosslinking systems have attributed encapsulated cell death to free radical damage. Our results indicate that photoinitiator radicals contribute to cell death in our printed hydrogels. Increasing the concentration of active photoinitiator radicals in the encapsulation conditions decreased cell viability (tested by increasing the photoinitiator concentration or by increasing the light source intensity). We found that HAVIC and HASSMC experience more general oxidative stress than HADMSC when encapsulated in photo-crosslinked hydrogels. Viability decreases as the intensity of oxidative stress experienced (measured by DCF relative fluorescence) increases in untreated photocrosslinking conditions, and this relationship exists independent of cell type and for each cell type. Atsumi et al found that more radical oxygen species were produced in submandibular-duct cells exposed to a more cytotoxic photoinitiator (Atsumi, Murata et al. 1998). In 2D culture they also found that reactive oxygen induced in cells was dependent on irradiation time and concentration of photoinitiator, and that the photocytotoxicity could be suppressed with a free radical scavenger hydroquinone. Lampe et al found that in 2D culture lactic acid could be added to the environment to scavenge free radicals produced by Irgacure 2959 and improved cell viability (Lampe, Namba et al. 2009). There have also been more elaborate strategies/inventions to mitigate oxidative damage in to cells in photo-crosslinking systems. Singh et al has developed protective nanospheres encapsulating catalase and superoxide dismutase and has tested them in 2D on keratinocytes (Singh, Singh et al. 2013) . Shin et al added 1.5nm graphene oxide sheets to cell encapsulating methacrylated gelatin hydrogels and

observed a protective effect from UV damage and improvement of viability, but also found that the graphene oxide reduced crosslinking efficiency (Shin, Aghaei-Ghareh-Bolagh et al. 2013). A treatment or additive to precursor solutions that prevents or mitigates damage to cells during photocrosslinking would broaden the application of 3D printing so that it could be used for sensitive cell types. However, interference with the hydrogel crosslinking, such as in the case of graphene oxide (Shin, Aghaei-Ghareh-Bolagh et al. 2013) or ascorbic acid (Sabnis, Rahimi et al. 2009), makes some radical-sink treatments strategies unsuitable for 3D printing. In the present study we investigated catalase pretreatment of cells prior to encapsulation as a strategy to reduce oxidative stress experienced by the cells without interfering with the crosslinking of the polymer precursor solution.

Treatment of HAVIC, HASSMC, and HADMSC prior to encapsulation with catalase almost eliminated general intracellular oxidative stress and hydrogels were still able to solidify/crosslink. However, this treatment with catalase did not rescue encapsulated cell viability. Catalase treatment gave a slight benefit to HAVIC encapsulated viability, and it reduced or did not affect HADMSC and HASSMC viability in the photo-encapsulation conditions tested. The dosage of catalase may be need to be optimized, and its possible normal cell functions utilizing free radicals were suppressed as the intracellular redox state impacts several signaling pathways and functions (Lampe, Namba et al. 2009) which could account for the reduction in viability. Another possible explanation is that while the catalase successfully reduced the intracellular oxidative stress in terms of hydrogen peroxide pathway, other types of oxidative stress that were not examined in

this study could be causing critical damage and the outer cell membrane in particular is still vulnerable to attack. Radicals produced by Irgacure are membrane impermeable and are suspected to cause damage by lipid peroxidation (Bryant, Nuttelman et al. 2000; Williams, Malik et al. 2005; Lampe, Namba et al. 2009). Less is known about the progression of VA086 radicals, but as an azo initiator it may also cause lipid peroxidation. In this study the fluorescence indicator of oxidative stress DCF is oxidized by cellular hydrogen peroxide, hydroxyl radicals, and radicals downstream from hydrogen peroxide. DCF is itself insensitive to oxidation by superoxide ( $O_2^-$ ) (Kirkland and Franklin 2001) or singlet molecular oxygen ( $O_2^*$ ) (Bilski, Belanger et al. 2002), but it can be considered an indirect indicator of these. It reacts with the downstream products of  $O_2^*$  reaction with cellular substrates that produce peroxy products and peroxy radicals, and it reacts with the hydrogen peroxide produced by dismutation of  $O_2^-$  (Kirkland and Franklin 2001; Bilski, Belanger et al. 2002). Catalase catalyzes the decomposition of hydrogen peroxide into water and oxygen. If lipid peroxidation is occurring at the outer membrane of the cells, unless that oxidation propagates into the interior of the cell, our diagnostic and rescue strategy misses the critical mechanism of damage.

Compared to VA086, Irgacure by weight has a more detrimental effect on cell viability for both primary valve cells and adipose derived stem cells. We investigated a range of photoinitiator concentrations that can produce similar mechanical property MEGEL/PEG-DA hydrogels using both Irgacure and VA086, the implication being that modulus and swelling ratio are proportional to the degree of crosslinking. Rouillard et al

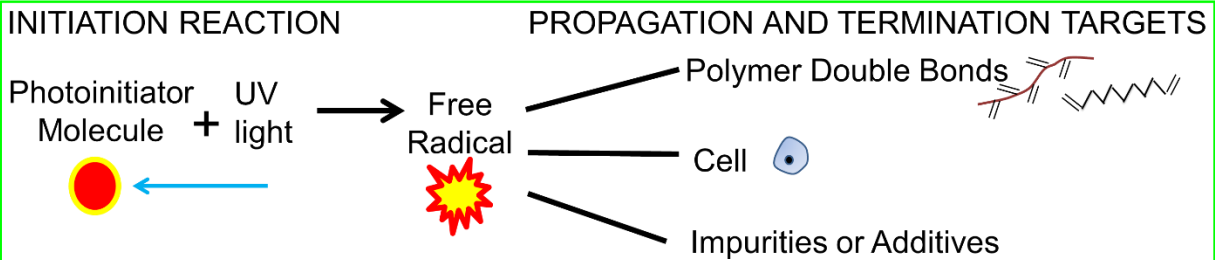
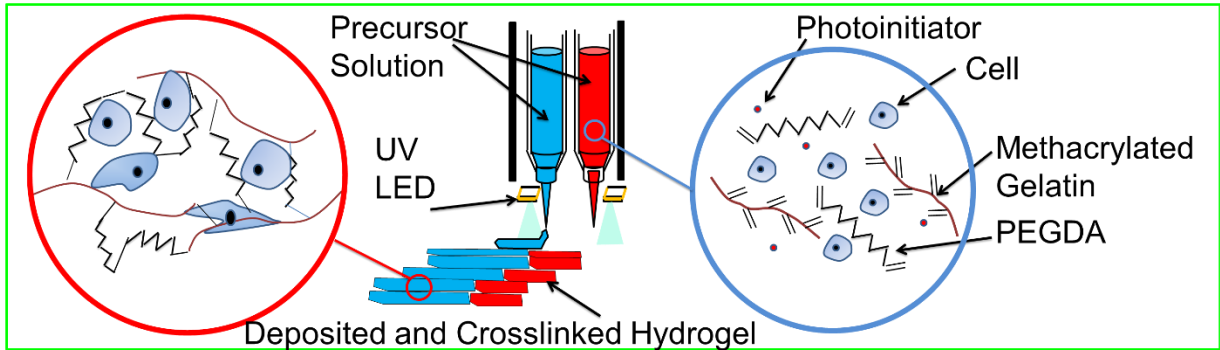
found that Irgacure 2959 was a more cytotoxic photoinitiator than VA086 by testing chondrocytes in both 2D and 3D culture and that Irgacure crosslinks hydrogels at weight fractions 10 times lower than VA086 (Rouillard, Berglund et al. 2011). They found that in methacrylated alginate hydrogels the aggregate modulus when prepared with 0.03% w/v Irgacure was not significantly different from those prepared with 0.3% w/v VA086 after 5 minutes of UV exposure time at  $2 \mu\text{W}/\text{cm}^2$  365 nm light intensity, but the viability was below 70% Irgacure hydrogel and greater than 90% in VA086 hydrogels after 48 hours in culture. Chandler et al found that to get comparable modulus of RGD modified methacrylated alginate, 7.5 times more VA086 needed to be used (0.04% w/v Irgacure compared to 0.3% w/v VA086), and that the corresponding viability of preadipocytes (3T3-L1 cells) in 2D culture treated with these concentrations was 2% and 82% (Chandler, Berglund et al. 2011). The modulus of our MEGEL/PEG-DA hydrogel crosslinked with the  $2 \text{ mW}/\text{cm}^2$  light source becomes significantly different between Irgacure and VA086 hydrogels at a slightly higher concentration ratio than the 1 to 10 that Rouillard et al observed. To get comparable modulus in the methacrylated gelatin hydrogels a ratio of 1 to 15 was needed (0.05% w/v Irgacure compared to 0.75% w/v VA086). This could be related to the viscosity of our precursor solution and the possible interference of the non-crosslinking alginate viscosity modifier or the polymer precursor type and weight ratio. At this comparable modulus, the viability of the three cell types at day 3 is HADMSC: Irgacure  $89.7 \pm 1.9$  and VA086  $92.5 \pm 1.6$ ; HAVIC: Irg  $66.4 \pm 2.3$  and VA086  $92.1 \pm 2.0$ ; and HASSMC: Irgacure  $61.2 \pm 1.6$  and VA086  $81.2 \pm 3.3$ . Additionally, in terms of modulus we observed that for a given light intensity there appears to be a saturation point for the photoinitiator concentration. Additional photoinitiator after that

point does not significantly increase the stiffness. Increasing the light intensity does increase the stiffness of the gel for each photoinitiator. However, by crosslinking VA086 hydrogel (1.0% w/v) at the higher light source, the modulus only increases to the modulus level of low intensity light Irgacure hydrogel modulus. In 1.0% VA086 precursor solution increasing the exposing light intensity from 2 mW/cm<sup>2</sup> and 136 mW/cm<sup>2</sup> caused the encapsulated viability to drop 16% for HAVIC, 29% for HASSMC, and 7% for HADMSC while there was a 26 kPa increase in modulus. For Irgacure hydrogels increasing the light intensity from 2 mW/cm<sup>2</sup> and 136 mW/cm<sup>2</sup> did not induce a significant drop in viability for HAVIC and HADMSC but induced a 18% drop in HASSMC percent viability while the hydrogel experienced a 80 kPa increase in modulus.

2D culture and treatment with a photoinitiator is commonly used as a screening tool to evaluate the feasibility of using that photoinitiator with a particular cell type in a photo-crosslinking hydrogel (Bryant, Nuttelman et al. 2000; Chandler, Berglund et al. 2011; Occhetta, Sadr et al. 2013). Exposure to a photoinitiator in 2D has been described as a worst case scenario for cells, where the maximum amount of free radical damage by the photoinitiator can occur (Williams, Malik et al. 2005). Occhetta et al used 30 times more VA086 compared to Irgacure 2959 (1.5% w/v compared to 0.05% w/v) to get comparable viability between the two photoinitiator types in their 2D tests with human umbilical vein endothelial cells (HUVEC) and bone marrow stromal cells (BMSC) prior to encapsulating in a MEGEL and PEG-DA hydrogel. The rate radicals are produced in solution depends on the concentration of the photoinitiator, the molar extinction

coefficient/absorptivity of the photoinitiator at a particular wavelength, the activation energy of the photoinitiator, the intensity of light, and the time of exposure to light (Bryant, Nuttelman et al. 2000). In a 3D hydrogel or encapsulating precursor solution, the radicals have more possible propagation and termination targets (Figure 4.33).

Polymer double bonds are the intended target, but competing targets in the precursor solution are the cells and any impurities or additives such as the alginate viscosity modifier. A higher extinction coefficient increases the rate of initiation at a given light intensity, and the molar extinction coefficient of Irgacure 2959 in water is  $6.7 \text{ mol}^{-1}\text{cm}^{-1}$  (at 365 nm) (Bryant, Nuttelman et al. 2000) and the molar extinction coefficient of VA086 is  $30 \text{ mol}^{-1}\text{cm}^{-1}$  (at 375 nm) (Wako Chemicals Technical Information). While the number of VA086 radicals produced in a given solution/lightsource combination was not quantified in 2D for this study, by increasing the light intensity we effectively increased the number of VA086 radicals in the hydrogel precursor solution (an over saturated VA086 initiator concentration). The effective radical concentration of VA086, and its efficiency in chain initiation for polymerization reaction in our hydrogel appears to be much less than Irgacure. Increasing the number of effective VA086 radicals, as evidenced by the increase in mechanical properties, decreased the viability of encapsulated cells. The effective cell damage of the VA086 radicals is not the same as Irgacure, but with the increase in light source intensity, we found we could get higher or equivalent viability in Irgacure hydrogels of much stiffer mechanical properties than the VA086 hydrogels. Bryant et al characterized photoinitiator solutions to do viability



Number of Radicals in Solution Depends on:	Free Radical Interactions Depend On:
Concentration of Photoinitiator	Availability of double bonds
Intensity of Light	Polymerization rate/Ability of radical to activate and propagate
Time of Exposure	Cell concentration,
Molar Extinction Coefficient	Membrane permeability of radical
Activation Energy	Membrane and intracellular antioxidants
	Additive concentration

**Figure 4.33 Schematic of precursor and crosslinked hydrogel environment.**

In the precursor solution upon exposure to the UV light free radicals are produced from the photoinitiator. The initiation reaction and the number of radicals it produces depends on concentration of photoinitiator, the intensity of light, and how long the light exposure is. Radical production also depends on the molar extinction coefficient and the activation energy of the photoinitiator. The free radicals can interact with multiple targets in a 3D hydrogel system. Additionally solution properties like temperature and viscosity can affect the rate of these reactions.

testing with the matched number of radicals produced by different photoinitiators (Bryant, Nuttelman et al. 2000). If this type of matched free radical number study was done on VA086 and Irgacure in conjunction with 3D crosslinking studies in different materials a more quantitative and generally applicable guide to photoinitiator selection could be defined.

Previously, studies have compared VA086 and Irgacure in terms of pair effects. For example mechanical effectiveness of photoinitiator is generally 10 to 1 and effective cell damage is 30 to 1 for Irgacure to VA086. In this study we observe a cell damage to mechanical gain ratio (Table 4.2). This ratio of cell damage to mechanical gain indicates that VA086 is actually a more detrimental photoinitiator in a hydrogel system because so much more of it is needed. However, it should be noted that we only calculate this damage ratio between two radical conditions for the two photoinitiators in one precursor combination for the 3 cell types. This was useful in demonstrating cell-type dependent sensitivity and that VA086 when compared to Irgacure in specific 3D conditions can produce a less crosslinked hydrogel with equivalent or greater detrimental effects on cell viability. More characterization and perhaps more sensitive mechanical characterization is needed to determine if this relationship between damage/mechanics is the same at higher and lower photoinitiator concentration and light intensity combinations. At the lower concentration initiator and light intensity VA086 does produce higher viability hydrogels than Irgacure. This suggests that hydrogel stiffness and cell viability slopes with increasing number of free radicals are different for the two photoinitiators. Additionally the mechanics/damage relationship of

**Table 4.2 Damage to mechanics ratio.** Decrease in cell viability corresponding to a jump in photoinitiator radicals induced by increasing the light intensity was divided by the increase in mechanical properties to give a damage to mechanical gain ratio.

<b>Light Intensity [mW/cm<sup>2</sup>]</b>	<b>Photoinitiator</b>	<b>Modulus [kPa]</b>	<b>Cell Type</b>	<b>Viability [%]</b>	<b>Damage/Mechanics Ratio [%]/[kPa]</b>
<b>2to136</b>	<b>VA086 1.0%</b>	19.3±2.8 to 45.6±5.2	<b>HAVIC</b>	23.4±3.4 to 7.43±1.2	16/26=0.62*
			<b>HASSMC</b>	74.4±2.9 to 45.1±4.6	29/26=1.1*
			<b>HADMSC</b>	83.5±4.8 to 76.5±6.1 NSD	7/26=0.27
	<b>Irgacure 2959 0.1%</b>	40.9±4.1, to 120.7±10.2	<b>HAVIC</b>	49.2±2.4 to 41.3±3.0 NSD	8/80=0.10
			<b>HASSMC</b>	62.0±1.8, to 44.8±5.7	18/80=0.23
			<b>HADMSC</b>	92.7±1.7 to 85.2±1.4 NSD	8/80=0.10

photocrosslinking conditions could be established for other polymer precursor materials and cell combinations. Mironi-Harpaz et al also observed the importance of crosslinking efficiency versus cytotoxicity in PEGDA and PEG-fibrinogen hydrogels when evaluating different photoinitiators (Mironi-Harpaz, Wang et al. 2012). Mironi-Harpaz et al compare 4 different photoinitiators (including Irgacure 2959) for their effects on shear modulus and crosslinking time and found that only Irgacure 2959 and I184 initiators could achieve high chondrocyte viability and suitably efficient photocrosslinking during the photopolymerization reactions (Mironi-Harpaz, Wang et al. 2012). Mironi-Harpaz et al look at the photocrosslinking kinetics with the exposure time to achieve comparable mechanics and the subsequent viability. By contrast the present study increased photoinitiator to achieve comparable mechanics and the subsequent viability. Different polymer precursors and weight ratios also have different crosslinking efficiencies with a given radical photoinitiator (Hockaday, Kang et al. 2012). Fully understanding the mechanics and cell damage induced by a photoinitiator in a particular material, perhaps in a standard set of characterizing tests so this information can be compared, could better guide printing of multi-material and multicellular constructs to mimic complex living tissue.

Nearly every 3D bio-printing study uses a custom material and fabrication strategy for the needs of the particular cell being used and the type of tissue being developed which has led to some degree of custom characterization. On the whole 3D bio-printing technology with its many different platforms currently involves a great deal of troubleshooting as investigators are rapidly eliminating non-working procedures and

refining encapsulation protocols with different materials. As researchers contribute to a growing body of knowledge and identify a growing number of printable material combinations, eventually common overlap will occur and comparable material/fabrication characterization could enable broader application of 3D printing. Precisely controlling crosslinking kinetics during fabrication and the resultant hydrogel mechanics will determine inductive properties of engineered tissues. Stiffness is just one micro-environmental property of a hydrogel that can affect the behavior of the resident cells and the subsequent tissue development. This is particularly important to tissue engineering strategies where stiffness is being used to drive cell behavior and differentiation (Engler, Sen et al. 2006; Chandler, Berglund et al. 2011; Park, Chu et al. 2011; Duan, Hockaday et al. 2013).

Additionally the mechanism of cell death and primary mode of cell damage in 3D hydrogels still needs to be identified and mitigated. We observed an increase in the calculated oxidative stress ratio with higher intensity light, and we observed that VA086 produced a higher intracellular oxidative stress ratio than Irgacure. These ratios are the divided averages of the different conditions to see the normalized high powered LED and VA086 condition and were not compared statistically. When just the relative oxidative fluorescence values and percentage of cells experiencing oxidative stress are considered, between conditions with more photoinitiator radicals (in Irgacure conditions since the VA086 data has to be excluded in this comparison), there is not a significant difference in intracellular oxidative stress. This indicates that Irgacure radicals are not causing intracellular oxidative stress. Cells did experience oxidative stress during the

handling of the cells for printing aside from the photo-encapsulation. While this may affect viability, HASSMC, which experienced the most oxidative stress also had the poorest response to the rescue attempt using treatment of catalase prior to encapsulation. This supports the conclusion that intracellular oxidative stress is not the main driver of cell death in our photo-crosslinking hydrogel system. Identifying where photoinitiator radicals (both VA086 and Irgacure radicals) are targeting and causing the most damage to cells could lead to a better rescue strategy and higher viability in photo-encapsulation fabrication techniques.

Engineering protection from a reaction oxygen species has been done in a 3D gels system, although it was for protection against external ROS attack as opposed to ROS produced as a byproduct of the fabrication of the hydrogel. Hume et al demonstrated that they could effectively protect PEG-DA encapsulated pancreatic cells from ROS external attack by incorporating a super oxide dismutase mimetic into the hydrogel itself(Hume and Anseth 2011). As a continuation of the study presented here, lipid peroxidation should be specifically stained for and compared between for VA086 and Irgacure 2959 photoinitiators. We suspect that a strategy to protect the cell membrane during the photo encapsulation process would significantly improve cell viability.

In our study we also tested longer term viability and metabolism in our hydrogels. As time in culture increases, the percent viability of HASSMC and HAVIC decreases in Irgacure photo-crosslinked hydrogels. Over the course of 7 days the metabolism of these tissue constructs decreases in all but the HADMSC populated VA086 hydrogels.

Additional variables characteristic of 3D culture, not examined here, may be affecting the viability of HADMSC, HASSMC, and HAVIC. For example the contribution of binding domains and density/presentation of these domains was not varied here and in the hydrogel used may actually be sub-optimal for valve interstitial cell culture. More bioactive and softer hydrogel photo-encapsulation (0.03% w/v Irgacure) have resulted in PAVIC viability closer to 80%. Studied here is one polymer mixture for printing, however, different polymer formulations may require more or less photoinitiator and more or less intense light source to enable fabrication of stable tissue engineered constructs (Hockaday, Kang et al. 2012).

#### **4.6 Conclusion**

This study further explores variables associated with photo-crosslinking hydrogels, relationships previously demonstrated or suspected by other investigators, for a MEGEL:PEG-DA 3350 mixture containing valve cells or mesenchymal stem cells. Contrary to numerous 2D cytotoxicity studies, we have demonstrated that when considered in a 3D hydrogel culture environment and fabrication setting, Irgacure 2959 rather than VA086 can produce more viable encapsulated cells. Intracellular oxidative stress was not significantly greater in hydrogel conditions of more Irgacure 2959 photoinitiator radicals. Normalized oxidative stress ratios suggest that increasing VA086 radicals induced higher intracellular oxidative stress. Suppression of intracellular oxidative stress using catalase pretreatment does not disrupt hydrogel crosslinking but it does not rescue cell viability.

#### **4.7 Future Directions**

Characterization to establish fabrication conditions that optimize cell viability and hydrogel solidification and to fully appreciate the consequences of these conditions on subsequent tissue is useful within the field of bioprinting and tissue engineering as a whole. The effects of fabrication conditions on other markers of functional health in the cells should be evaluated – such as cell differentiation, gene expression, extracellular matrix deposition following photocrosslinking. Identifying the primary mode of cell damage in photocrosslinking conditions and the radical sinking and protective effects of different polymers could lead to a means to improve cell viability. Two recommended future studies would be to (1) identify hydrogel material specific differences in ability to capture photoinitiator radicals and (2) test for lipid peroxidation and then pursue membrane targeted rescue strategies.

VA086 and Irgacure have different crosslinking efficiencies in the same solution and have different crosslinking efficiencies depending on the polymers in the precursor solution (Rouillard, Berglund et al. 2010; Chandler, Berglund et al. 2011). Encapsulated cell viability can be different using the same photoinitiator concentration using the same cell type but with different precursors in the solution. HAVIC photoencapsulated in methacrylated gelatin/methacrylated hyaluronic acid hydrogels have a viability over 90% at day 3 and day 7 when prepared with precursor solutions containing 0.05%w/v Irgacure 2959 that are exposed to 2 mW/cm<sup>2</sup> 365nm light (Duan, Kapetanovic et al. 2014) but in MEGEL/PEGDA for the same crosslinking conditions the viability was below 80%. In the precursor solutions there are competing reactions in terms of radical

targeting of polymer double bonds verses targeting of cells, and these reactions may not be equal. Some materials used in hydrogels are even cited for their antioxidant properties such as hyaluronan(Farnsworth, Bensard et al. 2012). While cells may prefer one hydrogel material over another for reasons such as availability of binding sites or network structure, there may also be a contribution of the material's ability to sink radicals away from the cells. To characterize multiple materials for the purposes of 3D bioprinting it would be useful to establish crosslinking and cell damage trends induced by a quantified number of photoinitiator radicals to generate standardized cell damage to mechanical gain ratios.

Lipid peroxidation is a major suspected mechanism of cell damage by Irgacure 2959 radicals. Testing of chondrocytes indicate that Irgacure 2959 in photocrosslinking conditions induced lipid peroxidation (Farnsworth, Bensard et al. 2012). Lipid peroxidation modifies the membranes and generates aldehydes, which unlike free radicals aldehydes are relatively long lived and unlike Irgacure radicals can diffuse from their site of origin in the lipid bilayer to react with intracellular targets(Balasubramanian, Bevers et al. 2001). To test for lipid peroxidation and pursue membrane targeted rescue strategies using membrane associated antioxidants, I recommend pretreatment of the cells with either melatonin or vitamin E prior to photoencapsulation and using diphenyl-1-pyrenoylphosphine (DPPP) and annexin V binding to screen for lipid peroxidation.

Melatonin could be explored as a pretreatment of cells prior to photoencapsulation to potentially reduce damage induced by photoinitiator radicals. Melatonin is an antioxidant that neutralizes directly several free radicals including superoxide anion, hydrogen peroxide, hydroxyl radical, singlet oxygen, peroxynitrite anion, nitric oxide, hypochlorous acid (Sokolovic, Djordjevic et al. 2013). Melatonin incorporates itself into the head-group region of the phospholipid bilayer where it reacts with radicals as an antioxidant defense, and it has been shown to stimulate production of intracellular antioxidants such as catalase (Col, Dinler et al. 2010; Drolle, Kucerka et al. 2013). In addition melatonin alters the biophysical properties of the membrane. Studies indicate that melatonin causes bilayer thinning, it introduces disorder into the membrane, and it increases membrane fluidity which could affect propagation of lipid peroxidation reactions (Drolle, Kucerka et al. 2013). Melatonin treatment of cells has previously been demonstrated to decrease the amount of cell membrane damage lipid peroxidation caused by UV-B light exposure and microwaves and to increase cell viability under these conditions (Ryoo, Suh et al. 2001; Sokolovic, Djordjevic et al. 2013). However, the anti-oxidative properties of melatonin depend on the cell type and the concentration of melatonin used, and prolonged incubation of cells in melatonin could cause damage to the cells (Krokosz, Grebowski et al. 2013). For a future photoencapsulation study a dose-melatonin study would need to be included for the different cell types.

The Vitamin E analog Trolox could be explored as a pretreatment of cells prior to photoencapsulation to potentially reduce or repair damage induced by photoinitiator radicals. Vitamin E is an antioxidant that prevents lipid peroxidation (Manevich, Sweitzer

et al. 2002), and in erythrocytes membrane lysis induced by oxidative stress is prevented by vitamin E supplements (Howard, McNeil et al. 2011).  $\alpha$ -tocopherol, the most common form of vitamin E, is lipid soluble and it partitions into the hydrophobic core of the plasma membrane bilayer. Upon incorporation of  $\alpha$ -tocopherol in to the membrane, membrane fluidity increases at surface and decreases in interior. The chromanol-head group of  $\alpha$ -tocopherol binds to the head group of phospholipids which limits their mobility within the membrane.  $\alpha$ -tocopherol (most common form of vitamin E) promoted plasma membrane repair and resealing after mechanical damage or laser induced injury. Trolox a biologically active analog of vitamin E (less understood biophysical mechanism of membrane association) has been used to promote membrane repair after short pre-incubation with cells. Trolox quickly associates with the cell membrane (after less than 15 minute incubation) while  $\alpha$ -tocopherol needs 24 hours or longer depending on the concentration to promote repair. Cells could be pre-treated with Trolox prior to photoencapsulation.

'Rescue' attempt experiments in VA086 and Irgacure photocrosslinking conditions should be performed with a live/dead viability assay for day 1 and day 3 time points in combination with a lipid peroxidation and membrane characterization. In a study with neuronal cells, vitamin E added at the same time as a toxins that cause lipid peroxidation, prevented lipid peroxidation did not prevent cell death (Slotkin and Seidler 2010). A toxin can have multiple mechanisms of cytotoxicity and cell damage. If lipid peroxidation oxidative stress is occurring in photoencapsulated cells to different degrees based on photoinitiator type and cell type, a functional test is needed to see if this is a

driving cause of observed differences in cell death. Running the day 1 and day 3 encapsulated viability study following treatment with melatonin or Trolox will help indicate if this is a mode of cell damage worth mitigating for the purposes of 3D bioprinting.

For our purposes either DPPP or BODIPY® 581/591 C11 could potentially work to quantify lipid peroxidation. DPPP is a probe used in live cells that localizes in cell membranes and becomes fluorescent in response to lipid peroxidation (Takahashi, Shibata et al. 2001; Manevich, Sweitzer et al. 2002) and BODIPY® 581/591 C11 and lipid peroxidation kit (C10445, Invitrogen). C11-BODIPY581/591 is a fluorescent fatty acid analog that upon free-radical induced oxidation shifts from red to green (Drummen, van Liebergen et al. 2002; Johnson 2010). In its reduced state C11-BODIPY581/591 has an excitation maxima at 581 and emission maxima at 591 nm and upon free radical-induced oxidation the probe shifts the excitation and emission to 488/510 nm. C11-BODIPY581/591 does preferentially labels mitochondrial membranes (a factor of 11-15 less in the plasma-membrane) (Drummen, van Liebergen et al. 2002). To assess membrane disruption caused by phospholipid peroxidation an annexin V binding assay can be used (Manevich, Sweitzer et al. 2002). Annexin V is a Ca<sup>2+</sup> dependent phospholipid-binding protein that has a high affinity for negatively charged phospholipids (van Engeland, Nieland et al. 1998). In normal viable cells the negatively charged phospholipid phosphatidylserine is on the cytoplasmic surface of the plasma membrane. In the intermediate stages of apoptosis phosphatidylserine is translocated from the inner to the outer part of the membrane and the membrane integrity is still

maintained (van Engeland, Nieland et al. 1998; Johnson 2010). Modification of the membrane where negative charged moieties are introduced promotes annexin V binding, and it has been shown that the amine-reactive aldehydes produced by lipid peroxidation can react with aminolipids to produce negatively charged adducts that bind annexin V (Balasubramanian, Bevers et al. 2001). Imaging for both lipid peroxidation and testing for annexin V binding of cells in photocrosslinking conditions could assess damage to cell membranes.

If treatments of the cells with antioxidants that associate with the membrane do not improve photoencapsulated cell viability, alternative strategies could be pursued. Studies have demonstrated a protective shell of pericellular matrix improves cell viability in photocrosslinking conditions (Villanueva, Bishop et al. 2009; Farnsworth, Bensard et al. 2012), transfection to over express protective membrane antioxidants can combat membrane targeted oxidative stress (Manevich, Sweitzer et al. 2002), and antioxidant enzymes can be stimulated/recruited to the plasma membrane to counteract lipid peroxidation (Hagmann, Kuczkowski et al. 2014). Identifying the primary mode of damage and then mitigating it for different cell types in hydrogel photoencapsulation would greatly expand the application of 3D printing technology, and this could potentially be done with antioxidant strategies targeting the membrane, modification of the membrane, or encasing the cells in a protective layer.

## REFERENCES

- Abramov, A. Y., A. Scorziello, et al. (2007). "Three distinct mechanisms generate oxygen free radicals in neurons and contribute to cell death during anoxia and reoxygenation." J Neurosci **27**(5): 1129-1138.
- Atsumi, T., J. Murata, et al. (1998). "Cytotoxicity of photosensitizers camphorquinone and 9-fluorenone with visible light irradiation on a human submandibular-duct cell line *in vitro*." Arch Oral Biol **43**(1): 73-81.
- Baier Leach, J., K. A. Bivens, et al. (2003). "Photocrosslinked hyaluronic acid hydrogels: Natural, biodegradable tissue engineering scaffolds." Biotechnology and Bioengineering **82**(5): 578-589.
- Baker, B. M. and C. S. Chen (2012). "Deconstructing the third dimension - how 3D culture microenvironments alter cellular cues." Journal of Cell Science **125**: 3015-3024.
- Bellis, A. D., B. P. Bernabe, et al. (2013). "Dynamic transcription factor activity profiling in 2D and 3D cell cultures." Biotechnology and Bioengineering **110**: 563-572.
- Benton, J. A., C. A. DeForest, et al. (2009). "Photo-crosslinking of gelatin macromers to synthesize porous hydrogels that promote valvular interstitial cell function." Tissue Eng Part A **15**(11): 3221-3230.
- Bilski, P., A. G. Belanger, et al. (2002). "Photosensitized oxidation of 2',7'-dichlorofluorescein: singlet oxygen does not contribute to the formation of fluorescent oxidation product 2',7'-dichlorofluorescein." Free Radic Biol Med **33**(7): 938-946.
- Bryant, S. J., C. R. Nuttelman, et al. (2000). "Cytocompatibility of UV and visible light photoinitiating systems on cultured NIH/3T3 fibroblasts *in vitro*." J Biomater Sci Polym Ed **11**(5): 439-457.
- Bunnell, B. A., M. Flaat, et al. (2008). "Adipose-derived stem cells: isolation, expansion and differentiation." Methods **45**(2): 115-120.
- Butcher, J. T. and R. M. Nerem (2004). "Porcine aortic valve interstitial cells in three-dimensional culture: comparison of phenotype with aortic smooth muscle cells." J Heart Valve Dis **13**(3): 478-485; discussion 485-476.
- Butcher, J. T., A. M. Penrod, et al. (2004). "Unique morphology and focal adhesion development of valvular endothelial cells in static and fluid flow environments." Arterioscler Thromb Vasc Biol **24**(8): 1429-1434.
- Butcher, J. T., C. A. Simmons, et al. (2008). "Mechanobiology of the aortic heart valve." J Heart Valve Dis **17**(1): 62-73.
- Carmichael, J., W. G. DeGraff, et al. (1987). "Evaluation of a tetrazolium-based semiautomated colorimetric assay: assessment of chemosensitivity testing." Cancer Res **47**(4): 936-942.
- Chandler, E. M., C. M. Berglund, et al. (2011). "Stiffness of photo-crosslinked RGD-alginate gels regulates adipose progenitor cell behavior." Biotechnol Bioeng **108**(7): 1683-1692.
- Chang, C. C., E. D. Boland, et al. (2011). "Direct-write bioprinting three-dimensional biohybrid systems for future regenerative therapies." Journal of Biomedical Materials Research Part B-Applied Biomaterials **98B**: 160-170.
- Chitcholtan, K., E. Asselin, et al. (2013). "Differences in growth properties of endometrial cancer in three dimensional (3D) culture and 2D cell monolayer." Experimental Cell Research **319**: 75-87.
- Colazzo, F., A. H. Chester, et al. (2010). "Induction of mesenchymal to endothelial transformation of adipose-derived stem cells." J Heart Valve Dis **19**(6): 736-744.

- Colazzo, F., P. Sarathchandra, et al. (2011). "Extracellular matrix production by adipose-derived stem cells: implications for heart valve tissue engineering." Biomaterials **32**(1): 119-127.
- Cruise, G. M., D. S. Scharp, et al. (1998). "Characterization of permeability and network structure of interfacially photopolymerized poly(ethylene glycol) diacrylate hydrogels." Biomaterials **19**(14): 1287-1294.
- Duan, B., L. A. Hockaday, et al. (2013). "3D bioprinting of heterogeneous aortic valve conduits with alginate/gelatin hydrogels." J Biomed Mater Res A **101**(5): 1255-1264.
- Duan, B., L. A. Hockaday, et al. (2013). "Stiffness and adhesivity control aortic valve interstitial cell behavior within hyaluronic acid based hydrogels." Acta Biomaterialia: <http://dx.doi.org/10.1016/j.actbio.2013.1004.1050>.
- Duan, B., E. Kapetanovic, et al. (2014). "Three-dimensional printed trileaflet valve conduits using biological hydrogels and human valve interstitial cells." Acta Biomater **10**(5): 1836-1846.
- Duan, B., M. Wang, et al. (2010). "Three-dimensional nanocomposite scaffolds fabricated via selective laser sintering for bone tissue engineering." Acta Biomater **6**(12): 4495-4505.
- Durst, C. A., M. P. Cuchiara, et al. (2011). "Flexural characterization of cell encapsulated PEG-DA hydrogels with applications for tissue engineered heart valves." Acta Biomater **7**(6): 2467-2476.
- Engler, A. J., S. Sen, et al. (2006). "Matrix elasticity directs stem cell lineage specification." Cell **126**(4): 677-689.
- Fedorovich, N. E., J. Alblas, et al. (2011). "Organ printing: the future of bone regeneration?" Trends in Biotechnology **29**: 601-606.
- Fedorovich, N. E., M. H. Oudshoorn, et al. (2009). "The effect of photopolymerization on stem cells embedded in hydrogels." Biomaterials **30**(3): 344-353.
- Gould, R. A., K. Chin, et al. (2012). "Cyclic strain anisotropy regulates valvular interstitial cell phenotype and tissue remodeling in three-dimensional culture." Acta Biomater **8**(5): 1710-1719.
- Gould, S. T. and K. S. Anseth (2013). "Role of cell-matrix interactions on VIC phenotype and tissue deposition in 3D PEG hydrogels." J Tissue Eng Regen Med.
- Guo, K., C. C. Chu, et al. (2005). "Synthesis and characterization of novel biodegradable unsaturated poly(ester amide)s." Journal of Polymer Science Part A: Polymer Chemistry **43**(7): 1463-1477.
- Hockaday, L. A., K. H. Kang, et al. (2012). "Rapid 3D printing of anatomically accurate and mechanically heterogeneous aortic valve hydrogel scaffolds." Biofabrication **4**(3): 035005.
- Hume, P. S. and K. S. Anseth (2011). "Polymerizable superoxide dismutase mimetic protects cells encapsulated in poly(ethylene glycol) hydrogels from reactive oxygen species-mediated damage." J Biomed Mater Res A **99**(1): 29-37.
- Hutson, C. B., J. W. Nichol, et al. (2011). "Synthesis and characterization of tunable poly(ethylene glycol): gelatin methacrylate composite hydrogels." Tissue Eng Part A **17**(13-14): 1713-1723.
- Kirkland, R. A. and J. L. Franklin (2001). "Evidence for redox regulation of cytochrome C release during programmed neuronal death: antioxidant effects of protein synthesis and caspase inhibition." J Neurosci **21**(6): 1949-1963.
- Kirkland, R. A., G. M. Saavedra, et al. (2007). "Rapid activation of antioxidant defenses by nerve growth factor suppresses reactive oxygen species during neuronal apoptosis: evidence for a role in cytochrome c redistribution." J Neurosci **27**(42): 11315-11326.
- Kloxin, A. M., J. A. Benton, et al. (2010). "In situ elasticity modulation with dynamic substrates to direct cell phenotype." Biomaterials **31**(1): 1-8.

- Koch, L., A. Deiwick, et al. (2012). "Skin tissue generation by laser cell printing." Biotechnology and Bioengineering **109**: 1855-1863.
- Kuzawa, C. W. (1998). "Adipose tissue in human infancy and childhood: An evolutionary perspective." Yearbook of Physical Anthropology, Vol 41 - 1998 **41**: 177-209.
- Lampe, K. J., R. M. Namba, et al. (2009). "Impact of lactic acid on cell proliferation and free radical-induced cell death in monolayer cultures of neural precursor cells." Biotechnol Bioeng **103**(6): 1214-1223.
- Latif, N., P. Sarathchandra, et al. (2007). "Characterization of structural and signaling molecules by human valve interstitial cells and comparison to human mesenchymal stem cells." J Heart Valve Dis **16**(1): 56-66.
- Leach, J. B. and C. E. Schmidt (2005). "Characterization of protein release from photo-crosslinkable hyaluronic acid-polyethylene glycol hydrogel tissue engineering scaffolds." Biomaterials **26**(2): 125-135.
- Lee, S. H., J. J. Moon, et al. (2008). "Three-dimensional micropatterning of bioactive hydrogels via two-photon laser scanning photolithography for guided 3D cell migration." Biomaterials **29**: 2962-2968.
- Luangphakdy, V., E. Walker, et al. (2013). "Evaluation of osteoconductive scaffolds in the canine femoral multi-defect model " Tissue Engineering Part A **19**: 634-648.
- Lund, A. W., B. Yener, et al. (2009). "The natural and engineered 3D microenvironment as a regulatory cue during stem cell fate determination." Tissue Engineering Part B-Reviews **15**: 371-380.
- Mallajosyula, J. K., D. Kaur, et al. (2008). "MAO-B elevation in mouse brain astrocytes results in Parkinson's pathology." PLoS One **3**(2): e1616.
- Manevich, Y., T. Sweitzer, et al. (2002). "1-Cys peroxiredoxin overexpression protects cells against phospholipid peroxidation-mediated membrane damage." Proc Natl Acad Sci U S A **99**(18): 11599-11604.
- Muller, A. M., M. Davenport, et al. (2009). "Platelet lysate as a serum substitute for 2D static and 3D perfusion culture of stromal vascular fraction cells from human adipose tissue." Tissue Engineering Part C **15**: 869-875.
- Nichol, J. W., S. T. Koshy, et al. (2010). "Cell-laden microengineered gelatin methacrylate hydrogels." Biomaterials **31**: 5536-5544.
- Occhetta, P., N. Sadr, et al. (2013). "Fabrication of 3D cell-laden hydrogel microstructures through photo-mold patterning." Biofabrication **5**(3): 035002.
- Park, J. S., J. S. Chu, et al. (2011). "The effect of matrix stiffness on the differentiation of mesenchymal stem cells in response to TGF-beta." Biomaterials **32**(16): 3921-3930.
- Quintanilla, R. A., T. A. Matthews-Roberson, et al. (2009). "Caspase-cleaved tau expression induces mitochondrial dysfunction in immortalized cortical neurons: implications for the pathogenesis of Alzheimer disease." J Biol Chem **284**(28): 18754-18766.
- Richards, J., I. El-Hamamsy, et al. (2013). "Side-specific endothelial-dependent regulation of aortic valve calcification interplay of hemodynamics and nitric oxide signaling." American Journal of Pathology **182**: 1922-1931.
- Rouillard, A. D., C. M. Berglund, et al. (2010). "Methods for Photo-crosslinking Alginate Hydrogel Scaffolds with High Cell Viability." Tissue Eng Part C Methods.
- Rouillard, A. D., C. M. Berglund, et al. (2011). "Methods for photo-crosslinking alginate hydrogel scaffolds with high cell viability." Tissue Eng Part C Methods **17**(2): 173-179.
- Santos, E., R. M. Hernandez, et al. (2012). "Novel advances in the design of three-dimensional bio-scaffolds to control cell fate: translation from 2D to 3D." Trends in Biotechnology **30**: 331-341.
- Shin, S. R., B. Aghaei-Ghareh-Bolagh, et al. (2013). "Cell-laden microengineered and mechanically tunable hybrid hydrogels of gelatin and graphene oxide." Adv Mater **25**(44): 6385-6391.

- Singh, S., C. Brocker, et al. (2013). "Aldehyde dehydrogenases in cellular responses to oxidative/electrophilic stress." Free Radic Biol Med **56**: 89-101.
- Singh, S., A. N. Singh, et al. (2013). "Biodegradable polycaprolactone (PCL) nanosphere encapsulating superoxide dismutase and catalase enzymes." Appl Biochem Biotechnol **171**(7): 1545-1558.
- Stephens, E. H., C. A. Durst, et al. (2011). "Mitral valvular interstitial cell responses to substrate stiffness depend on age and anatomic region." Acta Biomater **7**(1): 75-82.
- Swindle, M. M., A. Makin, et al. (2012). "Swine as models in biomedical research and toxicology testing." Vet Pathol **49**(2): 344-356.
- Torgersen, J., A. Ovsianikov, et al. (2012). "Photo-sensitive hydrogels for three-dimensional laser microfabrication in the presence of whole organisms." Journal of Biomedical Optics **17**: 105008.
- Wang, C., S. Yin, et al. (2010). "Differentiation of adipose-derived stem cells into contractile smooth muscle cells induced by transforming growth factor-beta1 and bone morphogenetic protein-4." Tissue Eng Part A **16**(4): 1201-1213.
- Wang, X., B. Su, et al. (2009). "Impaired balance of mitochondrial fission and fusion in Alzheimer's disease." J Neurosci **29**(28): 9090-9103.
- Williams, C. G., A. N. Malik, et al. (2005). "Variable cytocompatibility of six cell lines with photoinitiators used for polymerizing hydrogels and cell encapsulation." Biomaterials **26**(11): 1211-1218.

## CHAPTER 5

### ARBITRARY AND ANATOMICALLY BASED CONTROL OF INTERNAL HETEROGENEITY OF 3D PRINTED TISSUES

#### **5.1 Summary**

In this study we present methods to generate geometries exhibiting heterogeneous distribution of printable materials throughout a fabricated shape. These algorithms provide a tool for 3D printing of heterogeneous, anatomically relevant tissue engineered constructs. Using the first algorithm demonstrated, the target print image is generated through processing any image into printable vector format. We present a second algorithm that generates spatially heterogeneous gradients with multiple materials in arbitrary directions in 2D and 3D. We then present a combination algorithm that separates intrinsic tissue heterogeneity present in medical imaging scans of anatomical tissue into printable format files. The fabrication of these files was demonstrated using the Fab@Home<sup>TM</sup> platform by printing heterogeneous hydrogel scaffolds. We also present a method to quantify the fidelity of heterogeneous layers, and to quantify the blending of different materials that were printed.

#### **5.2 Introduction**

Heterogeneity is a critical functional characteristic of many living tissues. One of the primary drivers for exploration into 3D printing as a method for tissue engineering is the cellular, mechanical, and biochemical heterogeneity present in native tissue that cannot be replicated with traditional fabrication strategies like injection molding and shaping/suturing/gluing scaffolds by hand. 3D extrusion bioprinting enables a high level of geometric control and direct deposition of cells within tissue constructs (Skardal, Zhang et al. 2010; Fedorovich, Wijnberg et al. 2011; Schuurman, Khristov et al. 2011; Tirella, Vozzi et al. 2011; Fedorovich, Schuurman et al. 2012; Mannoer, Jiang et al.

2013; Ahn, Lee et al. 2014; Pati, Jang et al. 2014). A few strategies have advanced to evaluating the consequences of heterogeneity and multi-cellularity *in vivo* (Fedorovich, Wijnberg et al. 2011; Fedorovich, Schuurman et al. 2012). These studies have demonstrated that heterogeneous printing resulted in heterogeneous tissue formation during *in vivo* culture. ECM produced by the cells corresponded to the deposited cell type, and the scaffold mixture or hydrogel type could be used to direct and influence matrix production of encapsulated cells. Depending on the encapsulating scaffold material, cells maintained the original printed organization or migrated out of the pattern to different degrees.

Fab@Home™ is an open source extrusion based 3D printing platform that has recently been used to print heterogeneous tissue constructs. Materials that have been demonstrated with the platform for direct cell encapsulation and printing are methcrylated gelatin/methcrylated hyaluronic acid (Duan, Kapetanovic et al. 2014), four-armed PEG/hyaluronic acid/gelatin derivatives (Skardal, Zhang et al. 2010; Skardal, Zhang et al. 2010), alginate (Mannoor, Jiang et al. 2013), gelatin/alginate (Duan, Hockaday et al. 2013), and hydroxyapatite loaded gelatin/alginate (Wust, Godla et al. 2014). The primary file type used with the Fab@Home™ is a CAD drawing in Standard Tessellation Language (STL) format. This only contains the shell information of a shape, and the printer automatically plots and prints the outline of the shape and fills the layer with a single material. Interlocking and multiple STL files and similar files can be printed simultaneously to create multiple blocks of material in a single structure (Cohen, Malone et al. 2006; Hockaday, Kang et al. 2012; Duan, Kapetanovic et al. 2014). However, the Fab@Home™ has a second file format called a vector file. It is possible to control the information and material deposition within regional blocks with the vector printing.

In this study we develop and test algorithms designed to generate geometries exhibiting heterogeneous distribution of printable materials throughout a fabricated shape by utilizing the vector file format. Poly-(ethylene glycol)diacrylate (PEG-DA) and methacrylated gelatin (MeGel) photo-crosslinkable hydrogel precursors (Benton, DeForest et al. 2009; Hutson, Nichol et al. 2011) were combined with non-photo-crosslinking alginate to make a solution suitable for cell encapsulation and extrusion 3D printing. We previously demonstrated PEG-DA as a base polymer precursor for extrusion 3D printing of valve scaffolds (Hockaday, Kang et al. 2012). The potential for mechanical and/or molecular customization, coupled with their relatively low cost and biocompatibility, suggests PEG-DA could be an ideal material component for clinically relevant scale 3D tissue printing (Kloxin, Benton et al. 2010; Durst, Cuchiara et al. 2011); (Gunn, Turner et al. 2005; Peyton, Raub et al. 2006; Guo and Chu 2007). Gelatin is synthesized by partial breakdown of collagen, but it retains some bioactive features of collagen, particularly cell attachment/binding domains (Benton, DeForest et al. 2009). Gelatin can be modified for photo-crosslinking by incorporating double bond pendent groups on the gelatin chains to make methacrylated gelatin. Methacrylated gelatin (MeGel) hydrogels. MEGel hydrogels are enzymatically degradable and have been used to encapsulate valve interstitial cells (Benton, DeForest et al. 2009), and with the addition of PEG-DA the degradation properties are modifiable (Hutson, Nichol et al. 2011). These materials were 3D printed with and without encapsulated human adipose derived mesenchymal stem cells (HADMSC) using the Fab@Home™ printer to test arbitrary and image derived vector geometries to achieve material heterogeneity.

### ***5.3 Materials and Methods***

#### **5.3.1 Fab@Home™ 3D Printing Platform and Vector File Format**

A model 1 Fab@Home™ printer was used for testing geometries and fabricating hydrogel scaffolds. Detailed specifications and mechanics of the open-source

Fab@Home™ Model 1 extrusion based 3D printing platform can be found at [www.fabathome.org](http://www.fabathome.org) and in previous studies (Cohen, Malone et al. 2006; Malone 2007). Vector files can also be formatted into Fab files for printing in the Model 2 printer, but the model 1 was used for all data presented here. To enable heterogeneous printing we utilize a format in the Fab@Home™ called vector printing. In vector printing format, the user defines lines to be printed for a given layer using pairs of points. The start and end point are grouped with each other (Figure 5.1A). For a given layer the z coordinates are usually the same throughout the layer. When the vector file is uploaded to printer, the pair of coordinates is recognized and system will extrude material starting at the first point and ending at the second (Figure 5.1B). In contrast, when the user loads a file in Standard Tessellation Language (STL) format, which only contains the shell information of the shape, the printer automatically plots and prints the outline of a shape and fills the layer with a single material. Interlocking and multiple STL files and similar files can be printed simultaneously to create multiple blocks of material in a single structure (Cohen, Malone et al. 2006; Hockaday, Kang et al. 2012; Duan, Kapetanovic et al. 2014). However, with the vector printing it is possible to control the information and material deposition within those blocks.

### **5.3.2 Materials for Printing**

Silicone sealant was used as a testing material to check and troubleshoot printed geometries (GE Silicone Sealant II, Lowes Ithaca NY). Poly(ethylene glycol)-diacrylate (PEG-DA) and Methacrylated Gelatin (MEGEL) were used as the base polymer precursors for this study. PEG-DA700 hydrogel was used for test geometries when no cell encapsulation was needed for the experiment, and PEG-DA3350 in combination with MEGEL was used for direct cell bioprinting and photo-encapsulation of cells. 2-hydroxy-1(4-(hydroxyethoxy)phenyl)-2-methyl-1-propanone (Irgacure 2959, BASF Corporation, Newport, DE) which has previously been used with live cells in 3D

hydrogels was used as the photoinitiator (Rouillard, Berglund et al. 2010; Hutson, Nichol et al. 2011). Un-modified soluble alginate (LF10/60, FMC BioPolymer, Drammen, Norway) was mixed into polymer precursor solutions to temporarily increase viscosity during the printing extrusion process (Hockaday, Kang et al. 2012; Kang, Hockaday et al. 2013).

### **5.3.3 Precursor Solution Preparation for Printing without Cells**

For hydrogel printing without cells, the precursor solution consisted of 13.7 mM NaCl solution, 1.0%w/v photoinitiator, and 20%w/v PEG-DA 700MW. Red and blue food dye was added to precursor solutions for contrast and imaging heterogeneous scaffolds.

### **5.3.4 Polymer Synthesis and Solution Preparation for Cell Encapsulation**

In this study poly-(ethylene glycol)diacrylate molecular weight 3350 (PEG-DA3350) and methacrylated gelatin (MeGel) photo-crosslinkable hydrogel precursors (Benton, DeForest et al. 2009; Hutson, Nichol et al. 2011) were combined with non-photo-crosslinking alginate to make a solution suitable for cell encapsulation and extrusion 3D printing.

#### Synthesis

Methacrylated gelatin (MEGEL) was synthesized as previously described (Nichol, Koshy et al. 2010; Duan, Hockaday et al. 2013; Duan, Kapetanovic et al. 2014). Briefly, gelatin from bovine skin (Sigma) was dissolved at 10% (w/v) into distilled water at 40 °C and then methacrylic anhydride (MA, Sigma) (1:5 v/v to gelatin solution) was added drop by drop under stirred conditions at 40 °C for 1 hr. Polyethylene glycol diacrylate molecular weight 3350 was synthesized as previously described (PEG-DA 3350) (Cruise, Scharp et al. 1998; Guo, Chu et al. 2005). Poly(ethylene glycol) (PEG, Sigma) was dissolved in benzene (1.5 mmol of PEG in 150ml of benzene) and heated to 45 °C

with continuous stirring until completely dissolved. The solution was cooled to room temperature and triethylamine was added at 8 fold molar concentration (based on PEG diol end groups) to the PEG solution (12mmol). Acryloyl chloride (Sigma) at eightfold molar excess concentration was weighed out then diluted using benzene (1:40 acryloyl chloride to benzene) and added drop wise to the PEG solution through a drop funnel under an ice bath. The mixture was stirred overnight, and then the reaction stopped. The insoluble triethylamine was removed by filtration. PEG-DA was precipitated from the solution by the addition of petroleum ester (Sigma). The PEG-DA precipitate was collected using a funnel, re-dissolved in 20 ml of benzene, and precipitated again by adding petroleum ester. The precipitation process was repeated several times. After synthesis the MEGEL and PEG-DA products were dissolved in distilled water and transferred and sealed into dialysis tubing with a molecular weight cut off of 1000 Da. The polymers were dialyzed against distilled water for 5-7 days in 5 gallon containers with frequent water changes. The polymer product was then frozen at -20C and then lyophilized. Lyophilized polymers were stored at -20°C.

#### Preparation of Sterile Polymer Precursor Solution

Polymer solutions were prepared in a biosafety cabinet. Hydrogel precursor solutions were made 20%w/v polymer to solution, MEGEL:PEG-DA3350 1:1. Polymer precursors were weighed out dry and then sterilized for 1 hour using germicidal UV and then transferred into sterile 50 ml conical tubes. Irgacure 2959 was weighed out and dissolved in 70% ethanol to make stock solutions of 0.1g VA086/ml of ethanol solution and 0.015 g Irgacure/ml of ethanol solution which were then sterile filtered (Chandler, Berglund et al. 2011; Rouillard, Berglund et al. 2011). Stock solutions were stored at room temperature and used within 1 week. Photoinitiator stock solution was added to sterilized polymers to give a final concentration of 0.075%w/v Irgacure. The remaining solution volume was valve cell culture media. Polymer precursors, photoinitiator

solution, and media were combined in conical tube, the tube cap was wrapped with parafilm, and the tube placed into water bath at 37°C to dissolve.

### **5.3.5 Light Sources for Photo-crosslinking Printed Hydrogel Solutions**

For photo-crosslinking hydrogel constructs more than two layers. a low power 365 nm LED array built to mount on the syringe carriage, previously used for printing valve scaffolds [Biofabrication 2012], was built with 4 NCSU033B LEDs (Nichia America Corporation, Wixom, MI). The limiting resistance was set at 33  $\Omega$  per LED (calculated 376 mA forward current per LED and radiant flux at the LED was 233 mW, and at the print surface per LED 18.5mW/cm<sup>2</sup>). A Spectroline Lamp 365nm EN280L with a single bulb was used for photo-crosslinking printed hydrogels containing cells at 2 mW/cm<sup>2</sup> (intensity at stage/plate surface).

### **5.3.6 Adipose Derived Mesenchymal Cell Culture**

Direct cell encapsulation printing of heterogeneous scaffolds was demonstrated using adipose derived mesenchymal stem cells (ADMSC). ADMSC can be differentiated towards osteogenic, adipogenic, myogenic, chondrogenic, neurogenic, endothelial, and smooth muscle cell lineages (Colazzo, Chester et al. 2010; Wang, Yin et al. 2010). ADMSC have demonstrated similar phenotypic and functional characteristics to bone marrow mesenchymal stem cells (BMMSC), which are more established in the literature, but ADMSC isolation is less invasive (Bunnell, Flaas et al. 2008); (Colazzo, Chester et al. 2010). In addition, adipose tissue is present in infants, children, and adults (Kuzawa 1998). These characteristics suggest ADMSC are a potentially feasible cell source for tissue engineering replacement tissues that could be applicable to all three age groups. Cryopreserved HADMSC were purchased (Cat #:PT-5006, Lot#0F4505, Lonza, Walkersville). HADMSC were isolated from a 52 year old female donor and cryopreserved December 6, 2010. Greater than 90% of the cells were

positive for CD13, CD29, CD44, CD73, CD90, CD105, CD166. Less than 5% of cells were positive for CD14, CD31, and CD45. HADMSC were thawed and cultured using Dulbecco's Modified Eagle Medium: Nutrient Mixture F-12 (F12:DMEM, Invitrogen) supplemented with 10% FBS, 1% PS. HADMSC were passaged at just sub-confluent (~90%) and fed every 3-4 days. Cells were used at passages 4-8. HADMSC were expanded and maintained in flasks with and F12/DMEM media.

### **5.3.7 Cell Encapsulation and Handling for 3D Printing**

To test how cells were distributed throughout constructs when heterogeneous geometries were printed, cells were encapsulated in precursor solution, loaded into syringes, extruded into vector paths using the printer, and photo-crosslinked with the lamp at 2 mW/cm<sup>2</sup> for 5 minutes. Cells were rinsed with PBS, trypsinized from flasks that were 80-95% confluent, trypsin was inactivated with supplemented media, and cells were counted. Cells were spun down into a pellet (1000 RPM, 5min) and then incubated in working solution of 7 μM Cell Tracker Red or Cell Tracker Green in PBS for 20 minutes at 37°C, spun down (1000RPM, 5min), rinsed and re-suspended with PBS, spun down, and then encapsulated in prewarmed and dissolved MEGEL/PEG-DA3350 precursor solution at a concentration of 2.5 million cells/ml. Precursor solution containing the suspended cells was pipetted into syringes connected by Luer adapter with the stopper/piston removed from one side. 7.5%w/v alginate powder was added and stirred in with a sterile spatula. The syringe piston was reinserted, the bubbles squeezed out, and the viscous precursor solution was mixed back and forth between the two syringes to fully homogenize. Syringes were kept in the incubator at 37°C until ready to load into the printer syringe carriage. If the solution is allowed to cool, the MEGEL component solidifies and the photo-crosslinking does not work or is only partial. The Luer adapter was detached from the mixing syringe and reattached to a printing syringe. The gel was transferred to a printing syringe. Heating coils were applied to the

syringe barrels and tips to keep precursor gel warm. Wust et al previously demonstrated a heating setup with the Fab@Home™ for gelatin/alginate printing (Wust, Godla et al. 2014). Precursor solution was printed and then printed layers were exposed to UV lamp for 5 minutes. 20 ml of cell culture media was applied to submerge, hydrate, and loosen the hydrogel construct and was placed in the incubator. After 1 hour incubation in the media, the hydrogel constructs were transferred to 6-well plates containing fresh media. Plates were placed on a rocker in a walk-in incubator set at 37°C and 5% CO<sub>2</sub>. Media was exchanged after 24 hr and then hydrogels were fed every 48 hours. After printing, HADMSC hydrogel constructs were cultured in MCDB131 medium supplemented with 10% FBS, 1% PS, 0.25 µg/L recombinant human fibroblast growth factor basic (rhFGF-2; Invitrogen) and 5 µg/L recombinant human epidermal growth factor (rhEGF; Invitrogen).

### **5.3.8 First Algorithm: Conversion of Images to Printable Vectors**

Images can be converted into printable vector files using a custom algorithm. Photographs or images are converted into a 2D binary image (Figure 5.1C), and the algorithm identifies the different color regions and assigns materials. Coordinate points are designated within each region or dithered and then connected to create printable vector files. Silicone sealant geometries were extruded by the printer to test patterns specified by the vectors (Figure 5.1C and 5.1D). Regular and irregular shapes are possible with this printing format.

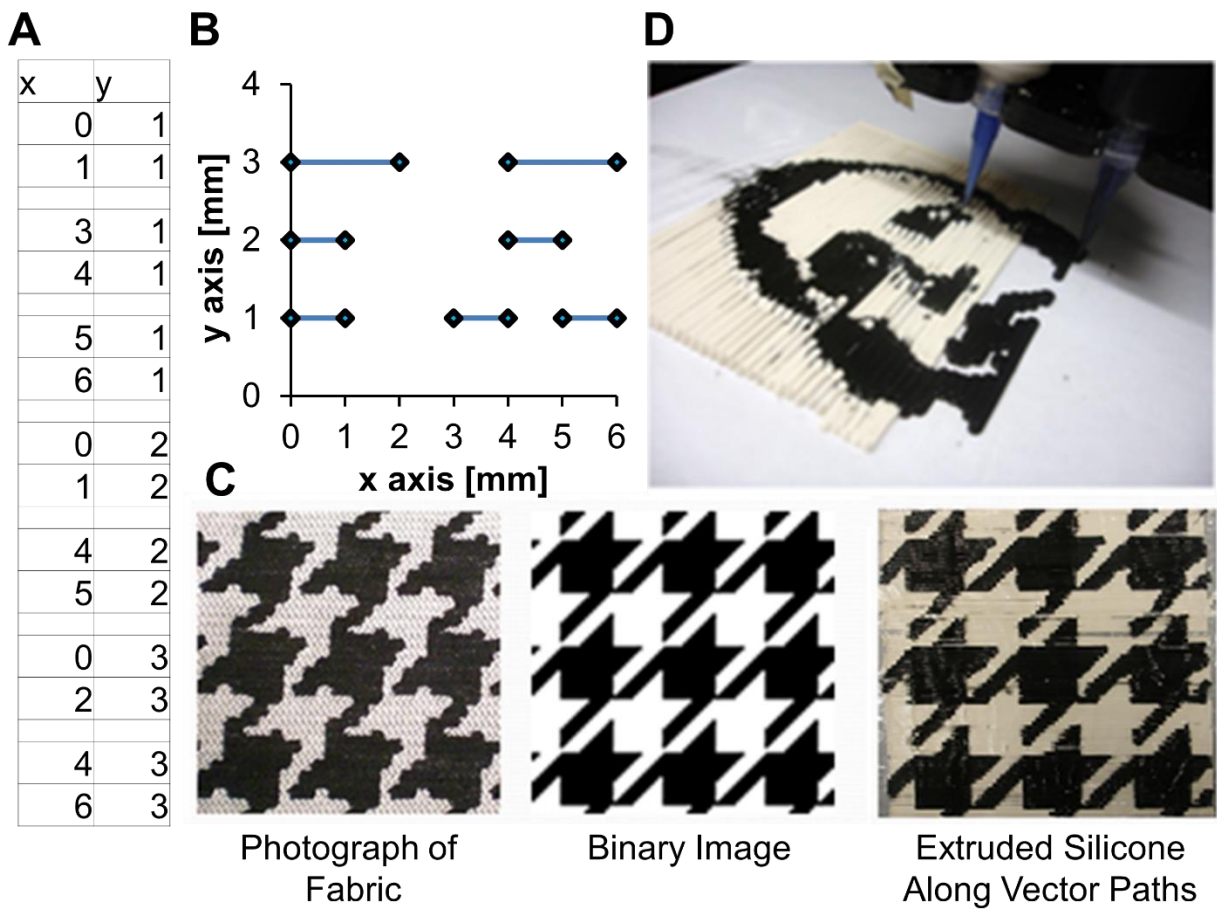


**Figure 5.1 Image defined heterogeneity - image based vector printing patterns in multiple materials.**

(A) In the Fab@Home™ vector printing format, the user defines lines to be printed. In the vector format, the start and end point are grouped with each other. (B) The printing platform recognizing this will observe this pair and will extrude material starting at the first point and ending at the second. (C) Images can be converted into printable files. In this example a photograph was converted to a 2D binary image, an algorithm identifies the different color regions and assigns materials. Coordinate points were designated within each region and then connected to create printable vector files. Silicone sealant was extruded by the printer into patterns specified by the vectors, right (C) and (D).

### **5.3.9 Second Algorithm: Application of Gradients within Shapes and Generation of Printable Vectors**

Functions are used to generate coordinate points within a shape assigned to different materials and those points are connected to vectors using a 2<sup>nd</sup> algorithm. This can be used to define gradients of material within a desired shape (Figure 5.2). Individual heterogeneous layers were printed with PEG-DA700 hydrogel solution mixed with red and green dye to visualize the pattern and to assess accuracy compared to the intended geometry (Figure 5.3A). Print parameters for the gradient print were: nozzle diameter 16G; deposition rate 0.004; path speed 7.5 mm/s; path width 1.0mm; and path height 0.8mm. Individual gradient layers were assessed directly after printing (uncrosslinked) to determine printer/pattern fidelity (Figure 5.3A and 5.3D). These layers when built up and photo-crosslinked to form a 3D gradient construct (Figure 5.3B) and were generated from a linear gradient function (Figure 5.3C). Hydrogel layers were imaged using an epifluorescence stereomicroscope (SteREO Discovery.V20; Zeiss, Germany). To assess fidelity the image of a target geometry and an image of a printed layer were appropriately scaled, overlapped, and compared in Matlab to calculate percent accuracy. This was done for circular and diagonal gradients to test the effect of pattern on accuracy.

### **5.3.10 Region Dither Vector (RDV) Algorithm: Converting Tissue Heterogeneity into Vectors**

We developed an algorithm that combines the ideas of algorithm 1 and 2 to extract tissue heterogeneity information from images (Figure 5.4). The more detailed process is summarized as a flowchart (Figure 5.5). The algorithm converts image slices, such as those from CT, into printer vector instructions. The object or tissue is first extracted from the image slices using a threshold defined by the user. The object is then separated into distinct materials using a dithering algorithm with the threshold defined

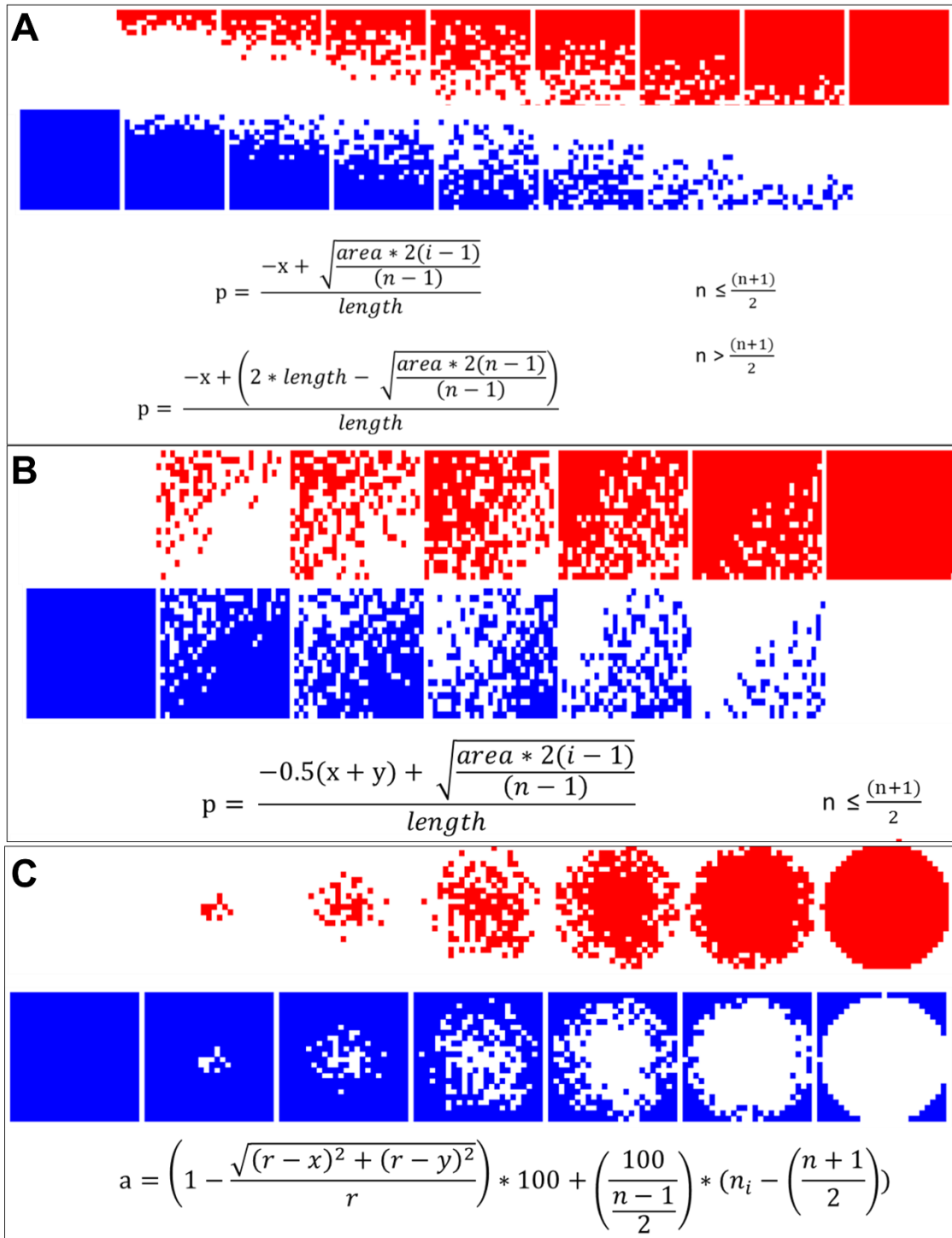


**Figure 5.2 Prescribed component heterogeneity - function generated geometries in Matlab and Excel.**

Functions can be applied within a shape to define gradients of material **(A)** Example of a linear gradient within a cube starting at one edge. Each layer is shown from left to right. **(B)** Example of a linear diagonal gradient within a cube starting at one corner. **(C)** Example of a circular/cone gradient within a cube.

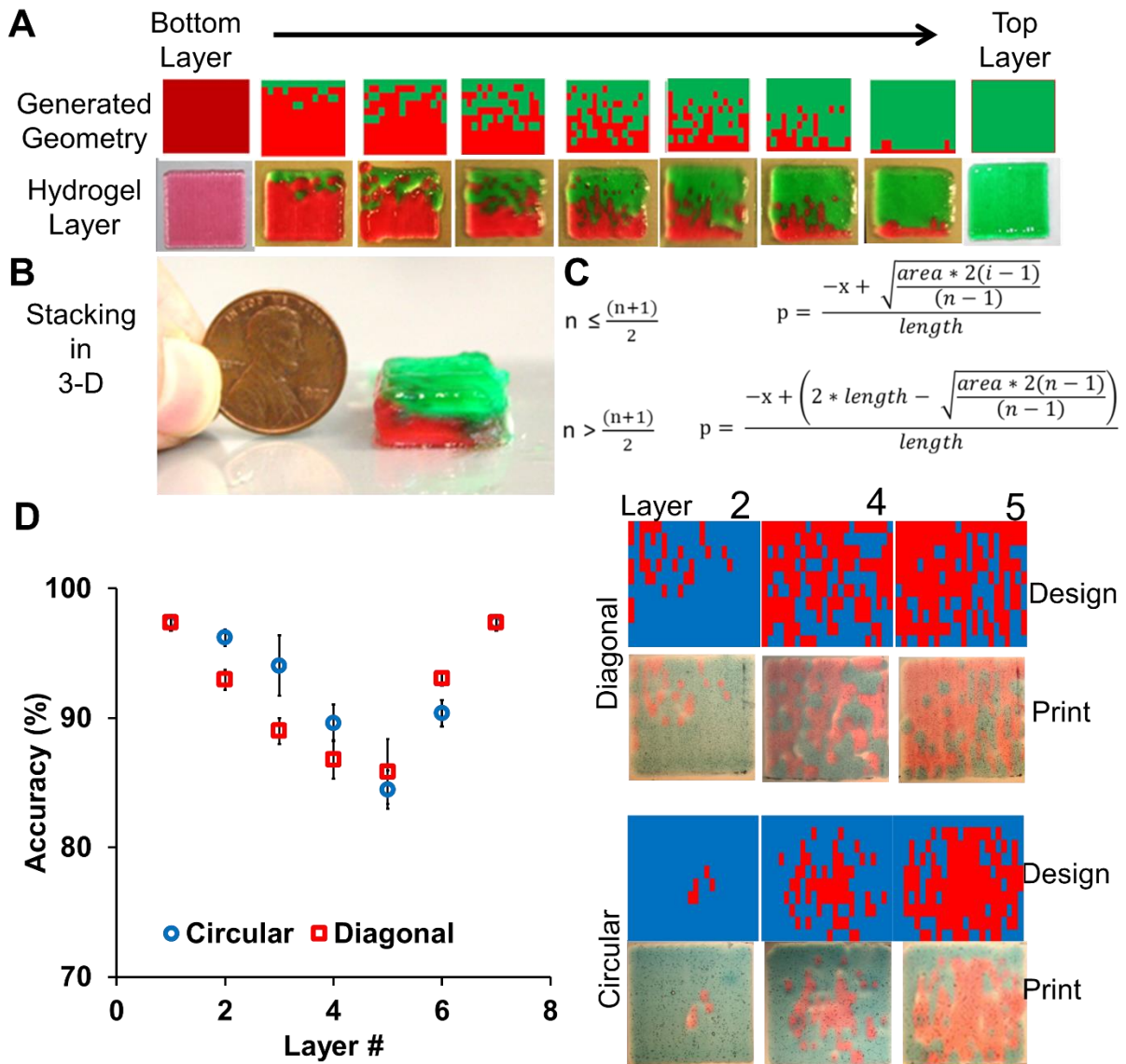


**Figure 5.3 Prescribed component heterogeneity - function generated geometries converted to vectors and fabricated in hydrogels.**

Functions can be applied within a shape to define gradients of material **(A)** Example of a linear gradient within a cube starting at one edge. Each layer is shown from left to right with the design of the layer shown above the printed hydrogel layer. Red and green dye was added to the hydrogel to visualize the pattern. **(B)** The layers shown in A were printed into a 3D photo-crosslinked hydrogel gradient structure. **(C)** Function defining material distribution printed in A and B. **(D)** Fidelity and Pixel value for red and green dye labeled hydrogels. Image of target geometry and printed layer overlap and compared to calculate percent accuracy for circular and diagonal gradients.

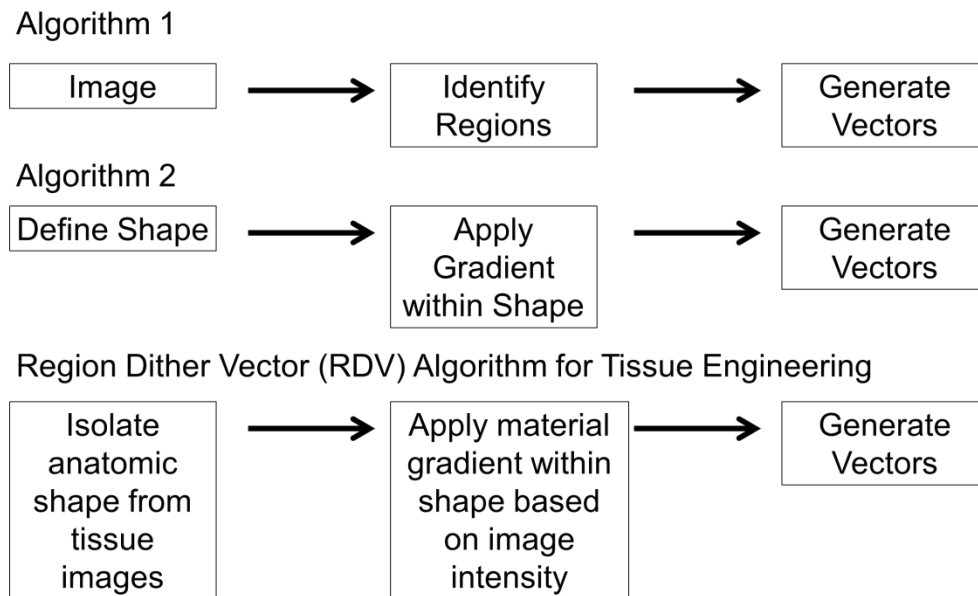


**Figure 5.4 Brief algorithm function schematic. The RDV algorithm combines two strategies for generating printable vector files.**

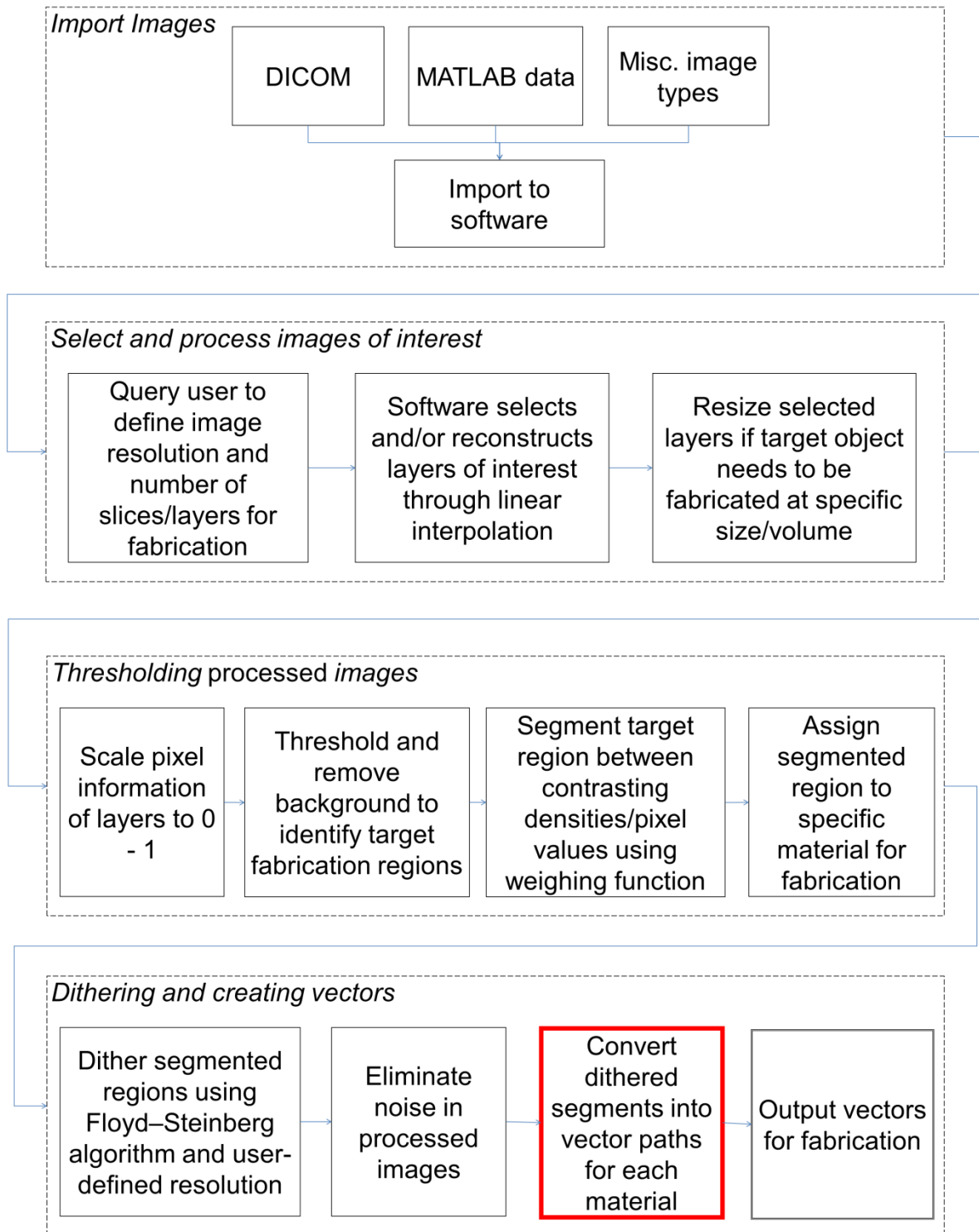


**Figure 5.5 RDV Algorithm. flowchart for fabricating geometries exhibiting anisotropic heterogeneity based on prescribed images.**

by the user. Since the printer has difficulty printing dots, all the holes and islands in the dithering results must be removed. This must be done with minimal distortion to the original shape. Lastly, the software outputs the printer instructions that will print the paths as defined by the dither results. More detail on the conversion of dithered points into vectors step (highlighted in red in the Figure 5.5 flowchart) is described in Figure 5.6.

The algorithm dithers images into coordinates/ or points associated with a material assignment. In the Figure 5.6 diagram, the dithered results or coordinate points are represented by red and blue boxes. Once images are dithered into coordinates that would be printed in different materials, the software creates vector paths for fabricating the target model. A starting segment is first selected and then compared to the neighboring segment (Figure 5.6A). If the segments are assigned to the same material, a vector between the segments will be created. This process repeats until sufficient numbers of vector paths have been generated for fabricating the target geometry. Directional priority is incorporated into algorithm to maximize efficiency and minimize error. (Figure 5.6B). Without directionality a non-ideal scenario of converting dithered segments into vectors can occur (Figure 5.6 B1). When comparing the starting segment to the adjacent one, the software needs to understand which direction it should search for segments with matching materials. If no directionality is specified, the resulting vector paths can exhibit numerous directional changes. This requires more movement of the printer tools, which can lead to inefficient and inaccurate fabrication. In Figure 5.6. B1, the vectors continuously change in directions, which is non-ideal for fabrication.

To enhance fabrication efficiency, we prioritize the direction that the program should search for matching coordinates (Figure 5.6B2). We first instruct the program to search

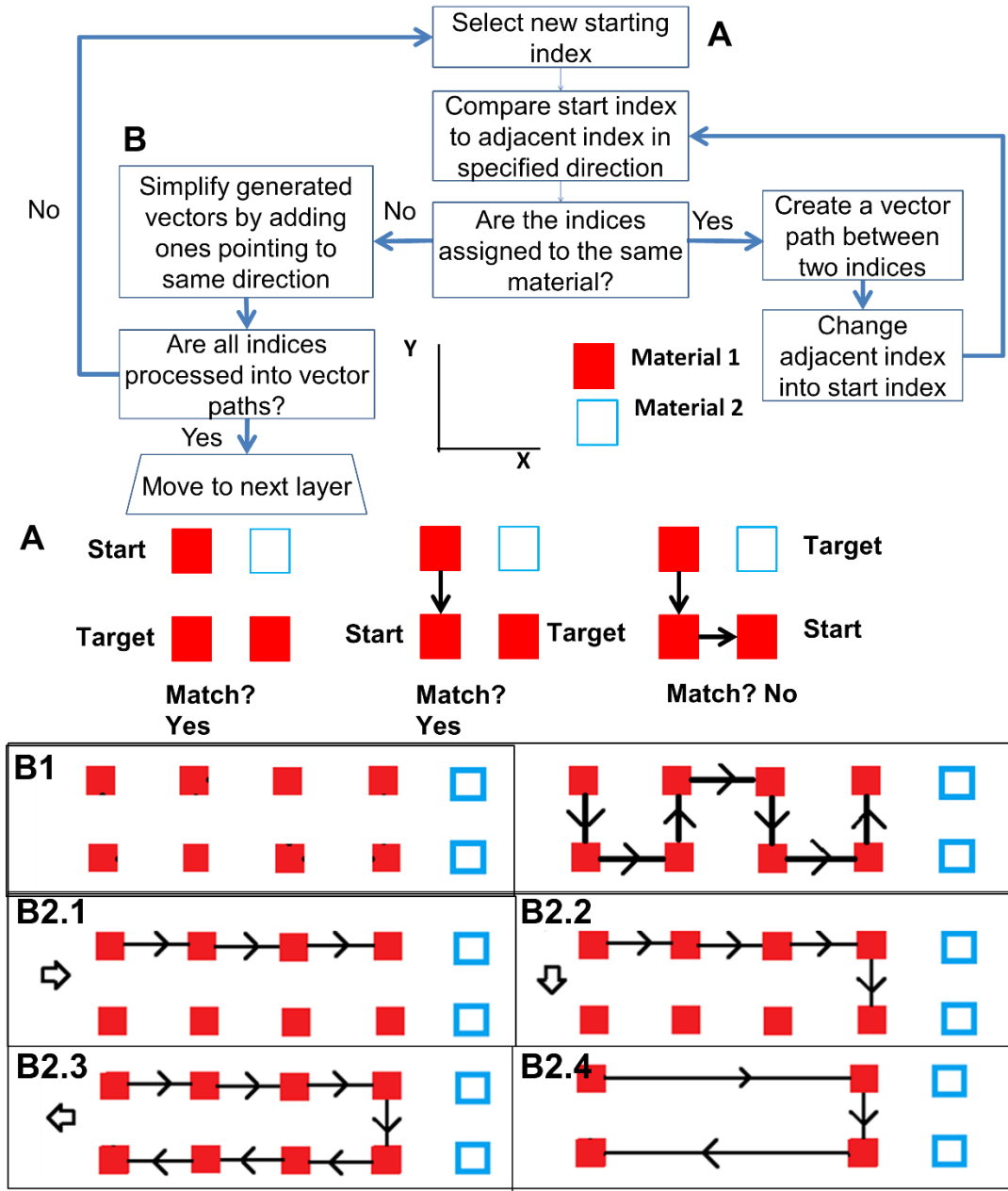


**Figure 5.6** Flowchart summary and diagram for converting dithered paths into vectors paths.

Once images are dithered into segments that would be printed in different materials, the software creates vector paths for fabricating the target model. **(A)** Starting coordinate is first selected and then compared to the neighboring coordinate. If the coordinates are assigned to the same material, a vector between the coordinates will be created. This process repeats until sufficient numbers of vector paths have been generated for fabricating the target geometry. **(B)** Directional priority is incorporated into algorithm to maximize efficiency and minimize error. **(B1)** Without directionality a non-ideal scenario of converting dithered coordinates into vectors can occur. **(B2)** By prioritizing the direction that the program should search for matching coordinates, smoother more continuous vector paths are created.

in the +x direction (Figure 5.6B2.1). The software compares the starting material coordinate to the adjacent one directly to the right, and if the materials match, a new vector path is created. This process continues until no more matching index can be found along the +x direction. The program then searches in the second direction (-y direction) (Figure 5.6B2.2), and vectors paths are created in the -y direction if matching material points are found. If there is no match, the software moves onto the next direction (-x direction) (Figure 5.6B2.3). Once all directions have been explored, the newly formed vectors along same directions are added to form continuous vector paths (Figure 5.6B2.4). A new material point that has not been processed is then selected as starting point, and the comparison process repeats until all coordinate points have been processed. By prioritizing the direction that the program should search for matching coordinates, smoother more continuous vector paths are created.

### **5.3.11 MicroCT and MRI Scanning of Aortic Valve Tissue**

A porcine aortic valve conduit obtained fresh at slaughter (Shirk Meats, Himrod, NY) was fixed in formalin and scanned with the leaflets in a partially open position via micro-CT at 100  $\mu\text{m}$  voxel size, 80 keV, 30 mA, 800 angles, 30 ms exposure time, 30 gain, and 20 offset (eXplore CT120; GE Healthcare, United Kingdom). For  $\mu\text{CT}$  the valve was positioned on a foam tray and scanned in air. For the MRI scan the same valve was embedded in agarose. 1.5% agarose was added to deionized water, the solution heated until the agarose dissolved, the solution partially cooled, and then used to embed the valve tissue. The MRI scan performed on the valve was type T1, resolution: of 0.2 mm x 0.2 mm with a slice thickness of 0.3 mm (Model: Signa HDxt, GE Medical Systems). MicroCT and MRI scans were processed using the RDV algorithm (Figure 5.7 and Figure 5.8).

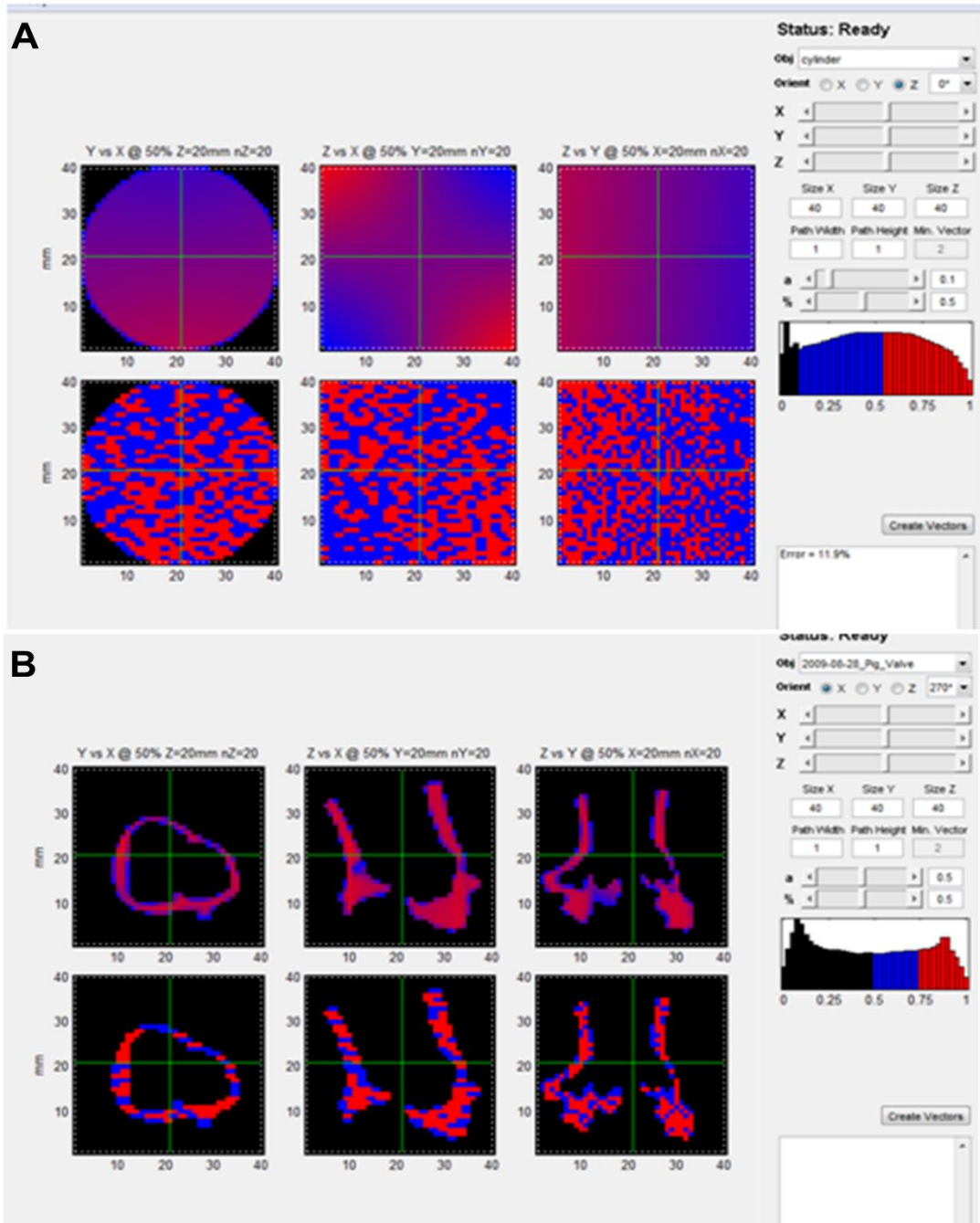


**Figure 5.7** User interface of RDV algorithm software written in Matlab.

**(A)** A cylinder exhibiting a gradient applied through the image is dithered into vertices. The top row represents the object with original data segmented out of the background for different planes (y versus x, z versus x, and z versus y), and the bottom row represents the dithering results. **(B)** Set of CT scans of a pig aortic heart valve, original data segmented out of background and then dithered into points at the resolution requested by the user for printing.

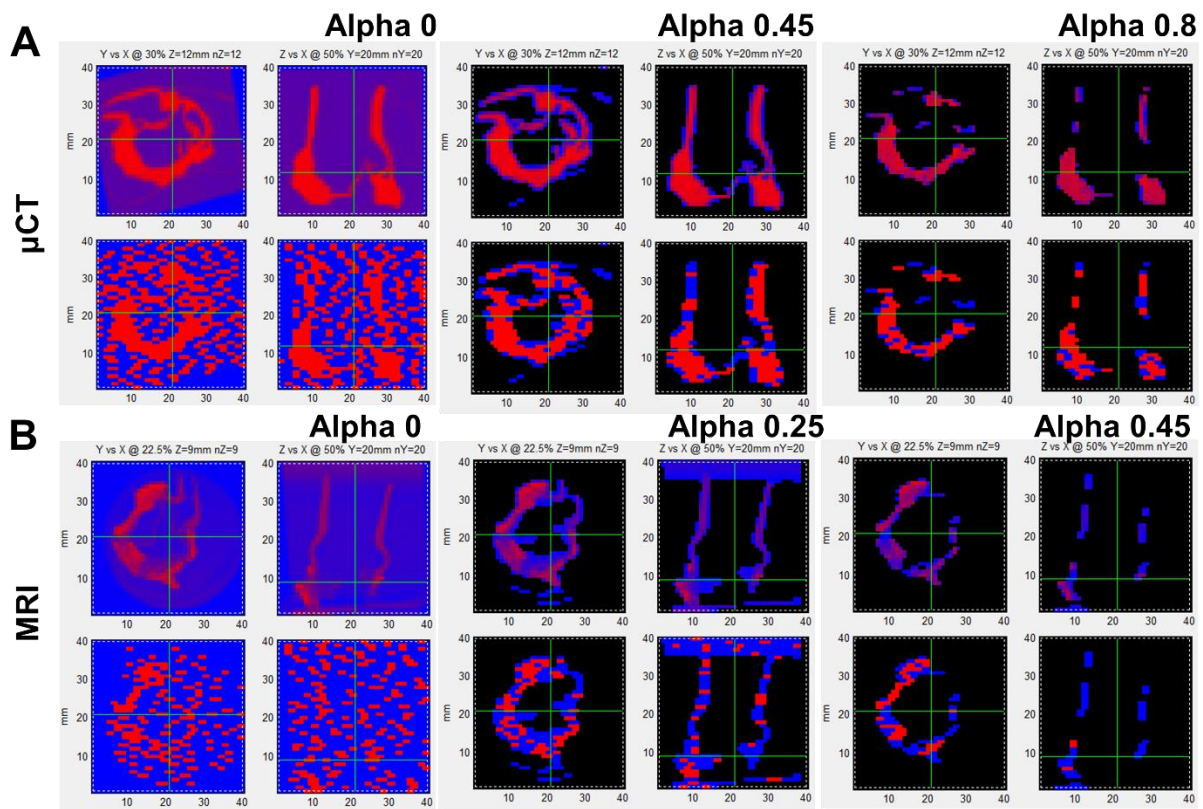


**Figure 5.8. Interpretation of  $\mu$ CT and MRI intensity values for heterogeneous vector generation.**

(A)  $\mu$ CT (B) MRI scan images of a fixed porcine aortic valve were dithered and converted to printable formats. The valve base with leaflets is shown with different threshold (alpha) settings (left to right) to segment out the tissue region from the background. Material distribution was arbitrarily set at 50:50 red and blue. For  $\mu$ CT the valve was scanned in air, and in MRI the valve was embedded in agarose.

Other parameters of the scan were: Series Description: 'SPGR 45deg nex=8, 0.2 x 0.2 x 0.3' ;Repetition Time: 31.6550; EchoTime: 7.4200; Number Of Averages: 8; Imaging Frequency: 127.7133; Imaged Nucleus: '1H'; Echo Number: 1; Magnetic Field Strength: 3; Device Serial Number: '0000000COR373216'; Software Version: '15\LX\MR Software release:15.0\_M4A\_0947.a'; Protocol Name: 'SPGR 45deg nex=8,0.2 x 0.2'; Receive Coil Name: 'HD WristCoil'.

### **5.3.12 Vector Printing MEGEL/PEG-DA Hydrogels**

Alternating line vector files were designed in Microsoft Excel as a simplified geometry to test heterogeneous path mixing and crosslinked scaffold fidelity. Previously assessment of fidelity and printing parameters has been done with single material constructs/scaffolds (Ballyns, Cohen et al. 2010; Hockaday, Kang et al. 2012; Kang, Hockaday et al. 2013). MEGEL/PEG-DA was used because of its cell compatibility and printability. We found that photo-crosslinking of hydrogel scaffolds bleaches food dye so a cellularized test was designed to assess fidelity after photo-crosslinking and pattern maintenance at time points in culture. (Refer back to Figure 5.3 for assessment of printed layers prior to photo-crosslinking or for non-photo-crosslinking hydrogels, and Figure 5.3.) Signs of color bleaching are visible in the base of the valve construct in Figure 5.9. The gelatin component in the hydrogel required the nickel chromium wire heating coils to be applied to the syringe barrel and tips to maintain temperature at 37°C during printing (Figure 5.10C). Without the heating coil the working time of the MEGEL/PEG-DA solution after it is removed from the water bath is very short, the viscosity will change as the solution cools (affecting deposition), and it will solidify in the syringes.

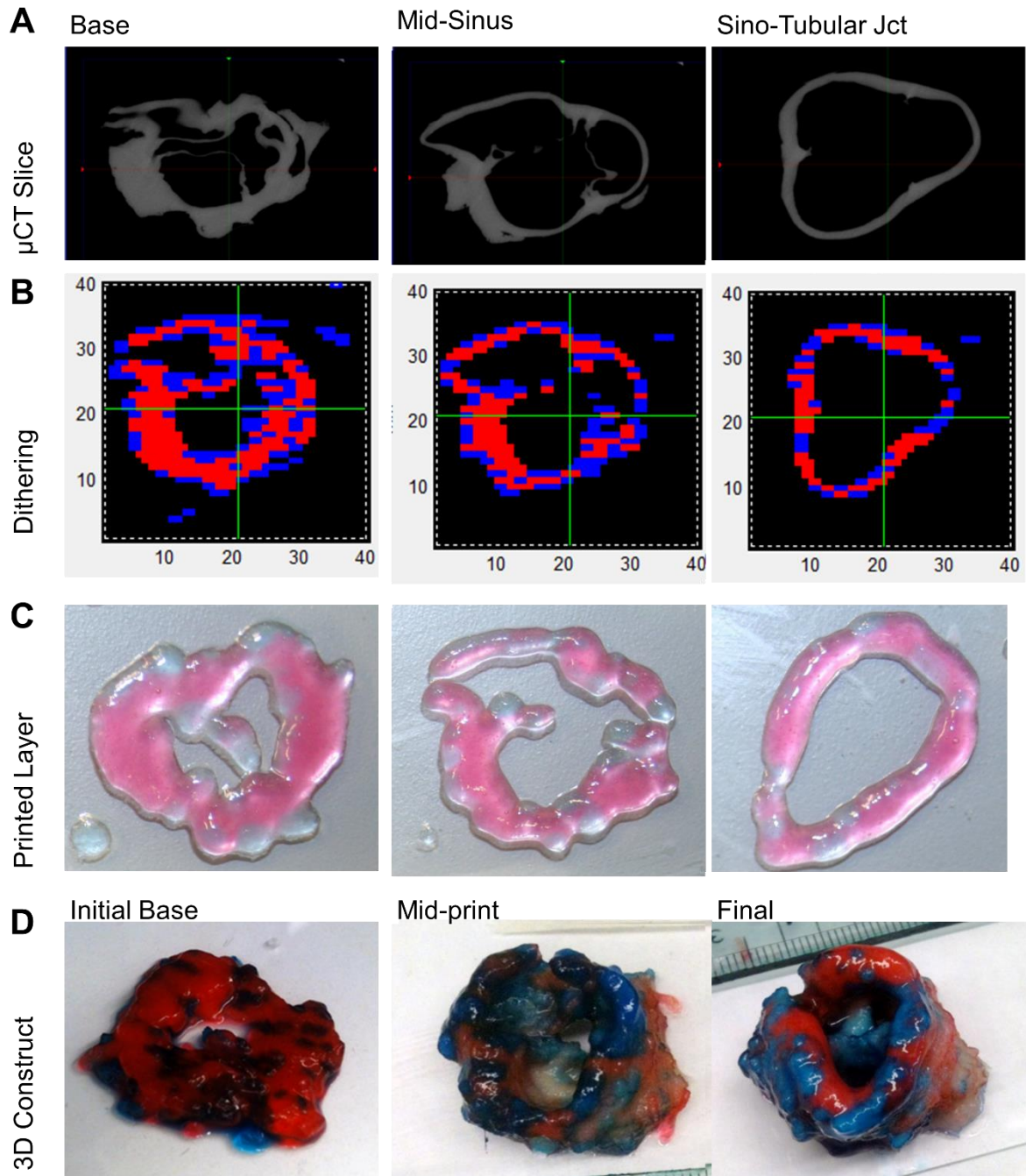


**Figure 5.9 Image defined material heterogeneity in printed hydrogel valve constructs.**

(A)  $\mu$ CT image slices in MicroView™ at base, mid sinus, and sinotubular junction of a porcine aortic heart valve (B) Defined tissue region and dithered material designation of valve slice generated in Yeh-Cheng algorithm. (C) Single heterogeneous valve layers printed in two different hydrogel solutions corresponding to  $\mu$ CT image slices. (D) 3D heterogeneous valve printed with hydrogel in stages. Left to right – initial printed layers, partially printed scaffold top view, final heterogeneous structure.

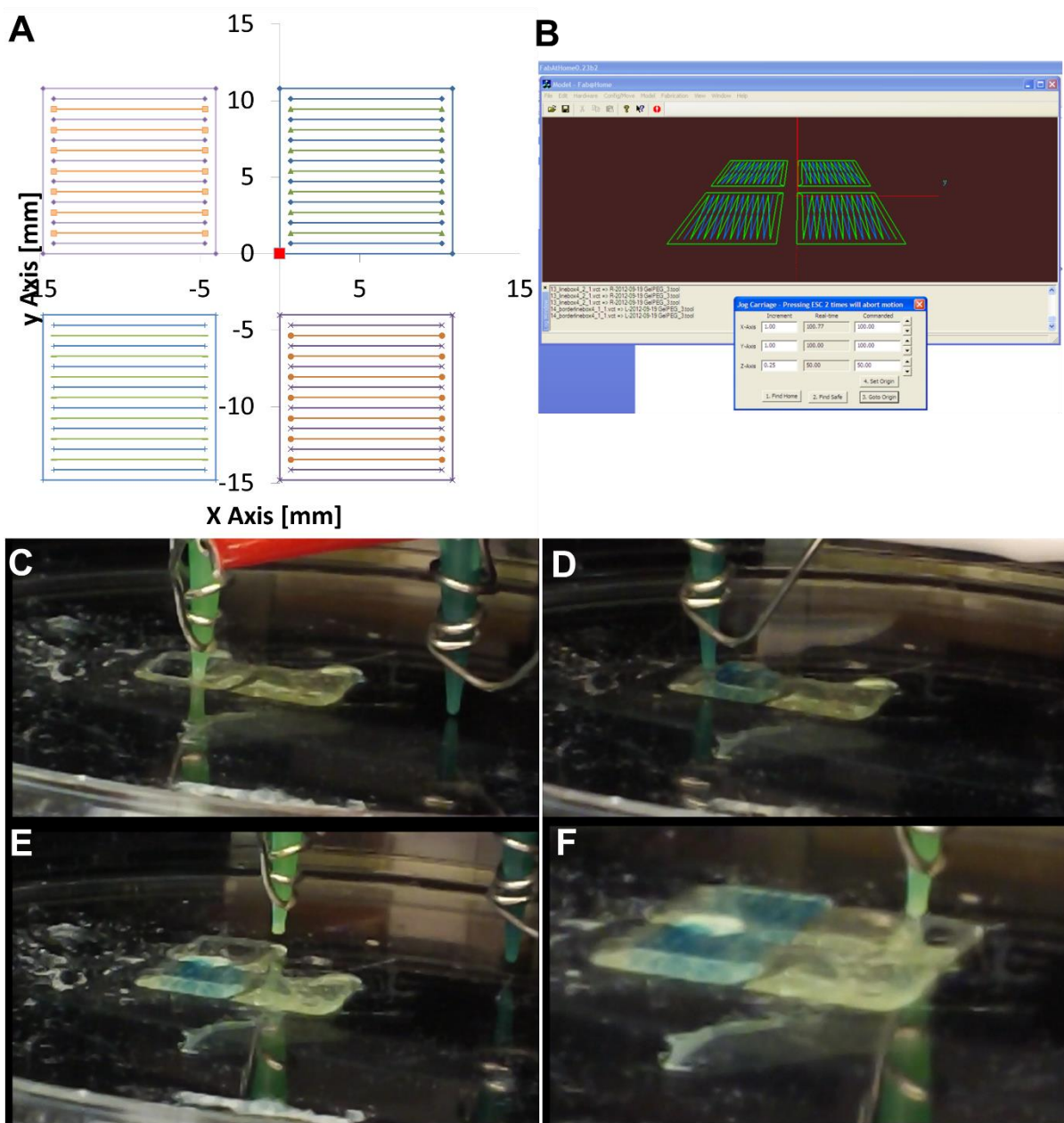


**Figure 5.10. Setup for printing line pattern heterogeneous hydrogel constructs**

(A) Vector paths were generated and plotted in Microsoft Excel and then formatted into vector files for printing. (B) The paths were grouped into files, and the priority set in Fab@Home program based on which materials and paths we wanted to be printed 1<sup>st</sup>. The first hydrogel precursor solution is used to trace out the border and the 1<sup>st</sup> set of lines (C), then the second material fills in the alternating lines (D) This repeats for 4 scaffolds per print (E), and (F). For this geometry a 0.625 path width, was used, and the printer syringes were loaded containing MEGEL/PEG-DA3350 0.075w/v% Irgacure (colorless here), and a solution of MEGEL/PEG-DA3350 0.75w/v% VA086 (blue dye added) each with a 0.800 mm tip. Heating coils were attached to the syringes to maintain the hydrogel temperature at 37C and keep the gelatin component a liquid.

### 5.3.13 Quantifying Cell Distribution within Crosslinked Heterogeneous Hydrogel Constructs

In order to use hydrogels for tissue engineering, and control the dimensions of fabricated constructs, we need to anticipate construct geometry, based on swelling and mixing introduced by the printer. Pattern accuracy for individual scaffolds after photocapsulation bioprinting and cell distribution within hydrogels was assessed using Image J and fluorescent imaging. HADSMC were tagged with either Cell Tracker Red or Cell Tracker Green dye and added to MEGEL/PEG-DA hydrogel precursor solution which was printed into a heterogeneous alternating line pattern scaffold. The construct was photo-crosslinked post-printing for 5 minutes at  $2 \text{ mW/cm}^2$ . The encapsulation solution was made with 0.075%w/v Irgacure. The compressive modulus of this hydrogel when crosslinked is  $42.0.3 \pm 8.2 \text{ kPa}$  in the 5 to 15% strain range and the estimated weight based swelling ratio of the hydrogel is 13.7 (Chapter 4). The HADMSC/MEGEL/PEG-DA3350 hydrogel constructs were cultured to 1, 2, and 3 days. Hydrogel constructs were imaged using an epifluorescence stereomicroscope (SteREO Discovery.V20; Zeiss, Germany).

A region count macro and the particle analysis function in Image J enables counting of cells in specific regions to analyze fluorescent images (Figure 5.11A). In image J the steps used to count the number of cells in printed regions to determine distribution were: 1<sup>st</sup> the image scale is set and the pixel/units are used to define the macro for an image taken at a particular magnification, 2<sup>nd</sup> the color channels are split for a given red/green stripe image, 3<sup>rd</sup> the dotted line tool is used to add a marker dot per each bin, 4<sup>th</sup> the channel image is thresholded so that the cells (which should be bright/higher intensities) are clear from the background fluorescence (which is actually pretty high for the hydrogels), and then 5<sup>th</sup> the macro which has arbitrary user defined size bins is used with the analysis particles function to count cells within a size range. The dotted line

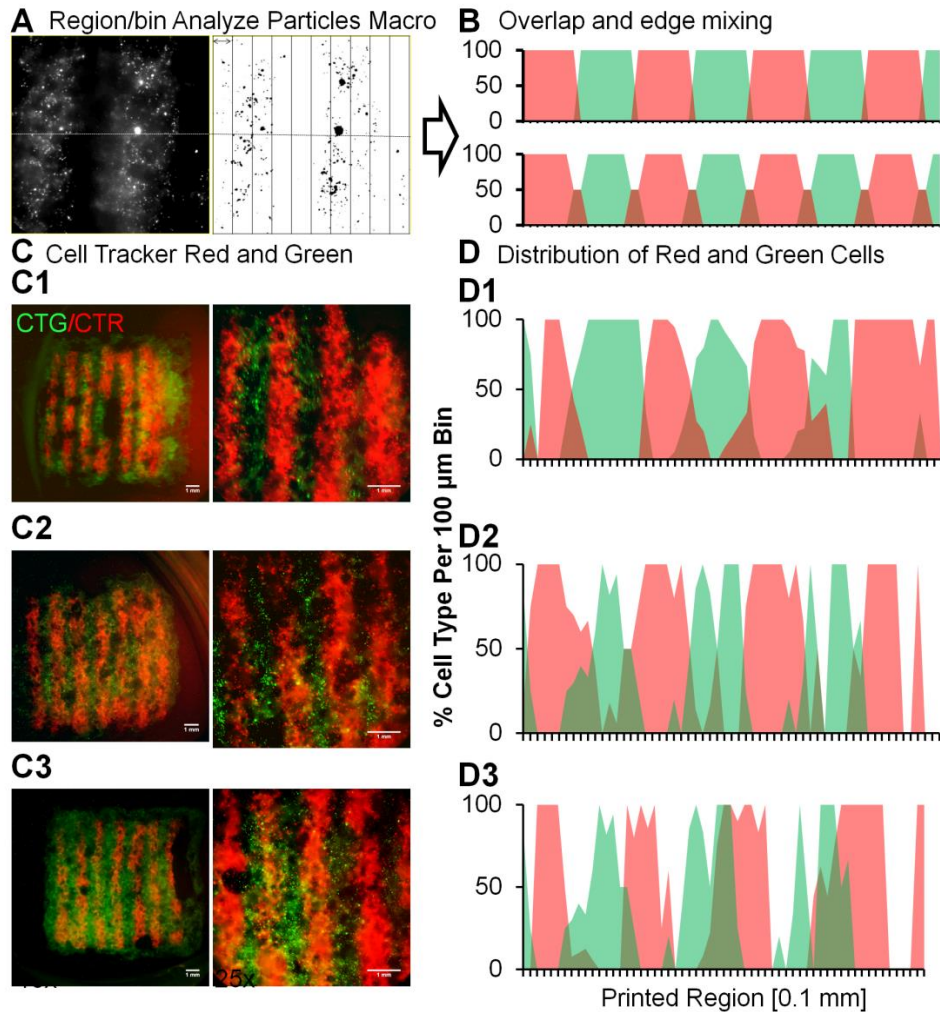


**Figure 5.11 Cell distribution within crosslinked heterogeneous hydrogel constructs.**

Pattern accuracy for individual scaffolds after printing and cell distribution within hydrogels was assessed using image J and fluorescent imaging. HADSMC were tagged with either Cell Tracker red or Cell Tracker Green dye and added to MEGEL/PEG-DA hydrogel precursor solution printed into a heterogeneous alternating line pattern scaffold, and photo-crosslinked for 5 minutes at  $2 \text{ mW/cm}^2$ . **(A)** A simple region count macro and the particle analysis function in Image J enables counting of cells in specific regions. Color channels (red or green) were thresholded and bin/counted to generate histograms of %cell type per  $100 \mu\text{m}$  wide column along the scaffold. **(B)** Theoretical red and green cell distribution through scaffold depending on tip size and path width. Mixing at the edges of the extruded lines occurs if tip size is greater than path width. **(C)** Representative images of line scaffolds printed with red and green labeled HADSMC and **(D)** the percentage of red and green cells across the scaffold corresponding to the 25X image, Top to bottom, scaffold cultured for 1, 2, 3 days. Left to right printed scaffold at 10X, 25X (used for analysis), and histogram. If compared to a 'no edge mixing model these scaffolds have 79%, 83%, 63% accuracy.

step is important so that every bin has at least one particle. This is subtracted out later. This is necessary so that empty bins (no cells counted) are reflected in the output data. The cell count data from image J (red and green in this case) is converted to a histogram of percentage of red and green per bin region of the scaffold. 25X images were analyzed in this study to generate histograms of %cell type per 100 $\mu$ m wide column along the scaffold. Theoretical red and green cell distribution through scaffold was estimated based on tip size, path width, and swelling of the hydrogel. The distribution of cells throughout the scaffold could also change depending on how well optimized the print parameters are (Kang, Hockaday et al. 2013). Mixing at the edges of the extruded lines is anticipated if the actual path width/path space (based on tip size, deposition rate, print speed, distance to stage, and viscosity of solution) is greater than the path space of the geometry (Figure 5.11B and Figure 5.12A). The theoretical distribution of cells through the scaffold was compared to the actual distribution of cells across the constructs to estimate the pattern fidelity of a given construct.

## **5.4 Results**

### **5.4.1 Layer Fidelity of Prescribed Component Heterogeneity**

Heterogeneous gradients can be printed directly into hydrogel scaffolds and high pattern fidelity results regardless of 3D gradient (Figure 5.3D). A diagonal gradient and a circular gradient design when compared to the printed hydrogel layer have similar accuracy changes through the scaffold. The average percent accuracy and standard deviation for the circular gradient layers decreased and then increased through the print (layer 1, 2, 3, 4, 5, 6, 7 percent accuracy was  $97.36\pm 0.62\%$ ,  $96.21\pm 0.63\%$ ,

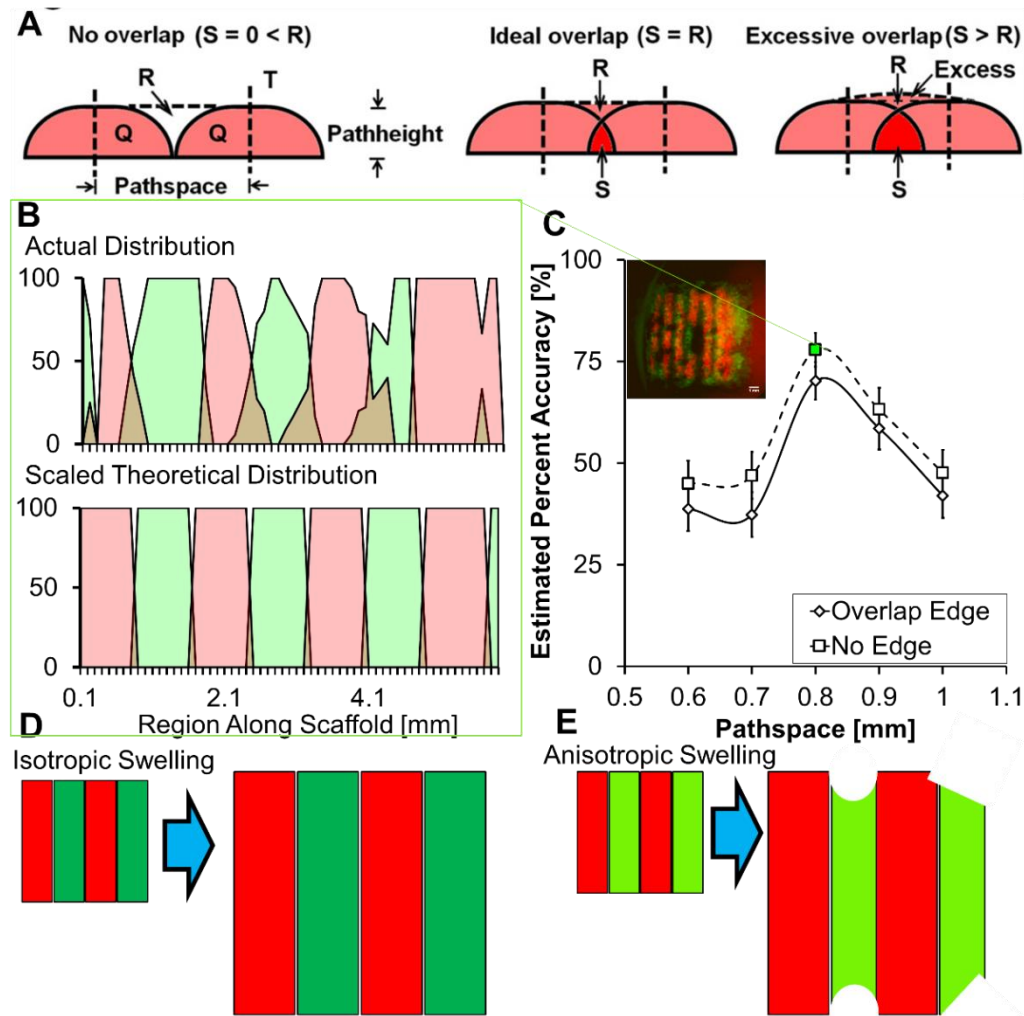


**Figure 5.12 Assessment of fabrication accuracy changes depending on path mixing during printing and the post-fabrication material properties of the hydrogel.**

**(A)** Boolean model of printed hydrogel lines for predicting optimal path space that yields uniform layer (Kang et al 20013). Q: half cross-sectional area of each line; R: void region between printed lines; S: overlapping region; T: rectangular region formed between the centers of the two lines. This model assumed that when lines are overlapped, the void region R is reduced by equal volume of the overlapping region S. Some path overlap is needed so that the discrete materials are contiguous, and the printed heterogeneous layer is sound. **(B)** Distribution of cells across day 1 printed scaffold (Figure 11C1) and the optimal scaled theoretical distribution are compared to obtain a percent error estimate. **(C)** Optimization of % accuracy estimate for the day 1 scaffold (Figure 11C1), comparing the percent accuracy versus the path space scaling with and without edge overlap. **(D)** Diagram of printed construct undergoing isotropic swelling. **(E)** Diagram of mechanically heterogeneous hydrogel construct experiencing anisotropic deformation due to non-uniform material swelling.

94.04±2.34%, 80.61±1.42, 84.47±1.46, 90.35±1.02, 97.36±0.62). The average percent accuracy and standard deviation for the diagonal gradient layers decreased and then increased through the print (layer 1, 2,3, 4, 5, 6, 7 percent accuracy was 97.36±0.62%, 96.95±0.78%, 89.25±1.01%, 80.79±1.49, 85.86±2.52, 93.06±0.55, 97.36±0.62).

#### **5.4.1 RDV Algorithm: Converting Tissue Heterogeneity into Vectors**

We used the RDV algorithm to process images into printable format through a user interface written in Matlab (Figure 5.7). This can be done for arbitrary shapes, such as a cylinder exhibiting a gradient applied through the image (Figure 5.7A) or medical images such as CT scans of a porcine aortic heart valve (Figure 5.7B). In each image, the top row represents the object with the original data segmented out of the background, and the bottom row represents the dithering results. At this interface the user can set the 'alpha' channel to segment out the tissue region from the background and the user sets the material distribution throughout the tissue region. Images from both  $\mu$ CT and MRI scans of an aortic valve were processed with the RDV algorithm software (Figure 5.8A and 5.8B). Tissue heterogeneity is detectable in both types of scans and can be converted to a dithered and printable format. For the scans used in this study when comparing between leaflets and the aortic valve sinus wall the difference is more pronounced for  $\mu$ CT scans. When the scans are run through the RDV algorithm to create printable vectors the  $\mu$ CT scans give more distinction between the root and the leaflet.

#### **5.4.2 Printing of Heterogeneous Anatomical Geometry**

The utility of the RDV algorithm was demonstrated by fabricating a heterogeneous valve construct using two hydrogel precursor solutions based on the  $\mu$ CT scan (Figure 5.9). The algorithm effectively identifies regions of heterogeneity in the images, it isolates the anatomic shape from the background, it applies a heterogeneous material gradient

throughout the valve geometry based on the intensity values present in each image slice (Figure 5.9B), and then generated printable vectors from that information. Each layer of the geometry when printed had discretized red and blue labeled hydrogel precursor solution throughout (Figure 5.9C). The heterogeneous layers were then deposited in 3D with simultaneous photocrosslinking with the low power LED array, to form a hydrogel valve construct (Figure 5.9D).

#### **5.4.3 Cell Distribution within Crosslinked Heterogeneous Hydrogel Constructs**

HADMSC were printed into a linear stripe pattern with MeGel/PEG-DA hydrogels so that a different gel cell mixture alternates with the other. (Figure 5.11C). A heterogeneous pattern was present in the scaffolds at 3 days in culture. The histograms of percentage of red and green cells across the scaffold corresponding to the 25X image (Figure 5.11D) show that the alternating pattern of cells is present at day 1, 2, and 3. To estimate fidelity it is possible to scale the theoretical distribution of cells within scaffold (Figure 5.12). If compared to a 'no edge mixing' model with the path space expanded to 0.8 these scaffolds have 78%, 83%, 63% accuracy.

The scaffolds were compared to a 'no edge mixing' model distribution with the path space expanded to 0.8 because the highest percent accuracy occurred at that scaling. The optimization data is shown for the day 1 scaffold (Figure 5.11C1), comparing the percent accuracy verses the path space scaling with and without edge overlap (Figure 5.12D and 5.12C). The printed scaffolds better matched the theoretical model with no edge mixing. While there is some edge mixing observed in the constructs (Figure 5.11D) the cell distribution does not match a 0.1 mm overlap. The estimated path space upon printing was nearly matched between the extrusion strand of deposited precursor solution and the geometry (~0.6 to 0.625) (Kang, Hockaday et al. 2013), so the degree of overlap should be minimal. These constructs were removed from culture and

imaged, and each construct was assessed for pattern fidelity. Although it was not done for this study, one could make comparisons between days, tracking the construct and baseline print fidelity day by day for a given material combination and geometry determined.

## **5.5 Discussion**

By combining the methods to print anatomical geometries and establish spatial and material gradients, we demonstrate the ability of 3D printing to fabricate truly heterogeneous tissue geometries. This capability is uniquely enabled by 3D printing and is not possible using molding or classical fabrication techniques. Researchers are rapidly expanding the capabilities of 3D printing, particularly in the area of engineering heterogeneity into tissue constructs (*Fedorovich, Wijnberg et al. 2011; Fedorovich, Schuurman et al. 2012; Lee, Ahn et al. 2014; Pati, Jang et al. 2014; Wust, Godla et al. 2014*). There are an expanding number of materials and handling methods for heterogeneous printing(*Lee, Ahn et al. 2014; Pati, Jang et al. 2014*) and imaging advances in the realm of soft tissues and hydrogels(*Feng, Taraban et al. 2011; Curtis, Zhang et al. 2012; Franquet, Avril et al. 2013; Kotecha, Klatt et al. 2013*). These advances could be used in conjunction with our image processing and path generation RDV algorithm to enable better engineering of living tissues.

In this study, tissue heterogeneity information was extracted from  $\mu$ CT and MRI images of an aortic heart valve and converted into printable format. The algorithm effectively identifies regions of heterogeneity in the images, it isolates the anatomic shape from the background, it applies a heterogeneous material gradient throughout the valve geometry based on the intensity values present in each image slice, and then it generates printable vectors from that information. We demonstrate image-derived and arbitrary heterogeneous vector geometries by 3D printing of heterogeneous hydrogel

constructs both with dye labeled precursor solution and fluorescent labeled encapsulated cells. 3D printing or additive manufacturing strategies have previously generated computer aided design (CAD) files of tissues from CT and MRI and have used them to fabricate implants and tissue engineered constructs. CT imaging and 3D printing of hard tissues has dominated in this area, incorporating higher level structure to mimic cortical and trabecular bone (Schieker, Seitz et al. 2006; Tarafder, Balla et al. 2013; Zhang, Jones et al. 2013). Soft tissue constructs have generally only used gross shape information from CT and MRI and variations in intensity and the information describing structural heterogeneity within the tissue is thresholded out/processed out (Ballyns, Gleghorn et al. 2008; Hockaday, Kang et al. 2012). Investigators have incorporated regional heterogeneity into vertebral disc, cartilage-bone, blood vessel-bone, and ear cartilage-electronic combination constructs using 3D printing (Cohen, Malone et al. 2006; Fedorovich, Wijnberg et al. 2011; Schuurman, Khristov et al. 2011; Fedorovich, Schuurman et al. 2012; Mannoor, Jiang et al. 2013). 3D printed constructs have also demonstrated control of internal structure within a bulk shape, and investigators have designed geometries to mimic tissue microstructure, microvasculature, capillary branching structure, and distribution of more than one cell type (Bianchi, Rosi et al. 2007; Cui and Boland 2009; Lee, Debasitis et al. 2009; Lee, Pinckney et al. 2009; Lee, Lee et al. 2010; Lee, Polio et al. 2010; Tirella, Vozzi et al. 2011; Gaetani, Doevendans et al. 2012; Koch, Deiwick et al. 2012; Marga, Jakab et al. 2012; Miller, Stevens et al. 2012; Blais, Parenteau-Bareil et al. 2013; Michael, Sorg et al. 2013). In these efforts a variety of techniques have been developed to control and introduce heterogeneity of strength and stiffness, fiber structure, bioactivity, and differentiation inductive properties of the microenvironment into tissue engineered constructs. Our algorithm could be applied with these other techniques and potentially adapted with the functional-tissue-unit concept. This would enable anatomically derived macroscopic tissue shape and internal structure of functionally heterogeneous tissues.

While the hydrogel scaffolds shown here were cellularly and spatially heterogeneous, they were mechanically homogeneous (Figure 5.9 and 5.11). The precursor solutions in a given layer had the same polymer formulation and the same photoinitiator concentration and photo-crosslinking was used so that the light energy delivered was uniform. The consequence of this is that the swelling of fabricated heterogeneous valve constructs and the HADMSC/hydrogel constructs is effectively isotropic (Figure 5.12D). The isotropic swelling makes it straight forward to demonstrate high fidelity per printed layer. Two types of heterogeneous layer fidelity analysis were demonstrated for a simplified geometry and with more complexly heterogeneous layers. Labeling hydrogel solution with dye or using cell tracking fluorescent labels enables assessment of print fidelity. However, it is important to consider that when printing with hydrogels with dissimilar swelling ratios anisotropic swelling may occur (Figure 5.12E). A predictive model to assess shape fidelity and guide iterative engineering will need to take this into account (Figure 5.13). To completely account for hydrogel swelling in 3D heterogeneous scaffolds, depending on the complexity of the tissue to be engineered, a finite elemental analysis model may be needed.

Additionally, non-uniform swelling may also induce stress in the structure. In our previous work where we fabricated valve constructs using an STL valve geometry, we observe a significant effect of swelling on valve volumetric and layer specific shape fidelity using  $\mu$ CT (*Hockaday, Kang et al. 2012*). Other studies indicate that assessment of whole tissue heterogeneous pattern fidelity post-fabrication and then post-remodeling using  $\mu$ CT or MRI could be possible. Wust et al printed heterogeneous hydrogel scaffolds and found that by adding hydroxyapatite into their extrusion solution they could change the radiopacity of the material and the contrast for  $\mu$ CT in order to assess the heterogeneous pattern within the printed construct after swelling (*Wust, Godla et al. 2014*). However, one of the problems with CT is the inability to distinguish

**A**

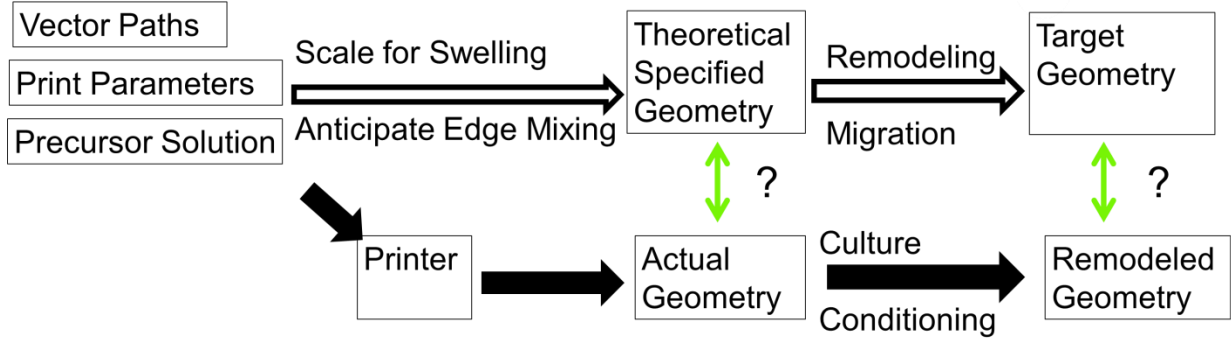


**Figure 5.13 Diagram of heterogeneous material printing scaffold shape fidelity and feedback.**

In order to use hydrogels for tissue engineering, and control the dimensions of fabricated constructs, we need to anticipate construct geometry, based on swelling and mixing introduced by the printer. The user controls the fabrication settings associated with the printer, the file geometry, and the materials and cells being used. Under these fabrication conditions a construct of a specific fidelity will be produced. When using hydrogels, the actual geometry post-fabrication and equilibrium with culture medium may differ significantly from printer input geometry. Therefore the user needs to anticipate contribution of swelling and mixing. In the context of tissue engineering important future work is to study the contribution of cell remodeling.

many soft tissues based on native contrast which are largely homogeneous in density (*Wathen, Foje et al. 2013*). For tissues where hydroxyapatite could introduce undesirable microenvironmental or differentiation characteristics (such as in heart valves where osteogenic differentiation is not ideal) MRI may be a better choice to assess heterogeneous pattern maintenance and remodeling. Studies have demonstrated that MR can be used to detect remodeling and differentiation in engineered tissues and to detect differences in modulus between different hydrogels (*Feng, Taraban et al. 2011; Curtis, Zhang et al. 2012; Kotecha, Klatt et al. 2013*). MR spectroscopy, imaging, and elastography could be used to analyze 3D printed hydrogel tissue remodeling and pattern maintenance in the entire structure.

When the MRI and  $\mu$ CT scans were run through the RDV algorithm to create printable vectors, we found that the  $\mu$ CT scans gave better distinction between the root and the leaflet. This is likely related to the fact that the  $\mu$ CT scans used here had a smaller slice thickness for the scan (0.1  $\mu$ CT scans verses 0.3 for the MRI scan) and was a better match for the dither and fabrication settings in the algorithm, and not an indication of feasibility, suitability, or capability of the imaging modality for this application. We demonstrate that we can extract heterogeneity from both MRI and  $\mu$ CT type images. However, identification of the physical or biological meaning of that information was not within the scope of this study. The intensity output of  $\mu$ CT is generally related to the material density and MRI image intensity is related to water proton relaxation time within a magnetic field after a radiofrequency pulse, diffusion, and water density (*Kotecha, Klatt et al. 2013*). Correlating image intensity values to fabricatable variables such as modulus or cell type is a critical next step in this research and for the application of this tissue heterogeneity algorithm. Ultimately  $\mu$ CT or MRI alone may be insufficient information to inform heterogeneous fabrication, and additional techniques

such as  $\mu$ CT detectable immunostaining to obtain 3D visualization of cell and molecular patterning within tissues (*Metscher and Muller 2011*) may be needed.

### **5.6 Conclusion**

The RDV algorithm presented in this study can be used to extract tissue heterogeneity and anatomic shape information from  $\mu$ CT and MRI images and convert those intensity values into a printable format for the scanned 3D tissue geometry. Image-derived and arbitrary heterogeneous vector geometries can be 3D printed into heterogeneous hydrogel constructs both with dye labeled precursor solution and fluorescent labeled encapsulated cells with high fidelity. This algorithm provides a tool for 3D printing heterogeneous, anatomically relevant tissue engineered constructs.

## REFERENCES

- Ahn, S., H. Lee, et al. (2014). "A direct cell printing supplemented with low-temperature processing method for obtaining highly porous three-dimensional cell-laden scaffolds." Journal of Materials Chemistry B **2**(18): 2773-2782.
- Ballyns, J. J., D. L. Cohen, et al. (2010). "An optical method for evaluation of geometric fidelity for anatomically shaped tissue-engineered constructs." Tissue Eng Part C Methods **16**(4): 693-703.
- Ballyns, J. J., J. P. Gleghorn, et al. (2008). "Image-guided tissue engineering of anatomically shaped implants via MRI and micro-CT using injection molding." Tissue Eng Part A **14**(7): 1195-1202.
- Benton, J. A., C. A. DeForest, et al. (2009). "Photo-crosslinking of gelatin macromers to synthesize porous hydrogels that promote valvular interstitial cell function." Tissue Eng Part A **15**(11): 3221-3230.
- Bianchi, F., M. Rosi, et al. (2007). "Microfabrication of fractal polymeric structures for capillary morphogenesis: applications in therapeutic angiogenesis and in the engineering of vascularized tissue." J Biomed Mater Res B Appl Biomater **81**(2): 462-468.
- Blais, M., R. Parenteau-Bareil, et al. (2013). "Concise review: tissue-engineered skin and nerve regeneration in burn treatment." Stem Cells Transl Med **2**(7): 545-551.
- Bunnell, B. A., M. Flaata, et al. (2008). "Adipose-derived stem cells: isolation, expansion and differentiation." Methods **45**(2): 115-120.
- Chandler, E. M., C. M. Berglund, et al. (2011). "Stiffness of photo-crosslinked RGD-alginate gels regulates adipose progenitor cell behavior." Biotechnol Bioeng **108**(7): 1683-1692.
- Cohen, D. L., E. Malone, et al. (2006). "Direct freeform fabrication of seeded hydrogels in arbitrary geometries." Tissue Eng **12**(5): 1325-1335.
- Colazzo, F., A. H. Chester, et al. (2010). "Induction of mesenchymal to endothelial transformation of adipose-derived stem cells." J Heart Valve Dis **19**(6): 736-744.
- Cruise, G. M., D. S. Scharp, et al. (1998). "Characterization of permeability and network structure of interfacially photopolymerized poly(ethylene glycol) diacrylate hydrogels." Biomaterials **19**(14): 1287-1294.
- Cui, X. and T. Boland (2009). "Human microvasculature fabrication using thermal inkjet printing technology." Biomaterials **30**(31): 6221-6227.
- Curtis, E. T., S. Zhang, et al. (2012). "Magnetic resonance elastography methodology for the evaluation of tissue engineered construct growth." J Vis Exp(60).
- Duan, B., L. A. Hockaday, et al. (2013). "3D bioprinting of heterogeneous aortic valve conduits with alginate/gelatin hydrogels." J Biomed Mater Res A **101**(5): 1255-1264.
- Duan, B., L. A. Hockaday, et al. (2013). "Stiffness and adhesivity control aortic valve interstitial cell behavior within hyaluronic acid based hydrogels." Acta Biomaterialia: <http://dx.doi.org/10.1016/j.actbio.2013.1004.1050>.
- Duan, B., E. Kapetanovic, et al. (2014). "Three-dimensional printed trileaflet valve conduits using biological hydrogels and human valve interstitial cells." Acta Biomater **10**(5): 1836-1846.

- Durst, C. A., M. P. Cuchiara, et al. (2011). "Flexural characterization of cell encapsulated PEG-DA hydrogels with applications for tissue engineered heart valves." Acta Biomater **7**(6): 2467-2476.
- Fedorovich, N. E., W. Schuurman, et al. (2012). "Biofabrication of osteochondral tissue equivalents by printing topologically defined, cell-laden hydrogel scaffolds." Tissue Eng Part C Methods **18**(1): 33-44.
- Fedorovich, N. E., H. M. Wijnberg, et al. (2011). "Distinct tissue formation by heterogeneous printing of osteo- and endothelial progenitor cells." Tissue Eng Part A **17**(15-16): 2113-2121.
- Feng, Y., M. Taraban, et al. (2011). "Linear Dependency of NMR Relaxation Rates on Shear Modulus in Hydrogels." Soft Matter **7**(21): 9890-9893.
- Franquet, A., S. Avril, et al. (2013). "A new method for the *in vivo* identification of mechanical properties in arteries from cine MRI images: theoretical framework and validation." IEEE Trans Med Imaging **32**(8): 1448-1461.
- Gaetani, R., P. A. Doevendans, et al. (2012). "Cardiac tissue engineering using tissue printing technology and human cardiac progenitor cells." Biomaterials **33**(6): 1782-1790.
- Gunn, J. W., S. D. Turner, et al. (2005). "Adhesive and mechanical properties of hydrogels influence neurite extension." J Biomed Mater Res A **72**(1): 91-97.
- Guo, K. and C. C. Chu (2007). "Controlled release of paclitaxel from biodegradable unsaturated poly(ester amide)s/poly(ethylene glycol) diacrylate hydrogels." J Biomater Sci Polym Ed **18**(5): 489-504.
- Guo, K., C. C. Chu, et al. (2005). "Synthesis and characterization of novel biodegradable unsaturated poly(ester amide)s." Journal of Polymer Science Part A: Polymer Chemistry **43**(7): 1463-1477.
- Hockaday, L. A., K. H. Kang, et al. (2012). "Rapid 3D printing of anatomically accurate and mechanically heterogeneous aortic valve hydrogel scaffolds." Biofabrication **4**(3): 035005.
- Hutson, C. B., J. W. Nichol, et al. (2011). "Synthesis and characterization of tunable poly(ethylene glycol): gelatin methacrylate composite hydrogels." Tissue Eng Part A **17**(13-14): 1713-1723.
- Kang, K. H., L. A. Hockaday, et al. (2013). "Quantitative optimization of solid freeform deposition of aqueous hydrogels." Biofabrication **5**(3): 035001.
- Kloxin, A. M., J. A. Benton, et al. (2010). "In situ elasticity modulation with dynamic substrates to direct cell phenotype." Biomaterials **31**(1): 1-8.
- Koch, L., A. Deiwick, et al. (2012). "Skin tissue generation by laser cell printing." Biotechnol Bioeng **109**(7): 1855-1863.
- Kotecha, M., D. Klatt, et al. (2013). "Monitoring cartilage tissue engineering using magnetic resonance spectroscopy, imaging, and elastography." Tissue Eng Part B Rev **19**(6): 470-484.
- Kuzawa, C. W. (1998). "Adipose tissue in human infancy and childhood: An evolutionary perspective." Yearbook of Physical Anthropology, Vol 41 - 1998 **41**: 177-209.
- Lee, H., S. Ahn, et al. (2014). "Enhancement of cell viability by fabrication of macroscopic 3D hydrogel scaffolds using an innovative cell-dispensing technique supplemented by preosteoblast-laden micro-beads." Carbohydr Polym **104**: 191-198.

- Lee, W., J. C. Debasitis, et al. (2009). "Multi-layered culture of human skin fibroblasts and keratinocytes through three-dimensional freeform fabrication." Biomaterials **30**(8): 1587-1595.
- Lee, W., V. Lee, et al. (2010). "On-demand three-dimensional freeform fabrication of multi-layered hydrogel scaffold with fluidic channels." Biotechnology and Bioengineering **105**(6): 1178-1186.
- Lee, W., J. Pinckney, et al. (2009). "Three-dimensional bioprinting of rat embryonic neural cells." Neuroreport **20**(8): 798-803.
- Lee, Y. B., S. Polio, et al. (2010). "Bio-printing of collagen and VEGF-releasing fibrin gel scaffolds for neural stem cell culture." Exp Neurol **223**(2): 645-652.
- Malone, E. L. H. (2007). "Fab@Home: the personal desktop fabricator kit." Rapid Prototyping Journal **13**(4): 245-255.
- Mannoor, M. S., Z. Jiang, et al. (2013). "3D Printed Bionic Ears." Nano Letters **13**(6): 2634-2639.
- Marga, F., K. Jakab, et al. (2012). "Toward engineering functional organ modules by additive manufacturing." Biofabrication **4**(2).
- Metscher, B. D. and G. B. Muller (2011). "MicroCT for molecular imaging: quantitative visualization of complete three-dimensional distributions of gene products in embryonic limbs." Dev Dyn **240**(10): 2301-2308.
- Michael, S., H. Sorg, et al. (2013). "Tissue Engineered Skin Substitutes Created by Laser-Assisted Bioprinting Form Skin-Like Structures in the Dorsal Skin Fold Chamber in Mice." PLoS One **8**(3): e57741.
- Miller, J. S., K. R. Stevens, et al. (2012). "Rapid casting of patterned vascular networks for perfusable engineered three-dimensional tissues." Nat Mater **11**(9): 768-774.
- Nichol, J. W., S. T. Koshy, et al. (2010). "Cell-laden microengineered gelatin methacrylate hydrogels." Biomaterials **31**: 5536-5544.
- Pati, F., J. Jang, et al. (2014). "Printing three-dimensional tissue analogues with decellularized extracellular matrix bioink." Nat Commun **5**: 3935.
- Peyton, S. R., C. B. Raub, et al. (2006). "The use of poly(ethylene glycol) hydrogels to investigate the impact of ECM chemistry and mechanics on smooth muscle cells." Biomaterials **27**(28): 4881-4893.
- Rouillard, A. D., C. M. Berglund, et al. (2010). "Methods for Photo-crosslinking Alginate Hydrogel Scaffolds with High Cell Viability." Tissue Eng Part C Methods.
- Rouillard, A. D., C. M. Berglund, et al. (2011). "Methods for photo-crosslinking alginate hydrogel scaffolds with high cell viability." Tissue Eng Part C Methods **17**(2): 173-179.
- Schieker, M., H. Seitz, et al. (2006). "Biomaterials as Scaffold for Bone Tissue Engineering." European Journal of Trauma **32**(2): 114-124.
- Schuurman, W., V. Khristov, et al. (2011). "Bioprinting of hybrid tissue constructs with tailorable mechanical properties." Biofabrication **3**(2): 021001.
- Skardal, A., J. Zhang, et al. (2010). "Photocrosslinkable hyaluronan-gelatin hydrogels for two-step bioprinting." Tissue Eng Part A **16**(8): 2675-2685.
- Skardal, A., J. Zhang, et al. (2010). "Bioprinting vessel-like constructs using hyaluronan hydrogels crosslinked with tetrahedral polyethylene glycol tetracrylates." Biomaterials **31**(24): 6173-6181.

- Tarafder, S., V. K. Balla, et al. (2013). "Microwave-sintered 3D printed tricalcium phosphate scaffolds for bone tissue engineering." J Tissue Eng Regen Med **7**(8): 631-641.
- Tirella, A., F. Vozzi, et al. (2011). "PAM2 (piston assisted microsyringe): a new rapid prototyping technique for biofabrication of cell incorporated scaffolds." Tissue Eng Part C Methods **17**(2): 229-237.
- Wang, C., S. Yin, et al. (2010). "Differentiation of adipose-derived stem cells into contractile smooth muscle cells induced by transforming growth factor-beta1 and bone morphogenetic protein-4." Tissue Eng Part A **16**(4): 1201-1213.
- Wathen, C. A., N. Foje, et al. (2013). "*In vivo* X-ray computed tomographic imaging of soft tissue with native, intravenous, or oral contrast." Sensors (Basel) **13**(6): 6957-6980.
- Wust, S., M. E. Godla, et al. (2014). "Tunable hydrogel composite with two-step processing in combination with innovative hardware upgrade for cell-based three-dimensional bioprinting." Acta Biomater **10**(2): 630-640.
- Zhang, Z., D. Jones, et al. (2013). "Hierarchical tailoring of strut architecture to control permeability of additive manufactured titanium implants." Mater Sci Eng C Mater Biol Appl **33**(7): 4055-4062.

## CHAPTER 6

### HEART VALVE BIOREACTORS FOR DYNAMIC CONDITIONING

Portions of this chapter was published as a book chapter titled “Aortic Heart Valve Tissue Regeneration” in *Tissue and Organ Regeneration: Advances in Micro and Nanotechnology* (Duan, Hockaday et al. 2014).

#### 6.1 Introduction

The classical tissue engineering concept is to fabricate a temporary scaffold that can support cell adhesion and signaling and eventually be remodeled into the patients’ own tissue. Heart valves are particularly challenging because the scaffold must function mechanically the moment it is implanted. The aortic valve is situated in one of the most demanding mechanical environments in the body (Butcher, Simmons et al. 2008). Tissue engineered heart valves have required dynamic *in vitro* conditioning in a bioreactor that simulates *in vivo* flow conditions prior to implantation (Gandaglia, Bagno et al. 2011). To fulfill strenuous requirements of geometry, mechanical strength, and biological function in aortic valve tissue engineering, successful strategies must thus consider cell source, scaffold parameters, fabrication techniques, and bioreactor design. This chapter will briefly review the functional characteristics of dynamic culture systems.

#### **6.2 Heart valve tissue bioreactors**

Native heart valves develop and function under dynamic conditions. Bioreactors designed to mimic the physiological stress and hemodynamics heart valves experience are integral to tissue engineering strategies for heart valve regeneration. Numerous

studies have demonstrated that TEHVs cultured in bioreactors have improved ECM content and organization, mechanical properties, and function upon implantation compared to those that are statically cultured (Hoerstrup, Sodian et al. 2000; Flanagan, Cornelissen et al. 2007; Flanagan, Sachweh et al. 2009; Ramaswamy, Gottlieb et al. 2010; Schmidt, Dijkman et al. 2010). The magnitude and distribution of mechanical loading and flow changes during the cardiac cycle, and it changes during the course of heart valve development, as shown in Figure 6.1 and Table 6.1 (Brewer, Mentzer et al. 1977; Dagum, Green et al. 1999; Aikawa, Whittaker et al. 2006). Two main classes of bioreactors have been used for these studies: component bioreactors and whole organ bioreactors.

### **6.2.1 Component bioreactors**

Component bioreactors are designed to apply a single specific mechanical stimuli to identify how and by what mechanism it effects cell differentiation and/or scaffold remodeling. Biomechanical components of the environment tested with specialized bioreactors include cyclic stretch, cyclic flexure, and oscillating shear stress and flow (Berry, Steen et al. 2010). Some of the major findings of these three types of partial tissue bioreactor studies are summarized in Table 6.2.

To apply defined fluid shear stress to tissues and cell seeded scaffolds, different designs of a parallel plate flow chamber combined with a pump have been used. Butcher et al found that valve endothelial cells align perpendicular to flow while vascular endothelial cells align parallel to flow within 24 hours when steady, unidirectional shear stress (20 dynes/cm<sup>2</sup>) is applied (Butcher, Penrod et al. 2004). They also found that the signaling pathways mediating the alignment response was different between the two cell types (Butcher and Nerem 2006).

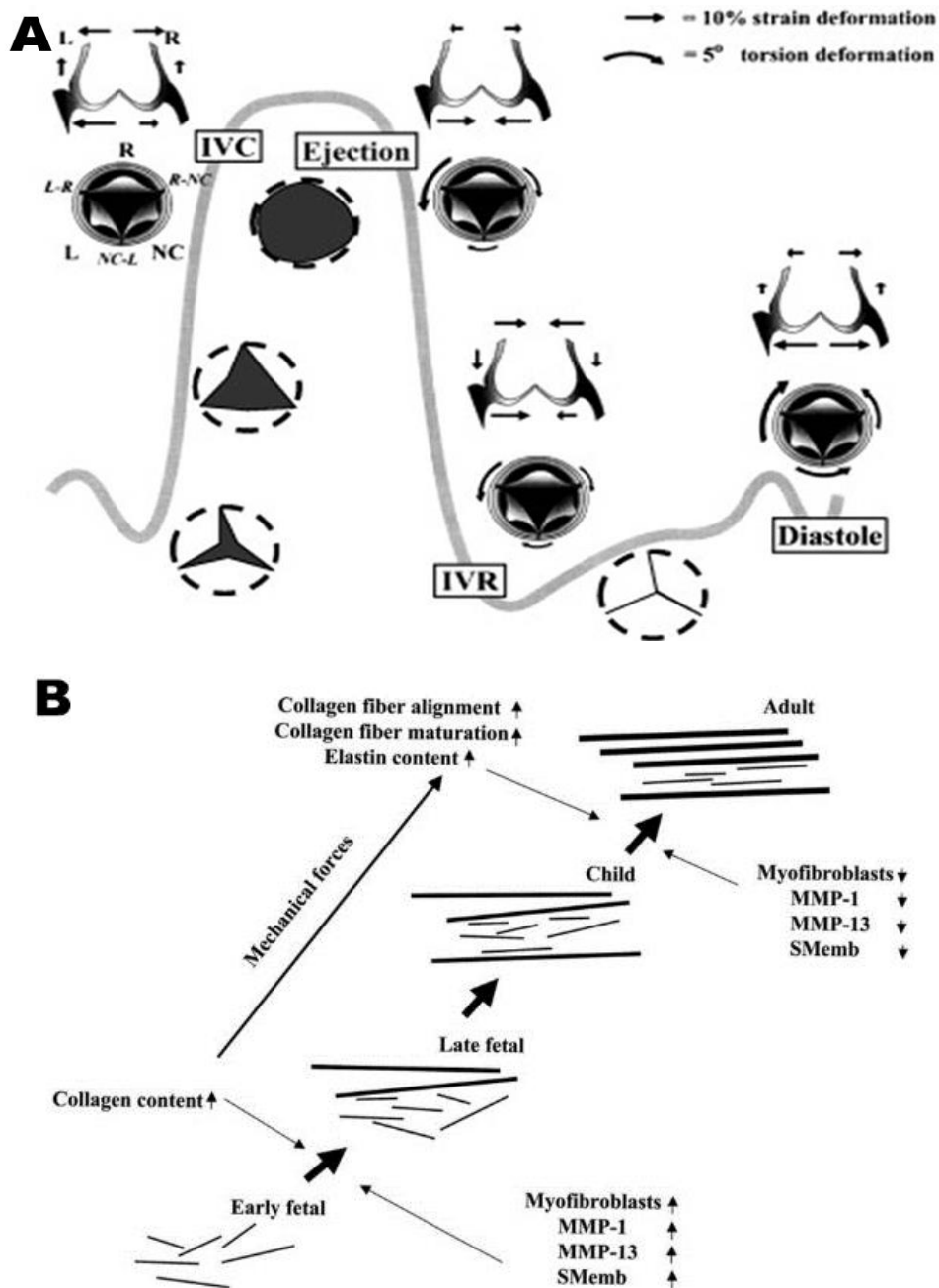


**Figure 6.1 Native valve loading and flow conditions change during cardiac cycle and as the valve develops.**

(A) In addition to the leaflets, the aortic root and sinuses deform during the cardiac cycle (Dagum, Green et al. 1999; Butcher, Mahler et al. 2011). (B) Changing mechanical forces during cardiac valve development are tied to matrix organization and cell activity. Modified from (Aikawa, Whittaker et al. 2006).

**Table 6.1. Native valve loading and flow conditions change as the valve develops**

<b>Age/Stage</b>	<b>Aorta Blood Pressure Sys/Dias</b>	<b>Pulmonary Artery Blood Pressure Sys/Dias</b>	<b>Heart Rate [bpm]</b>
<b>Fetal</b>	50/15 mmHg	50/15 mmHg	140-180
<b>Postnatal</b>	70/40 mmHg	30/15 mmHg	100-160
<b>Toddler (2 years old)</b>	95-105/53-66mm Hg	?	80-140
<b>Adult</b>	120/80 mmHg	20/9 mmHg	60-80

(Dagum, Green et al. 1999; Aikawa, Whittaker et al. 2006; Kovacs, Berghold et al. 2009; Butcher, Mahler et al. 2011).

**Table 6.2 Miniaturized/partial tissue bioreactors**

Bioreactor types	Cell/scaffold types	Bioreactor features in specific study	Mechanistic findings	Ref.
Flow	Cell Monolayer (VEC)	Steady, laminar, unidirectional shear stress (20 dynes/cm <sup>2</sup> )	Valve endothelial cells are distinct from vascular endothelial cells in behavior and signaling pathways. Valve endothelial cells align perpendicular to flow.	(Butcher, Penrod et al. 2004)
Flow	VIC + VEC collagen slab construct	Steady, laminar, unidirectional shear stress (20 dynes/cm <sup>2</sup> )	Valvular interstitial cells proliferate when not in communication with valvular endothelial cells. VIC ECM secretion is dependent on endothelial cells and on flow.	(Butcher and Nerem 2006)
Flow	PGA fiber scaffold aortic myofibroblasts	Flow rate 250-500ml/min	Collagen synthesis increases in response to shear	(Jockenhoevel, Zund et al. 2002)
Stretch (Flexcell)	Confluent VICs and MSC plated on collagen I coated membrane	Flexible membrane culture surface stretched across posts by applied vacuum. 0.6 Hz; radial stretch 7, 10, 14, 20%	VIC and MSC increase collagen synthesis in response to cyclic stretch	(Ku, Johnson et al. 2006)
Stretch (Flexcell)	PGA fiber scaffold coated with P4HB seeded with human venous myofibroblasts with fibrin gel cell carrier	Scaffold ends reinforced and attached to Flexcell well with silicone rubber. Intermittent straining at 4% 1Hz.	Intermittent straining engineered tissues increased collagen production, crosslink density, collagen organization, and mechanical properties faster than constrained controls. Stronger tissues in shorter culture time.	(Rubbens, Mol et al. 2009; Syedain and Tranquillo 2009)
Uniaxial Stretch (linear actuator)	Aortic valve leaflet circumferential direction	10%,15%, 20% strain at 1.167 Hz (70 beats/min)	10% cyclic stretch 'normal' maintains native matrix remodeling activity. Cell proliferation and apoptosis increase as cyclic stretch increases from normal to pathologic levels (15%, 20%). Increase in matrix remodeling enzyme activity and expression at elevated cyclic stretch (15, 20%).	(Balachandran, Sucusky et al. 2009)

**Table 6.2 Continued**

Bioreactor types	Cell/scaffold types	Bioreactor features in specific study	Mechanistic findings	Ref.
Stretch (linear actuator)	Aortic valve leaflets circumferential direction	Uniaxial tension delivered with actuating arm. Tissues threaded with stainless steel springs. 15% stretch, 1 Hz	Cyclic stretch + biochemical factor TGFβ1 increase contractile and biosynthetic proteins in VICs	(Merryman, Lukoff et al. 2007)
Stretch (biaxial)	Mitral VIC or chordal cells seed in collagen gels	10% strain, 1.167 Hz. Alternate stretch and relaxation every 24 hrs. Collagen gel anchored by mesh holders.	GAG secretion up regulated during cyclic stretch and down regulated during relaxation. VICs adapt to high cyclic strains indicated by proportion of GAG classes changing. For chordal cell constructs GAG classes remain consistent.	(Gupta, Werdenberg et al. 2008)
Stretch (Biaxial and anisotropy)	Aortic VIC seeded into collagen gels	Equibiaxial and controlled anisotropic strain. Collagen gel anchored/formed in a compression spring.	Increasing anisotropy of biaxial strain increases cell orientation and collagen fiber alignment along principal directions of strain. Cells orient before fibers reorganize. Results suggest strain field anisotropy regulates VIC fibroblast phenotype, proliferation, apoptosis, and matrix organization.	(Gould, Chin et al. 2012)
Flex (linear actuator)	PGA vs PLLA scaffolds each coated with P4HB (No cells)	Three point bending with controlled strain rate. 1Hz	Decrease in stiffness both materials after 2, 3, 5 weeks of flexure.	(Engelmayr, Hildebrand et al. 2003)
Flex (linear actuator)	Ovine vascular smooth muscle cells seeded into PGA and PLLA scaffolds	Three point bending, flexure angle 62%, 1 Hz. Multiple wells to hold rectangular specimens (isolated from each other)	Cyclic flexure increased effective stiffness, collagen, vimentin expression of cell seeded scaffolds	(Engelmayr, Rabkin et al. 2005)

**Table 6.2 Continued**

Bioreactor types	Cell/scaffold types	Bioreactor features in specific study	Mechanistic findings	Ref.
Flow + Stretch + Flex (Bending and stretch with a linear actuator, shear flow induced by a paddle wheel.)	Bone marrow mesenchymalstem cells from juvenile sheep seeded into PGA and PLLA scaffolds	Can study flex, stretch, flow each independently or coupled. 12 rectangular scaffolds at once. Spiral metal binders threaded through ends of scaffolds. 0.012–1.875 dynes/cm <sup>2</sup> . Up to 75% tensile strain.	Cyclic flexure and laminar flow synergistically accelerate BMSC mediated tissue formation. Collagen content and effective stiffness was higher for flex-flow conditions compared to flex and flow only conditions. Comparable collagen and effective stiffness for flex only conditions to SMC seeded scaffolds.	(Engelmayr, Sales et al. 2006; Engelmayr, Soletti et al. 2008)

Jockenhoevel *et al* included a second nutrient chamber and a multi-frame set up to hold multiple seeded scaffolds (Jockenhoevel, Zund et al. 2002). An infusion pump removed media from the nutrient chamber and a gravity feed replenished it. It was found that aortic myofibroblasts seeded into a PGA hydrogel scaffold responded to shear stress by producing hydroxyproline, indicating collagen deposition.

The effects of defined tensile strain on native and engineered valve tissues and cells have been studied using a variety of stretch bioreactor designs. These bioreactors deform the tissue or culture using either a pressure/vacuum or a linear actuator and have varying degrees of geometric control. The commercially available Flexcell bioreactor deforms flexible membranes that are set into a multi-well plate. A vacuum applied to the underside of the well deforms the membrane across a post. The flexible membrane setup has been used to condition cell monolayers (Ku, Johnson et al. 2006) and has been adapted to condition engineered heart valve tissues (Rubbens, Mol et al. 2009). A recent bioreactor specifically designed to hold hydrogel based tissues, deforms a silicone rubber slab that can hold different mold shapes to control strain direction to introduce anisotropy into tissues (Gould, Chin et al. 2012).

During each cardiac cycle, bending stresses are caused by the reversal of the curvature of the leaflets when leaflets open and close in response to pressure gradient changes (Deck, Thubrikar et al. 1988; Butcher, Mahler et al. 2011). Dynamic flexure bioreactors have enabled study of cell seeded scaffolds for valve engineering and valve tissues in bending. The flexure and bending mode of these bioreactors is generally driven by a linear actuator. Engelmayr *et al.* developed multiple bioreactors for testing

scaffolds in flexure (Engelmayr, Hildebrand et al. 2003; Engelmayr, Rabkin et al. 2005; Engelmayr, Sales et al. 2006; Engelmayr, Soletti et al. 2008). The flex bioreactor applies 3 point bending to a scaffold inside a well.

### **6.2.2 Whole valve scale bioreactors**

Whole valve scale bioreactors, while not able to target mechanisms of a specific stimulus, simulate the entire hemodynamic and mechanical microenvironment on TEHV to understand how cells and scaffold materials would interact and remodel towards clinically useful valve conduits. Aspects of this 3D environment include (1) leaflet stretching and deformation during opening and coaptation; (2) deformation of the valve root and pressure induced vessel stretch; (3) non laminar flow in the coronary sinuses (Berry, Steen et al. 2010). They are generally comprised of the following basic components: (1) a driving force or pump for fluid movement; (2) a reservoir usually containing culture media; (3) a holder or test section containing the heart valve; (4) a fluid capacitance to store and release energy every pump cycle; (5) a resistance element to help control the overall system pressure, and (6) a means of gas exchange (Berry, Steen et al. 2010). The culture bioreactor must also maintain physiological temperature and maintain sterility throughout long term culture. The different designs of bioreactors produce different hemodynamics conditions, degrees of control, and throughput. There are four main bioreactor types- pneumatic diaphragm/balloon, plate-piston, pump and splash, as shown in Figure 6.2 and summarized in Table 6.3.

Pneumatic diaphragm or balloon bioreactors use a deformable elastic membrane to drive fluid through a flow loop (Figure 6.2A). With this type of design it is possible to

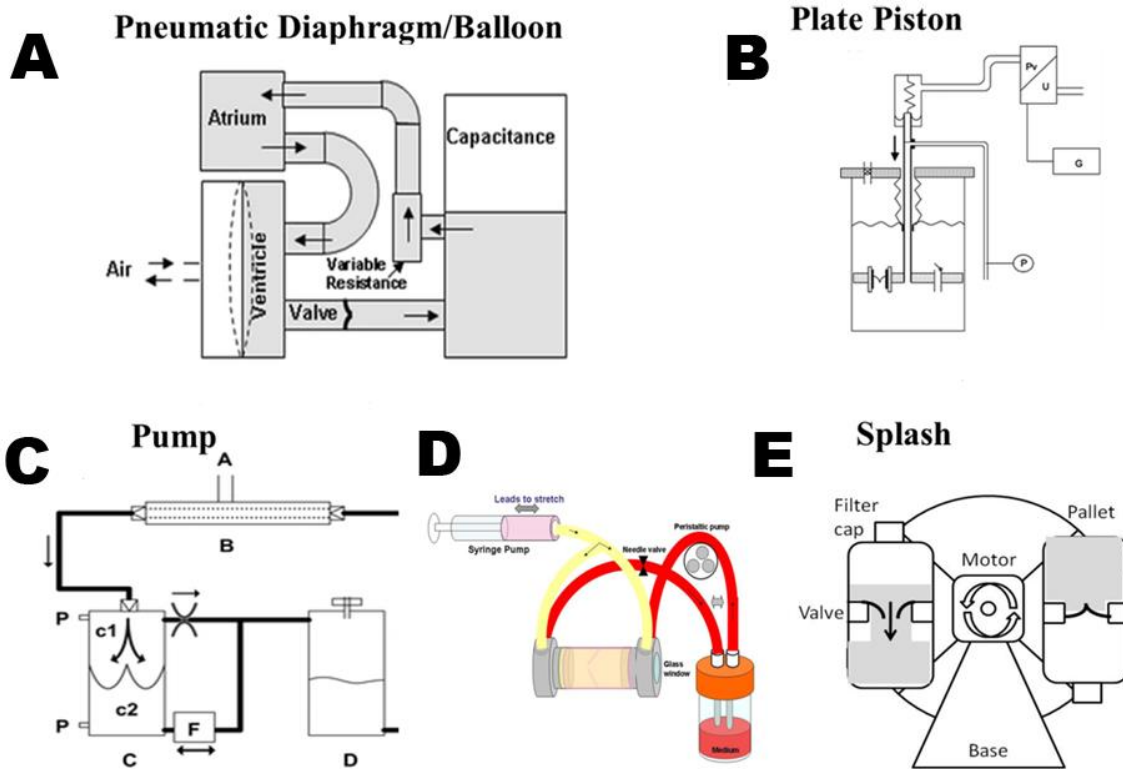


**Figure 6.2 Four main bioreactor types.**

**(A)** Pneumatic diaphragm/balloon (Hildebrand, Wu et al. 2004); **(B)** plate piston (Durst and Grande-Allen 2010; Schleicher, Sammler et al. 2010); **(C-D)** pump driven (Kortsmit, Rutten et al. 2009; Syedain and Tranquillo 2009) and **(E)** splash (Sutherland, Perry et al. 2005; Barzilla, McKenney et al. 2010).

**Table 6.3. Whole valve bioreactors**

Operation/ Components	Cell/scaffold types	Hemodynamic/ Biomechanical conditions	Mechanistic findings/features of study	Ref.
<b>Pneumatic Diaphragm</b>				
Diaphragm between an air chamber and media chamber deforms to pulse media through a valve.	Trileaflet valve construct of bio-absorbable polymers seeded with ovine myofibroblasts and endothelial cells	Systole 10-240 mmHg , 0.05 L/min to 2.0 L/min	Constructs cultured for 14 days in gradually increasing pulsatile flow, then implanted into the pulmonary position of lambs, were functional up to 5 months. At 20 weeks ECM and DNA content equal to and greater than native, and the mechanical strength comparable to native valves.	(Hoerstrup, Sodian et al. 2000; Hoerstrup, Sodian et al. 2000)
Air driven diaphragm deforms to pulse fluid through valve, and system also includes a capacitance chamber to control transvalvular pressure	1 <sup>st</sup> study PGA/PLA scaffold seeded with ovine smooth muscle cells, 2 <sup>nd</sup> study PGA/PLLA trileaflet valve scaffold seeded with bone marrow MSCs	Systole/Diastole 35/20 mmHg-125/85 mmHg, 0-6 L/min. Valves cultured under pulmonary artery conditions although the bioreactor has a wide range of possible conditions	3 weeks static and then 3 weeks bioreactor culture. Media supplemented with bFGF and AA2P accelerated collagen formation compared to standard media. Dynamic conditioning increases collagen production. Note: Reduction in GAG content with increased culture time. Note: Flexibility of scaffold material a limitation for replicating deformation and motion of native leaflets	(Hildebrand, Wu et al. 2004; Ramaswamy, Gottlieb et al. 2010)
Air driven diaphragm deforms to pulse fluid through valve, and system also includes a capacitance chamber to control transvalvular pressure. Universal valve holder mounting design	Decellularized porcine scaffolds seeded with porcine aortic endothelial cells	Systole/Diastole 40/15 mmHg-80/70 mmHg, 5-23 ml stroke volume	17 days of bioreactor culture. Cells adhere and form cobblestone morphology, but incomplete endothelialization, probably due to low seeding concentration. Valve opening and closing monitored with video system.	(Sierad, Simionescu et al. 2010)

**Table 6.3 Continued**

Operation/ Components	Cell/scaffold types	Hemodynamic/ Biomechanical conditions	Mechanistic findings/features of study	Ref.
Balloon				
Pressure chamber with bladder on the outflow side of the valve. Negative pressure causes back flow on the valve to close it, positive pressure to get flow through open valve.	Decellularized porcine valves seeded with ovine carotid artery endothelial cells and myofibroblasts	Systole/Diastole 60/40 mmHg-180/120 mmHg, 25 ml/min-3L/min	Hydrodynamic reseeding of a scaffold more effective than static reseeding. Hydrodynamic seeded scaffolds had more cell mass, collagen and elastin content, and strength than static controls.	(Zeltinger, Landeen et al. 2001; Schenke-Layland, Opitz et al. 2003)
Silicone blub compressed by piston <ul style="list-style-type: none"> <li>• TE valve holder</li> <li>• compliance chamber and resistance</li> <li>• reservoir with aerator</li> <li>• mechanical valve</li> </ul>	Checked system for biocompatibility using endothelial cells. Bioreactor materials put into media for 2 weeks for leaching, and media then fed o cells	Systole/Diastole 120/80 mmHg-40/25mmHg, 1.68L/min-3.44L/min, Stroke volume: 35-76ml	The rubber sealing material and rubber used for left ventricle was cytotoxic. Ethylene oxide (EtO) vs glutaraldehyde (2%) (GA) sterilization of all the bioreactor materials: silicone tubing, silicone ventricle, rubber sealing, Teflon sealing, Plexiglass, glue, glued pieces of Plexiglass and/or polyvinyl chloride [PVC]), PVC tubes, and PVC angles.	(Dumont, Yperman et al. 2002)
Plate-Piston				
Plate-Piston	Tested with commercial bio-prosthetic and mechanical valves	Systole/Diastole 120/80mmHg 180/100mmHg, ΔP: 0-120mmHg. Vertical movement range associated with stroke volume.	Bioreactor evaluated with an aqueous xanthan gum solution to give media blood- like rheological properties and a blood-like salt solution. Valves opening and closing monitored with video system.	(Durst and Grande-Allen 2010; Schleicher, Sammler et al. 2010)

**Table 6.3 Continued**

Operation/ Components	Cell/scaffold types	Hemodynamic/ Biomechanical conditions	Mechanistic findings/features of study	Ref.
Pump Deformation + Flow latex tube <ul style="list-style-type: none"> <li>• TEHV mount</li> <li>• Flow circuit for stretch</li> <li>• Flow circuit or nutrient supply</li> <li>• reciprocating syringe pump</li> <li>• peristaltic pump</li> </ul>	Fibrin based valve construct seeded with human dermal fibroblasts	Cyclic loading of valve root. 0-15% Root Strain Low flow rate 10- 15ml/min	3 weeks of cyclic stretching with incrementally increasing strain amplitude. TEHV leaflets after culture had circumferential fiber alignment and had tensile stiffness and anisotropy similar to sheep pulmonary valves.	(Syedain and Tranquillo 2009)
Pump Deformation w/Fluid Minimal flow/shear	Human saphenous vein cells seeded into PGA/P4Hb scaffolds using fibrin cell carrier.	Diastole. Applied pressure difference over leaflets. Dynamic trans- valvular pressure: 0- 80mmHg. Dynamic Strain 0-25% Low shear stress	Dynamically loaded leaflets have higher UTS, modulus, and tissue formation compared non loaded tissue strips after 4 weeks of culture Mechanical behavior of loaded leaflets non-linear and strips was linear. Prestrain induced by the stent (3-5%) also affects the mechanical and tissue organization.	(Mol, Driessen et al. 2005)

**Table 6.3 Continued**

Operation/ Components	Cell/scaffold types	Hemodynamic/ Biomechanical conditions	Mechanistic findings/features of study	Ref.
Pump (continued)				
<p>Developed a proportional integral-derivative (PID) feedback controller to regulate deformation in their TEHV bioreactor system. Results indicated a good correspondence between the measured and the prescribed deformation values</p>	<p>Molded valve scaffold of PGA coated with P4HB, then coated with PCL and bonded to a polycarbonate cylinder, which was seeded with human saphenous vein endothelial cells using fibrin cell carrier.</p>	<p>Diastole. Applied pressure difference over leaflets. Up to 100 mmHg transvalvular pressure. Slow media circulation 4ml/min.</p>	<p>12 days culture in low speed media circulation then dynamic pressure differences applied for 16 days at 1 Hz. With increased culture time the leaflets became less stiff, more flexible, and less leaky. No significant modulus difference between loading protocols, but anisotropic mechanical properties (circumferential vs radial) induced by both. Study goal to facilitate development of an optimal conditioning protocol using deformation feedback.</p>	<p>(Kortsmit, Rutten et al. 2009)</p>
<ul style="list-style-type: none"> <li>• Capacitance chamber</li> <li>• Pulsatile pump</li> <li>• Cell seeding inlets</li> <li>• Fits into Incubator. Direct control of flow rate using pulsatile pump. Roller pump enabled gas exchange in an oxygenation chamber</li> </ul>	<p>Decellularized ovine pulmonary valves seeded with jugular vein endothelial cells</p>	<p>Mean system pressure was maintained at 25±4 mmHg, 0.1 L/min to 2.0 L/min</p>	<p>Valves were seeded using the bioreactor and then implanted into lambs for 3 months. Valves were completely endothelialized following bioreactor culture. Found that moderate pulsatile flow with bioreactor stimulated EC proliferation, and high flow damaged endothelium and caused loss of cellularity. After explant both reseeded valves and bare decellularized valves had interstitial cells, but a confluent monolayer of EC only present on recellularized valves. More thrombotic formations on bare decellularized valves.</p>	<p>(Lichtenberg, Cebotari et al. 2006; Lichtenberg, Tudorache et al. 2006)</p>

**Table 6.3 continued**

Operation/ Components	Cell/scaffold types	Hemodynamic/ Biomechanical conditions	Mechanistic findings/features of study	Ref.
Splash				
As the chamber rotates, the culture medium flows past the tissue surface, imparting normal and shear forces to the surface and causing deformation of the organ culture.	Porcine mitral valve segments including strut chordae	3ml/s	Native mitral valves lose microstructure and ECM expression patterns when cultured under static conditions and were better maintained in dynamic culture. Proliferation of cells throughout the leaflet was also effected.	(Barzilla, Acevedo et al. 2010; Barzilla, McKenney et al. 2010)

induce leaflet stretching and coaptation and to create non laminar the flow in the valve sinuses. The most elaborate of this type of design models the left side of the heart (Hildebrand, Wu et al. 2004; Ramaswamy, Gottlieb et al. 2010; Sierad, Simionescu et al. 2010). In this design media is drawn from an 'atrium' media reservoir in to a 'ventricle' chamber where air deforms a diaphragm in a 'ventricle' chamber which pushes media through an aortic valve construct. A pressurized capacitance tank following the valve allows for control of transvalvular pressure and fluid recycles to the atrium reservoir. Systole and diastole can be mimicked with this type of design, and it enables a high degree of flow and pressure control. One of the major disadvantages of a pneumatic diaphragm/balloon design is that a large number of components are needed to achieve a high level of control. As these bioreactors become increasingly intricate the bioreactor system get larger (Hoerstrup, Sodian et al. 2000; Hoerstrup, Sodian et al. 2000; Hildebrand, Wu et al. 2004; Sierad, Simionescu et al. 2010). If the system must fit into a culture incubator to regulate temperature and CO<sub>2</sub>, size becomes one of the major limitations to high-throughput culture of multiple valves.

A plate-piston bioreactor physically moves valves through liquid to condition them (Figure 6.2B) (Schleicher, Sammler et al. 2010). Multiple valves are mounted in a plate that is submerged in liquid. A steel tube that is driven up and down by a piston is attached to the plate. By moving the valve back and forth through the liquid it is possible to mimic systole and diastole, leaflet stretching and coaptation, and flow eddies in the sinuses. The vertical range of movement in the system is coupled to the stroke volume for this system. This design has the benefit of being relatively high throughput although

the multiple valves are not isolated from one another. The piston-plate bioreactor design enables a wide range of loading conditions and enable loading of multiple valves simultaneously (Schleicher, Sammler et al. 2010). The major disadvantage of the system is that the valves are not isolated from one another during culture which means it is difficult to test multiple conditions (for example cell type or media composition) and contamination would affect the entire set of TEHVs. Additionally the plate-piston periodically requires time to reset position which can alter the 'cardiac' cycle conditions.

Pump bioreactors like diaphragm bioreactors move fluid through flow loops. For convenient sterile culture the syringe pumps and peristaltic pumps have been incorporated into these designs. Lichtenberg *et al* designed a bioreactor specifically for seeding TEHV with a pulsatile pump, valve reservoir and holder, and oxygenation compliance chamber (Lichtenberg, Cebotari et al. 2006; Lichtenberg, Tudorache et al. 2006). Cell inlets were incorporated above and below the heart valve. Several pump bioreactor designs mimic both valve leaflet and root deformation with particular emphasis on the diastolic phase of the cardiac cycle (Figure 6.2C,D) (Mol, Driessen et al. 2005; Kortsmi, Rutten et al. 2009; Syedain and Tranquillo 2009). Diastolic pressure differences can be applied over the leaflets, with minimal shear flow using a bioreactor consisting of a valve holding container and a medium container. Using a pump a pulse of media of controlled volume and pressure is applied to the outflow side of the leaflets, and the valve deformation can be regulated (Kortsmi, Rutten et al. 2009) (Figure 6.2C). In another bioreactor design there are two separate flow loops-a stretch circuit for applying strain to the valve root wall and leaflets, and a flow circuit for nutrient supply

(Figure 6.2D) (Syedain and Tranquillo 2009). The Syedain design is one of the few that specifically attempts to recreate valve root deformation biomechanics. The advantage of these pump driven bioreactor designs is that they are very compact compared to other bioreactors and multiple systems can fit into an incubator. Pump driven systems have been used to replicate specific elements of the cardiac cycle such as blood flow through the leaflets during systole (Lichtenberg, Tudorache et al. 2006), diastolic loading (Kortsmit, Rutten et al. 2009) and root deformation (Syedain and Tranquillo 2009) and several compact designs have been demonstrated. However, duplicating the full cardiac cycle with a pump driven design may involve the same component and complexity increase associated with control that effects the diaphragm/balloon bioreactors.

The final bioreactor type is a splash bioreactor (Figure 6.2E). A valve segment is mounted between two chambers, one of which is filled with media. As the chamber rotates, the culture medium flows past the tissue surface, imparting normal and shear forces to the surface and causing deformation of the valve leaflet (Barzilla, McKenney et al. 2010). The splash bioreactor has the advantage of having self-contained sterile conditioning of individual valves, and can be scaled up to have multiple chambers for high-throughput (Barzilla, McKenney et al. 2010). However, the current splash bioreactor design is more suited to the mitral valve, and may not be suitable for aortic or pulmonary TEHV. It does not allow for control of pressure, flow rate, or stroke volume.

### **6.3 Conclusions**

*In vitro* bioreactor studies have demonstrated that hemodynamic conditioning affects TEHV development and can improve tissue function. However, optimal magnitudes of biomechanical conditioning still need to be identified. *In vitro* conditioning is critically important for TEHV strategies that begin with cellularized scaffolds unable to immediately function under physiologic levels of cyclic stretch, flexure, and shear stress upon implantation (Flanagan, Cornelissen et al. 2007; Flanagan, Sachweh et al. 2009). Many of the new materials developed for valve and stem cell culture (Benton, Kern et al. 2009; Kloxin, Tibbitt et al. 2010; Kloxin, Tibbitt et al. 2010; Pedron, Kasko et al. 2010), if fabricated into scaffolds may fall into this category. As the field of biomaterials expands, the need for high throughput *in vitro* evaluation and conditioning of different materials for TEHV is also expanding.

## REFERENCES

- Aikawa, E., P. Whittaker, et al. (2006). "Human semilunar cardiac valve remodeling by activated cells from fetus to adult - Implications for postnatal adaptation, pathology, and tissue engineering." Circulation **113**: 1344-1352.
- Balachandran, K., P. Sucusky, et al. (2009). "Elevated cyclic stretch alters matrix remodeling in aortic valve cusps: implications for degenerative aortic valve disease." American Journal of Physiology-Heart and Circulatory Physiology **296**: H756-H764.
- Barzilla, J. E., F. E. Acevedo, et al. (2010). "Organ culture as a tool to identify early mechanisms of serotonergic valve disease." Journal of Heart Valve Disease **19**: 626-635.
- Barzilla, J. E., A. S. McKenney, et al. (2010). "Design and validation of a novel splashing bioreactor system for use in mitral valve organ culture." Annals of Biomedical Engineering **38**: 3280-3294.
- Benton, J. A., H. B. Kern, et al. (2009). "Statins block calcific nodule formation of valvular interstitial cells by inhibiting alpha-smooth muscle actin expression." Arteriosclerosis Thrombosis and Vascular Biology **29**: 1950-1957.
- Berry, J. L., J. A. Steen, et al. (2010). "Bioreactors for development of tissue engineered heart valves." Annals of Biomedical Engineering **38**: 3272-3279.
- Brewer, R. J., R. M. Mentzer, et al. (1977). "*In vivo* study of the dimensional changes of the aortic valve leaflets during the cardiac cycle." Journal OF Thoracic and Cardiovascular Surgery **74**: 645-650.
- Butcher, J. T., G. J. Mahler, et al. (2011). "Aortic valve disease and treatment: The need for naturally engineered solutions." Advanced Drug Delivery Reviews **63**: 242-268.
- Butcher, J. T. and R. M. Nerem (2006). "Valvular endothelial cells regulate the phenotype of interstitial cells in co-culture: Effects of steady shear stress." Tissue Engineering **12**: 905-915.
- Butcher, J. T., A. M. Penrod, et al. (2004). "Unique morphology and focal adhesion development of valvular endothelial cells in static and fluid flow environments." Arteriosclerosis Thrombosis and Vascular Biology **24**: 1429-1434.
- Butcher, J. T., C. A. Simmons, et al. (2008). "Review - Mechanobiology of the aortic heart valve." Journal of Heart Valve Disease **17**: 62-73.
- Dagum, P., G. R. Green, et al. (1999). "Deformational dynamics of the aortic root - Modes and physiologic determinants." Circulation **100**: S54-62.
- Deck, J. D., M. J. Thubrikar, et al. (1988). "Structure, stress, and tissue-repair in aortic valve leaflets." Cardiovascular Research **22**: 7-16.
- Dumont, K., J. Yperman, et al. (2002). "Design of a new pulsatile bioreactor for tissue engineered aortic heart valve formation." Artificial Organs **26**: 710-714.
- Durst, C. A. and K. J. Grande-Allen (2010). "Design and physical characterization of a synchronous multivalve aortic valve culture system." Annals of Biomedical Engineering **38**: 319-325.

- Engelmayr, G. C., D. K. Hildebrand, et al. (2003). "A novel bioreactor for the dynamic flexural stimulation of tissue engineered heart valve biomaterials." Biomaterials **24**: 2523-2532.
- Engelmayr, G. C., E. Rabkin, et al. (2005). "The independent role of cyclic flexure in the early *in vitro* development of an engineered heart valve tissue." Biomaterials **26**: 175-187.
- Engelmayr, G. C., V. L. Sales, et al. (2006). "Cyclic flexure and laminar flow synergistically accelerate mesenchymal stem cell-mediated engineered tissue formation: Implications for engineered heart valve tissues." Biomaterials **27**: 6083-6095.
- Engelmayr, G. C., L. Soletti, et al. (2008). "A novel flex-stretch-flow bioreactor for the study of engineered heart valve tissue mechanobiology." Annals of Biomedical Engineering **36**: 700-712.
- Flanagan, T. C., C. Cornelissen, et al. (2007). "The *in vitro* development of autologous fibrin-based tissue-engineered heart valves through optimised dynamic conditioning." Biomaterials **28**: 3388-3397.
- Flanagan, T. C., J. S. Sachweh, et al. (2009). "*In vivo* remodeling and structural characterization of fibrin-based tissue-engineered heart valves in the adult sheep model." Tissue Engineering Part A **15**: 2965-2976.
- Gandaglia, A., A. Bagno, et al. (2011). "Cells, scaffolds and bioreactors for tissue-engineered heart valves: a journey from basic concepts to contemporary developmental innovations " European Journal of Cardio-thoracic Surgery **39**: 523-531.
- Gould, R. A., K. Chin, et al. (2012). "Cyclic strain anisotropy regulates valvular interstitial cell phenotype and tissue remodeling in three-dimensional culture." Acta Biomaterialia **8**: 1710-1719.
- Gupta, V., J. A. Werdenberg, et al. (2008). "Reversible secretion of glycosaminoglycans and proteoglycans by cyclically stretched valvular cells in 3D culture." Annals of Biomedical Engineering **36**: 1092-1103.
- Hildebrand, D. K., Z. J. J. Wu, et al. (2004). "Design and hydrodynamic evaluation of a novel pulsatile bioreactor for biologically active heart valves." Annals of Biomedical Engineering **32**: 1039-1049.
- Hoerstrup, S. P., R. Sodian, et al. (2000). "Functional living trileaflet heart valves grown *in vitro*." Circulation **102**: III44-49.
- Hoerstrup, S. P., R. Sodian, et al. (2000). "New pulsatile bioreactor for *in vitro* formation of tissue engineered heart valves." Tissue Engineering **6**: 75-79.
- Jockenhoevel, S., G. Zund, et al. (2002). "Cardiovascular tissue engineering: A new Laminar flow chamber for *in vitro* improvement of mechanical tissue properties." ASAIO Journal **48**: 8-11.
- Kloxin, A. M., M. W. Tibbitt, et al. (2010). "Synthesis of photodegradable hydrogels as dynamically tunable cell culture platforms." Nature Protocols **5**: 1867-1887.
- Kloxin, A. M., M. W. Tibbitt, et al. (2010). "Tunable hydrogels for external manipulation of cellular microenvironments through controlled photodegradation." Advanced Materials **22**: 61-+.
- Kortsmit, J., M. C. M. Rutten, et al. (2009). "Deformation controlled load application in heart valve tissue engineering." Tissue Engineering Part C-Method **15**: 707-716.

- Kovacs, G., A. Berghold, et al. (2009). "Pulmonary arterial pressure during rest and exercise in healthy subjects: a systematic review." European Respiratory Journal **34**: 888-894.
- Ku, C. H., P. H. Johnson, et al. (2006). "Collagen synthesis by mesenchymal stem cells and aortic valve interstitial cells in response to mechanical stretch." Cardiovascular Research **71**: 548-556.
- Lichtenberg, A., S. Cebotari, et al. (2006). "Flow-dependent re-endothelialization of tissue-engineered heart valves." Journal of Heart Valve Disease **15**: 287-293.
- Lichtenberg, A., I. Tudorache, et al. (2006). "Preclinical testing of tissue-engineered heart valves re-endothelialized under simulated physiological conditions." Circulation **114**: I559-I565.
- Merryman, W. D., H. D. Lukoff, et al. (2007). "Synergistic effects of cyclic tension and transforming growth factor-beta 1 on the aortic valve myofibroblast." Cardiovascular Pathology **16**: 268-276.
- Mol, A., N. J. B. Driessen, et al. (2005). "Tissue engineering of human heart valve leaflets: A novel bioreactor for a strain-based conditioning approach." Annals of Biomedical Engineering **33**: 1778-1788.
- Pedron, S., A. M. Kasko, et al. (2010). "Effect of heparin oligomer chain length on the activation of valvular interstitial cells." Biomacromolecules **11**: 1692-1695.
- Ramaswamy, S., D. Gottlieb, et al. (2010). "The role of organ level conditioning on the promotion of engineered heart valve tissue development in-vitro using mesenchymal stem cells." Biomaterials **31**: 1114-1125.
- Rubbens, M. P., A. Mol, et al. (2009). "Intermittent straining accelerates the development of tissue properties in engineered heart valve tissue." Tissue Engineering Part A **15**: 999-1008.
- Schenke-Layland, K., F. Opitz, et al. (2003). "Complete dynamic repopulation of decellularized heart valves by application of defined physical signals-an *in vitro* study." Cardiovascular Research **60**: 497-509.
- Schleicher, M., G. Sammler, et al. (2010). "Simplified pulse reactor for real-time long-term *in vitro* testing of biological heart valves." Annals of Biomedical Engineering **38**: 1919-1927.
- Schmidt, D., P. Dijkman, et al. (2010). "Minimally-invasive implantation of living tissue engineered heart valves A comprehensive approach from autologous vascular cells to stem cells." Journal of the American College of Cardiology **56**: 510-520.
- Sierad, L. N., A. Simionescu, et al. (2010). "Design and testing of a pulsatile conditioning system for dynamic endothelialization of polyphenol-stabilized tissue engineered heart valves." Cardiovascular Engineering and Technology **1**: 138-153.
- Sierad, L. N., A. Simionescu, et al. (2010). "Design and testing of a pulsatile conditioning system for dynamic endothelialization of polyphenol-stabilized tissue engineered heart valves." Cardiovascular Engineering and Technology **1**: 138-153.
- Syedain, Z. H. and R. T. Tranquillo (2009). "Controlled cyclic stretch bioreactor for tissue-engineered heart valves." Biomaterials **30**: 4078-4084.
- Webster, T. J. K. A. Z. L. G. (2014). "Tissue and organ regeneration : advances in micro- and nanotechnology." from <http://dx.doi.org/10.1201/b15595>.

Zeltinger, J., L. K. Landeen, et al. (2001). "Development and characterization of tissue-engineered aortic valves." Tissue Engineering 7: 9-22.

## CHAPTER 7

### BIOREACTOR FOR PARALLEL DYNAMIC CONDITIONING OF ADULT AND PEDIATRIC SIZED 3D PRINTED HYDROGEL HEART VALVES

Portions of this chapter were previously published in *Advanced Drug Delivery Reviews* (Butcher, Mahler et al. 2011) and in the book chapter entitled “Aortic Heart Valve Tissue Regeneration” (Duan, Hockaday et al. 2014) in *Tissue and Organ Regeneration: Advances in Micro and Nanotechnology*.

#### **7.1 Summary**

In this study we demonstrate a dynamic conditioning system specifically for the culture of 3D bioprinted and *ex-vivo* native tissue heart valves. The custom water driven diaphragm-type bioreactor was engineered with a conditioning chamber specifically designed for ultrasound monitoring of valve root wall and leaflet motion and tissue strain. The parameters of the flexible control and water driven flow loop system can be scaled or throttled to enable dynamic culture of aortic and pulmonary valves at adult or pediatric stroke volume and flow rates. Additionally the system can be scaled for parallel conditioning in multiple reactor chambers containing individual valves. Physiological systolic and diastolic loading conditions can be achieved or diastolic only loading conditions can be induced with the control setup. This will enable exploration into the optimal conditions and loading regimes needed to drive remodeling and tissue development in 3D printed hydrogel valves. 3D bioprinted heart valves composed of methacrylated gelatin, methacrylated hyaluronic acid, and PEGDA were cultured up to 14 days under static and dynamic conditions to validate the system and to induce remodeling in bioprinted valves.

## **7.2 Introduction**

Heart valves are a particularly challenging target for tissue engineering because the engineered tissue must function mechanically the moment it is implanted. The aortic and pulmonary valves are situated in two of the most demanding mechanical environments in the body (Butcher, Simmons et al. 2008). Tissue engineered heart valve strategies depend heavily on dynamic *in vitro* conditioning in a bioreactor that simulates *in vivo* flow conditions prior to implantation to drive cell remodeling and matrix deposition to meet these demands (Gandaglia, Bagno et al. 2011). Native heart valves develop and function under dynamic conditions. Bioreactors designed to mimic the physiological stress and hemodynamics heart valves experience are integral to tissue engineering strategies for heart valve regeneration. Numerous studies have demonstrated that TEHVs cultured in bioreactors have improved ECM content and organization, mechanical properties, and function upon implantation compared to those that are statically cultured (Hoerstrup, Sodian et al. 2000; Flanagan, Cornelissen et al. 2007; Flanagan, Sachweh et al. 2009; Ramaswamy, Gottlieb et al. 2010; Schmidt, Dijkman et al. 2010). The magnitude and distribution of mechanical loading and flow changes during the cardiac cycle, and it changes during the course of heart valve development (Brewer, Mentzer et al. 1977; Dagum, Green et al. 1999; Aikawa, Whittaker et al. 2006). While upon implantation a TEHV must function at full aortic and ventricular pressures and stroke volume, for driving tissue development a more fetal-like set of hemodynamic conditions may be needed depending on the starting materials of the valve (Aikawa, Whittaker et al. 2006). Compared to other possible TEHV strategy materials, hydrogels in particular are mechanically weak, and tissue development and remodeling activity by the cells is necessary before valves can withstand physiological

conditions (Butcher, Mahler et al. 2011; Syedain 2011). The Tranquillo group has demonstrated that cell remodeling can be effectively harnessed in a fibrin hydrogel to reorganize and deposit more matrix so that the resultant tissue is mechanically robust enough to be decellularized and function under pulmonary conditions (Syedain, Bradee et al. 2013; Syedain, Meier et al. 2013).

Classical TEHV strategies are limited by their fabrication methods and materials. For autologous biological polymeric valves, tissue contraction of the leaflets resulted in valve insufficiency (Flanagan, Sachweh et al. 2009). In contrast, a persistent problem for synthetic polymeric fiber TEHV is that the material has been too stiff for the leaflets or the leaflets have stiffened over time resulting in stenotic function (Sutherland, Perry et al. 2005; Schmidt, Dijkman et al. 2010). Using one material means that the even superficial regional mechanical differences present in native tissue, such as compliant leaflets and the stiff root, are neglected and the microenvironment could limit heterogeneous differentiation of seeded cells and result in undesirable remodeling behaviors (Butcher, Mahler et al. 2011). For the field of TEHV to move forward there is a need for better mimicry of root and leaflet mechanical function and better control cell-scaffold interactions/remodeling. 3D printing is of interest as a tool both because it enables mechanistic and biological investigation in 3D at multiple scales, such as at the cell level (Lee, Moon et al. 2008; Torgersen, Ovsianikov et al. 2012) and the tissue level (Chang, Boland et al. 2011; Fedorovich, Alblas et al. 2011)), and because it could translate into a means for fabricating living tissue with native heterogeneity at a scale suitable for clinical use (Koch, Deiwick et al. 2012; Luangphakdy, Walker et al. 2013).

In our previous work and in Chapter 5 we demonstrate the capability of 3D printing to create complexly heterogeneous heart valve constructs, but the consequences of this heterogeneity must be evaluated.

In this study, we present the characterization of water driven diaphragm-type whole valve bioreactor that was designed and built for the pulsatile conditioning of 3D printed hydrogel heart valves, inspired by diaphragm-type reactors demonstrated by Hoerstrup et al and Sierad et al (Hoerstrup, Sodian et al. 2000; Sierad, Simionescu et al. 2010).

3D printed hydrogel valves were cultured in the characterized bioreactor conditioning system. Human adipose derived mesenchymal stem cells (HADMSC) were combined with poly-(ethylene glycol)diacrylate (PEG-DA), methacrylated gelatin (MEGEL), and methacrylated hyaluronic acid (MEHA) photo-crosslinkable hydrogel precursors (Benton, DeForest et al. 2009; Hutson, Nichol et al. 2011) to make a solution suitable for extrusion 3D printing. PEG-based hydrogels have been used to study heart valve interstitial cells response to mechanical properties in both 2D and encapsulate 3D in-vitro studies (Kloxin, Benton et al. 2010; Durst, Cuchiara et al. 2011). A vast potential for mechanical and/or molecular hydrogels are enzymatically degradable and have been used to encapsulate valve interstitial cells (Benton, DeForest et al. 2009), and with the addition of PEG-DA the degradation properties are modifiable (Hutson, Nichol et al. 2011). MEHA has attractive bioactive features and varying the ratios of MEGEL and MEHA have previously been demonstrated to modulate resultant hydrogel mechanical properties, precursor solution viscosity and 3D printed scaffold fidelity, and cell

phenotype within (Duan, Kapetanovic et al. 2014). Bioprinted valves were dynamically and statically cultured up to 14 days.

### **7.3 Materials and Methods**

#### **7.3.1 Heart Valve Bioreactor Design Overview**

A water driven diaphragm-type whole valve bioreactor was designed and built for the pulsatile conditioning of 3D printed hydrogel heart valves. The design was largely based on pneumatic diaphragm-type reactors demonstrated by Hoerstrup et al and Sierad et al (Hoerstrup, Sodian et al. 2000; Sierad, Simionescu et al. 2010). Sierad et al and Hoerstrup et al used an air driven diaphragm pump to move culture medium through a tissue engineered heart valve. In this study, a water driven system instead of an air driven system was used to enable fast frequency response. Air driven systems have a slight disadvantage compared to piston or post systems due to the compressibility of air (Schleicher, Sammler et al. 2010; Gould, Chin et al. 2012). At room temperature and at 37°C for the culture incubator, water is effectively incompressible. With a fast frequency response a reactor could mimic the faster heart rate of the pediatric and fetal cardiac system, so that hemodynamic conditions could be selected in the full range of pediatric to adult loading and flow conditions. In the native valve loading and flow conditions change as the valve develops (Dagum, Green et al. 1999; Aikawa, Whittaker et al. 2006; Kovacs, Berghold et al. 2009; Butcher, Mahler et al. 2011).

In our heart valve bioreactor design a pump driven water flow loop is used to circulate media in a sterile media loop (Figure 7.1). The media loop is separated from the water

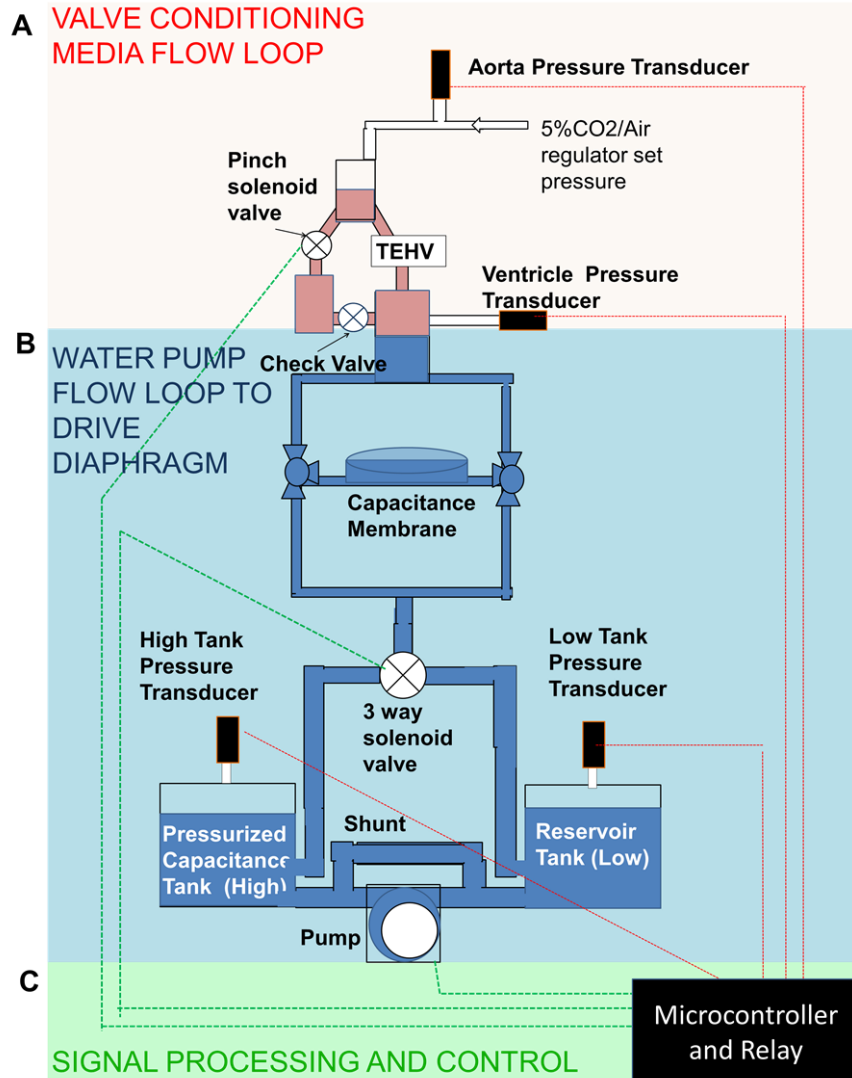


**Figure 7.1** Over view of the heart valve bioreactor conditioning system which uses a pump driven water flow loop to circulate media in a sterile media loop.

**(A)** The media loop is separated from the water loop with a silicone diaphragm. Water is pumped into the base of the valve conditioning chamber, this deflects/deforms the silicone diaphragm in the ‘ventricle’ and pushes media through the TEHV into a pressurized aortic chamber, the media circulates back to a reservoir of culture media. One way check valves only allow media to flow from the media reservoir into the ‘ventricle’ chamber of the conditioning chamber. **(B)** The water flow loop is driven by a pump. The pump moves water from the reservoir or ‘low’ tank to pressurize a capacitance ‘high’ tank. The 3-way solenoid switches between this high pressure source and this low pressure sink to provide an oscillating pulse of water to the base of the conditioning chamber. This pulse is analogous to one cardiac cycle. A shunt is included so that once the system is shut down the tank pressures will equilibrate. **(C)** Signal processing of the pressure transducer information and control of the system is enabled by a microcontroller and a timer relay. A computer is connected to the microcontroller to record pressure data.

loop with a silicone diaphragm (7.1A). Water is pumped into the base of the valve conditioning chamber; this deflects/deforms the silicone diaphragm in the 'ventricle' and pushes media through the TEHV into a pressurized aortic chamber. The media circulates back to a reservoir of culture media. One way check valves only allow media to flow from the media reservoir into the 'ventricle' chamber of the conditioning chamber. The water flow loop is driven by a pump (7.1B). The pump moves water from the reservoir or 'low' tank to pressurize a capacitance 'high' tank. The 3-way solenoid switches between this high pressure source and this low pressure sink to provide an oscillating pulse of water to the base of the conditioning chamber. This pulse is analogous to one cardiac cycle. A shunt is included so that once the system is shut down the tank pressures will equilibrate. Signal processing of the pressure transducer information and control of the system is enabled by a microcontroller and a timer relay (7.1C). A computer is connected to the microcontroller to record pressure data. Pressurized gas (CO<sub>2</sub>/Air) was applied to set the aortic or outflow track pressure to get a transvalvular pressure.

### **7.3.2 Heart valve conditioning chamber and holder for 3D printed hydrogel or ex vivo heart valves**

The conditioning chamber and holder assembly is designed so that the heart valve can be loaded with pressures that mimic the ventricle, aorta, and the chest cavity. At the beginning of the diastolic phase, pressure should be higher on the aortic side of the valve leaflets compared to the ventricular side (Figure 7.2A). Under this condition the valve leaflets will close. In the human body the circulatory system is pressurized relative to the chest cavity, and the root wall experiences stress and deformation based on the relative pressure changes between an aorta and the chest cavity (Dagum, Green et al. 1999). Although it was not monitored in the study presented here, a line for a body cavity pressure transducer was included on the side of the bioreactor chamber. Top

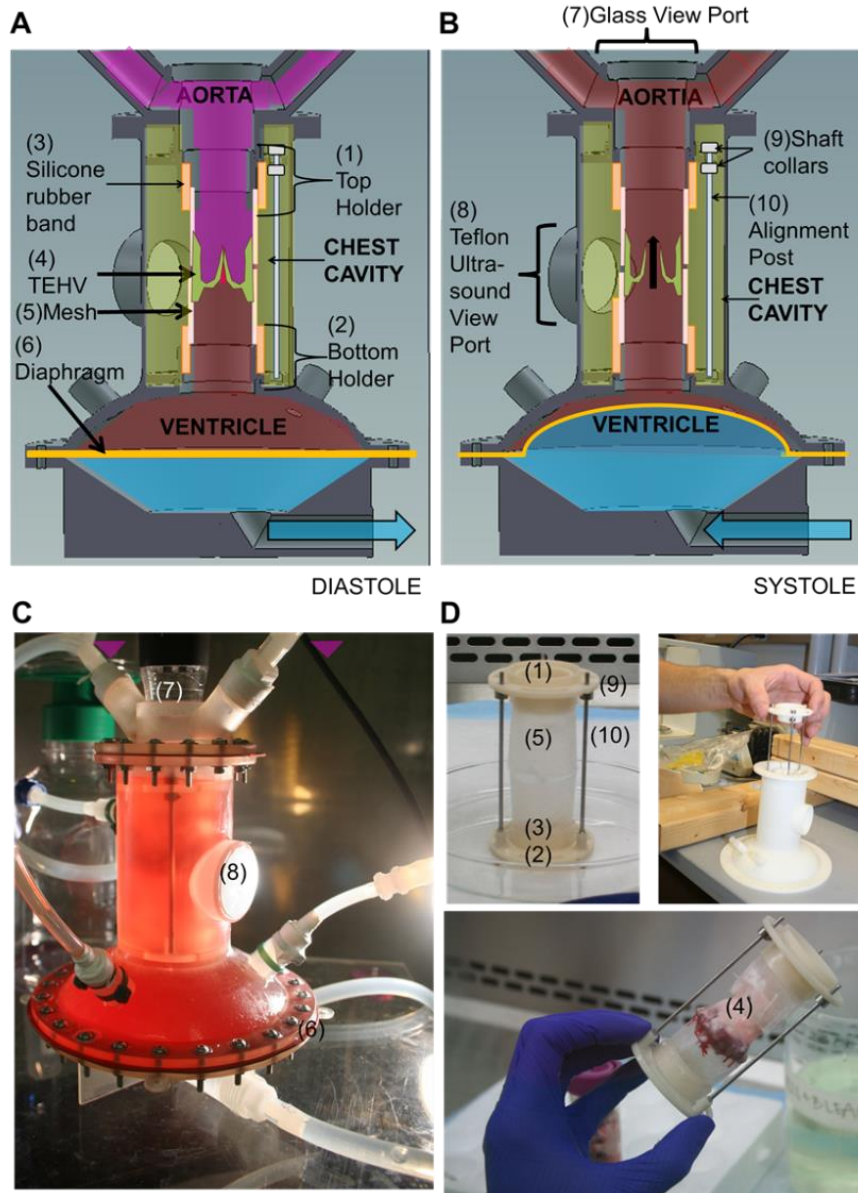


**Figure 7.2 Component diagram of Heart valve conditioning chamber and holder for 3D printed hydrogel or ex-vivo heart valves.**

A) Diastolic pressure phase. Top (1) and bottom (2) holder parts are fabricated out of the same material as the chamber parts. (2) Silicone rubber band (tightly fit over the tube part of the holders and a sleeve of GE Teflon mesh/membrane. (5) PDMS is applied to secure it. (4) The engineered or ex-vivo valve. (6) The silicone rubber diaphragm. (B) Systolic pressure phase. (C) The function and motion of the tissue can be observed using an optical viewport (7) and a Teflon ultrasound viewport (8). (D) The height of the holder is set using stainless steel shaft collars with set screws. (9) The three stainless steel alignment posts. (10) The holders follow a track when the valve assembly is loaded into the body of the conditioning chamber and the posts were positioned in the holder to not obscure the ultrasound port.

(Figure 7.2A1) and bottom (Figure 7.2A2) holder parts are fabricated out of the same material as the chamber parts. They are designed to slide in following a track along the reactor wall to fit into the main body of the reactor chamber (Figure 7.2D). The holders fit into and can seal with the openings from the ventricle and the aorta when the aortic part is bolted to the body of the chamber. A silicone rubber band (Figure 7.2A3) is cut from large silicone tubing and tightly fit over the tube part of the holders and a sleeve of GE Teflon mesh/membrane. PDMS is applied to secure it (Figure 7.2A5). The Teflon mesh is used to attach the engineered or *ex-vivo* valve (Figure 7.2A4) into the holder assembly. The valve is secured to the mesh using sutures for native heart valves and tissue glue for the 3D printed hydrogel valves. The diaphragm (Figure 7.2A6) of the ventricle chamber is made with a 1mm thick sheet of silicone rubber that is tightly bolted between the two flanges of the base. During the diastolic phase the diaphragm retracts as water is drawn out of the base. During the systolic phase pressure should be higher on the ventricular side of the valve leaflets compared to the aortic side. Under this condition the valve leaflets will open (Figure 7.2B). During the systolic phase, the diaphragm retracts as water is drawn out of the base. On the media side of the diaphragm, media is drawn from a reservoir into the ventricle in response to the dropping ventricle pressure induced by the diaphragm retraction. The function and motion of the tissue can be observed using an optical viewport (Figure 7.2C7) and a Teflon ultrasound viewport (Figure 7.2C8). The height of the holder is set using stainless steel shaft collars with set screws (Figure 7.2D9) and three stainless steel alignment posts (Figure 7.2D10). The holders follow a track when the valve assembly is loaded into the body of the conditioning chamber and the posts were positioned in the holder to not obscure the ultrasound port.

### **7.3.3 Media Flow Loop and Aortic Pressurization**

The conditioning chamber is setup to mimic the systolic and diastolic loading conditions of the cardiac cycle. Pressurized 5%CO<sub>2</sub>/air is injected into the conditioning chamber to pressurize the aortic side of the valve (Airgas, Ithaca) and achieve a transvalvular pressure during diastolic loading. This applied aortic side pressure is a set with a regulator (Airgas, Ithaca). Media cycles through the conditioning chamber and the TEHV in a flow loop that is driven by and separated from a water loop with a silicone diaphragm. During systole water is pumped into the base of the valve conditioning chamber, this deflects/deforms the silicone diaphragm in the 'ventricle' and pushes media through the TEHV into a pressurized aortic chamber (Figure 7.3A). Media circulates back to a reservoir of culture media and pressure is periodically vented from the reservoir through a pinch valve and sterile filter. One-way check valves only allow media to flow from the media reservoir into the 'ventricle' chamber of the conditioning chamber. During the diastolic phase (7.3B), pressure should be higher on the aortic side of the valve leaflets compared to the ventricular side. Transducers are connected to the ventricle and the aortic chambers to record pressure. During the systolic phase the diaphragm retracts as water is drawn out of the base. Media is drawn from the reservoir into the ventricular chamber through the one-way check valves.

### **7.3.4 Two Control Strategies for Pulsatile Conditioning: Timer Relay and Pressure Relief**

Two control strategies were investigated for bioreactor conditioning. First a control strategy was investigated where the frequency of diastolic loading and system venting is pressure independent (Figure 7.4A). Second a control strategy where diastolic loading depends on a pressure feedback signal to the microcontroller (Figure 7.4B). In the first strategy, all solenoid valves are controlled using a timer relay (Figure 7.4A). A time delay repeat cycle relay is used to control the pulse of the switching of the 3-way

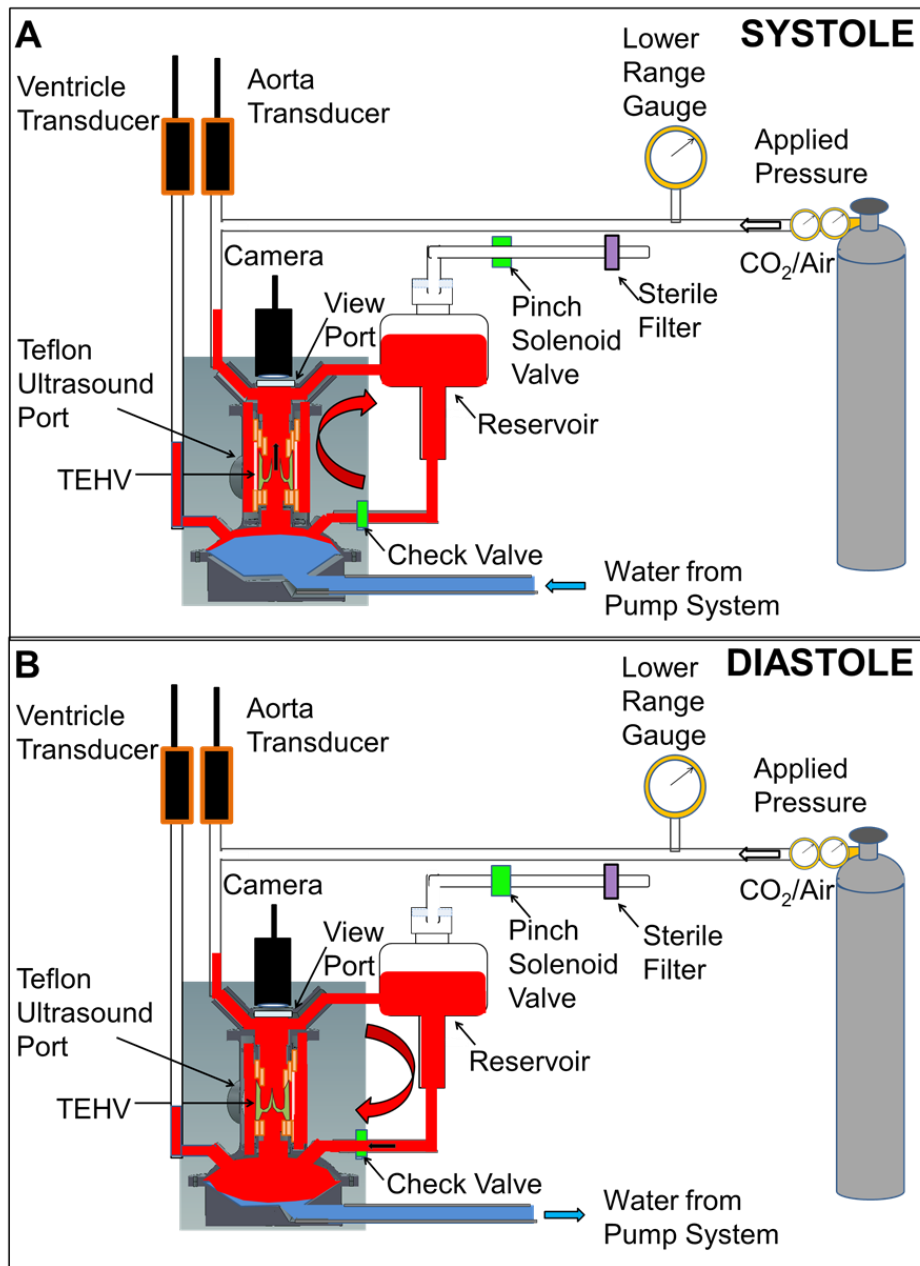


**Figure 7.3 Media flow loop and aortic pressurization diagram.**

(A) During systole water is pumped into the base of the valve conditioning chamber, this deflects/defirms the silicone diaphragm in the ‘ventricle’ and pushes media through the TEHV into a pressurized aortic chamber. Media circulates back to a reservoir of culture media, and pressure is periodically vented from the reservoir through a pinch valve and sterile filter. One-way check valves only allow media to flow from the media reservoir into the ‘ventricle’ chamber of the conditioning chamber. (B) During the systolic phase the diaphragm retracts as water is drawn out of the base. Media is drawn from the reservoir into the ventricular chamber through the one-way check valves.

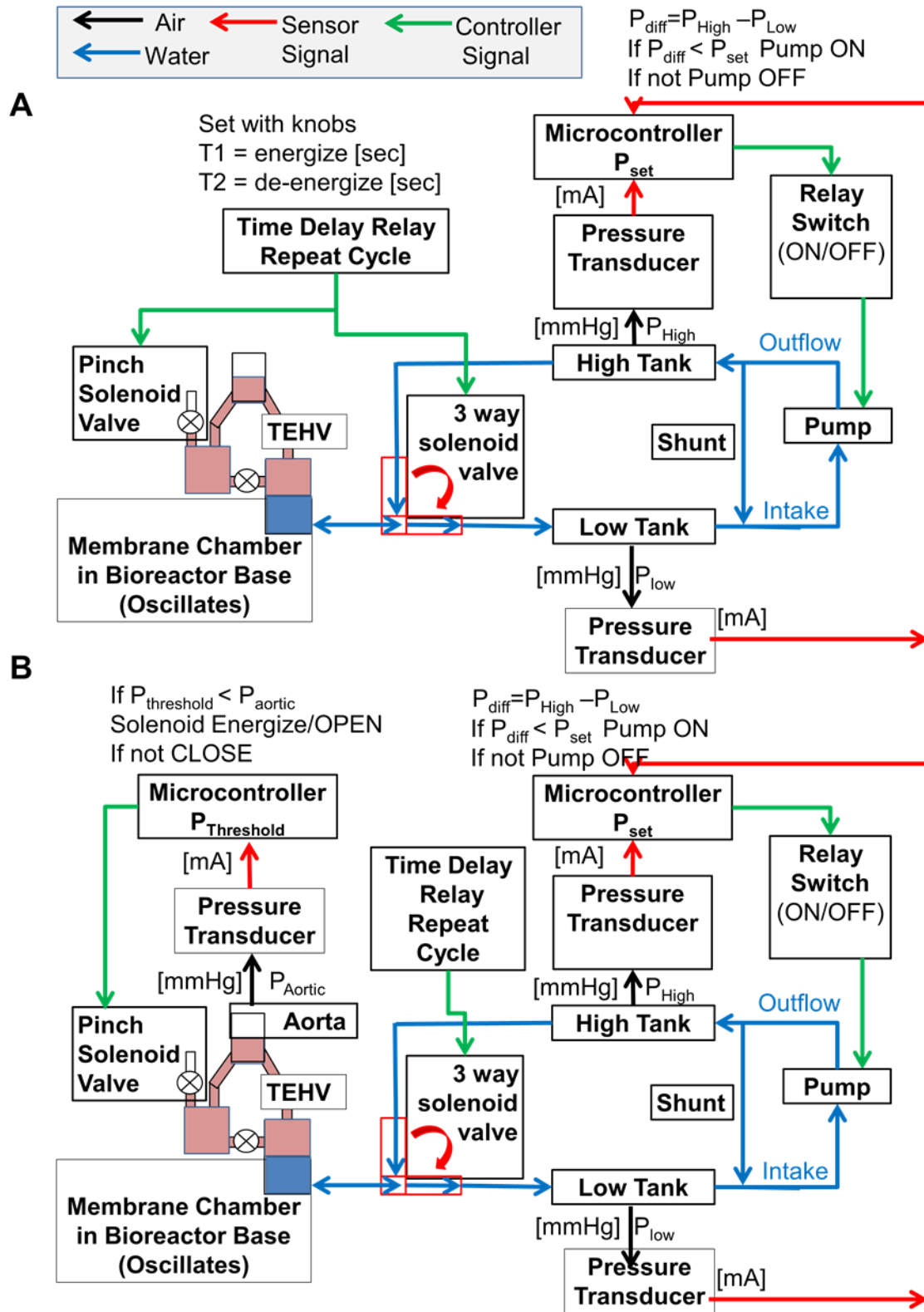


Figure 7.4 Two strategies for bioreactor system control: pressure independent (A) Strategy 1. (B) Strategy 2.

solenoid valve and the opening/closing of the pinch valve. The microcontroller signals the pump to move water from the 'low' tank to pressurize a 'high' tank based on signals from the pressure transducers. The 3-way solenoid switches between this high pressure source and this low pressure sink to provide an oscillating pulse of water to the base of the conditioning chamber. This pulse is analogous to one diastolic and systolic cycle. This is one 'beat' in terms of heart rate. The timer relay can be connected so that power or the energize signal alternates between the 3-way solenoid and the pinch valve solenoid. The pinch valve solenoid vents pressure from media reservoir and aorta with each beat in this setup. The consequence of this is the frequency of the delivered ventricular pulse and frequency of diastolic loading is independent of any pressures in the system.

For the first strategy, the functional steps of the system are: (1) the pump fills the water capacitance tank or 'High' tank with water; (2) the High tank becomes pressurized and pressure drops in the water reservoir or 'Low' tank; (3) the 3-way solenoid valve switches to connect the high tank to the bioreactor base, driving a pulse of fluid into the bioreactor base which deforms the silicone diaphragm and pressurizes the ventricle; (4) the 3-way solenoid valve switches to connect the low tank to the bioreactor base, and water is drawn out of the bioreactor base to the Low tank and the ventricle pressure drops. Meanwhile the time delay relay alternately energizes the 3-way solenoid and then the pinch valve. Aortic pressure is delivered from a 5%CO<sub>2</sub>/air tank which is set by a regulator at the tank. On step three when the 3-way solenoid switches to High tank source, the pinch valve closes. On step four when the 3-way Solenoid switches to the Low Tank sink the pinch valve opens. It is important to keep in mind when ordering, wiring the setup, and programming the microcontroller that the solenoids are sold in either an open/energized or open/de-energized assembly. The pinch valve use here is an open/energized valve type.

As an alternative control strategy, a value can be set in the microcontroller so that the pinch valve solenoid opens when pressure in the aortic chamber passes a user defined pressure threshold (Figure 7.4B). As in the first strategy, the pump is controlled by the microcontroller and the ventricular pulse from the 3-way solenoid is controlled by the timer relay. In the alternative setup the signal from the aortic pressure transducer is compared to a set pressure, if  $P_{\text{aortic}}$  is greater than  $P_{\text{threshold}}$  then pinch valve opens if  $P_{\text{aorta}}$  less than or equal to  $P_{\text{threshold}}$  then the solenoid remains closed.

### **7.3.5 Micro-controller for Regulation of Ventricular and Aortic Pressure**

During the development of the bioreactor system and in our initial characterization studies, we used two DAQ boards and Simulink/Matlab program in combination with a timer relay for the control of the electronics and data acquisition. We found that the DAQ boards were very sensitive to electromagnetic interference from the solenoids and the system was vulnerable to timeout errors. We believe this was associated with working in conjunction with a non-dedicated computer. The electronics control setup was converted to a microcontroller (Figure 7.5). The microcontroller was designed using an ATmega1284P chip on the prototype board which is used in the Cornell ECE 4760 class and programmed with C. The microcontroller was custom fabricated at Cornell at Bruce Land's laboratory in the ECE department. Four industrial pressure transducers (Dwyer Instruments, IN, ordered from Zoro tools) are each connected to a resistor and the voltage signal is read by the microcontroller and converted to a pressure measurement. The microcontroller reads the signals sent from the pressure transducers using built-in Analog-Digital-Convertor and sends out the control signal for the pump and the pinch solenoid valve through the junction box. The junction box energizes the circuit by using a relay switch. The microcontroller allows for a more compact system that only needs to be connected to a computer to take a data sample. The interface for setting the

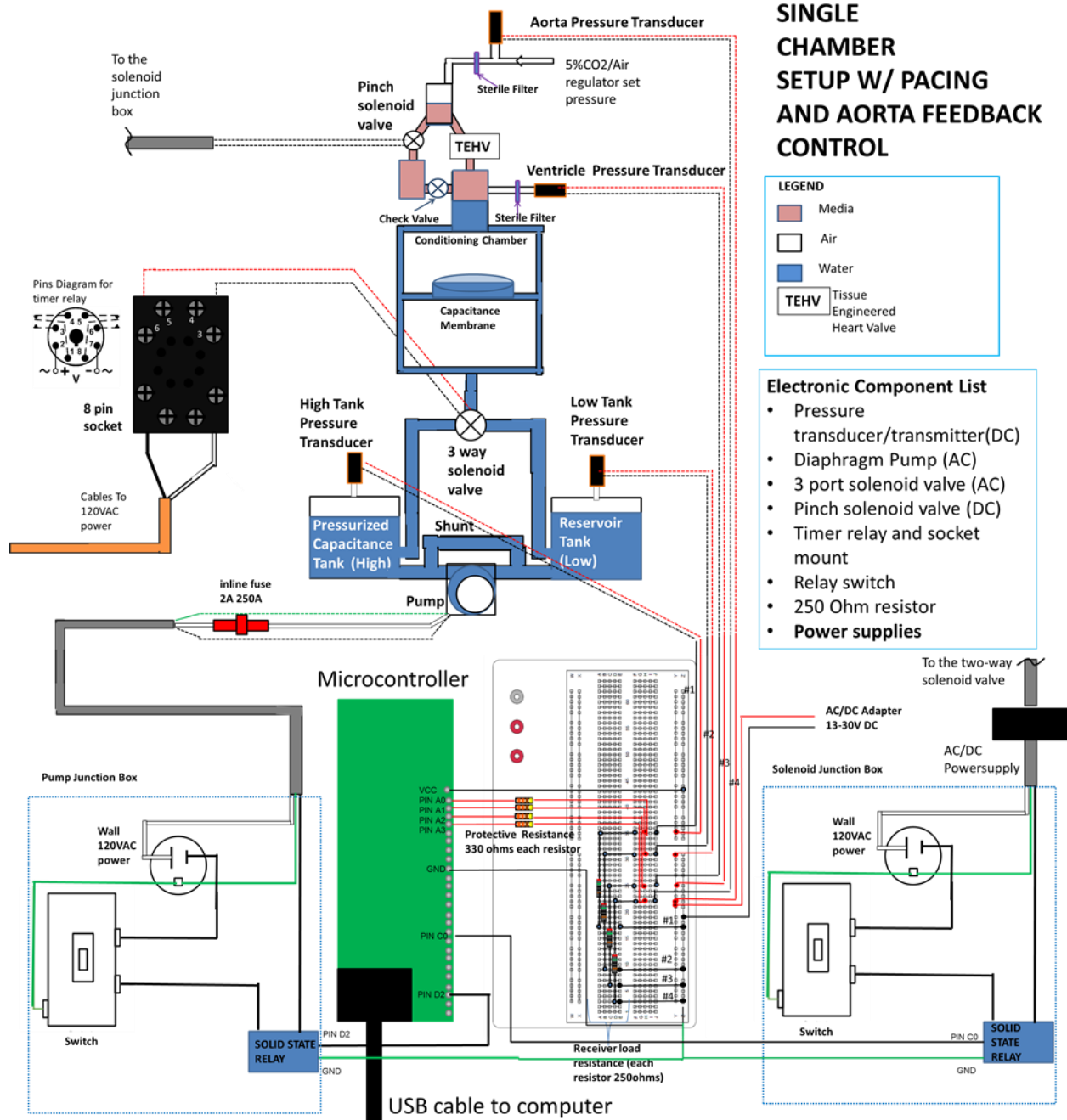


Figure 7.5 Electronics diagram for single conditioning chamber.

pressure and pump and pump conditions is written in Matlab. The user is prompted to change the  $P_{diff}$  setting, the delta setting, the aortic pressure threshold, and the data acquisition time. After the data acquisition period the system runs automatically at the set parameters. Up to 2 weeks of data can be logged in one acquisition period.

### **7.3.6 Characterizing Water Pump Flow Loop System to Drive Diaphragm in Media Loop**

The pump driven water flow loop of the bioreactor system was characterized to determine operating volumes and pressures. The pump pressurizes the high tank, drawing water from the low tank. The 3-way solenoid controls an alternating pulse of high pressure water from the 'High' tank and a sink/suction pulse back to the 'Low' tank. Depending on the pressure on the media side of the membrane there will be volume drift when the system equilibrates. Volume offset of the system was measured at a neutral (room) pressure by detaching the reactor/diaphragm chamber and connecting a graduated column for measuring volume. Deviation/drift in the system as well as the periodic oscillation/deflection needed to flex the silicone diaphragm was quantified using a video camera and tracking the rise and fall of the volume. Volume was measured with increasing pressure difference settings (at a set delta = 2). Pressure difference ( $P_{diff}$ ) was the difference between the high tank pressure and the low tank pressure ( $P_{diff} = P_{High} - P_{Low}$ ). Volume drift was measured with increasing delta settings (at a set  $P_{diff} = 150\text{mmHg}$ ). Delta describes the sensitivity or anticipation of the pump turning on to maintain  $P_{diff}$ . For these tests the sink time ( $t_{sink}$ ) and the source time ( $t_{source}$ ) were equal and set at 1 second. These times  $t_{sink}$  and  $t_{source}$  describes switching the connection between graduated column from high tank and the low tank and the time for each connection. In a connected chamber setup, the sink time is analogous to the diastolic

phase of the bioreactor cycle  $t_{\text{sink}} = t_{\text{diastolic}}$  and the source time is analogous to the ventricular phase of the bioreactor cycle  $t_{\text{source}} = t_{\text{diastolic}}$ .

### **7.3.7 Measurement of Ventricular Stroke Volume for Different Size Conditioning Chambers**

To establish dynamic conditioning ranges achievable by the system, stroke volume was measured for a miniature and large base reactor design. A graduated column to measure volume was connected to the aortic outlet of the conditioning chamber. For these tests a 1-mm thick silicone diaphragm, was bolted into the base, the sink and source time of delivered water pulse from the pump system was 1 sec ( $T_{\text{systolic}} = T_{\text{source}} = 1$  sec and  $T_{\text{diastolic}} = T_{\text{sink}} = 1$  sec). Also, the effect of applied pressure on the stroke volume was tested. 80 mmHg of aortic pressure was applied on the media side of the silicone membrane for the large base conditioning chamber. The setup tested had ¼" diameter tubing out of the high tank and low tank connected to the 3-way solenoid valve. This test was to determine the delivered stroke volume of the diaphragm so the test was run without a heart valve separating the aortic and ventricular chambers and the reservoir was disconnected so the check valves at the inlet lines of the ventricle remain closed.

### **7.3.8 Systolic Flow Rate in Heart Valve Bioreactor Calculated from Stroke Volume and Cycle Time**

Stroke volume is coupled to the time allowed for source and sink to act through the 3-way solenoid. The stroke volume is how much volume is moved when the diaphragm moves from the retracted position to the inflated position. The time this takes is  $t_{\text{systolic}}$ . The sink and source time, also known as the diastolic and systolic times are matched and when added together equal the cycle time. From the stroke volume data it is

possible to calculate an estimated systolic flow rate and then extrapolate the stroke volumes for shorter cycle times.

$$\text{Systolic Flow Rate} = \frac{\text{StrokeVolume}}{\left(\frac{t_{\text{cycle}}}{2}\right)}$$

$$t_{\text{systolic}} = t_{\text{diastolic}} = t_{\text{sink}} = t_{\text{source}}$$

$$t_{\text{cycle}} = t_{\text{systolic}} + t_{\text{diastolic}}$$

Using the slope of the stroke volume versus  $P_{\text{diff}}$  trend, the stroke volume at higher pressure settings can be calculated. These calculations were also scaled using Poiseuille's law to estimate the effect of a larger tubing size (1/2") for the sink and source tube out of the high tank and low tank.

$$R = \frac{8\eta\Delta x}{\pi r^4}$$

R= resistance to fluid movement,  $\eta$ =viscosity,  $\Delta x$ =change in distance, and r =radius of the tube.

This is treated as a hydraulic circuit where  $V=IR$ . The change in pressure is analogous to voltage. The volumetric flow rate is analogous to current. Effective resistance in the tube is inversely proportional to the fourth power of the radius. Doubling the radius reduces the resistance to fluid movement by a factor of 16.

### **7.3.9 Testing the Holder and Ultrasound Port and Characterizing Bioreactor System Pressure with Heart Valves**

Whole porcine aortic and pulmonary valves and whole ovine aortic and pulmonary valves were obtained fresh at slaughter from Shirk Meats, Himrod, NY. The aortic valves and pulmonary valves were isolated from the heart using very sharp scissors.

Blood was rinsed away with cold sterile PBS, making sure to remove blood clots. The whole valve (root and leaflets intact) was placed into a container of sterile PBS with protease inhibitor. Protease Inhibitor solution was prepared prior to isolation, with 1 protease inhibitor cocktail tablet per 50 ml of 1XPBS and sterile filtered (Roche, USA). The valves in inhibitor solution were placed into a cooler with ice for transport to the lab. At the lab, the valves were trimmed to a desired length of aortic or pulmonary root before mounting into the reactor holder. For pressure characterization tests, valves were tested within 48 hours of isolation or were frozen and thawed the day of the characterization experiment.

#### **7.3.10 Bioreactor System Pressure Characterization**

A range of input parameters were tested to characterize the pressure response of the bioreactor system. Porcine and ovine sheep valves were sutured into the mesh of the holder assembly and used for the characterization tests.  $P_{diff}$  settings in the flow loop were tested (10, 25, 50, 75, 100, 150, 200, 250, and 300 mmHg) for the miniature and large chamber designs. An aortic pressure of 0, 80, or 160 mmHg was applied. Two control setups were tested, the alternating solenoid/timer relay setup and the aortic pressure feedback setup. Data was recorded from four transducers which were connected to the high tank, the low tank, the aortic chamber, and the ventricular chamber. The sampling rate was 44 samples per second. At the beginning of each test, the capacitance membrane was connected to the flow loop for 10 cycles of the pump. The flow loop was then switched from the capacitance membrane to the bioreactor chamber base.

### **7.3.11 Optical Imaging of Heart Valves in Bioreactor Chamber**

A VMS-004D - 400x USB Microscope with adjustable focus was used to capture video and still images through the glass optical port of heart valves being conditioned in the reactor (Veho, Dayton Ohio).

### **7.3.12 Ultrasound Imaging of Heart Valves in Bioreactor Chamber**

The ultrasound port of the bioreactor chamber was tested at the Cornell University Veterinary Hospital for animals. Water soluble ultrasound transmission gel (Aquasonic 100, Parker Laboratories, Fairfield NJ) was applied to the side port of the reactor and a 5 MHz probe. The probe could be rotated to obtain different cross-sectional views of the valve. The reactor tested in this study had one ultrasound port in the side port position. From this position it is possible to use tissue doppler to look at the valve wall and leaflet motion. The chamber is fabricated so that the optical viewport in the aortic chamber can be replaced with a Teflon ultrasound port. From this position in the outflow tract of the valve it would be possible to obtain velocity information for the flow

### **7.3.13 Heart Valve and Mesenchymal Cell Culture**

Biocompatibility testing and direct cell printing encapsulation with dynamic culture conditions were tested with both primary aortic valve interstitial cells and adipose derived mesenchymal stem cells (ADMSC). Valve interstitial cells (VIC) are the main cell type that populates valve leaflets (Butcher, Simmons et al. 2008). Primary valve cells have been used to study mechanistic and remodeling behavior as well as to establish tissue engineering targets (Stephens, Durst et al. 2011; Gould, Chin et al. 2012; Duan, Hockaday et al. 2013; Gould and Anseth 2013). Heart valves are non-sacrificial, and for the purposes of tissue engineering, a heart valve cell source other than primary valve cells is needed. A recent study profiled ECM gene expression of ADMSC and VICs in response to strain. They found that the two cell types have the

capacity to synthesize and remodel the surrounding matrix and the two cell types have comparable response to mechanical stimulus (Latif, Sarathchandra et al. 2007; Colazzo, Sarathchandra et al. 2011). ADSC can be differentiated towards osteogenic, adipogenic, myogenic, chondrogenic, neurogenic, endothelial, and smooth muscle cell lineages (Colazzo, Chester et al. 2010; Wang, Yin et al. 2010). ADMSC have demonstrated similar phenotypic and functional characteristics to bone marrow mesenchymal stem cells (BMMSC), which are more established in the literature, but ADMSC isolation is less invasive (Bunnell, Flaas et al. 2008) (Colazzo, Chester et al. 2010). In addition, adipose tissue is present in infants, children, and adults (Kuzawa 1998). These characteristics suggest ADMSC are a potentially feasible cell source for TEHV that could be applicable to all three age groups.

Porcine aortic valve interstitial cells (PAVIC) were isolated via collagenase digestion as previously described (Butcher and Nerem 2004; Butcher, Penrod et al. 2004; Richards, El-Hamamsy et al. 2013). PAVIC were cultured with Dulbecco's Modified Eagle's Medium (DMEM; Invitrogen, Carlsbad, CA) supplemented with 10% fetal bovine serum (FBS; Invitrogen) and 1% penicillin/streptomycin (PS; Invitrogen). Cells were fed every 2-3 days and were used at passage number 4-8.

Cryopreserved HADMSC were purchased (Cat #:PT-5006, Lot#0F4505) Lonza, Walkersville). HADMSC were isolated from a 52 year old female donor and cryopreserved December 6, 2010. Greater than 90% of the cells were positive for CD13, CD29, CD44, CD73, CD90, CD105, and CD166. Less than 5% of cells were positive for CD14, CD31, and CD45. (Note: According to the certificate of analysis for HADMSC 23 hour doubling time). HADMSC were thawed and cultured using Dulbecco's Modified Eagle Medium: Nutrient Mixture F-12 (F12:DMEM, Invitrogen)

supplemented with 10% FBS, 1% PS. HADMSC were passaged at just sub-confluent (~90%) and fed every 3-4 days. Cells were used at passage number 4-8.

PAVIC and HADMSC were expanded and maintained in flasks with DMEM, and F12/DMEM media respectively.

### **7.3.14 Biocompatibility Testing of Media Flow Loop and Conditioning Chamber Parts**

In this bioreactor design there are many parts that come in to contact with cell culture media and cells. Biocompatibility testing was done to determine what materials to fabricate the conditioning chamber out of and what materials, parts, and glues were appropriate for the fittings and the holder of the media loop part of the reactor. Conditioned media and material-in-well biocompatibility testing of bioreactor materials were carried out with PAVIC. PAVIC are fast dividing and in the Chapter 4 viability tests they were the most sensitive cell type to encapsulation conditions. Cells were conditioned with media in 2D culture, imaged with a phase contrast microscope at day 1 - 7, and then assessed with an MTT assay.

#### Conditioned media experiments

Media was conditioned in contact with materials to be used in bioreactor valve conditioning chamber before it was used to treat cells in 2D culture (Darnell, Sun et al. 2013). The test was designed so that any leaching or toxins will become more concentrated as the test progresses because the conditioned media plus material is kept in the incubator throughout the experiment. Conditioned media is decanted from the material and media stock. Materials to be tested were cut into 8-10 mm squares, washed/scrubbed/rinsed and then sterilized using hydrogen peroxide (VHP® MD140X Biodecontamination Unit, Steris Life Sciences, Mentor OH). Six sterilized material

squares and 40 ml of DMEM media were placed in a vented cap vial in the incubator for 3 days before the media was applied to PAVIC plated into 24-well plates for one week. Media was decanted from the condition stock solution and used to feed the 24-well plates every other day.

#### Material-in well experiments

Materials were also cultured with the cells directly. Cell appearance and well coverage was assessed. MTT results from these tests were inconsistent because the material in the well sometimes mechanically disrupted or scrapes the cells or covered different area of the well.

#### MTT Assay

3-[4,5-dimethylthiazol-2-yl]-2,5- diphenyltetrazolium bromide; thiazolyl blue (MTT, Sigma-Aldrich) assay was used to measure cell metabolism of cells in biocompatibility and conditioned media experiments (Duan, Wang et al. 2010). MTT is yellow in solution and then is converted to a dark blue water insoluble MTT formazan by mitochondrial dehydrogenase of living metabolically active cells (Carmichael, DeGraff et al. 1987). Cells that are actively proliferating have an increased metabolic activity while cells that have been exposed to toxins will have decreased metabolic activity. MTT assay does not distinguish between cytostatic (growth inhibitory) and cytotoxic (lethal) effects of a treatment. MTT solution was prepared at a concentration of 5 mg MTT powder/ml in PBS and sterile filtered before use. Cell monolayers in 24-well plates were rinsed with PBS then each well was filled with 1 ml of media. 1/10 media volume of MTT solution (0.1 ml) was added to each well and incubated for 2 hours at 37°C. Media MTT solution was removed and 500 µl of Dimethyl Sulfoxide (DMSO, Sigma-Aldrich) was added per well to dissolve the formazan. 100 µl aliquots of solution were pipetted into a 96-well

plate and the absorbance of the solution was analyzed using a multi-detection microplate reader (BioTek Synergy HT) at 570 nm. Three to four wells per condition were analyzed. Results were compared using ANOVA and student's t-test.

### **7.3.15 Simplified Interlocking Valve Geometry**

A hydrogel heart valve with a simplified geometry was designed for a first demonstration of the bioreactor system with hydrogel valve conditioning. The simplified valve geometry was designed in Solidworks. It had two component STL parts that fit together: (1) three flat radially symmetric leaflets separated by a slight gap and (2) one tubular root conduit with no sinuses. This geometry had a slightly reinforced hinge point where the leaflet meets the root and the gap between the leaflets was slightly larger compared to the flat profile valve in our previous work (Duan, Kapetanovic et al. 2014).

### **7.3.16 Precursor Solution Preparation for Printing 3D Hydrogel Valves**

The hydrogel valve geometry was printed with 700PEGDA solution for the initial handling tests of the 3D printed valves in the bioreactor. MEGEL/MEHA/PEGDA precursor solution was then used to encapsulate HADMSC for direct cell printing into the valve geometry. The leaflets were printed out of a softer MEGEL/MEHA/PEGDA8000 combination and the root was printed in a stiffer MEGEL/MEHA/PEGDA8000 combination.

#### Methacrylation of HA and gelatin and PEGDA Synthesis

MEHA (Novozymes, ~1200 kDa) was synthesized by a modification of a previously published preparation (Smeds, Pfister-Serres et al. 2001; Brigham, Bick et al. 2009; Duan, Hockaday et al. 2013). Briefly, 10 ml methacrylic anhydride (MA, Sigma) was reacted with HA aqueous solution at 40 °C for 6 hr and the pH of mixture during reaction was maintained at 8.5 by adding 5N NaOH. MEGEL was synthesized as previously

described (Nichol, Koshy et al. 2010; Duan, Hockaday et al. 2013). Briefly, gelatin from bovine skin (Sigma) was dissolved at 10% (w/v) into distilled water at 40 °C and then MA (1:5 v/v to gelatin solution) was added drop by drop under stirred conditions at 40 °C for 1 hour. The obtained MEHA or MEGEL solutions were dialyzed for 3 days and lyophilized. Polyethylene glycol diacrylate molecular weight 3350 was synthesized as previously described (PEGDA 3350) (Cruise, Scharp et al. 1998; Guo, Chu et al. 2005). Poly(ethylene glycol) (PEG, Sigma) was dissolved in benzene (1.5 mmol of PEG in 150 ml of benzene) and heated to 45 °C with continuous stirring until completely dissolved. The solution was cooled to room temperature and triethylamine was added at eight-fold molar concentration (based on PEG diol end groups) to the PEG solution (12 mmol). Acryloyl chloride (Sigma) at eight-fold molar excess concentration was weighed out then diluted using benzene (1:40 acryloyl chloride to benzene) and added drop wise to the PEG solution through a drop funnel under an ice bath. The mixture was stirred overnight, and then the reaction stopped. The insoluble triethylamine was removed by filtration. PEGDA was precipitated from the solution by the addition of petroleum ester (Sigma). The PEGDA precipitate was collected using a funnel, re-dissolved in 20 ml of benzene, and precipitated again by adding petroleum ester. The precipitation process was repeated several times.

After synthesis the MEHA, MEGEL, and PEGDA products were dissolved in distilled water and transferred and sealed into dialysis tubing with a molecular weight cut off of 1000 Da. The polymers were dialyzed against distilled water for 5-7 days in 5 gallon containers with frequent water changes. The polymer product was then frozen at -20C and then lyophilized. Lyophilized polymers were stored at -20°C.

### PEGDA700MW Hydrogel Precursor Solution

For hydrogel printing without cells, the precursor solution consisted of 13.7 mM NaCl solution, .0%w/v photoinitiator, and 20%w/v PEG-DA 700MW. Un-modified soluble alginate (LF10/60, FMC BioPolymer, Drammen, Norway) was mixed into precursor solution, 10%w/v, to temporarily increase viscosity during the printing extrusion process (Hockaday, Kang et al. 2012; Kang, Hockaday et al. 2013).

### MEGEL/MEHA/PEGDA Sterile Hydrogel Precursor Solution

Polymer solutions were prepared with 4%w/v:10%w/v: 5%w/v MEHA:MEGEL:PEGDA in solution for hydrogel printing with encapsulated HADMSC. 8000MW PEGDA was used for the leaflets and 3350 MW PEGDA was used for the root. Polymer precursors were weighed out dry and then sterilized for 1 hour using germicidal UV and then transferred into sterile 50-ml conical tubes. Photoinitiators 2,2'-Azobis[2-methyl-N-(2-hydroxyethyl)propionamide] (VA-086, Wako Chemicals) and 2-hydroxy-1(4-(hydroxyethoxy)phenyl)-2-methyl-1-propanone (Irgacure 2959, BASF Corporation, Newport, DE) were weighed out and dissolved in 70% ethanol to make stock solutions 0.015g Irgacure/ml of ethanol solution which was then sterile filtered (Chandler, Berglund et al. 2011; Rouillard, Berglund et al. 2011). Stock solutions were stored at room temperature and used within 1 week. Photoinitiator stock solution was added to sterilized polymers to give a final concentration of 0.1% w/v Irgacure for the valve root, and 0.02%w/v for the valve leaflet. The remaining solution volume was made up by F12:DMEM cell culture media. Polymer precursors, photoinitiator solution, and media were combined in conical tube, the tube cap was wrapped with parafilm, and the tube placed into water bath at 37°C to dissolve.

### **7.3.17 Encapsulation and 3D Bioprinting of HADMSC into Hydrogel Valves**

To test 3D bioprinted hydrogel valves in the bioreactor conditioning system and to study the effects of dynamic culture on remodeling in these constructs, cells were encapsulated in precursor solution printed into a heterogeneous simplified valve geometry, and crosslinked the high power LED array. Two valves were printed with each experiment – one designated for dynamic culture and one designate for static culture. Cells were rinsed with PBS, trypsinized from flasks that were 80 - 95% confluent, then the trypsin was inactivated with supplemented media and cells were counted. Cells were spun down into a pellet (1000 RPM, 5 min). Cells were suspend in a small amount of media and then suspended in warmed 37°C precursor solution so that the concentration was 2.5 million cells/ml of precursor solution. Precursor solution was prepared in syringes connected by a Luer lock adapter with the stopper/piston removed from one side. Cells and precursors were stirred together with a sterile spatula. The syringe piston was reinserted, the solution gently mixed, and the bubbles were squeezed out. One syringe was detached from the Luer adapter and the precursor solution was transferred to a printing syringe. Precursor solution was printed and then printed layers were exposed to a high powered LED array (136 mW/cm<sup>2</sup> at the print surface, Chapter 3) was used to photo-crosslink the hydrogel while material was being deposited and for 5 minutes of post-extrusion. Twenty milliliters of cell culture media was applied to submerge, hydrate, and loosen the hydrogel construct and was placed in the incubator. After one hour incubation the media was exchanged for fresh. Media was exchanged after 24 hours and then the hydrogel valve designated for dynamic culture was installed in the bioreactor for 14 days of stimulation and the static culture valve was maintained in the incubator at 37°C, 5% CO<sub>2</sub>, and was fed every 48 hours for 14 days.

### **7.3.18 3D Printed Hydrogel Valve Attachment into Bioreactor Holder Assembly**

3D printed hydrogel valves were attached into the bioreactor holder assembly using 3MTM Vetbond™ tissue adhesive to bond the conduit root to the Teflon mesh. The Vetbond™ tissue adhesive is a n-butyl cyanoacrylate that polymerizes in seconds after contact with tissue and body fluids. The glue was tested for biocompatibility with both a direct material contact and a conditioned media experiment, and the cells were imaged with a phase contrast microscope at day 2,4, and 7 days of culture. For the direct glue experiment, 1 cm<sup>2</sup> square of GE Health Expanded polytetrafluoroethylene (ePTFE) membrane was bonded to the surface of the 6-well plate with 50 µl VetBond and PAVIC were seeded into the wells. For the conditioned media experiment, three 2 cm<sup>2</sup> squares of ePTFE membrane with 50 µl of polymerized applied VetBond glue were soaked in DMEM media. Media is conditioned for 3 days prior to application to cells for the conditioned media experiment. Conditioned media is decanted from the material plus media tube every other day. Any leaching or toxins will become more concentrated as the test progresses.

### **7.3.19 Cell viability, collagen, and glycosaminoglycan (GAG) secretion**

Cultured valves were stained with LIVE/DEAD Viability and Cytotoxicity Kit (Invitrogen) to determine viability of cells after 7 days and 14 days in culture. Green fluorescent Calcein-AM (LIVE) staining indicates intracellular esterase activity and red fluorescent ethidium homodimer-1 (DEAD) indicates loss of plasma membrane integrity. Dye working solution was prepared at a concentration of 4 µM DEAD and 2 µM LIVE in PBS warmed to 37°C. Media was aspirated from wells containing gel disks and dye working solution was applied directly to gels. Working solution submerged gels were incubated for 30 minutes at 37°C. Dye solution was aspirated and gels were rinsed with warmed PBS. PBS was aspirated and warmed culture media was added to wells. LIVE/DEAD stained valve portions were imaged using confocal laser scanning microscopy (25X H<sub>2</sub>O

objective, LSM 710, Carl Zeiss). Dimethylmethylene blue (DMMB) assay was performed to measure the sulfated GAG production in the hydrogel valves after 7 days and 14 days culture (Farndale, Buttle et al. 1986; Hui, Cheung et al. 2008). Pieces of the valve constructs were digested with 300  $\mu\text{g/ml}$  papain in 50 mM phosphate buffer (pH 6.5), containing 5 mM cysteine and 5 mM EDTA for 16 h at 60 °C. GAG concentration was calculated by calibrating against a standard curve obtained with shark chondroitin sulfate (Sigma). A hydroxyproline assay was used to determine if there were the changes in collagen content between the static and dynamically cultured valves, as previously described (Reddy and Enwemeka 1996; Sinthuvanich, Haines-Butterick et al. 2012).

### **7.3.20 Statistics**

JMP PRO was used to make statistical comparisons. The Student's t-test was applied to the data sets. Standard error of the mean was calculated and is displayed on graphs. Fit least squares regression analysis was done on the stroke volume trends results to compare slopes.

## **7.4 Results**

### **7.4.1 Characterization of Water Pump Flow Loop System to Drive Diaphragm Deflection in Media Loop**

When first turned on, the water loop system takes a few minutes and several cycles of the pump to equilibrate. Increasing the pressure difference between the high tank and low tank (set by the controller) increases the amount of volume drift (Figure 7.6A). The periodic deflection of the volume also varies during the cycle of the pump. This is related to the oscillation around the pressure difference setting. The volume deviation was 12 ml and 150 ml for a  $P_{\text{diff}}$  pressure setting of 50 mmHg and 250 mmHg respectively. The average volume deflection was 6 ml and 13 ml for a  $P_{\text{diff}}$  pressure setting of 50 mmHg and 250 mmHg respectively. Changing the delta setting affected

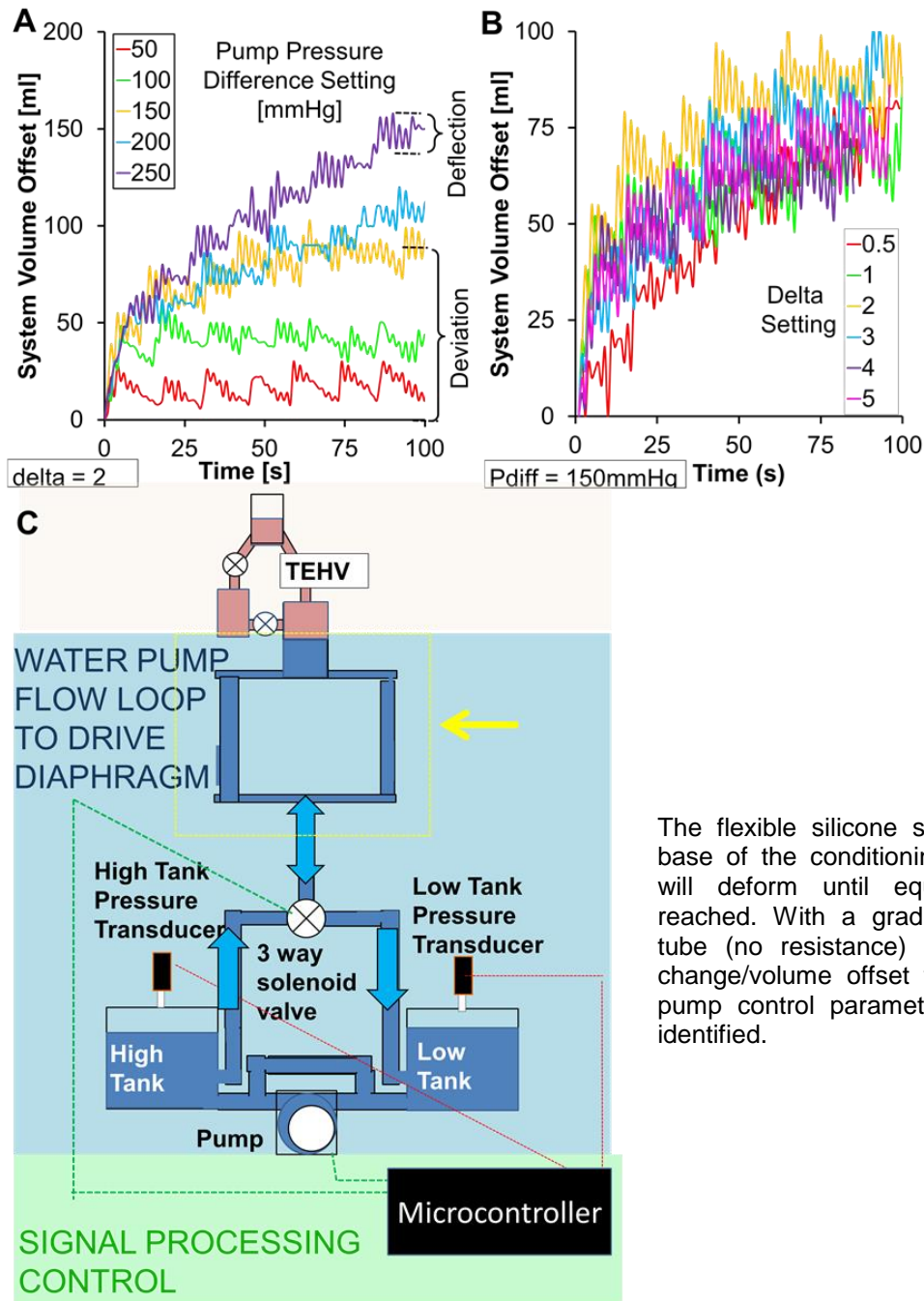


**Figure 7.6** Characterizing water pump flow loop system to drive diaphragm in media loop.

(A) Volume drift was plotted against time for different pressure difference settings ( $P_{diff} = \text{Hightank} - \text{Low tank}$ ). (B) Volume drift was plotted against time for different delta settings in the controller program. (Delta describe the sensitivity or anticipation of the pump turning on to maintain  $P_{diff}$ .) (C) Pressure drift affects the water pressure in the tubing lines indicated by the yellow arrow and box.

the pressure deviation inconsistently and did not affect the deflection except at the lower pressure setting (Figure 7.6.B). Pressure drift affects the water pressure in the tubing lines leading up to the base of the conditioning chamber (Figure 7.2C, indicated by the yellow arrow and box). The flexible silicone sheet in the base of the conditioning chamber will deform until equilibrium is reached. At higher pressure settings the volume deviation could over flex the diaphragm depending on the size of the reactor base (Figure 7.7).

Ideally the deflection of the membrane is within the dimensions of the base (Figure 7.7A). Water from the pump system will deform the silicone diaphragm. It will retract or expand as water moves to from higher pressure to lower pressure. This will simulate expansion and contraction of the heart ventricle on the media side of the silicone. High deviation and/or deflection will over flex the diaphragm where it begins to impact against the chamber walls (Figure 7.7B). This will affect the stroke volume of the ventricle chamber. Also, if the membrane deforms beyond the base and into the inflow and outflow ports, wear and break down of the silicone sheet may occur. This leads to the inclusion of an additional capacitance membrane/silicone diaphragm in the water flow loop (Figure 7.7C.2). When the pump system (Figure 7.7C.3) is first turned on the capacitance membrane expands with the extra deviation volume (Figure 7.7C.2), then the flow loop is switched/connected to the bioreactor chamber base when the volume has equilibrated (Figure 7.7C.1). Left side is the schematic diagram and right side are the images of the actual conditioning chamber with attached pressure transducers, the capacitance membrane (pale green), and the tank setup. Two diverting 3-port ball valves were used to switch the flow loop from the capacitance membrane to the bioreactor chamber base.

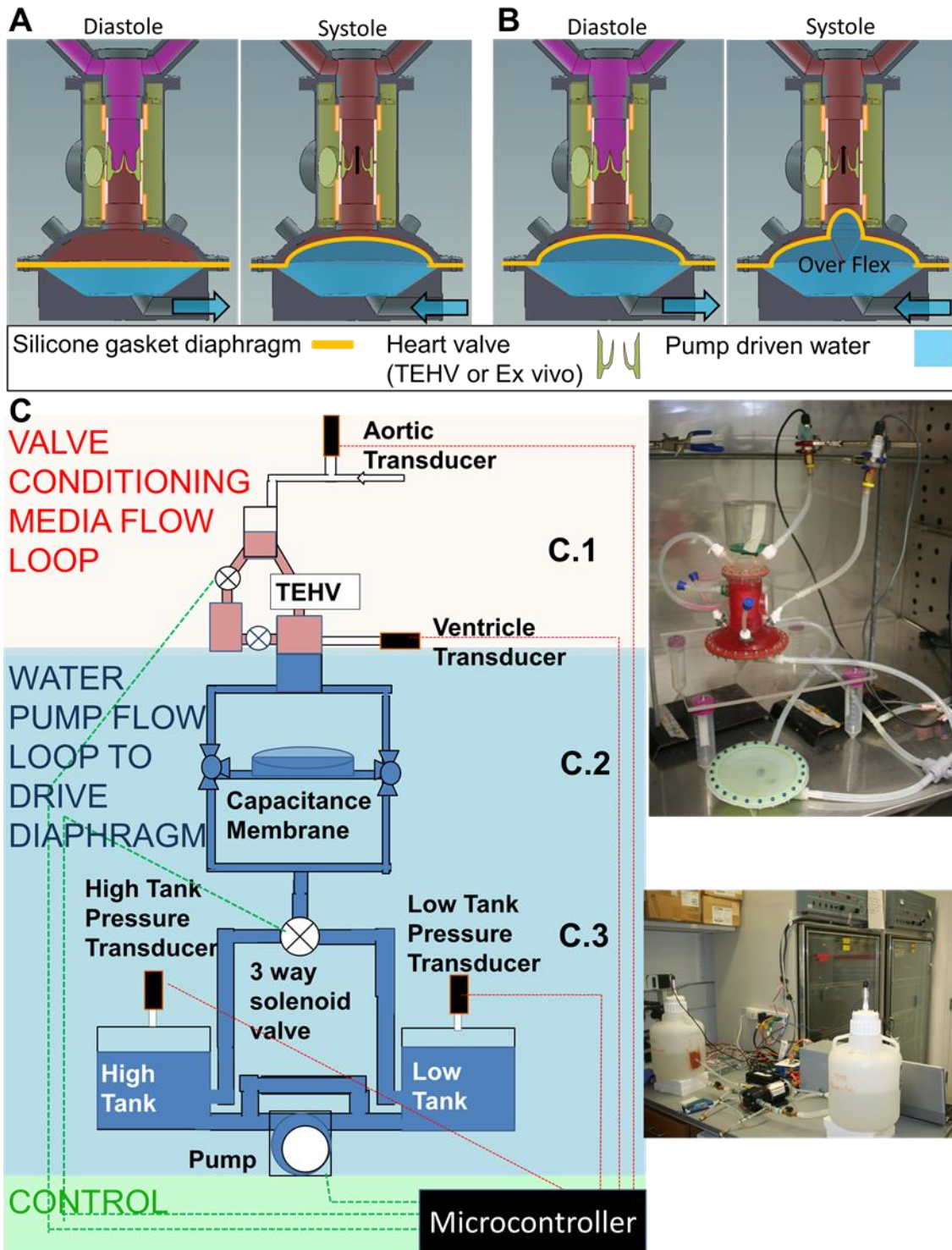


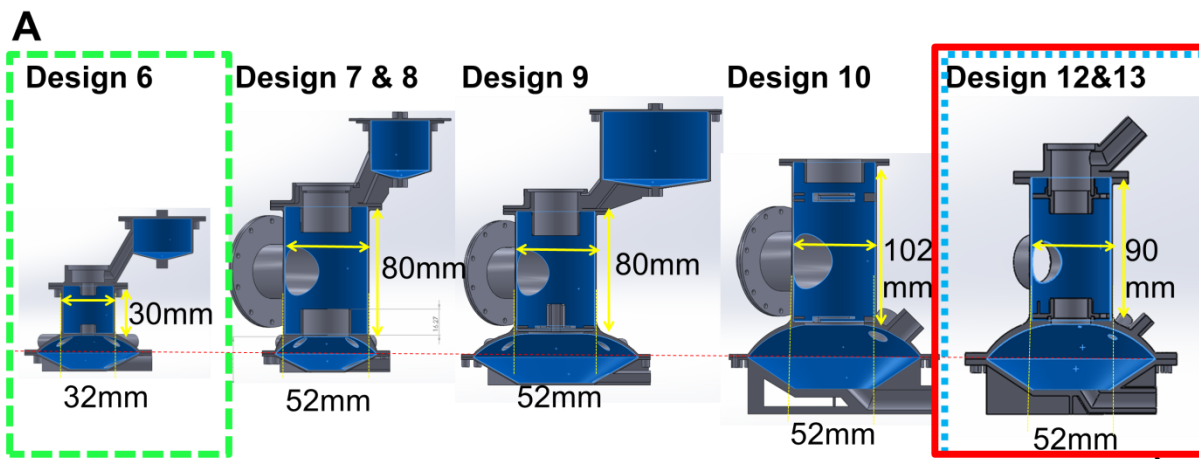
Figure 7.7 Schematic representation of diaphragm state

#### **7.4.2 Ventricular Stroke Volume for Different Size Conditioning Chambers**

The conditioning chamber design became larger as our design progressed, building in extra capacity to condition both adult and pediatric heart valves (Figure 7.8A). The conditioning chamber design 6 was optimized for minimal media usage. The working volume was 85 ml, not including a media reservoir. Inclusion of an ultrasound port, room for a aligned holder frame, and expansion of the base of the reactor increased the working volume to 478 ml. The maximum possible stroke volume is set by the dimensions of the reactor base. For the miniature bioreactor this is 37 ml and for the large base reactor this is 287 ml. Stroke volume as a function of the pressure difference setting in the water pump system followed a similar trend for the miniature base reactor (design 6) and the larger base reactor (design 12) (Figure 7.8B). Applied aortic pressure increases the slope of the trend, and stroke volume increases with  $P_{diff}$  setting more sharply with applied pressure. Standard least squares regression (using the full factorial macro in JMP) indicates slope is significantly different between the no aortic pressure large base stroke volume trend and the applied aortic large reactor base stroke volume trend.

#### **7.4.3 Systolic Flow Rate in Heart Valve Bioreactor**

The size of the conditioning chamber base size sets a limit on the stroke volume and flow rate. The bioreactor base and tubing can be scaled for a large range of stroke volumes and systolic flow rates through the TEHV. The estimated systolic flow rate and stroke volumes for shorter cycle times, at higher pressure settings, and for larger sink and source tubing are summarized in Table 7.2. Shortening the cycle time decreases the stroke volume. Systolic flow rate increases with pressure setting for miniature and large base reactors, and applied aortic pressure decreases the flow rate and stroke



<b>Aortic Chamber</b>	24 ml	35 ml	181 ml	NA	N/A
<b>Holder Chamber</b>	24 ml	170 ml	170 ml	217 ml	191 ml
<b>Base</b>	37 ml	37 ml	178 ml	219 ml	287 ml

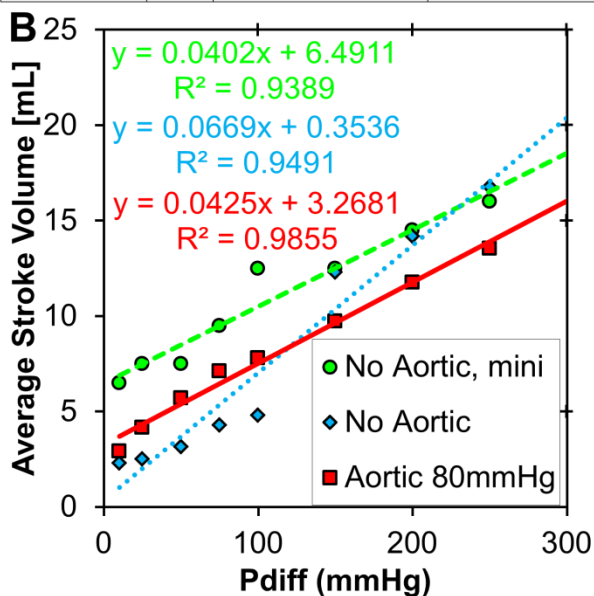


**Figure 7.8 Heart valve bioreactor base and chamber design progression and stroke volume.**

(A) The conditioning chamber design 6 was optimized for minimal media usage. The working volume was 85 ml, not including a media reservoir. Inclusion of an ultrasound port, room for a aligned holder frame , and expanding the base of the reactor increased the working volume to 478 ml. (B) Stroke volume of a small base reactor (design 6) was compared to a larger base reactor (design 12). For these tests a 1mm thick silicone diaphragm, was bolted into the base,  $T_{\text{systolic}} = T_{\text{source}} = 1$  sec and  $T_{\text{diastolic}} = T_{\text{sink}} = 1$  sec.

**Table 7.2 Extrapolated stroke volume and flow rate based on heart valve bioreactor base design, delivered pressure, and tank tubing.**

<b>Pdiff [mmHg]</b>	250							500	25
<b>Cycle Time [sec]</b>	0.25	0.5	1	2	3	4	6	2	2
<b>Mini Base Stroke Volume [ml]</b>	2	4	8	17	25	33	N/A	27	7
<b>Large Base Stroke volume [ml]</b>	2	4	9	17	26	34	51	34	2
<b>80 mmHg Applied Aortic Pressure, Large Base Stroke Volume [ml]</b>	2	3	7	14	21	28	42	25	4
<b>Mini Systolic Flow Rate [ml/sec]</b>	17							27	7
<b>Large Systolic Flow Rate [ml/sec]</b>	17							34	2
<b>Large AP 80 Systolic Flow Rate [ml/sec]</b>	14							25	4
<b>w/ Double Tube Tank Diameter (1/2")</b>									
<b>Large Systolic Flow Rate [ml/sec]</b>	273							541	32
<b>Large AP 80 Systolic Flow Rate [ml/sec]</b>	222							392	69
<b>Large Stroke Volume [ml]</b>	34	68	137	273	410	547	820	541	32
<b>Large AP 80 Stroke Volume[ml]</b>	28	56	111	222	333	445	667	392	69

volume. In the no applied aortic pressure condition, the flow rate increases from 2 ml/sec to 17 ml/sec for  $P_{diff}$  at 25 and 250 mmHg respectively. When 80 mmHg aortic pressure is applied, the flow rate increases from 2ml/sec to 14 ml/sec for  $P_{diff}$  at 25 and 250 mmHg respectively. The effect of a larger tubing size (1/2") for the sink and source tube out of the high tank and low tank had a dramatic effect on flow rates and possible stroke volumes. The tubing size works as a throttle in the system. If larger systolic flow rate is needed the tank tubing can be increased. In this system setting unmatched sink and source times eventually over-inflate or suck down the membrane. In the tested setup, the water flow loop is symmetric with the tubing lines. If an asymmetric diastolic and systolic time were desired flow rates in and out of the reactor base could be mismatched.

#### **7.4.4 Porcine Valve Sutured into Holder Assembly**

To test the bioreactor system a porcine valve was sutured into the holder assembly and loaded into the reactor. The valve was positioned in the holder/mesh so that the leaflets and sinus are in the line of sight of the ultrasound port. The base was preassembled and the check valves were installed. There were seven main steps to the assembly of the holder and insertion into the bioreactor chamber. First, the height of holder was set with the first three shaft collars on the three alignment posts (Figure 7.9A). 2<sup>nd</sup> the base of the heart valve was sutured into the Teflon mesh of the bottom holder, and then the aorta/sinotubular junction was sutured into the Teflon mesh of the top holder (7.9B). 3<sup>rd</sup>, the valve needed to be checked for buckling in case the suturing was uneven and re-sutured if necessary (Figure 7.9C). 4<sup>th</sup> the holder was fixed onto the alignment posts with the remaining three shaft collars using a hex key to tighten the set screws with (Figure 7.9D,E). 5<sup>th</sup> the holder assembly was inserted into the body of the conditioning chamber along the guide track (Figure 7.9F). 6<sup>th</sup> the chamber was filled with enough liquid to submerge the valve (PBS for pressure characterization, media for culture tests)

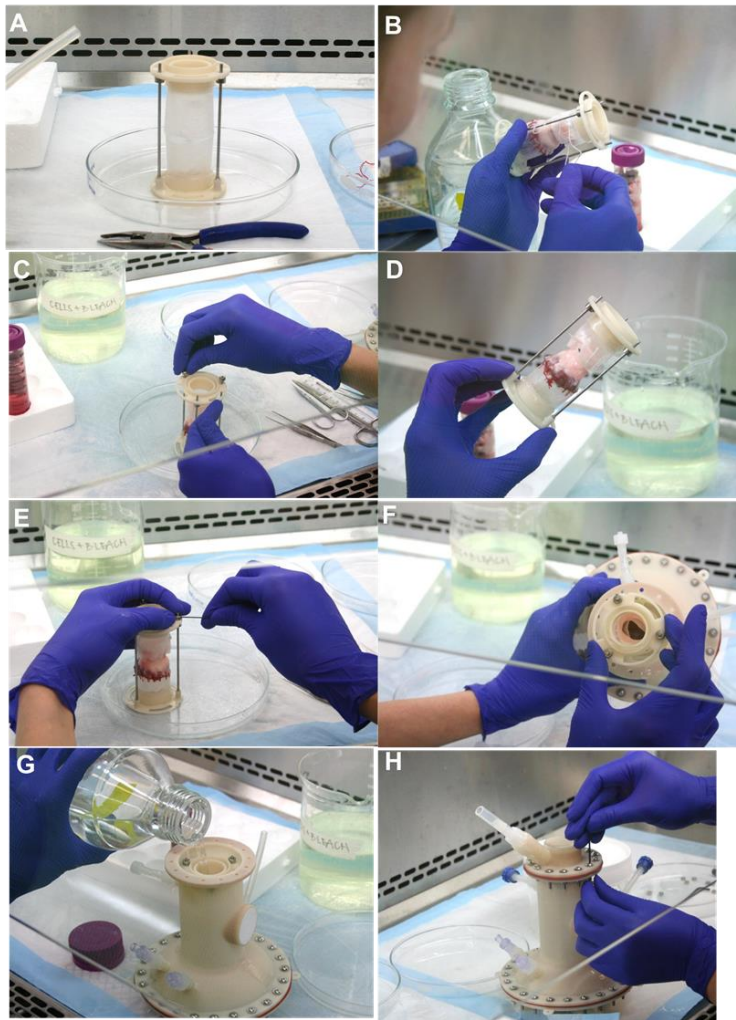


**Figure 7.9 Testing the holder setup with a porcine heart valve and system pressure characterization.**

To test the bioreactor system a porcine valve was sutured into the holder assembly and loaded into the reactor. The assembly steps were: (A) The height of holder was set with the first three shaft collars on the three alignment posts. (B) The base of the heart valve was sutured into the Teflon mesh of the bottom holder, and then the aorta/sinotubular junction was sutured into the Teflon mesh of the top holder. (C) The valve was checked for buckling caused by uneven suturing. (D) The holder was fixed onto the alignment posts with the remaining three shaft collars by (E) tightening the set screws with a hex key. (F) Holder assembly was inserted into the body of the conditioning chamber along the guide track. (G) The chamber was filled with enough liquid to submerge the valve (PBS for pressure characterization only, media for culture tests). (H) The aortic top piece flanges were mated with the body flanges, with a silicone gasket in between, and the bolt/washer/nuts were tightened.

(Figure 7.9G). 7<sup>th</sup> the aortic top piece flanges were mated with the body flanges with a silicone gasket in between and the nuts were tightened on the bolts and washers. This assembly was connected to the transducer tubing and reservoir, and then to the pump apparatus.

#### **7.4.5 Optical and Ultrasound Imaging of Heart Valve in Hard -walled Bioreactor Chamber.**

Optical imaging and ultrasound imaging of the valve in the holder setup within the bioreactor conditioning chamber was possible (bioreactor chamber design 12/13). A portable USB microscope was used to image the valve through the glass optical port in the top of the aortic part of the conditioning chamber (7.10B). This microscope could be set up in the incubator and mounted on a stand. For video and still frame imaging the reactor could be lit with a lamp because the bioreactor Steralloy material was translucent. By imaging through the glass port the leaflet appearance and movement during systole is clearly visible (7.11A). Leaflet coaptation of the porcine valve during diastole is visible with the microscope imaging (7.11B).

A 5 MHz ultrasound probe, normally used for transthoracic echocardiograms, was used to image the valve through the Teflon port on the side of the reactor chamber (Figure 7.10B). The bioreactor conditioning chamber and media flow loop was fairly portable, and could be moved in and out of the incubator and reconnected to the electronics and water flow loop as needed. The bioreactor conditioning chamber and flow loop was transported to the veterinary hospital for the ultrasound imaging. By imaging through the ultrasound port the leaflet motion during systole is visible in the transverse plane or short axis (7.11C.1) and in the sagittal plane or long axis (7.11D.1). Tissue and tissue movement is clear. Bubbles were injected and circulated through the valve for contrast. to observe liquid movement. The coaptation of the leaflets is evident in both the short



**Figure 7.10** Microscope and ultrasound imaging of valve in bioreactor.

(A) A USB microscope was used to image the valve through the glass optical port in the top of the aortic part of the conditioning chamber. (B) A 5 MHz ultrasound probe was used to image the valve through the Teflon port through the side of the reactor chamber.

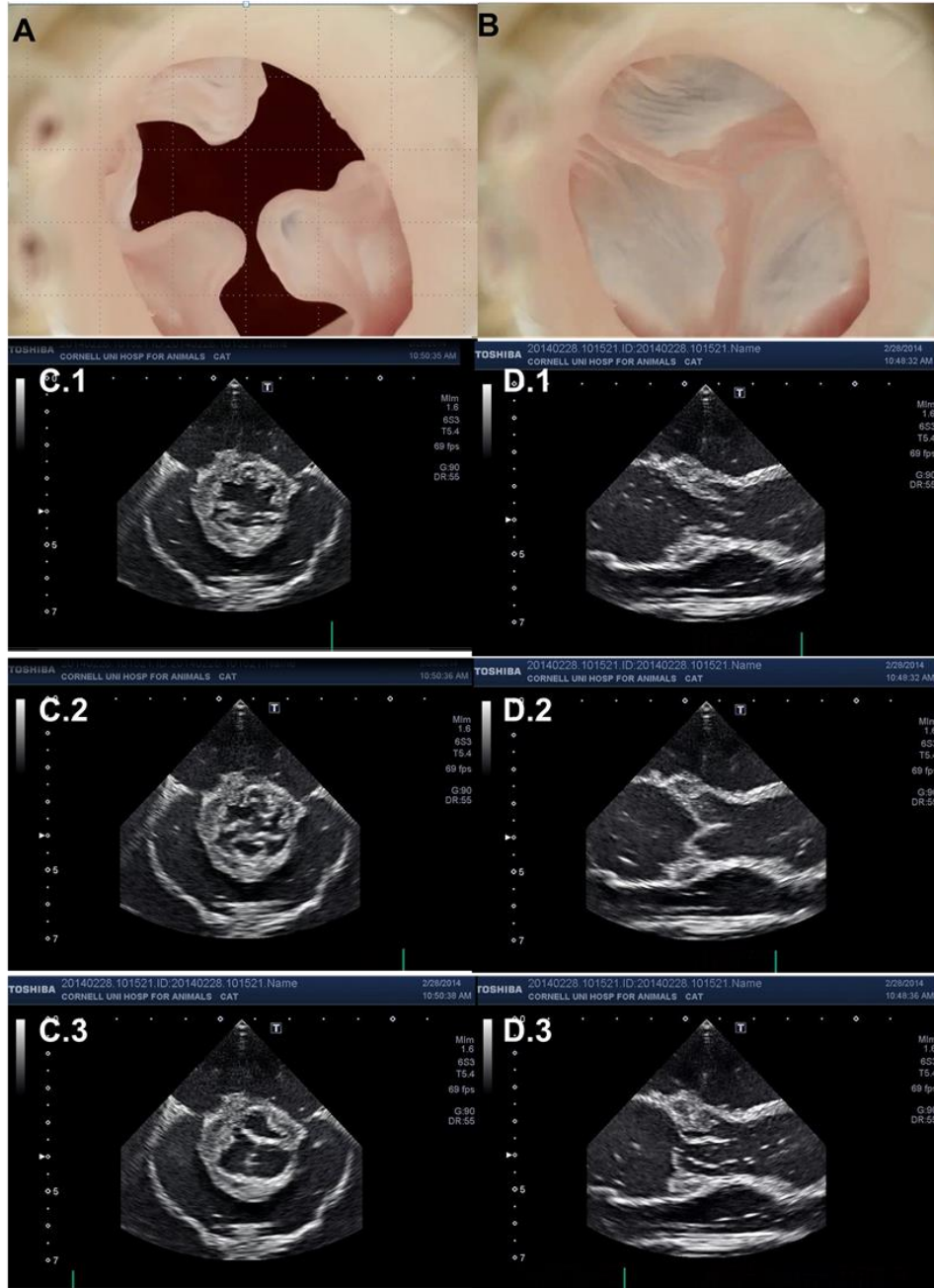


**Figure 7.11 Microscope and ultrasound images of systole and diastole**

(A) By imaging through the glass port leaflet appearance of the porcine valve used for validation and movement during systole is clearly visible. (B) Leaflet coaptation of the porcine valve during diastole is visible with the microscope imaging. (C and D) By imaging through the ultrasound port the leaflet motion during systole is visible in the transverse plane or short axis (C.1) and in the sagittal plane or long axis (D.1). Bubbles can be injected and circulated through the valve for contrast. The coaptation of the leaflets is evident in both the short axis (C.2, C.3) and the long axis (D.2, D.3). Diastolic loading of the valve once the leaflets have coapted shows deformation of the valve root and leaflets (D.3).

axis (7.11C.2, 7.11C.3) and the long axis (7.11D.2, 7.11D.3). Diastolic loading of the valve once the leaflets have coapted shows deformation of the valve root and leaflets (7.11D.3). The picture on the ultrasound monitor shows the displayed 'beam' from the transducer the ultrasound port and structures at the bottom of the images are furthest away. The focal zone, where the area of greatest resolution is, is marked by a small carat on the left side of the images. It was possible to adjust this focal zone to be right in the center of the valve, and to section on either side (images were shown here of the center section). The stainless steel posts are acceptably positioned in the reactor so they do not obscure the image. In the short axis view (7.11C) although the three posts around the valve are visible to the ultrasound.

#### 7.4.6 Aortic and Ventricular Pressure Ranges of Bioreactor for Changing Flow Loop and Applied Pressure Parameters

##### Alternating solenoid timer relay control setup

Pressure traces were recorded for a 10mmHg  $P_{diff}$  setting with no applied aortic pressure for the high tank, low tank, ventricle, and aortic chambers for the alternating solenoid/timer relay control setup (7.12A). The sink and source time for the flow loop was matched so that  $t_{systolic} = t_{diastolic}$  which was set to 1 sec. With the alternating solenoid control setup the pinch solenoid opens at the same time that the diaphragm expands and pushes fluid out of the ventricle. The high and low tank pressures fluctuate as the pump turns on and off to maintain the  $P_{diff}$ . The pump fills the high tank by drawing liquid from the low tank, and the rise of the pressure in the high tank is matched by the fall of the pressure in the low tank. At the low (10 mmHg)  $P_{diff}$  setting the change in the actual pressure difference between the high tank and the low tank during the pump cycle visibly affects the pressures in the ventricle and aortic chambers. Pressure traces were recorded for a 150 mmHg  $P_{diff}$  setting with no applied aortic pressure for the high tank,

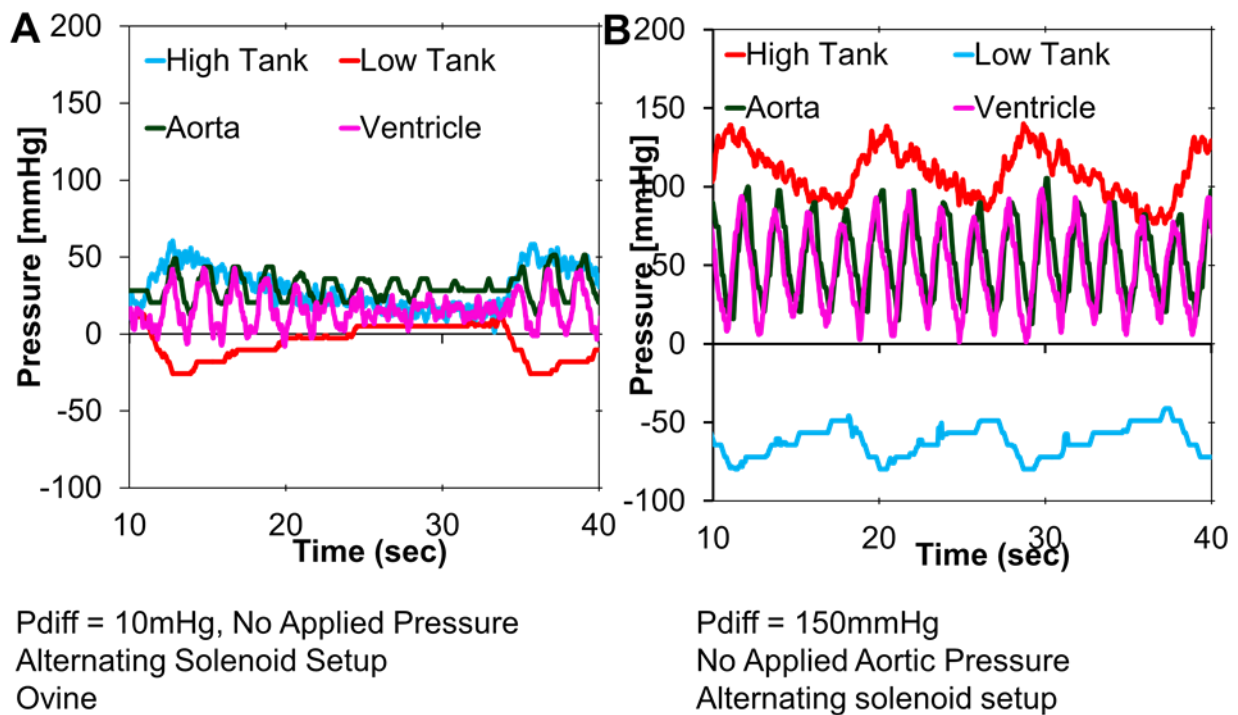


**Figure 7.12 Representative pressure traces of high tank, low tank, aortic, and ventricular chambers in an alternating solenoid control setup.**

(A) Pressure traces were recorded for a 10mmHg  $P_{diff}$  setting with no applied aortic pressure for the high tank, low tank, ventricle, and aortic chambers. The sink and source time for the flow loop was matched so that  $t_{systolic} = t_{diastolic}$  which was set to 1 sec. With the alternating solenoid control setup the the pinch solenoid opens at the same time that the diaphragm expands and pushes fluid out of the ventricle. (B) Pressure traces were recorded for a 150 mmHg  $P_{diff}$  setting with no applied aortic pressure for the high tank, low tank, ventricle, and aortic chambers.

low tank, ventricle, and aortic chambers for the alternating solenoid/timer relay control setup (7.12B). At the higher (150 mmHg)  $P_{diff}$  setting an effect of the oscillating pressure difference between the high tank and the low tank during the pump cycle is still present in the ventricle and aortic pressure traces but it is less pronounced. When there is no applied aortic pressure the aortic pressure follows the rise in ventricle pressure.

Pressure traces were also plotted showing just the aortic and ventricle pressures (7.13). The pressure profile of a 75 mmHg  $P_{diff}$  setting with no applied aortic pressure (7.13A) and the pressure profile of a 150 mmHg ( $P_{diff}$ ) setting are similar with the ventricle pressure leading the aortic pressure. When 78 mm Hg pressure is applied to the aorta using the pressurized tank of 5% CO<sub>2</sub>/air the ventricle and aortic pressures both shift up for both a 75 mmHg  $P_{diff}$  condition and a 150 mmHg  $P_{diff}$  condition (Figure 7.13B and D respectively). With the alternating solenoid control setup the pinch solenoid opens at the same time that the diaphragm expands and pushes fluid out of the ventricle. Under a pressurized aortic condition, when the pinch valve opens it vents the pressure. As a result the rise and fall of the aortic and ventricular pressure are more in phase. The pressure traces of the applied pressure conditions indicate that the aortic pressure remains higher than the ventricular pressure. However, in the viewport it was possible to see that the valve is opening and closing with and without applied aortic pressure for 75 and 150 mmHg  $P_{diff}$  settings. There also does not appear to be regurgitation of liquid back into the ventricle through the leaflets. This indicates that the pressure traces shown by the transducers are offset from the pressures experienced at the valve leaflets. For the leaflets to open and fluid to flow through the heart valve, pressure on the ventricle side must overcome the pressure on the aortic side.

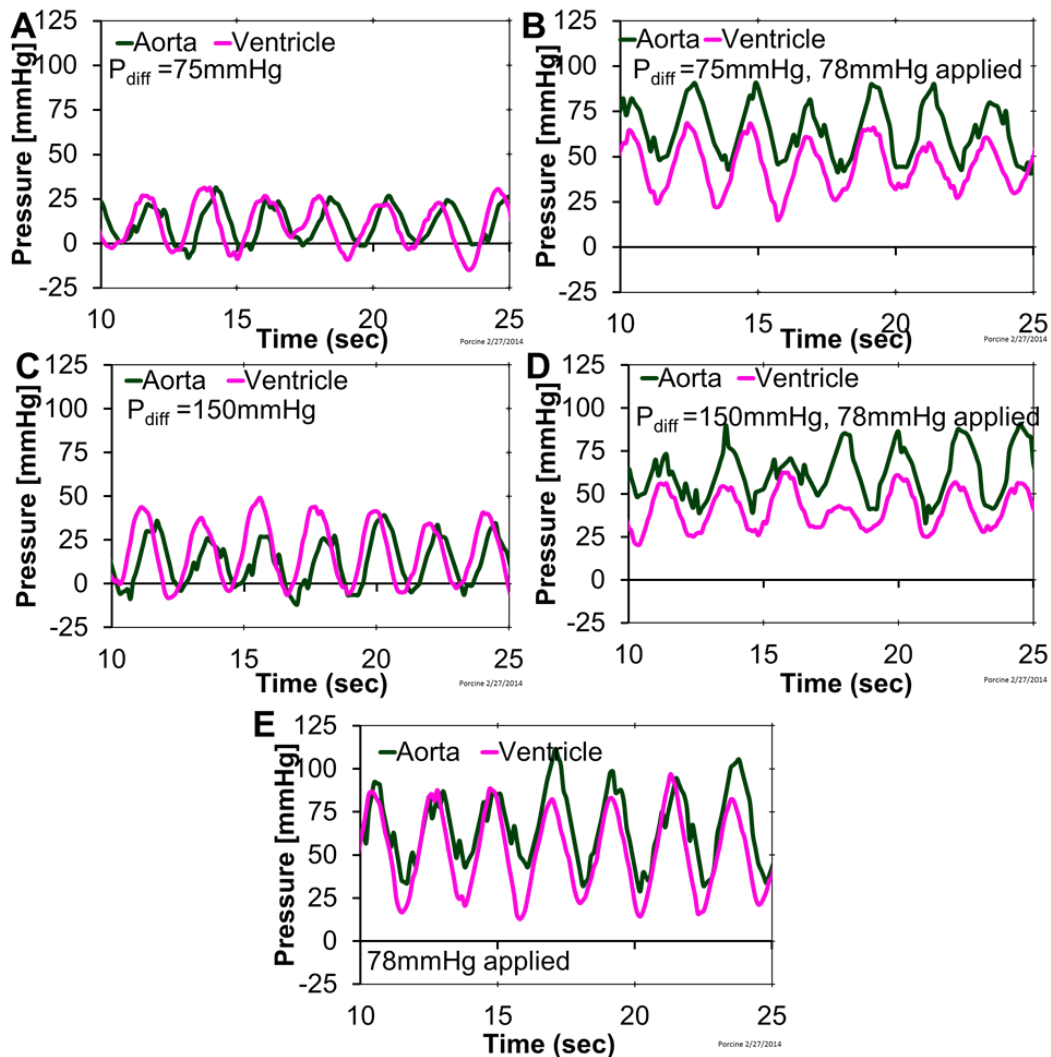


**Figure 7.13** Representative pressure traces of aortic and ventricular chambers in an alternating solenoid control setup with applied aortic pressure.

(A) Pressure traces were recorded for a 75 mmHg  $P_{diff}$  setting with no applied aortic pressure for the ventricle and aortic chambers. (B) Pressure traces were recorded for a 75 mmHg  $P_{diff}$  setting with 78 mmHg applied aortic pressure for the ventricle and aortic chambers. (C) Pressure traces were recorded for a 75 mmHg  $P_{diff}$  setting with no applied aortic pressure for the ventricle and aortic chambers (D) Pressure traces were recorded for a 150 mmHg  $P_{diff}$  setting with no applied aortic pressure for the high tank, low tank, ventricle, and aortic chambers. With the alternating solenoid control setup the pinch solenoid opens at the same time that the diaphragm expands and pushes fluid out of the ventricle. For (A), (B), (C), and (D) the sink and source time for the flow loop was matched so that  $t_{systolic} = t_{diastolic} = 1 \text{ sec}$ . (E) To investigate a diastolic loading only condition pressure traces were recorded with the flow loop disconnected from the base (connected to the capacitance membrane instead) with the regulator for the applied aortic pressure set at 78 mmHg.

To investigate a diastolic loading only condition, pressure traces were recorded with the flow loop disconnected from the base (connected to the capacitance membrane instead) with the regulator for the applied aortic pressure set at 78 mmHg (Figure 7.13E). In this situation the aortic pressure leads the ventricular pressure. Media does move around the valve and which is how the ventricular pressure follows the aortic pressure. Water or media can flow around the valve a few ways. The valve is held in a Teflon mesh that water (or media) will pass through the mesh at pressures greater than 38 mmHg. There are small equilibrium holes between the chest cavity and the ventricle chamber. For aortic valves, the coronary ostia allow flow from the aorta into the chest cavity of the reactor. There could be gaps in the sutures.

#### Aortic pressure feedback control setup

The aortic pressure feedback control setup was tested by setting a threshold for the aortic pressure, setting the regulator on the tank for the applied aortic pressure at that number, and then running the system at the 10-300 mmHg range of  $P_{diff}$  settings. The pressure traces show that this control strategy (at least at the settings explored) gives a more physiological simulation of cardiac conditions (in terms of the Wiggers diagram) (Figure 7.14). The pressure traces show that an offset between the aortic pressure and the ventricle pressure can be maintained, and that when the ventricle contracts the pressure rises to meet the aortic pressure. The logic of the microcontroller is that if  $P_{threshold}$  less than  $P_{aortic}$  then the pinch solenoid valve will energize and open, allowing flow through the tubing vent out of the reservoir, and if the  $P_{threshold}$  is equal to or greater than the  $P_{aortic}$ , the solenoid will remain closed. It should be noted that the regulator pressure gauges do not have a very fine scale so there is some margin of error for how precisely we are able to set the applied aortic pressure at 80 mmHg and 160mmHg. When the pressure delivered by the regulator was set at 80 mmHg and the pressure relief threshold in the microcontroller was set to match the applied aortic pressure, a 75

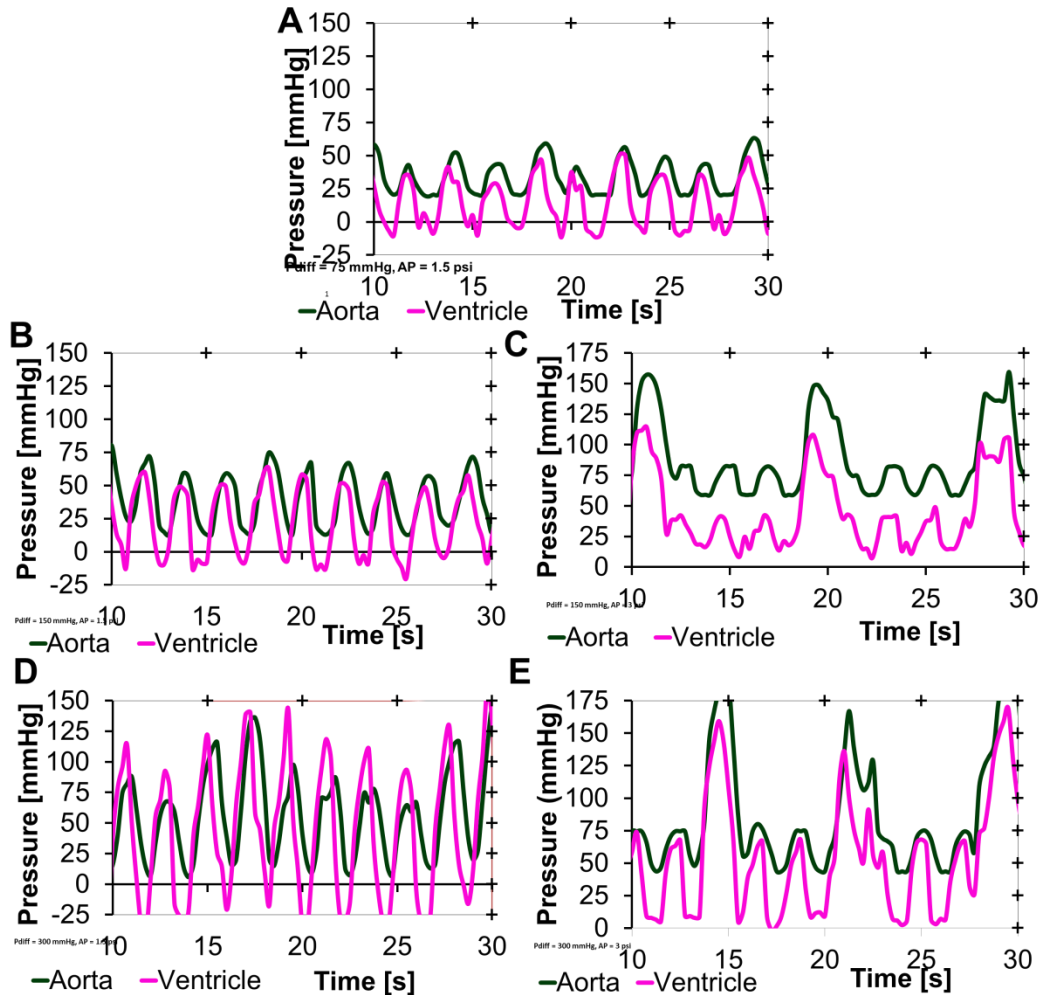


**Figure 7.14 Representative pressure traces of aortic and ventricular chambers in an aortic pressure feedback control setup.**

The pressure relief threshold in the microcontroller was set to match the applied aortic pressure. (A) Pressure traces were recorded for the ventricle and aortic chambers with a 75 mmHg  $P_{diff}$  setting in the flow loop with applied aortic pressure of 80mmHg. The pinch valve was controlled by the microcontroller and the pressure relief threshold was set at 80mmHg. (B) Pressure traces were recorded for the ventricle and aortic chambers with a 150 mmHg  $P_{diff}$  setting, 80mmHg applied aortic pressure, and a 80mmHg relief threshold. (C) Pressure traces were recorded for the ventricle and aortic chambers with a 150mmHg  $P_{diff}$  setting, 160 mmHg applied aortic pressure, and a 160 mmHg relief threshold. (D) Pressure traces were recorded for the ventricle and aortic chambers with a 300mmHg  $P_{diff}$  setting, 80 mmHg applied aortic pressure, and a 80 mmHg relief threshold. (E) Pressure traces were recorded for the ventricle and aortic chambers with a 300mmHg  $P_{diff}$  setting, 160 mmHg applied aortic pressure, and a 160 mmHg relief threshold. With the pressure feedback control setup the pinch solenoid opens at the same time that the diaphragm expands and pushes fluid out of the ventricle. For all traces shown the sink and source time for the flow loop were matched so that  $t_{systolic} = t_{diastolic} = 1$  sec.

mmHg  $P_{diff}$  setting in the flow loop triggers the pressure relief solenoid to energize with each beat (Figure 7.14A). Pressure traces recorded for the ventricle and aortic chambers with a 150 mmHg  $P_{diff}$  setting, 80 mmHg applied aortic pressure, and a 80 mmHg relief threshold show that the peak ventricle and aortic pressure for a given beat can be increased compared to 7.14A by increasing the  $P_{diff}$  setting and that the pinch valve will vent with each beat (Figure 7.14B). Setting the parameters at 150 mmHg  $P_{diff}$ , 160 mmHg applied aortic pressure, and a 160 mmHg relief threshold shows that there is a delay/recovery phase when the much higher aortic pressure is applied (Figure 7.14C). This is also evident for the 300mmHg  $P_{diff}$  setting tests where 80 mmHg was the applied aortic pressure and relief threshold setting(Figure 7.14.D) and 160 mmHg was the applied aortic pressure and relief threshold setting (Figure 7.14.E). With the pressure feedback control setup, the diaphragm expands and pushes fluid out of the ventricle and the aortic pressure rises, triggering the opening of the pinch solenoid. For all traces shown in this set of experiments the sink and source time for the flow loop were matched so that  $t_{systolic} = t_{diastolic} = 1$  sec.

#### **7.4.7 Biocompatibility Testing of Media Flow Loop and Conditioning Chamber Parts**

Materials that were biocompatible and could be used in contact with media were subsequently chosen for bioreactor assembly and fabrication (Table 7.1). During the design phase of the chamber and holder assembly, possible materials were explored with conditioned media experiments and MTT assay. (Figure 7.15, Figure 7.16A, Figure 7.17A). For the fabrication of the bioreactor chamber, we found that the Durable Fine plastic Ponoko 3D printed material and the Quickparts SLA materials tested were all detrimental to PAVIC viability (Figure 7.15, Figure 7.16B). Once we found that the standard commercially 3D printed and SLA parts were not compatible with valve cells,

**Table 7.1 Media loop: Parts in Contact with Cell Culture Media/Bioreactor Interior**

Part in Bioreactor Setup	Material	Manufacturer	Part Number/ID	Critical Specifications	Sterilization
Cast Chamber Parts	Quickparts/Hapco Steralloy cast chamber parts	Quickparts 3D Systems, Atlanta GA. Hapco, Haover MA.	Steralloy 2463	gel time: 20min, hardness Shore: 80D, resin viscosity: 6700cps, Demold time: 6-12 hours or 2-4 hrs at 50°C	H2O2
Mesh connecting holder to valve	ePTFE Membrane Laminated to Polypropylene	GE Healthcare Bio-Sciences, Pittsburg, PA.	QL230	bonds with tissue glue and suturing; biocompatible with VIC; Pore Size: 5.0um; Air permeability: 5.5-8.0 cfm at 125Pa; Water entry Pressure: >0.7 psi	
Ultrasound Port	1/4" Teflon	McMaster-Carr, Cleveland, OH	8545K1	longitudinal speed of sound 1376 m s <sup>-1</sup> compared with 1540 m s <sup>-1</sup> in soft tissue	
Optical Port	Heat-Resistant Borosilicate Glass disc 1-1/4" Diameter, 1/4" Thick		8477K71	glass resists clouding and pitting, highly chemical and heat resistant, and low rate of thermal expansion	H2O2 or Autoclave
Diaphragm	extreme temperature silicone rubber sheet		3788T42	1mm thick	
Shaft collars for holder	Stainless Steel		57485K11	corrosion resistance	
Glue on fittings and holder	Polydimethylsiloxane (PDMS) Sylgard 184 silicone elastomer kit	Dow Corning	3097358-1004	formed at a concentration of 20:1 base to curing agent, degassed, poured applied, and solidified at 70°C overnight	
Luer lock and barbed fittings 1/8"	Natural Kynar PVDF	Value Plastics, Fort Collins, CO.	S230-J1A	1/4-28 UNF Thread with 5/16" Hex to 200 Series Barb, 1/8" (3.2 mm) ID Tubing,	
Check valves, 1/8"	Polycarbonate w/Silicone Disc		VPS5401068N	420 mL/min flow rate at 1M head, 30 psi back pressure, 1/4 13mmHg cracking pressure	H2O2
Pressure Transducers	Stainless Steel	Dwyer Instruments	628-08-GH-P1-E1-S1	Output: 4-20 mA 2-wire, Range: 0-30 psig, Power Supply: 13-30 VDC	Spray with 70% Ethanol and UV sterilize 1 hour

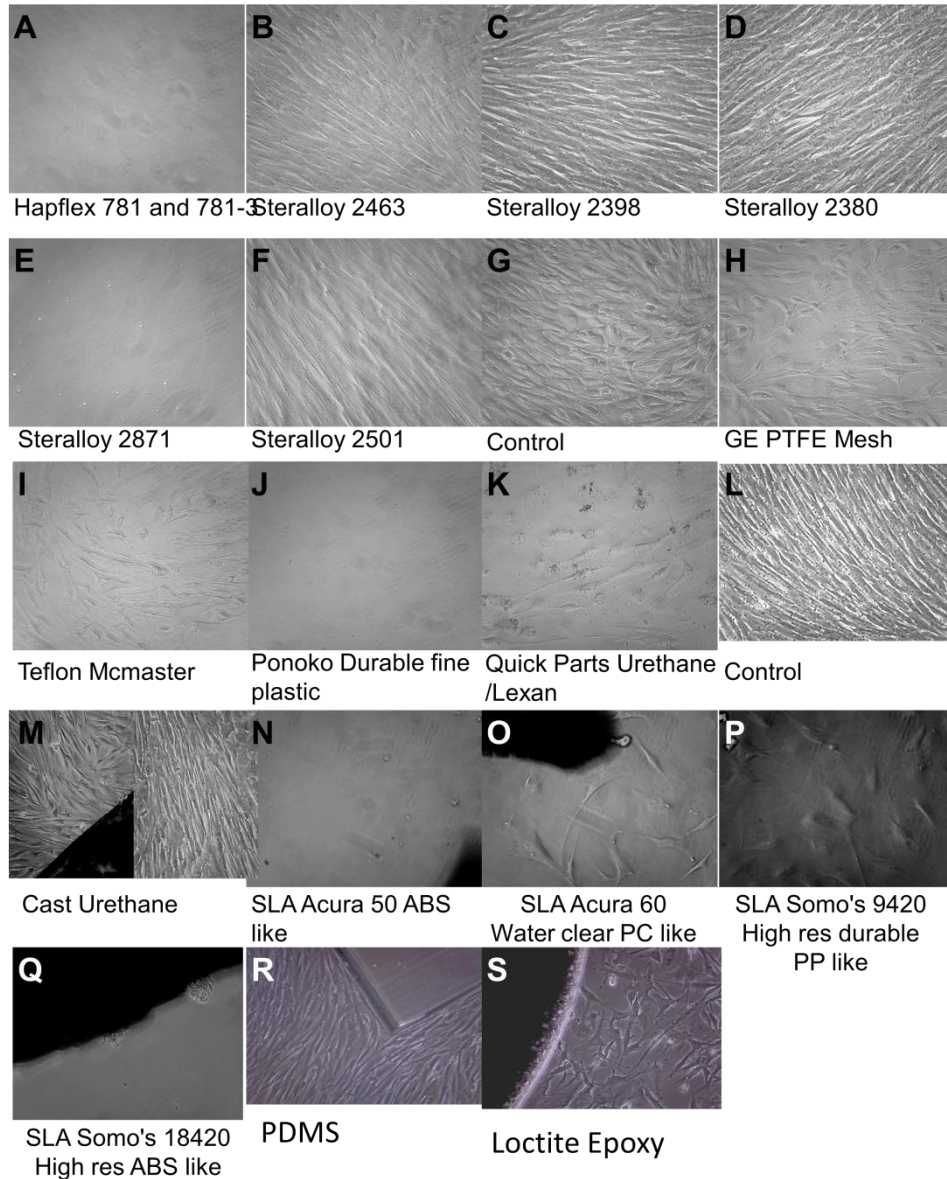


**Figure 7.15 Representative images of biocompatibility well experiments.**

Materials that were tested with conditioned media experiments were: (A) Hapflex 781 and 781-3, (B) Steralloy 2463, (C) Steralloy 2398, (D) Steralloy 2380, (E) Steralloy 2871, and (F) Steralloy 2501. (images A-F were taken at day 4 of conditioned media treatment for wells seeded at  $2.0 \times 10^4$  cells/cm<sup>2</sup>). Conditioned media experiments with a sparser cell density were used test materials: (G) Control, (H) GE PTFE Mesh, (I) Teflon McMaster-Carr for ultrasound port, (J) Ponoko durable fine plastic, (K) Quickparts Urethane/Lexan (Note: cells died and peeled off in sheets after 24 hours in conditioned media). (images G-K were taken at day 6 of conditioned media treatment for wells seeded at  $1.0 \times 10^4$  cells/cm<sup>2</sup>). Material in well experiment were also used to test materials: (L) Control (M) Quickparts Cast Urethane/Lexan, (N) Quickparts SLA Acura 50 ABS like, (O) Quickparts SLA Acura 60 Water clear PC like, (P) Quickparts SLA Somo's 9420, High res durable PP like, (Q) Quickparts SLA Somo's 18420, High resolution ABS like, (R) Sylgard PDMS, and (S) Loctite Epoxy. Images L-N were taken 6 days after wells were seeded.

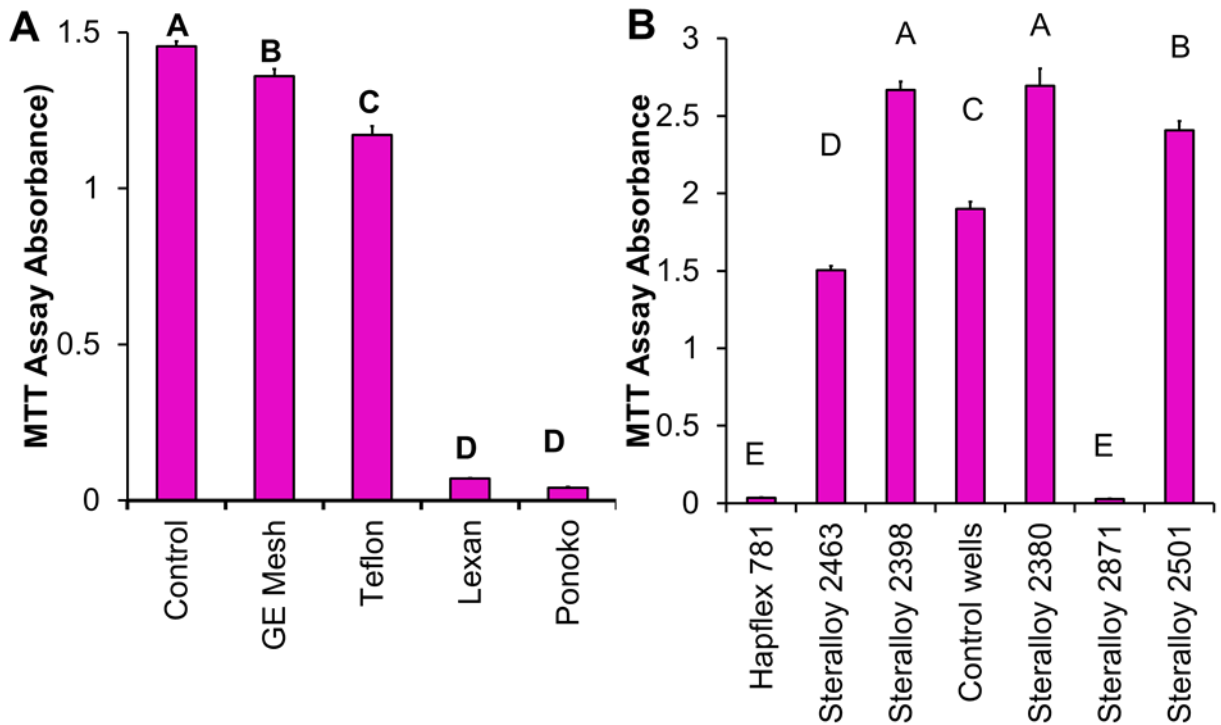


**Figure 7.16 MTT assay biocompatibility screening of bioreactor materials.**

Cell metabolism of PAVIC treated with conditioned media was assessed for chamber and holder materials. (A) During the design phase of the chamber and holder assembly, possible materials were explored with conditioned media experiments and MTT assay. Wells seeded at  $1.0 \times 10^4$  cells/cm<sup>2</sup> were assayed at day 7 of conditioned media treatment. (B) Once we found that the standard commercially 3D printed and SLA parts were not compatible with valve cells, specialty resins previously used in food and medical equipment for cast parts were explored with conditioned media experiments and MTT assay. Wells were seeded at  $2.0 \times 10^4$  cells/cm<sup>2</sup>. Statistical comparisons were made using Student's t-test and non matching letters indicate significance  $p < 0.05$ . Graph error bars indicate standard error of the mean.

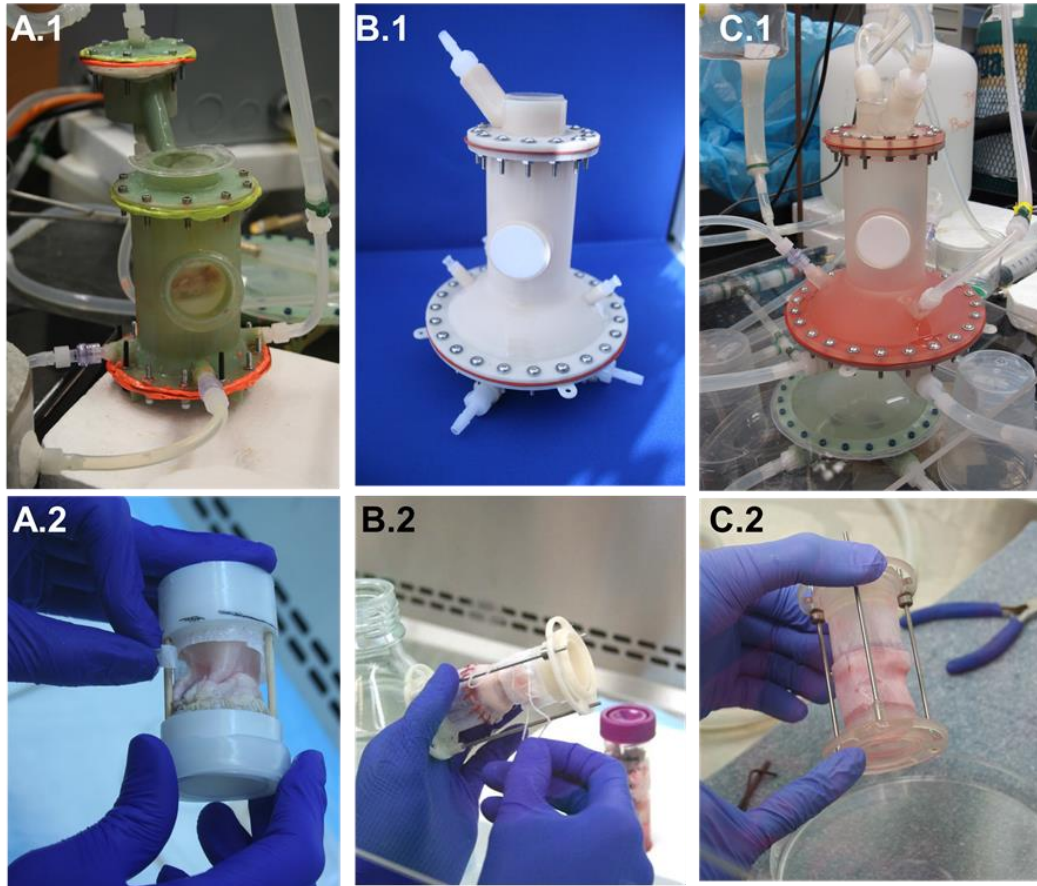


**Figure 7.17. Bioreactor chamber fabrication and material selection progression.**

(A.1) Initial testing of chamber design and prototyping was done with Ponoko fabricated parts made of Durable Fine Plastic. These parts were made with a UV cured greenish resin that is printed on an Objet Connex 3D printing machine. The Ponoko Durable Fine Plastic was not compatible with valve cells. Over time it absorbed water, and with repeated clamping of the bolts the flanges eventually deform. A silicone putty was used to pack the gaskets to get a seal for pressurization in the early prototypes made with the Durable Fine plastic. (A.2) Valve holder assemblies were initially built out of available materials in lab to refine the Solidworks designs prior to fabrication. (B) Quickparts SLA fabricated parts were used to check the design prior to casting multiple bioreactor chambers. (B.1 and B.2) The PP-like, Durable Accura 25 / VisiJet SLFlex SLA parts were water tight and could be pressurized for testing. (C) Once the design was refined multiple Steralloy 2463 chambers were fabricated so that the parallel conditioning system could be setup with biocompatible parts. Quickparts fabricates SLA parts of all the components, makes RTV silicone rubber molds, and then casts the parts. (C.1) The final bioreactor chamber is translucent so that bubbles and media levels within are visible to the outside. (C.2) The holder made of 2643 bonds well to PDMS allowing for the attachment of the Teflon mesh.

specialty resins previously used in food and medical equipment for cast parts were explored with conditioned media experiments and MTT assay (Figure 7.16B).

While we did find that coating the Ponoko plastic with PDMS and curing it in an oven overnight improved biocompatibility, the Ponoko parts also experienced significant warping over time (Figure 7.17A.1). Several of the specialty casting Steralloy resins (Hapco, Hanover MA) were biocompatible with the cells. Steralloy FDG-2398, Steralloy FDG-2380, Steralloy FDG-2501 all had higher MTT results than the control (Figure 7.16B). From the images it appeared that Steralloy 2380 introduced a particulate or some kind of debris into culture. The MTT absorbance was less than control for Steralloy 2463, but the cell morphology was characteristic of healthy PAVIC and there was less debris that was seen in 2398 and 2380. Steralloy 2463 was chosen for the bioreactor chamber because it was easier for Quickparts to handle. Steralloy 2463 as an uncured resin is ~25% less viscous compared to 2398, it is much easier to process, and it has a hardness of 80D which is the same as the 2501. RTV molding as a prototyping process is good for fabricating 1 - 100 parts. Once the molds are made, the cost of fabricating parts goes down dramatically. Quickparts fabricates SLA parts of all the components, uses the SLA parts as the negative to make RTV silicone rubber molds, gets the needed specialty resin from HAPCO, and then casts the parts.

Quickparts SLA fabricated parts were used to check the design prior to committing resources to casting multiple bioreactor chambers in the biocompatible material. The PP-like, Durable Accura 25 / VisiJet SLFlex SLA parts were water tight and could be pressurized for testing (7.17B.1 and 6.17B.2). Once the design was refined, multiple Steralloy 2463 chambers were fabricated so that the parallel conditioning system could be setup with biocompatible parts (7.17C). The final bioreactor chamber is translucent so

that bubbles and media levels within are visible to the outside (7.17C.1). The holder made of 2643 bonds well to PDMS allowing for the attachment of the Teflon mesh to the holder 7.17C.2).

#### **7.4.8 3D Printed Hydrogel Valve Attachment into Biocompatible Bioreactor Holder**

PEGDA700 precursor solutions and MEGEL/MEHA/PEGDA precursor solutions were successfully printed into two part STL geometries. UV light applied during the printing (Figure 7.18A) and for 5 minutes after the hydrogel was extruded (Figure 7.18B). An ice water cooling heat sink keeps the temperature of the LEDs stable so that light intensity should be constant during the whole fabrication process (Figure 7.16C). The 3D printed hydrogel heart valves in PEGDA700 were sufficiently crosslinked after printing and 5 minutes additional crosslinking enabled handling and incorporation into the holders (Figure 7.19). Tissue glue was used to attach the 3D printed hydrogel valve into the Teflon mesh of the holder. Tissue glue compatibility was screened with 2D PAVIC culture and showed that cytotoxicity of the glue was inconsistent (Figure 7.19A). Near glue and mesh in direct media contact conditions wells either had very few attached cells or wells were confluent cells by day 7. PAVIC in wells treated with conditioned media from tissue glue bonded to Teflon mesh reached confluence by day 7 (Figure 7.19 B) Control wells seeded at the same density as the treatment groups reached confluence by day 7 (Figure 7.19C). The 3D printed PEGDA700 valve was successfully bonded onto the top holder mesh using tissue glue (Figure 7.19E). The glue was injected between the mesh and the conduit wall. Then the bottom holder mesh was fitted over the sides of the printed valve. The second set of shaft collars locked the holder in place and the assembly was loaded into the bioreactor body. The PEGDA 700

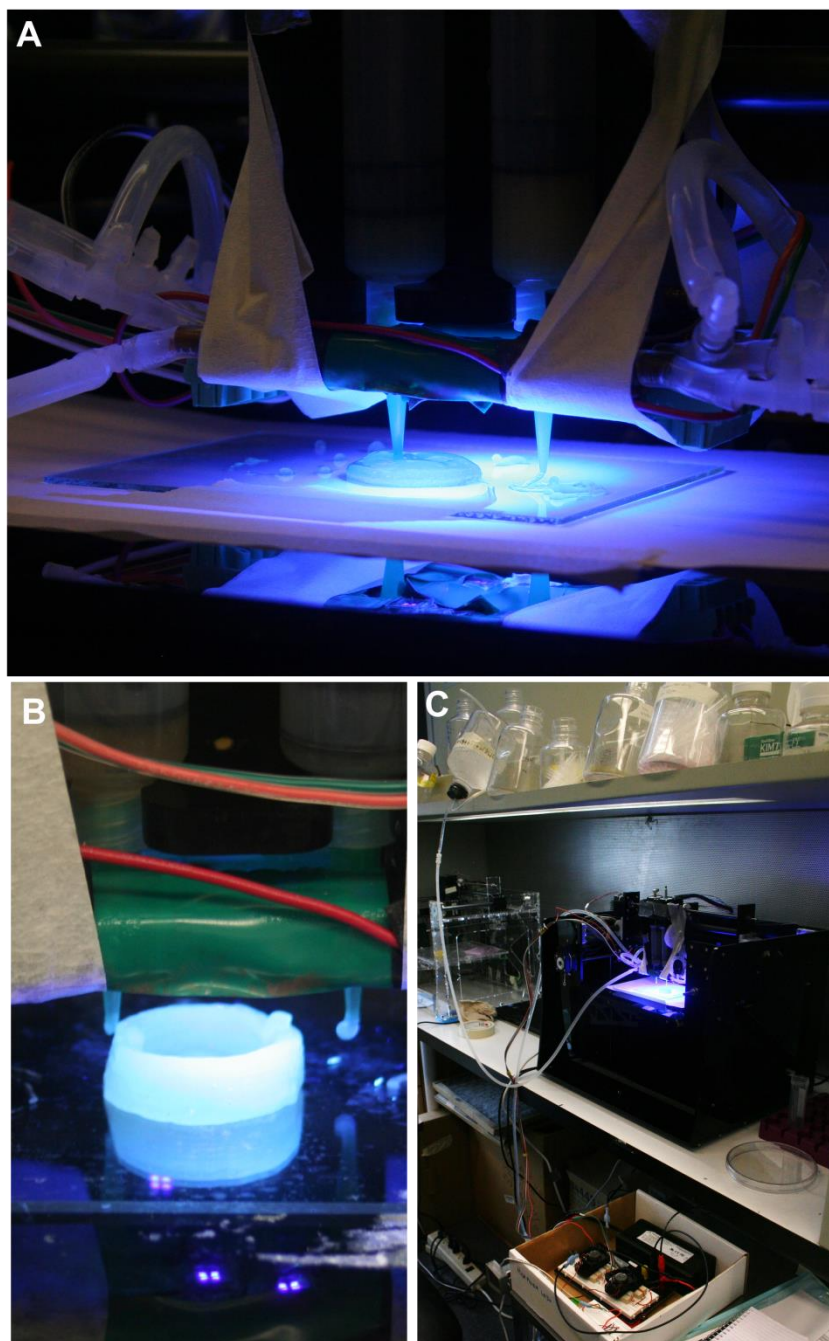


**Figure 7.18 High power LED printing of hydrogel valves for conditioning.**

**(A)** A solution of MEGEL/MEHA/PEGDA3350 was printed into a simplified interlocking STL hydrogel valve geometry using the Fab@Home™ extrusion 3D printer. The root was printed with a stiffer hydrogel composition than the leaflets. A high powered LED array was mounted on the carriage so that photo-crosslinking occurred during printing. **(B)** An additional 5 minutes of post-print-crosslinking was applied with the LEDs centered over the printed valve. **(C)** An ice water cooling heat sink is built into the high powered LED array circuit. The power supply and resistor bed as well as the water supply are kept outside of the laminar flow hood.

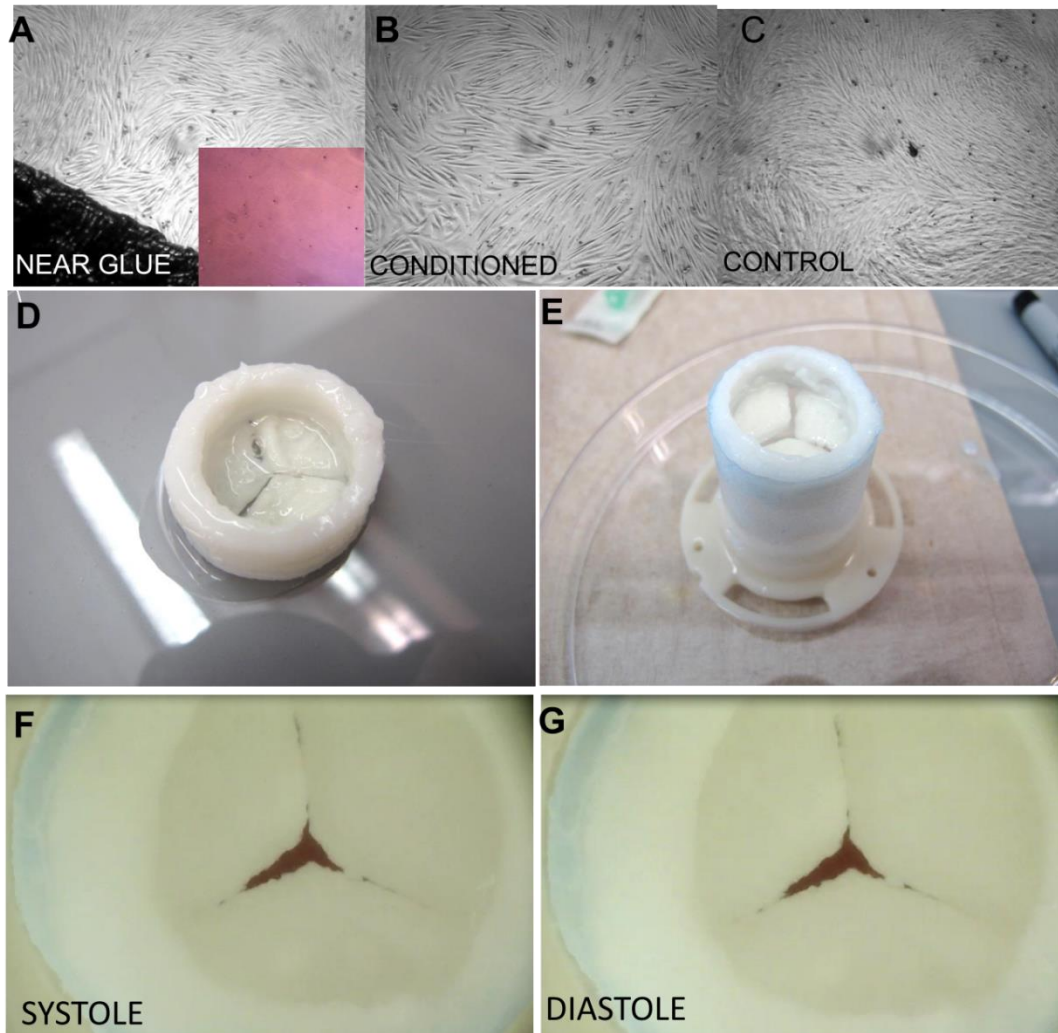


**Figure 7.19 3D printed hydrogel valve sealing into bioreactor holder assembly.**

Tissue glue was used to attach the 3D printed hydrogel valve into the teflon mesh of the holder. Tissue glue compatibility was screened with 2D PAVIC culture, (A) Near glue and mesh in direct media contact conditions wells either had very few attached cells or wells were confluent cells by day 7. (B) PAVIC in wells treated with conditioned media from tissue glue bonded to Teflon mesh reached confluence by day 7. (C) Control wells seeded at the same density as the treatment groups reached confluence by day 7. (D) A simplified valve geometry was 3D printed with a PEGDA700 solution with 1% Irgacure. (E) The 3D printed PEGDA700 valve was 1<sup>st</sup> bonded onto the top holder mesh using tissue glue. The glue was injected between the mesh and the conduit wall. 2<sup>nd</sup> the bottom holder mesh was fitted over the sides of the printed valve. The second set of shaft collars locked the holder in place and the assembly was loaded into the bioreactor body. (F) The PEGDA 700 Valve was tested in the bioreactor setup up to a 250 mmHg Pdiff setting with no applied aortic pressure. The leaflet movement for the stiff PEGDA700 leaflets during the systolic (F) and diastolic (G) phases of the conditioning cycle at 250mmHg was slight.

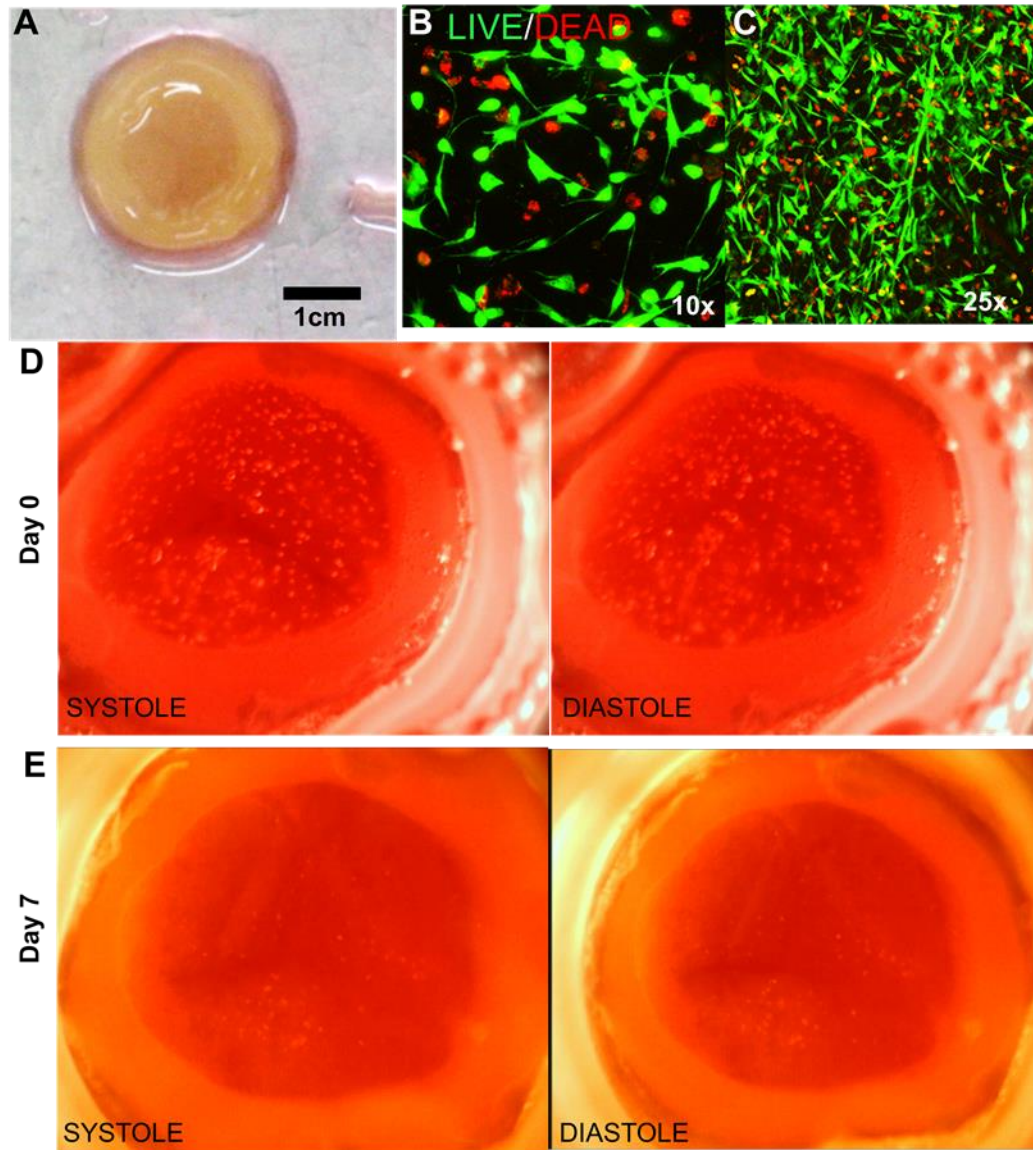


**Figure 7.20 Dynamic culture of 3D bioprinted heterogeneous hydrogel valves printed with encapsulated HADMSC.**

HADMSC were encapsulated into MEGEL/MEHA/PEGDA solutions and printed into simplified valve geometries. For each experiment a pair of valves were printed, one for dynamic and one for static conditioning for 14 days. (A) The valve root and leaflets were printed out of different precursor solutions so that the leaflets are more compliant than the root. A static conditioned bioprinted valve was stained using Live/Dead after 7 days of culture and imaged with a 25X (B) and 10X. (C) confocal objective. (D) Snapshots were taken of a dynamically conditioning bioprinted valve during systole and diastole directly after it was installed in the reactor and conditioning was initiated. Low stroke volume and pressure conditions were used, and the conditioning parameters were set at  $P_{diff} = 25\text{mmHg}$ , no applied aortic pressure, and  $t_{svstolic} = t_{dastolic} = 1\text{ sec}$ , and an open vent (no aortic threshold).

Valve was tested in the bioreactor setup up to a 250 mmHg  $P_{diff}$  setting with no applied aortic pressure. The leaflet movement for the stiff PEGDA700 leaflets during the systolic (Figure 7.19F) and diastolic (Figure 7.19G) phases of the conditioning cycle at 250 mmHg was slight.

#### **7.4.9 Dynamic Conditioning of 3D Bioprinting Hydrogel Valves with Encapsulated of HADMSC**

HADMSC encapsulated into MEGEL/MEHA/PEGDA solutions were successfully printed into simplified valve geometries. For each experiment, a pair of valves were printed, one for dynamic and one for static conditioning for 14 days of culture. The valve root and leaflets were printed out of different precursor solutions so that the leaflets are more compliant than the root (Figure 7.20A). A static condition bioprinted valve was stained using Live/Dead after 7 days and high viability was present indicating the printing results in high viability valves. Snapshots of dynamically conditioning bioprinted valve during systole and diastole directly after it was installed in the reactor and conditioning was initiated show leaflet movement and flexure (Figure 7.20D). Low stroke volume and pressure conditions were used so that conditions would be very gentle, and the conditioning parameters were set at  $P_{diff}= 25$  mmHg, no applied aortic pressure, and  $t_{systolic}=t_{diastolic}=1$  sec, and an open vent (no aortic threshold). Snapshots taken of the dynamically conditioning bioprinted valve at day 7 of culture show clear media and leaflet movement and flexure (Figure 7.20D).

### **7.5 Discussion**

Previous work has shown that 3D printing can be used to fabricate viable mechanically and cellularly heterogeneous and hydrogel heart valves (Hockaday, Kang et al. 2012; Duan, Hockaday et al. 2013; Duan, Kapetanovic et al. 2014). Critical for the advancement of a 3D printed TEHV strategy into animal models and then to clinic is an

understanding of 3D print valve remodeling and optimum hemodynamic conditions to drive appropriate and necessary tissue development. In this study we demonstrate a dynamic conditioning system specifically for the culture of 3D bioprinted heart valves. Mechanically heterogeneous MEHA/MEGEL/PEGDA hydrogel valves were printed with encapsulated HADMSC and subjected to dynamic conditioning for up to 14 days to validate the system and to induce remodeling in bioprinted valves. Investigators are developing an expanding number of encapsulating and tunable synthetic hydrogel material technologies, and have evaluated many of them for valve and mesenchymal stem cell culture (Benton, Fairbanks et al. 2009; Benton, Kern et al. 2009; Lin and Anseth 2009; Kloxin, Benton et al. 2010; Kloxin, Tibbitt et al. 2010; Kloxin, Tibbitt et al. 2010; Pedron, Kasko et al. 2010). The validation our 3D printing and conditioning approach using naturally and synthetically derived polymers, indicates that perhaps material technologies that have thus far been confined to small dimensional mechanistic studies could be fabricated into living tissues at a scale suitable for clinical use. These technologies include hydrogels with photo-releasable tethered functional groups that allow for control of cell-material interactions (Kloxin, Tibbitt et al. 2010), and photo-polymerizable hydrogels with bound peptide moieties to affect and enhance affinity protein binding which would allow for retention and sustained release of growth factors from implanted scaffolds (Lin and Anseth 2009).

Ultrasound assessment of valve root wall and leaflet motion and tissue during systolic and diastolic loading was enabled by a rigid Teflon ultrasound port or acoustic 'window' built into the reactor conditioning chamber. The Teflon window can also be moved to the top of the aortic chamber so that flow velocity information can be obtained. Other studies have used ultrasound to monitor TEHV following implantation into animal models (Syedain 2011) and acoustic windows have been built into pulse duplicator

systems for Doppler flow mapping studies of prosthetic valves (Giuliatti, Gallo et al. 2000). Ultrasound echocardiography has been used to assess the performance of molded fibrin hydrogel TEHVs (Syedain 2011), in-body TEHV (Nakayama, Takewa et al. 2014), and nonwoven polymeric fiber scaffold TEHV (Gottlieb, Kunal et al. 2010), once they had been implanted into animal models. These studies have assessed coaptation and valve closure and have characterized the flow profile and regurgitation of the valves under physiological conditions. Subsequent 3D printed valve studies with our system can evaluate flow profiles over time in culture and study the effects of different loading/cardiac cycle conditions to assess functional or non-functional remodeling. This ultrasound port could also potentially be used for strain mapping of 3D printed heart valves. This has previously been done for myocardium and the ventricles (D'Hooge, Heimdal et al. 2000; Weidemann, Eyskens et al. 2002; Sutherland, Di Salvo et al. 2004; Larsen, Petersen et al. 2006), and it is possible that it could be done for heart valves. The conditioning chamber and holder in our system was specifically designed so that outflow tract, ventricular, and body cavity pressures surrounding the valve can be mimicked. Although it was not monitored in the study presented here, a line for a body cavity pressure transducer was included on the side of the bioreactor chamber. Quantifying tissue strain could be useful for understanding whole hydrogel valve remodeling and in particular for studying the biological implications of valve shape (Chapter 3) (Hockaday, Kang et al. 2012), printer-material-specified mechanics (Chapter 4), complex heterogeneity (Chapter 5), and dynamic conditioning variables.

The water driven diaphragm-type bioreactor presented in this study was engineered with flexible control parameters and water driven flow loop system. The reactor system can be scaled or throttled to enable dynamic culture of aortic and pulmonary valves at adult or pediatric stroke volume and flow rates (Figure 7.21). We characterize the system for a throttled flow rate and stroke volume output and extrapolate for the higher flow setup. We can duplicate the range of 34 week fetal stroke volume to adult stroke volume. The size of the conditioning chamber and diaphragm base is actually bigger than needed with at least 150 ml extra capacity built in. In human adults ~100 ml is the maximum stroke volume of the left ventricle, ~40-70 ml for children (age 8-16)(Sproul and Simpson 1964), and 0.02 ml-2.7 ml for a fetus(12 weeks to 34 weeks)(Molina, Faro et al. 2008) . Additionally the system can be scaled for parallel conditioning in multiple reactor chambers containing individual valves (Figure 7.22). Physiological systolic and diastolic loading conditions can be achieved or diastolic only loading conditions can be induced with two electronics setups that we demonstrate in this study. The alternating solenoid control setup enables cyclic diastolic loading, and the pressure relief control setup enables a more physiological profile. Cyclic and diastolic loading has been demonstrated as a strategy to determine optimal loading conditions and to study tissue deformation (Mol, Driessen et al. 2005; Kortsmits, Rutten et al. 2009). In combination with the ultrasound port in our bioreactor, these types of deformation studies could better determine optimal and precise loading conditions in the reactors needed to drive remodeling and tissue development in 3D printed hydrogel valves.

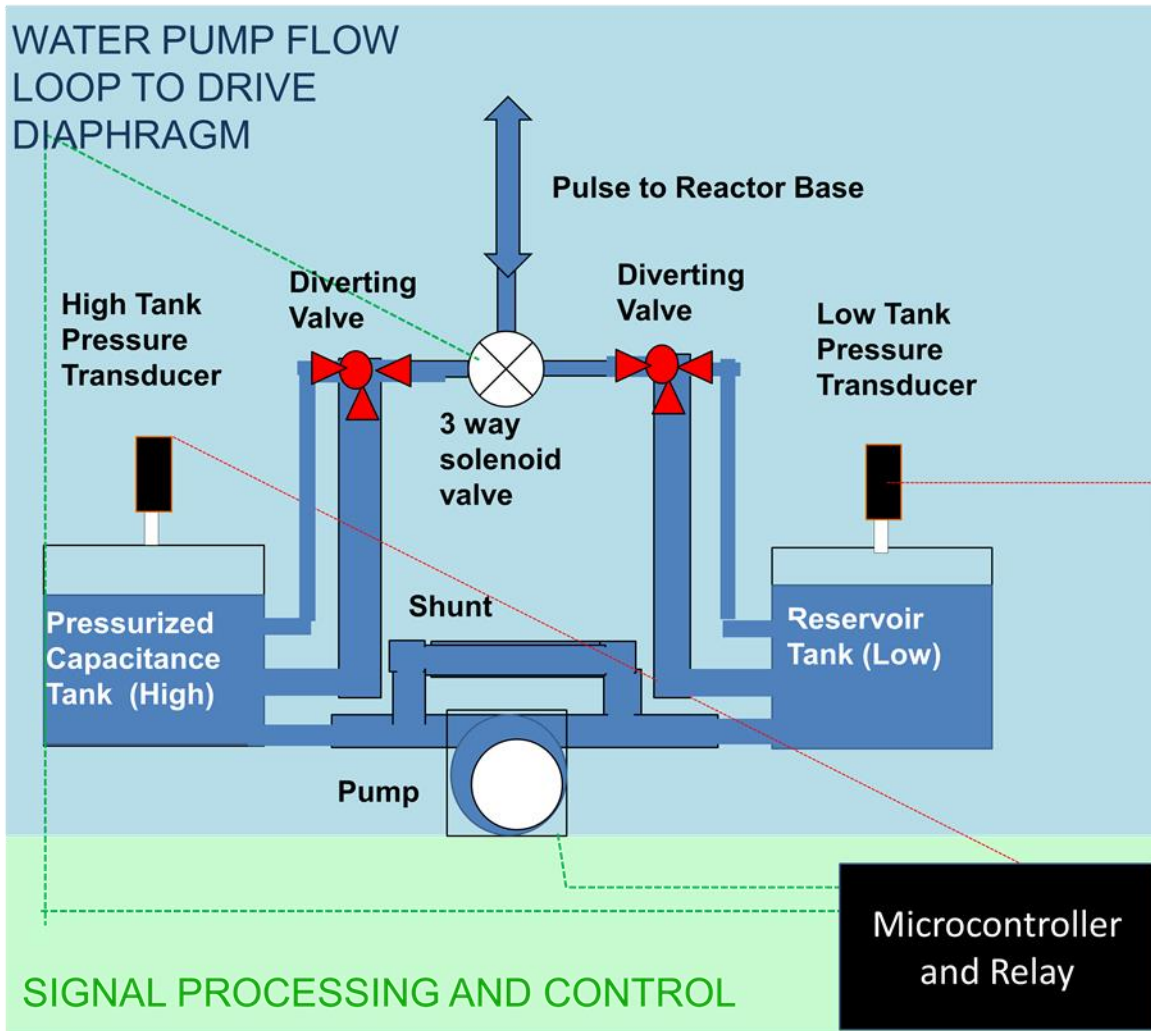


Figure 7.21 Heart valve bioreactor conditioning system with a built in flow throttle in the pump driven water flow loop.

To set ranges of stroke volume when circulating media in the sterile media loop a throttle switch can be used in the water flow loop. Two tubes from the high tank and two tubes from the low tank are connected with three way diverting valves the outlets of which both lead to the 3-way solenoid valve. If a low flow setup is desired the flow loop can be throttled and the diverting valves set to connect the smaller, high resistance tubes to from the 3-way solenoid ports to the sink and source tanks.

## **7.6 Conclusion**

In this study we demonstrate a dynamic conditioning system specifically for the culture of 3D bioprinted and *ex-vivo* native tissue heart valves. The custom water driven diaphragm-type bioreactor was engineered with a conditioning chamber specifically designed for ultrasound monitoring of valve root wall and leaflet motion and tissue strain. The parameters of the flexible control and water driven flow loop system can be scaled or throttled to enable dynamic culture of aortic and pulmonary valves at adult or pediatric stroke volume and flow rates. Additionally the system can be scaled for parallel conditioning in multiple reactor chambers containing individual valves. Physiological systolic and diastolic loading conditions can be achieved or diastolic only loading conditions can be induced with the control setup. This will enable exploration into the optimal conditions and loading regimes needed to drive remodeling and tissue development in 3D printed hydrogel valves. 3D bioprinted heart valves composed of methacrylated gelatin, methacrylated hyaluronic acid, and PEGDA were cultured up to 14 days under static and dynamic conditions to validate the system and to induce remodeling in bioprinted valves.



## REFERENCES

- Abramov, A. Y., A. Scorziello, et al. (2007). "Three distinct mechanisms generate oxygen free radicals in neurons and contribute to cell death during anoxia and reoxygenation." J Neurosci **27**(5): 1129-1138.
- Administration, F. a. D. (October 2004). Report to Congress: Barriers to the Availability of Medical Devices Intended for the Treatment or Diagnosis of Diseases and Conditions that Affect Children. U. S. D. o. H. a. H. Services.
- Ahmann, K. A., J. S. Weinbaum, et al. "Fibrin degradation enhances vascular smooth muscle cell proliferation and matrix deposition in fibrin-based tissue constructs fabricated *in vitro*." Tissue Eng Part A **16**(10): 3261-3270.
- Ahn, S., H. Lee, et al. (2014). "A direct cell printing supplemented with low-temperature processing method for obtaining highly porous three-dimensional cell-laden scaffolds." Journal of Materials Chemistry B **2**(18): 2773-2782.
- Aikawa, E., P. Whittaker, et al. (2006). "Human semilunar cardiac valve remodeling by activated cells from fetus to adult - Implications for postnatal adaptation, pathology, and tissue engineering." Circulation **113**: 1344-1352.
- Aikawa, E., P. Whittaker, et al. (2006). "Human semilunar cardiac valve remodeling by activated cells from fetus to adult: implications for postnatal adaptation, pathology, and tissue engineering." Circulation **113**(10): 1344-1352.
- Alsoufi, B., Z. Al-Halees, et al. (2009). "Mechanical valves versus the Ross procedure for aortic valve replacement in children: propensity-adjusted comparison of long-term outcomes." J Thorac Cardiovasc Surg **137**(2): 362-370 e369.
- Arcaute, K., B. K. Mann, et al. (2006). "Stereolithography of three-dimensional bioactive poly(ethylene glycol) constructs with encapsulated cells." Ann Biomed Eng **34**(9): 1429-1441.
- Atsumi, T., J. Murata, et al. (1998). "Cytotoxicity of photosensitizers camphorquinone and 9-fluorenone with visible light irradiation on a human submandibular-duct cell line *in vitro*." Arch Oral Biol **43**(1): 73-81.
- Azadani, A. N., S. Chitsaz, et al. (2012). "Biomechanical comparison of human pulmonary and aortic roots." Eur J Cardiothorac Surg.
- Azagarsamy, M. A., D. L. Alge, et al. (2012). "Photocontrolled nanoparticles for on-demand release of proteins." Biomacromolecules **13**: 2219-2224.
- Baier Leach, J., K. A. Bivens, et al. (2003). "Photocrosslinked hyaluronic acid hydrogels: Natural, biodegradable tissue engineering scaffolds." Biotechnology and Bioengineering **82**(5): 578-589.
- Baker, B. M. and C. S. Chen (2012). "Deconstructing the third dimension - how 3D culture microenvironments alter cellular cues." Journal of Cell Science **125**: 3015-3024.
- Balachandran, K., P. Sucusky, et al. (2009). "Elevated cyclic stretch alters matrix remodeling in aortic valve cusps: implications for degenerative aortic valve disease." American Journal of Physiology-Heart and Circulatory Physiology **296**: H756-H764.
- Balguid, A., A. Mol, et al. (2009). "Hypoxia induces near-native mechanical properties in engineered heart valve tissue." Circulation **119**(2): 290-297.
- Ballyns, J. J. and L. J. Bonassar (2009). "Image-guided tissue engineering." J Cell Mol Med **13**(8A): 1428-1436.
- Ballyns, J. J. and L. J. Bonassar (2011). "Dynamic compressive loading of image-guided tissue engineered meniscal constructs." Journal of Biomechanics **44**: 509-516.
- Ballyns, J. J., D. L. Cohen, et al. "An optical method for evaluation of geometric fidelity for anatomically shaped tissue-engineered constructs." Tissue Eng Part C Methods **16**(4): 693-703.

- Ballyns, J. J., D. L. Cohen, et al. (2010). "An optical method for evaluation of geometric fidelity for anatomically shaped tissue-engineered constructs." Tissue Eng Part C Methods **16**(4): 693-703.
- Ballyns, J. J., D. L. Cohen, et al. (2010). "An optical method for evaluation of geometric fidelity for anatomically shaped tissue-engineered constructs." Tissue Eng Part C **16**(4): 693-703.
- Ballyns, J. J., D. L. Cohen, et al. (2010). "An optical method for evaluation of geometric fidelity for anatomically shaped tissue-engineered constructs" " Tissue Engineering Part C-Method **16**: 693-703.
- Ballyns, J. J., J. P. Gleghorn, et al. (2008). "Image-guided tissue engineering of anatomically shaped implants via MRI and micro-CT using injection molding " Tissue Engineering Part A **14**: 1195-1202.
- Ballyns, J. J., J. P. Gleghorn, et al. (2008). "Image-guided tissue engineering of anatomically shaped implants via MRI and micro-CT using injection molding." Tissue Eng Part A **14**(7): 1195-1202.
- Barzilla, J. E., F. E. Acevedo, et al. (2010). "Organ culture as a tool to identify early mechanisms of serotonergic valve disease." Journal of Heart Valve Disease **19**: 626-635.
- Barzilla, J. E., A. S. McKenney, et al. (2010). "Design and validation of a novel splashing bioreactor system for use in mitral valve organ culture." Annals of Biomedical Engineering **38**: 3280-3294.
- Bellhouse, B. J., F. H. Bellhouse, et al. (1968). "Fluid mechanics of the aortic root with application to coronary flow." Nature **219**(5158): 1059-1061.
- Bellis, A. D., B. P. Bernabe, et al. (2013). "Dynamic transcription factor activity profiling in 2D and 3D cell cultures." Biotechnology and Bioengineering **110**: 563-572.
- Benton, J. A., C. A. DeForest, et al. (2009). "Photo-crosslinking of gelatin macromers to synthesize porous hydrogels that promote valvular interstitial cell function." Tissue Eng Part A **15**(11): 3221-3230.
- Benton, J. A., B. D. Fairbanks, et al. (2009). "Characterization of valvular interstitial cell function in three dimensional matrix metalloproteinase degradable PEG hydrogels." Biomaterials **30**(34): 6593-6603.
- Benton, J. A., H. B. Kern, et al. (2009). "Statins block calcific nodule formation of valvular interstitial cells by inhibiting alpha-smooth muscle actin expression." Arteriosclerosis Thrombosis and Vascular Biology **29**: 1950-1957.
- Benton, J. A., H. B. Kern, et al. (2009). "Statins block calcific nodule formation of valvular interstitial cells by inhibiting alpha-smooth muscle actin expression." Arterioscler Thromb Vasc Biol **29**(11): 1950-1957.
- Berry, J. L., J. A. Steen, et al. (2010). "Bioreactors for development of tissue engineered heart valves." Annals of Biomedical Engineering **38**: 3272-3279.
- Bianchi, F., M. Rosi, et al. (2007). "Microfabrication of fractal polymeric structures for capillary morphogenesis: applications in therapeutic angiogenesis and in the engineering of vascularized tissue." J Biomed Mater Res B Appl Biomater **81**(2): 462-468.
- Billiar, K. L. and M. S. Sacks (2000). "Biaxial mechanical properties of the native and glutaraldehyde-treated aortic valve cusp: Part II--A structural constitutive model." J Biomech Eng **122**(4): 327-335.
- Billiet, T., M. Vandenhaute, et al. (2012). "A review of trends and limitations in hydrogel-rapid prototyping for tissue engineering." Biomaterials **33**: 6020-6041.
- Bilski, P., A. G. Belanger, et al. (2002). "Photosensitized oxidation of 2',7'-dichlorofluorescein: singlet oxygen does not contribute to the formation of fluorescent oxidation product 2',7'-dichlorofluorescein." Free Radic Biol Med **33**(7): 938-946.

- Black, A. F., V. Hudon, et al. (1999). "A novel approach for studying angiogenesis: A human skin equivalent with a capillary-like network." Cell Biology and Toxicology **15**: 81-90.
- Blais, M., R. Parenteau-Bareil, et al. (2013). "Concise review: tissue-engineered skin and nerve regeneration in burn treatment." Stem Cells Transl Med **2**(7): 545-551.
- Boettcher-Haberzeth, S., T. Biedermann, et al. (2010). "Tissue engineering of skin." Burns **36**: 450-460.
- Bottio, T., V. Tarzia, et al. "The changing hydrodynamic performance of the decellularized intact porcine aortic root: considerations on in-vitro testing." J Heart Valve Dis **19**(4): 485-491.
- Bowles, R. D., R. M. Williams, et al. (2010). "Self-assembly of aligned tissue-engineered annulus fibrosus and intervertebral disc composite via collagen gel contraction." Tissue Eng Part A **16**(4): 1339-1348.
- Brewer, R. J., R. M. Mentzer, et al. (1977). "*In vivo* study of the dimensional changes of the aortic valve leaflets during the cardiac cycle." Journal OF Thoracic and Cardiovascular Surgery **74**: 645-650.
- Brigham, M. D., A. Bick, et al. (2009). "Mechanically robust and bioadhesive collagen and photocrosslinkable hyaluronic acid semi-interpenetrating networks." Tissue Engineering Part A **15**: 1645-1653.
- Browning, M. B. and E. Cosgriff-Hernandez (2012). "Development of a biostable replacement for PEGDA hydrogels." Biomacromolecules **13**(3): 779-786.
- Browning, M. B., T. Wilems, et al. (2011). "Compositional control of poly(ethylene glycol) hydrogel modulus independent of mesh size." J Biomed Mater Res A **98**(2): 268-273.
- Bryant, S. J. and K. S. Anseth (2002). "Hydrogel properties influence ECM production by chondrocytes photoencapsulated in poly(ethylene glycol) hydrogels." J Biomed Mater Res **59**(1): 63-72.
- Bryant, S. J., C. R. Nuttelman, et al. (2000). "Cytocompatibility of UV and visible light photoinitiating systems on cultured NIH/3T3 fibroblasts *in vitro*." J Biomater Sci Polym Ed **11**(5): 439-457.
- Bunnell, B. A., M. Flaas, et al. (2008). "Adipose-derived stem cells: isolation, expansion and differentiation." Methods **45**(2): 115-120.
- Burdick, J. A. and K. S. Anseth (2002). "Photoencapsulation of osteoblasts in injectable RGD-modified PEG hydrogels for bone tissue engineering." Biomaterials **23**(22): 4315-4323.
- Butcher, J. T., G. J. Mahler, et al. (2011). "Aortic valve disease and treatment: The need for naturally engineered solutions." Advanced Drug Delivery Reviews **63**: 242-268.
- Butcher, J. T., G. J. Mahler, et al. (2011). "Aortic valve disease and treatment: the need for naturally engineered solutions." Adv Drug Deliv Rev **63**(4-5): 242-268.
- Butcher, J. T. and R. M. Nerem (2004). "Porcine aortic valve interstitial cells in three-dimensional culture: comparison of phenotype with aortic smooth muscle cells." J Heart Valve Dis **13**(3): 478-485; discussion 485-476.
- Butcher, J. T. and R. M. Nerem (2006). "Valvular endothelial cells regulate the phenotype of interstitial cells in co-culture: effects of steady shear stress." Tissue Eng **12**(4): 905-915.
- Butcher, J. T. and R. M. Nerem (2006). "Valvular endothelial cells regulate the phenotype of interstitial cells in co-culture: Effects of steady shear stress." Tissue Engineering **12**: 905-915.
- Butcher, J. T., A. M. Penrod, et al. (2004). "Unique morphology and focal adhesion development of valvular endothelial cells in static and fluid flow environments." Arterioscler Thromb Vasc Biol **24**(8): 1429-1434.

- Butcher, J. T., A. M. Penrod, et al. (2004). "Unique morphology and focal adhesion development of valvular endothelial cells in static and fluid flow environments." Arteriosclerosis Thrombosis and Vascular Biology **24**: 1429-1434.
- Butcher, J. T., C. A. Simmons, et al. (2008). "Mechanobiology of the aortic heart valve." J Heart Valve Dis **17**(1): 62-73.
- Butcher, J. T., C. A. Simmons, et al. (2008). "Review - Mechanobiology of the aortic heart valve." Journal of Heart Valve Disease **17**: 62-73.
- Butscher, A., M. Bohner, et al. (2011). "Structural and material approaches to bone tissue engineering in powder-based three-dimensional printing." Acta Biomaterialia **7**: 907-920.
- Cai, H., G. Azangwe, et al. (2005). "Skin cell culture on an ear-shaped scaffold created by fused deposition modelling." Bio-medical Materials and Engineering **15**: 375-380.
- Cameron, D. E. and L. A. Vricella (2007). "What is the proper place of the Ross procedure in our modern armamentarium?" Curr Cardiol Rep **9**(2): 93-98.
- Carabello, B. A. and W. J. Paulus (2009). "Aortic stenosis." Lancet **373**(9667): 956-966.
- Carapetis, J. R. (2008). "Rheumatic heart disease in Asia." Circulation **118**(25): 2748-2753.
- Carapetis, J. R., A. C. Steer, et al. (2005). "The global burden of group A streptococcal diseases." Lancet Infect Dis **5**(11): 685-694.
- Carmichael, J., W. G. DeGraff, et al. (1987). "Evaluation of a tetrazolium-based semiautomated colorimetric assay: assessment of chemosensitivity testing." Cancer Res **47**(4): 936-942.
- Chan, V., P. Zorlutuna, et al. (2010). "Three-dimensional photopatterning of hydrogels using stereolithography for long-term cell encapsulation." Lab Chip **10**(16): 2062-2070.
- Chanda, J., R. Kuribayashi, et al. (1997). "Valved conduit in the descending thoracic aorta in juvenile sheep: a useful, cost-effective model for accelerated calcification study in systemic circulation." Biomaterials **18**(19): 1317-1321.
- Chandler, E. M., C. M. Berglund, et al. (2011). "Stiffness of photocrosslinked RGD-alginate gels regulates adipose progenitor cell behavior." Biotechnol Bioeng **108**(7): 1683-1692.
- Chang, C. C., E. D. Boland, et al. (2011). "Direct-write bioprinting three-dimensional biohybrid systems for future regenerative therapies." Journal of Biomedical Materials Research Part B-Applied Biomaterials **98B**: 160-170.
- Cheng, A., P. Dagum, et al. (2007). "Aortic root dynamics and surgery: from craft to science." Philos Trans R Soc Lond B Biol Sci **362**(1484): 1407-1419.
- Chitcholtan, K., E. Asselin, et al. (2013). "Differences in growth properties of endometrial cancer in three dimensional (3D) culture and 2D cell monolayer." Experimental Cell Research **319**: 75-87.
- Christie, G. W. (1992). "Anatomy of aortic heart valve leaflets: the influence of glutaraldehyde fixation on function." Eur J Cardiothorac Surg **6 Suppl 1**: S25-32; discussion S33.
- Christie, G. W. and B. G. Barratt-Boyes (1995). "Mechanical properties of porcine pulmonary valve leaflets: how do they differ from aortic leaflets?" Ann Thorac Surg **60**(2 Suppl): S195-199.
- Chue, W. L., G. R. Campbell, et al. (2004). "Dog peritoneal and pleural cavities as bioreactors to grow autologous vascular grafts." J Vasc Surg **39**(4): 859-867.
- Ciorba, A. and A. Martini (2006). "Tissue engineering and cartilage regeneration for auricular reconstruction." International Journal of Pediatric Otorhinolaryngology **70**: 1507-1515.
- Cipitria, A., C. Lange, et al. (2012). "Porous scaffold architecture guides tissue formation." J Bone Miner Res **27**(6): 1275-1288.

- Clark, E. B. (1996). "Pathogenetic mechanisms of congenital cardiovascular malformations revisited." Semin Perinatol **20**(6): 465-472.
- Cohen, D. L., W. Lo, et al. (2011). "Increased mixing improves hydrogel homogeneity and quality of three-dimensional printed constructs " Tissue Engineering Part C-Method **17**: 239-248.
- Cohen, D. L., E. Malone, et al. (2006). "Direct freeform fabrication of seeded hydrogels in arbitrary geometries." Tissue Engineering **12**: 1325-1335.
- Cohen, D. L., E. Malone, et al. (2006). "Direct freeform fabrication of seeded hydrogels in arbitrary geometries." Tissue Eng **12**(5): 1325-1335.
- Colazzo, F., A. H. Chester, et al. (2010). "Induction of mesenchymal to endothelial transformation of adipose-derived stem cells." Journal of Heart Valve Disease **19**: 736-744.
- Colazzo, F., A. H. Chester, et al. (2010). "Induction of mesenchymal to endothelial transformation of adipose-derived stem cells." J Heart Valve Dis **19**(6): 736-744.
- Colazzo, F., P. Sarathchandra, et al. (2011). "Extracellular matrix production by adipose-derived stem cells: Implications for heart valve tissue engineering." Biomaterials **32**: 119-127.
- Colazzo, F., P. Sarathchandra, et al. (2011). "Extracellular matrix production by adipose-derived stem cells: implications for heart valve tissue engineering." Biomaterials **32**(1): 119-127.
- Colvee, E. and J. M. Hurle (1983). "Malformations of the semilunar valves produced in chick embryos by mechanical interference with cardiogenesis. An experimental approach to the role of hemodynamics in valvular development." Anat Embryol (Berl) **168**(1): 59-71.
- Courtney, T., M. S. Sacks, et al. (2006). "Design and analysis of tissue engineering scaffolds that mimic soft tissue mechanical anisotropy." Biomaterials **27**(19): 3631-3638.
- Cruise, G. M., D. S. Scharp, et al. (1998). "Characterization of permeability and network structure of interfacially photopolymerized poly(ethylene glycol) diacrylate hydrogels." Biomaterials **19**(14): 1287-1294.
- Cui, X. and T. Boland (2009). "Human microvasculature fabrication using thermal inkjet printing technology." Biomaterials **30**(31): 6221-6227.
- Cui, X. F. and T. Boland (2009). "Human microvasculature fabrication using thermal inkjet printing technology." Biomaterials **30**: 6221-6227.
- Cui, X. F., K. Breitenkamp, et al. (2012). "Direct human cartilage repair using three-dimensional bioprinting technology." Tissue engineering Part A **18**: 1304-1312.
- Curtis, E. T., S. Zhang, et al. (2012). "Magnetic resonance elastography methodology for the evaluation of tissue engineered construct growth." J Vis Exp(60).
- D'Alessandro, D., S. Danti, et al. (2012). "Histologic characterization of human ear ossicles for the development of tissue-engineered replacements " Otology & Neurotology **33**: 1458-1468.
- D'Hooge, J., A. Heimdal, et al. (2000). "Regional strain and strain rate measurements by cardiac ultrasound: principles, implementation and limitations." Eur J Echocardiogr **1**(3): 154-170.
- Dagum, P., G. R. Green, et al. (1999). "Deformational dynamics of the aortic root: modes and physiologic determinants." Circulation **100**(19 Suppl): II54-62.
- Dagum, P., G. R. Green, et al. (1999). "Deformational dynamics of the aortic root - Modes and physiologic determinants." Circulation **100**: S54-62.
- Dajani, A. S. and K. A. Taubert (1992). "Re: Letter to the editor by Dr. Steven M. Pollack and author's response from Drs. Thomas J. Pallasch and Jorgen Slots. Committee on Rheumatic Fever, Endocarditis, and Kawasaki Disease of the American Heart Association." J Periodontol **63**(5): 488.
- Darnell, M. C., J. Y. Sun, et al. (2013). "Performance and biocompatibility of extremely tough alginate/polyacrylamide hydrogels." Biomaterials **34**(33): 8042-8048.

- Dasi, L. P., H. A. Simon, et al. (2009). "Fluid mechanics of artificial heart valves." Clin Exp Pharmacol Physiol **36**(2): 225-237.
- de Simone, G., R. B. Devereux, et al. (1997). "Stroke volume and cardiac output in normotensive children and adults. Assessment of relations with body size and impact of overweight." Circulation **95**(7): 1837-1843.
- Deck, J. D., M. J. Thubrikar, et al. (1988). "Structure, stress, and tissue-repair in aortic valve leaflets." Cardiovascular Research **22**: 7-16.
- Derby, B. (2012). "Printing and prototyping of tissues and scaffolds " Science **338**: 921-926.
- Devarajan, K., M. L. Forrest, et al. (2013). "Adenovector-mediated gene delivery to human umbilical cord mesenchymal stromal cells induces inner ear cell phenotype." Cellular Reprogramming **15**: 43-54.
- Dhariwala, B., E. Hunt, et al. (2004). "Rapid prototyping of tissue-engineering constructs, using photopolymerizable hydrogels and stereolithography." Tissue Eng **10**(9-10): 1316-1322.
- Dohmen, P. M., A. Lembcke, et al. (2002). "Ross operation with a tissue-engineered heart valve." Ann Thorac Surg **74**(5): 1438-1442.
- Duan, B., L. A. Hockaday, et al. (2013). "3D bioprinting of heterogeneous aortic valve conduits with alginate/gelatin hydrogels." J Biomed Mater Res A **101**(5): 1255-1264.
- Duan, B., L. A. Hockaday, et al. (2013). "3D bioprinting of heterogeneous aortic valve conduits with alginate/gelatin hydrogels." Journal of Biomedical Materials Research Part A **101A**: 1255-1264.
- Duan, B., L. A. Hockaday, et al. (2014). "Aortic Heart Valve Tissue Regeneration." Tissue and Organ Regeneration: Advances in Micro and Nanotechnology.
- Duan, B., L. A. Hockaday, et al. (2013). "Stiffness and adhesivity control aortic valve interstitial cell behavior within hyaluronic acid based hydrogels." Acta Biomaterialia: <http://dx.doi.org/10.1016/j.actbio.2013.1004.1050>.
- Duan, B., E. Kapetanovic, et al. (2014). "Three-dimensional printed trileaflet valve conduits using biological hydrogels and human valve interstitial cells." Acta Biomater **10**(5): 1836-1846.
- Duan, B., M. Wang, et al. (2010). "Three-dimensional nanocomposite scaffolds fabricated via selective laser sintering for bone tissue engineering." Acta Biomater **6**(12): 4495-4505.
- Dumont, K., J. Yperman, et al. (2002). "Design of a new pulsatile bioreactor for tissue engineered aortic heart valve formation." Artificial Organs **26**: 710-714.
- Durst, C. A., M. P. Cuchiara, et al. (2011). "Flexural characterization of cell encapsulated PEGDA hydrogels with applications for tissue engineered heart valves." Acta Biomater **7**(6): 2467-2476.
- Durst, C. A. and K. J. Grande-Allen (2010). "Design and physical characterization of a synchronous multivalve aortic valve culture system." Annals of Biomedical Engineering **38**: 319-325.
- Eckert, C. E., B. T. Mikulis, et al. (2011). "Three-dimensional quantitative micromorphology of pre- and post-implanted engineered heart valve tissues." Ann Biomed Eng **39**(1): 205-222.
- El-Hamamsy, I., Z. Eryigit, et al. (2010). "Long-term outcomes after autograft versus homograft aortic root replacement in adults with aortic valve disease: a randomised controlled trial." Lancet **376**(9740): 524-531.
- Emani, S., J. E. Mayer, et al. (2011). "Gene regulation of extracellular matrix remodeling in human bone marrow stem cell-seeded tissue-engineered grafts." Tissue Engineering Part A **17**: 2379-2388.
- Engelmayr, G. C., D. K. Hildebrand, et al. (2003). "A novel bioreactor for the dynamic flexural stimulation of tissue engineered heart valve biomaterials." Biomaterials **24**: 2523-2532.

- Engelmayr, G. C., E. Rabkin, et al. (2005). "The independent role of cyclic flexure in the early *in vitro* development of an engineered heart valve tissue." Biomaterials **26**: 175-187.
- Engelmayr, G. C., V. L. Sales, et al. (2006). "Cyclic flexure and laminar flow synergistically accelerate mesenchymal stem cell-mediated engineered tissue formation: Implications for engineered heart valve tissues." Biomaterials **27**: 6083-6095.
- Engelmayr, G. C., L. Soletti, et al. (2008). "A novel flex-stretch-flow bioreactor for the study of engineered heart valve tissue mechanobiology." Annals of Biomedical Engineering **36**: 700-712.
- Engler, A. J., S. Sen, et al. (2006). "Matrix elasticity directs stem cell lineage specification." Cell **126**(4): 677-689.
- Erdbrugger, W., W. Konertz, et al. (2006). "Decellularized xenogenic heart valves reveal remodeling and growth potential *in vivo* ." Tissue Eng **12**(8): 2059-2068.
- Farndale, R. W., D. J. Buttle, et al. (1986). "Improved quantitation and discrimination of sulphated glycosaminoglycans by use of dimethylmethylene blue." Biochimica et Biophysica Acta **883**: 173-177.
- Fedorovich, N. E., J. Alblas, et al. (2011). "Organ printing: the future of bone regeneration?" Trends in Biotechnology **29**: 601-606.
- Fedorovich, N. E., M. H. Oudshoorn, et al. (2009). "The effect of photopolymerization on stem cells embedded in hydrogels." Biomaterials **30**(3): 344-353.
- Fedorovich, N. E., W. Schuurman, et al. (2012). "Biofabrication of osteochondral tissue equivalents by printing topologically defined, cell-laden hydrogel scaffolds." Tissue Eng Part C Methods **18**(1): 33-44.
- Fedorovich, N. E., W. Schuurman, et al. (2012). "Biofabrication of osteochondral tissue equivalents by printing topologically defined, cell-laden hydrogel scaffolds." Tissue Engineering Part C-Methods **18**: 33-44.
- Fedorovich, N. E., H. M. Wijnberg, et al. (2011). "Distinct tissue formation by heterogeneous printing of osteo- and endothelial progenitor cells." Tissue Eng Part A **17**(15-16): 2113-2121.
- Fedorovich, N. E., H. M. Wijnberg, et al. (2011). "Distinct tissue formation by heterogeneous printing of osteo- and endothelial progenitor cells " Tissue Engineering Part A **17**: 2113-2121.
- Feng, Y., M. Taraban, et al. (2011). "Linear Dependency of NMR Relaxation Rates on Shear Modulus in Hydrogels." Soft Matter **7**(21): 9890-9893.
- Filho AL, C. P., Noritomi PY, Silva JVL, Colangelo NW, Kang H, Lipson H, Butcher JT, Malone E, Neto PI. ( 2009). "Construction and Adaptation of an Open Source Rapid Prototyping Machine for Biomedical Research Purposes - a Multinational Collaborative Development." Advanced Research in Virtual and Rapid Prototyping.
- Flanagan, T. C., C. Cornelissen, et al. (2007). "The *in vitro* development of autologous fibrin-based tissue-engineered heart valves through optimised dynamic conditioning." Biomaterials **28**: 3388-3397.
- Flanagan, T. C., J. S. Sachweh, et al. (2009). "*In vivo* remodeling and structural characterization of fibrin-based tissue-engineered heart valves in the adult sheep model." Tissue Eng Part A **15**(10): 2965-2976.
- Flanagan, T. C., J. S. Sachweh, et al. (2009). "*In vivo* remodeling and structural characterization of fibrin-based tissue-engineered heart valves in the adult sheep model." Tissue Engineering Part A **15**: 2965-2976.
- Franquet, A., S. Avril, et al. (2013). "A new method for the *in vivo* identification of mechanical properties in arteries from cine MRI images: theoretical framework and validation." IEEE Trans Med Imaging **32**(8): 1448-1461.
- Frigiola, A., A. Varrica, et al. (2010). "Neo-aortic Valve and Root Complex Evolution After Ross Operation in Infants, Children, and Adolescents." Ann Thorac Surg **90**(4): 1278-1285.

- Gaetani, R., L. Barile, et al. (2009). "New perspectives to repair a broken heart." Cardiovascular & Hematological Agents in Medicinal Chemistry **7**: 91-107.
- Gaetani, R., P. A. Doevendans, et al. (2012). "Cardiac tissue engineering using tissue printing technology and human cardiac progenitor cells." Biomaterials **33**(6): 1782-1790.
- Gaetani, R., P. A. Doevendans, et al. (2012). "Cardiac tissue engineering using tissue printing technology and human cardiac progenitor cells." Biomaterials **33**: 1782-1790.
- Gandaglia, A., A. Bagno, et al. (2011). "Cells, scaffolds and bioreactors for tissue-engineered heart valves: a journey from basic concepts to contemporary developmental innovations " European Journal of Cardio-thoracic Surgery **39**: 523-531.
- Gauvin, R., Y. C. Chen, et al. (2012). "Microfabrication of complex porous tissue engineering scaffolds using 3D projection stereolithography." Biomaterials **33**(15): 3824-3834.
- Genes, N. G., J. A. Rowley, et al. (2004). "Effect of substrate mechanics on chondrocyte adhesion to modified alginate surfaces." Arch Biochem Biophys **422**(2): 161-167.
- Giuliatti, S., L. Gallo, Jr., et al. (2000). "A pulsatile flow model for *in vitro* quantitative evaluation of prosthetic valve regurgitation." Braz J Med Biol Res **33**(3): 341-346.
- Glen, S., J. Burns, et al. (2004). "Prevalence and development of additional cardiac abnormalities in 1448 patients with congenital ventricular septal defects." Heart **90**(11): 1321-1325.
- Gottlieb, D., T. Kunal, et al. "*In vivo* monitoring of function of autologous engineered pulmonary valve." J Thorac Cardiovasc Surg **139**(3): 723-731.
- Gottlieb, D., T. Kunal, et al. (2010). "*In vivo* monitoring of function of autologous engineered pulmonary valve." J Thorac Cardiovasc Surg **139**(3): 723-731.
- Gould, R. A., K. Chin, et al. (2012). "Cyclic strain anisotropy regulates valvular interstitial cell phenotype and tissue remodeling in three-dimensional culture." Acta Biomater **8**(5): 1710-1719.
- Gould, R. A., K. Chin, et al. (2012). "Cyclic strain anisotropy regulates valvular interstitial cell phenotype and tissue remodeling in three-dimensional culture." Acta Biomaterialia **8**: 1710-1719.
- Gould, S. T. and K. S. Anseth (2013). "Role of cell-matrix interactions on VIC phenotype and tissue deposition in 3D PEG hydrogels." J Tissue Eng Regen Med.
- Groeber, F., M. Holeiter, et al. (2011). "Skin tissue engineering - *In vivo* and *in vitro* applications." Advanced Drug Delivery Reviews **63**: 352-366.
- Grunkemeier, G. L., H. H. Li, et al. (2000). "Long-term performance of heart valve prostheses." Curr Probl Cardiol **25**(2): 73-154.
- Grunkemeier, G. L., H. H. Li, et al. (1999). "Heart valve replacement: a statistical review of 35 years' results." J Heart Valve Dis **8**(5): 466-470; discussion 470-461.
- Gunatillake, P. A. and R. Adhikari (2003). "Biodegradable synthetic polymers for tissue engineering." Eur Cell Mater **5**: 1-16; discussion 16.
- Gunn, J. W., S. D. Turner, et al. (2005). "Adhesive and mechanical properties of hydrogels influence neurite extension." J Biomed Mater Res A **72**(1): 91-97.
- Guo, K. and C. C. Chu (2005). "Synthesis and characterization of novel biodegradable unsaturated poly(ester amide)/poly(ethylene glycol) diacrylate hydrogels." Journal of Polymer Science Part A: Polymer Chemistry **43**(17): 3932-3944.
- Guo, K. and C. C. Chu (2007). "Controlled release of paclitaxel from biodegradable unsaturated poly(ester amide)s/poly(ethylene glycol) diacrylate hydrogels." J Biomater Sci Polym Ed **18**(5): 489-504.
- Guo, K., C. C. Chu, et al. (2005). "Synthesis and characterization of novel biodegradable unsaturated poly(ester amide)s." Journal of Polymer Science Part A: Polymer Chemistry **43**(7): 1463-1477.

- Gupta, V., J. A. Werdenberg, et al. (2008). "Reversible secretion of glycosaminoglycans and proteoglycans by cyclically stretched valvular cells in 3D culture." Annals of Biomedical Engineering **36**: 1092-1103.
- Haddad, B., A. H. Pakravan, et al. (2013). "A systematic review of tissue engineered meniscus: Cell-based preclinical models " Current Stem Cell Research & Therapy **8**: 222-231.
- Haglund, L., J. Moir, et al. (2011). "Development of a bioreactor for axially loaded intervertebral disc organ culture " Tissue Engineering Part C-Method **17**: 1011-1019.
- Hahn, M. S., M. K. McHale, et al. (2007). "Physiologic pulsatile flow bioreactor conditioning of poly(ethylene glycol)-based tissue engineered vascular grafts." Ann Biomed Eng **35**(2): 190-200.
- Hammermeister, K., G. K. Sethi, et al. (2000). "Outcomes 15 years after valve replacement with a mechanical versus a bio-prosthetic valve: final report of the Veterans Affairs randomized trial." J Am Coll Cardiol **36**(4): 1152-1158.
- Hayashida, K., K. Kanda, et al. (2007). "Development of an *in vivo* tissue-engineered, autologous heart valve (the biovalve): preparation of a prototype model." J Thorac Cardiovasc Surg **134**(1): 152-159.
- Hayman, E. G., M. D. Pierschbacher, et al. (1985). "Vitronectin--a major cell attachment-promoting protein in fetal bovine serum." Exp Cell Res **160**(2): 245-258.
- Hildebrand, D. K., Z. J. J. Wu, et al. (2004). "Design and hydrodynamic evaluation of a novel pulsatile bioreactor for biologically active heart valves." Annals of Biomedical Engineering **32**: 1039-1049.
- Hinton, R. B. and K. E. Yutzey (2011). "Heart Valve Structure and Function in Development and Disease." Annual Review of Physiology **73**(1): null.
- Hockaday, L. A., K. H. Kang, et al. (2012). "Rapid 3D printing of anatomically accurate and mechanically heterogeneous aortic valve hydrogel scaffolds." Biofabrication **4**(3): 035005.
- Hockaday, L. A., K. H. Kang, et al. (2012). "Rapid 3D printing of anatomically accurate and mechanically heterogeneous aortic valve hydrogel scaffolds." Biofabrication **4**: 035005.
- Hoerstrup, S. P., R. Sodian, et al. (2000). "Functional living trileaflet heart valves grown *in vitro*." Circulation **102**: III44-49.
- Hoerstrup, S. P., R. Sodian, et al. (2000). "Functional living trileaflet heart valves grown *in vitro*." Circulation **102**(19 Suppl 3): III44-49.
- Hoerstrup, S. P., R. Sodian, et al. (2000). "New pulsatile bioreactor for *in vitro* formation of tissue engineered heart valves." Tissue Engineering **6**: 75-79.
- Hoerstrup, S. P., R. Sodian, et al. (2000). "New pulsatile bioreactor for *in vitro* formation of tissue engineered heart valves." Tissue Eng **6**(1): 75-79.
- Hoffman-Kim, D., M. S. Maish, et al. (2005). "Comparison of three myofibroblast cell sources for the tissue engineering of cardiac valves." Tissue Engineering **11**: 288-301.
- Hoffman, J. I. (1995). "Incidence of congenital heart disease: II. Prenatal incidence." Pediatr Cardiol **16**(4): 155-165.
- Hoffman, J. I. and S. Kaplan (2002). "The incidence of congenital heart disease." J Am Coll Cardiol **39**(12): 1890-1900.
- Hollister, S. J. (2005). "Porous scaffold design for tissue engineering." Nat Mater **4**(7): 518-524.
- Hong, T., M. S. Maish, et al. (2000). "Reproducible echocardiography in juvenile sheep and its application in the evaluation of a pulmonary valve homograft implant." Contemp Top Lab Anim Sci **39**(5): 20-25.

- Hou, Y., C. A. Schoener, et al. (2010). "Photo-cross-linked PDMSstar-PEG hydrogels: synthesis, characterization, and potential application for tissue engineering scaffolds." Biomacromolecules **11**(3): 648-656.
- Huebsch, N., P. R. Arany, et al. (2010). "Harnessing traction-mediated manipulation of the cell/matrix interface to control stem-cell fate." Nat Mater **9**(6): 518-526.
- Hui, T. Y., K. M. C. Cheung, et al. (2008). "*In vitro* chondrogenic differentiation of human mesenchymal stem cells in collagen microspheres: Influence of cell seeding density and collagen concentration." Biomaterials **29**: 3201-3212.
- Hume, P. S. and K. S. Anseth (2011). "Polymerizable superoxide dismutase mimetic protects cells encapsulated in poly(ethylene glycol) hydrogels from reactive oxygen species-mediated damage." J Biomed Mater Res A **99**(1): 29-37.
- Hutson, C. B., J. W. Nichol, et al. (2011). "Synthesis and characterization of tunable poly(ethylene glycol): gelatin methacrylate composite hydrogels." Tissue Eng Part A **17**(13-14): 1713-1723.
- Ilbawi, A. M., D. E. Spicer, et al. (2007). "Morphologic study of the ascending aorta and aortic arch in hypoplastic left hearts: surgical implications." J Thorac Cardiovasc Surg **134**(1): 99-105.
- Jashari, R., Y. Goffin, et al. (2010). "European homograft bank: twenty years of cardiovascular tissue banking and collaboration with transplant coordination in Europe." Transplant Proc **42**(1): 183-189.
- Jockenhoevel, S., G. Zund, et al. (2002). "Cardiovascular tissue engineering: A new Laminar flow chamber for *in vitro* improvement of mechanical tissue properties." ASAIO Journal **48**: 8-11.
- Kanemaru, S., H. Umeda, et al. (2013). "Improvement of eustachian tube function by tissue-engineered regeneration of mastoid air cells." Laryngoscope **123**: 472-476.
- Kang, K. H., L. A. Hockaday, et al. (2013). "Quantitative optimization of solid freeform deposition of aqueous hydrogels." Biofabrication **5**: 035001.
- Kang, K. H., L. A. Hockaday, et al. (2013). "Quantitative optimization of solid freeform deposition of aqueous hydrogels." Biofabrication **5**(3): 035001.
- Karamlou, T., K. Jang, et al. (2005). "Outcomes and associated risk factors for aortic valve replacement in 160 children: a competing-risks analysis." Circulation **112**(22): 3462-3469.
- Kirkland, R. A. and J. L. Franklin (2001). "Evidence for redox regulation of cytochrome C release during programmed neuronal death: antioxidant effects of protein synthesis and caspase inhibition." J Neurosci **21**(6): 1949-1963.
- Kirkland, R. A., G. M. Saavedra, et al. (2007). "Rapid activation of antioxidant defenses by nerve growth factor suppresses reactive oxygen species during neuronal apoptosis: evidence for a role in cytochrome c redistribution." J Neurosci **27**(42): 11315-11326.
- Kloxin, A. M., J. A. Benton, et al. (2010). "In situ elasticity modulation with dynamic substrates to direct cell phenotype." Biomaterials **31**(1): 1-8.
- Kloxin, A. M., A. M. Kasko, et al. (2009). "Photodegradable hydrogels for dynamic tuning of physical and chemical properties." Science **324**: 59-63.
- Kloxin, A. M., C. J. Kloxin, et al. (2010). "Mechanical properties of cellularly responsive hydrogels and their experimental determination." Adv Mater **22**(31): 3484-3494.
- Kloxin, A. M., K. J. R. Lewis, et al. (2012). "Responsive culture platform to examine the influence of microenvironmental geometry on cell function in 3D." Integrative Biology **4**: 1540-1549.
- Kloxin, A. M., M. W. Tibbitt, et al. (2010). "Synthesis of photodegradable hydrogels as dynamically tunable cell culture platforms." Nature Protocols **5**: 1867-1887.
- Kloxin, A. M., M. W. Tibbitt, et al. (2010). "Synthesis of photodegradable hydrogels as dynamically tunable cell culture platforms." Nat Protoc **5**(12): 1867-1887.

- Kloxin, A. M., M. W. Tibbitt, et al. (2010). "Tunable hydrogels for external manipulation of cellular microenvironments through controlled photodegradation." Advanced Materials **22**: 61-+.
- Kloxin, A. M., M. W. Tibbitt, et al. (2010). "Tunable hydrogels for external manipulation of cellular microenvironments through controlled photodegradation." Adv Mater **22**(1): 61-66.
- Koch, L., A. Deiwick, et al. (2012). "Skin tissue generation by laser cell printing." Biotechnology and Bioengineering **109**: 1855-1863.
- Koch, L., A. Deiwick, et al. (2012). "Skin tissue generation by laser cell printing." Biotechnol Bioeng **109**(7): 1855-1863.
- Konstantinov, I. E., T. Karamlou, et al. (2006). "Truncus arteriosus associated with interrupted aortic arch in 50 neonates: a Congenital Heart Surgeons Society study." Ann Thorac Surg **81**(1): 214-222.
- Konuma, T., E. J. Devaney, et al. (2009). "Performance of CryoValve SG decellularized pulmonary allografts compared with standard cryopreserved allografts." Ann Thorac Surg **88**(3): 849-854; discussion 554-845.
- Kortsmit, J., M. C. Rutten, et al. (2009). "Deformation-controlled load application in heart valve tissue engineering." Tissue Eng Part C Methods **15**(4): 707-716.
- Kortsmit, J., M. C. M. Rutten, et al. (2009). "Deformation controlled load application in heart valve tissue engineering." Tissue Engineering Part C-Method **15**: 707-716.
- Kosaki, K., A. Mendoza, et al. (1996). "Cervical flexion: its contribution to normal and abnormal cardiac morphogenesis." Teratology **54**(3): 135-144.
- Kotecha, M., D. Klatt, et al. (2013). "Monitoring cartilage tissue engineering using magnetic resonance spectroscopy, imaging, and elastography." Tissue Eng Part B Rev **19**(6): 470-484.
- Koul, B., C. J. Lindholm, et al. (2002). "Ross operation for bicuspid aortic valve disease in adults: is it a valid surgical option?" Scand Cardiovasc J **36**(1): 48-52.
- Kovacs, G., A. Berghold, et al. (2009). "Pulmonary arterial pressure during rest and exercise in healthy subjects: a systematic review." European Respiratory Journal **34**: 888-894.
- Ku, C. H., P. H. Johnson, et al. (2006). "Collagen synthesis by mesenchymal stem cells and aortic valve interstitial cells in response to mechanical stretch." Cardiovascular Research **71**: 548-556.
- Kuzawa, C. W. (1998). "Adipose tissue in human infancy and childhood: An evolutionary perspective." Yearbook of Physical Anthropology, Vol 41 - 1998 **41**: 177-209.
- L'Heureux, N., S. Paquet, et al. (1998). "A completely biological tissue-engineered human blood vessel." Faseb Journal **12**: 47-56.
- Labarthe, D. R. and S. B. Dunbar (2012). "Global cardiovascular health promotion and disease prevention 2011 and beyond." Circulation **125**: 2667-2676.
- Lampe, K. J., R. M. Namba, et al. (2009). "Impact of lactic acid on cell proliferation and free radical-induced cell death in monolayer cultures of neural precursor cells." Biotechnol Bioeng **103**(6): 1214-1223.
- Larsen, L. U., O. B. Petersen, et al. (2006). "Strain rate derived from color Doppler myocardial imaging for assessment of fetal cardiac function." Ultrasound Obstet Gynecol **27**(2): 210-213.
- Latif, N., P. Sarathchandra, et al. (2007). "Characterization of structural and signaling molecules by human valve interstitial cells and comparison to human mesenchymal stem cells." J Heart Valve Dis **16**(1): 56-66.
- Leach, J. B. and C. E. Schmidt (2005). "Characterization of protein release from photocrosslinkable hyaluronic acid-polyethylene glycol hydrogel tissue engineering scaffolds." Biomaterials **26**(2): 125-135.
- Lee, H., S. Ahn, et al. (2014). "Enhancement of cell viability by fabrication of macroscopic 3D hydrogel scaffolds using an innovative cell-dispensing technique

- supplemented by preosteoblast-laden micro-beads." Carbohydr Polym **104**: 191-198.
- Lee, S. H., J. J. Moon, et al. (2008). "Three-dimensional micropatterning of bioactive hydrogels via two-photon laser scanning photolithography for guided 3D cell migration." Biomaterials **29**: 2962-2968.
- Lee, S. J., H. W. Kang, et al. (2008). "Application of microstereolithography in the development of three-dimensional cartilage regeneration scaffolds." Biomedical Microdevices **10**: 233-241.
- Lee, S. J., J. W. Rhie, et al. (2008). "Development of three-dimensional alginate encapsulated chondrocyte hybrid scaffold using microstereolithography." Journal of Manufacturing Science and Engineering-Transactions of the ASME **130**: 021007.
- Lee, W., J. C. Debasitis, et al. (2009). "Multi-layered culture of human skin fibroblasts and keratinocytes through three-dimensional freeform fabrication." Biomaterials **30**(8): 1587-1595.
- Lee, W., J. C. Debasitis, et al. (2009). "Multi-layered culture of human skin fibroblasts and keratinocytes through three-dimensional freeform fabrication." Biomaterials **30**: 1587-1595.
- Lee, W., V. Lee, et al. (2010). "On-demand three-dimensional freeform fabrication of multi-layered hydrogel scaffold with fluidic channels." Biotechnology and Bioengineering **105**(6): 1178-1186.
- Lee, W., V. Lee, et al. (2010). "On-demand three-dimensional freeform fabrication of multi-layered hydrogel scaffold with fluidic channels " Biotechnology and Bioengineering **105**: 1178-1186.
- Lee, W., J. Pinckney, et al. (2009). "Three-dimensional bioprinting of rat embryonic neural cells " Neuroreport **20**: 798-803.
- Lee, W., J. Pinckney, et al. (2009). "Three-dimensional bioprinting of rat embryonic neural cells." Neuroreport **20**(8): 798-803.
- Lee, Y. B., S. Polio, et al. (2010). "Bio-printing of collagen and VEGF-releasing fibrin gel scaffolds for neural stem cell culture." Exp Neurol **223**(2): 645-652.
- Lee, Y. B., S. Polio, et al. (2010). "Bio-printing of collagen and VEGF-releasing fibrin gel scaffolds for neural stem cell culture." Experimental Neurology **223**: 645-652.
- Leong, K. F., C. M. Cheah, et al. (2003). "Solid freeform fabrication of three-dimensional scaffolds for engineering replacement tissues and organs." Biomaterials **24**: 2363-2378.
- Liao, J., E. M. Joyce, et al. (2008). "Effects of decellularization on the mechanical and structural properties of the porcine aortic valve leaflet." Biomaterials **29**(8): 1065-1074.
- Lichtenberg, A., S. Cebotari, et al. (2006). "Flow-dependent re-endothelialization of tissue-engineered heart valves." Journal of Heart Valve Disease **15**: 287-293.
- Lichtenberg, A., I. Tudorache, et al. (2006). "Preclinical testing of tissue-engineered heart valves re-endothelialized under simulated physiological conditions." Circulation **114**: I559-I565.
- Lin, C. C. and K. S. Anseth (2009). "Controlling Affinity Binding with Peptide-Functionalized Poly(ethylene glycol) Hydrogels." Adv Funct Mater **19**(14): 2325.
- Liu, V. A. and S. N. Bhatia (2002). "Three-Dimensional Photopatterning of Hydrogels Containing Living Cells." Biomedical Microdevices **4**(4): 257-266.
- Liu, Y., L. Zhang, et al. (2010). "*In vitro* engineering of human ear-shaped cartilage assisted with CAD/CAM technology." Biomaterials **31**: 2176-2183.
- Luangphakdy, V., E. Walker, et al. (2013). "Evaluation of osteoconductive scaffolds in the canine femoral multi-defect model " Tissue Engineering Part A **19**: 634-648.
- Lund, A. W., B. Yener, et al. (2009). "The natural and engineered 3D microenvironment as a regulatory cue during stem cell fate determination." Tissue Engineering Part B-Reviews **15**: 371-380.

- Lupinetti, F. M., J. Warner, et al. (1997). "Comparison of human tissues and mechanical prostheses for aortic valve replacement in children." Circulation **96**(1): 321-325.
- Ma, P. X. and J. H. Elisseeff (2005). Scaffolding in tissue engineering. Boca Raton, Taylor&Francis.
- MacNeil, S. and S. N. V. I. P. D. n. P. F. 2007 (2007). "Progress and opportunities for tissue-engineered skin." Nature **445**: 874-880.
- Maish, M. S., D. Hoffman-Kim, et al. (2003). "Tricuspid valve biopsy: A potential source of cardiac myofibroblast cells for tissue-engineered cardiac valves." Journal of Heart Valve Disease **12**: 264-269.
- Mallajosyula, J. K., D. Kaur, et al. (2008). "MAO-B elevation in mouse brain astrocytes results in Parkinson's pathology." PLoS One **3**(2): e1616.
- Malone, E. and H. Lipson (2007). "Fab@Home: The Personal Desktop Fabricator Kit." Rapid Prototyping J **13**: 244-255.
- Malone, E. L. H. (2007). "Fab@Home: the personal desktop fabricator kit." Rapid Prototyping Journal **13**(4): 245-255.
- Manevich, Y., T. Sweitzer, et al. (2002). "1-Cys peroxiredoxin overexpression protects cells against phospholipid peroxidation-mediated membrane damage." Proc Natl Acad Sci U S A **99**(18): 11599-11604.
- Mannoor, M. S., Z. Jiang, et al. (2013). "3D Printed Bionic Ears." Nano Letters **13**(6): 2634-2639.
- Mannoor, M. S., Z. W. Jiang, et al. (2013). "3D printed bionic ears." Nano Letters **13**: 2634-2639.
- Marga, F., K. Jakab, et al. (2012). "Toward engineering functional organ modules by additive manufacturing." Biofabrication **4**: 022001.
- Marga, F., K. Jakab, et al. (2012). "Toward engineering functional organ modules by additive manufacturing." Biofabrication **4**(2).
- Marijon, E., P. Ou, et al. (2007). "Prevalence of rheumatic heart disease detected by echocardiographic screening." N Engl J Med **357**(5): 470-476.
- Mariner, P. D., E. Johannesen, et al. (2012). "Manipulation of miRNA activity accelerates osteogenic differentiation of hMSCs in engineered 3D scaffolds." Journal of Tissue Engineering and Regenerative Medicine **6**: 314-324.
- Matthews, P. B., A. N. Azadani, et al. (2010). "Comparison of porcine pulmonary and aortic root material properties." Ann Thorac Surg **89**(6): 1981-1988.
- Mavrilas, D. and Y. Missirlis (1991). "An approach to the optimization of preparation of bio-prosthetic heart valves." J Biomech **24**(5): 331-339.
- Mayosi, B. M. (2007). "Contemporary trends in the epidemiology and management of cardiomyopathy and pericarditis in sub-Saharan Africa." Heart **93**(10): 1176-1183.
- McAllister, T. N., M. Maruszewski, et al. (2009). "Effectiveness of haemodialysis access with an autologous tissue-engineered vascular graft: a multicentre cohort study." Lancet **373**: 1440-1446.
- McBride, K. L., L. Marengo, et al. (2005). "Epidemiology of noncomplex left ventricular outflow tract obstruction malformations (aortic valve stenosis, coarctation of the aorta, hypoplastic left heart syndrome) in Texas, 1999-2001." Birth Defects Res A Clin Mol Teratol **73**(8): 555-561.
- Merryman, W. D., H. D. Lukoff, et al. (2007). "Synergistic effects of cyclic tension and transforming growth factor-beta 1 on the aortic valve myofibroblast." Cardiovascular Pathology **16**: 268-276.
- Messier, R. H., B. L. Bass, et al. (1994). "Dual structural and functional phenotypes of the porcine aortic-valve interstitial population-Characteristics of the leaflet myofibroblast." Journal of Surgical Research **57**: 1-21.
- Metscher, B. D. and G. B. Muller (2011). "MicroCT for molecular imaging: quantitative visualization of complete three-dimensional distributions of gene products in embryonic limbs." Dev Dyn **240**(10): 2301-2308.

- Meuris, B., S. Ozaki, et al. (2001). "Influence of species, environmental factors, and tissue cellularity on calcification of porcine aortic wall tissue." Semin Thorac Cardiovasc Surg **13**(4 Suppl 1): 99-105.
- Meuris, B., S. Ozaki, et al. (2003). "Bio-prosthetic tissue calcification: influence of blood contact and arterial pressure. an experimental study in rats and sheep." J Heart Valve Dis **12**(3): 392-399; discussion 399.
- Michael, S., H. Sorg, et al. (2013). "Tissue Engineered Skin Substitutes Created by Laser-Assisted Bioprinting Form Skin-Like Structures in the Dorsal Skin Fold Chamber in Mice." PLoS One **8**(3): e57741.
- Michael, S., H. Sorg, et al. (2013). "Tissue engineered skin substitutes created by laser-assisted bioprinting form skin-like structures in the dorsal skin fold chamber in mice " Plos One **8**: e57741.
- Miller, D. V., W. D. Edwards, et al. (2006). "Endothelial and smooth muscle cell populations in a decellularized cryopreserved aortic homograft (SynerGraft) 2 years after implantation." J Thorac Cardiovasc Surg **132**(1): 175-176.
- Miller, J. S., K. R. Stevens, et al. (2012). "Rapid casting of patterned vascular networks for perfusable engineered three-dimensional tissues." Nat Mater **11**(9): 768-774.
- Miller, J. S., K. R. Stevens, et al. (2012). "Rapid casting of patterned vascular networks for perfusable engineered three-dimensional tissues." Nature Materials **11**: 768-774.
- Mocumbi, A. O., M. B. Ferreira, et al. (2008). "A population study of endomyocardial fibrosis in a rural area of Mozambique." N Engl J Med **359**(1): 43-49.
- Mol, A., N. J. Driessen, et al. (2005). "Tissue engineering of human heart valve leaflets: a novel bioreactor for a strain-based conditioning approach." Ann Biomed Eng **33**(12): 1778-1788.
- Mol, A., N. J. B. Driessen, et al. (2005). "Tissue engineering of human heart valve leaflets: A novel bioreactor for a strain-based conditioning approach." Annals of Biomedical Engineering **33**: 1778-1788.
- Molina, F. S., C. Faro, et al. (2008). "Heart stroke volume and cardiac output by four-dimensional ultrasound in normal fetuses." Ultrasound Obstet Gynecol **32**(2): 181-187.
- Muller, A. M., M. Davenport, et al. (2009). "Platelet lysate as a serum substitute for 2D static and 3D perfusion culture of stromal vascular fraction cells from human adipose tissue." Tissue Engineering Part C **15**: 869-875.
- Nakayama, Y., Y. Takewa, et al. (2014). "In-body tissue-engineered aortic valve (Biovalve type VII) architecture based on 3D printer molding." Journal of Biomedical Materials Research Part B: Applied Biomaterials: n/a-n/a.
- Nakayama, Y., Y. Takewa, et al. (2014). "In-body tissue-engineered aortic valve (Biovalve type VII) architecture based on 3D printer molding." J Biomed Mater Res B Appl Biomater.
- Naso, F., A. Gandaglia, et al. "Differential distribution of structural components and hydration in aortic and pulmonary heart valve conduits: Impact of detergent-based cell removal." Acta Biomater **6**(12): 4675-4688.
- Neidert, M. R. and R. T. Tranquillo (2006). "Tissue-engineered valves with commissural alignment." Tissue Eng **12**(4): 891-903.
- Nichol, J. W., S. T. Koshy, et al. (2010). "Cell-laden microengineered gelatin methacrylate hydrogels." Biomaterials **31**: 5536-5544.
- Nimeskern, L., H. Martinez Avila, et al. (2013). "Mechanical evaluation of bacterial nanocellulose as an implant material for ear cartilage replacement." Journal of Mechanical Behavior of Biomedical Materials **22**: 12-21.
- Nimeskern, L., G. J. van Osch, et al. (2013). "Quantitative evaluation of mechanical properties in tissue-engineered auricular cartilage." Tissue Engineering Part B-Reviews: DOI: 10.1089/ten.teb.2013.0117.

- Norotte, C., F. S. Marga, et al. (2009). "Scaffold-free vascular tissue engineering using bioprinting." Biomaterials **30**: 5910-5917.
- O'Brien, M. F., S. Goldstein, et al. (1999). "The SynerGraft valve: a new acellular (nongluteraldehyde-fixed) tissue heart valve for autologous recellularization first experimental studies before clinical implantation." Semin Thorac Cardiovasc Surg **11**(4 Suppl 1): 194-200.
- O'Cearbhaill, E. D., M. Murphy, et al. (2010). "Behavior of human mesenchymal stem cells in fibrin-based vascular tissue engineering constructs." Ann Biomed Eng **38**(3): 649-657.
- Occhetta, P., N. Sadr, et al. (2013). "Fabrication of 3D cell-laden hydrogel microstructures through photo-mold patterning." Biofabrication **5**(3): 035002.
- Ouyang, D. W., C. T. Salerno, et al. (1998). "Long-term evaluation of orthotopically implanted stentless bio-prosthetic aortic valves in juvenile sheep." J Invest Surg **11**(3): 175-183.
- Owens, S. T., C. Gomez-Fifer, et al. (2006). "Thrombus formation in the native aortic root in patients with hypoplastic left heart syndrome." Pediatr Cardiol **27**(3): 385-387.
- Padera R F i J r , S. F. J., Ed. (2008). Pathology of Cardiac Surgery. Cardiac Surgery in the Adult. . New York, McGraw-Hill.
- Park, J. S., J. S. Chu, et al. (2011). "The effect of matrix stiffness on the differentiation of mesenchymal stem cells in response to TGF-beta." Biomaterials **32**(16): 3921-3930.
- Pati, F., J. Jang, et al. (2014). "Printing three-dimensional tissue analogues with decellularized extracellular matrix bioink." Nat Commun **5**: 3935.
- Pedron, S., A. M. Kasko, et al. (2010). "Effect of heparin oligomer chain length on the activation of valvular interstitial cells." Biomacromolecules **11**: 1692-1695.
- Pedron, S., A. M. Kasko, et al. (2010). "Effect of heparin oligomer chain length on the activation of valvular interstitial cells." Biomacromolecules **11**(6): 1692-1695.
- Perry, T. E., S. Kaushal, et al. (2003). "Bone marrow as a cell source for tissue engineering heart valves." Annals of Thoracic Surgery **75**: 761-767.
- Peyton, S. R., C. B. Raub, et al. (2006). "The use of poly(ethylene glycol) hydrogels to investigate the impact of ECM chemistry and mechanics on smooth muscle cells." Biomaterials **27**(28): 4881-4893.
- Pibarot, P. and J. G. Dumesnil (2006). "Prosthesis-patient mismatch: definition, clinical impact, and prevention." Heart **92**(8): 1022-1029.
- Quintanilla, R. A., T. A. Matthews-Roberson, et al. (2009). "Caspase-cleaved tau expression induces mitochondrial dysfunction in immortalized cortical neurons: implications for the pathogenesis of Alzheimer disease." J Biol Chem **284**(28): 18754-18766.
- Rahimtoola, S. H. (2010). "Choice of prosthetic heart valve in adults an update." J Am Coll Cardiol **55**(22): 2413-2426.
- Rajani, B., R. B. Mee, et al. (1998). "Evidence for rejection of homograft cardiac valves in infants." J Thorac Cardiovasc Surg **115**(1): 111-117.
- Ramaswamy, S., D. Gottlieb, et al. (2010). "The role of organ level conditioning on the promotion of engineered heart valve tissue development in-vitro using mesenchymal stem cells." Biomaterials **31**: 1114-1125.
- Ramaswamy, S., D. Gottlieb, et al. (2010). "The role of organ level conditioning on the promotion of engineered heart valve tissue development in-vitro using mesenchymal stem cells." Biomaterials **31**(6): 1114-1125.
- Reddy, G. K. and C. S. Enwemeka (1996). "A simplified method for the analysis of hydroxyproline in biological tissues." Clin Biochem **29**(3): 225-229.
- Reiffel, A. J., C. Kafka, et al. (2013). "High-fidelity tissue engineering of patient-specific auricles for reconstruction of pediatric microtia and other auricular deformities." Plos One **8**: e56506.

- Ribeiro, P. S., K. H. Jacobsen, et al. (2008). "Priorities for women's health from the Global Burden of Disease study." Int J Gynaecol Obstet **102**(1): 82-90.
- Richards, J., I. El-Hamamsy, et al. (2013). "Side-specific endothelial-dependent regulation of aortic valve calcification interplay of hemodynamics and nitric oxide signaling." American Journal of Pathology **182**: 1922-1931.
- Rieder, E., M. T. Kasimir, et al. (2004). "Decellularization protocols of porcine heart valves differ importantly in efficiency of cell removal and susceptibility of the matrix to recellularization with human vascular cells." J Thorac Cardiovasc Surg **127**(2): 399-405.
- Rieder, E., G. Seebacher, et al. (2005). "Tissue engineering of heart valves: decellularized porcine and human valve scaffolds differ importantly in residual potential to attract monocytic cells." Circulation **111**(21): 2792-2797.
- Roberts, W. C. and J. M. Ko (2005). "Frequency by decades of unicuspid, bicuspid, and tricuspid aortic valves in adults having isolated aortic valve replacement for aortic stenosis, with or without associated aortic regurgitation." Circulation **111**(7): 920-925.
- Robinson, P. S., S. L. Johnson, et al. (2007). "Functional Tissue-Engineered Valves from Cell-Remodeled Fibrin with Commissural Alignment of Cell-Produced Collagen." Tissue Eng.
- Rogers, C. I., J. V. Pagaduan, et al. (2011). "Single-monomer formulation of polymerized polyethylene glycol diacrylate as a nonadsorptive material for microfluidics." Anal Chem **83**(16): 6418-6425.
- Rosano, A., L. D. Botto, et al. (2000). "Infant mortality and congenital anomalies from 1950 to 1994: an international perspective." J Epidemiol Community Health **54**(9): 660-666.
- Ross, D. N. (1967). "Replacement of aortic and mitral valves with a pulmonary autograft." Lancet **2**(7523): 956-958.
- Rouillard, A. D., C. M. Berglund, et al. (2010). "Methods for Photo-crosslinking Alginate Hydrogel Scaffolds with High Cell Viability." Tissue Eng Part C Methods.
- Rouillard, A. D., C. M. Berglund, et al. (2011). "Methods for photo-crosslinking alginate hydrogel scaffolds with high cell viability." Tissue Eng Part C Methods **17**(2): 173-179.
- Rowley, J. A., G. Madlambayan, et al. (1999). "Alginate hydrogels as synthetic extracellular matrix materials." Biomaterials **20**(1): 45-53.
- Rubbens, M. P., A. Mol, et al. (2009). "Intermittent straining accelerates the development of tissue properties in engineered heart valve tissue." Tissue Engineering Part A **15**: 999-1008.
- Sacks, M. S., F. J. Schoen, et al. (2009). "Bioengineering challenges for heart valve tissue engineering." Annu Rev Biomed Eng **11**: 289-313.
- Sales, V. L., B. A. Mettler, et al. (2010). "Endothelial progenitor cells as a sole source for ex vivo seeding of tissue-engineered heart valves." Tissue Engineering Part A **16**: 257-267.
- Sales, V. L., B. A. Mettler, et al. (2010). "Endothelial progenitor cells as a sole source for ex vivo seeding of tissue-engineered heart valves." Tissue Eng Part A **16**(1): 257-267.
- Sani, M. U., K. M. Karaye, et al. (2007). "Prevalence and pattern of rheumatic heart disease in the Nigerian savannah: an echocardiographic study." Cardiovasc J Afr **18**(5): 295-299.
- Santos, E., R. M. Hernandez, et al. (2012). "Novel advances in the design of three-dimensional bio-scaffolds to control cell fate: translation from 2D to 3D." Trends in Biotechnology **30**: 331-341.
- Sauren, A. A., M. C. van Hout, et al. (1983). "The mechanical properties of porcine aortic valve tissues." J Biomech **16**(5): 327-337.

- Sayk, F., I. Bos, et al. (2005). "Histopathologic findings in a novel decellularized pulmonary homograft: an autopsy study." Ann Thorac Surg **79**(5): 1755-1758.
- Schaefermeier, P. K., D. Szymanski, et al. (2009). "Design and fabrication of three-dimensional scaffolds for tissue engineering of human heart valves." Eur Surg Res **42**(1): 49-53.
- Schechner, J. S., S. K. Crane, et al. (2003). "Engraftment of a vascularized human skin equivalent." Faseb Journal **17**: 2250-2256.
- Schenke-Layland, K., F. Opitz, et al. (2003). "Complete dynamic repopulation of decellularized heart valves by application of defined physical signals-an *in vitro* study." Cardiovascular Research **60**: 497-509.
- Schieker, M., H. Seitz, et al. (2006). "Biomaterials as Scaffold for Bone Tissue Engineering." European Journal of Trauma **32**(2): 114-124.
- Schleicher, M., G. Sammler, et al. (2010). "Simplified pulse reactor for real-time long-term *in vitro* testing of biological heart valves." Annals of Biomedical Engineering **38**: 1919-1927.
- Schmidt, D., J. Achermann, et al. (2008). "Cryopreserved amniotic fluid-derived cells: A life-long autologous fetal stem cell source for heart valve tissue engineering." Journal of Heart Valve Disease **17**: 446-455.
- Schmidt, D., J. Achermann, et al. (2008). "Cryopreserved amniotic fluid-derived cells: a lifelong autologous fetal stem cell source for heart valve tissue engineering." J Heart Valve Dis **17**(4): 446-455; discussion 455.
- Schmidt, D., C. Breyman, et al. (2004). "Umbilical cord blood derived endothelial progenitor cells for tissue engineering of vascular grafts." Annals of Thoracic Surgery **78**: 2094-2098.
- Schmidt, D., P. Dijkman, et al. (2010). "Minimally-invasive implantation of living tissue engineered heart valves A comprehensive approach from autologous vascular cells to stem cells." Journal of the American College of Cardiology **56**: 510-520.
- Schmidt, D., P. E. Dijkman, et al. (2010). "Minimally-invasive implantation of living tissue engineered heart valves: a comprehensive approach from autologous vascular cells to stem cells." J Am Coll Cardiol **56**(6): 510-520.
- Schmidt, D., A. Mol, et al. (2006). "Living autologous heart valves engineered from human prenatally harvested progenitors." Circulation **114**(1 Suppl): I125-131.
- Schmidt, D., A. Mol, et al. (2006). "Living autologous heart valves engineered from human prenatally harvested progenitors." Circulation **114**: I125-I131.
- Schmidt, D., A. Mol, et al. (2006). "Engineering of biologically active living heart valve leaflets using human umbilical cord-derived progenitor cells." Tissue Engineering **12**: 3223-3232.
- Schmidt, D., U. A. Stock, et al. (2007). "Tissue engineering of heart valves using decellularized xenogeneic or polymeric starter matrices." Philos Trans R Soc Lond B Biol Sci **362**(1484): 1505-1512.
- Schoen, F. J. (2006). "New frontiers in the pathology and therapy of heart valve disease: 2006 Society for Cardiovascular Pathology, Distinguished Achievement Award Lecture, United States-Canadian Academy of Pathology, Atlanta, GA, February 12, 2006." Cardiovasc Pathol **15**(5): 271-279.
- Schoen, F. J. (2008). "Evolving concepts of cardiac valve dynamics: the continuum of development, functional structure, pathobiology, and tissue engineering." Circulation **118**(18): 1864-1880.
- Schuurman, W., V. Khristov, et al. (2011). "Bioprinting of hybrid tissue constructs with tailorable mechanical properties." Biofabrication **3**(2): 021001.
- Seeger, J. M. and N. Klingman (1985). "Improved endothelial cell seeding with cultured cells and fibronectin-coated grafts." J Surg Res **38**(6): 641-647.
- Seliktar, D., R. A. Black, et al. (2000). "Dynamic mechanical conditioning of collagen-gel blood vessel constructs induces remodeling *in vitro*." Ann Biomed Eng **28**(4): 351-362.

- Seliktar, D., R. M. Nerem, et al. (2001). "The role of matrix metalloproteinase-2 in the remodeling of cell-seeded vascular constructs subjected to cyclic strain." Ann Biomed Eng **29**(11): 923-934.
- Shin, S. R., B. Aghaei-Ghareh-Bolagh, et al. (2013). "Cell-laden microengineered and mechanically tunable hybrid hydrogels of gelatin and graphene oxide." Adv Mater **25**(44): 6385-6391.
- Shinoka, T., C. K. Breuer, et al. (1995). "Tissue engineering heart valves: valve leaflet replacement study in a lamb model." Annals of Thoracic and Surgery **60**: S513-516.
- Shinoka, T., P. X. Ma, et al. (1996). "Tissue-engineered heart valves. Autologous valve leaflet replacement study in a lamb model." Circulation **94**(9 Suppl): II164-168.
- Shinoka, T., D. ShumTim, et al. (1997). "Tissue-engineered heart valve leaflets - Does cell origin affect outcome?" Circulation **96**: 102-107.
- Sierad, L., A. Simionescu, et al. "Design and Testing of a Pulsatile Conditioning System for Dynamic Endothelialization of Polyphenol-Stabilized Tissue Engineered Heart Valves." Cardiovascular Engineering and Technology **1**(2): 138.
- Sierad, L. N., A. Simionescu, et al. (2010). "Design and testing of a pulsatile conditioning system for dynamic endothelialization of polyphenol-stabilized tissue engineered heart valves." Cardiovascular Engineering and Technology **1**: 138-153.
- Sierad, L. N., A. Simionescu, et al. (2010). "Design and Testing of a Pulsatile Conditioning System for Dynamic Endothelialization of Polyphenol-Stabilized Tissue Engineered Heart Valves." Cardiovasc Eng Technol **1**(2): 138-153.
- Sierad, L. N., A. Simionescu, et al. (2010). "Design and testing of a pulsatile conditioning system for dynamic endothelialization of polyphenol-stabilized tissue engineered heart valves." Cardiovascular Engineering and Technology **1**: 138-153.
- Simon, P., M. T. Kasimir, et al. (2003). "Early failure of the tissue engineered porcine heart valve SYNERGRAFT in pediatric patients." Eur J Cardiothorac Surg **23**(6): 1002-1006; discussion 1006.
- Singh, S., C. Brocker, et al. (2013). "Aldehyde dehydrogenases in cellular responses to oxidative/electrophilic stress." Free Radic Biol Med **56**: 89-101.
- Singh, S., A. N. Singh, et al. (2013). "Biodegradable polycaprolactone (PCL) nanosphere encapsulating superoxide dismutase and catalase enzymes." Appl Biochem Biotechnol **171**(7): 1545-1558.
- Sinthuvanich, C., L. A. Haines-Butterick, et al. (2012). "Iterative design of peptide-based hydrogels and the effect of network electrostatics on primary chondrocyte behavior." Biomaterials **33**(30): 7478-7488.
- Skardal, A., J. Zhang, et al. (2010). "Photocrosslinkable hyaluronan-gelatin hydrogels for two-step bioprinting." Tissue Eng Part A **16**(8): 2675-2685.
- Skardal, A., J. Zhang, et al. (2010). "Bioprinting vessel-like constructs using hyaluronan hydrogels crosslinked with tetrahedral polyethylene glycol tetracrylates." Biomaterials **31**(24): 6173-6181.
- Skardal, A., J. X. Zhang, et al. (2010). "Photocrosslinkable hyaluronan-gelatin hydrogels for two-step bioprinting." Tissue engineering Part A **16**: 2675-2685.
- Smeds, K. A., A. M. Pfister-Serres, et al. (2001). "Photocrosslinkable polysaccharides for in situ hydrogel formation." Journal of Biomedical Materials Research **55**: 254-255.
- Sodian, R., S. P. Hoerstrup, et al. (2000). "Early *in vivo* experience with tissue-engineered trileaflet heart valves." Circulation **102**(19 Suppl 3): III22-29.
- Sodian, R., S. P. Hoerstrup, et al. (2000). "Evaluation of biodegradable, three-dimensional matrices for tissue engineering of heart valves." Asaio J **46**(1): 107-110.

- Sodian, R., M. Loebe, et al. (2002). "Application of stereolithography for scaffold fabrication for tissue engineered heart valves." ASAIO J **48**(1): 12-16.
- Sodian, R., P. Schaefermeier, et al. (2010). "Use of human umbilical cord blood-derived progenitor cells for tissue-engineered heart valves." Ann Thorac Surg **89**(3): 819-828.
- Sodian, R., J. S. Sperling, et al. (1999). "Tissue engineering of a trileaflet heart valve-early *in vitro* experiences with a combined polymer." Tissue Eng **5**(5): 489-494.
- Sproul, A. and E. Simpson (1964). "Stroke Volume and Related Hemodynamic Data in Normal Children." Pediatrics **33**: 912-918.
- Stamm, C., A. Khosravi, et al. (2004). "Biomatrix/polymer composite material for heart valve tissue engineering." Ann Thorac Surg **78**(6): 2084-2092; discussion 2092-2083.
- Stankus, J. J., J. Guan, et al. (2006). "Microintegrating smooth muscle cells into a biodegradable, elastomeric fiber matrix." Biomaterials **27**(5): 735-744.
- Steinboff, G., U. Stock, et al. (2000). "Tissue engineering of pulmonary heart valves on allogenic acellular matrix conduits: *in vivo* restoration of valve tissue." Circulation **102**(19 Suppl 3): III50-55.
- Stephens, E. H., C. A. Durst, et al. "Mitral valvular interstitial cell responses to substrate stiffness depend on age and anatomic region." Acta Biomater **7**(1): 75-82.
- Stephens, E. H., C. A. Durst, et al. (2011). "Mitral valvular interstitial cell responses to substrate stiffness depend on age and anatomic region." Acta Biomater **7**(1): 75-82.
- Sterodimas, A. and J. de Faria (2013). "Human auricular tissue engineering in an immunocompetent animal model " Aesthetic Surgery Journal **33**: 283-289.
- Stock, U. A., M. Nagashima, et al. (2000). "Tissue-engineered valved conduits in the pulmonary circulation." J Thorac Cardiovasc Surg **119**(4 Pt 1): 732-740.
- Sumikura, H., Y. Nakayama, et al. (2014). "*In vitro* evaluation of a novel autologous aortic valve (biovalve) with a pulsatile circulation circuit." Artif Organs **38**(4): 282-289.
- Sutherland, F. W., T. E. Perry, et al. (2005). "From stem cells to viable autologous semilunar heart valve." Circulation **111**(21): 2783-2791.
- Sutherland, F. W. H., T. E. Perry, et al. (2005). "From stem cells to viable autologous semilunar heart valve." Circulation **111**: 2783-2791.
- Sutherland, G. R., G. Di Salvo, et al. (2004). "Strain and strain rate imaging: a new clinical approach to quantifying regional myocardial function." J Am Soc Echocardiogr **17**(7): 788-802.
- Swarts, J. D., C. M. Alper, et al. (2013). "Panel 2: Eustachian tube, middle ear, and mastoid-anatomy, physiology, pathophysiology, and pathogenesis " Otolaryngology-Head and Neck Surgery **148**: E26-E36.
- Swindle, M. M., A. Makin, et al. (2012). "Swine as models in biomedical research and toxicology testing." Vet Pathol **49**(2): 344-356.
- Syedain, Z. H., A. R. Bradee, et al. (2013). "Decellularized tissue-engineered heart valve leaflets with recellularization potential." Tissue Eng Part A **19**(5-6): 759-769.
- Syedain, Z. H., L. A. Meier, et al. (2013). "Tubular heart valves from decellularized engineered tissue." Ann Biomed Eng **41**(12): 2645-2654.
- Syedain, Z. H. and R. T. Tranquillo (2009). "Controlled cyclic stretch bioreactor for tissue-engineered heart valves." Biomaterials **30**: 4078-4084.
- Syedain, Z. H. L. M. T. J. S. L. R. P. S. R. G. R. B. R. W. T. R. T. (2011). "Implantation of a Tissue-engineered Heart Valve from Human Fibroblasts Exhibiting Short Term Function in the Sheep Pulmonary Artery." Cardiovascular Engineering and Technology **2**(2): 101-112.

- Tan, J. Y., C. K. Chua, et al. (2013). "Fabrication of channeled scaffolds with ordered array of micro-pores through microsphere leaching and indirect Rapid Prototyping technique " Biomedical Microdevices **15**: 83-96.
- Tanner, K., N. Sabrine, et al. (2005). "Cardiovascular malformations among preterm infants." Pediatrics **116**(6): e833-838.
- Tarafder, S., V. K. Balla, et al. (2013). "Microwave-sintered 3D printed tricalcium phosphate scaffolds for bone tissue engineering." J Tissue Eng Regen Med **7**(8): 631-641.
- Tayalia, P., C. R. Mendonca, et al. (2008). "3D Cell-Migration Studies using Two-Photon Engineered Polymer Scaffolds." Advanced Materials **20**(23): 4494-4498.
- Taylor, P. A., P. Batten, et al. (2003). "The cardiac valve interstitial cell." International Journal of Biochemistry & Cell Biology **35**: 113-118.
- Taylor, P. M., S. P. Allen, et al. (2000). "Phenotypic and functional characterization of interstitial cells from human heart valves, pericardium and skin." Journal of Heart Valve Disease **9**: 150-158.
- Tedder, M. E., J. Liao, et al. (2009). "Stabilized collagen scaffolds for heart valve tissue engineering." Tissue Eng Part A **15**(6): 1257-1268.
- Tedder, M. E., A. Simionescu, et al. (2010). "Assembly and Testing of Stem Cell-Seeded Layered Collagen Constructs for Heart Valve Tissue Engineering." Tissue Eng Part A.
- Teh, B. M., R. J. Marano, et al. (2013). "Tissue engineering of the tympanic membrane." Tissue Engineering Part B-Reviews **19**: 116-132.
- Thubrikar, M., L. P. Boshier, et al. (1979). "The mechanism of opening of the aortic valve." J Thorac Cardiovasc Surg **77**(6): 863-870.
- Thubrikar, M., S. P. Nolan, et al. (1980). "The cyclic changes and structure of the base of the aortic valve." Am Heart J **99**(2): 217-224.
- Tibbitt, M. W. and K. S. Anseth (2012). "Dynamic microenvironments: The fourth dimension " Science Translational Medicine **4**: 160ps124.
- Tirella, A., F. Vozzi, et al. (2011). "PAM2 (piston assisted microsyringe): a new rapid prototyping technique for biofabrication of cell incorporated scaffolds." Tissue Eng Part C Methods **17**(2): 229-237.
- Torgersen, J., A. Ovsianikov, et al. (2012). "Photo-sensitive hydrogels for three-dimensional laser microfabrication in the presence of whole organisms." Journal of Biomedical Optics **17**: 105008.
- van Geemen, D., A. Driessen-Mol, et al. (2012). "Variation in tissue outcome of ovine and human engineered heart valve constructs: relevance for tissue engineering." Regen Med **7**(1): 59-70.
- Veinot, J. P. (2006). "Pathology of inflammatory native valvular heart disease." Cardiovasc Pathol **15**(5): 243-251.
- Verter, F. (Copyright 2000 - 2010 December 7, 2010). "Parent's Guide to Cord Blood Foundation - With Emphasis on how to Evaluate Bank Services." from <http://parentsguidecordblood.org/content/usa/banklists/index.shtml?navid=14>.
- Vesely, I. (2000). "Aortic root dilation prior to valve opening explained by passive hemodynamics." J Heart Valve Dis **9**(1): 16-20.
- Vricella, L. A., J. A. Williams, et al. (2005). "Early experience with valve-sparing aortic root replacement in children." Ann Thorac Surg **80**(5): 1622-1626; discussion 1626-1627.
- Wang, C., S. Yin, et al. (2010). "Differentiation of adipose-derived stem cells into contractile smooth muscle cells induced by transforming growth factor-beta1 and bone morphogenetic protein-4." Tissue Eng Part A **16**(4): 1201-1213.
- Wang, Q., A. J. McGoron, et al. (2010). "A novel small animal model for biocompatibility assessment of polymeric materials for use in prosthetic heart valves." J Biomed Mater Res A **93**(2): 442-453.

- Wang, X., B. Su, et al. (2009). "Impaired balance of mitochondrial fission and fusion in Alzheimer's disease." J Neurosci **29**(28): 9090-9103.
- Wang, X. H., Y. N. Yan, et al. (2006). "Generation of three-dimensional hepatocyte/gelatin structures with rapid prototyping system." Tissue Engineering **12**: 83-90.
- Wang, X. H., Y. N. Yan, et al. (2007). "Rapid prototyping as a tool for manufacturing bioartificial livers." Trends in Biotechnology **25**: 505-513.
- Wathen, C. A., N. Foje, et al. (2013). "*In vivo* X-ray computed tomographic imaging of soft tissue with native, intravenous, or oral contrast." Sensors (Basel) **13**(6): 6957-6980.
- Weber, B., M. Y. Emmert, et al. (2012). "Prenatally engineered autologous amniotic fluid stem cell-based heart valves in the fetal circulation." Biomaterials **33**: 4031-4043.
- Weber, B., S. M. Zeisberger, et al. (2011). "Prenatally harvested cells for cardiovascular tissue engineering: Fabrication of autologous implants prior to birth." Placenta **32**: S316-S319.
- Weidemann, F., B. Eyskens, et al. (2002). "Quantification of regional left and right ventricular radial and longitudinal function in healthy children using ultrasound-based strain rate and strain imaging." J Am Soc Echocardiogr **15**(1): 20-28.
- Williams, C. G., A. N. Malik, et al. (2005). "Variable cytocompatibility of six cell lines with photoinitiators used for polymerizing hydrogels and cell encapsulation." Biomaterials **26**(11): 1211-1218.
- Wilson, C. E., C. A. van Blitterswijk, et al. (2011). "Scaffolds with a standardized macro-architecture fabricated from several calcium phosphate ceramics using an indirect rapid prototyping technique " Journal of Materials Science-Materials in Medicine **22**: 97-105.
- Wust, S., M. E. Godla, et al. (2014). "Tunable hydrogel composite with two-step processing in combination with innovative hardware upgrade for cell-based three-dimensional bioprinting." Acta Biomater **10**(2): 630-640.
- Wylie, R. G., S. Ahsan, et al. (2011). "Spatially controlled simultaneous patterning of multiple growth factors in three-dimensional hydrogels." Nature Materials **10**: 799-806.
- Xu, C., W. Chai, et al. (2012). "Scaffold-free inkjet printing of three-dimensional zigzag cellular tubes." Biotechnology and Bioengineering: n/a-n/a.
- Xu, C. X., W. X. Chai, et al. (2012). "Scaffold-free inkjet printing of three-dimensional zigzag cellular tubes." Biotechnology and Bioengineering **109**: 3152-3160.
- Xu, T., C. A. Gregory, et al. (2006). "Viability and electrophysiology of neural cell structures generated by the inkjet printing method." Biomaterials **27**: 3580-3588.
- Xue, J. X., B. Feng, et al. (2013). "Engineering ear-shaped cartilage using electrospun fibrous membranes of gelatin/polycaprolactone." Biomaterials **34**: 2624-2631.
- Yacoub, M. H. and J. J. Takkenberg (2005). "Will heart valve tissue engineering change the world?" Nat Clin Pract Cardiovasc Med **2**(2): 60-61.
- Yamanami, M., Y. Yahata, et al. "Preparation of in-vivo tissue-engineered valved conduit with the sinus of Valsalva (type IV biovalve)." J Artif Organs **13**(2): 106-112.
- Yamanami, M., Y. Yahata, et al. (2010). "Preparation of in-vivo tissue-engineered valved conduit with the sinus of Valsalva (type IV biovalve)." J Artif Organs **13**(2): 106-112.
- Ye, X., Q. Zhao, et al. (2009). "Enhancement of mesenchymal stem cell attachment to decellularized porcine aortic valve scaffold by *in vitro* coating with antibody against CD90: a preliminary study on antibody-modified tissue-engineered heart valve." Tissue Eng Part A **15**(1): 1-11.
- Yeong, W. Y., C. K. Chua, et al. (2004). "Rapid prototyping in tissue engineering: challenges and potential " Trends in Biotechnology **22**: 643-652.

- Yusuf, S., S. Reddy, et al. (2001). "Global burden of cardiovascular diseases - Part I: General considerations, the epidemiologic transition, risk factors, and impact of urbanization." Circulation **104**: 2746-2753.
- Yusuf, S., M. Vaz, et al. (2004). "Tackling the challenge of cardiovascular disease burden in developing countries." Am Heart J **148**(1): 1-4.
- Zeltinger, J., L. K. Landeen, et al. (2001). "Development and characterization of tissue-engineered aortic valves." Tissue Engineering **7**: 9-22.
- Zhang, H., L. Wang, et al. (2011). "Controllable properties and microstructure of hydrogels based on crosslinked poly(ethylene glycol) diacrylates with different molecular weights." Journal of Applied Polymer Science **121**(1): 531-540.
- Zhang, T., Y. N. Yan, et al. (2007). "Three-dimensional gelatin and gelatin/hyaluronan hydrogel structures for traumatic brain injury." Journal of Bioactive and Compatible Polymers **22**: 19-29.
- Zhang, Z., D. Jones, et al. (2013). "Hierarchical tailoring of strut architecture to control permeability of additive manufactured titanium implants." Mater Sci Eng C Mater Biol Appl **33**(7): 4055-4062.
- Zilla, P., J. Brink, et al. (2008). "Prosthetic heart valves: catering for the few." Biomaterials **29**(4): 385-406.
- Zimmermann, W. H., K. Schneiderbanger, et al. (2002). "Tissue engineering of a differentiated cardiac muscle construct." Circulation Research **90**: 223-230.

## CHAPTER 8

### CONCLUSIONS AND FUTURE DIRECTIONS

#### ***8.1 One Step Closer to a Viable TEHV***

Heart valve disease is a tremendous national and global burden. Worldwide 80% of all cardiovascular disease cases occur in developing countries (Yusuf, Vaz et al. 2004), causing more than 19% of deaths, and causing more deaths than war and malaria combined (Ribeiro, Jacobsen et al. 2008). In Western countries the population primarily suffers from aging related degenerative valve disease, but the vast majority of aortic valve disease patients in the developing world are children and young adults (Cohen, Malone et al. 2006; Zilla, Brink et al. 2008). Additionally, valve related congenital heart defects in the US and worldwide are a serious clinical burden affecting 1/100 live births. Prosthetic replacement is essentially the only treatment for a critically damaged or malformed valve, and current aortic valve replacement options for pediatric patients are grimly inadequate. Nearly 20% of children with prosthetic valves die within 10 years of aortic valve replacement and an additional 40% require repeat surgical operations (Alsoufi, Al-Halees et al. 2009) (Karamlou, Jang et al. 2005; Vricella, Williams et al. 2005). Tissue engineering has the potential to generate living heart valve replacements capable of growth and integration critically needed to treat children with valve disease.

Over the last 15 years, researchers have developed and implemented novel synthetic polymers as scaffolds for engineered heart valves. Although much progress has been made, a persistent problem is the difficulty incorporating native-like heterogeneity and controlled remodeling into TEHV. I hope this work using a 3D printing approach that has the capacity to generate complex 3D geometries with extrudable materials and

encapsulated cells will help move the field of TEHV forward towards fully functional and clinically applicable tissue engineered heart valves. The fabrication strategy in this work demonstrates tools to incorporate heterogeneity directly into engineered tissues and suggests a means to evaluate subsequent remodeling through dynamic conditioning and ultrasound,  $\mu$ CT and MRI evaluation of the tissue.

### ***8.2 Need for Predictive Swelling, Growth, and Remodeling Models to Guide 3D Printing of Complex Geometries***

In Chapter 3, we demonstrated that 3D printing and photo-crosslinking hydrogels can be used to rapidly fabricate anatomical scaffolds on a tissue implant scale exhibiting mechanical heterogeneity and cytocompatibility. We used  $\mu$ CT to evaluate adult and pediatric sized valve constructs and find that the photo-crosslinking approach enables a high degree of geometric control and the hydrogel material swelling does affect scaffold fidelity. In this study and in two other subsequent studies from our group, the valve geometries printed were interlocking STL type files where heterogeneity existed between the two parts (the root and the leaflet) but within these parts the material was homogeneous (Hockaday, Kang et al. 2012; Duan, Hockaday et al. 2013; Duan, Kapetanovic et al. 2014). In Chapter 5 we described the generation of complex heterogeneous valve structures with full control of the interior material distribution based on native heterogeneity. We observed in Chapter 5 that hydrogel swelling had to be compensated for when assessing fidelity of heterogeneous patterns within printed geometries. Chapter 4 mechanical testing showed that for a polymer precursor mixture with a fixed amount of polymer weight to volume ratio that a variation in the photoinitiator type, concentration, and light source could more than double the weight based swelling ratio.

Future work should involve modeling geometric compensation for swelling and 3D evaluation of heterogeneous material effect on 3D shape and internal structure. There are a growing number of people using the Fab@Home™ 3D printing platform for extrusion printing of hydrogels. Materials that have been demonstrated with the platform for direct cell encapsulation and printing are methcrylated gelatin/methcrylated hyaluronic acid (Duan, Kapetanovic et al. 2014), four-armed PEG/hyaluronic acid/gelatin derivatives (Skardal, Zhang et al. 2010; Skardal, Zhang et al. 2010), alginate (Mannoor, Jiang et al. 2013), gelatin/alginate (Duan, Hockaday et al. 2013), and hydroxyapatite loaded gelatin/alginate (Wust, Godla et al. 2014).

As more materials are investigated and their handling properties are evaluated, the applicability of 3D printing to tissue engineering broadens. Each of these materials have different swelling and mechanical properties. With the stated goal of engineering heterogeneity into living tissues – there is going to be an almost inherent material mismatch. In other words engineering mechanical or encapsulating material type heterogeneity directly into printed scaffolds will by design mean that the scaffold will have anisotropic response to a number of possible conditions. These conditions could include surrounding media and mechanical loading. Additionally hydrogel mechanical properties change with remodeling and degradation. Depending on the hydrogel type, mechanisms and rate of degradation, populating cell activity and function (such as contractility), this can manifest itself in expansion swelling (Anseth, Metters et al. 2002) or tissue contraction (Flanagan, Sachweh et al. 2009). Computational modeling has been used to develop a growth and remodeling model for embryonic valve cushion response to blood flow induced loading of the tissue (Buskohl, Jenkins et al. 2012). Possible future work to better inform 3D printing strategies could include a swelling and shape deformation model, a heterogeneous material mechanics finite element analysis model, and a growth model for hydrogel TEHV.

Additional studies could be done with the line printing to incorporate bead tracking combined with cell tracking. This could be used to differentiate between the effects of cell migration from the effects of gel viscosity and mixing and the effects of construct swelling. Fluorescent beads or microspheres for tracer studies are commercially available. FluoSpheres<sup>®</sup> are manufactured at different sizes, with cell culture compatibility, and are relatively immune to photobleaching (Johnson 2010). The bead size used would be larger than what cells will ingest/phagocytose. Cells and beads would be suspended in each precursor solution and the patterns printed into a heterogeneous layer. The layers would be imaged immediately after photocrosslinking and 1 hour incubation in culture media to establish a baseline cell and bead distribution and pattern fidelity. The scaffolds would be imaged after 24 hours in culture and over several days. The beads and the cells will shift based on changes in the polymer scaffold structure. If the cells remodel the matrix or if the matrix degrades causing changes in the hydrogel swelling that should be reflected by a shift in the bead and cell distribution throughout the hydrogel structure. Cell migration could be indicated by a shift in distribution throughout the hydrogel structure different from the bead distribution.

### ***8.3 Additional Studies to Identify Mechanism of Cell Type Specific Response to Photoencapsulation and Characterizing Material Sinking of Initiator Radicals***

In the Chapter 3 study, the scaffolds were seeded with cells from the outside and in general the overall infiltration and integration of cells within the printed material was poor, certainly orders of magnitude less than actual tissue. The other critical feature of this type of seeding strategy is there is no control in terms of cell placement throughout the hydrogel. In subsequent studies (Chapter 4, 5, and 7 and our other associated studies (Duan, Hockaday et al. 2013; Duan, Kapetanovic et al. 2014)) direct cell printing was investigated. Direct cell printing enabled control of cell distribution within patterned layers, with high fidelity to the user specified geometry (>80%

accuracy). The encapsulated viability of 3D printed cells in photocrosslinked hydrogels was tested for more than one cell type relevant to tissue engineering heart valves. In Chapter 4, ranges of cell viability for two primary valve cell types and a mesenchymal stem cell type were determined in response to photo-crosslinking variables of light intensity, photoinitiator type, and photoinitiator concentration. Contrary to numerous 2D cytotoxicity studies, the findings presented in this chapter indicate that in a MEGEL:PEGDA3350 hydrogel culture environment and 3D fabrication setting, Irgacure 2959 can produce more viable encapsulated cells than VA086 in a higher stiffness hydrogel.

Intracellular oxidative stress was not significantly greater in hydrogel conditions of more Irgacure 2959 photoinitiator radicals. Normalized oxidative stress ratios suggest that increasing VA086 radicals induced higher intracellular oxidative stress. Our findings also demonstrate that suppression of intracellular oxidative stress using catalase pretreatment does not disrupt hydrogel crosslinking, but it does not rescue cell viability from photoinitiator damage. Two recommended future studies following this work presented in this thesis are to 1) test for lipid peroxidation and then pursue membrane targeted rescue strategies and 2) identify hydrogel material specific differences in ability to capture photoinitiator radicals. Photoinitiator radical induced damage is most likely occurring at the outside membrane of cells, and identification for the type of damage could lead to damage mitigating strategies. From the comparison of the results presented in Chapter 4 to outside studies, we suspect that different hydrogel materials may have different characteristic abilities to act as a sinks for photoinitiator radicals in 3D photoencapsulation conditions. Under similar photoinitiator concentrations different investigators have seen dramatically different results in viability based on the 3D material being used to encapsulate the cells.

#### ***8.4 Evaluating the Biological Consequences of Complex Heterogeneity in a Hemodynamic Environment***

In Chapter 5, a Region Dither Vector (RDV) algorithm that separates intrinsic tissue heterogeneity present in medical imaging scans of anatomical tissue into printable format files is demonstrated by 3D printing heterogeneous hydrogel scaffolds. We also presented a method to quantify the fidelity of heterogeneous layers, and to quantify the degree of cell mixing and blending of different materials within the layer. The biological consequence of this 3D printed complex heterogeneity in bioprinted valves was not evaluated in this work.

A dynamic conditioning system specifically for the culture of 3D bioprinted heart valves was developed for this purpose. The reactor is capable of fetal-like high frequency. The bioreactor system was validated in Chapter 7 using simplified geometry 3D bioprinted heart valves composed of methacrylated gelatin, methacrylated hyaluronic acid, and PEGDA. The valves were cultured up to 14 days under static and dynamic conditions. Evaluating the function and remodeling of a complex medical imaging derived heterogeneous bioprinted heart valve in a dynamic culture environment would be the culmination of all the work presented here. The bioreactor conditioning system has optical and acoustic windows for imaging hydrogel valve development and remodeling with light microscopy and ultrasound. Whole valve function under different bioreactor loading regimes would be assessed first at different days of culture, and then conditioned valves would be assessed for viability, GAG content, collagen content, immunohistochemistry, and gene expression. Ultimately, control of cells within their microenvironment is the purpose of utilizing the 3D printing technology in a TEHV application, and much more work needs to be done for full understanding of the biological effects of fabrication input and output parameters.

### ***8.5 Proposed MRI Study to Evaluate Engineered Valve Heterogeneity Compared to Native***

In Chapter 5, the RDV algorithm presented in this study was used to extract tissue heterogeneity and anatomic shape information from  $\mu$ CT and MRI images and convert those intensity values into a printable format for the scanned 3D tissue geometry. However, further study needs to be done to correlate those intensity values with biological distributions with the tissue. Towards the goal of investigating the consequence of native-tissue-derived complex shape and internal material distribution on TEHV remodeling, a pilot study proposal has been accepted by the Cornell Magnetic Resonance Imaging Facility (CMRIF). The goal is to use MRI to characterize native and engineered heart valve tissue heterogeneity. MRI may be a better choice to assess heterogeneous pattern maintenance and remodeling. Studies have demonstrated that MR can be used to detect remodeling and differentiation in engineered tissues and to detect differences in modulus between different hydrogels (Feng, Taraban et al. 2011; Curtis, Zhang et al. 2012; Kotecha, Klatt et al. 2013). MR spectroscopy, imaging, and elastography could be used to analyze 3D printed hydrogel tissue remodeling and pattern maintenance in the entire structure. In the pilot study, MRI scans will be used to determine if heterogeneities can be revealed in native valve tissue, if engineered hydrogel tissues can be distinguished from each other, and to study 3D printed valve remodeling.

### ***8.6 Conclusion***

If subsequent studies build upon the work presented here, these results bring a 3D printed hydrogel TEHV strategy one step closer to a living replacement for the treatment of pediatric valve disease. This work demonstrates a 3D printing approach that generates complex 3D geometry tissue constructs using extrudable materials and encapsulated cells based on native valve tissue heterogeneity. As a fabrication strategy

3D printing overcomes the limitations associated with classical heart valve tissue engineering. The viability experiments and bioreactor validation studies presented in this work provide a range of fabrication and conditioning parameters that can be utilized for the fabrication and dynamic culture of 3D bioprinted heart valves. Our studies indicate that the bioprinted valves can be produced with high viability HADMSC (human adipose derived mesenchymal stem cell) for the purposes of a TEHV or with HAVIC and HASSMC for the purpose of *in vitro* testing and study.

## REFERENCES

- Abramov, A. Y., A. Scorziello, et al. (2007). "Three distinct mechanisms generate oxygen free radicals in neurons and contribute to cell death during anoxia and reoxygenation." J Neurosci **27**(5): 1129-1138.
- Administration, F. a. D. (October 2004). Report to Congress: Barriers to the Availability of Medical Devices Intended for the Treatment or Diagnosis of Diseases and Conditions that Affect Children. U. S. D. o. H. a. H. Services.
- Ahmann, K. A., J. S. Weinbaum, et al. "Fibrin degradation enhances vascular smooth muscle cell proliferation and matrix deposition in fibrin-based tissue constructs fabricated in vitro." Tissue Eng Part A **16**(10): 3261-3270.
- Ahn, S., H. Lee, et al. (2014). "A direct cell printing supplemented with low-temperature processing method for obtaining highly porous three-dimensional cell-laden scaffolds." Journal of Materials Chemistry B **2**(18): 2773-2782.
- Aikawa, E., P. Whittaker, et al. (2006). "Human semilunar cardiac valve remodeling by activated cells from fetus to adult - Implications for postnatal adaptation, pathology, and tissue engineering." Circulation **113**: 1344-1352.
- Aikawa, E., P. Whittaker, et al. (2006). "Human semilunar cardiac valve remodeling by activated cells from fetus to adult: implications for postnatal adaptation, pathology, and tissue engineering." Circulation **113**(10): 1344-1352.
- Alsoufi, B., Z. Al-Halees, et al. (2009). "Mechanical valves versus the Ross procedure for aortic valve replacement in children: propensity-adjusted comparison of long-term outcomes." J Thorac Cardiovasc Surg **137**(2): 362-370 e369.
- Anseth, K. S., A. T. Metters, et al. (2002). "In situ forming degradable networks and their application in tissue engineering and drug delivery." Journal of Controlled Release **78**(1-3): 199-209.
- Arcaute, K., B. K. Mann, et al. (2006). "Stereolithography of three-dimensional bioactive poly(ethylene glycol) constructs with encapsulated cells." Ann Biomed Eng **34**(9): 1429-1441.
- Atsumi, T., J. Murata, et al. (1998). "Cytotoxicity of photosensitizers camphorquinone and 9-fluorenone with visible light irradiation on a human submandibular-duct cell line in vitro." Arch Oral Biol **43**(1): 73-81.
- Awad, H. A., D. L. Butler, et al. (2000). "In vitro characterization of mesenchymal stem cell-seeded collagen scaffolds for tendon repair: effects of initial seeding density on contraction kinetics." J Biomed Mater Res **51**(2): 233-240.
- Azadani, A. N., S. Chitsaz, et al. (2012). "Biomechanical comparison of human pulmonary and aortic roots." Eur J Cardiothorac Surg.
- Azagarsamy, M. A., D. L. Alge, et al. (2012). "Photocontrolled nanoparticles for on-demand release of proteins." Biomacromolecules **13**: 2219-2224.
- Baier Leach, J., K. A. Bivens, et al. (2003). "Photocrosslinked hyaluronic acid hydrogels: Natural, biodegradable tissue engineering scaffolds." Biotechnology and Bioengineering **82**(5): 578-589.
- Baker, B. M. and C. S. Chen (2012). "Deconstructing the third dimension - how 3D culture microenvironments alter cellular cues." Journal of Cell Science **125**: 3015-3024.
- Balachandran, K., P. Sucusky, et al. (2009). "Elevated cyclic stretch alters matrix remodeling in aortic valve cusps: implications for degenerative aortic valve disease." American Journal of Physiology-Heart and Circulatory Physiology **296**: H756-H764.
- Balasubramanian, K., E. M. Bevers, et al. (2001). "Binding of annexin V to membrane products of lipid peroxidation." Biochemistry **40**(30): 8672-8676.

- Balguid, A., A. Mol, et al. (2009). "Hypoxia induces near-native mechanical properties in engineered heart valve tissue." Circulation **119**(2): 290-297.
- Ballyns, J. J. and L. J. Bonassar (2009). "Image-guided tissue engineering." J Cell Mol Med **13**(8A): 1428-1436.
- Ballyns, J. J. and L. J. Bonassar (2011). "Dynamic compressive loading of image-guided tissue engineered meniscal constructs." Journal of Biomechanics **44**: 509-516.
- Ballyns, J. J., D. L. Cohen, et al. (2010). "An optical method for evaluation of geometric fidelity for anatomically shaped tissue-engineered constructs." Tissue Eng Part C **16**(4): 693-703.
- Ballyns, J. J., D. L. Cohen, et al. (2010). "An optical method for evaluation of geometric fidelity for anatomically shaped tissue-engineered constructs." Tissue Engineering Part C-Method **16**: 693-703.
- Ballyns, J. J., D. L. Cohen, et al. (2010). "An optical method for evaluation of geometric fidelity for anatomically shaped tissue-engineered constructs." Tissue Eng Part C Methods **16**(4): 693-703.
- Ballyns, J. J., J. P. Gleghorn, et al. (2008). "Image-guided tissue engineering of anatomically shaped implants via MRI and micro-CT using injection molding." Tissue Engineering Part A **14**: 1195-1202.
- Ballyns, J. J., J. P. Gleghorn, et al. (2008). "Image-guided tissue engineering of anatomically shaped implants via MRI and micro-CT using injection molding." Tissue Eng Part A **14**(7): 1195-1202.
- Barzilla, J. E., F. E. Acevedo, et al. (2010). "Organ culture as a tool to identify early mechanisms of serotonergic valve disease." Journal of Heart Valve Disease **19**: 626-635.
- Barzilla, J. E., A. S. McKenney, et al. (2010). "Design and validation of a novel splashing bioreactor system for use in mitral valve organ culture." Annals of Biomedical Engineering **38**: 3280-3294.
- Bellhouse, B. J., F. H. Bellhouse, et al. (1968). "Fluid mechanics of the aortic root with application to coronary flow." Nature **219**(5158): 1059-1061.
- Bellis, A. D., B. P. Bernabe, et al. (2013). "Dynamic transcription factor activity profiling in 2D and 3D cell cultures." Biotechnology and Bioengineering **110**: 563-572.
- Benton, J. A., C. A. DeForest, et al. (2009). "Photocrosslinking of gelatin macromers to synthesize porous hydrogels that promote valvular interstitial cell function." Tissue Eng Part A **15**(11): 3221-3230.
- Benton, J. A., B. D. Fairbanks, et al. (2009). "Characterization of valvular interstitial cell function in three dimensional matrix metalloproteinase degradable PEG hydrogels." Biomaterials **30**(34): 6593-6603.
- Benton, J. A., H. B. Kern, et al. (2009). "Statins block calcific nodule formation of valvular interstitial cells by inhibiting alpha-smooth muscle actin expression." Arterioscler Thromb Vasc Biol **29**(11): 1950-1957.
- Benton, J. A., H. B. Kern, et al. (2009). "Statins block calcific nodule formation of valvular interstitial cells by inhibiting alpha-smooth muscle actin expression." Arteriosclerosis Thrombosis and Vascular Biology **29**: 1950-1957.
- Berry, J. L., J. A. Steen, et al. (2010). "Bioreactors for development of tissue engineered heart valves." Annals of Biomedical Engineering **38**: 3272-3279.
- Bianchi, F., M. Rosi, et al. (2007). "Microfabrication of fractal polymeric structures for capillary morphogenesis: applications in therapeutic angiogenesis and in the engineering of vascularized tissue." J Biomed Mater Res B Appl Biomater **81**(2): 462-468.
- Billiar, K. L. and M. S. Sacks (2000). "Biaxial mechanical properties of the native and glutaraldehyde-treated aortic valve cusp: Part II--A structural constitutive model." J Biomech Eng **122**(4): 327-335.

- Billiet, T., M. Vandenhaute, et al. (2012). "A review of trends and limitations in hydrogel-rapid prototyping for tissue engineering." Biomaterials **33**: 6020-6041.
- Bilski, P., A. G. Belanger, et al. (2002). "Photosensitized oxidation of 2',7'-dichlorofluorescein: singlet oxygen does not contribute to the formation of fluorescent oxidation product 2',7'-dichlorofluorescein." Free Radic Biol Med **33**(7): 938-946.
- Black, A. F., V. Hudon, et al. (1999). "A novel approach for studying angiogenesis: A human skin equivalent with a capillary-like network." Cell Biology and Toxicology **15**: 81-90.
- Blais, M., R. Parenteau-Bareil, et al. (2013). "Concise review: tissue-engineered skin and nerve regeneration in burn treatment." Stem Cells Transl Med **2**(7): 545-551.
- Boettcher-Haberzeth, S., T. Biedermann, et al. (2010). "Tissue engineering of skin." Burns **36**: 450-460.
- Bottio, T., V. Tarzia, et al. "The changing hydrodynamic performance of the decellularized intact porcine aortic root: considerations on in-vitro testing." J Heart Valve Dis **19**(4): 485-491.
- Bowles, R. D., R. M. Williams, et al. (2010). "Self-assembly of aligned tissue-engineered annulus fibrosus and intervertebral disc composite via collagen gel contraction." Tissue Eng Part A **16**(4): 1339-1348.
- Brewer, R. J., R. M. Mentzer, et al. (1977). "In vivo study of the dimensional changes of the aortic valve leaflets during the cardiac cycle." Journal OF Thoracic and Cardiovascular Surgery **74**: 645-650.
- Brigham, M. D., A. Bick, et al. (2009). "Mechanically robust and bioadhesive collagen and photocrosslinkable hyaluronic acid semi-interpenetrating networks." Tissue Engineering Part A **15**: 1645-1653.
- Browning, M. B. and E. Cosgriff-Hernandez (2012). "Development of a biostable replacement for PEGDA hydrogels." Biomacromolecules **13**(3): 779-786.
- Browning, M. B., T. Wilems, et al. (2011). "Compositional control of poly(ethylene glycol) hydrogel modulus independent of mesh size." J Biomed Mater Res A **98**(2): 268-273.
- Bryant, S. J. and K. S. Anseth (2002). "Hydrogel properties influence ECM production by chondrocytes photoencapsulated in poly(ethylene glycol) hydrogels." J Biomed Mater Res **59**(1): 63-72.
- Bryant, S. J., C. R. Nuttelman, et al. (2000). "Cytocompatibility of UV and visible light photoinitiating systems on cultured NIH/3T3 fibroblasts in vitro." J Biomater Sci Polym Ed **11**(5): 439-457.
- Bunnell, B. A., M. Flaas, et al. (2008). "Adipose-derived stem cells: isolation, expansion and differentiation." Methods **45**(2): 115-120.
- Burdick, J. A. and K. S. Anseth (2002). "Photoencapsulation of osteoblasts in injectable RGD-modified PEG hydrogels for bone tissue engineering." Biomaterials **23**(22): 4315-4323.
- Buskohl, P. R., J. T. Jenkins, et al. (2012). "Computational simulation of hemodynamic-driven growth and remodeling of embryonic atrioventricular valves." Biomech Model Mechanobiol **11**(8): 1205-1217.
- Butcher, J. T., G. J. Mahler, et al. (2011). "Aortic valve disease and treatment: The need for naturally engineered solutions." Advanced Drug Delivery Reviews **63**: 242-268.
- Butcher, J. T., G. J. Mahler, et al. (2011). "Aortic valve disease and treatment: the need for naturally engineered solutions." Adv Drug Deliv Rev **63**(4-5): 242-268.
- Butcher, J. T. and R. M. Nerem (2004). "Porcine aortic valve interstitial cells in three-dimensional culture: comparison of phenotype with aortic smooth muscle cells." J Heart Valve Dis **13**(3): 478-485; discussion 485-476.

- Butcher, J. T. and R. M. Nerem (2006). "Valvular endothelial cells regulate the phenotype of interstitial cells in co-culture: Effects of steady shear stress." Tissue Engineering **12**: 905-915.
- Butcher, J. T. and R. M. Nerem (2006). "Valvular endothelial cells regulate the phenotype of interstitial cells in co-culture: effects of steady shear stress." Tissue Eng **12**(4): 905-915.
- Butcher, J. T., A. M. Penrod, et al. (2004). "Unique morphology and focal adhesion development of valvular endothelial cells in static and fluid flow environments." Arteriosclerosis Thrombosis and Vascular Biology **24**: 1429-1434.
- Butcher, J. T., A. M. Penrod, et al. (2004). "Unique morphology and focal adhesion development of valvular endothelial cells in static and fluid flow environments." Arterioscler Thromb Vasc Biol **24**(8): 1429-1434.
- Butcher, J. T., C. A. Simmons, et al. (2008). "Mechanobiology of the aortic heart valve." J Heart Valve Dis **17**(1): 62-73.
- Butcher, J. T., C. A. Simmons, et al. (2008). "Review - Mechanobiology of the aortic heart valve." Journal of Heart Valve Disease **17**: 62-73.
- Butscher, A., M. Bohner, et al. (2011). "Structural and material approaches to bone tissue engineering in powder-based three-dimensional printing." Acta Biomaterialia **7**: 907-920.
- Cai, H., G. Azangwe, et al. (2005). "Skin cell culture on an ear-shaped scaffold created by fused deposition modelling." Bio-medical Materials and Engineering **15**: 375-380.
- Cameron, D. E. and L. A. Vricella (2007). "What is the proper place of the Ross procedure in our modern armamentarium?" Curr Cardiol Rep **9**(2): 93-98.
- Carabello, B. A. and W. J. Paulus (2009). "Aortic stenosis." Lancet **373**(9667): 956-966.
- Carapetis, J. R. (2008). "Rheumatic heart disease in Asia." Circulation **118**(25): 2748-2753.
- Carapetis, J. R., A. C. Steer, et al. (2005). "The global burden of group A streptococcal diseases." Lancet Infect Dis **5**(11): 685-694.
- Carmichael, J., W. G. DeGraff, et al. (1987). "Evaluation of a tetrazolium-based semiautomated colorimetric assay: assessment of chemosensitivity testing." Cancer Res **47**(4): 936-942.
- Chan, V., P. Zorlutuna, et al. (2010). "Three-dimensional photopatterning of hydrogels using stereolithography for long-term cell encapsulation." Lab Chip **10**(16): 2062-2070.
- Chanda, J., R. Kuribayashi, et al. (1997). "Valved conduit in the descending thoracic aorta in juvenile sheep: a useful, cost-effective model for accelerated calcification study in systemic circulation." Biomaterials **18**(19): 1317-1321.
- Chandler, E. M., C. M. Berglund, et al. (2011). "Stiffness of photocrosslinked RGD-alginate gels regulates adipose progenitor cell behavior." Biotechnol Bioeng **108**(7): 1683-1692.
- Chang, C. C., E. D. Boland, et al. (2011). "Direct-write bioprinting three-dimensional biohybrid systems for future regenerative therapies." Journal of Biomedical Materials Research Part B-Applied Biomaterials **98B**: 160-170.
- Cheng, A., P. Dagum, et al. (2007). "Aortic root dynamics and surgery: from craft to science." Philos Trans R Soc Lond B Biol Sci **362**(1484): 1407-1419.
- Chitcholtan, K., E. Asselin, et al. (2013). "Differences in growth properties of endometrial cancer in three dimensional (3D) culture and 2D cell monolayer." Experimental Cell Research **319**: 75-87.
- Christie, G. W. (1992). "Anatomy of aortic heart valve leaflets: the influence of glutaraldehyde fixation on function." Eur J Cardiothorac Surg **6 Suppl 1**: S25-32; discussion S33.

- Christie, G. W. and B. G. Barratt-Boyes (1995). "Mechanical properties of porcine pulmonary valve leaflets: how do they differ from aortic leaflets?" Ann Thorac Surg **60**(2 Suppl): S195-199.
- Chue, W. L., G. R. Campbell, et al. (2004). "Dog peritoneal and pleural cavities as bioreactors to grow autologous vascular grafts." J Vasc Surg **39**(4): 859-867.
- Ciorba, A. and A. Martini (2006). "Tissue engineering and cartilage regeneration for auricular reconstruction." International Journal of Pediatric Otorhinolaryngology **70**: 1507-1515.
- Cipitria, A., C. Lange, et al. (2012). "Porous scaffold architecture guides tissue formation." J Bone Miner Res **27**(6): 1275-1288.
- Clark, E. B. (1996). "Pathogenetic mechanisms of congenital cardiovascular malformations revisited." Semin Perinatol **20**(6): 465-472.
- Cohen, D. L., W. Lo, et al. (2011). "Increased mixing improves hydrogel homogeneity and quality of three-dimensional printed constructs " Tissue Engineering Part C-Method **17**: 239-248.
- Cohen, D. L., E. Malone, et al. (2006). "Direct freeform fabrication of seeded hydrogels in arbitrary geometries." Tissue Eng **12**(5): 1325-1335.
- Cohen, D. L., E. Malone, et al. (2006). "Direct freeform fabrication of seeded hydrogels in arbitrary geometries." Tissue Engineering **12**: 1325-1335.
- Col, C., K. Dinler, et al. (2010). "Oxidative stress and lipid peroxidation products: effect of pinealectomy or exogenous melatonin injections on biomarkers of tissue damage during acute pancreatitis." Hepatobiliary Pancreat Dis Int **9**(1): 78-82.
- Colazzo, F., A. H. Chester, et al. (2010). "Induction of mesenchymal to endothelial transformation of adipose-derived stem cells." J Heart Valve Dis **19**(6): 736-744.
- Colazzo, F., A. H. Chester, et al. (2010). "Induction of mesenchymal to endothelial transformation of adipose-derived stem cells." Journal of Heart Valve Disease **19**: 736-744.
- Colazzo, F., P. Sarathchandra, et al. (2011). "Extracellular matrix production by adipose-derived stem cells: implications for heart valve tissue engineering." Biomaterials **32**(1): 119-127.
- Colazzo, F., P. Sarathchandra, et al. (2011). "Extracellular matrix production by adipose-derived stem cells: Implications for heart valve tissue engineering." Biomaterials **32**: 119-127.
- Colvee, E. and J. M. Hurlle (1983). "Malformations of the semilunar valves produced in chick embryos by mechanical interference with cardiogenesis. An experimental approach to the role of hemodynamics in valvular development." Anat Embryol (Berl) **168**(1): 59-71.
- Courtney, T., M. S. Sacks, et al. (2006). "Design and analysis of tissue engineering scaffolds that mimic soft tissue mechanical anisotropy." Biomaterials **27**(19): 3631-3638.
- Cruise, G. M., D. S. Scharp, et al. (1998). "Characterization of permeability and network structure of interfacially photopolymerized poly(ethylene glycol) diacrylate hydrogels." Biomaterials **19**(14): 1287-1294.
- Cui, X. and T. Boland (2009). "Human microvasculature fabrication using thermal inkjet printing technology." Biomaterials **30**(31): 6221-6227.
- Cui, X. F. and T. Boland (2009). "Human microvasculature fabrication using thermal inkjet printing technology." Biomaterials **30**: 6221-6227.
- Cui, X. F., K. Breitenkamp, et al. (2012). "Direct human cartilage repair using three-dimensional bioprinting technology." Tissue engineering Part A **18**: 1304-1312.
- Curtis, E. T., S. Zhang, et al. (2012). "Magnetic resonance elastography methodology for the evaluation of tissue engineered construct growth." J Vis Exp(60).
- D'Alessandro, D., S. Danti, et al. (2012). "Histologic characterization of human ear ossicles for the development of tissue-engineered replacements " Otology & Neurotology **33**: 1458-1468.

- D'Hooge, J., A. Heimdal, et al. (2000). "Regional strain and strain rate measurements by cardiac ultrasound: principles, implementation and limitations." Eur J Echocardiogr **1**(3): 154-170.
- Dagum, P., G. R. Green, et al. (1999). "Deformational dynamics of the aortic root: modes and physiologic determinants." Circulation **100**(19 Suppl): II54-62.
- Dagum, P., G. R. Green, et al. (1999). "Deformational dynamics of the aortic root - Modes and physiologic determinants." Circulation **100**: S54-62.
- Dajani, A. S. and K. A. Taubert (1992). "Re: Letter to the editor by Dr. Steven M. Pollack and author's response from Drs. Thomas J. Pallasch and Jorgen Slots. Committee on Rheumatic Fever, Endocarditis, and Kawasaki Disease of the American Heart Association." J Periodontol **63**(5): 488.
- Darnell, M. C., J. Y. Sun, et al. (2013). "Performance and biocompatibility of extremely tough alginate/polyacrylamide hydrogels." Biomaterials **34**(33): 8042-8048.
- Dasi, L. P., H. A. Simon, et al. (2009). "Fluid mechanics of artificial heart valves." Clin Exp Pharmacol Physiol **36**(2): 225-237.
- de Simone, G., R. B. Devereux, et al. (1997). "Stroke volume and cardiac output in normotensive children and adults. Assessment of relations with body size and impact of overweight." Circulation **95**(7): 1837-1843.
- Deck, J. D., M. J. Thubrikar, et al. (1988). "Structure, stress, and tissue-repair in aortic valve leaflets." Cardiovascular Research **22**: 7-16.
- Derby, B. (2012). "Printing and prototyping of tissues and scaffolds " Science **338**: 921-926.
- Devarajan, K., M. L. Forrest, et al. (2013). "Adenovector-mediated gene delivery to human umbilical cord mesenchymal stromal cells induces inner ear cell phenotype." Cellular Reprogramming **15**: 43-54.
- Dhariwala, B., E. Hunt, et al. (2004). "Rapid prototyping of tissue-engineering constructs, using photopolymerizable hydrogels and stereolithography." Tissue Eng **10**(9-10): 1316-1322.
- Dijkman, P. E., A. Driessen-Mol, et al. (2012). "Decellularized homologous tissue-engineered heart valves as off-the-shelf alternatives to xeno- and homografts." Biomaterials **33**(18): 4545-4554.
- Dohmen, P. M., A. Lembcke, et al. (2002). "Ross operation with a tissue-engineered heart valve." Ann Thorac Surg **74**(5): 1438-1442.
- Drolle, E., N. Kucerka, et al. (2013). "Effect of melatonin and cholesterol on the structure of DOPC and DPPC membranes." Biochim Biophys Acta **1828**(9): 2247-2254.
- Drummen, G. P., L. C. van Liebergen, et al. (2002). "C11-BODIPY(581/591), an oxidation-sensitive fluorescent lipid peroxidation probe: (micro)spectroscopic characterization and validation of methodology." Free Radic Biol Med **33**(4): 473-490.
- Duan, B., L. A. Hockaday, et al. (2013). "3D bioprinting of heterogeneous aortic valve conduits with alginate/gelatin hydrogels." J Biomed Mater Res A **101**(5): 1255-1264.
- Duan, B., L. A. Hockaday, et al. (2013). "3D bioprinting of heterogeneous aortic valve conduits with alginate/gelatin hydrogels." Journal of Biomedical Materials Research Part A **101A**: 1255-1264.
- Duan, B., L. A. Hockaday, et al. (2014). "Aortic Heart Valve Tissue Regeneration." Tissue and Organ Regeneration: Advances in Micro and Nanotechnology.
- Duan, B., L. A. Hockaday, et al. (2013). "Stiffness and adhesivity control aortic valve interstitial cell behavior within hyaluronic acid based hydrogels." Acta Biomaterialia: <http://dx.doi.org/10.1016/j.actbio.2013.1004.1050>.
- Duan, B., E. Kapetanovic, et al. (2014). "Three-dimensional printed trileaflet valve conduits using biological hydrogels and human valve interstitial cells." Acta Biomater **10**(5): 1836-1846.

- Duan, B., E. Kapetanovic, et al. (2014). "Three-dimensional printed trileaflet valve conduits using biological hydrogels and human valve interstitial cells." Acta Biomaterialia **10**(5): 1836-1846.
- Duan, B., M. Wang, et al. (2010). "Three-dimensional nanocomposite scaffolds fabricated via selective laser sintering for bone tissue engineering." Acta Biomater **6**(12): 4495-4505.
- Dumont, K., J. Yperman, et al. (2002). "Design of a new pulsatile bioreactor for tissue engineered aortic heart valve formation." Artificial Organs **26**: 710-714.
- Durst, C. A., M. P. Cuchiara, et al. (2011). "Flexural characterization of cell encapsulated PEGDA hydrogels with applications for tissue engineered heart valves." Acta Biomater **7**(6): 2467-2476.
- Durst, C. A. and K. J. Grande-Allen (2010). "Design and physical characterization of a synchronous multivalve aortic valve culture system." Annals of Biomedical Engineering **38**: 319-325.
- Eckert, C. E., B. T. Mikulis, et al. (2011). "Three-dimensional quantitative micromorphology of pre- and post-implanted engineered heart valve tissues." Ann Biomed Eng **39**(1): 205-222.
- El-Hamamsy, I., Z. Eryigit, et al. (2010). "Long-term outcomes after autograft versus homograft aortic root replacement in adults with aortic valve disease: a randomised controlled trial." Lancet **376**(9740): 524-531.
- Emani, S., J. E. Mayer, et al. (2011). "Gene regulation of extracellular matrix remodeling in human bone marrow stem cell-seeded tissue-engineered grafts." Tissue Engineering Part A **17**: 2379-2388.
- Engelmayr, G. C., D. K. Hildebrand, et al. (2003). "A novel bioreactor for the dynamic flexural stimulation of tissue engineered heart valve biomaterials." Biomaterials **24**: 2523-2532.
- Engelmayr, G. C., E. Rabkin, et al. (2005). "The independent role of cyclic flexure in the early in vitro development of an engineered heart valve tissue." Biomaterials **26**: 175-187.
- Engelmayr, G. C., V. L. Sales, et al. (2006). "Cyclic flexure and laminar flow synergistically accelerate mesenchymal stem cell-mediated engineered tissue formation: Implications for engineered heart valve tissues." Biomaterials **27**: 6083-6095.
- Engelmayr, G. C., L. Soletti, et al. (2008). "A novel flex-stretch-flow bioreactor for the study of engineered heart valve tissue mechanobiology." Annals of Biomedical Engineering **36**: 700-712.
- Engler, A. J., S. Sen, et al. (2006). "Matrix elasticity directs stem cell lineage specification." Cell **126**(4): 677-689.
- Erdbrugger, W., W. Konertz, et al. (2006). "Decellularized xenogenic heart valves reveal remodeling and growth potential in vivo." Tissue Eng **12**(8): 2059-2068.
- Farndale, R. W., D. J. Buttle, et al. (1986). "Improved quantitation and discrimination of sulphated glycosaminoglycans by use of dimethylmethylene blue." Biochimica et Biophysica Acta **883**: 173-177.
- Farnsworth, N., C. Bensard, et al. (2012). "The role of the PCM in reducing oxidative stress induced by radical initiated photoencapsulation of chondrocytes in poly(ethylene glycol) hydrogels." Osteoarthritis Cartilage **20**(11): 1326-1335.
- Fedorovich, N. E., J. Alblas, et al. (2011). "Organ printing: the future of bone regeneration?" Trends in Biotechnology **29**: 601-606.
- Fedorovich, N. E., M. H. Oudshoorn, et al. (2009). "The effect of photopolymerization on stem cells embedded in hydrogels." Biomaterials **30**(3): 344-353.
- Fedorovich, N. E., W. Schuurman, et al. (2012). "Biofabrication of osteochondral tissue equivalents by printing topologically defined, cell-laden hydrogel scaffolds." Tissue Eng Part C Methods **18**(1): 33-44.

- Fedorovich, N. E., W. Schuurman, et al. (2012). "Biofabrication of osteochondral tissue equivalents by printing topologically defined, cell-laden hydrogel scaffolds." Tissue Engineering Part C-Methods **18**: 33-44.
- Fedorovich, N. E., H. M. Wijnberg, et al. (2011). "Distinct tissue formation by heterogeneous printing of osteo- and endothelial progenitor cells." Tissue Eng Part A **17**(15-16): 2113-2121.
- Fedorovich, N. E., H. M. Wijnberg, et al. (2011). "Distinct tissue formation by heterogeneous printing of osteo- and endothelial progenitor cells " Tissue Engineering Part A **17**: 2113-2121.
- Feng, Y., M. Taraban, et al. (2011). "Linear Dependency of NMR Relaxation Rates on Shear Modulus in Hydrogels." Soft Matter **7**(21): 9890-9893.
- Filho AL, C. P., Noritomi PY, Silva JVL, Colangelo NW, Kang H, Lipson H, Butcher JT, Malone E, Neto PI. ( 2009). "Construction and Adaptation of an Open Source Rapid Prototyping Machine for Biomedical Research Purposes - a Multinational Collaborative Development." Advanced Research in Virtual and Rapid Prototyping.
- Flanagan, T. C., C. Cornelissen, et al. (2007). "The in vitro development of autologous fibrin-based tissue-engineered heart valves through optimised dynamic conditioning." Biomaterials **28**: 3388-3397.
- Flanagan, T. C., J. S. Sachweh, et al. (2009). "In vivo remodeling and structural characterization of fibrin-based tissue-engineered heart valves in the adult sheep model." Tissue Eng Part A **15**(10): 2965-2976.
- Flanagan, T. C., J. S. Sachweh, et al. (2009). "In vivo remodeling and structural characterization of fibrin-based tissue-engineered heart valves in the adult sheep model." Tissue Engineering Part A **15**: 2965-2976.
- Franquet, A., S. Avril, et al. (2013). "A new method for the in vivo identification of mechanical properties in arteries from cine MRI images: theoretical framework and validation." IEEE Trans Med Imaging **32**(8): 1448-1461.
- Frigiola, A., A. Varrica, et al. (2010). "Neo-aortic Valve and Root Complex Evolution After Ross Operation in Infants, Children, and Adolescents." Ann Thorac Surg **90**(4): 1278-1285.
- Gaetani, R., L. Barile, et al. (2009). "New perspectives to repair a broken heart." Cardiovascular & Hematological Agents in Medicinal Chemistry **7**: 91-107.
- Gaetani, R., P. A. Doevendans, et al. (2012). "Cardiac tissue engineering using tissue printing technology and human cardiac progenitor cells." Biomaterials **33**(6): 1782-1790.
- Gaetani, R., P. A. Doevendans, et al. (2012). "Cardiac tissue engineering using tissue printing technology and human cardiac progenitor cells." Biomaterials **33**: 1782-1790.
- Gandaglia, A., A. Bagno, et al. (2011). "Cells, scaffolds and bioreactors for tissue-engineered heart valves: a journey from basic concepts to contemporary developmental innovations " European Journal of Cardio-thoracic Surgery **39**: 523-531.
- Gauvin, R., Y. C. Chen, et al. (2012). "Microfabrication of complex porous tissue engineering scaffolds using 3D projection stereolithography." Biomaterials **33**(15): 3824-3834.
- Genes, N. G., J. A. Rowley, et al. (2004). "Effect of substrate mechanics on chondrocyte adhesion to modified alginate surfaces." Arch Biochem Biophys **422**(2): 161-167.
- Giuliatti, S., L. Gallo, Jr., et al. (2000). "A pulsatile flow model for in vitro quantitative evaluation of prosthetic valve regurgitation." Braz J Med Biol Res **33**(3): 341-346.
- Glen, S., J. Burns, et al. (2004). "Prevalence and development of additional cardiac abnormalities in 1448 patients with congenital ventricular septal defects." Heart **90**(11): 1321-1325.
- Gottlieb, D., T. Kunal, et al. "In vivo monitoring of function of autologous engineered pulmonary valve." J Thorac Cardiovasc Surg **139**(3): 723-731.

- Gottlieb, D., T. Kunal, et al. (2010). "In vivo monitoring of function of autologous engineered pulmonary valve." J Thorac Cardiovasc Surg **139**(3): 723-731.
- Gould, R. A., K. Chin, et al. (2012). "Cyclic strain anisotropy regulates valvular interstitial cell phenotype and tissue remodeling in three-dimensional culture." Acta Biomater **8**(5): 1710-1719.
- Gould, R. A., K. Chin, et al. (2012). "Cyclic strain anisotropy regulates valvular interstitial cell phenotype and tissue remodeling in three-dimensional culture." Acta Biomaterialia **8**: 1710-1719.
- Gould, S. T. and K. S. Anseth (2013). "Role of cell-matrix interactions on VIC phenotype and tissue deposition in 3D PEG hydrogels." J Tissue Eng Regen Med.
- Groeber, F., M. Holeiter, et al. (2011). "Skin tissue engineering - In vivo and in vitro applications." Advanced Drug Delivery Reviews **63**: 352-366.
- Grunkemeier, G. L., H. H. Li, et al. (2000). "Long-term performance of heart valve prostheses." Curr Probl Cardiol **25**(2): 73-154.
- Grunkemeier, G. L., H. H. Li, et al. (1999). "Heart valve replacement: a statistical review of 35 years' results." J Heart Valve Dis **8**(5): 466-470; discussion 470-461.
- Gunatillake, P. A. and R. Adhikari (2003). "Biodegradable synthetic polymers for tissue engineering." Eur Cell Mater **5**: 1-16; discussion 16.
- Gunn, J. W., S. D. Turner, et al. (2005). "Adhesive and mechanical properties of hydrogels influence neurite extension." J Biomed Mater Res A **72**(1): 91-97.
- Guo, K. and C. C. Chu (2005). "Synthesis and characterization of novel biodegradable unsaturated poly(ester amide)/poly(ethylene glycol) diacrylate hydrogels." Journal of Polymer Science Part A: Polymer Chemistry **43**(17): 3932-3944.
- Guo, K. and C. C. Chu (2007). "Controlled release of paclitaxel from biodegradable unsaturated poly(ester amide)s/poly(ethylene glycol) diacrylate hydrogels." J Biomater Sci Polym Ed **18**(5): 489-504.
- Guo, K., C. C. Chu, et al. (2005). "Synthesis and characterization of novel biodegradable unsaturated poly(ester amide)s." Journal of Polymer Science Part A: Polymer Chemistry **43**(7): 1463-1477.
- Gupta, V., J. A. Werdenberg, et al. (2008). "Reversible secretion of glycosaminoglycans and proteoglycans by cyclically stretched valvular cells in 3D culture." Annals of Biomedical Engineering **36**: 1092-1103.
- Haddad, B., A. H. Pakravan, et al. (2013). "A systematic review of tissue engineered meniscus: Cell-based preclinical models " Current Stem Cell Research & Therapy **8**: 222-231.
- Haglund, L., J. Moir, et al. (2011). "Development of a bioreactor for axially loaded intervertebral disc organ culture " Tissue Engineering Part C-Method **17**: 1011-1019.
- Hagmann, H., A. Kuczkowski, et al. (2014). "Breaking the chain at the membrane: paraoxonase 2 counteracts lipid peroxidation at the plasma membrane." FASEB J **28**(4): 1769-1779.
- Hahn, M. S., M. K. McHale, et al. (2007). "Physiologic pulsatile flow bioreactor conditioning of poly(ethylene glycol)-based tissue engineered vascular grafts." Ann Biomed Eng **35**(2): 190-200.
- Hammermeister, K., G. K. Sethi, et al. (2000). "Outcomes 15 years after valve replacement with a mechanical versus a bioprosthetic valve: final report of the Veterans Affairs randomized trial." J Am Coll Cardiol **36**(4): 1152-1158.
- Hayashida, K., K. Kanda, et al. (2007). "Development of an in vivo tissue-engineered, autologous heart valve (the biovalve): preparation of a prototype model." J Thorac Cardiovasc Surg **134**(1): 152-159.
- Hayman, E. G., M. D. Pierschbacher, et al. (1985). "Vitronectin--a major cell attachment-promoting protein in fetal bovine serum." Exp Cell Res **160**(2): 245-258.

- Hildebrand, D. K., Z. J. J. Wu, et al. (2004). "Design and hydrodynamic evaluation of a novel pulsatile bioreactor for biologically active heart valves." Annals of Biomedical Engineering **32**: 1039-1049.
- Hinton, R. B. and K. E. Yutzey (2011). "Heart Valve Structure and Function in Development and Disease." Annual Review of Physiology **73**(1): null.
- Hockaday, L. A., K. H. Kang, et al. (2012). "Rapid 3D printing of anatomically accurate and mechanically heterogeneous aortic valve hydrogel scaffolds." Biofabrication **4**(3): 035005.
- Hockaday, L. A., K. H. Kang, et al. (2012). "Rapid 3D printing of anatomically accurate and mechanically heterogeneous aortic valve hydrogel scaffolds." Biofabrication **4**: 035005.
- Hoerstrup, S. P., R. Sodian, et al. (2000). "Functional living trileaflet heart valves grown in vitro." Circulation **102**: III44-49.
- Hoerstrup, S. P., R. Sodian, et al. (2000). "Functional living trileaflet heart valves grown in vitro." Circulation **102**(19 Suppl 3): III44-49.
- Hoerstrup, S. P., R. Sodian, et al. (2000). "New pulsatile bioreactor for in vitro formation of tissue engineered heart valves." Tissue Engineering **6**: 75-79.
- Hoerstrup, S. P., R. Sodian, et al. (2000). "New pulsatile bioreactor for in vitro formation of tissue engineered heart valves." Tissue Eng **6**(1): 75-79.
- Hoffman-Kim, D., M. S. Maish, et al. (2005). "Comparison of three myofibroblast cell sources for the tissue engineering of cardiac valves." Tissue Engineering **11**: 288-301.
- Hoffman, J. I. (1995). "Incidence of congenital heart disease: II. Prenatal incidence." Pediatr Cardiol **16**(4): 155-165.
- Hoffman, J. I. and S. Kaplan (2002). "The incidence of congenital heart disease." J Am Coll Cardiol **39**(12): 1890-1900.
- Hollister, S. J. (2005). "Porous scaffold design for tissue engineering." Nat Mater **4**(7): 518-524.
- Hong, T., M. S. Maish, et al. (2000). "Reproducible echocardiography in juvenile sheep and its application in the evaluation of a pulmonary valve homograft implant." Contemp Top Lab Anim Sci **39**(5): 20-25.
- Hou, Y., C. A. Schoener, et al. (2010). "Photo-cross-linked PDMSstar-PEG hydrogels: synthesis, characterization, and potential application for tissue engineering scaffolds." Biomacromolecules **11**(3): 648-656.
- Howard, A. C., A. K. McNeil, et al. (2011). "Promotion of plasma membrane repair by vitamin E." Nat Commun **2**: 597.
- Huebsch, N., P. R. Arany, et al. (2010). "Harnessing traction-mediated manipulation of the cell/matrix interface to control stem-cell fate." Nat Mater **9**(6): 518-526.
- Hui, T. Y., K. M. C. Cheung, et al. (2008). "In vitro chondrogenic differentiation of human mesenchymal stem cells in collagen microspheres: Influence of cell seeding density and collagen concentration." Biomaterials **29**: 3201-3212.
- Hume, P. S. and K. S. Anseth (2011). "Polymerizable superoxide dismutase mimetic protects cells encapsulated in poly(ethylene glycol) hydrogels from reactive oxygen species-mediated damage." J Biomed Mater Res A **99**(1): 29-37.
- Hutson, C. B., J. W. Nichol, et al. (2011). "Synthesis and characterization of tunable poly(ethylene glycol): gelatin methacrylate composite hydrogels." Tissue Eng Part A **17**(13-14): 1713-1723.
- Ilbawi, A. M., D. E. Spicer, et al. (2007). "Morphologic study of the ascending aorta and aortic arch in hypoplastic left hearts: surgical implications." J Thorac Cardiovasc Surg **134**(1): 99-105.
- Jashari, R., Y. Goffin, et al. (2010). "European homograft bank: twenty years of cardiovascular tissue banking and collaboration with transplant coordination in Europe." Transplant Proc **42**(1): 183-189.

- Jockenhoevel, S., G. Zund, et al. (2002). "Cardiovascular tissue engineering: A new Laminar flow chamber for in vitro improvement of mechanical tissue properties." ASAIO Journal **48**: 8-11.
- Johnson, I. D. (2010). The Molecular Probes Handbook: A Guide to Fluorescent Probes and Labeling Technologies, 11th Edition, Life Technologies Corporation.
- Kanemaru, S., H. Umeda, et al. (2013). "Improvement of eustachian tube function by tissue-engineered regeneration of mastoid air cells." Laryngoscope **123**: 472-476.
- Kang, K. H., L. A. Hockaday, et al. (2013). "Quantitative optimization of solid freeform deposition of aqueous hydrogels." Biofabrication **5**: 035001.
- Kang, K. H., L. A. Hockaday, et al. (2013). "Quantitative optimization of solid freeform deposition of aqueous hydrogels." Biofabrication **5**(3): 035001.
- Karamlou, T., K. Jang, et al. (2005). "Outcomes and associated risk factors for aortic valve replacement in 160 children: a competing-risks analysis." Circulation **112**(22): 3462-3469.
- Kirkland, R. A. and J. L. Franklin (2001). "Evidence for redox regulation of cytochrome C release during programmed neuronal death: antioxidant effects of protein synthesis and caspase inhibition." J Neurosci **21**(6): 1949-1963.
- Kirkland, R. A., G. M. Saavedra, et al. (2007). "Rapid activation of antioxidant defenses by nerve growth factor suppresses reactive oxygen species during neuronal apoptosis: evidence for a role in cytochrome c redistribution." J Neurosci **27**(42): 11315-11326.
- Kloxin, A. M., J. A. Benton, et al. (2010). "In situ elasticity modulation with dynamic substrates to direct cell phenotype." Biomaterials **31**(1): 1-8.
- Kloxin, A. M., A. M. Kasko, et al. (2009). "Photodegradable hydrogels for dynamic tuning of physical and chemical properties." Science **324**: 59-63.
- Kloxin, A. M., C. J. Kloxin, et al. (2010). "Mechanical properties of cellularly responsive hydrogels and their experimental determination." Adv Mater **22**(31): 3484-3494.
- Kloxin, A. M., K. J. R. Lewis, et al. (2012). "Responsive culture platform to examine the influence of microenvironmental geometry on cell function in 3D." Integrative Biology **4**: 1540-1549.
- Kloxin, A. M., M. W. Tibbitt, et al. (2010). "Synthesis of photodegradable hydrogels as dynamically tunable cell culture platforms." Nature Protocols **5**: 1867-1887.
- Kloxin, A. M., M. W. Tibbitt, et al. (2010). "Synthesis of photodegradable hydrogels as dynamically tunable cell culture platforms." Nat Protoc **5**(12): 1867-1887.
- Kloxin, A. M., M. W. Tibbitt, et al. (2010). "Tunable hydrogels for external manipulation of cellular microenvironments through controlled photodegradation." Advanced Materials **22**: 61-+.
- Kloxin, A. M., M. W. Tibbitt, et al. (2010). "Tunable hydrogels for external manipulation of cellular microenvironments through controlled photodegradation." Adv Mater **22**(1): 61-66.
- Koch, L., A. Deiwick, et al. (2012). "Skin tissue generation by laser cell printing." Biotechnology and Bioengineering **109**: 1855-1863.
- Koch, L., A. Deiwick, et al. (2012). "Skin tissue generation by laser cell printing." Biotechnol Bioeng **109**(7): 1855-1863.
- Konstantinov, I. E., T. Karamlou, et al. (2006). "Truncus arteriosus associated with interrupted aortic arch in 50 neonates: a Congenital Heart Surgeons Society study." Ann Thorac Surg **81**(1): 214-222.
- Konuma, T., E. J. Devaney, et al. (2009). "Performance of CryoValve SG decellularized pulmonary allografts compared with standard cryopreserved allografts." Ann Thorac Surg **88**(3): 849-854; discussion 554-845.
- Kortsmit, J., M. C. Rutten, et al. (2009). "Deformation-controlled load application in heart valve tissue engineering." Tissue Eng Part C Methods **15**(4): 707-716.

- Kortsmit, J., M. C. M. Rutten, et al. (2009). "Deformation controlled load application in heart valve tissue engineering." Tissue Engineering Part C-Method **15**: 707-716.
- Kosaki, K., A. Mendoza, et al. (1996). "Cervical flexion: its contribution to normal and abnormal cardiac morphogenesis." Teratology **54**(3): 135-144.
- Kotecha, M., D. Klatt, et al. (2013). "Monitoring cartilage tissue engineering using magnetic resonance spectroscopy, imaging, and elastography." Tissue Eng Part B Rev **19**(6): 470-484.
- Koul, B., C. J. Lindholm, et al. (2002). "Ross operation for bicuspid aortic valve disease in adults: is it a valid surgical option?" Scand Cardiovasc J **36**(1): 48-52.
- Kovacs, G., A. Berghold, et al. (2009). "Pulmonary arterial pressure during rest and exercise in healthy subjects: a systematic review." European Respiratory Journal **34**: 888-894.
- Krokosz, A., J. Grebowski, et al. (2013). "Can melatonin delay oxidative damage of human erythrocytes during prolonged incubation?" Adv Med Sci **58**(1): 134-142.
- Ku, C. H., P. H. Johnson, et al. (2006). "Collagen synthesis by mesenchymal stem cells and aortic valve interstitial cells in response to mechanical stretch." Cardiovascular Research **71**: 548-556.
- Kuzawa, C. W. (1998). "Adipose tissue in human infancy and childhood: An evolutionary perspective." Yearbook of Physical Anthropology, Vol 41 - 1998 **41**: 177-209.
- L'Heureux, N., S. Paquet, et al. (1998). "A completely biological tissue-engineered human blood vessel." Faseb Journal **12**: 47-56.
- Labarthe, D. R. and S. B. Dunbar (2012). "Global cardiovascular health promotion and disease prevention 2011 and beyond." Circulation **125**: 2667-2676.
- Lampe, K. J., R. M. Namba, et al. (2009). "Impact of lactic acid on cell proliferation and free radical-induced cell death in monolayer cultures of neural precursor cells." Biotechnol Bioeng **103**(6): 1214-1223.
- Larsen, L. U., O. B. Petersen, et al. (2006). "Strain rate derived from color Doppler myocardial imaging for assessment of fetal cardiac function." Ultrasound Obstet Gynecol **27**(2): 210-213.
- Latif, N., P. Sarathchandra, et al. (2007). "Characterization of structural and signaling molecules by human valve interstitial cells and comparison to human mesenchymal stem cells." J Heart Valve Dis **16**(1): 56-66.
- Leach, J. B. and C. E. Schmidt (2005). "Characterization of protein release from photocrosslinkable hyaluronic acid-polyethylene glycol hydrogel tissue engineering scaffolds." Biomaterials **26**(2): 125-135.
- Lee, H., S. Ahn, et al. (2014). "Enhancement of cell viability by fabrication of macroscopic 3D hydrogel scaffolds using an innovative cell-dispensing technique supplemented by preosteoblast-laden micro-beads." Carbohydr Polym **104**: 191-198.
- Lee, S. H., J. J. Moon, et al. (2008). "Three-dimensional micropatterning of bioactive hydrogels via two-photon laser scanning photolithography for guided 3D cell migration." Biomaterials **29**: 2962-2968.
- Lee, S. J., H. W. Kang, et al. (2008). "Application of microstereolithography in the development of three-dimensional cartilage regeneration scaffolds." Biomedical Microdevices **10**: 233-241.
- Lee, S. J., J. W. Rhie, et al. (2008). "Development of three-dimensional alginate encapsulated chondrocyte hybrid scaffold using microstereolithography." Journal of Manufacturing Science and Engineering-Transactions of the ASME **130**: 021007.
- Lee, W., J. C. Debasitis, et al. (2009). "Multi-layered culture of human skin fibroblasts and keratinocytes through three-dimensional freeform fabrication." Biomaterials **30**(8): 1587-1595.

- Lee, W., J. C. Debasitis, et al. (2009). "Multi-layered culture of human skin fibroblasts and keratinocytes through three-dimensional freeform fabrication." Biomaterials **30**: 1587-1595.
- Lee, W., V. Lee, et al. (2010). "On-demand three-dimensional freeform fabrication of multi-layered hydrogel scaffold with fluidic channels." Biotechnology and Bioengineering **105**(6): 1178-1186.
- Lee, W., V. Lee, et al. (2010). "On-demand three-dimensional freeform fabrication of multi-layered hydrogel scaffold with fluidic channels " Biotechnology and Bioengineering **105**: 1178-1186.
- Lee, W., J. Pinckney, et al. (2009). "Three-dimensional bioprinting of rat embryonic neural cells " Neuroreport **20**: 798-803.
- Lee, W., J. Pinckney, et al. (2009). "Three-dimensional bioprinting of rat embryonic neural cells." Neuroreport **20**(8): 798-803.
- Lee, Y. B., S. Polio, et al. (2010). "Bio-printing of collagen and VEGF-releasing fibrin gel scaffolds for neural stem cell culture." Exp Neurol **223**(2): 645-652.
- Lee, Y. B., S. Polio, et al. (2010). "Bio-printing of collagen and VEGF-releasing fibrin gel scaffolds for neural stem cell culture." Experimental Neurology **223**: 645-652.
- Leong, K. F., C. M. Cheah, et al. (2003). "Solid freeform fabrication of three-dimensional scaffolds for engineering replacement tissues and organs." Biomaterials **24**: 2363-2378.
- Liao, J., E. M. Joyce, et al. (2008). "Effects of decellularization on the mechanical and structural properties of the porcine aortic valve leaflet." Biomaterials **29**(8): 1065-1074.
- Lichtenberg, A., S. Cebotari, et al. (2006). "Flow-dependent re-endothelialization of tissue-engineered heart valves." Journal of Heart Valve Disease **15**: 287-293.
- Lichtenberg, A., I. Tudorache, et al. (2006). "Preclinical testing of tissue-engineered heart valves re-endothelialized under simulated physiological conditions." Circulation **114**: I559-I565.
- Lin, C. C. and K. S. Anseth (2009). "Controlling Affinity Binding with Peptide-Functionalized Poly(ethylene glycol) Hydrogels." Adv Funct Mater **19**(14): 2325.
- Liu, V. A. and S. N. Bhatia (2002). "Three-Dimensional Photopatterning of Hydrogels Containing Living Cells." Biomedical Microdevices **4**(4): 257-266.
- Liu, Y., L. Zhang, et al. (2010). "In vitro engineering of human ear-shaped cartilage assisted with CAD/CAM technology." Biomaterials **31**: 2176-2183.
- Luangphakdy, V., E. Walker, et al. (2013). "Evaluation of osteoconductive scaffolds in the canine femoral multi-defect model " Tissue Engineering Part A **19**: 634-648.
- Lund, A. W., B. Yener, et al. (2009). "The natural and engineered 3D microenvironment as a regulatory cue during stem cell fate determination." Tissue Engineering Part B-Reviews **15**: 371-380.
- Lupinetti, F. M., J. Warner, et al. (1997). "Comparison of human tissues and mechanical prostheses for aortic valve replacement in children." Circulation **96**(1): 321-325.
- Ma, P. X. and J. H. Elisseeff (2005). Scaffolding in tissue engineering. Boca Raton, Taylor&Francis.
- MacNeil, S. and S. N. V. I. P. D. n. P. F. 2007 (2007). "Progress and opportunities for tissue-engineered skin." Nature **445**: 874-880.
- Maish, M. S., D. Hoffman-Kim, et al. (2003). "Tricuspid valve biopsy: A potential source of cardiac myofibroblast cells for tissue-engineered cardiac valves." Journal of Heart Valve Disease **12**: 264-269.
- Mallajosyula, J. K., D. Kaur, et al. (2008). "MAO-B elevation in mouse brain astrocytes results in Parkinson's pathology." PLoS One **3**(2): e1616.
- Malone, E. and H. Lipson (2007). "Fab@Home: The Personal Desktop Fabricator Kit." Rapid Prototyping J **13**: 244-255.
- Malone, E. L. H. (2007). "Fab@Home: the personal desktop fabricator kit." Rapid Prototyping Journal **13**(4): 245-255.

- Manevich, Y., T. Sweitzer, et al. (2002). "1-Cys peroxiredoxin overexpression protects cells against phospholipid peroxidation-mediated membrane damage." Proc Natl Acad Sci U S A **99**(18): 11599-11604.
- Mannoor, M. S., Z. Jiang, et al. (2013). "3D Printed Bionic Ears." Nano Letters **13**(6): 2634-2639.
- Mannoor, M. S., Z. W. Jiang, et al. (2013). "3D printed bionic ears." Nano Letters **13**: 2634–2639.
- Marga, F., K. Jakab, et al. (2012). "Toward engineering functional organ modules by additive manufacturing." Biofabrication **4**: 022001.
- Marga, F., K. Jakab, et al. (2012). "Toward engineering functional organ modules by additive manufacturing." Biofabrication **4**(2).
- Marijon, E., P. Ou, et al. (2007). "Prevalence of rheumatic heart disease detected by echocardiographic screening." N Engl J Med **357**(5): 470-476.
- Mariner, P. D., E. Johannesen, et al. (2012). "Manipulation of miRNA activity accelerates osteogenic differentiation of hMSCs in engineered 3D scaffolds." Journal of Tissue Engineering and Regenerative Medicine **6**: 314-324.
- Matthews, P. B., A. N. Azadani, et al. (2010). "Comparison of porcine pulmonary and aortic root material properties." Ann Thorac Surg **89**(6): 1981-1988.
- Mavrilas, D. and Y. Missirlis (1991). "An approach to the optimization of preparation of bioprosthetic heart valves." J Biomech **24**(5): 331-339.
- Mayosi, B. M. (2007). "Contemporary trends in the epidemiology and management of cardiomyopathy and pericarditis in sub-Saharan Africa." Heart **93**(10): 1176-1183.
- McAllister, T. N., M. Maruszewski, et al. (2009). "Effectiveness of haemodialysis access with an autologous tissue-engineered vascular graft: a multicentre cohort study." Lancet **373**: 1440-1446.
- McBride, K. L., L. Marengo, et al. (2005). "Epidemiology of noncomplex left ventricular outflow tract obstruction malformations (aortic valve stenosis, coarctation of the aorta, hypoplastic left heart syndrome) in Texas, 1999-2001." Birth Defects Res A Clin Mol Teratol **73**(8): 555-561.
- Merryman, W. D., H. D. Lukoff, et al. (2007). "Synergistic effects of cyclic tension and transforming growth factor-beta 1 on the aortic valve myofibroblast." Cardiovascular Pathology **16**: 268-276.
- Merryman, W. D., I. Youn, et al. (2006). "Correlation between heart valve interstitial cell stiffness and transvalvular pressure: implications for collagen biosynthesis." Am J Physiol Heart Circ Physiol **290**(1): H224-231.
- Messier, R. H., B. L. Bass, et al. (1994). "Dual structural and functional phenotypes of the porcine aortic-valve interstitial population-Characteristics of the leaflet myofibroblast." Journal of Surgical Research **57**: 1-21.
- Metscher, B. D. and G. B. Muller (2011). "MicroCT for molecular imaging: quantitative visualization of complete three-dimensional distributions of gene products in embryonic limbs." Dev Dyn **240**(10): 2301-2308.
- Meuris, B., S. Ozaki, et al. (2001). "Influence of species, environmental factors, and tissue cellularity on calcification of porcine aortic wall tissue." Semin Thorac Cardiovasc Surg **13**(4 Suppl 1): 99-105.
- Meuris, B., S. Ozaki, et al. (2003). "Bioprosthetic tissue calcification: influence of blood contact and arterial pressure. an experimental study in rats and sheep." J Heart Valve Dis **12**(3): 392-399; discussion 399.
- Michael, S., H. Sorg, et al. (2013). "Tissue Engineered Skin Substitutes Created by Laser-Assisted Bioprinting Form Skin-Like Structures in the Dorsal Skin Fold Chamber in Mice." PLoS One **8**(3): e57741.
- Michael, S., H. Sorg, et al. (2013). "Tissue engineered skin substitutes created by laser-assisted bioprinting form skin-like structures in the dorsal skin fold chamber in mice " Plos One **8**: e57741.

- Miller, D. V., W. D. Edwards, et al. (2006). "Endothelial and smooth muscle cell populations in a decellularized cryopreserved aortic homograft (SynerGraft) 2 years after implantation." J Thorac Cardiovasc Surg **132**(1): 175-176.
- Miller, J. S., K. R. Stevens, et al. (2012). "Rapid casting of patterned vascular networks for perfusable engineered three-dimensional tissues." Nat Mater **11**(9): 768-774.
- Miller, J. S., K. R. Stevens, et al. (2012). "Rapid casting of patterned vascular networks for perfusable engineered three-dimensional tissues." Nature Materials **11**: 768-774.
- Mironi-Harpaz, I., D. Y. Wang, et al. (2012). "Photopolymerization of cell-encapsulating hydrogels: crosslinking efficiency versus cytotoxicity." Acta Biomater **8**(5): 1838-1848.
- Mocumbi, A. O., M. B. Ferreira, et al. (2008). "A population study of endomyocardial fibrosis in a rural area of Mozambique." N Engl J Med **359**(1): 43-49.
- Mol, A., N. J. Driessen, et al. (2005). "Tissue engineering of human heart valve leaflets: a novel bioreactor for a strain-based conditioning approach." Ann Biomed Eng **33**(12): 1778-1788.
- Mol, A., N. J. B. Driessen, et al. (2005). "Tissue engineering of human heart valve leaflets: A novel bioreactor for a strain-based conditioning approach." Annals of Biomedical Engineering **33**: 1778-1788.
- Molina, F. S., C. Faro, et al. (2008). "Heart stroke volume and cardiac output by four-dimensional ultrasound in normal fetuses." Ultrasound Obstet Gynecol **32**(2): 181-187.
- Muller, A. M., M. Davenport, et al. (2009). "Platelet lysate as a serum substitute for 2D static and 3D perfusion culture of stromal vascular fraction cells from human adipose tissue." Tissue Engineering Part C **15**: 869-875.
- Nakayama, Y., Y. Takewa, et al. (2014). "In-body tissue-engineered aortic valve (Biovalve type VII) architecture based on 3D printer molding." Journal of Biomedical Materials Research Part B: Applied Biomaterials: n/a-n/a.
- Nakayama, Y., Y. Takewa, et al. (2014). "In-body tissue-engineered aortic valve (Biovalve type VII) architecture based on 3D printer molding." J Biomed Mater Res B Appl Biomater.
- Naso, F., A. Gandaglia, et al. "Differential distribution of structural components and hydration in aortic and pulmonary heart valve conduits: Impact of detergent-based cell removal." Acta Biomater **6**(12): 4675-4688.
- Neidert, M. R. and R. T. Tranquillo (2006). "Tissue-engineered valves with commissural alignment." Tissue Eng **12**(4): 891-903.
- Nichol, J. W., S. T. Koshy, et al. (2010). "Cell-laden microengineered gelatin methacrylate hydrogels." Biomaterials **31**: 5536-5544.
- Nimeskern, L., H. Martinez Avila, et al. (2013). "Mechanical evaluation of bacterial nanocellulose as an implant material for ear cartilage replacement." Journal of Mechanical Behavior of Biomedical Materials **22**: 12-21.
- Nimeskern, L., G. J. van Osch, et al. (2013). "Quantitative evaluation of mechanical properties in tissue-engineered auricular cartilage." Tissue Engineering Part B-Reviews: DOI: 10.1089/ten.teb.2013.0117.
- Nirmalanandhan, V. S., M. S. Levy, et al. (2006). "Effects of cell seeding density and collagen concentration on contraction kinetics of mesenchymal stem cell-seeded collagen constructs." Tissue Eng **12**(7): 1865-1872.
- Norotte, C., F. S. Marga, et al. (2009). "Scaffold-free vascular tissue engineering using bioprinting." Biomaterials **30**: 5910-5917.
- O'Brien, M. F., S. Goldstein, et al. (1999). "The SynerGraft valve: a new acellular (nonglutaraldehyde-fixed) tissue heart valve for autologous recellularization first experimental studies before clinical implantation." Semin Thorac Cardiovasc Surg **11**(4 Suppl 1): 194-200.

- O'Cearbhaill, E. D., M. Murphy, et al. (2010). "Behavior of human mesenchymal stem cells in fibrin-based vascular tissue engineering constructs." Ann Biomed Eng **38**(3): 649-657.
- Occhetta, P., N. Sadr, et al. (2013). "Fabrication of 3D cell-laden hydrogel microstructures through photo-mold patterning." Biofabrication **5**(3): 035002.
- Ouyang, D. W., C. T. Salerno, et al. (1998). "Long-term evaluation of orthotopically implanted stentless bioprosthetic aortic valves in juvenile sheep." J Invest Surg **11**(3): 175-183.
- Owens, S. T., C. Gomez-Fifer, et al. (2006). "Thrombus formation in the native aortic root in patients with hypoplastic left heart syndrome." Pediatr Cardiol **27**(3): 385-387.
- Padera R F i J r , S. F. J., Ed. (2008). Pathology of Cardiac Surgery. Cardiac Surgery in the Adult. . New York, McGraw-Hill.
- Park, J. S., J. S. Chu, et al. (2011). "The effect of matrix stiffness on the differentiation of mesenchymal stem cells in response to TGF-beta." Biomaterials **32**(16): 3921-3930.
- Pati, F., J. Jang, et al. (2014). "Printing three-dimensional tissue analogues with decellularized extracellular matrix bioink." Nat Commun **5**: 3935.
- Pedron, S., A. M. Kasko, et al. (2010). "Effect of heparin oligomer chain length on the activation of valvular interstitial cells." Biomacromolecules **11**: 1692-1695.
- Pedron, S., A. M. Kasko, et al. (2010). "Effect of heparin oligomer chain length on the activation of valvular interstitial cells." Biomacromolecules **11**(6): 1692-1695.
- Perry, T. E., S. Kaushal, et al. (2003). "Bone marrow as a cell source for tissue engineering heart valves." Annals of Thoracic Surgery **75**: 761-767.
- Peyton, S. R., C. B. Raub, et al. (2006). "The use of poly(ethylene glycol) hydrogels to investigate the impact of ECM chemistry and mechanics on smooth muscle cells." Biomaterials **27**(28): 4881-4893.
- Pibarot, P. and J. G. Dumesnil (2006). "Prosthesis-patient mismatch: definition, clinical impact, and prevention." Heart **92**(8): 1022-1029.
- Quintanilla, R. A., T. A. Matthews-Roberson, et al. (2009). "Caspase-cleaved tau expression induces mitochondrial dysfunction in immortalized cortical neurons: implications for the pathogenesis of Alzheimer disease." J Biol Chem **284**(28): 18754-18766.
- Rahimtoola, S. H. (2010). "Choice of prosthetic heart valve in adults an update." J Am Coll Cardiol **55**(22): 2413-2426.
- Rajani, B., R. B. Mee, et al. (1998). "Evidence for rejection of homograft cardiac valves in infants." J Thorac Cardiovasc Surg **115**(1): 111-117.
- Ramaswamy, S., D. Gottlieb, et al. (2010). "The role of organ level conditioning on the promotion of engineered heart valve tissue development in-vitro using mesenchymal stem cells." Biomaterials **31**: 1114-1125.
- Ramaswamy, S., D. Gottlieb, et al. (2010). "The role of organ level conditioning on the promotion of engineered heart valve tissue development in-vitro using mesenchymal stem cells." Biomaterials **31**(6): 1114-1125.
- Reddy, G. K. and C. S. Enwemeka (1996). "A simplified method for the analysis of hydroxyproline in biological tissues." Clin Biochem **29**(3): 225-229.
- Reiffel, A. J., C. Kafka, et al. (2013). "High-fidelity tissue engineering of patient-specific auricles for reconstruction of pediatric microtia and other auricular deformities." Plos One **8**: e56506.
- Ribeiro, P. S., K. H. Jacobsen, et al. (2008). "Priorities for women's health from the Global Burden of Disease study." Int J Gynaecol Obstet **102**(1): 82-90.
- Richards, J., I. El-Hamamsy, et al. (2013). "Side-specific endothelial-dependent regulation of aortic valve calcification interplay of hemodynamics and nitric oxide signaling." American Journal of Pathology **182**: 1922-1931.

- Rieder, E., M. T. Kasimir, et al. (2004). "Decellularization protocols of porcine heart valves differ importantly in efficiency of cell removal and susceptibility of the matrix to recellularization with human vascular cells." J Thorac Cardiovasc Surg **127**(2): 399-405.
- Rieder, E., G. Seebacher, et al. (2005). "Tissue engineering of heart valves: decellularized porcine and human valve scaffolds differ importantly in residual potential to attract monocytic cells." Circulation **111**(21): 2792-2797.
- Roberts, W. C. and J. M. Ko (2005). "Frequency by decades of unicuspid, bicuspid, and tricuspid aortic valves in adults having isolated aortic valve replacement for aortic stenosis, with or without associated aortic regurgitation." Circulation **111**(7): 920-925.
- Robinson, P. S., S. L. Johnson, et al. (2007). "Functional Tissue-Engineered Valves from Cell-Remodeled Fibrin with Commissural Alignment of Cell-Produced Collagen." Tissue Eng.
- Rogers, C. I., J. V. Pagaduan, et al. (2011). "Single-monomer formulation of polymerized polyethylene glycol diacrylate as a nonadsorptive material for microfluidics." Anal Chem **83**(16): 6418-6425.
- Rosano, A., L. D. Botto, et al. (2000). "Infant mortality and congenital anomalies from 1950 to 1994: an international perspective." J Epidemiol Community Health **54**(9): 660-666.
- Ross, D. N. (1967). "Replacement of aortic and mitral valves with a pulmonary autograft." Lancet **2**(7523): 956-958.
- Rouillard, A. D., C. M. Berglund, et al. (2010). "Methods for Photocrosslinking Alginate Hydrogel Scaffolds with High Cell Viability." Tissue Eng Part C Methods.
- Rouillard, A. D., C. M. Berglund, et al. (2011). "Methods for photocrosslinking alginate hydrogel scaffolds with high cell viability." Tissue Eng Part C Methods **17**(2): 173-179.
- Rowley, J. A., G. Madlambayan, et al. (1999). "Alginate hydrogels as synthetic extracellular matrix materials." Biomaterials **20**(1): 45-53.
- Rubbens, M. P., A. Mol, et al. (2009). "Intermittent straining accelerates the development of tissue properties in engineered heart valve tissue." Tissue Engineering Part A **15**: 999-1008.
- Ryoo, Y. W., S. I. Suh, et al. (2001). "The effects of the melatonin on ultraviolet-B irradiated cultured dermal fibroblasts." J Dermatol Sci **27**(3): 162-169.
- Sabnis, A., M. Rahimi, et al. (2009). "Cytocompatibility studies of an in situ photopolymerized thermoresponsive hydrogel nanoparticle system using human aortic smooth muscle cells." J Biomed Mater Res A **91**(1): 52-59.
- Sacks, M. S., F. J. Schoen, et al. (2009). "Bioengineering challenges for heart valve tissue engineering." Annu Rev Biomed Eng **11**: 289-313.
- Sakai, S., Y. Liu, et al. (2013). "Horseradish peroxidase/catalase-mediated cell-laden alginate-based hydrogel tube production in two-phase coaxial flow of aqueous solutions for filament-like tissues fabrication." Biofabrication **5**(1): 015012.
- Sakata, N., K. Miyamoto, et al. (1998). "Oxidative damage of vascular smooth muscle cells by the glycated protein-cupric ion system." Atherosclerosis **136**(2): 263-274.
- Sales, V. L., B. A. Mettler, et al. (2010). "Endothelial progenitor cells as a sole source for ex vivo seeding of tissue-engineered heart valves." Tissue Engineering Part A **16**: 257-267.
- Sales, V. L., B. A. Mettler, et al. (2010). "Endothelial progenitor cells as a sole source for ex vivo seeding of tissue-engineered heart valves." Tissue Eng Part A **16**(1): 257-267.
- Sani, M. U., K. M. Karaye, et al. (2007). "Prevalence and pattern of rheumatic heart disease in the Nigerian savannah: an echocardiographic study." Cardiovasc J Afr **18**(5): 295-299.

- Santos, E., R. M. Hernandez, et al. (2012). "Novel advances in the design of three-dimensional bio-scaffolds to control cell fate: translation from 2D to 3D." Trends in Biotechnology **30**: 331-341.
- Sauren, A. A., M. C. van Hout, et al. (1983). "The mechanical properties of porcine aortic valve tissues." J Biomech **16**(5): 327-337.
- Sayk, F., I. Bos, et al. (2005). "Histopathologic findings in a novel decellularized pulmonary homograft: an autopsy study." Ann Thorac Surg **79**(5): 1755-1758.
- Schaefermeier, P. K., D. Szymanski, et al. (2009). "Design and fabrication of three-dimensional scaffolds for tissue engineering of human heart valves." Eur Surg Res **42**(1): 49-53.
- Schechner, J. S., S. K. Crane, et al. (2003). "Engraftment of a vascularized human skin equivalent." Faseb Journal **17**: 2250-2256.
- Schenke-Layland, K., F. Opitz, et al. (2003). "Complete dynamic repopulation of decellularized heart valves by application of defined physical signals-an in vitro study." Cardiovascular Research **60**: 497-509.
- Schieker, M., H. Seitz, et al. (2006). "Biomaterials as Scaffold for Bone Tissue Engineering." European Journal of Trauma **32**(2): 114-124.
- Schleicher, M., G. Sammler, et al. (2010). "Simplified pulse reactor for real-time long-term in vitro testing of biological heart valves." Annals of Biomedical Engineering **38**: 1919-1927.
- Schmidt, D., J. Achermann, et al. (2008). "Cryopreserved amniotic fluid-derived cells: A life-long autologous fetal stem cell source for heart valve tissue engineering." Journal of Heart Valve Disease **17**: 446-455.
- Schmidt, D., J. Achermann, et al. (2008). "Cryopreserved amniotic fluid-derived cells: a lifelong autologous fetal stem cell source for heart valve tissue engineering." J Heart Valve Dis **17**(4): 446-455; discussion 455.
- Schmidt, D., C. Breymann, et al. (2004). "Umbilical cord blood derived endothelial progenitor cells for tissue engineering of vascular grafts." Annals of Thoracic Surgery **78**: 2094-2098.
- Schmidt, D., P. Dijkman, et al. (2010). "Minimally-invasive implantation of living tissue engineered heart valves A comprehensive approach from autologous vascular cells to stem cells." Journal of the American College of Cardiology **56**: 510-520.
- Schmidt, D., P. E. Dijkman, et al. (2010). "Minimally-invasive implantation of living tissue engineered heart valves: a comprehensive approach from autologous vascular cells to stem cells." J Am Coll Cardiol **56**(6): 510-520.
- Schmidt, D., A. Mol, et al. (2006). "Living autologous heart valves engineered from human prenatally harvested progenitors." Circulation **114**: I125-I131.
- Schmidt, D., A. Mol, et al. (2006). "Living autologous heart valves engineered from human prenatally harvested progenitors." Circulation **114**(1 Suppl): I125-131.
- Schmidt, D., A. Mol, et al. (2006). "Engineering of biologically active living heart valve leaflets using human umbilical cord-derived progenitor cells." Tissue Engineering **12**: 3223-3232.
- Schmidt, D., U. A. Stock, et al. (2007). "Tissue engineering of heart valves using decellularized xenogeneic or polymeric starter matrices." Philos Trans R Soc Lond B Biol Sci **362**(1484): 1505-1512.
- Schneider, P. J. and J. D. Deck (1981). "Tissue and cell renewal in the natural aortic valve of rats: an autoradiographic study." Cardiovasc Res **15**(4): 181-189.
- Schoen, F. J. (1997). "Aortic valve structure-function correlations: role of elastic fibers no longer a stretch of the imagination." J Heart Valve Dis **6**(1): 1-6.
- Schoen, F. J. (2006). "New frontiers in the pathology and therapy of heart valve disease: 2006 Society for Cardiovascular Pathology, Distinguished Achievement Award Lecture, United States-Canadian Academy of Pathology, Atlanta, GA, February 12, 2006." Cardiovasc Pathol **15**(5): 271-279.

- Schoen, F. J. (2008). "Evolving concepts of cardiac valve dynamics: the continuum of development, functional structure, pathobiology, and tissue engineering." Circulation **118**(18): 1864-1880.
- Schuurman, W., V. Khristov, et al. (2011). "Bioprinting of hybrid tissue constructs with tailorable mechanical properties." Biofabrication **3**(2): 021001.
- Seeger, J. M. and N. Klingman (1985). "Improved endothelial cell seeding with cultured cells and fibronectin-coated grafts." J Surg Res **38**(6): 641-647.
- Seliktar, D., R. A. Black, et al. (2000). "Dynamic mechanical conditioning of collagen-gel blood vessel constructs induces remodeling in vitro." Ann Biomed Eng **28**(4): 351-362.
- Seliktar, D., R. M. Nerem, et al. (2001). "The role of matrix metalloproteinase-2 in the remodeling of cell-seeded vascular constructs subjected to cyclic strain." Ann Biomed Eng **29**(11): 923-934.
- Shin, S. R., B. Aghaei-Ghareh-Bolagh, et al. (2013). "Cell-laden microengineered and mechanically tunable hybrid hydrogels of gelatin and graphene oxide." Adv Mater **25**(44): 6385-6391.
- Shinoka, T., C. K. Breuer, et al. (1995). "Tissue engineering heart valves: valve leaflet replacement study in a lamb model." Annals of Thoracic and Surgery **60**: S513-516.
- Shinoka, T., P. X. Ma, et al. (1996). "Tissue-engineered heart valves. Autologous valve leaflet replacement study in a lamb model." Circulation **94**(9 Suppl): II164-168.
- Shinoka, T., D. ShumTim, et al. (1997). "Tissue-engineered heart valve leaflets - Does cell origin affect outcome?" Circulation **96**: 102-107.
- Sierad, L., A. Simionescu, et al. "Design and Testing of a Pulsatile Conditioning System for Dynamic Endothelialization of Polyphenol-Stabilized Tissue Engineered Heart Valves." Cardiovascular Engineering and Technology **1**(2): 138.
- Sierad, L. N., A. Simionescu, et al. (2010). "Design and testing of a pulsatile conditioning system for dynamic endothelialization of polyphenol-stabilized tissue engineered heart valves." Cardiovascular Engineering and Technology **1**: 138-153.
- Sierad, L. N., A. Simionescu, et al. (2010). "Design and Testing of a Pulsatile Conditioning System for Dynamic Endothelialization of Polyphenol-Stabilized Tissue Engineered Heart Valves." Cardiovasc Eng Technol **1**(2): 138-153.
- Sierad, L. N., A. Simionescu, et al. (2010). "Design and testing of a pulsatile conditioning system for dynamic endothelialization of polyphenol-stabilized tissue engineered heart valves." Cardiovascular Engineering and Technology **1**: 138-153.
- Simon, P., M. T. Kasimir, et al. (2003). "Early failure of the tissue engineered porcine heart valve SYNERGRAFT in pediatric patients." Eur J Cardiothorac Surg **23**(6): 1002-1006; discussion 1006.
- Singh, S., C. Brocker, et al. (2013). "Aldehyde dehydrogenases in cellular responses to oxidative/electrophilic stress." Free Radic Biol Med **56**: 89-101.
- Singh, S., A. N. Singh, et al. (2013). "Biodegradable polycaprolactone (PCL) nanosphere encapsulating superoxide dismutase and catalase enzymes." Appl Biochem Biotechnol **171**(7): 1545-1558.
- Sinthuvanich, C., L. A. Haines-Butterick, et al. (2012). "Iterative design of peptide-based hydrogels and the effect of network electrostatics on primary chondrocyte behavior." Biomaterials **33**(30): 7478-7488.
- Skardal, A., J. Zhang, et al. (2010). "Photocrosslinkable hyaluronan-gelatin hydrogels for two-step bioprinting." Tissue Eng Part A **16**(8): 2675-2685.
- Skardal, A., J. Zhang, et al. (2010). "Bioprinting vessel-like constructs using hyaluronan hydrogels crosslinked with tetrahedral polyethylene glycol tetracrylates." Biomaterials **31**(24): 6173-6181.

- Skardal, A., J. X. Zhang, et al. (2010). "Photocrosslinkable hyaluronan-gelatin hydrogels for two-step bioprinting." Tissue engineering Part A **16**: 2675-2685.
- Slotkin, T. A. and F. J. Seidler (2010). "Oxidative stress from diverse developmental neurotoxicants: antioxidants protect against lipid peroxidation without preventing cell loss." Neurotoxicol Teratol **32**(2): 124-131.
- Smeds, K. A., A. M. Pfister-Serres, et al. (2001). "Photocrosslinkable polysaccharides for in situ hydrogel formation." Journal of Biomedical Materials Research **55**: 254-255.
- Sodian, R., S. P. Hoerstrup, et al. (2000). "Early in vivo experience with tissue-engineered trileaflet heart valves." Circulation **102**(19 Suppl 3): III22-29.
- Sodian, R., S. P. Hoerstrup, et al. (2000). "Evaluation of biodegradable, three-dimensional matrices for tissue engineering of heart valves." Asaio J **46**(1): 107-110.
- Sodian, R., M. Loebe, et al. (2002). "Application of stereolithography for scaffold fabrication for tissue engineered heart valves." ASAIO J **48**(1): 12-16.
- Sodian, R., P. Schaefermeier, et al. (2010). "Use of human umbilical cord blood-derived progenitor cells for tissue-engineered heart valves." Ann Thorac Surg **89**(3): 819-828.
- Sodian, R., J. S. Sperling, et al. (1999). "Tissue engineering of a trileaflet heart valve-early in vitro experiences with a combined polymer." Tissue Eng **5**(5): 489-494.
- Sokolovic, D., B. Djordjevic, et al. (2013). "Melatonin protects rat thymus against oxidative stress caused by exposure to microwaves and modulates proliferation/apoptosis of thymocytes." Gen Physiol Biophys **32**(1): 79-90.
- Sproul, A. and E. Simpson (1964). "Stroke Volume and Related Hemodynamic Data in Normal Children." Pediatrics **33**: 912-918.
- Stamm, C., A. Khosravi, et al. (2004). "Biomatrix/polymer composite material for heart valve tissue engineering." Ann Thorac Surg **78**(6): 2084-2092; discussion 2092-2083.
- Stankus, J. J., J. Guan, et al. (2006). "Microintegrating smooth muscle cells into a biodegradable, elastomeric fiber matrix." Biomaterials **27**(5): 735-744.
- Steinboff, G., U. Stock, et al. (2000). "Tissue engineering of pulmonary heart valves on allogenic acellular matrix conduits: in vivo restoration of valve tissue." Circulation **102**(19 Suppl 3): III50-55.
- Stephens, E. H., C. A. Durst, et al. "Mitral valvular interstitial cell responses to substrate stiffness depend on age and anatomic region." Acta Biomater **7**(1): 75-82.
- Stephens, E. H., C. A. Durst, et al. (2011). "Mitral valvular interstitial cell responses to substrate stiffness depend on age and anatomic region." Acta Biomater **7**(1): 75-82.
- Sterodimas, A. and J. de Faria (2013). "Human auricular tissue engineering in an immunocompetent animal model." Aesthetic Surgery Journal **33**: 283-289.
- Stock, U. A., M. Nagashima, et al. (2000). "Tissue-engineered valved conduits in the pulmonary circulation." J Thorac Cardiovasc Surg **119**(4 Pt 1): 732-740.
- Sumikura, H., Y. Nakayama, et al. (2014). "In vitro evaluation of a novel autologous aortic valve (biovalve) with a pulsatile circulation circuit." Artif Organs **38**(4): 282-289.
- Sutherland, F. W., T. E. Perry, et al. (2005). "From stem cells to viable autologous semilunar heart valve." Circulation **111**(21): 2783-2791.
- Sutherland, F. W. H., T. E. Perry, et al. (2005). "From stem cells to viable autologous semilunar heart valve." Circulation **111**: 2783-2791.
- Sutherland, G. R., G. Di Salvo, et al. (2004). "Strain and strain rate imaging: a new clinical approach to quantifying regional myocardial function." J Am Soc Echocardiogr **17**(7): 788-802.

- Swarts, J. D., C. M. Alper, et al. (2013). "Panel 2: Eustachian tube, middle ear, and mastoid-anatomy, physiology, pathophysiology, and pathogenesis " Otolaryngology-Head and Neck Surgery **148**: E26-E36.
- Swindle, M. M., A. Makin, et al. (2012). "Swine as models in biomedical research and toxicology testing." Vet Pathol **49**(2): 344-356.
- Syedain, Z. H., A. R. Bradee, et al. (2013). "Decellularized tissue-engineered heart valve leaflets with recellularization potential." Tissue Eng Part A **19**(5-6): 759-769.
- Syedain, Z. H., L. A. Meier, et al. (2013). "Tubular heart valves from decellularized engineered tissue." Ann Biomed Eng **41**(12): 2645-2654.
- Syedain, Z. H. and R. T. Tranquillo (2009). "Controlled cyclic stretch bioreactor for tissue-engineered heart valves." Biomaterials **30**: 4078-4084.
- Syedain, Z. H. L. M. T. J. S. L. R. P. S. R. G. R. B. R. W. T. R. T. (2011). "Implantation of a Tissue-engineered Heart Valve from Human Fibroblasts Exhibiting Short Term Function in the Sheep Pulmonary Artery." Cardiovascular Engineering and Technology **2**(2): 101-112.
- Takahashi, M., M. Shibata, et al. (2001). "Estimation of lipid peroxidation of live cells using a fluorescent probe, diphenyl-1-pyrenylphosphine." Free Radic Biol Med **31**(2): 164-174.
- Tan, J. Y., C. K. Chua, et al. (2013). "Fabrication of channeled scaffolds with ordered array of micro-pores through microsphere leaching and indirect Rapid Prototyping technique " Biomedical Microdevices **15**: 83-96.
- Tanner, K., N. Sabrine, et al. (2005). "Cardiovascular malformations among preterm infants." Pediatrics **116**(6): e833-838.
- Tarafder, S., V. K. Balla, et al. (2013). "Microwave-sintered 3D printed tricalcium phosphate scaffolds for bone tissue engineering." J Tissue Eng Regen Med **7**(8): 631-641.
- Tayalia, P., C. R. Mendonca, et al. (2008). "3D Cell-Migration Studies using Two-Photon Engineered Polymer Scaffolds." Advanced Materials **20**(23): 4494-4498.
- Taylor, P. A., P. Batten, et al. (2003). "The cardiac valve interstitial cell." International Journal of Biochemistry & Cell Biology **35**: 113-118.
- Taylor, P. M., S. P. Allen, et al. (2000). "Phenotypic and functional characterization of interstitial cells from human heart valves, pericardium and skin." Journal of Heart Valve Disease **9**: 150-158.
- Tedder, M. E., J. Liao, et al. (2009). "Stabilized collagen scaffolds for heart valve tissue engineering." Tissue Eng Part A **15**(6): 1257-1268.
- Tedder, M. E., A. Simionescu, et al. (2010). "Assembly and Testing of Stem Cell-Seeded Layered Collagen Constructs for Heart Valve Tissue Engineering." Tissue Eng Part A.
- Teh, B. M., R. J. Marano, et al. (2013). "Tissue engineering of the tympanic membrane." Tissue Engineering Part B-Reviews **19**: 116-132.
- Thubrikar, M., L. P. Boshier, et al. (1979). "The mechanism of opening of the aortic valve." J Thorac Cardiovasc Surg **77**(6): 863-870.
- Thubrikar, M., S. P. Nolan, et al. (1980). "The cyclic changes and structure of the base of the aortic valve." Am Heart J **99**(2): 217-224.
- Tibbitt, M. W. and K. S. Anseth (2012). "Dynamic microenvironments: The fourth dimension " Science Translational Medicine **4**: 160ps124.
- Tirella, A., F. Vozzi, et al. (2011). "PAM2 (piston assisted microsyringe): a new rapid prototyping technique for biofabrication of cell incorporated scaffolds." Tissue Eng Part C Methods **17**(2): 229-237.
- Torgersen, J., A. Ovsianikov, et al. (2012). "Photo-sensitive hydrogels for three-dimensional laser microfabrication in the presence of whole organisms." Journal of Biomedical Optics **17**: 105008.

- van Engeland, M., L. J. Nieland, et al. (1998). "Annexin V-affinity assay: a review on an apoptosis detection system based on phosphatidylserine exposure." Cytometry **31**(1): 1-9.
- van Geemen, D., A. Driessen-Mol, et al. (2012). "Variation in tissue outcome of ovine and human engineered heart valve constructs: relevance for tissue engineering." Regen Med **7**(1): 59-70.
- Veinot, J. P. (2006). "Pathology of inflammatory native valvular heart disease." Cardiovasc Pathol **15**(5): 243-251.
- Verter, F. (Copyright 2000 - 2010 December 7, 2010). "Parent's Guide to Cord Blood Foundation - With Emphasis on how to Evaluate Bank Services." from <http://parentsguidecordblood.org/content/usa/banklists/index.shtml?navid=14>.
- Vesely, I. (2000). "Aortic root dilation prior to valve opening explained by passive hemodynamics." J Heart Valve Dis **9**(1): 16-20.
- Villanueva, I., N. L. Bishop, et al. (2009). "Medium osmolarity and pericellular matrix development improves chondrocyte survival when photoencapsulated in poly(ethylene glycol) hydrogels at low densities." Tissue Eng Part A **15**(10): 3037-3048.
- Vricella, L. A., J. A. Williams, et al. (2005). "Early experience with valve-sparing aortic root replacement in children." Ann Thorac Surg **80**(5): 1622-1626; discussion 1626-1627.
- Wang, C., S. Yin, et al. (2010). "Differentiation of adipose-derived stem cells into contractile smooth muscle cells induced by transforming growth factor-beta1 and bone morphogenetic protein-4." Tissue Eng Part A **16**(4): 1201-1213.
- Wang, Q., A. J. McGoron, et al. (2010). "A novel small animal model for biocompatibility assessment of polymeric materials for use in prosthetic heart valves." J Biomed Mater Res A **93**(2): 442-453.
- Wang, X., B. Su, et al. (2009). "Impaired balance of mitochondrial fission and fusion in Alzheimer's disease." J Neurosci **29**(28): 9090-9103.
- Wang, X. H., Y. N. Yan, et al. (2006). "Generation of three-dimensional hepatocyte/gelatin structures with rapid prototyping system." Tissue Engineering **12**: 83-90.
- Wang, X. H., Y. N. Yan, et al. (2007). "Rapid prototyping as a tool for manufacturing bioartificial livers." Trends in Biotechnology **25**: 505-513.
- Wathen, C. A., N. Foje, et al. (2013). "In vivo X-ray computed tomographic imaging of soft tissue with native, intravenous, or oral contrast." Sensors (Basel) **13**(6): 6957-6980.
- Weber, B., M. Y. Emmert, et al. (2012). "Prenatally engineered autologous amniotic fluid stem cell-based heart valves in the fetal circulation." Biomaterials **33**: 4031-4043.
- Weber, B., S. M. Zeisberger, et al. (2011). "Prenatally harvested cells for cardiovascular tissue engineering: Fabrication of autologous implants prior to birth." Placenta **32**: S316-S319.
- Weidemann, F., B. Eyskens, et al. (2002). "Quantification of regional left and right ventricular radial and longitudinal function in healthy children using ultrasound-based strain rate and strain imaging." J Am Soc Echocardiogr **15**(1): 20-28.
- Williams, C. G., A. N. Malik, et al. (2005). "Variable cytocompatibility of six cell lines with photoinitiators used for polymerizing hydrogels and cell encapsulation." Biomaterials **26**(11): 1211-1218.
- Wilson, C. E., C. A. van Blitterswijk, et al. (2011). "Scaffolds with a standardized macro-architecture fabricated from several calcium phosphate ceramics using an indirect rapid prototyping technique " Journal of Materials Science-Materials in Medicine **22**: 97-105.
- Wust, S., M. E. Godla, et al. (2014). "Tunable hydrogel composite with two-step processing in combination with innovative hardware upgrade for cell-based three-dimensional bioprinting." Acta Biomater **10**(2): 630-640.

- Wylie, R. G., S. Ahsan, et al. (2011). "Spatially controlled simultaneous patterning of multiple growth factors in three-dimensional hydrogels." Nature Materials **10**: 799-806.
- Xu, C., W. Chai, et al. (2012). "Scaffold-free inkjet printing of three-dimensional zigzag cellular tubes." Biotechnology and Bioengineering: n/a-n/a.
- Xu, C. X., W. X. Chai, et al. (2012). "Scaffold-free inkjet printing of three-dimensional zigzag cellular tubes." Biotechnology and Bioengineering **109**: 3152-3160.
- Xu, T., C. A. Gregory, et al. (2006). "Viability and electrophysiology of neural cell structures generated by the inkjet printing method." Biomaterials **27**: 3580-3588.
- Xue, J. X., B. Feng, et al. (2013). "Engineering ear-shaped cartilage using electrospun fibrous membranes of gelatin/polycaprolactone." Biomaterials **34**: 2624-2631.
- Yacoub, M. H. and J. J. Takkenberg (2005). "Will heart valve tissue engineering change the world?" Nat Clin Pract Cardiovasc Med **2**(2): 60-61.
- Yamanami, M., Y. Yahata, et al. "Preparation of in-vivo tissue-engineered valved conduit with the sinus of Valsalva (type IV biovalve)." J Artif Organs **13**(2): 106-112.
- Yamanami, M., Y. Yahata, et al. (2010). "Preparation of in-vivo tissue-engineered valved conduit with the sinus of Valsalva (type IV biovalve)." J Artif Organs **13**(2): 106-112.
- Ye, X., Q. Zhao, et al. (2009). "Enhancement of mesenchymal stem cell attachment to decellularized porcine aortic valve scaffold by in vitro coating with antibody against CD90: a preliminary study on antibody-modified tissue-engineered heart valve." Tissue Eng Part A **15**(1): 1-11.
- Yeong, W. Y., C. K. Chua, et al. (2004). "Rapid prototyping in tissue engineering: challenges and potential" Trends in Biotechnology **22**: 643-652.
- Yusuf, S., S. Reddy, et al. (2001). "Global burden of cardiovascular diseases - Part I: General considerations, the epidemiologic transition, risk factors, and impact of urbanization." Circulation **104**: 2746-2753.
- Yusuf, S., M. Vaz, et al. (2004). "Tackling the challenge of cardiovascular disease burden in developing countries." Am Heart J **148**(1): 1-4.
- Zeltinger, J., L. K. Landeen, et al. (2001). "Development and characterization of tissue-engineered aortic valves." Tissue Engineering **7**: 9-22.
- Zhang, H., L. Wang, et al. (2011). "Controllable properties and microstructure of hydrogels based on crosslinked poly(ethylene glycol) diacrylates with different molecular weights." Journal of Applied Polymer Science **121**(1): 531-540.
- Zhang, T., Y. N. Yan, et al. (2007). "Three-dimensional gelatin and gelatin/hyaluronan hydrogel structures for traumatic brain injury." Journal of Bioactive and Compatible Polymers **22**: 19-29.
- Zhang, Z., D. Jones, et al. (2013). "Hierarchical tailoring of strut architecture to control permeability of additive manufactured titanium implants." Mater Sci Eng C Mater Biol Appl **33**(7): 4055-4062.
- Zilla, P., J. Brink, et al. (2008). "Prosthetic heart valves: catering for the few." Biomaterials **29**(4): 385-406.
- Zimmermann, W. H., K. Schneiderbanger, et al. (2002). "Tissue engineering of a differentiated cardiac muscle construct." Circulation Research **90**: 223-230.

## APPENDIX A

### BIOPRINTER TEAM

The bioprinter project has been a team effort. It is important to at least briefly describe which parts people worked on and describe some of the contributions to the progress of the 3D valve printing work as a whole. Jonathan Butcher started his laboratory at Cornell University in 2007. The valve bioprinting project was conceived by Dr. Butcher, Dr. Hod Lipson, and Dr. Lawrence Bonassar shortly thereafter. When I first joined the bioprinter team in fall of 2008, I was mentored by the other 3 students who were currently working on the project: Phil Cheung, Nick Colangelo, and Kevin Kang. My role and the team dynamics have changed as I have progressed from a trainee to a team leader responsible for training and mentoring other students. On the bioprinter team I have had privilege of working with 23 talented scientists (Appendix Figure A.1). The list of these scientists follows.

Nicholas Colangelo (2007, 2008, 2009, 2010) – worked on pluronic, UPEA, and PEGDA material biocompatibility cell surface seeding experiments, initial encapsulation testing, SEM imaging, and hydrogel tensile testing.

Phillip Y.C Cheng (2008, 2009) – worked on developing protocols for generating 3D geometries, exploring and identifying 3D printable materials, 3D printing hydrogel valves out of PEGDA, and developing initial heterogeneous dithering code.

Kevin Heeyong Kang (2008, 2009, 2010, 2011) - worked on investigating alginate solubility, optimizing printing techniques for STL printing and vector printing of hydrogel materials, refining protocols and code for better shape and gradient information extraction from medical image files, application of heterogeneous printing of hydrogels, 3D printing hydrogel valves, and testing effects of viscosity and shear on cell viability.

Christopher Caiola (2010) – worked on collagen isolation and investigation into collagen printing.

Dave Filipiak (2009) - worked on development of a prototype design, solidworks modeling, and video simulation for a rotating cassette bioreactor.

Edward Yip (2009) – worked on development of a prototype design for a rotating cassette bioreactor and a clamp holder assembly.

Jagannath Padmanabhan (2009) – worked on screening a GMA-chitosan material for cell encapsulation in hydrogels.

Jhalak Agarwal (2010,2011) – worked on initial light intensity calculations and light meter protocols, testing of photocrosslinking efficiency, and printing optimization.

Kevin Yeh (2009) – worked on programming the heterogeneous dithering code into a format for converting DICOM images into printable material gradients, and assembly of the model 2 Fab@Home™.

Kevin Lamott (2009) – worked on development of a pneumatic bioreactor design in solidworks with a silicone diaphragm driven ventricle and ball valve aortic return.

Bin Duan (2010, 2011, 2012, 2013, 2014) – worked on adapting biocompatible hydrogel materials for 3D printing, 3D printing valve and blood vessel constructs, synthesizing, combining polymers to improve bioactivity of printed constructs, and printed valve conditioning validation studies.. Edi Kapetanovic (2011,2012), Anya Laibangyang (2012, 2013, 2014), Shoshanna Das (2013,2014), and Charlie Xu (2013, 2014) have worked with Duan on these aspects of the project.

Lauren Lee (2011, 2013) – worked on histological staining and parafilm sectioning of hydrogels, compression mechanical testing, and observations of material clogging in direct printing of encapsulated cell studies that motivated different handling protocols of polymer precursors.

Scott Newman (2011, 2012) – worked on Solidworks modeling and prototyping during reiterative testing and modification of the diaphragm driven bioreactor conditioning chamber and TEHV holder assembly.

Patrick Armstrong (2011) – worked on cell photoencapsulation live/dead studies using PAVIC and compression mechanical testing.

Mohammed Cherkaoui (2011) – worked on a mathematical model to describe the bioreactor conditioning chamber and pump system, programming a DAQ board/Simulink control system for the reactor, building a pump and capacitance tank flow loop to drive the conditioning chamber.

Harshal Sawant (2012) – worked on troubleshooting and characterizing the DAQ board program and electronics and flow loop, and biocompatibility screening of commercial SLA materials and glues and components for the fabrication of the conditioning chamber.



**Figure A.1 Bioprinter team 2008-2014.**

(A) 2008 team is pictured left to right LA Hockaday, KH Kang, PYC Cheung, NW Colangelo. (B) 2009 team is pictured left to right D Filipiak, NW Colangelo, LA Hockaday, KH Kang, E Yip, C Caiola was not present for the team picture. (C) 2010 team is pictured left to right LA Hockaday, J Agarwal, K Yeh, JT Butcher principle investigator, K LaMott, B Duan, and KH Kang. J Padmanabhnan was not present for the team picture. (D) 2011 team is pictured. Left to right top row in the picture is the Duan family (Bin, Ellie, Angela), J Agarwal, LA Hockaday, KH Kang. Left to right bottom row in the picture is E Kapetanovic, S Newman, P Armstrong, L Lee, M Cherkaoui. (E) 2013 team is pictured. Left to right top row in the picture is LA Hockaday, A Kaldany, L Lee, C Xu, B Duan. Left to right bottom row is S Das, A Laibangyang, D Cheung, and K Li. A team picture was not taken for 2012 which included Harshal Sawant.

Alain Kaldany (2012, 2013, 2014) – worked on troubleshooting the DAQ board program and electronics, flow loop and pressure characterization, and biocompatibility screening of components in the TEHV holder in the conditioning chamber.

Kang Li (2013, 2014) – worked on converting the bioreactor electronics control setup from a DAQ board assembly to a microcontroller.

Daniel Cheung (2013, 2014) - worked on Solidworks design modifications to the bioreactor chamber, pressure characterization of the conditioning chamber, and printed valve conditioning validation studies.

People on the bioprinter team before I joined the project who should not go unacknowledged include Jamie Brennan (2007) who worked on initial tensile testing of hydrogels, and Johnson Chiu (2007) and Albert Liang (2007) who worked on assembly of the Model 1 Fab@Home™ printers.

## APPENDIX B

### BIOREACTOR PARTS AND ASSEMBLY

#### ***B.1 Summary***

Assembly of the bioreactor heart valve conditioning system 1<sup>st</sup> requires assembly of the water flow loop and assembly of the control system; 2<sup>nd</sup> requires connection of transducers and pump to the control system with the tubes and wires appropriately routed for benchtop or incubator testing; 3<sup>rd</sup> requires assembly and sterilization of the bioreactor conditioning chamber and holder; 4<sup>th</sup> requires installment of a prosthetic, 3D bioprinted, or isolated valve into the holder mesh; 5<sup>th</sup> requires assembly of the bioreactor chamber and filling of the media flow loop with culture media or PBS depending on the needs of the test; 6<sup>th</sup> requires the assembled conditioning chamber is connected to the control system, applied pressure tank assembly, and water flow loop. I recommend assembling the bioreactor conditioning chamber and checking for leaks, then partially disassembling for sterilization, and then reassembling the chamber and installing valve for the actual test. Leaks can be related to defects and bubbles in the silicone sealant bead and rotation of the fitting.

#### ***B.2 Assembly of Bioreactor Pump Driven Water Flow Loop***

Order tanks, tubing, diverting valves, tubing adapters, adapters from VWR, McMaster, and Grainger Silicone sealant can be obtained at the hardware store. (Refer to the parts list, Table B.1) Tools needed for the water flow loop assembly include a drill, a pipe tap, adjustable wrench, Allen wrenches, small pliers, and 3 mm Miltex biopsy punches. Steps 1 to 5 describe the basic steps for building the water flow loop that drives the expansion and contraction of the silicone diaphragm in the base of the bioreactor conditioning chamber.

**Table B.1 Parts in Bioreactor**

<b>Parts in Contact with Cell Culture Media/Bioreactor Interior</b>					
<b>Part</b>	<b>Material</b>	<b>Manufacturer/ Seller</b>	<b>Part Number/ID</b>	<b>Critical Specifications</b>	<b>Sterilization</b>
Cast Conditioning Chamber Parts	Quickparts/ Hapco Steralloy cast chamber parts, Steralloy 2463	Quickparts 3D Systems, Atlanta GA. Hapco	Body_Design 13_no twist_fill port supports	gel time: 20min, hardness Shore: 80D, resin viscosity: 6700cps, Demold time: 6-12 hours or 2-4 hrs at 50°C	H2O2
			Aorta_Design 13_no twist		
			Base_Design 13_supports		
			Holder Universal Bottom_Design 13_no twist		
			Holder Universal Top_Design 13_no twist		
Mesh connecting holder to valve	ePTFE Membrane Laminated to Polypropylene	GE Healthcare Bio-Sciences, Pittsburgh, Pennsylvania. Dx Assay Enabling Technologies	QL230	bonds with tissue glue and suturing; biocompatible with VIC; Pore Size: 5.0um; Air permeability: 5.5-8.0 cfm at 125Pa; Water entry Pressure: >0.7 psi	H2O2

**Table B.1 continued.**

<b>Part</b>	<b>Material</b>	<b>Manufacturer/ Seller</b>	<b>Part Number/ID</b>	<b>Critical Specifications</b>	<b>Sterilization</b>
Ultrasound Port	1/4" Teflon	McMaster-Carr, Cleveland, OH	8545K1	longitudinal speed of sound 1376 m s <sup>-1</sup> compared with 1540 m s <sup>-1</sup> in soft tissue	H2O2
Optical Port	Heat-Resistant Borosilicate Glass disc 1- 1/4" Diameter, 1/4" Thick		8477K71	glass resists clouding and pitting, highly chemical and heat resistant, and low rate of thermal expansion	H2O2 or Autoclave (sealed into chamber port so H2O2 sterilized)
Diaphragm	extreme temperature silicone rubber sheet		3788T42	1mm thick	H2O2 or Autoclave
Shaft collars for holder posts	Stainless Steel		57485K11	corrosion resistance	H2O2 or Autoclave
Holder posts	Stainless Steel		3180T31	17-4 PH Stainless Steel Tight-Tolerance Rod, 2mm Diameter	H2O2 or Autoclave (assembled with holder H2O2 sterilization)
Glue on fittings and holder	Polydimethylsil oxane (PDMS) Sylgard 184 silicone elastomer kit	Dow Corning	3097358-1004	formed at a concentration of 20:1 base to curing agent, degassed, poured applied, and solidified at 70°C overnight	H2O2 or Autoclave

**Table B.1 continued.**

<b>Part</b>	<b>Material</b>	<b>Manufacturer/ Seller</b>	<b>Part Number/ID</b>	<b>Critical Specifications</b>	<b>Sterilization</b>
Barb to hex thread fittings 1/8"	Natural Kynar PVDF	Value Plastics, Fort Collins, CO.	S230-J1A	1/4-28 UNF Thread with 5/16" Hex to 200 Series Barb, 1/8" (3.2 mm) ID Tubing,	H2O2 and Autoclave
	Natural Kynar PVDF		MTLL230-J1A	Male Luer Integral Lock Ring to 200 Series Barb, 1/8" (3.2 mm) ID Tubing, Natural Kynar PVDF	H2O2 and Autoclave
Female luer to hex thread fittings 1/8"	Natural Kynar PVDF		18FTLL-J1A	Female Luer Thread Style with 7/16" Hex to 1/8-27 NPT Thread, Natural Kynar PVDF	H2O2 and Autoclave
Check valves, 1/8"	Polycarbonate w/Silicone Disc		VPS5401068N	420 mL/min flow rate at 1M head, 30 psi back pressure, 1/4 13mmHg cracking pressure	H2O2
Pressure Transducers	Stainless Steel		Dwyer Instruments	628-08-GH-P1-E1-S1	Output: 4-20 mA 2-wire, Range: 0-30 psig, Power Supply: 13-30 VDC, 1/4" NPT male thread
Luer end caps	Plastic	Nordson EFD	7012194	end caps	H2O2
Tubing	Silicone Rubber	McMaster-Carr, Cleveland, OH		High-Temperature Silicone Rubber Tubing, Soft,, Semi-Clear White	Autoclave (H2O2 for short open end lengths)
			5236K83	1/8" ID, 1/4" OD	
			5054K784	9 mm ID, 11 mm OD	
			51135K77	1/4" ID, 3/8" OD	
			51135K35	3/8" ID, 1/2" OD,	
			51135K43	1/2" ID, 3/4" OD,	
			51135K51	3/4" ID, 1" OD	
5236K239	1" ID, 1-1/8" OD				

Table B.1 Continued

Parts for Applied Aortic Pressure and Relief					
Part	Material	Manufacturer /Seller	Part Number/ID	Critical Specifications	Sterilization
CO2/Air tank		Airgas	X02AR95C3000993	Ct 5% Hydrogen Balance Argon Size 300 Certified Standard-spec CGA 350	N/A
CO2/Air tank Regulator	Brass	Airgas	Y12C144A590	Regulator High Purity 2-Stage Low-Flow 3000PSI Brass, 0-10 Del Range, CGA-590	N/A
Pinch Solenoid Valve (DC)		McMaster-Carr, Cleveland, OH	5431T132	Pinch-Style Aluminum Solenoid Valve for Tubing, Normally Closed, for 3/8" Tube OD x 1/4" Tube ID, 24 VDC	N/A
Water Flow Loop and Pump Parts					
Nalgene® Carboys	Low-Density Polyethylene (LDPE)	VWR, Thermo Scientific	16333-080	10 L (2.6 gal.) 83B cap size, handles, serrated tubing outlet is molded in one piece with bottle for strength and leak-resistance. Outlet low on bottle for more complete drainage. Made for 12.7mm (1/2") I.D. tubing	N/A
Brass Push-on Hose Fitting	Brass	McMaster-Carr, Cleveland, OH	91465K91	1/4" Hose ID x 1/4" NPTF Male Pipe	N/A
Female/male pipe adapter (1/4")	Brass		50785K27	Medium-Pressure Brass Threaded Pipe Fitting, 1/4 Female x 1/4 Male Pipe Size, Adapter, NPT	N/A

**Table B.1 continued.**

<b>Part</b>	<b>Material</b>	<b>Manufacturer /Seller</b>	<b>Part Number/ID</b>	<b>Critical Specifications</b>	<b>Sterilization</b>
Diverting ball valve (switch flow between throttle and high flow)	PVC	McMaster-Carr, Cleveland, OH	4757K52	Miniature PVC Ball Valve, 3-Port, NPT Female x Female x Female, 1/4" Pipe Size	N/A
Barb/male pipe adapter for for diverting valve (throttle)	Polyethylene		2808K34	Super-Flow Polyethylene Barbed Tube Fitting, Straight for 1/4" Tube ID x 1/2 Male Pipe Size	H2O2
Diverting ball valve (switch flow between capacitance membrane and base chamber)	PVC		4757K57	Miniature PVC Ball Valve, Diverting, 3-Port, Barb, for 1/4" Tube ID	N/A
Barb/male pipe adapter 1/4"	Polyethylene		2808K27	Super-Flow Polyethylene Barbed Tube Fitting, Straight for 1/4" Tube ID x 1/4 Male Pipe Size	
Button head socket cap screws			98164A434 (but should up grade to a harder grade)	Type 316 Stainless Steel Button-Head Socket Cap Screw 4-40 Thread, 3/4" Long	
Hex nuts	Stainless Steel		91841A005	18-8 Stainless Steel Machine Screw Hex Nut 4-40 Thread Size, 1/4" Width, 3/32" Height	

Table B.1 continued

Part	Material	Manufacturer /Seller	Part Number/ID	Critical Specifications	Sterilization
Tee (connecting tank 1/2", pump 1/2", shunt lines 1/4")	Stainless Steel	McMaster-Carr, Cleveland, OH	5670K37	Type 303 Stainless Steel Barbed Tube Fitting, Reducing Tee for 1/2" x 1/4" Tube ID	
Elbow connector	Nylon		5463K594	Durable Nylon Tight-Seal Barbed Tube Fitting, 90 Degree Elbow for 1/4" Tube ID	
Flat washer	Stainless Steel		92141A005	18-8 Stainless Steel General Purpose Flat Washer, Number 4 Screw Size, 5/16" OD, .02"-.04" Thick	
Tooth washer	Stainless Steel		91757A101	18-8 Stainless STL Internal-Tooth Lock Washer NO. 4 Screw Size, .27" OD, .01"-.02" Thick	
Flange ring	ABS-Natural, Manufactured Plastic Prototypes	Quickparts 3D Systems, Atlanta GA. Hapco	Base Ring_Design 13_24 bolts	Tensile strength 6,500 psi, flexure strength 10,600psi, flexure modulus 331,000psi, heat deflection temperature 190 °F, Vical softening point 210 °F	
Biopsy punch		Integra Miltex/VWR		3 mm	
Water Diaphragm Pump		Flojet Instruments/G rainger	FLOJET Pump Model: 4300-501/Grainger Item # 4YD41	115 Volts AC 50/60Hz, 1.5 Amps, Flow 14.4 LPM, 45 PSI Max	

**Table B.1 continued.**

<b>Part</b>	<b>Material</b>	<b>Manufacturer /Seller</b>	<b>Part Number/ID</b>	<b>Critical Specifications</b>	<b>Sterilization</b>
3-way solenoid		Parker Hannifin Corporation/Mcmaster Carr	Parker:71295SN2ENJ1 NOC111P3/Mcmaster: 7889K28	Directional Control 3-Port Stainless Steel Solenoid Valve, Buna-N Seal, Normally Closed, 1/4 NPT Female port, 25 PSI, 120 VAC, valves have wire leads, and draw a max. of 0.42 amps	N/A

### **B.2.1 Step 1 Drill and tap Nalgene tank walls and caps for adapters, and tap outlets for the capacitance membrane base.**

This is to setup the high pressure water source tank and the low pressure water sink tank. The tanks have one barbed tubing outlet low on the bottle already – this is for the tubing to pump connection. Additional outlets on the tank walls (2 per tank) that are drilled and then threaded with a pipe tap are for the sink and source tubes. The holes should be cut low on the tank walls to install an adapter for ¼” tubing and ½” tubing for each tank for a high flow and a throttled flow tube. These holes should be level with each other. The caps should be drilled in the center for ¼” adapters and this is to attach the pressure transducers.

The capacitance membrane chamber is built using the same cast part as the conditioning chamber base. Tap/thread the two outlets so that 1/2” male pipe/barb adapters can be installed.

### **B.2.2 Step 2 Seal adapters with silicone sealant to tanks, pressure transducers, and capacitance membrane chamber.**

**Day 1** - Apply a bead of silicon sealant on the threads of the pressure transducer male thread connection and screw into the female threads of the male/female pipe adapter intended for the tank cap connection. Wrap around Teflon pipe tape around the joint. Allow to cure at least overnight.

For each wall flow outlet apply a bead of silicone sealant to a large nylon washer and apply a bead of silicone sealant to the male threads of the male/barb adapter. Screw the adapter into the appropriate tapped/threaded hole in the wall of the Nalgene tank through the washer. If needed apply more silicone sealant (Note: The washer reinforces the wall/adapter joint. Without the washer the wall is not thick enough for a good

mechanical hold. Consequently any connecting/reconnecting/tension on the tubing can loosen the adapter and lead to leaking around the fitting). Allow adapters to cure at least overnight.

Manual switch valves will be installed for each flow outlet of the tank. This enables us to open and close off flow for each outlet of the tank if the system needs to be moved, disassembled, or emptied. It will add resistance to the flow loop. For each switch valve (1/2" between tank and pump, 1/4" between the throttle diverting valve and the solenoid sink and source connections), seal in a barbed adapter on both ends. Apply a bead of silicone sealant to the threads of the male end of the adapter, screw into the female threads of the valve switch (this may require the wrench), and wrap the joints with Teflon tape.

For a throttle/high flow assembly seal in 3 barbed adapters into a manual 3-way diverting valve. For the adapters all three have 1/2" male threaded connections pipe connections, and then one has a barb are is for 1/2"ID tubing and two have barbs for 1/4" ID tubing.

A three way solenoid valve switches the connection between flow from the source tank and to the sink tank. The solenoid has female 1/4" pipe thread connection ports so male pipe/barb tubing adapters need to be sealed in to the assembly to connect it to the flow loop. Apply a bead of silicone sealant to the threads of the male end of the adapter, screw into the female threads of the valve switch (this may require the wrench), and wrap the joints with Teflon tape.

Seal adapters into the capacitance membrane chamber base ports. Apply silicone sealant on the threads of the 1/2" male pipe/barb adapters and screw in to the base

ports (may need the wrench but keep in mind that forcing the tap or angling it wrong can snap the port). Wrap with Teflon tape and allow curing overnight.

**Day 2** - For each tank cap apply a bead of silicone sealant to a large nylon washer and apply a bead of silicone sealant to the male threads of the male/female adapter and pressure transducer assembly. Screw the male adapter into the tapped/threaded hole in the wall of the Nalgene tank through the washer. If needed apply more silicone sealant. Allow to cure for 24 hours.

### **B.2.3 Step 3 Assemble capacitance membrane chamber.**

Cut a disc out of the silicone rubber sheet (1 mm thick) matching the diameter of the flange of the cast base part. Flip the base part upside down and place on top of silicone rubber sheet disk. Align the edges. Using the 3 mm diameter biopsy punch, form holes neat holes in the silicone matching with the 24 bolt holes in the flange. Sandwich the silicone between the base flange and the ABS-like base ring part, line up the holes, and then tighten with bolts. For each bolt hole the bolt should insert through a flat washer, through the base ring flange, through the silicone diaphragm, through the base part flange, thread into a hex nut, then a toothed washer, and a second hex nut. Tighten the nut and bolt using a pair of pliers and an Allen wrench. Need strong bolt and nut material to keep from stripping the caps of the bolts.

### **B.2.4 Step 4: Assemble the water flow loop.**

Cut silicone rubber tubing tubing to connect the components of the flow loop together (Refer to Table B.2 for suggested tubing lengths). Cut the tubing so that the system is symmetric. Attach the tubing to the barb ends of the adapters. Changing the lengths of the tubing may change the resistance in the flow loop which could change which may

affect the stroke volume and flow rate (so the characterization should be checked for the different setups). Tighten zipties on the tubing and the 1/2" barb adapters.

### **B.2.5 Build electronics control setup.**

A list of the Bioreactor electronics and signal processing parts is provided in Table B.3. During the development of the bioreactor system and in initial characterization studies, we used two DAQ boards and Simulink/Matlab program (See Cherkaoui Masters of Engineering Project Report 2012 and Sawant Masters of Engineering Project Report 2013) in combination with a timer relay for the control of the electronics and data acquisition. We found that the DAQ boards were very sensitive to electromagnetic interference from the solenoids and the system was vulnerable to timeout errors. We believe this was associated with working in conjunction with a non-dedicated computer. The electronics control setup was converted to a microcontroller. The microcontroller was designed using an ATmega1284P chip on the prototype board which is used in the Cornell ECE 4760 class and programmed with C (See Li Masters of Engineering Project Report). The microcontroller was custom fabricated at Cornell at Bruce Land's laboratory in the ECE department. Four industrial pressure transducers (Dwyer Instruments, IN, ordered from Zoro tools) are each connected to a resistor and the voltage signal is read by the microcontroller and converted to a pressure measurement. The microcontroller reads the signals sent from the pressure transducers using built-in Analog-Digital-Convertor and sends out the control signal for the pump and the pinch solenoid valve through the junction box. The junction box energizes the circuit by using a relay switch. The microcontroller allows for a more compact system that only needs to be connected to a computer to take a data sample. The interface for setting the pressure and pump and pump conditions is written in Matlab. The user is prompted to change the Pdiff setting, the delta setting, the aortic pressure threshold, and the data

**Table B.2 Tubing Cheat Sheet for Water Flow Loop**

<b>Connection</b>	<b>Tubing Size</b>	<b>Tubing Length</b>
High tank to switch valve adapter barb	1/2"	40cm
Switch valve to tee		
Tee to pump barb	1/2"	10cm
Switch valve to pump barb, Inlet	1/2"	10cm
Low tank to switch valve adapter barb	1/2"	40cm
Switch valve to tee	1/2"	10cm
Tee to pump barb	1/2"	10cm
Switch valve to pump barb, Outlet	1/2"	10cm
Reducing tee to shunt elbow	1/4"	15cm
Shunt	1/4"	46 cm
<b>Single Flow Setting Setup</b>		
High tank to switch valve adapter for source line	1/4"	60 cm
Low tank to switch valve adapter for sink line	1/4"	60 cm
Source line from switch valve to 3-way solenoid	1/4"	60cm
Sink line from switch valve to 3-way solenoid	1/4"	60cm
<b>Throttle/Highflow Setup</b>		
Throttle line high tank to 3-way diverting valve	1/4"	60 cm
High flow line high tank to 3-way diverting valve	1/2"	60 cm
Source line from diverting valve to 3-way solenoid	1/4"	60cm
Throttle line low tank to 3-way diverting valve	1/4"	60cm
High flow line low tank to 3-way diverting valve	1/2"	60cm
Sink line from diverting valve to 3-way solenoid	1/4"	60cm
<b>Single Conditioning Chamber setup</b>		
3-way solenoid to 1/4" tee	1/4"	~80cm (initial bench testing), ~275 cm to route into the incubator
tee to three way diverting valve (two)	1/4"	15 cm
diverting valve to capacitance membrane (two)	1/4"	45cm
diverting valve to chamber base (two)	1/4"	45 cm

**Table B.3 Bioreactor Electronics and Signal Processing Parts Not in Contact with Media or Water**

<b>Microcontroller</b>			
<b>Part</b>	<b>Manufacturer/Seller</b>	<b>Part Number/ID</b>	<b>Critical Specifications</b>
ATmega 1284P chip	Bruce Land Laboratory		
Prototype Board			
330 Ohm protective resistor			
USB cable			
<b>Junction Box</b>			
Wall switch	Grainger	6X063	LEVITON Wall Switch, 1-Pole, Toggle, Brown
Receptacle		6A702	LEVITON Receptacle, 20A, 125V, 5-20R, 2P, 3W, 1PH
Box		6XC61	RACO Box, Plastic 2 Gang
Wall plate		1LXT1	HUBBELL WIRING DEVICE- KELLEMS Wall Plate, 2Gang, Nylon, Ivory
Solid State Relay		6C900	OMRON Relay, Solid State
Extension cord		5XFP9	NO BRAND NAME ASSIGNED Extension Cord, 6ft, 16/3, 13A, SJT, Black
<b>Connector Wires and Timer Relay</b>			
250 Ohm reciever load resistance	Digikey	WHA250FECT-ND	RES 250 OHM 1/2W 1% AXIAL
3M Breadboard	Digikey		
Powersupply for transducers	Radioshack/Enercell		AC/DC Adapter 13-30V DC, 1A
Plug-in Timer Relay Repeat Cycle	McMaster Carr/Macromatic	7630K12	Plug-in Timer Relay, Repeat Cycle, 120V AC/DC Control, .1 to 10 Seconds
Relay Socket	McMaster Carr	7122K11	8-Pin Circular, 2.6" High x 1.5" Wide x 1.1" Deep
Inline fuse to protect pump	Radioshack		Inline fuse 2A 250A

**Table B.3 continued**

<b>Part</b>	<b>Manufacturer/Seller</b>	<b>Part Number/ID</b>	<b>Critical Specifications</b>
Power supply for pinch valve	Digikey	2 Power Supply AC/DC (LED Drivers), disconnected HighLED printing driver to use on heart valve bioreactor but need to rebuild LED circuit and 2nd electronics setup	
Terminal block for easier connections in incubator (pinch solenoid)	7527K44		300 VAC/VDC Terminal Block 3 Circuits, 3/8" Center-to-Center, 20 Amps
cover for terminal block	7527K827		Cover for 3/8" Center-to-Center, 3 Circuit 300 VAC/VDC Terminal Block
cover for terminal block	7527K828		Cover for 3/8" Center-to-Center, 4 Circuit 300 VAC/VDC Terminal Block
Terminal block for easier connections in incubator (transducers)	7527K44		300 VAC/VDC Terminal Block 4 Circuits, 3/8" Center-to-Center, 20 Amps
Easy connect male wires	7548K462		Terminals Connected to Wire Male Quick-Disconnect on One End, 24" L, 14 AWG, Black
Easy connect female wires	7548K362		Terminals Connected to Wire Fem Quick-Disconnect on One End, 24" L, 14 AWG, Black
Connector for pinch solenoid valve	4985K15		Solenoid Valve Connector DIN Type A Fem Plug, 2 Pole, 250V AC/DC, 1/2" NPT Thrd

**Table B.3 continued.**

<b>Part</b>	<b>Manufacturer/Seller</b>	<b>Part Number/ID</b>	<b>Critical Specifications</b>
Shielded cables to route into incubator	6452T26		Cable-Tray-Rated Control Cable Shielded, Includes Three 14-Gauge Wires, 10 ft. Length
Shielded cables to route into incubator	6452T27		Cable-Tray-Rated Control Cable Shielded, Includes Four 14-Gauge Wires, 10 ft. Length

acquisition time. After the data acquisition period the system runs automatically at the set parameters. Up to 2 weeks of data can be logged in one acquisition period.

Wire the electronics according to the diagram in Figure B.1 for a single conditioning chamber with an aortic feedback control setup and according to the diagram in Figure 7.22 for a parallel conditioning chamber with an aortic feedback control setup. The parallel setup shown in 7.22 assumes that the valves and therefore the conditions in each chamber will be similar because only one aortic and ventricle transducer is shown. It would be better for quantification for each chamber to have a set of aortic and ventricular transducers. Wire the electronics according to the diagram in Figure B.2 for a single conditioning chamber with a time delay repeat cycle relay setup used to control the pulse of the switching of the 3-way solenoid valve and the opening/closing of the pinch valve.

### ***B.3 Partial assembly of bioreactor conditioning chamber and holder assembly and sterilization of media flow loop parts.***

#### **B.3.1 Step 1 Drill and tap the cast conditioning chamber base part outlets, aortic part outlet, body part outlets, and media reservoir.**

Tap and thread the cast conditioning chamber base part. Tap/thread the two outlets so that 1/2" male pipe/barb adapters can be installed.

Tap and thread the cast conditioning chamber body part. Tap/thread the 3 outlets on the 'ventricle' wall so that 1/8" thread/luer adapters can be installed. Tap/thread the single outlet on the side wall of the body part so that 1/8" thread/luer adapters can be installed.

Tap and thread the cast conditioning chamber aorta part. Tap/thread the single outlet so that 1/4" male pipe/barb adapter can be installed.

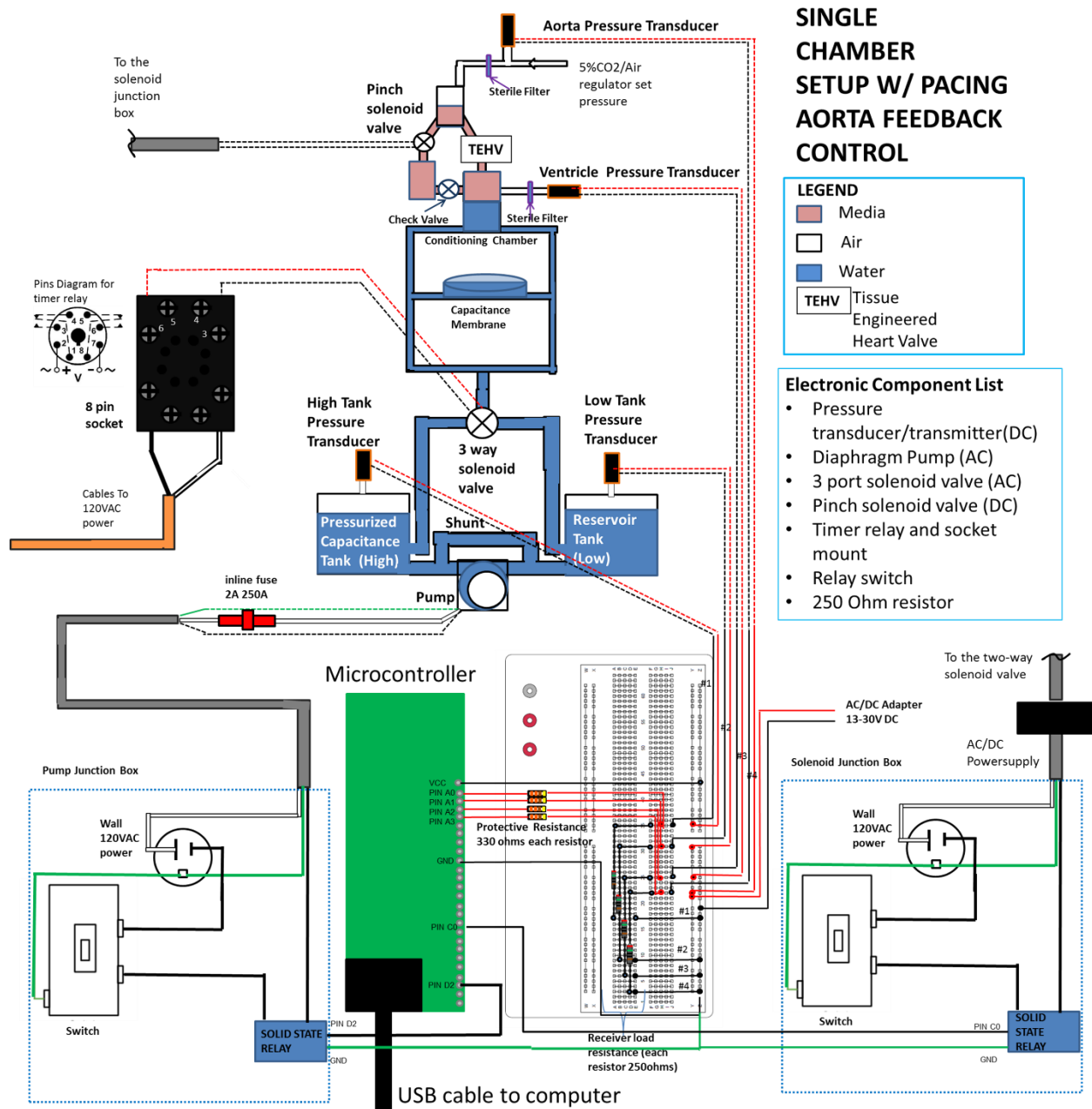


**Figure B.1 Bioreactor electronics setup for pressure feedback control of diastolic loading.**

In this control strategy, a value can be set in the microcontroller so that the pinch valve solenoid opens when pressure in the aortic chamber passes a user defined pressure threshold. This allows for pressure feedback control of diastolic loading of the TEHV. The pump is controlled by the microcontroller and the ventricular pulse from the 3-way solenoid is controlled by the timer relay.

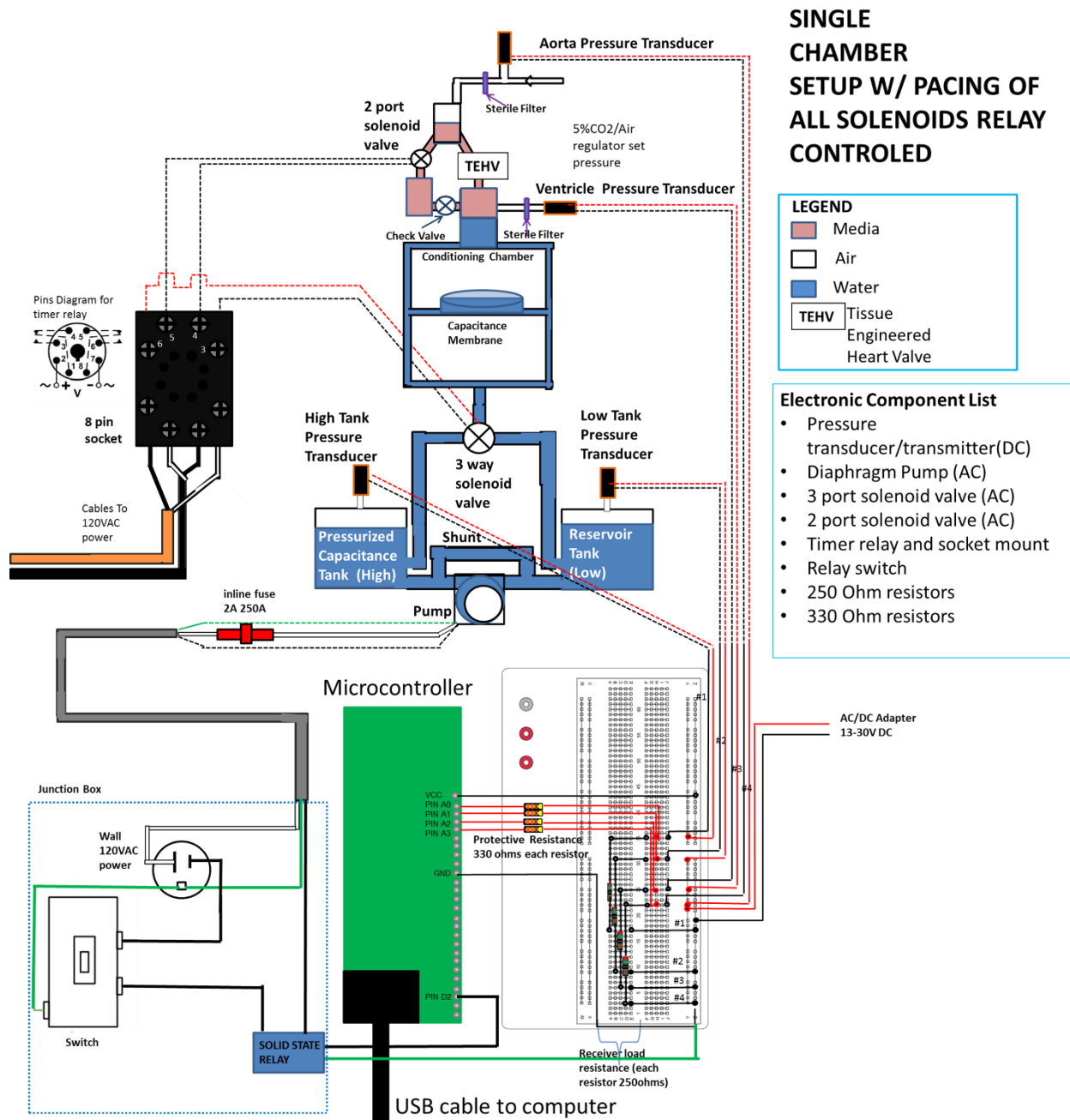


**Figure B.2 Electronics setup for bioreactor system control: pressure independent control of diastolic loading.**

A time delay repeat cycle relay is used to control the pulse of the switching of the 3-way solenoid valve and the opening/closing of the pinch valve. The microcontroller signals the pump to move water from the 'low' tank to pressurize a 'high' tank based on signals from the pressure transducers. The timer relay is connected so that power or the energize signal alternates between the 3-way solenoid and the 2-way solenoid. The pinch valve solenoid which vents pressure after the aorta vents with each beat in this setup. The consequence of this is the frequency of the delivered ventricular pulse and diastolic loading is independent of any pressures in the system.

Tap media reservoir container so that 1/4" male pipe/barb adapters, and 1/8" luer to hex thread fittings can be installed.

Cut out and sand down a Teflon disk for the ultrasound port. Make sure it fits tightly into the side inset port.

### **B.3.2 Step 2 Seal adapters into ports of bioreactor chamber and reservoir parts.**

**Day 1** - Apply PDMS on the threads of 1/4" male pipe/barb adapters and screw in to the base ports (may need the wrench but keep in mind that forcing the tap or angling it wrong can snap the port). Allow curing overnight in the oven (60C) and then wrap with Teflon tape.

Seal the 1/8"hex thread adapters into the body ports. (This may require the wrench but keep in mind that forcing or or angling it wrong can snap the port). Fittings were clamped for additional mechanical hold as per Figure B.3. PDMS is applied to the threads, the threads and fitting are screwed in to the port, additional PDMS is applied around the fitting, a short length of silicone tubing is slid over the hex and the protruding port of the cast part. The silicone rubber is Zip-tied (clamped tightly) over the cast port and over the hex part of the fitting. This is to keep fitting from rotating with vibration due to the cyclic pulse through the system. Allow curing overnight in the oven (60C) and then wrap with Teflon tape.

Apply PDMS on the threads of a 1/4" male pipe/barb adapters and screw in to the aorta part outlet ports. Allow curing overnight in the oven (60C) and then wrap with Teflon tape.



**Figure B.3 Fittings were clamped for additional mechanical hold in addition to PDMS sealing of luer fittings.**

PDMS is applied to the threads, the threads and fitting are screwed in to the port,, additional PDMS is applied around the fitting, a short length of silicone tubing is slid over the hex and the protruding port of the cast part. The silicone rubber is Zip-tied (clamped tightly) over the cast port and over the hex part of the fitting. This is to keep fitting from rotating with vibration due to the cyclic pulse through the system

Apply PDMS in a bead in the inset/shelf of the ultrasound port on the body of the bioreactor and in the inset/shelf of the optical port on the aorta part. Insert the Teflon disk in the side view port and the glass disk in the top view port. Allow curing overnight in the oven (60C).

Apply PDMS on the threads of 1/8", 1/4" male pipe/barb adapters and screw in to the reservoir parts. Allow curing overnight in the oven (60C) and then wrap with Teflon tape. Using silicone rubber tubing pieces, telescope and size the holders to match the size of the valve. Cut two pieces of Teflon mesh to fit into top and bottom holder assembly. For the mesh at the maximum diameter apply PDMS on the edges of Teflon mesh and around the cylindrical protrusion of the holder part then clamp the mesh into place using a rubber band cut from the silicone rubber tubing. Apply additional PDMS to seal it into place. Allow curing overnight in the oven (60C).

**Day 2** - Cut 3 posts for the holder using a hack saw and then wash and rinse vigorously. Apply PDMS to the post peg-holes in the bottom holder part, and insert posts. Allow curing overnight in the oven (60C).

### **B.3.3 Step 3 Assemble conditioning chamber base.**

Cut a disc out of the silicone rubber sheet (1mm thick) matching the diameter of the flange of the cast base part. Flip the base part upside down and place on top of silicone rubber sheet disk. Align the edges. Using the 3 mm diameter biopsy punch, form holes neat holes in the silicone matching with the 24 bolt holes in the flange. Cut a gasket ring for the aortic/body flanges. Flip the body part upside down and place on top of silicone rubber sheet. Align the edges. Using the 3 mm diameter biopsy punch, form neat holes in the silicone matching with the bolt holes in the flanges.

Wash and rinse all the chamber parts. Assemble the base prior to sterilization. Sandwich the silicone between the base flange and the body chamber part, line up the holes, and then tighten with bolts. For each bolt hole the bolt should insert through a flat washer, through the body flange, through the silicone diaphragm, through the base part flange, thread into a hex nut, then a toothed washer, and a second hex nut. Tighten the nut and bolt using a pair of pliers and an Allen wrench. Need strong bolt and nut material to keep from stripping the caps of the bolts.

#### **B.3.4 Step 4 - Sterilization of bioreactor conditioning chamber, reservoir, and tubing.**

Cast parts must be sterilized using hydrogen peroxide sterilization at the Vet school instead of an autoclave.  $H_2O_2$  does not have the same penetration as ethylene oxide, and the parts need to be prepared for sterilization with short distances in mind. Also the parts must be completely dry for the sterilization. After washing and rinsing parts thoroughly, use pressurized air to dry and then put in the oven to dry all the way before packaging the parts up in Tyvek sleeves for sterilization. The check valves and cap ends are sterilized with  $H_2O_2$  loose in a sleeve.

Autoclave the tubing and adapter parts (when not sealed into the chamber parts). Also autoclave pliers, Allen wrenches, tweezers, spatulas, and gloves for assembly.

For the pressure transducers, sterilize before connecting into the sterile flow loop setup. The tubing is removed from each transducer (and autoclaved). The transducer is sprayed with 70% ethanol and then swabbed down. The transducer is oriented in the biosafety cabinet with the tubing adapter pointed up. The transducer is then exposed to the germicidal UV light for a least 1 hour.

#### ***B.4 Installment of a valve into the holder mesh and media flow loop and chamber assembly.***

All the sterilized tubing and check valves and reservoir connections are attached before handling the valve.

Chapter 7 and Figure 7.9 describe the loading of the valves into the chamber assembly. Working in the biosafety cabinet a prosthetic, 3D bioprinted, or an isolated valve can be loaded into the holder mesh. The chamber is then partially filled with media. The aortic part is then bolted into place (with the silicone rubber gasket in place). The bioreactor chamber and media flow loop is filled with culture media or PBS depending on the needs of the test. Connect the sterilized pressure transducers to the reactor in the hood.

#### ***B.5 Transfer the conditioning chamber setup to the large incubator and connect to electronics and applied aortic pressure line.***

The incubator needs to be scrubbed down with Alconox, sprayed down with 70% ethanol, and allowed to dry the day before the test. The week of and the morning of the experiment, turn on the incubator to make sure that it reaches and holds at temperature (37C). Once the valve is loaded and the conditioning chamber is fully assembled the system can be moved to the incubator. Note the only opening should be through a sterile filter leading to the aortic pressure inlet connection, and a sterile filter at the end of the pinch valve line for the vent. Connect the pressure transducers to the terminal blocks in the incubator connected to the microcontroller, connect the applied pressure tank assembly to the aorta of the conditioning chamber, and insert the vent tubing into pinch valve, and connect the water flow loop to the base of the reactor. Note: Running into the incubator through a side port are 4 lines – the aortic pressure line, the transducer line, the sink/source line of the water flow loop, and the pinch solenoid line.

Once the reactor is connected, initialize the microcontroller. Observe the valve and check the system for leaks. Open the valve on the applied aortic pressure. Check for leaks. Close the incubator door and then open the valve to the CO<sub>2</sub> on the incubator tanks.

## APPENDIX C

### HIGH POWER LED ARRAY AND HEAT SINK ASSEMBLY

The high powered LED array was built to enable higher intensity exposure during extrusion printing. The first version rapidly over heated (Figure C.1), and as a result I built a water cooled heat sink (Figure C.2) to keep the LEDs cool. The heat sink was built to fit on the syringe carriage with the high powered LED array. Copper tubing was soldered to a copper plate and liquid heat sinking compound was layered together (Figure C.3). High powered LED array intensities were estimated for different resistances (Figure C.4).

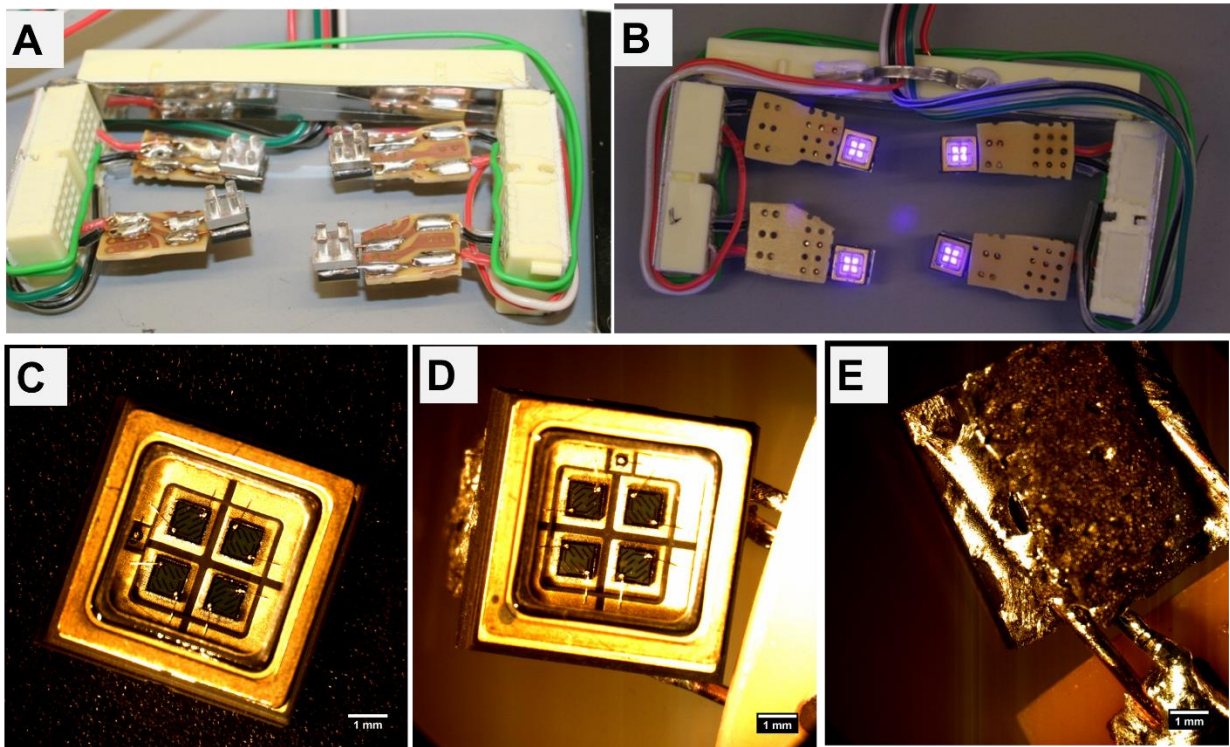


**Figure C.1** First version of high powered LED array was built with small heat sinks and rapidly overheated.

(A) Small gauge wires soldered to a PCB board, and anchored in a bread board. (B) After 1-2 minutes the LEDs run at 70% current the LEDs will begin to melt loose from their solder connections (C) LED before soldering. (D and E) Solder has shifted on the wires when the LED heats up.

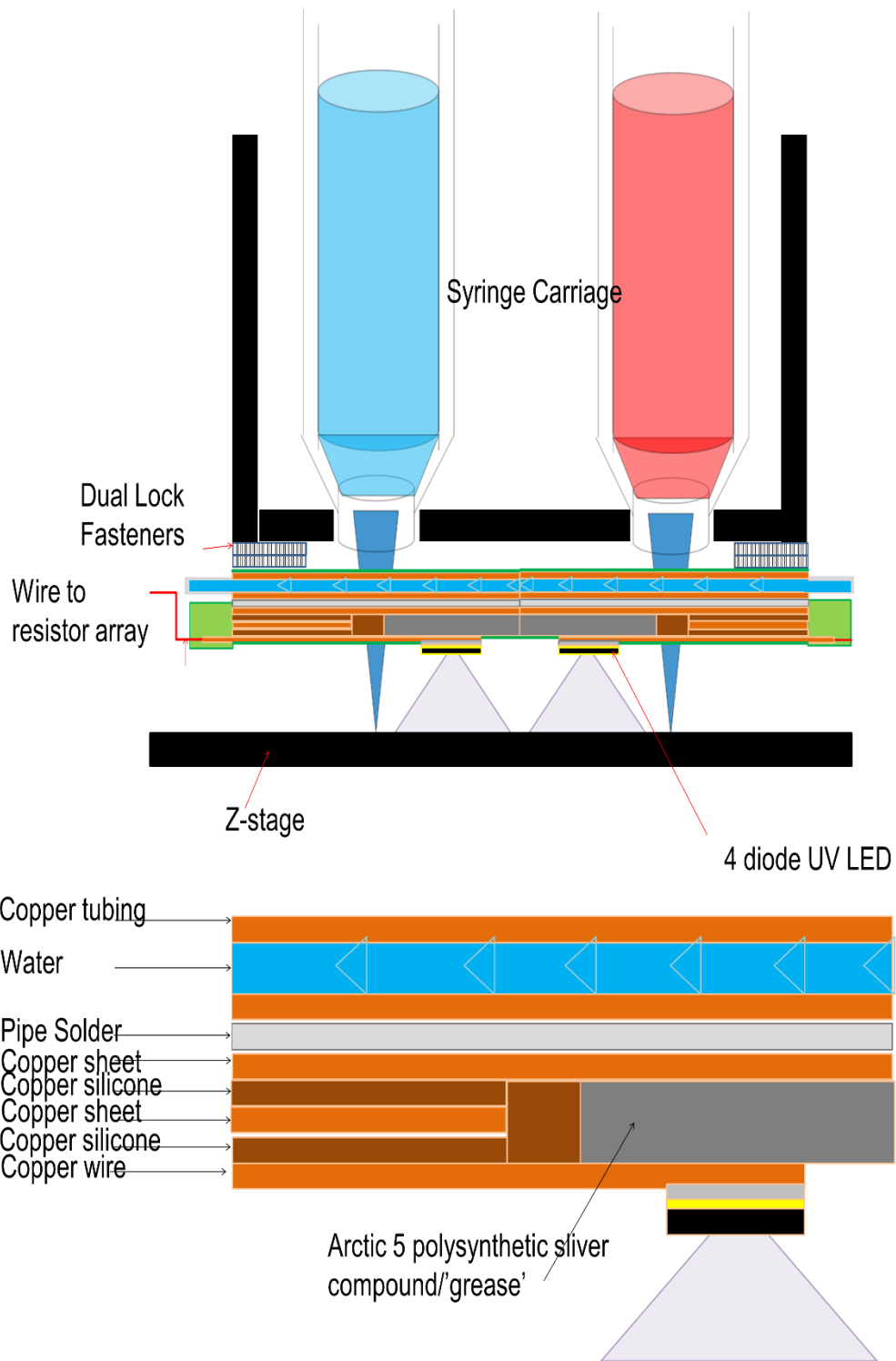


**Figure C.2 High powered LED schematic.**

**(A)** LED array mounts on the syringe carriage with 3M dual lock fasteners. **(B)** Cross section diagram of the heat sink array assembly.

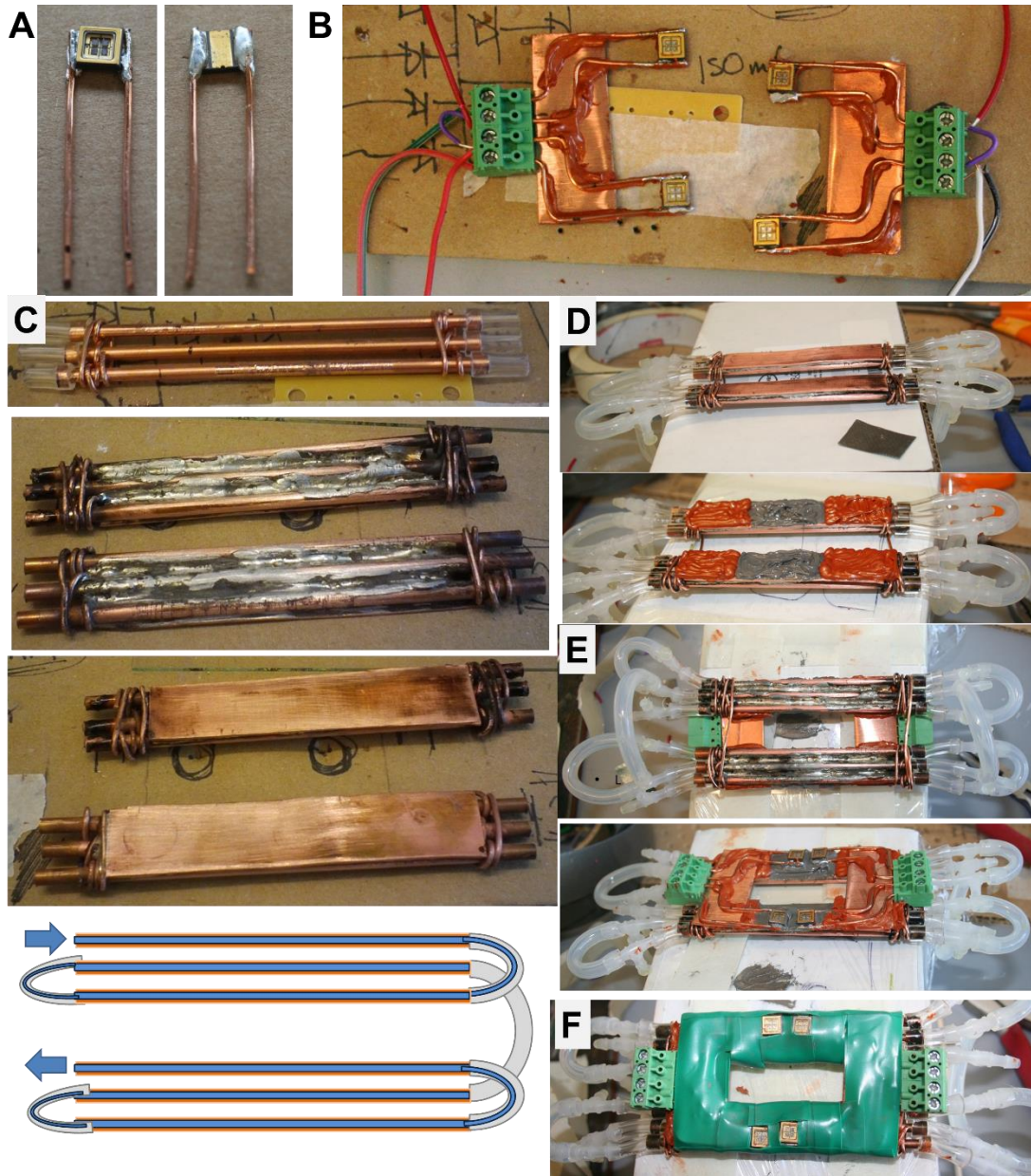
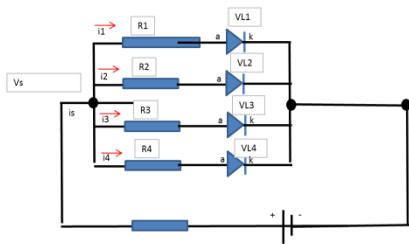
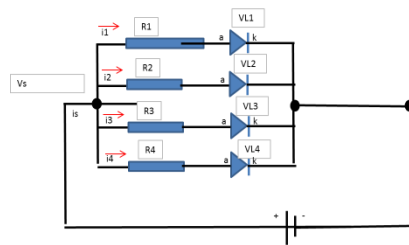


**Figure C.3 Water cooling loop and copper heat sink.**

**(A)** Solder large copper wires (to maximize heat sinking by wires) to LEDs **(B)** Route wires so can be held in pin connectors **(C)** Copper tubing align using copper wire and silicone tubing. Remove silicone tubing and use pipe solder to fill gaps between copper tubing and heat sink plate. **(D)** Attach silicone tubing and tees to route water through copper tubing lay a bead of copper filled (Ultra copper) silicone sealant and a bead of arctic silver thermal compound on heatsink plate side. **(E)** Press the wire/copper plate/LED circuit into the sealant/thermal compound (tape down to hold in contact overnight for curing). **(F)** Wrap/encase in electrical tape so the live wires will not be exposed power supply is a 2 Amp LED Driver and parallel resistor.

Nichia UV LED NC4U133A				Forward Current vs Relative Radiant Flux	
Lot# = BAI054-UaP9d31a				Forward Current [mA]	Relative Radiant Flux
Specs	Min	Max		500	1
Peak Wavelength	360	370[nm]		1000	2
Radiant Flux	1240	1370[mW]	$y=mx+b$		
Forward Voltage	14.1	15.7[V]	$m$		0.002
Maximum Forward Current		700[mA]	$b$		0



$V_s$	$R_1=R_2=R_3=R_4$	$R_{LEDs}$	$R_{lim}$	$R_{total}$	$I_s=(V_s-V_{LED})/R_{total}$	$i_1=i_2=i_3=i_4$	Radiant Flux at LED ( $P_s$ )	Distance from LED	$P_{d,r}$	Each LED Resistor Power Dissipated	Voltage across Resistor	Limiting Resistor Power Dissipated
[V]	[Ohms]	[Ohm]	[Ohm]	[Ohm]	[mA]	[mA]	[mW]	[cm]	[mW/cm <sup>2</sup> ]	[W]	[V]	[W]
30	50	13	5	18	857	214	531	1	42	2	4	4
25	10	3	3	6	1818	455	1127	1	90	2	5	10
36	60	15	0	15	1400	350	868	1	69	7	0	0
36	100	25	0	25	840	210	521	1	41	4	0	0

Figure C.4 High powered LED array intensity calculation estimates for different resistances.

## APPENDIX D

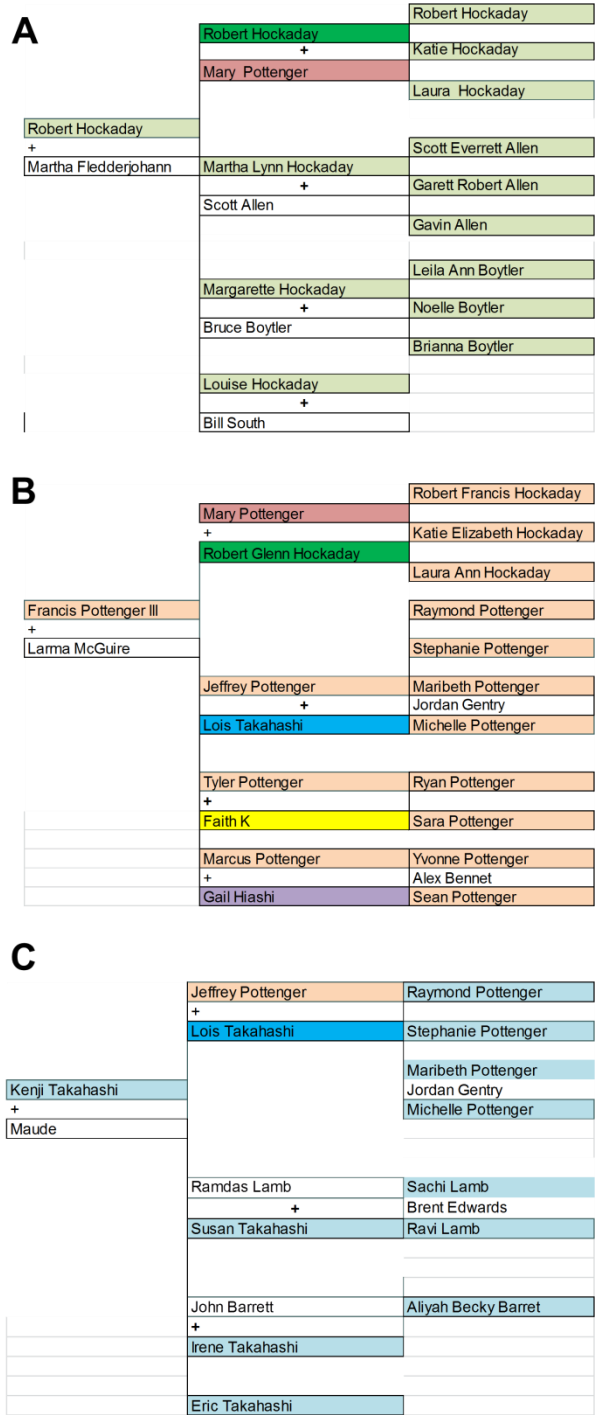


**Figure D.1. Family Tree Cheat Sheet for (A) Hockaday (B) Pottenger, and (C)Takahashi..**